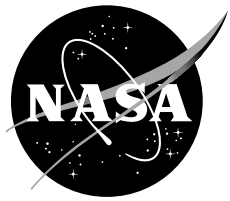


NASA/TM-1999-208764



Cone-Probe Rake Design and Calibration for Supersonic Wind Tunnel Models

Mark J. Won

The NASA STI Program Office . . . in Profile

Since its founding, NASA has been dedicated to the advancement of aeronautics and space science. The NASA Scientific and Technical Information (STI) Program Office plays a key part in helping NASA maintain this important role.

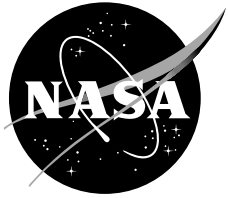
The NASA STI Program Office is operated by Langley Research Center, the Lead Center for NASA's scientific and technical information. The NASA STI Program Office provides access to the NASA STI Database, the largest collection of aeronautical and space science STI in the world. The Program Office is also NASA's institutional mechanism for disseminating the results of its research and development activities. These results are published by NASA in the NASA STI Report Series, which includes the following report types:

- **TECHNICAL PUBLICATION.** Reports of completed research or a major significant phase of research that present the results of NASA programs and include extensive data or theoretical analysis. Includes compilations of significant scientific and technical data and information deemed to be of continuing reference value. NASA's counterpart of peer-reviewed formal professional papers but has less stringent limitations on manuscript length and extent of graphic presentations.
- **TECHNICAL MEMORANDUM.** Scientific and technical findings that are preliminary or of specialized interest, e.g., quick release reports, working papers, and bibliographies that contain minimal annotation. Does not contain extensive analysis.
- **CONTRACTOR REPORT.** Scientific and technical findings by NASA-sponsored contractors and grantees.
- **CONFERENCE PUBLICATION.** Collected papers from scientific and technical conferences, symposia, seminars, or other meetings sponsored or cosponsored by NASA.
- **SPECIAL PUBLICATION.** Scientific, technical, or historical information from NASA programs, projects, and missions, often concerned with subjects having substantial public interest.
- **TECHNICAL TRANSLATION.** English-language translations of foreign scientific and technical material pertinent to NASA's mission.

Specialized services that complement the STI Program Office's diverse offerings include creating custom thesauri, building customized databases, organizing and publishing research results . . . even providing videos.

For more information about the NASA STI Program Office, see the following:

- Access the NASA STI Program Home Page at <http://www.sti.nasa.gov>
- E-mail your question via the Internet to help@sti.nasa.gov
- Fax your question to the NASA Access Help Desk at (301) 621-0134
- Telephone the NASA Access Help Desk at (301) 621-0390
- Write to:
NASA Access Help Desk
NASA Center for AeroSpace Information
7121 Standard Drive
Hanover, MD 21076-1320



Cone-Probe Rake Design and Calibration for Supersonic Wind Tunnel Models

Mark J. Won

Ames Research Center, Moffett Field, California

National Aeronautics and
Space Administration

Ames Research Center
Moffett Field, California 94035-1000

Acknowledgments

The author acknowledges the significant contributions of Max Amaya in providing extensive test support and data analysis during the calibration phase of wind tunnel testing. The author also acknowledges David G. Tuttle and the wind tunnel staff at the NASA Langley Unitary Plan Wind Tunnel facility, who were primarily responsible for acquiring the high quality wind tunnel data shown in this document and provided outstanding engineering and technical services throughout all phases of testing.

Available from:

NASA Center for AeroSpace Information
7121 Standard Drive
Hanover, MD 21076-1320
(301) 621-0390

National Technical Information Service
5285 Port Royal Road
Springfield, VA 22161
(703) 487-4650

CONE-PROBE RAKE DESIGN AND CALIBRATION FOR SUPersonic WIND TUNNEL MODELS

Mark J. Won

Ames Research Center

SUMMARY

A series of experimental investigations were conducted at the NASA Langley Unitary Plan Wind Tunnel (UPWT) to calibrate cone-probe rakes designed to measure the flow field on 1–2% scale, high-speed wind tunnel models from Mach 2.15 to 2.4. The rakes were developed from a previous design that exhibited unfavorable measurement characteristics caused by a high probe spatial density and flow blockage from the rake body. Calibration parameters included Mach number, total pressure recovery, and flow angularity. Reference conditions were determined from a localized UPWT test section flow survey using a 10° supersonic wedge probe. Test section Mach number and total pressure were determined using a novel iterative technique that accounted for boundary layer effects on the wedge surface. Cone-probe measurements were correlated to the surveyed flow conditions using analytical functions and recursive algorithms that resolved Mach number, pressure recovery, and flow angle to within ± 0.01 , $\pm 1\%$ and $\pm 0.1^\circ$, respectively, for angles of attack and sideslip between $\pm 8^\circ$. Uncertainty estimates indicated the overall cone-probe calibration accuracy was strongly influenced by the propagation of measurement error into the calculated results.

SYMBOLS

M	Mach number
P	static pressure
P_t	total pressure
PR	pressure ratio parameter
U	uncertainty
y, z	test section coordinates
α	angle of attack
β	angle of sideslip
γ	ratio of specific heats
δ	turning or inclination angle
ε	elevation angle (gravity axis)
θ	oblique shock angle
μ	tunnel upflow
ξ	tunnel crossflow
σ	standard deviation
ϕ	roll angle
ψ	yaw angle

INTRODUCTION

The five-hole cone probe has been commonly used for measuring subsonic and supersonic flow fields. Flow angularity, Mach number, and total pressure are deduced from a single pitot pressure and four static pressures located on a conical head. In many wind tunnel model applications, cone-probes have been calibrated and used to map internal and external flows on various aircraft components over a range of Mach numbers (refs. 1–5).

Typically, the cone-probes must resolve the flow field in sufficient detail to extract flow gradient and directional information for comparison with computational or analytical predictions. For supersonic flow measurement applications, careful attention to probe spacing and rake body design is required to ensure the measurements are free of instrument-related flow interference or disturbances. Achieving these goals on cone-probe assemblies designed for high-speed testing on 1–2% scale wind tunnel models poses a difficult engineering challenge.

The following sections describe the methods developed for calibrating cone-probes for small scale, high-speed wind tunnel model applications. Experimental data collected from two successful cone-probe rakes are compared to measurements from a third cone-probe rake design. Details of a test section flow survey which was conducted in support of the cone-probe calibrations are also presented. The experimental data quality for both flow survey and cone-probe test entries is discussed in terms of the absolute uncertainty in Mach number, pressure recovery, and flow angularity.

TEST DESCRIPTION

General

The cone-probe calibrations were conducted at the NASA Langley Unitary Plan Wind Tunnel (UPWT) in December 1997. To achieve the desired cone-probe data quality, detailed knowledge of the UPWT test section flow quality was required to properly correlate tunnel conditions with cone-probe measurements. Historical data describing the flow quality in each test section was insufficient to meet this requirement. Therefore, the cone-probe calibration effort was preceded by a localized flow survey during October 1997 in UPWT Test Sections (TS) 1 and 2 using a pressure-instrumented supersonic wedge probe.

As part of the initial flow survey of each UPWT test section, a 16 cone-probe rake assembly was tested to coincide with the probe calibration effort. Unfortunately, flow interference from the rake body adversely affected the majority of the cone-probe pressure measurements, rendering the data invalid for useful correlation and analysis. Subsequently, the calibration was suspended until a new rake design was developed to eliminate the interference effects. Cone-probe testing eventually resumed following the construction of two new rake assemblies with improved performance characteristics.

Facility Calibration Background

The Langley UPWT is a closed-circuit pressure tunnel, with two 4-ft by 4-ft test sections (TS1, TS2). Mach number is controlled using a sliding block nozzle upstream of each test section. Several comprehensive flow surveys were conducted in TS 1 and 2 at selected conditions and tunnel stations (ref. 6). As reported by reference 6 in 1981, the Mach number survey was accurate to ± 0.01 and ± 0.004 for TS 1 and 2, respectively, while test section flow angularity was reportedly accurate to within $\pm 0.1^\circ$ in both test sections. The Mach number and flow angularity profiles in TS 1 and 2 were qualitatively mapped at selected stations. Although these results have been published, the spatial flow distributions could not be sufficiently resolved or interpolated with reasonable accuracy for cone-probe correlation purposes.

In past UPWT flow surveys, the local test section Mach number for flow settings above Mach 2.0 was determined by assuming a perfect (unity) nozzle-test section total pressure recovery. This approach relied on adiabatic normal shock theory to calculate the Mach number from multiple test section pitot pressures together with the settling chamber stagnation pressure. By neglecting the stagnation losses, however, the local test section total pressure and Mach number results were subject to errors. As depicted in figure 1, a 1% decay in the average test section total pressure recovery (P_{t1}/P_{t0}) corresponds to a -0.01 to -0.015 decrement in the ideal Mach number computed from normal shock theory for test section Mach numbers between 2.0 and 2.5. By ignoring stagnation pressure losses, the reported test section Mach number uncertainty was likely to be higher than initially reported in reference 6.

Wedge Probe

To accurately establish the test section total pressure and Mach number for cone-probe calibration (independently of tunnel settling chamber pressure), an instrumented wedge probe featuring a 10° half-angle was employed. The wedge probe used to survey the flow in each Langley UPWT test section was originally constructed as one of six probes for calibrating the NASA Ames UPWT 9-ft by 7-ft (9 X 7) supersonic wind tunnel in 1993. These probes were derivatives of a previous wedge built for an earlier pilot calibration of the 9 X 7 (ref. 7). The 10° wedge probes were designed to measure test section flow conditions at Mach numbers between 1.5 and 2.6 when aligned parallel to the nominal stream direction.

The original 9 X 7 wedge design was based on similar wedge hardware developed for surveying the flow in the NASA Lewis 10-ft by 10-ft supersonic wind tunnel (ref. 8). Similar wedge probes have been designed and tested with different instrumentation features to measure the flow at other supersonic wind tunnel facilities (refs. 4, 9, and 10).

The actual wedge used for the Langley UPWT flow surveys was designated as Wedge #1. The wedge featured an average half-angle of 10.1063° which was derived from Ames metrology measurements performed prior to the 1993 9 X 7 UPWT calibration. For reference purposes, the two inclined wedge surfaces were designated as surfaces "A" and "B." As shown in figure 2, the wedge probe instrumentation consisted of paired surface static pressure orifices (P_{2A} , P_{2B}), surface pitot probes (P_{t3A} , P_{t3B}), and outboard pitot probes (P_{t2nA} , P_{t2nB}). The wedge static pressure orifices and

pitot probes had exposed hole diameters of 0.04 in., each with its own service tubing for obtaining separate pressure measurements.

Cone-Probe Rakes

The five-hole cone-probes were selected and designed to measure the Mach number, total pressure, and flow angularity at Mach numbers above 2 and flow angles within a $\pm 15^\circ$ range. The stainless steel probe barrel had an external diameter of 0.125 in., and was tipped by a pressure instrumented 40° conical head. The pressure instrumentation consisted on each probe of a single 0.016 in. diameter pitot centered at the tip of a truncated conical apex with four equally spaced static pressure taps having hole diameters of 0.015 in.

As shown in figure 3, the initial rake assembly consisted of a 4-by-4 probe array containing 16 equally spaced cone-probes. The collective probe arrangement was designed to map the flow field within a 1.125 in. by 1.125 in. square periphery. Relying on shock theory and reference data for conical surfaces (refs. 4 and 11), the probe spacing was selected to ensure each instrumented conical head remained free of incident shock impingement from neighboring cone-probes at design conditions.

As previously mentioned, two new rake assemblies were constructed after unsatisfactory pressure measurements were obtained from the 16-probe rake. Both rakes were designed with features to alleviate flow blockage and instabilities which could potentially propagate forward of the rake body. As a principal risk reduction measure, the projected frontal area occupied by the rake was reduced by decreasing the probe density. As illustrated in figure 4, one of the modified rakes (rake 1) arranged the probes into a 2-by-4 rectangular pattern. Slots were incorporated into the probe holders to bleed and stabilize any shocks formed within the rake body. To further mitigate the adverse effects of flow interference, the probe tips were positioned farther upstream of the rake body leading edge.

The second modified cone-probe rake (rake 2) was designed and constructed to function as a backup to the first rake, in the event adverse flow blockage effects were not completely eliminated. As shown in figure 5, the second rake assembly featured a 2-by-3 rectangular probe spacing which encompassed the same peripheral area as the 2-by-4 rake. With increased vertical spacing between probes, larger vent slots were incorporated in the probe holder to increase rake body channel flow bleed-off effectiveness and promote shock stability. The probe length forward of the rake body leading edge was identical to the primary modified rake. Both modified cone-probe rake assemblies were designed to map the flow field within a 0.8-in. by 1.2-in. rectangular region.

Model Installation and Articulation

A schematic and photograph of the wedge installation for the UPWT test section flow survey is depicted in figure 6. The wedge and sting adapter were collectively rolled together (through angle ϕ_S) using the roll coupling mechanism, and translated laterally (in the y-direction) using the tunnel's model support strut. This arrangement permitted the wedge to be centered along the test section vertical symmetry plane at two different heights (+z-direction) above the tunnel floor. The wedge tip

was maintained at a constant tunnel axial station by positioning the wedge leading edge at the upstream frame of test section window number 6. The vertical separation distance between the two survey locations was bounded between $z = 16.24$ in. and $z = 19.73$ in. from wedge tip to wedge tip at a neutral wedge elevation. For additional roll orientations, the wedge was rotated about the forward end of the dog-leg adapter (through angle ϕ_W) in 90° increments; the total model roll angle, ϕ_M , resulted from the combined rotation ($\phi_W + \phi_S$). The various combinations of roll coupling and manual wedge rotations employed to survey the test section are illustrated in figure 7.

At each vertical location, the wedge was articulated in either pitch (ϵ) or yaw (ψ) directions (relative to the test section centerline) to acquire data over a $\pm 2^\circ$ range. For tunnel upflow angle determination (z -direction), the wedge was rotated to either $\phi_M = 0^\circ$ or 180° and pitched through ϵ in 0.25° increments at a nominally zero yaw angle. Tunnel crossflow was established in a similar fashion by rotating the wedge to either $\phi_M = 90^\circ$ or -90° , then yawing through ψ in 0.25° increments at a nominally zero pitch angle. For pitch rotations, the upright wedge orientation was defined with wedge surface A facing the tunnel ceiling ($+z$ direction, $\phi_M = 0^\circ$). In the transverse direction, the upright orientation was defined with wedge surface A facing $+y$ direction ($\phi_M = 90^\circ$). At yaw angles other than zero, the model support strut was translated to maintain the center of rotation about the wedge leading edge and within ± 1 in. of the test section vertical symmetry plane.

The cone-probe rake installation is depicted in figure 8. For each rake installation, the rake assembly was attached to the sting adapter in place of the dog-leg adapter used during wedge testing. The roll coupling mechanism was not actuated for cone-probe testing; the rake was maintained at $\phi_S = \phi_M = 0^\circ$ during articulation. At a neutral pitch and yaw orientation, the cone-probe tips were positioned in the center of test section window number 6. Each rake was parametrically pitched in ϵ every 1° over a $\pm 12^\circ$ range, at constant ψ from -8° to 8° in 2° increments. At yaw angles other than zero, the model support strut was translated to maintain the center of rotation about the middle of the rake probe array and within ± 1 in. of the test section vertical symmetry plane.

As illustrated in figure 9, the two wedge measurement locations above the test section floor defined a spatial region for interpolating Mach number, total pressure, and stream angle for cone-probe calibration. Due to the model articulation arrangement, both wedge and cone-probes were vertically displaced in the z -direction when rotated by the model pitch mechanism. Since the same angle source was used to measure model angle of attack in the tunnel for both wedge and cone-probe tests, the cone-probe and wedge positions were related to each other by calibrating the sting adapter position above the floor as a function of model pitch elevation, $z_{ref}(\epsilon)$. The measured sting adapter vertical displacement to model pitch angle relation is shown in figure 10. In addition to vertical travel, both wedge and cone-probe rake also translated along the test section centerline when elevated by the tunnel pitch mechanism. Since the wedge and rake were exposed to the same flow conditions over a common test section region during pitch rotations, no axial position adjustments were performed to maintain the model at a constant tunnel station during model articulation.

Instrumentation and Data System

Each UPWT test section retained its own dedicated data acquisition system and instrumentation suite that was centered around a Modcomp 88100 Open Architecture System. Data acquisition and

real time data reduction for the test operational mode of the tunnel were performed utilizing a Modcomp 88100 computer complex that was interfaced to Neff 620 analog amplifier conditioning units and Pressure Systems Inc. (PSI) 8400 System Processors (SP). Final data reduction and post-processing functions were accomplished on Sun Ultra 2 SPARC II workstations linked to the Langley network (LaRCNET).

The tunnel total pressure was derived from one of two pitot probes located in the settling chamber of each test section. Each settling chamber pressure was measured by a vacuum-referenced Ruska Series 6000 quartz differential pressure transducer. Tunnel humidity was obtained from a General Eastern SPECTRA L1 Hygrometer. Tunnel total temperature was measured by an Instrulab 25-ohm platinum resistance thermometer. No corrections for thermal transfer, flow losses or other dissipative effects were applied to these tunnel measurements.

In both wedge and cone-probe tests, the primary gravity-axis model elevation angle (ϵ) was measured by an AlliedSignal Q-Flex Model QA1402 accelerometer. The Q-Flex was installed in a housing attached to the sting adapter at a single location for all sting roll orientations. Model yaw (ψ) was determined from tunnel strut yaw mechanism resolver readings. Model sting roll (ϕ_s) was measured from resolvers located in the roll-coupling mechanism. Due to the relatively low aerodynamic forces produced by the wedge and cone-probe rake, model and support system elastic deflections upstream of the respective angle measurement sources were not actively measured.

Installed pitch and roll calibrations were performed using the Langley digital Angle Measurement System (AMS) that featured simultaneous pitch-roll measurement capability (through 360°). Figure 11 shows the AMS used to reference the wedge probe orientation in the test section. Similar to the Q-Flex mounting, the AMS sensor's precision base was attached directly onto the sting adapter at a single location for all roll orientations. This arrangement eliminated the requirement for a leveling plate, and avoided angle measurement bias errors associated with multiple leveling surfaces and attachment points. By relying on the AMS's simultaneous pitch-roll measurement capability, separate accelerometer calibration data were obtained at each 90° sting-roll increment. The accelerometer and AMS combination employed during model leveling and angle calibration provided better than $\pm 0.01^\circ$ zeroing repeatability between subsequent model changes.

All wedge and cone-probe pressures were measured by 32-port, rack-mounted ± 5 psid PSI S3200 electronic scanner modules (ESPs); 5 psid and 15 psia PSI Pressure Calibration Units (PCUs) provided the reference and calibration pressures. A dedicated set of PSI scanners and PCUs were located in an ambient environment above each UPWT test section. As depicted in figure 12, a single ESP module was allocated to the wedge and cone-probe pitot instrumentation for high-range pressure measurement, with the reference pressure vented to atmosphere. Three ESP modules were assigned to the wedge and cone-probe static taps for low-range pressure measurement, with the reference pressure set to 5 psia during normal scanner operation.

The atmospheric and 5 psia reference pressures were individually measured by Ruska Series 6200 portable digital pressure gauge. Throughout wedge and cone-probe testing, daily ESP module calibrations were performed to maintain a nominal pressure measurement tolerance of ± 0.005 psid, relative to known, monitored conditions. Selected pressure ports from each ESP module were pneumatically connected to individual Ruska 6200 pressure gauges which monitored scanner

operational stability and drift throughout wind tunnel testing. The monitored pressure levels were controlled using MKS Type 250 pressure controllers.

Tunnel and model conditions were recorded in data frames, where each frame represented a single scan of a particular type of measurement containing analog or ESP data. The Modcomp data sampling rate for all Neff analog input channels was maintained at 30 frames/sec, averaged over a 2-second interval for each data point (60 frames averaged/point). The maximum attainable ESP data transmission rate between Modcomp and the 8400 SP was limited to 40 frames/sec, which was averaged over a 2-second interval (80 frames averaged/point). Each ESP data frame acquired by the Modcomp system represented a single, unaveraged measurement of all ESP port pressures.

Tunnel Conditions

For each tunnel Mach number setting (M_{set}), the nominal flow conditions in both UPWT TS 1 and 2 were held constant during the test section survey and cone-probe calibrations. The Reynolds number per foot was sustained at 4 million by adjusting the tunnel total pressure (P_{t0}) for each M_{set} . Tunnel humidity was controlled to sustain a dewpoint of -18°F at all tunnel conditions, with the total temperature maintained at a nominal 125°F . Both wedge and cone-probe tests were designed to acquire data at nominal test section Mach numbers of 2.15, 2.29, and 2.40. Due to the tunnel operating limitations, testing at the Mach number setting of 2.15 was conducted in TS 1, while testing at Mach number settings of 2.29 and 2.40 was performed in TS 2.

No attempt was made to experimentally assess the nature of the boundary layer on either wedge surface during the Langley UPWT flow surveys. Based on experience gained from Ames 9 X 7 wedge testing using sublimation and fluorescent oil flow visualization techniques, the boundary layer was found to be uniform and laminar, provided that the wedge surface remained polished and free of foreign surface deposits. An analytical treatment of the viscous contributions to the calculated flow variables is applied to the wedge data, as discussed in the following section.

MACH NUMBER FROM WEDGE MEASUREMENTS

Governing Equations

Referring to figure 13, the governing equations for determining the supersonic freestream Mach number, M_1 , and total pressure, P_{t1} , are based on inviscid, adiabatic normal and oblique shock theories. Convenient expressions are given in reference 11 to implicitly relate M_1 to the oblique shock incident angle (θ), the pressures measured by the wedge instrumentation (P_{t2n} , P_{t3} , P_2), and the supersonic turning angle (δ). These are given below, assuming a value for the ratio of specific heats (γ) of 1.4:

$$\frac{P_{t3}}{P_2} = \left(\frac{6M_2^2}{5} \right)^{\frac{7}{2}} \left(\frac{6}{7M_2^2 - 1} \right)^{\frac{5}{2}} \quad (\text{Pitot-Rayleigh formula}) \quad (1)$$

$$M_2^2 = \frac{36M_1^4 \sin^2 \theta - 5(M_1^2 \sin^2 \theta - 1)(7M_1^2 \sin^2 \theta + 5)}{(7M_1^2 \sin^2 \theta - 1)(M_1^2 \sin^2 \theta + 5)} \quad (2)$$

$$\cot \delta = \tan \theta \left[\frac{6M_1^2}{5(M_1^2 \sin^2 \theta - 1)} - 1 \right] \quad (3)$$

$$\frac{P_2}{P_{t1}} = \frac{7M_1^2 \sin^2 \theta - 1}{6} \left(\frac{5}{M_1^2 + 5} \right)^{\frac{7}{2}} \quad (4)$$

$$\frac{P_{t2n}}{P_{t1}} = \left(\frac{6M_1^2}{M_1^2 + 5} \right)^{\frac{7}{2}} \left(\frac{6}{7M_1^2 - 1} \right)^{\frac{5}{2}} \quad (\text{Normal shock recovery}) \quad (5)$$

$$M_2^2 \sin^2(\theta - \delta) = \frac{M_1^2 \sin^2 \theta + 5}{(7M_1^2 \sin^2 \theta - 1)} \quad (6)$$

Equations 4 and 5 can be combined to express the freestream pitot and post-oblique shock static pressures in terms of the freestream Mach number and oblique shock angle:

$$\frac{P_{t2n}}{P_2} = \frac{6}{7M_1^2 \sin^2 \theta - 1} \left(\frac{6M_1^2}{5} \right)^{\frac{7}{2}} \left(\frac{6}{7M_1^2 - 1} \right)^{\frac{5}{2}} \quad (7)$$

Similarly, equations 1 and 7 can be rearranged and combined to relate the normal shock and post-oblique shock pitot pressures to the freestream Mach number, post-oblique shock Mach number, and oblique shock angle:

$$\frac{P_{t3}}{P_{t2n}} = \frac{7M_1^2 \sin^2 \theta - 1}{6} \left(\frac{M_2}{M_1} \right)^7 \left(\frac{7M_1^2 - 1}{7M_2^2 - 1} \right)^{\frac{5}{2}} \quad (8)$$

General Mach Calculation Methods

Due to the implicit dependency of the freestream conditions on the normal and oblique shock pressures and turning angle, a recursive approach must be utilized to solve for M_1 . With foreknowledge of the measured pressures (P_{t2n} , P_{t3} , P_2) and turning angle (δ), M_1 may be determined from one of two methods:

I: Pitot-Pitot Method, using P_{t2n} , P_{t3} and δ together with equations 2, 3, 6, and 8

II: Pitot-Static Method, using P_{t2n} , P_2 and δ together with equations 3 and 7

Under ideal circumstances, both methods should yield identical values for M_1 ; differences in the Mach number computed between the two methods typically arise from pressure measurement errors and turning angle uncertainty. For each method, the process begins by equating M_1 to a Mach iteration variable, $M_{1\text{iter}}$, which is initially set to a nominal Mach number (such as the wind tunnel Mach number setting). In a similar fashion, the oblique shock angle, θ , is equated to its iteration counterpart, θ_{iter} , and initialized to an angle near 60° to ensure solution convergence. The relevant governing equations are then solved by numerical iteration until the desired residual levels are reached. The general procedure for computing M_1 using Methods I and II is described in Appendices A and B, respectively.

Mach from Complementary Wedge Variables

Calculation of the freestream Mach can be refined using Method I and II relationships based on figure 14, which identifies the complementary wedge surface pressure and geometric variables. M_1 can be computed for each wedge surface's instrument set (P_{t3A} - P_{2A} , P_{t3B} - P_{2B}) utilizing the appropriate iterative schemes. Ideally, the Mach number, M_{1A} , from surface "A" pressure instrumentation should equal the Mach number, M_{1B} , from surface "B" pressure instrumentation. Under ideal circumstances, the converged freestream Mach number solutions from Methods I and II, $M_{1,I}$ and $M_{1,II}$, respectively, should produce identical results: $M_{1,I} = M_{1A,I} = M_{1B,I} = M_{1,II} = M_{1A,II} = M_{1B,II}$.

Fundamentally, M_{1A} , and M_{1B} are computed using the wedge's geometric vertex half-angle, δ_w , and angle of attack, α_w , to define their respective oblique shock turning angles, δ_A and δ_B :

$$\delta_A = \delta_w - \alpha_w \quad (9)$$

$$\delta_B = \delta_w + \alpha_w \quad (10)$$

Here, α_w is measured between the stream direction and the wedge's semi-vertex reference datum defining δ_w .

As shown in figure 15, the presence of a boundary layer on the inclined wedge surfaces effectively "inflates" the wedge's total inclusive vertex angle, thereby increasing the oblique shock incident angle for a constant M_1 . To account for the boundary layer, a viscous flow deflection increment, $\Delta\delta_{\text{Weff}}$, can be presumed on both surfaces A and B, to produce oblique shock angles, $\theta_{A\text{eff}}$ and $\theta_{B\text{eff}}$, respectively. Then, the effective wedge vertex half-angle, δ_{Weff} , can be expressed as the sum of the geometric wedge half-angle and the viscous flow deflection increment:

$$\delta_{\text{Weff}} = \delta_w + \Delta\delta_{\text{Weff}} \quad (11)$$

A corresponding effective angle of attack, α_{Weff} , can be introduced to reflect the change in the indicated flow direction sensed by the wedge pressure instrumentation due to the boundary layer's presence. Together with the wedge half-angle, the effective shock turning angles, $\delta_{A\text{eff}}$ and $\delta_{B\text{eff}}$, may be defined relative to the wedge symmetry plane:

$$\delta_{A\text{eff}} = \delta_{\text{Weff}} - \alpha_{\text{Weff}} \quad (12)$$

$$\delta_{\text{Beff}} = \delta_{\text{Weff}} + \alpha_{\text{Weff}} \quad (13)$$

Mach Number Balancing

If sufficient information is available regarding the effective inclination of the wedge surfaces relative to the mean flow direction, either Method I or II should be sufficient for computing the freestream Mach number. However, since $\Delta\delta_{\text{Weff}}$ cannot be experimentally or analytically determined with sufficient accuracy, an iterative technique (Method III) can be adopted to compute M_1 strictly from wedge pressure measurements. The process reduces the requirement for bookkeeping the wedge surface inclinations relative to the model angle measurement source, therefore avoiding the introduction of angle measurement errors from multiple angle sources.

For a given set of wedge pressures, the Method III Mach number ($M_{1,\text{III}}$) calculation routine relies on symmetry to ensure $M_{1,I} = M_{1A,I} = M_{1B,I}$, $M_{1,II} = M_{1A,II} = M_{1B,II}$, and $M_{1,I} = M_{1,II}$. Thus, if P_{t2n} , P_{t3} , and P_2 are known for surfaces A and B, then a unique value of $\delta_{\text{Weff}} \pm \alpha_{\text{Weff}}$ exists which produces identical M_1 values in both Method I and II calculations. This trait is illustrated in figure 16 over a representative Mach number and angle range for a 10° half-angle wedge. The $M_{1,I} = M_{1A,I} = M_{1B,I}$ condition is obtained by adjusting the wedge angle of attack, $\alpha_{\text{Weff},I}$, using Method I for given values of δ_{Weff} , P_{t3A} , P_{t2nA} , P_{t3B} , and P_{t2nB} . Similarly, the $M_{1,II} = M_{1A,II} = M_{1B,II}$ condition is obtained by adjusting a corresponding wedge angle of attack, $\alpha_{\text{Weff},II}$ (which is not necessarily identical to $\alpha_{\text{Weff},I}$) using Method II for given values of δ_{Weff} , P_{2A} , P_{t2nA} , P_{2B} , and P_{t2nB} . The final $M_{1,I} = M_{1,II}$ condition is satisfied by varying $\Delta\delta_{\text{Weff}}$ in equation 11 to obtain an identical solution for M_1 between Methods I and II.

Since small pressure measurement errors are commonly associated with pressure instrumentation (refs. 12–14), Method III may not converge on a $M_{1,\text{III}} = M_{1,I} = M_{1,II}$ solution if both Methods I and II assume $\alpha_{\text{Weff},I} = \alpha_{\text{Weff},II}$ and share a common $\Delta\delta_{\text{Weff}}$. Therefore, separate and unique values for $\alpha_{\text{Weff},I}$ and $\alpha_{\text{Weff},II}$ must be computed and retained by each respective method to account for the measurement discrepancies. Alternately, an $M_{1,\text{III}}$ solution can be obtained by employing identical α_{Weff} , but distinct δ_{Weff} , values in the calculations performed for Methods I and II. In the remaining discussions, the former approach ($\alpha_{\text{Weff},I} \neq \alpha_{\text{Weff},II}$) is considered for all data reductions.

The Method III Mach number computation begins by initially conditioning several of the input variables utilized by both Methods I and II. Due to the distance and location of the P_{t2nA} and P_{t2nB} pitot probes, relative to the wedge centerline, both freestream normal shock pitot pressures must be either averaged or interpolated to obtain a representative freestream pitot pressure in the vicinity of the wedge surface pressure instrumentation.

Starting values for the oblique shock turning angles (δ_{Aeff} and δ_{Beff}) must be also provided for the Method III calculation process. For convenience, $\Delta\delta_{\text{Weff}}$ may be initialized to zero ($\delta_{\text{Weff}} = \delta_w$). Likewise, $\alpha_{\text{Weff},I}$ and $\alpha_{\text{Weff},II}$ may be both initially equated to α_w , or some other model angle of attack measured in the same plane and direction as the wedge half-angle.

Once the appropriate parameters have been initialized, the M_1 balancing process proceeds by utilizing the measured P_{t3A} , P_{t3B} , P_{2A} , and P_{2B} , as well as the previously described $M_{1\text{iter}}$ and θ_{iter}

start-up values, to compute the terms in the Method I and II M_1 calculation routines. Residuals from the first computation cycle are used to update the iteration variables on the subsequent computational cycle. This process is performed repeatedly until the $M_{1,III} \approx M_{1,I} \approx M_{1,II}$ has been obtained. The general calculation process for Method III is described in Appendix C, with sample numerical calculations given in Appendix D.

POST-TEST DATA PROCESSING AND ANALYSIS

Post-test data processing and analysis were performed on an Apple Macintosh PowerPC G3 computer. The computational algorithms for evaluating the wedge and cone-probe data were developed using National Instruments LabVIEW software, which featured a high-level, graphical user interface (GUI) language with built-in analytical functions. Additional data processing was accomplished using Microsoft Excel's spreadsheet and plotting functions.

TEST SECTION SURVEY RESULTS

Normal Shock Pitot Pressure Distribution

Figure 17 shows the settling chamber referenced normal shock pitot recovery distributions at the test section vertical centerline ($y = 24$ in.) and constant horizontal stations ($z = 16.24, 19.73$ in.) for the three Mach number settings. The pressures were mapped from separate P_{t2nA} and P_{t2nB} measurements obtained from the multiple wedge orientations depicted in figure 7. Variations in the local pitot pressure along the z -direction were greater than the estimated measurement uncertainty associated with the wedge pitot and settling chamber pressures. The distributions are indicative of the flow nonuniformity within the surveyed region of each respective test section.

Flow Angularity

The approach for determining the tunnel upflow, μ , and crossflow, ξ , relied on deriving the sensitivity of the wedge surface A to B static pressure ratio, P_{2A}/P_{2B} , to a corrected wedge angle of attack, α_{Wcorr} . Since there was greater confidence in the pitch angle (ϵ) measurement accuracy, α_{Wcorr} was obtained from wedge pitch data runs only ($\phi_M = 0^\circ, 180^\circ, \psi = 0^\circ$). From this set of data, the corrected angle of attack was obtained by relating P_{2A}/P_{2B} to the wedge angle of attack, α_W , defined by:

$$\alpha_W = \epsilon \cos(\phi_M)$$

As shown in figure 18, α_{Wcorr} represented the midpoint between upright and inverted $\alpha_W - P_{2A}/P_{2B}$ polars at $z = 16.24$ in. and $z = 19.73$ in. for constant P_{2A}/P_{2B} . An analytical expression describing $\alpha_{Wcorr}(P_{2A}/P_{2B})$ for both wedge locations above the test section floor was obtained at each Mach number through regression analysis. μ and ξ were determined by respectively relating ϵ and ψ to $\alpha_{Wcorr}(P_{2A}/P_{2B})$ for each tunnel Mach number, as depicted in figure 19. The test section

flow angle was presumed to coincide with $\alpha_{Wcorr}(P_{2A}/P_{2B}) = 0^\circ$ for wedge articulation in the pitch and yaw directions.

Figures 20 and 21, respectively, show the assumed linear upflow, $\mu(z)$, and crossflow, $\xi(z)$, distributions extracted from wedge measurements at $z = 16.24$ in. and $z = 19.73$ in. at each tunnel Mach number setting. UPWT TS 1 exhibited the largest upflow angle of nearly 1.5° . Crossflow varied between $\pm 0.2^\circ$ in both test sections. The magnitudes and trends were in general agreement with the nominal tunnel flow angles described in reference 6.

Mach Number and Pressure Recovery

In order to compute the freestream Mach number from the wedge pressures, a fourth-order polynomial regression was first applied to the normal shock pitot pressure distribution along the test section centerline ($y = 24$ in.), shown in figure 17. This analytical representation describing $P_{t2n}(z)/P_{t0}$ was used to interpolate P_{t2n} from wedge position information and tunnel settling chamber pressure, P_{t0} . Values for z were referenced to the wedge leading edge height above the test section floor, and determined from $z_{ref}(\epsilon)$ in figure 10, together with wedge and sting adapter dimensions.

Establishing P_{t2n} from the spatial distribution was preferred over the numerical averaging of P_{t2nA} and P_{t2nB} due to the pressure measurement uncertainty associated with the lateral separation distance between the outboard pitot probes and wedge surface instrumentation. As shown in figure 22, the analytical $P_{t2n}(z)/P_{t0}$ distribution gave a better approximation of the normal shock pressure within close proximity of the wedge surface static and pitot instrumentation.

Figure 23 compares the Method I, II, and III Mach numbers with the ideal Mach number computed from $P_{t2n}(z)/P_{t0}$ using equation 5 (assuming perfect recovery, $P_{t1} = P_{t0}$). To preclude the introduction of errors associated with flow angularity, the assumed linear distributions were constructed from measurements made within $\pm 0.25^\circ$ of the computed upflow and crossflow angles at each wedge position above the test section floor. The Mach gradient for all methods was steepest for TS 2 at $M_{set} = 2.29$, with the Mach number being higher at the survey location closest to the tunnel floor.

Ideally, the test section Mach number should have been identical for all calculation methods at all flow conditions. At a tunnel Mach setting of 2.15 in TS 1, the Mach numbers for Methods I, II, and III were reasonably close to each other, with the exception of the ideal Mach, which was higher than the others, as would be expected. However, the Method I, II, and III-computed Mach numbers for TS 2 diverged with increasing Mach. At $M_{set} = 2.40$, the Method I Mach number exceeded the ideal Mach value. Excluding the ideal Mach number, the Method III approach was an overall compromise between Method I and II results.

The freestream total pressure recovery, P_{t1}/P_{t0} , computed from the corresponding Mach number methods and $P_{t2n}(z)/P_{t0}$ using equation 5 is shown in figure 24. Similar to the Mach number, linear pressure recovery distributions in the z -direction were defined by data within $\pm 0.25^\circ$ of the computed tunnel flow angles. The recovery trends reflected the variations in Mach number obtained

from Methods I, II, and III. At $M_{\text{set}} = 2.40$, the total pressure recovery computed from the Method I Mach number was greater than unity, yielding overshoots on the order of 1 to 1.5%.

Wedge Measurement Discrepancies

Figure 25 shows the viscous flow deflection increment, $\Delta\delta_{\text{Weff}}$, resulting from the Method III calculation process for the various wedge roll orientations as a function of wedge tip position above the test section floor. The largest increment is on the order of $+0.3^\circ$ at $M_{\text{set}} = 2.40$. However, at Mach number settings of 2.15 and 2.29, the increment is less than zero. A positive wedge half-angle increment could be explained as the effective boundary layer displacement on the wedge surface sensed by the pressure instrumentation. For negative half-angle increments at the mid and lower Mach number settings, other contributing factors must be taken into account.

One plausible explanation for the observed anomaly considers the Mach number sensitivity to wedge surface inclination and pressure measurement errors. The Mach number sensitivity to pressure variations is compared between Methods I and II in figure 26. Referring to figure 13, the curves are representative of the experimental flow conditions and wedge surface inclinations. The sensitivities were obtained by evaluating the governing equations for the Method I and II Mach number using central-differencing approximations.

The Method I Mach number sensitivity to the surface pitot pressure error, $(\Delta M_1/M_1)/(\Delta P_{t3}/P_{t3})$, decreases with increasing wedge deflection angle, and is relatively invariant with Mach number at a given wedge angle. In contrast, the Method II Mach number sensitivity to the surface static pressure error, $(\Delta M_1/M_1)/(\Delta P_2/P_2)$, becomes increasingly negative with increasing wedge deflection angle and Mach number. The increasing magnitude of the Method II Mach number sensitivity with Mach number could explain the method-dependent variations observed in figure 23.

In general, pitot pressures are less susceptible than surface static pressures to measurement errors from instrumentation misalignment or geometry (ref. 12). Static pressures are strongly influenced by orifice size, rounding or chamfering, flushness, and hole alignment (ref. 14). Depending on the wedge surface inclination and Mach number, such static pressure measurement errors could have adversely affected the computed Mach number, possibly accounting for total pressure recoveries greater than unity and the negative values of $\Delta\delta_{\text{Weff}}$, described above.

The Method III Mach number calculation technique assumes equal weighting of pressure measurement error between the wedge surface static and pitot instrumentation. Determining the magnitude of these errors and the proper weighting in the Method III calculations would have required additional experimental testing, which was beyond the scope of the test section flow survey objectives.

CONE-PROBE PERFORMANCE COMPARISONS

Figure 27 shows the static to pitot pressure ratio pitch polars (for taps A and C) for the initial 16-probe cone-probe rake assembly tested at $M_{\text{set}} = 2.40$ and $\psi = 0^\circ$. Theoretically, the polar shape for each static pressure tap should have been continuous over the entire $\pm 12^\circ$ pitch range. Successful

correlation of the cone-probe angle of attack to the measured pressures was critically dependent on this trait. However, it is evident from the figure that probes located near the center of the 4-by-4 array (probes 2, 3, 6, 7, and 10) had polars which departed from the desired trends, exhibiting erratic changes in magnitude between consecutive data points. Similar pressure polar behavior was also observed at Mach numbers of 2.15 and 2.29 and in the transverse probe taps, B and D, as well. Figure 28 illustrates the relationship between the location of the affected probes and the downstream blockage area in the 16-probe rake body.

Figures 29 and 30 show the static tap pressure polars for the respective 8- and 6-probe rakes at $M_{set} = 2.40$ and $\psi = 0^\circ$. Unlike the 16-probe rake, the pressure polar discontinuities were absent from the modified rakes at all flow conditions. The shadowgraphs in figure 31 illustrate the qualitative differences in the flow structure between the 16-probe rake and the modified rakes at various tunnel Mach settings. Although the incident shocks shed by the probe tips in the 16-probe rake did not appear to impinge on the pressure-instrumented conical surface between adjacent probes, the flow between the probes appeared chaotic and populated by multiple shock reflections and waves. Similar qualities were also observed in the 4-by-4 probe array at other Mach numbers and rake orientations. In contrast, the incident and reflected shocks from the probe tips on rakes 1 and 2 were coherent and well-defined. Disturbances which plagued the static pressure taps on the 16-probe rake were apparently attenuated by the reduced probe density, increased probe length, and addition of rake body slots.

CONE-PROBE CALIBRATION

Reference Flow Conditions

The cone-probes were calibrated against the local test section flow distribution derived from the wedge measurements in the z-direction. From cone-probe rake dimensions and the relationship shown in figure 10, z represented the distance from the test section floor to each probe tip, and was determined from $z_{ref}(\epsilon)$, together with rake, probe, and sting adapter dimensions. Using this relationship, the cone-probe measurements could be referenced to the local test section flow angles, $\mu(z)$ and $\xi(z)$, Mach number, $M_1(z)$, and total pressure recovery, $P_{t1}(z)/P_{t0}$, based on the respective linear distributions shown in figures 20, 21, 23, and 24. $M_1(z)$ and $P_{t1}(z)/P_{t0}$ were established from the Method III calculation results. The coefficients representing the linear test section flow distribution for $\mu(z)$, $\xi(z)$, $M_1(z)$, and $P_{t1}(z)/P_{t0}$ are tabulated in table 1.

The effective cone-probe angles of attack, α_C , and sideslip, β_C , were calculated from the cosine transformation of Euler angles expressed in terms of the known angles $\mu(z)$, $\xi(z)$, ϵ , ψ , and ϕ_M , following the angle convention illustrated in figure 32:

$$\begin{aligned}\tan \alpha_C &= \frac{\tan(\epsilon + \epsilon_F) \cos \phi_M}{\cos[\psi - \xi(z)]} + \sin \phi_M \tan[\psi - \xi(z)] \\ \tan \beta_C &= \frac{\tan(\epsilon + \epsilon_F) \sin \phi_M}{\cos[\psi - \xi(z)]} - \cos \phi_M \tan[\psi - \xi(z)]\end{aligned}\quad (14)$$

where

$$\tan \epsilon_F = \tan \mu(z) \cos \xi(z)$$

Compressibility Correlation

With reference to figure 33, the cone-probe Mach number sensitivity was derived using a compressibility parameter, PR_T , defined by the average cone-probe static pressure normalized by the pitot pressure:

$$PR_T = \frac{(P_A + P_B + P_C + P_D)}{4P_{tY}} \quad (15)$$

Figures 34 and 35 show the effect of cone-probe angle of attack and sideslip on the compressibility parameter; the trends are similar to those reported in reference 5 for Mach numbers near 2.40. To correct for the changes in PR_T due to flow angularity at a constant Mach number, the compressibility parameter was related to the longitudinal and directional sensitivity parameters, PR_{AC} and PR_{BD} , respectively:

$$\begin{aligned}PR_{AC} &= \frac{P_A - P_C}{P_{tY}} \\ PR_{BD} &= \frac{P_B - P_D}{P_{tY}}\end{aligned}\quad (16)$$

As defined in figure 33, PR_{AC} represented the probe's sensitivity to angle of attack, whereas PR_{BD} described the probe's sensitivity to angle of sideslip. By combining these parameters, an effective flow inclination parameter, PR_{ACBD} , was defined to correlate the probe's sensitivity to combined changes in angle of attack and sideslip:

$$PR_{ACBD} = (PR_{AC}^2 + PR_{BD}^2)^{\frac{1}{2}} \quad (17)$$

The compressibility parameter's relationship to the effective inclination parameter is shown in figures 36 and 37 for rakes 1 and 2, respectively, for angles of attack between $\pm 12^\circ$ and angles of sideslip between $\pm 8^\circ$. At each test section Mach number setting, the data scatter between PR_T and PR_{ACBD} differs from probe to probe in both rakes. This behavior was attributed to probe misalignment (relative to the rake body orientation) and measurement errors associated with static pressure orifice asymmetry. Under ideal circumstances, the data points would have collapsed onto a single curve for each Mach number.

To improve the correlation between the compressibility and inclination parameters described by equation 17, the effective inclination parameter was redefined to account for probe misalignment effects and pressure tap errors by introducing a corrected inclination parameter, PRACBDcorrT:

$$PR_{ACBDcorrT} = \left[(PR_{AC} + PR_{ACbiasT})^2 + (PR_{BD} + PR_{BDbiasT})^2 \right]^{\frac{1}{2}} \quad (18)$$

$PR_{ACbiasT}$ and $PR_{BDbiasT}$ were bias components in the respective cone-probe longitudinal and directional sensitivity parameters, and were assumed to be unique for each probe and invariant with flow angle at a constant Mach number. For data obtained at a constant M_{set} , these bias terms were determined by parametrically adjusting $PR_{ACbiasT}$ and $PR_{BDbiasT}$ in equation 18 until the standard deviation for a cubic regression relating PR_T to $PR_{ACBDcorrT}$ converged to acceptable levels. The analytical expression which was found to yield the least PR_T data scatter for all probes took the following implicit form:

$$PR_T = l_{T0} + l_{T1}x_T + l_{T2}x_T^2 + l_{T3}x_T^3, \text{ where } x_T = PR_{ACBDcorrT} PR_T^7 \quad (19)$$

Since data irregularities were present at extreme angles of attack and compromised the overall quality of the regression, the numerical analysis was limited to cone-probe angles of attack and sideslip within $\pm 8^\circ$. Curves of $PRT(PRACBDcorrT)$ obtained from the PRACbiasT and PRBDbiasT iteration using equation 19 are shown in figures 38 and 39 for rakes 1 and 2, respectively.

Once the compressibility parameter had been correlated to the corrected inclination parameter, the effects of flow angularity was established. Referring to figure 40, the offset coefficient, l_{T0} , in equation 19 defined the fundamental compressibility parameter, PR_{T0} , which was assumed to be invariant with flow angularity and dependent only on Mach number. The remaining higher order terms represented the flow angularity increment, ΔPR_T , to the fundamental compressibility parameter. After rearranging and substituting terms in equation 19, the fundamental compressibility parameter was expressed as:

$$PR_{T0} = PR_T - \Delta PR_T = PR_T - (l_{T1}x_T + l_{T2}x_T^2 + l_{T3}x_T^3) \quad (20)$$

Since the cone-probes had been calibrated at three separate tunnel Mach number settings (2.15, 2.29, and 2.40), three corresponding values of PR_{T0} were obtained for each cone-probe to express $PR_{ACbiasT}$, $PR_{BDbiasT}$, l_{T1} , l_{T2} , and l_{T3} as quadratic functions of PR_{T0} :

$$\begin{aligned} PR_{ACbiasT} &= j_{T0} + j_{T1} PR_{T0} + j_{T2} PR_{T0}^2 \\ PR_{BDbiasT} &= k_{T0} + k_{T1} PR_{T0} + k_{T2} PR_{T0}^2 \\ l_{T1} &= m_{T0} + m_{T1} PR_{T0} + m_{T2} PR_{T0}^2 \\ l_{T2} &= n_{T0} + n_{T1} PR_{T0} + n_{T2} PR_{T0}^2 \\ l_{T3} &= q_{T0} + q_{T1} PR_{T0} + q_{T2} PR_{T0}^2 \end{aligned}$$

The second-order coefficients for $PR_{ACbiasT}$, $PR_{BDbiasT}$, l_{T1} , l_{T2} , and l_{T3} are listed in tables 2 and 3 for rakes 1 and 2, respectively.

By assuming that $PR_{ACbiasT}$, $PR_{BDbiasT}$, l_{T1} , l_{T2} , and l_{T3} were solely dependent on PR_{T0} for each probe, PR_{T0} was determined by numerically solving the resulting implicit relation in equation 20:

$$PR_T - (l_{T1}x_T + l_{T2}x_T^2 + l_{T3}x_T^3) - PR_{T0} = 0 \quad (21)$$

A sample calculation for PR_{T0} is included in Appendix E.

Mach Number Correlation

The Mach number was correlated to the cone-probe pressures following the general method employed in reference 5, which expressed the Mach number as an empirical function of the compressibility parameter at zero flow incidence. Consequently, $M_1(z)$ was explicitly derived as a function of the fundamental compressibility parameter to eliminate the effects of flow angularity. Since the calibration data was obtained at Mach numbers of 2.15, 2.29, and 2.40, the correlation accuracy was dependent on the analytical relationship between $M_1(z)$ and PR_{T0} . From conical shock relations provided reference 11, values for the freestream Mach number were computed for a 40° cone as a function of the theoretical PR_{T0} to extrapolate for conditions beyond the experimental Mach number range. A polynomial regression of the collective data set containing both experimental and supplemental data expressed the calibrated cone-probe Mach number, M_{1Ccal} , as a fourth-order polynomial function of the fundamental compressibility parameter:

$$M_{1Ccal} = C_{M0} + C_{M1} PR_{T0} + C_{M2} PR_{T0}^2 + C_{M3} PR_{T0}^3 + C_{M4} PR_{T0}^4 \quad (22)$$

The coefficients derived for M_{1Ccal} are listed in table 4 for both cone-probe rakes.

Figures 41 and 42 illustrate the analytical Mach number dependency on the fundamental compressibility parameter for rakes 1 and 2, respectively. The two-standard deviation, $2\sigma(M_{1Ccal})$, calculated from the residuals between M_{1Ccal} and $M_1(z)$ is shown in figures 43 and 44 for rakes 1 and 2, respectively. This statistic was a general measure of the cone-probe Mach number resolution, rather than an indicator of the absolute Mach number calibration accuracy. The calibrated Mach number residuals were within a $2\sigma(M_{1Ccal})$ of ± 0.01 for Mach numbers above 2.29. Probes 5 and 6 on rake 1 and probe 3 on rake 2 exhibited higher M_{1Ccal} deviations at $M_{set} = 2.15$ over the $\pm 8^\circ$ angle of attack and sideslip range.

Total Pressure Correlation

Figures 45 and 46 show the effect of cone-probe angle of attack and sideslip on the compressibility parameter; the trends are similar to those reported in ref. 5 for Mach numbers near 2.40. Similar to the compressibility parameter, the cone-probe pitot pressure, P_{tY} , was correlated to PR_{ACBD} to represent the variation with flow angularity. Figures 47 and 48 show the pitot pressure variation with the effective inclination parameter for rakes 1 and 2, respectively, at constant tunnel Mach numbers. The data scatter was considered an artifact of both probe misalignment and

measurement error due to probe inclination to the mean flow direction. This behavior has been observed for sharp-edged pitot probes with conical tips (ref. 13).

To improve the correlation between the pitot pressure and inclination parameter, an effective inclination parameter, $PR_{ACBDcorrY}$, was introduced to correct for probe misalignment effects and flow angularity at a constant Mach number:

$$PR_{ACBDcorrY} = \left[(PR_{AC} + PR_{ACbiasY})^2 + (PR_{BD} + PR_{BDbiasY})^2 \right]^{1/2} \quad (23)$$

The relationship between P_{tY} and $PR_{ACBDcorrY}$ was based on the model presented in figure 49. The pitot pressure variation was expressed in terms of $\Delta P_{tY}/P_{tY}$, which analytically described the deviation from the maximum pitot pressure due to flow inclination at constant Mach number. As in the compressibility parameter correlation, $PR_{ACbiasY}$ and $PR_{BDbiasY}$ were the bias offsets complementing the respective cone-probe longitudinal and directional sensitivity parameters, and accounted for the P_{tY} data scatter with flow inclination at a constant Mach number. For data obtained at a constant M_{set} , these bias terms were determined for each cone-probe by parametrically adjusting $PR_{ACbiasY}$ and $PR_{BDbiasY}$ in equation 23 until the standard deviation for a cubic regression relating $\Delta P_{tY}/P_{tY}$ to $PR_{ACBDcorrY}$ converged to within acceptable levels. The cubic relationship took the following form:

$$\Delta P_{tY}/P_{tY} = l_{Y0} + l_{Y1}x_Y + l_{Y2}x_Y^2 + l_{Y3}x_Y^3, \text{ where } x_Y = PR_{ACBDcorrY} \quad (24)$$

For each iteration cycle, $\Delta P_{tY}/P_{tY}$ was determined from a separate cubic regression of $P_{tY}(PR_{ACBDcorrY})$:

$$P_{tY} = l_{Yabs0} + l_{Yabs1}x_Y + l_{Yabs2}x_Y^2 + l_{Yabs3}x_Y^3 \quad (25)$$

From this expression, P_{tYmax} , the maximum value of $P_{tY}(PR_{ACBDcorrY})$ for $x_Y \geq 0$, was determined; for positive, real values of x_Y , P_{tYmax} was derived by solving equation 25 for x_{Ymax} which yielded the maximum $P_{tY}(PR_{ACBDcorrY})$:

$$x_{Ymax} = \frac{-l_{Yabs2} + \sqrt{l_{Yabs2}^2 - 3l_{Yabs1}l_{Yabs3}}}{3l_{Yabs3}} \quad (26)$$

Then

$$P_{tYmax} = l_{Yabs0} + l_{Yabs1}x_{Ymax} + l_{Yabs2}x_{Ymax}^2 + l_{Yabs3}x_{Ymax}^3$$

Otherwise, $P_{tYmax} = l_{Yabs0}$ for non-real or negative values of x_Y . Once P_{tYmax} was computed, $\Delta P_{tY}/P_{tY}$ could be calculated to evaluate equation 24:

$$\Delta P_{tY}/P_{tY} = P_{tYmax}/P_{tY} - 1 \quad (27)$$

Similar to the PR_T analysis, the analysis of $\Delta P_{tY}/P_{tY}(PR_{ACBDcorrY})$ and P_{tYmax} was limited to nominal cone-probe angles of attack and sideslip within $\pm 8^\circ$. Curves of $P_{tY}/P_{t0}(PR_{ACBDcorrY})$ resulting from the converged solution of equation 24 are shown in figures 50 and 51 for rakes 1 and 2, respectively.

To account for compressibility effects, $PR_{ACbiasY}$, $PR_{BDbiasY}$, l_{Y0} , l_{Y1} , l_{Y2} , and l_{Y3} were expressed as analytical functions of PR_{T0} for each probe. Since the cone-probes were calibrated at three separate tunnel Mach numbers (2.15, 2.29, and 2.40), $PR_{ACbiasY}$, $PR_{BDbiasY}$, l_{Y0} , l_{Y1} , l_{Y2} , and l_{Y3} were related to the three corresponding values of PR_{T0} using a second-order polynomial function obtained through regression analysis:

$$\begin{aligned} PR_{ACbiasY} &= j_{Y0} + j_{Y1} PR_{T0} + j_{Y2} PR_{T0}^2 \\ PR_{BDbiasY} &= k_{Y0} + k_{Y1} PR_{T0} + k_{Y2} PR_{T0}^2 \\ l_{Y0} &= m_{Y0} + m_{Y1} PR_{T0} + m_{Y2} PR_{T0}^2 \\ l_{Y1} &= n_{Y0} + n_{Y1} PR_{T0} + n_{Y2} PR_{T0}^2 \\ l_{Y2} &= q_{Y0} + q_{Y1} PR_{T0} + q_{Y2} PR_{T0}^2 \\ l_{Y3} &= r_{Y0} + r_{Y1} PR_{T0} + r_{Y2} PR_{T0}^2 \end{aligned}$$

The second-order coefficients for $PR_{ACbiasY}$, $PR_{BDbiasY}$, l_{Y0} , l_{Y1} , l_{Y2} , and l_{Y3} resulting from the minimization of $\Delta P_{tY}/P_{tY}$ ($PR_{ACBDcorrY}$) at each Mach number are listed in tables 5 and 6 for rakes 1 and 2, respectively.

Once the flow inclination correction had been obtained, the corrected pitot pressure, P_{tYcorr} , was equated to P_{tYmax} and solved by combining equations 24 and 27:

$$P_{tYcorr} = (1 + l_{Y0} + l_{Y1}x_Y + l_{Y2}x_Y^2 + l_{Y3}x_Y^3)P_{tY} \quad (28)$$

From P_{tYcorr} and the explicit relation for M_{1Ccal} given in equation 22, the calibrated cone-probe freestream total pressure, P_{t1Ccal} , was calculated from the one-dimensional normal shock equation:

$$P_{t1Ccal} = P_{tYcorr} \left(\frac{M_{1Ccal}^2 + 5}{6M_{1Ccal}^2} \right)^{\frac{7}{2}} \left(\frac{7M_{1Ccal}^2 - 1}{6} \right)^{\frac{5}{2}} \quad (29)$$

The two-standard deviation, $2\sigma(P_{t1Ccal}/P_{t0})$, of the residuals between the calibrated cone-probe total pressure recovery, P_{t1Ccal}/P_{t0} , and the reference test section total pressure recovery distribution, $P_{t1}(z)/P_{t0}$, is depicted in figures 52 and 53 for rakes 1 and 2, respectively. This statistic was a general measure of the correlation's ability to resolve the freestream total pressure, rather than an indicator of the absolute total pressure calibration accuracy. The calibrated total pressure recovery residuals were typically within a $2\sigma(P_{t1Ccal}/P_{t0})$ of ± 0.01 ($\pm 1\%$ of the settling chamber pressure) for Mach

numbers above 2.29. On most probes, the deviation between the cone-probe and wedge-surveyed freestream pressure recovery remained relatively invariant with probe angle of attack and sideslip. Probes 5 and 6 on rake 1 and probes 1 and 3 on rake 2 exhibited higher P_{t1Ccal}/P_{t0} deviations at $M_{set} = 2.15$ over the $\pm 8^\circ$ angle of attack and sideslip range.

Angle of Attack Correlation

Due to the size and arrangement of the probes in the rake assembly, the actual angle of attack for each cone-probe could not be directly measured with sufficient accuracy. For simplicity, the angle of attack for each probe was referenced to its effective angle of attack, α_C . Since any probe misalignment relative to the α_C reference datum was most likely to be small, any probe offset angle in the pitch direction would presumably appear as a bias error in the cone-probe pressures. Referring to figure 32, α_C was approximately proportional to the longitudinal sensitivity parameter, PR_{AC} . This observation is illustrated in figures 54 and 55 for rakes 1 and 2, respectively, at a nominal angle of sideslip of 0° and tunnel Mach number of 2.40. Similar trends were exhibited at other Mach numbers as well.

To avoid increased fit errors from data irregularities at higher angles, the cone-probe angle of attack analysis was limited to data within a model pitch range of $\pm 8^\circ$. From this reduced data set, the calibrated cone-probe angle of attack, α_{Ccal} , was analytically correlated to the measured cone-probe pressures in the following manner:

$$\alpha_{Ccal} = \alpha_0 - \Delta\alpha_B - \Delta\alpha_{corr} \quad (30)$$

The first term on the right side of equation 30 represented the linear variation of the effective cone-probe angle of attack with the longitudinal sensitivity parameter. α_0 was derived from the regression of α_C with PR_{AC} at a nominal β_C of zero for each tunnel Mach number setting:

$$\alpha_0 = a_0 + a_1 PR_{AC} \quad (31)$$

The second term in equation 30 corrected for probe angle of attack variations due to crossflow. For each data run at a nominally constant ψ , $\Delta\alpha_B$ was determined from a fourth-order polynomial regression relating $(\alpha_C - \alpha_0)$ to PR_{AC} at a constant M_{set} :

$$\Delta\alpha_B = \alpha_C - \alpha_0 = b_0 + b_1 PR_{AC} + b_2 P_{t0} PR_{AC}^2 + b_3 P_{t0} PR_{AC}^3 + b_4 P_{t0} PR_{AC}^4 \quad (32)$$

Since PR_{BD} was assumed to be nearly invariant with angle of attack, each coefficient in equation 32 was correlated to the average directional sensitivity parameter, PR_{BDavg} , using a sixth-order regression of the form:

$$b_i = c_{0i} + c_{1i} PR_{BDavg} + c_{2i} PR_{BDavg}^2 + c_{3i} PR_{BDavg}^3 + c_{4i} PR_{BDavg}^4 + c_{5i} PR_{BDavg}^5 + c_{6i} PR_{BDavg}^6 \quad (33)$$

where $i = 0$ to 4

For each cone-probe, PR_{BDavg} was computed at a nominally constant ψ for each tunnel Mach number condition.

The last term in equation 30 corrects for any residuals resulting from the α_C , α_0 , and $\Delta\alpha_B$ relationship with PR_{AC} at a constant M_{set} :

$$\Delta\alpha_{\text{corr}} = \alpha_0 - \alpha_C - \Delta\alpha_B = d_0 + d_1 \text{PR}_{\text{AC}} + d_2 \text{PR}_{\text{AC}}^2 + d_3 \text{PR}_{\text{AC}}^3 + d_4 \text{PR}_{\text{AC}}^4 \quad (34)$$

To capture the α_C sensitivity to Mach number, the a, c, and d coefficients obtained at each of the three tunnel Mach numbers (2.15, 2.29, and 2.40) were analytically related to the corresponding values of PR_{T0} using a quadratic function obtained from regression analysis:

$$a_0 = C_{0,a0} + C_{1,a0} \text{PR}_{T0} + C_{2,a0} \text{PR}_{T0}^2$$

$$a_1 = C_{0,a1} + C_{1,a1} \text{PR}_{T0} + C_{2,a1} \text{PR}_{T0}^2$$

$$c_{0i} = C_{0,c0} + C_{1,c0} \text{PR}_{T0} + C_{2,c0} \text{PR}_{T0}^2$$

$$c_{1i} = C_{0,c1} + C_{1,c1} \text{PR}_{T0} + C_{2,c1} \text{PR}_{T0}^2$$

$$c_{2i} = C_{0,c2} + C_{1,c2} \text{PR}_{T0} + C_{2,c2} \text{PR}_{T0}^2$$

$$c_{3i} = C_{0,c3} + C_{1,c3} \text{PR}_{T0} + C_{2,c3} \text{PR}_{T0}^2$$

$$c_{4i} = C_{0,c4} + C_{1,c4} \text{PR}_{T0} + C_{2,c4} \text{PR}_{T0}^2$$

$$c_{5i} = C_{0,c5} + C_{1,c5} \text{PR}_{T0} + C_{2,c5} \text{PR}_{T0}^2$$

$$c_{6i} = C_{0,c6} + C_{1,c6} \text{PR}_{T0} + C_{2,c6} \text{PR}_{T0}^2$$

$$d_0 = C_{0,d0} + C_{1,d0} \text{PR}_{T0} + C_{2,d0} \text{PR}_{T0}^2$$

$$d_1 = C_{0,d1} + C_{1,d1} \text{PR}_{T0} + C_{2,d1} \text{PR}_{T0}^2$$

$$d_2 = C_{0,d2} + C_{1,d2} \text{PR}_{T0} + C_{2,d2} \text{PR}_{T0}^2$$

$$d_3 = C_{0,d3} + C_{1,d3} \text{PR}_{T0} + C_{2,d3} \text{PR}_{T0}^2$$

$$d_4 = C_{0,d4} + C_{1,d4} \text{PR}_{T0} + C_{2,d4} \text{PR}_{T0}^2$$

The second-order coefficients for a, c, and d are listed in tables 7 and 8 for rakes 1 and 2, respectively.

The two-standard deviation, $2\sigma(\alpha_{\text{Ccal}})$, calculated from the residual between α_{Ccal} and α_C is shown in figures 56 and 57 for rakes 1 and 2, respectively. Similar to the Mach number and total pressure results, this statistic was a general measure of the correlation method's ability to resolve the

cone-probe angle of attack, rather than being an indicator of the absolute angle of attack calibration accuracy. Over the $\pm 8^\circ$ angle of attack and sideslip range, the effective cone-probe angle of attack residuals were within a $2\sigma(\alpha_{C\text{cal}})$ of $\pm 0.1^\circ$. For most probes, the deviation between the calibrated cone-probe angle of attack and α_C remained relatively invariant with probe angle of attack and sideslip. Most excursions from this trend occurred at the extreme probe attitude angles and at the tunnel Mach number setting of 2.15.

Angle of Sideslip Correlation

Similar to the angle of attack correlation, the angle of sideslip for each cone-probe was referenced to the effective angle of sideslip, β_C . As a consequence, any probe misalignment in the yaw direction would appear as a bias error in the local cone-probe pressures. Referring to figure 32, β_C was nominally proportional to the directional sensitivity parameter, PR_{BD} . This observation is illustrated in figures 58 and 59, which are the respective cross-plots of figures 54 and 55 for rakes 1 and 2 at a nominal angle of attack of 0° and tunnel Mach number of 2.40. Similar trends were also obtained at other Mach numbers.

To avoid increased fit errors from data irregularities at higher angles, the cone-probe angle of sideslip analysis was limited to data within a model pitch range of $\pm 8^\circ$. From this reduced data set, the calibrated cone-probe angle of sideslip, $\beta_{C\text{cal}}$, was analytically correlated to the measured cone-probe pressures in the following manner:

$$\beta_{C\text{cal}} = \beta_0 - \Delta\beta_A - \Delta\beta_{\text{corr}} \quad (35)$$

The first term on the right side of equation 35 described the linear variation of β_C with PR_{BD} . β_0 was derived from the regression of β_C with PR_{BD} at a nominal angle of attack of zero for each tunnel Mach number condition:

$$\beta_0 = e_0 + e_1 PR_{BD} \quad (36)$$

The second term in equation 35 corrected for probe angle of sideslip variations due to angle of attack. $\Delta\beta_A$ was determined from a fourth-order polynomial regression relating $(\beta_C - \beta_0)$ to PR_{BD} at a constant M_{set} and angle of attack:

$$\Delta\beta_A = \beta_C - \beta_0 = f_0 + f_1 PR_{BD} + f_2 PR_{BD}^2 + f_3 PR_{BD}^3 + f_4 PR_{BD}^4 \quad (37)$$

Since PR_{AC} was assumed to be nearly invariant with angle of sideslip, each coefficient in equation 37 was correlated to an average longitudinal sensitivity parameter, $PR_{AC\text{avg}}$, using a sixth-order regression of the form:

$$f_i = g_{0i} + g_{1i} PR_{AC\text{avg}} + g_{2i} PR_{AC\text{avg}}^2 + g_{3i} PR_{AC\text{avg}}^3 + g_{4i} PR_{AC\text{avg}}^4 + g_{5i} PR_{AC\text{avg}}^5 + g_{6i} PR_{AC\text{avg}}^6 \quad (38)$$

where $i = 0$ to 4

For each cone-probe, PR_{ACavg} was computed at a nominally constant ϵ for each tunnel Mach number condition.

The last term in equation 35 corrected for any residuals, which resulted from relating β_C , β_0 , and $\Delta\beta_A$ to PR_{BD} at a constant tunnel Mach number:

$$\Delta\beta_{\text{corr}} = \beta_0 - \beta_C - \Delta\beta_A = h_0 + h_1 \text{PR}_{\text{BD}} + h_2 \text{PR}_{\text{BD}}^2 + h_3 \text{PR}_{\text{BD}}^3 + h_4 \text{PR}_{\text{BD}}^4 \quad (39)$$

To capture the β_C sensitivity to Mach number, the e, g, and h coefficients obtained at each of the three tunnel Mach numbers (2.15, 2.29, and 2.40) were analytically related to the corresponding values of PR_{T0} using a quadratic function obtained from regression analysis:

$$e_0 = C_{0,e0} + C_{1,e0} \text{PR}_{\text{T0}} + C_{2,e0} \text{PR}_{\text{T0}}^2$$

$$e_1 = C_{0,e1} + C_{1,e1} \text{PR}_{\text{T0}} + C_{2,e1} \text{PR}_{\text{T0}}^2$$

$$g_{0i} = C_{0,g0} + C_{1,g0} \text{PR}_{\text{T0}} + C_{2,g0} \text{PR}_{\text{T0}}^2$$

$$g_{1i} = C_{0,g1} + C_{1,g1} \text{PR}_{\text{T0}} + C_{2,g1} \text{PR}_{\text{T0}}^2$$

$$g_{2i} = C_{0,g2} + C_{1,g2} \text{PR}_{\text{T0}} + C_{2,g2} \text{PR}_{\text{T0}}^2$$

$$g_{3i} = C_{0,g3} + C_{1,g3} \text{PR}_{\text{T0}} + C_{2,g3} \text{PR}_{\text{T0}}^2$$

$$g_{4i} = C_{0,g4} + C_{1,g4} \text{PR}_{\text{T0}} + C_{2,g4} \text{PR}_{\text{T0}}^2$$

$$g_{5i} = C_{0,g5} + C_{1,g5} \text{PR}_{\text{T0}} + C_{2,g5} \text{PR}_{\text{T0}}^2$$

$$g_{6i} = C_{0,g6} + C_{1,g6} \text{PR}_{\text{T0}} + C_{2,g6} \text{PR}_{\text{T0}}^2$$

$$h_0 = C_{0,h0} + C_{1,h0} \text{PR}_{\text{T0}} + C_{2,h0} \text{PR}_{\text{T0}}^2$$

$$h_1 = C_{0,h1} + C_{1,h1} \text{PR}_{\text{T0}} + C_{2,h1} \text{PR}_{\text{T0}}^2$$

$$h_2 = C_{0,h2} + C_{1,h2} \text{PR}_{\text{T0}} + C_{2,h2} \text{PR}_{\text{T0}}^2$$

$$h_3 = C_{0,h3} + C_{1,h3} \text{PR}_{\text{T0}} + C_{2,h3} \text{PR}_{\text{T0}}^2$$

$$h_4 = C_{0,h4} + C_{1,h4} \text{PR}_{\text{T0}} + C_{2,h4} \text{PR}_{\text{T0}}^2$$

The second-order coefficients for e, g, and h are listed in tables 9 and 10 for rakes 1 and 2, respectively.

The two-standard deviation, $2\sigma(\beta_{\text{Ccal}})$, calculated from the residuals between β_{Ccal} and β_C is shown in figures 60 and 61 for rakes 1 and 2, respectively. As with the other cone-probe parameters, this statistic quantified the angle of sideslip resolution for the correlation method, rather than serving

as a measure of the absolute angle of sideslip calibration accuracy. Over the $\pm 8^\circ$ angle of attack and sideslip range, the effective cone-probe angle of sideslip residuals were within a $2\sigma(\beta_{C\text{cal}})$ of $\pm 0.1^\circ$. The deviation between the calibrated cone-probe angle of sideslip and β_C remained relatively invariant with probe angle of attack and sideslip on both rakes. Most excursions from this observation occurred at the extreme probe attitude angles.

UNCERTAINTY ANALYSIS

General Measurement Accuracy

Performing a comprehensive, end-to-end uncertainty analysis for each instrument and data acquisition process was essentially impractical. Instead, reasonable engineering judgments were made as to which measurement variables were most likely have a significant impact on the test section flow survey and cone-probe calibration quality. In many circumstances, various quality and control procedures were instituted prior to and during wind tunnel testing to ensure experimental deviations were within acceptable limits. Calibration information and test data pertaining to the dominant error sources were evaluated for propagating the measurement uncertainties into the computed results. Instrument and calibration working standard accuracies were estimated from UPWT installed calibration results and archived Langley metrology data. Comparisons with the manufacturer's specifications were made to assess the short-term accuracy and long-term stability of the measurement device, relative to the duration of each particular wind tunnel test entry. In all cases, the most conservative (highest uncertainty) figures were assumed in the analyses.

Uncertainties were estimated at the 95% confidence level, following the methods established in refs. 14–16. The total measurement uncertainty was expressed as the root-sum-square (RSS) of the bias and precision limits. Where applicable, correlated bias limits were included for measurement variables and computed parameters sharing common data paths or reference sources. A coverage factor of 2 was applied in estimating the precision limits for each independent measurement variable. Partial derivatives involving complex, implicit equations or recursive algorithms were evaluated using second-order accurate, central-difference approximations; the computational stepsizes were evaluated and selected to avoid numerical round-off errors, while minimizing the approximation error due to truncation (ref. 17).

Table 11 summarizes the estimated uncertainty for the measurement devices employed for both wedge and cone-probe tests. The tabulated results are limited to the static (wind-off) performance of the data acquisition devices and equipment. The estimates exclude errors associated with dynamic phenomena typically experienced during actual wind-on testing, such as flow unsteadiness, heat transfer, and vibration. The effects of pressure tubing delay time on sampling duration, gravimetric pressure variations (due to transducer elevation above/below test article) and leakage during test section depressurization were also neglected from these estimates.

Test Section Flow Angularity Uncertainties

The test section upflow uncertainty, U_μ , was estimated from a combination of the regression residuals produced by the $\epsilon - \alpha_{W\text{corr}}$ relationships (shown in fig. 19) and the measurement uncertainty of ϵ . Figure 62 shows the overall data scatter about the analytical expression for $\epsilon(\alpha_{W\text{corr}})$, with the error bars representing the total uncertainty in ϵ based on the static performance of the Q-flex accelerometer. Within $\pm 0.5^\circ$ of the presumed local upflow direction, U_μ was estimated to be $\pm 0.05^\circ$ in the surveyed region of each test section for all Mach number settings. Since the wedge was repeatedly tested at selected conditions, the random deviations represent the short- and mid-term data repeatability. Compared to the size of the error bars, the relatively larger data scatter indicates the upflow uncertainty comprised mostly wind-on data precision error.

Similar to the upflow uncertainty, the test section crossflow uncertainty, U_ξ , was estimated from a combination of the regression residuals resulting from the $\psi - \alpha_{W\text{corr}}$ correlation (shown in fig. 19) and the measurement uncertainty of ψ . Figure 63 shows the deviations about the analytical function for $\psi(\alpha_{W\text{corr}})$, with the error bars representing the total uncertainty in ψ based on the static performance of the tunnel strut yaw mechanism. Within $\pm 0.5^\circ$ of the presumed local crossflow direction, U_ξ was estimated to be $\pm 0.12^\circ$ in the surveyed region of both test sections for all Mach number settings. In contrast to the upflow error, the static measurement uncertainty for ψ dominated the wind-on measurement precision error, as characterized by the relative difference in magnitudes between the error bars and the data scatter.

Test Section Mach and Recovery Uncertainties

The test section Mach number uncertainty (U_{M1}) and total pressure recovery uncertainty ($U_{Pt1/Pt0}$) were estimated from the residuals about their respective linear distributions, shown in figures 23 and 24. The propagation of the wind-off pressure measurement bias and precision limits into the Method III Mach number computation algorithm were included.

Figure 64 shows the Method III Mach number deviation about the presumed linear distribution, with error bars representing the computational variations resulting from the pressure measurement uncertainties. For data acquired at wedge orientations within $\pm 0.25^\circ$ of the presumed local upflow and crossflow directions, U_{M1} was estimated to be ± 0.005 in the surveyed region of each test section for all Mach number settings. The comparable size of the error bars and data scatter indicates the Mach number uncertainty was equally composed of both wind-on measurement precision and calculation errors.

Figure 65 shows the total pressure recovery scatter about the presumed linear distribution, with error bars representing the computational variations resulting from the pressure measurement uncertainties. For data acquired at wedge orientations within $\pm 0.25^\circ$ of the presumed local upflow and crossflow directions, $U_{Pt1/Pt0}$ was estimated to be ± 0.01 ($\pm 1\%$ of P_{t0}) in the surveyed region of each test section for all Mach number settings. Unlike the Mach number uncertainty, the total pressure recovery uncertainty was dominated by calculation errors arising from the propagated pressure measurement uncertainties.

Although disparities existed between the Method I and II Mach number and total pressure recovery results, these deviations were excluded from the uncertainty analysis, since they were by-products of the interim solutions leading to the Method III results. Uncertainties from wedge pitot and static pressure measurement errors resulting from probe and orifice geometry were also neglected from the analyses, since these effects could not be quantified without additional experimental work.

Cone-Probe Mach Number and Pressure Recovery Uncertainties

The absolute uncertainty of the calibrated cone-probe Mach number (U_{M1c}) was estimated from the M_{1Ccal} correlation residuals, the uncertainty of the reference Mach number (U_{M1}), and the uncertainty resulting from the propagation of the wind-off bias and precision limits into the M_{1Ccal} calculations. U_{M1c} was estimated as the sum of $2\sigma(M_{1Ccal})$ and the RSS of U_{M1} and a statistic representing the nominal M_{1Ccal} calculation uncertainty. The latter term was expressed as the sum of the average and two-standard deviation of the calculation uncertainties computed from all data points contained within a prescribed cone-probe angle of attack and sideslip range.

The variation of U_{M1c} over selected ranges of cone-probe angles of attack and sideslip is presented in figures 68 and 69 for rakes 1 and 2, respectively. For many probes, the calculation uncertainty accounted for the majority of U_{M1c} , and was primarily due to the sensitivity of PR_{T0} and M_{1Ccal} to small cone-probe pressure changes. The absolute uncertainty in the calibrated cone-probe Mach number generally increased with increasing Mach number, typically ranging from ± 0.01 to ± 0.04 for both rakes.

Similar to the Mach number uncertainty, the absolute uncertainty of the calibrated cone-probe total pressure recovery ($U_{Pt1c/Pt0}$) was estimated from correlation residuals for P_{t1Ccal}/P_{t0} , the uncertainty of the reference test section total pressure recovery ($U_{Pt1/Pt0}$), and the uncertainty resulting from the propagation of the wind-off bias and precision limits through the P_{t1Ccal}/P_{t0} calculation process. $U_{Pt1c/Pt0}$ was estimated as the sum of $2\sigma(P_{t1Ccal}/P_{t0})$ and the RSS of $U_{Pt1/Pt0}$ and a statistic representing the nominal P_{t1Ccal}/P_{t0} calculation uncertainty. The last uncertainty component was the sum of the average and two-standard deviation of the calculation uncertainty computed from all data points contained within a prescribed cone-probe angle of attack and sideslip range.

The variation of $U_{Pt1c/Pt0}$ over selected ranges of cone-probe angles of attack and sideslip is shown in figures 68 and 69 for rakes 1 and 2, respectively. For all probes on both rakes, the calculation uncertainty accounted for nearly all of $U_{Pt1c/Pt0}$, and was approximately an order of magnitude greater than the correlation resolution defined by $2\sigma(P_{t1Ccal}/P_{t0})$. The relatively large P_{t1Ccal}/P_{t0} calculation uncertainty resulted from the accumulation of ESP system measurement errors in the calculation of PR_{T0} , M_{1Ccal} , and P_{tYcorr} . The contribution of the P_{t0} measurement uncertainty to $U_{Pt1c/Pt0}$ was relatively insignificant compared to the ESP system effect. The cone-probe total pressure recovery accuracy generally decreased with increasing Mach number, typically ranging from ± 0.03 to ± 0.1 ($\pm 3\%$ to $\pm 10\%$ of P_{t0}) for both rakes.

Cone-Probe Flow Angle Uncertainties

The absolute uncertainty of calibrated cone-probe angle of attack (U_{α_c}) was derived from the sum of $2\sigma(\alpha_{C_{cal}})$ and the RSS of the α_C uncertainty and $\alpha_{C_{cal}}$ calculation uncertainty resulting from the propagation of the wind-off bias and precision limits through the $\alpha_{C_{cal}}$ calculation process. The α_C uncertainty was obtained from the RSS of the bias and precision limits determined from equation 14. The variation of U_{α_c} over selected ranges of cone-probe angles of attack and sideslip is presented in figures 70 and 71 for rakes 1 and 2, respectively. At moderate angles of attack and sideslip, U_{α_c} was typically invariant with Mach number, and ranged between $\pm 0.1^\circ$ and $\pm 0.25^\circ$.

The calibrated cone-probe angle of sideslip total uncertainty (U_{β_c}) was derived from the sum of $2\sigma(\beta_{C_{cal}})$ and the RSS of the β_C uncertainty and the $\beta_{C_{cal}}$ calculation uncertainty resulting from the propagation of the wind-off bias and precision limits through the $\beta_{C_{cal}}$ calculation process. The β_C uncertainty was estimated by computing the RSS of the bias and precision limits from equation 14. The variation of U_{β_c} over selected ranges of cone-probe angles of attack and sideslip is presented in figures 72 and 73 for rakes 1 and 2, respectively. At moderate angles of attack and sideslip, $U_{\beta_{C_{cal}}}$ was typically invariant with Mach number, and ranged between $\pm 0.1^\circ$ and $\pm 0.2^\circ$.

CONCLUSIONS

A series of experimental investigations were conducted at the NASA Langley UPWT to calibrate cone-probe rakes for measuring the flow field on 1–2% scale, high-speed wind tunnel models between Mach 2.15 and 2.4. Reference conditions were established from test section flow measurements using a 10° supersonic wedge probe. All testing was performed at a constant Reynolds number per foot and humidity level.

The measured test section flow angularity was comparable to angularity measurements reported in previous UPWT calibration efforts. Three methods were used to calculate the freestream Mach number from wedge pressure measurements. The methods accounted for stagnation pressure losses between the tunnel settling chamber and test section. Method-dependent differences increased with test section Mach number, with Method III yielding the best compromise in Mach number and pressure recovery among the various methods. Testing a different wedge probe featuring a steeper half-angle than 10° would significantly reduce the Method I Mach number sensitivity to wedge surface pressure and inclination perturbations between Mach 2 and 2.5, but would aggravate the Method II Mach number sensitivity to similar effects over the same Mach range.

Two successful cone-probe rake assemblies were developed from an earlier 16-probe rake assembly that exhibited irregular pressure variations with flow incidence. Probe density and channel-flow blockage effects were found to have a profound impact on rake design and cone-probe data quality. Analytical expressions were developed to correlate cone-probe pressures to the reference flow conditions established from the test section flow surveys using the wedge probe. Recursive calculation techniques were required to establish the effect of compressibility and flow angularity on the measured flow parameters. The correlation algorithms resolved Mach number, pressure recovery, and flow angle to within ± 0.01 , $\pm 1\%$ and $\pm 0.1^\circ$, respectively, for cone-probe angles of attack and sideslip between $\pm 8^\circ$.

An uncertainty analysis was performed to estimate the absolute uncertainty of the test section flow survey and cone-probe calibration at the 95% confidence interval. UPWT test section upflow, crossflow, Mach number, and total pressure recovery had respective uncertainties of $\pm 0.05^\circ$, $\pm 0.12^\circ$, ± 0.005 , and $\pm 1\%$ (of tunnel settling chamber total pressure). Cone-probe angles of attack and sideslip were accurate to within $\pm 0.25^\circ$ and $\pm 0.2^\circ$, respectively. The calibrated cone-probe Mach number and total pressure uncertainty levels, respectively, varied from ± 0.01 to ± 0.04 and $\pm 3\%$ to $\pm 10\%$ (of tunnel settling chamber total pressure), generally increasing with Mach number on most probes. The estimated uncertainty for each of the calibrated cone-probe flow quantities in both rake designs was affected by the propagation of measurement errors into the calculated flow variables.

REFERENCES

1. Antonatos, P. P.; Surber, L. E.; and Stava, D. J.: Inlet/Airframe Interference and Integration. AGARD-LS-53, May 1972.
2. Smeltzer, D. B.: Top-Mounted Inlet Performance for a V/STOL Fighter/Attack Aircraft Configuration. NASA TM-88210, Jan. 1987.
3. VanDuine, A. A.; Rhoades, W. W.; and Swan, W. C.: Configuration Aspects of Propulsion Installation on Supersonic Transports. AGARD-CP-71-71, Sept. 1970.
4. Volluz, R. J.: Section 20 Wind Tunnel Instrumentation and Operation, Handbook of Supersonic Aerodynamics. NAVORD Report 1488, Vol. 6, 1961.
5. Centolanzi, F. J.: Characteristics of a 40° Cone for Measuring Mach Number, Total Pressure, and Flow Angles at Supersonic Speeds. NACA TN-3967, May 1957.
6. Jackson, C. M., Jr.; Corlett, W. A.; and Monta, W. J.: Description and Calibration of the Langley Unitary Plan Wind Tunnel. NASA TP-1905, Nov. 1981.
7. Hansley, J. F., Jr.: Pilot Calibration of the 9- by 7-Foot Test Section of the Ames Unitary Plan Wind Tunnel. Presented at the 54th Semi-Annual Meeting of the Supersonic Tunnel Association, Oct. 1980.
8. Cubbison, R. W.; and Meleason, E. T.: Water Condensation Effects of Heated Vitiated Air on Flow in a Large Supersonic Wind Tunnel. NASA TM X-1636, Aug. 1968.
9. Reed, T. D.; Pope, T. C.; and Cooksey, J. M.: Calibration of Transonic and Supersonic Wind Tunnels. NASA CR-2920, Nov. 1977.
10. Bobbitt, P. J.; and Darden, C. M.: A Wedge Shaped Supersonic Flow Field Probe. NASA CP-10133, Feb. 1994.
11. Ames Research Staff: Equations, Tables and Charts for Compressible Flow. NACA Report 1135, 1953.
12. Goldstein, R. J.: Fluid Mechanics Measurements. Second Edition, Taylor and Francis, Washington, D.C., 1996.
13. Gracey, W.: Wind Tunnel Investigation of a Number of Total-Pressure Tubes at High Angles of Attack – Subsonic, Transonic and Supersonic Speeds. NACA TN-3641, May 1956.

14. Saravanamuttoo, H. I. H.: Recommended Practices for Measurement of Gas Path Pressures and Temperatures for Performance Assessment of Aircraft Turbine Engines and Components. AGARD-AR-245, June 1990.
15. Working Group 15 of the AGARD Fluid Dynamics Panel: Quality Assessment for Wind Tunnel Testing, AGARD-AR-304, July 1994.
16. Coleman, H. W.; and Steele, W. G.: Experimentation and Uncertainty Analysis for Engineers. John Wiley & Sons, New York, 1989.
17. Maron, M. J.: Numerical Analysis, A Practical Approach, Macmillan Publishing Co., New York, 1982.

APPENDIX A

METHOD I MACH CALCULATION

All angles are in units of radians.

A. Iterate on $\cot\delta$ to solve for θ

Step 1: calculate $(\cot\delta)_{\text{iter}}$ by substituting $M_{1\text{iter}}$ for M_1 and θ_{iter} for θ in Eqn. 3

Step 2: calculate the $\cot\delta$ residual, $\text{ERR}(\cot\delta) = 1 - (\cot\delta)_{\text{iter}} / \cot\delta$

Step 3: if $|\text{ERR}(\cot\delta)| > 10^{-6}$, update θ_{iter} to $\theta_{\text{iter}} = \theta_{\text{iter}} - 0.01 * \text{ERR}(\cot\delta)$ and repeat Steps 1–2 by substituting the last updated value for θ_{iter} on each successive iteration cycle

B. Iterate on P_{t3}/P_{t2n} to solve for M_1 (from Eqn. 2)

Step 4: solve for $M_{2\text{iter}}$ by substituting $M_{1\text{iter}}$ for M_1 and the updated θ_{iter} (from Step 3) for θ in Eqn. 2

Step 5: calculate $(P_{t3}/P_{t2n})_{\text{iter}}$ by substituting $M_{1\text{iter}}$ for M_1 and $M_{2\text{iter}}$ for M_2 in Eqn. 8

Step 6: calculate the P_{t3}/P_{t2n} residual, $\text{ERR}(P_{t3}/P_{t2n}) = 1 - (P_{t3}/P_{t2n})_{\text{iter}} / (P_{t3}/P_{t2n})$

Step 7: if $|\text{ERR}(P_{t3}/P_{t2n})| > 10^{-6}$, update $M_{1\text{iter}}$ to $M_{1\text{iter}} = M_{1\text{iter}} + \text{ERR}(P_{t3}/P_{t2n})$ and repeat Steps 4–6 by substituting the last updated values for $M_{1\text{iter}}$ and θ_{iter} on each successive iteration cycle

C. Iterate on $M_2^2 \sin^2(\theta - \delta)$ to solve for M_1 (from Eqn. 6)

Step 8: calculate the left-hand side (LHS) of Eqn. 6 by substituting the last updated value for $M_{2\text{iter}}$ (from Step 4) for M_2 and θ_{iter} (from Step 3) for θ

Step 9: calculate the right-hand side (RHS) of Eqn. 6 by substituting the last updated value for $M_{1\text{iter}}$ (from Step 7) for M_1 and θ_{iter} (from Step 3) for θ

Step 10: calculate the Eqn. 6 residual, $\text{ERR}(\text{Eqn. 6}) = 1 - \text{LHS}(\text{Eqn. 6}) / \text{RHS}(\text{Eqn. 6})$

Step 11: if $|\text{ERR}(\text{Eqn. 6})| > 10^{-5}$, update the value of $M_{1\text{iter}}$ prior to Part B to $M_{1\text{iter}} = M_{1\text{iter}} - \text{ERR}(\text{Eqn. 6})$ and repeat Steps 1–10 by substituting the last updated values for $M_{1\text{iter}}$ and θ_{iter} on each successive iteration cycle

Once a solution has been reached at Step 11, equate $M_1 = M_{1\text{iter}}$.

APPENDIX B

METHOD II MACH CALCULATION

All angles are in units of radians.

A. Iterate on $\cot\delta$ to solve for θ

Step 1: calculate $(\cot\delta)_{\text{iter}}$ by substituting $M_{1\text{iter}}$ for M_1 and θ_{iter} for θ in Eqn. 3

Step 2: calculate the $\cot\delta$ residual, $\text{ERR}(\cot\delta) = 1 - (\cot\delta)_{\text{iter}} / \cot\delta$

Step 3: if $|\text{ERR}(\cot\delta)| > 10^{-6}$, update θ_{iter} to $\theta_{\text{iter}} = \theta_{\text{iter}} - 0.01 * \text{ERR}(\cot\delta)$ and repeat Steps 1–2 by substituting the last updated value for θ_{iter} on each successive iteration cycle

B. Iterate on P_{t2n}/P_2 to solve for M_1

Step 4: calculate $(P_{t2n}/P_2)_{\text{iter}}$ by substituting $M_{1\text{iter}}$ for M_1 and the updated θ_{iter} (from Step 3) for θ in Eqn. 7

Step 5: calculate the P_{t2n}/P_2 residual, $\text{ERR}(P_{t2n}/P_2) = (P_{t2n}/P_2)_{\text{iter}} - P_{t2n}/P_2$

Step 6: if $|\text{ERR}(P_{t2n}/P_2)| > 10^{-5}$, update $M_{1\text{iter}}$ to $M_{1\text{iter}} = M_{1\text{iter}} - 0.1 * \text{ERR}(P_{t2n}/P_2)$ and repeat Steps 1–5 by substituting the last updated values for $M_{1\text{iter}}$ and θ_{iter} on each successive iteration cycle

Once a solution has been reached at Step 6, equate $M_1 = M_{1\text{iter}}$.

APPENDIX C

METHOD III MACH CALCULATION

All angles are in units of radians.

A. Iterate on $\alpha_{W\text{eff},I}$ to solve for $M_{1A,I} = M_{1B,I} = M_{1,I}$

Step 1: calculate $\delta_{A\text{eff}}$ by substituting $\Delta\delta_{W\text{eff}}$ and $\alpha_{W\text{eff},I}$ into Eqn. 12

Step 2: calculate $\delta_{B\text{eff}}$ by substituting $\Delta\delta_{W\text{eff}}$ and $\alpha_{W\text{eff},I}$ into Eqn. 13

Step 3: calculate $M_{1A,I}$ by substituting $\delta_{A\text{eff}}$ for δ and \underline{P}_{t2n} for P_{t2n} , then performing Steps 1–11 of the pitot-pitot method (Method I) until a solution is obtained

Step 4: calculate $M_{1B,I}$ by substituting $\delta_{B\text{eff}}$ for δ and \underline{P}_{t2n} for P_{t2n} , then performing Steps 1–11 of Method I until a solution is obtained

Step 5: calculate the $M_{1,I}$ residual, $\text{ERR}(M_{1,I}) = M_{1A,I} - M_{1B,I}$

Step 6: if $|\text{ERR}(M_{1,I})| > 10^{-5}$, update $\alpha_{W\text{eff},I}$ to $\alpha_{W\text{eff},I} = \alpha_{W\text{eff},I} - 0.1 * \text{ERR}(M_{1,I})$ and repeat Steps 1–5 by substituting the last updated values for $M_{1\text{iter}}$, θ_{iter} and $\alpha_{W\text{eff},I}$ on each successive iteration cycle; otherwise, set $M_{1,I} = M_{1A,I}$

B. Iterate on $\alpha_{W\text{eff},II}$ to solve for $M_{1A,II} = M_{1B,II} = M_{1,II}$

Step 7: calculate $\delta_{A\text{eff}}$ by substituting $\Delta\delta_{W\text{eff}}$ and $\alpha_{W\text{eff},II}$ into Eqn. 12

Step 8: calculate $\delta_{B\text{eff}}$ by substituting $\Delta\delta_{W\text{eff}}$ and $\alpha_{W\text{eff},II}$ into Eqn. 13

Step 9: calculate $M_{1A,II}$ by substituting $\delta_{A\text{eff}}$ for δ and \underline{P}_{t2n} for P_{t2n} , then performing Steps 1–6 of the pitot-static method (Method II) until a solution is obtained

Step 10: calculate $M_{1B,II}$ by substituting $\delta_{B\text{eff}}$ for δ and \underline{P}_{t2n} for P_{t2n} , then performing Steps 1–6 of Method II until a solution is obtained

Step 11: calculate the $M_{1,II}$ residual, $\text{ERR}(M_{1,II}) = M_{1A,II} - M_{1B,II}$

Step 12: if $|\text{ERR}(M_{1,II})| > 10^{-5}$, update $\alpha_{W\text{eff},II}$ to $\alpha_{W\text{eff},II} = \alpha_{W\text{eff},II} + 0.1 * \text{ERR}(M_{1,II})$ and repeat Steps 7–12 by substituting the last updated values for $M_{1\text{iter}}$, θ_{iter} and $\alpha_{W\text{eff},II}$ on each successive iteration cycle; otherwise, set $M_{1,II} = M_{1A,II}$

C. Iterate on $\Delta\delta_{\text{Weff}}$ to solve for $M_{1,\text{I}} = M_{1,\text{II}} = M_1$

Step 13: using the results from Steps 6 and 12, calculate the M_1 residual $\text{ERR}(M_1) = M_{1,\text{I}} - M_{1,\text{II}}$

Step 14: if $|\text{ERR}(M_1)| > 10^{-5}$, update $\Delta\delta_{\text{Weff}}$ to $\Delta\delta_{\text{Weff}} = \Delta\delta_{\text{Weff}} + 0.1 * \text{ERR}(M_1)$ and repeat
Steps 1–13 by substituting the last updated values for $M_{1,\text{iter}}$, θ_{iter} and $\Delta\delta_{\text{Weff}}$ on each
successive iteration cycle; otherwise, set $M_1 = M_{1,\text{I}}$

APPENDIX D

SAMPLE CALCULATION FOR METHOD III

To demonstrate the process required for computing the freestream Mach number following the steps outlined for Method III, consider the input values given below, which are representative of the measured conditions for an instrumented 10° half-angle wedge tested at a nominal wind tunnel Mach number setting of 2.40:

$$P_{t2nA} = 11.3352 \text{ psia}$$

$$P_{t2nB} = 11.3128 \text{ psia}$$

$$P_{t3A} = 15.4106 \text{ psia}$$

$$P_{t3B} = 14.2464 \text{ psia}$$

$$P_{2A} = 3.0196 \text{ psia}$$

$$P_{2B} = 2.3911 \text{ psia}$$

$$\epsilon = \psi = -2.00^\circ$$

$$\delta_W = 10.1063^\circ$$

For convenience, the freestream pitot pressure, P_{t2n} , will be represented by the average of P_{t2nA} and P_{t2nB} for inclusion into the Method I and II calculations:

$$P_{t2n} = 11.3240 \text{ psia}$$

Angularity parameters are initialized to their starting values (in units of radians):

$$\alpha_{Weff,I} = \alpha_{Weff,II} = \epsilon = -0.0349 \text{ rad}$$

$$\delta_W = 0.1764 \text{ rad}$$

$$\Delta\delta_{Weff} = 0 \text{ rad}$$

$$\theta_{Aeff} = \theta_{Beff} = \theta_{iter} = 1.00 \text{ rad}$$

Since the ideal tunnel Mach number setting is known, let $M_{1iter} = 2.40$ for the first iteration cycle. Now that the initial conditions have been established, the calculations for Method III may begin:

A. Iterate on $\alpha_{\text{Weff},I}$ to solve for $M_{1A,I} = M_{1B,I} = M_{1,I}$

$$\text{Step 1: } \delta_{\text{Aeff}} = 0 + 0.1764 + 0.0349 = 0.2113$$

$$\text{Step 2: } \delta_{\text{Beff}} = 0 + 0.1764 - 0.0349 = 0.1415$$

Step 3: Iterate to solve for $M_{1A,I}$ from Method I

A. Iterate on $\cot\delta_{\text{Aeff}}$ to solve for θ_{Aeff}

Step 1:

$$(\cot\delta_A)_{\text{iter}} = \tan(1.00) \left\{ \frac{6 * 2.40^2}{5[2.40^2 \sin^2(1.00) - 1]} - 1 \right\} = 1.9394$$

$$\text{Step 2: } \text{ERR}(\cot\delta_{\text{Aeff}}) = 1 - 1.9394/\cot(0.2113) = 0.5840$$

Step 3: Since $|\text{ERR}(\cot\delta_{\text{Aeff}})| > 10^{-6}$, update $\theta_{\text{iter}} = 1.00 - 0.01 * 0.5840 = 0.9942$
and repeat Method I Steps 1–2; after 341 iterations, the following solution is obtained: $\theta_{\text{iter}} = \theta_{\text{Aeff}} = 0.6129$

B. Iterate on P_{t3A}/P_{t2n} to solve for $M_{1A,I}$ (from Eqn. 2)

Step 4:

$$M_{2_{\text{iter}}} = \left\{ \frac{36 * 2.40^4 \sin^2(0.6129)}{\left[7 * 2.40^2 \sin^2(0.6129) - 1 \right] \left[2.40^2 \sin^2(0.6129) + 5 \right]} - \frac{5[2.40^2 \sin^2(0.6129) - 1][7 * 2.40^2 \sin^2(0.6129) + 5]}{\left[7 * 2.40^2 \sin^2(0.6129) - 1 \right] \left[2.40^2 \sin^2(0.6129) + 5 \right]} \right\}^{\frac{1}{2}} = 1.9137$$

Step 5:

$$\begin{aligned} \frac{P_{t3A}}{P_{t2n}} &= \left[\frac{7 * 2.40^2 \sin^2(0.6129) - 1}{6} \right] \left(\frac{1.9137}{2.40} \right)^7 \left(\frac{7 * 2.40^2 - 1}{7 * 1.9137^2 - 1} \right)^{\frac{5}{2}} \\ &= 1.3567 \end{aligned}$$

$$\text{Step 6: } \text{ERR}(P_{t3A}/P_{t2n}) = 1 - 1.3567/(15.4106/11.3240) = .0031$$

Step 7: Since $|\text{ERR}(P_{t3A}/P_{t2n})| > 10^{-6}$, update $M_1 = 2.40 + 0.0031 = 2.4031$ and repeat Method I

Steps 4–6; after 15 iterations, the following solutions are obtained:

$$M_{1\text{iter}} = 2.4071, M_{2\text{iter}} = 1.9161$$

C. Iterate on $M_2^2 \sin^2(\theta_{\text{Beff}} - \delta_{\text{Aeff}})$ to solve for $M_{1A,I}$ (from Eqn. 6)

$$\text{Step 8: LHS(Eqn. 6)} = 1.9161^2 \sin^2(0.6129 - 0.2113) = 0.5610$$

Step 9:

$$\text{RHS(Eqn.6)} = \frac{2.4071^2 \sin^2(0.6129) + 5}{7 * 2.4071^2 \sin^2(0.6129) - 1} = 0.5569$$

$$\text{Step 10: } \text{ERR(Eqn. 6)} = 1 - 0.5610/0.5569 = -0.0073$$

Step 11: Since $|\text{ERR(Eqn. 6)}| > 10^{-5}$, update $M_{1\text{iter}} = 2.40 + 0.0073 = 2.4073$ and repeat Method I Steps 1–10; after 9 iterations, the following solution is obtained: $M_{1\text{iter}} = M_{1A,I} = 2.4133$

Step 4: Iterate to solve for $M_{1B,I}$ from Method I

A. Iterate on $\cot \delta_{\text{Beff}}$ for θ_{Beff}

Step 1:

$$(\cot \delta_B)_{\text{iter}} = \tan(1.00) \left\{ \frac{6 * 2.40^2}{5[2.40^2 \sin^2(1.00) - 1]} - 1 \right\} = 1.9394$$

$$\text{Step 2: } \text{ERR}(\cot \delta_{\text{Beff}}) = 1 - 1.9394/\cot(0.1415) = 0.7238$$

Step 3: Since $|\text{ERR}(\cot \delta_{\text{Beff}})| > 10^{-6}$, update $\theta_{\text{iter}} = 1.00 - 0.01 * 0.7238 = 0.9928$ and repeat Method I Steps 1–2; after 236 iterations, the following solution is obtained: $\theta_{\text{iter}} = \theta_{\text{Beff}} = 0.5453$

B. Iterate on P_{t3B}/P_{t2n} to solve for $M_{1B,I}$ (from Eqn. 2)

Step 4:

$$M_{2\text{iter}} = \left\{ \frac{36 * 2.40^4 \sin^2(0.5453)}{7 * 2.40^2 \sin^2(0.5453) - 1} \right\} \left[\frac{5[2.40^2 \sin^2(0.5453) - 1][7 * 2.40^2 \sin^2(0.5453) + 5]}{7 * 2.40^2 \sin^2(0.5453) - 1} \right]^{\frac{1}{2}} = 2.0752$$

Step 5:

$$\begin{aligned}\frac{P_{t3B}}{P_{t2n}} &= \left[\frac{7 * 2.40^2 \sin^2(0.5453) - 1}{6} \right] \left(\frac{2.0752}{2.40} \right)^7 \left(\frac{7 * 2.40^2 - 1}{7 * 2.0752^2 - 1} \right)^{\frac{5}{2}} \\ &= 1.2540\end{aligned}$$

Step 6: $\text{ERR}(P_{t3B}/P_{t2n}) = 1 - 1.2540/(14.2464/11.3240) = 0.0033$

Step 7: Since $|\text{ERR}(P_{t3B}/P_{t2n})| > 10^{-6}$, update $M_1 = 2.40 + 0.0034 = 2.4033$ and repeat Method I Steps 4–6; after 14 iterations, the following solutions are obtained: $M_{1\text{iter}} = 2.4071$ $M_{2\text{iter}} = 2.0778$

C. Iterate on $M_2^2 \sin^2(\theta_{\text{Beff}} - \delta_{\text{Beff}})$ to solve for $M_{1B,I}$ (from Eqn. 6)

Step 8: $\text{LHS}(\text{Eqn 6}) = 2.0778^2 \sin^2(0.5453 - 0.1415) = 0.6667$

Step 9:

$$\text{RHS}(\text{Eqn.6}) = \frac{2.4071^2 \sin^2(0.5453) + 5}{7 * 2.4071^2 \sin^2(0.5453) - 1} = 0.6617$$

Step 10: $\text{ERR}(\text{Eqn. 6}) = 1 - 0.6667/0.6617 = -0.0076$

Step 11: Since $|\text{ERR}(\text{Eqn. 6})| > 10^{-5}$, update $M_{1\text{iter}} = 2.40 + 0.0076 = 2.4076$ and repeat Method I Steps 1–10; after 15 iterations, the following solution is obtained: $M_{1\text{iter}} = M_{1B,I} = 2.4202$

Step 5: $\text{ERR}(M_{1,I}) = 2.4133 - 2.4202 = -0.0069$

Step 6: Since $|\text{ERR}(M_{1,I})| > 10^{-5}$, update $\alpha_{\text{Weff},I} = -0.0349 + 0.1 * 0.0069 = -0.0342$ rad and repeat Method III Steps 1–5; after 5 iterations, the following solutions are obtained: $M_{1A,I} = M_{1B,I} = M_{1,I} = 2.4156$, $\alpha_{\text{Weff},I} = -0.0343$ rad

B. Iterate on $\alpha_{\text{Weff},II}$ to solve for $M_{1A,II} = M_{1B,II} = M_{1,II}$

Step 7: $\delta_{\text{Aeff}} = 0 + 0.1764 - 0.0349 = 0.2113$

Step 8: $\delta_{\text{Beff}} = 0 + 0.1764 + 0.0349 = 0.1415$

Step 9: Iterate for $M_{1A,II}$ from Method II

A. Iterate on $\cot\delta_{A\text{eff}}$ to solve for $\theta_{A\text{eff}}$

Step 1:

$$(\cot\delta_A)_{\text{iter}} = \tan(1.00) \left\{ \frac{6 * 2.40^2}{5[2.40^2 \sin^2(1.00) - 1]} - 1 \right\} = 1.9394$$

Step 2: $\text{ERR}(\cot\delta_{A\text{eff}}) = 1 - 1.9394/\cot(0.2113) = 0.5840$

Step 3: Since $|\text{ERR}(\cot\delta_{A\text{eff}})| > 10^{-6}$, update $\theta_{\text{iter}} = 1.00 - 0.01 * 0.5840 = 0.9942$
and repeat Method I Steps 1–2; after 341 iterations, the following solution
is obtained: $\theta_{\text{iter}} = \theta_{A\text{eff}} = 0.6129$

B. Iterate on P_{t2n}/P_{2A} to solve for $M_{1A,II}$

Step 4:

$$\begin{aligned} \frac{P_{t2n}}{P_{2A}} &= \left[\frac{6}{7 * 2.40^2 \sin^2(0.6129) - 1} \right] \left(\frac{6 * 2.40^2}{5} \right)^{\frac{7}{2}} \left(\frac{6}{7 * 2.40^2 - 1} \right)^{\frac{5}{2}} \\ &= 3.8391 \end{aligned}$$

Step 5: $\text{ERR}(P_{t2n}/P_{2A}) = 3.8391 - 11.3240/3.0196 = 0.0890$

Step 6: Since $|\text{ERR}(P_{t2n}/P_{2A})| > 10^{-6}$, update $M_{1\text{iter}} = 2.40 - 0.1 * 0.0890 = 2.3911$
and repeat Method II Steps 1–5; after 38 iterations, the following solution
is obtained: $M_{1\text{iter}} = M_{1A,II} = 2.3589$

Step 10: Iterate to solve for $M_{1B,II}$ from Method II

A. Iterate on $\cot\delta_{B\text{eff}}$ for $\theta_{B\text{eff}}$

Step 1:

$$(\cot\delta_B)_{\text{iter}} = \tan(1.00) \left\{ \frac{6 * 2.40^2}{5[2.40^2 \sin^2(1.00) - 1]} - 1 \right\} = 1.9394$$

Step 2: $\text{ERR}(\cot\delta_{B\text{eff}}) = 1 - 1.9394/\cot(0.1415) = 0.7238$

Step 3: Since $|ERR(\cot\delta_{Beff})| > 10^{-6}$, update $\theta_{iter} = 1.00 - 0.01*0.7238 = 0.9928$
and repeat Method I Steps 1–2; after 236 iterations, the following solution
is obtained: $\theta_{iter} = \theta_{Beff} = 0.5453$

B. Iterate on P_{t2n}/P_{2B} to solve for $M_{1B,II}$

Step 4:

$$\frac{P_{t2n}}{P_{2B}} = \left[\frac{6}{7 * 2.40^2 \sin^2(0.5453) - 1} \right] \left(\frac{6 * 2.40^2}{5} \right)^{\frac{7}{2}} \left(\frac{6}{7 * 2.40^2 - 1} \right)^{\frac{5}{2}}$$

$$= 4.8110$$

Step 5: $ERR(P_{t2n}/P_{2B}) = 4.8110 - 11.3240/2.3911 = 0.0751$

Step 6: Since $|ERR(P_{t2n}/P_{2B})| > 10^{-6}$, update $M_1 = 2.40 - 0.1*0.0751 = 2.3925$
and repeat Method II Steps 1–5; after 26 iterations, the following solution
is obtained: $M_{1iter} = M_{1B,II} = 2.3750$

Step 11: $ERR(M_{1,II}) = 2.3589 - 2.3750 = -0.0161$

Step 12: Since $|ERR(M_{1,I})| > 10^{-5}$, update $\alpha_{Weff,II} = -0.0349 - 0.1*0.0161 = -0.0365$ rad
and repeat Method III Steps 7–12; after 3 iterations, the following solutions are
obtained: $M_{1A,II} = M_{1B,II} = M_{1,II} = 2.3671$, $\alpha_{Weff,II} = -0.0364$ rad

C. Iterate on $\Delta\delta_{Weff}$ to solve for $M_{1,I} = M_{1,II} = M_1$

Step 13: $ERR(M_1) = 2.4156 - 2.3671 = 0.0485$

Step 14: Since $|ERR(M_1)| > 10^{-5}$, update $\Delta\delta_{Weff} = 0 + 0.1*0.0485 = 0.0048$ and
repeat Method III Steps 1–13; after 3 iterations, the following solutions are
obtained: $M_{1,I} = M_{1,II} = M_1 = 2.3916$, $\Delta\delta_{Weff} = 0.0046$ rad = 0.261° ,
 $\alpha_{Weff,I} = -0.0359$ rad = -2.057° , $\alpha_{Weff,II} = -0.0364$ rad = -2.086°

APPENDIX E

SAMPLE COMPRESSIBILITY PARAMETER CALCULATION

To demonstrate the calculation process for determining the cone-probe fundamental compressibility parameter, probe 4 on rake 1 will be analyzed. The following probe data are provided for the computations:

$$P_{t0} = 18.645 \text{ psia}$$

$$P_{tY} = 12.0886 \text{ psia}$$

$$P_A = 4.8990 \text{ psia}$$

$$P_B = 3.0313 \text{ psia}$$

$$P_C = 2.8279 \text{ psia}$$

$$P_D = 4.2387 \text{ psia}$$

The compressibility parameter is computed from Eqn. 15:

$$PR_T = \frac{4.8990 + 3.0313 + 2.8279 + 4.2387}{4 * 12.0886} = 0.31014$$

The longitudinal and directional sensitivity parameters are computed from Eqn. 16:

$$PR_{AC} = \frac{4.8990 - 2.8279}{12.0886} = 0.17133$$

$$PR_{BD} = \frac{3.0313 - 4.2387}{12.0886} = -0.099879$$

To calculate the fundamental compressibility parameter in Eqn. 21, the quadratic coefficients in table 2 (probe 4, rake 1) and an initial guess for PR_{T0} are required to initiate the iterative computations. For the first iteration cycle, $PR_{T0} = 0.28000$ is assumed:

$$PR_{ACbiasT} = 5.15935 - 36.2706 * 0.28000 + 63.2252 * 0.28000^2 = -0.0395623$$

$$PR_{BDbiasT} = 0.10258 - 0.064912 * 0.28000 - 0.598695 * 0.28000^2 = 0.0374670$$

$$l_{T1} = 3.07195E+04 - 2.09517E+05 * 0.28000 + 3.56703E+05 * 0.28000^2 = 20.25520$$

$$l_{T2} = -6.77677E+08 + 4.76863E+09 * 0.28000 - 8.33091E+09 * 0.28000^2 = 4.39606E+06$$

$$l_{T3} = 8.06312E+12 - 5.56876E+13*0.28000 + 9.58164E+13*0.28000^2 = -1.74022E+10$$

From Eqn. 18:

$$PR_{ACBDcorrT} = [(0.17133 - 0.0395623)^2 + (-0.099879 + 0.0374670)^2]^{1/2} = 0.14580$$

From Eqn. 19:

$$x_T = 0.14580 * 0.31014^7 = 4.02407E-05$$

Equating Eqn. 21 to the arbitrary variable, G:

$$\begin{aligned} G &= PR_T - (l_{T1}x_T + l_{T2}x_T^2 + l_{T3}x_T^3) - PR_{T0} \\ &= 0.31014 - (20.25520 * 4.02407E-05 + 4.39606E+06 * 4.02407E-05^2 \\ &\quad - 1.74022E+10 * 4.02407E-05^3) - 0.28000 = 0.023340 \end{aligned}$$

Since $G \neq 0$, the value for PR_{T0} is updated by incrementing its initial value by G:

$$PR_{T0} = 0.28000 + 0.023340 = 0.30334$$

The new value for PR_{T0} is then used in the next iteration cycle, repeating the process until $G \approx 0$ is reached. Subsequent calculation results are tabulated below, with PR_{T0} incremented by G between consecutive iterations. A reasonable solution for PR_{T0} is obtained after five computational cycles, yielding $PR_{T0} = 0.30711$.

Iteration	0	1	2	3	4	5
PR_{T0}	0.28000	0.30334	0.30730	0.30709	0.30711	0.30711
$PR_{ACbiasT}$	-0.0395623	-0.0252966	-0.0160486	-0.0165702	-0.0165271	-0.0165306
$PR_{BDbiasT}$	0.0374670	0.0278005	0.0260969	0.0261846	0.0261774	0.0261780
l_{T1}	20.25520	-13.30272	19.53804	17.58502	17.74599	17.73289
l_{T2}	4.39606E+06	2.26916E+06	1.00869E+06	1.07957E+06	1.07371E+06	1.07419E+06
l_{T3}	-1.74022E+10	-1.25949E+10	-1.43006E+09	-2.07467E+09	-2.02147E+09	-2.02580E+09
$PR_{ACBDcorrT}$	0.14580	0.16285	0.17192	0.17141	0.17145	0.17145
x_T	4.02407E-05	4.49469E-05	4.74491E-05	4.73087E-05	4.73203E-05	4.73194E-05
G	2.3340E-02	3.9571E-03	-2.0263E-04	1.6817E-05	-1.3675E-06	1.1139E-07

Table 1. Linear coefficients for referenced test section flow conditions

Flow Parameter	UPWT TS	1	2	2
	M_{set}	2.15	2.29	2.40
Upflow, $\mu(z)$	Slope (deg/in)	3.36039E-02	2.07784E-02	4.93372E-02
	Intercept (deg)	7.65491E-01	-2.17092E-01	-9.43008E-01
Crossflow, $\xi(z)$	Slope (deg/in)	9.16905E-03	1.60458E-02	1.31805E-02
	Intercept (deg)	-2.25905E-01	-1.82585E-01	-1.21052E-01
Mach Number, $M_1(z)$	Slope (1/in)	-3.22233E-04	-2.84782E-03	-6.72053E-04
	Intercept	2.14666E+00	2.32673E+00	2.40666E+00
Recovery, $P_{t1}(z)/P_{t0}$	Slope (1/in)	4.09665E-04	-3.93429E-04	-1.08764E-04
	Intercept	9.79078E-01	9.90679E-01	9.90974E-01

Table 2. Coefficients for the rake 1 fundamental compressibility parameter

Probe	PR _{ACbiasT}			PR _{BDbiasT}		
	j _{T0}	j _{T1}	j _{T2}	k _{T0}	k _{T1}	k _{T2}
1	3.87742E+00	-2.66679E+01	4.63012E+01	2.86931E+00	-1.89661E+01	3.11012E+01
2	5.28361E-01	-3.49127E+00	6.07979E+00	-3.30830E+00	2.45834E+01	-4.51360E+01
3	8.49070E-01	-5.68873E+00	8.95443E+00	2.22154E+00	-1.50582E+01	2.52124E+01
4	5.15935E+00	-3.62706E+01	6.32252E+01	1.02580E-01	-6.49120E-02	-5.98695E-01
5	5.63140E+00	-3.93874E+01	6.80277E+01	-6.68240E-01	5.53303E+00	-1.07184E+01
6	8.59335E+00	-6.04494E+01	1.05093E+02	7.61857E+00	-5.32185E+01	9.21083E+01
7	1.97692E+00	-1.44429E+01	2.66561E+01	3.79681E+00	-2.59426E+01	4.32231E+01
8	4.78194E+00	-3.45141E+01	6.24782E+01	-3.79044E+00	2.70781E+01	-4.79276E+01

Probe	l _{T1}			l _{T2}		
	m _{T0}	m _{T1}	m _{T2}	n _{T0}	n _{T1}	n _{T2}
1	1.58058E+03	-9.24322E+03	1.29533E+04	1.38249E+08	-7.94744E+08	1.14496E+09
2	-1.83096E+04	1.26027E+05	-2.16348E+05	1.52206E+09	-1.02663E+10	1.73077E+10
3	1.67459E+04	-1.14558E+05	1.95501E+05	-1.68057E+07	3.72535E+08	-1.02077E+09
4	3.07195E+04	-2.09517E+05	3.56703E+05	-6.77677E+08	4.76863E+09	-8.33091E+09
5	-6.01080E+03	4.09694E+04	-6.94673E+04	1.26761E+09	-8.39949E+09	1.39224E+10
6	-1.22838E+04	8.46945E+04	-1.45400E+05	1.65003E+09	-1.11961E+10	1.89905E+10
7	2.63328E+04	-1.83701E+05	3.19977E+05	-2.79863E+08	2.18200E+09	-4.15443E+09
8	3.44547E+04	-2.39254E+05	4.14789E+05	-3.26454E+08	2.54921E+09	-4.84185E+09

Probe	l _{T3}		
	q _{T0}	q _{T1}	q _{T2}
1	6.37023E+11	-5.79083E+12	1.19568E+13
2	-2.35611E+13	1.59432E+14	-2.69461E+14
3	-7.11149E+12	4.52070E+13	-7.19047E+13
4	8.06312E+12	-5.56876E+13	9.58164E+13
5	-2.24793E+13	1.50161E+14	-2.50657E+14
6	-2.74790E+13	1.87227E+14	-3.18675E+14
7	-2.06300E+12	1.15934E+13	-1.57623E+13
8	-1.47602E+12	7.09834E+12	-7.43957E+12

Table 3. Coefficients for the rake 2 fundamental compressibility parameter

Probe	PR _{ACbiasT}			PR _{BDbiasT}		
	j _{T0}	j _{T1}	j _{T2}	k _{T0}	k _{T1}	k _{T2}
1	9.93132E+00	-7.02481E+01	1.25008E+02	1.11886E+00	-7.90968E+00	1.44470E+01
2	9.00664E-01	-5.68633E+00	8.77864E+00	-2.09080E+00	1.36876E+01	-2.14667E+01
3	1.82968E+00	-1.18867E+01	1.81672E+01	2.64358E+00	-1.91381E+01	3.52681E+01
4	8.45330E-01	-5.51382E+00	8.62861E+00	-3.58330E+00	2.43530E+01	-4.07843E+01
5	3.19486E-01	-2.03997E+00	3.04712E+00	1.33559E+00	-9.54829E+00	1.73636E+01
6	3.21875E-01	-2.01510E+00	3.12523E+00	-4.91985E+00	3.47691E+01	-6.14264E+01

Probe	l _{T1}			l _{T2}		
	m _{T0}	m _{T1}	m _{T2}	n _{T0}	n _{T1}	n _{T2}
1	2.06233E+04	-1.46753E+05	2.60069E+05	-3.18328E+08	2.56042E+09	-4.98197E+09
2	-4.70170E+03	3.00921E+04	-4.80485E+04	5.16231E+08	-3.26680E+09	5.17226E+09
3	1.53285E+03	-1.01725E+04	1.70501E+04	6.25352E+08	-4.15146E+09	6.89531E+09
4	9.64282E+03	-6.57495E+04	1.11863E+05	2.88196E+08	-1.74190E+09	2.62960E+09
5	2.69995E+04	-1.85611E+05	3.18400E+05	-2.36035E+08	1.91786E+09	-3.73149E+09
6	5.19332E+02	-3.03113E+03	4.38688E+03	9.65690E+08	-6.38848E+09	1.05800E+10

Probe	l _{T3}		
	q _{T0}	q _{T1}	q _{T2}
1	5.75679E+10	-4.22371E+12	1.33308E+13
2	-7.26511E+12	4.67084E+13	-7.50726E+13
3	-1.05745E+13	7.12439E+13	-1.19932E+14
4	-6.39594E+12	4.09404E+13	-6.55337E+13
5	-5.84456E+12	3.56734E+13	-5.42728E+13
6	-1.74805E+13	1.16582E+14	-1.94380E+14

Table 4. Coefficients for the correlated cone-probe Mach number

Rake 1

Probe	C_{M0}	C_{M1}	C_{M2}	C_{M3}	C_{M4}
1	2.33044E+02	-3.14176E+03	1.62034E+04	-3.74331E+04	3.25984E+04
2	2.80307E+02	-3.73303E+03	1.89423E+04	-4.29993E+04	3.67824E+04
3	3.70722E+02	-5.03217E+03	2.59138E+04	-5.95573E+04	5.14687E+04
4	3.64916E+02	-4.97030E+03	2.56820E+04	-5.92071E+04	5.13040E+04
5	1.76437E+02	-2.30498E+03	1.15905E+04	-2.61944E+04	2.23870E+04
6	3.29945E+02	-4.44655E+03	2.27815E+04	-5.21623E+04	4.49662E+04
7	7.72448E+02	-1.06503E+04	5.53223E+04	-1.27858E+05	1.10859E+05
8	6.53954E+02	-9.06530E+03	4.73970E+04	-1.10290E+05	9.62826E+04

Rake 2

Probe	C_{M0}	C_{M1}	C_{M2}	C_{M3}	C_{M4}
1	4.65158E+02	-6.38506E+03	3.31650E+04	-7.67892E+04	6.67872E+04
2	-7.55773E+01	1.09500E+03	-5.58619E+03	1.23522E+04	-1.00548E+04
3	3.08335E+02	-4.20947E+03	2.18715E+04	-5.07838E+04	4.43704E+04
4	1.56175E+02	-2.13051E+03	1.11995E+04	-2.63645E+04	2.33454E+04
5	4.57895E+02	-6.27249E+03	3.25119E+04	-7.51096E+04	6.51741E+04
6	3.32854E+02	-4.51493E+03	2.32649E+04	-5.35244E+04	4.63107E+04

Table 5. Coefficients for the rake 1 correlated pitot pressure

Probe	PR _{ACbiasY}			PR _{BDbiasY}		
	j _{Y0}	j _{Y1}	j _{Y2}	k _{Y0}	k _{Y1}	k _{Y2}
1	8.29654E+00	-5.45409E+01	9.02695E+01	7.04530E+00	-4.27674E+01	6.50728E+01
2	1.59908E+00	-1.30324E+01	2.63212E+01	-1.21605E+01	8.33190E+01	-1.42183E+02
3	-5.43298E+00	3.82491E+01	-6.67566E+01	-6.91918E+00	4.86581E+01	-8.45437E+01
4	-1.22145E+01	8.35608E+01	-1.43777E+02	2.80416E+00	-2.02750E+01	3.75520E+01
5	-1.03334E+01	7.32933E+01	-1.28354E+02	-4.72693E+00	3.27423E+01	-5.59399E+01
6	-8.72178E+00	6.12402E+01	-1.07246E+02	-2.26857E+00	1.28667E+01	-1.69234E+01
7	3.78072E+01	-2.54995E+02	4.29077E+02	7.12244E+01	-4.94571E+02	8.59493E+02
8	-1.41770E+01	9.95480E+01	-1.75158E+02	3.57808E+01	-2.47096E+02	4.27543E+02

Probe	l _{Y0}			l _{Y1}		
	m _{Y0}	m _{Y1}	m _{Y2}	n _{Y0}	n _{Y1}	n _{Y2}
1	7.89082E-01	-5.24939E+00	8.72743E+00	-8.32726E+00	5.56242E+01	-9.28902E+01
2	1.65910E-01	-1.19790E+00	2.16107E+00	7.84932E-02	1.55938E+00	-6.42128E+00
3	-3.35901E-01	2.33696E+00	-4.05133E+00	1.58962E+01	-1.09923E+02	1.89773E+02
4	1.49569E-01	-1.06437E+00	1.89135E+00	-1.80404E+01	1.26471E+02	-2.20702E+02
5	-6.82582E-01	4.71575E+00	-8.11587E+00	2.41466E+01	-1.66767E+02	2.87483E+02
6	1.00458E+00	-6.92463E+00	1.19246E+01	-3.00658E+01	2.07259E+02	-3.56780E+02
7	3.52092E+00	-2.44043E+01	4.22494E+01	-4.24751E+01	2.97986E+02	-5.21706E+02
8	1.66867E+00	-1.14532E+01	1.96400E+01	-4.25231E+01	2.95437E+02	-5.12372E+02

Probe	l _{Y2}			l _{Y3}		
	q _{Y0}	q _{Y1}	q _{Y2}	r _{Y0}	r _{Y1}	r _{Y2}
1	5.62939E+01	-3.88147E+02	6.68547E+02	-1.27378E+02	8.78309E+02	-1.50763E+03
2	4.27282E+01	-3.10965E+02	5.63794E+02	-1.66779E+02	1.18952E+03	-2.11200E+03
3	-4.56012E+01	3.10908E+02	-5.29136E+02	-1.27297E+01	1.03173E+02	-2.00380E+02
4	8.80715E+01	-6.18125E+02	1.07876E+03	-1.88754E+02	1.32376E+03	-2.30389E+03
5	-9.49885E+01	6.54664E+02	-1.12669E+03	9.91666E+01	-6.82282E+02	1.17691E+03
6	2.24289E+02	-1.54151E+03	2.64535E+03	-5.75457E+02	3.95735E+03	-6.79059E+03
7	1.41764E+02	-9.99892E+02	1.75922E+03	-2.23568E+02	1.58096E+03	-2.78707E+03
8	1.60641E+02	-1.12022E+03	1.94994E+03	-3.34916E+02	2.33956E+03	-4.07337E+03

Table 6. Coefficients for the rake 2 correlated pitot pressure

Probe	PR _{ACbiasY}			PR _{BDbiasY}		
	j _{Y0}	j _{Y1}	j _{Y2}	k _{Y0}	k _{Y1}	k _{Y2}
1	1.48164E+02	-1.06940E+03	1.92808E+03	-2.59948E+01	1.81374E+02	-3.15152E+02
2	-9.41593E+00	6.09611E+01	-9.76655E+01	-1.66137E+01	1.09317E+02	-1.79442E+02
3	-1.39187E+01	9.48970E+01	-1.61171E+02	-1.70108E+01	1.16641E+02	-1.99094E+02
4	-2.30889E+01	1.56052E+02	-2.62947E+02	-9.71864E+00	6.27243E+01	-1.00263E+02
5	-2.77804E+00	2.17327E+01	-4.09851E+01	1.29981E+00	-8.66107E+00	1.58137E+01
6	-9.28830E+00	6.56415E+01	-1.15690E+02	-5.98352E+00	3.90973E+01	-6.31288E+01

Probe	l _{Y0}			l _{Y1}		
	m _{Y0}	m _{Y1}	m _{Y2}	n _{Y0}	n _{Y1}	n _{Y2}
1	6.45120E+01	-4.64419E+02	8.35403E+02	-1.42209E+02	1.02574E+03	-1.84881E+03
2	-6.62600E-01	4.41139E+00	-7.31172E+00	1.63948E+01	-1.08607E+02	1.79199E+02
3	-9.25139E-01	6.59552E+00	-1.17371E+01	1.13087E+01	-8.00691E+01	1.41381E+02
4	9.13222E-01	-6.17167E+00	1.04271E+01	-2.20381E+01	1.48465E+02	-2.49878E+02
5	-1.56077E-01	1.09013E+00	-1.89314E+00	5.16780E+00	-3.59794E+01	6.22707E+01
6	5.25079E-01	-3.63955E+00	6.30702E+00	-1.16770E+01	7.99787E+01	-1.36973E+02

Probe	l _{Y2}			l _{Y3}		
	q _{Y0}	q _{Y1}	q _{Y2}	r _{Y0}	r _{Y1}	r _{Y2}
1	3.92529E+01	-3.01366E+02	5.76542E+02	1.30659E+02	-8.86298E+02	1.49963E+03
2	-4.89702E+01	3.24488E+02	-5.34262E+02	1.05893E+01	-6.77587E+01	1.06358E+02
3	-5.40714E+01	3.78970E+02	-6.62078E+02	4.28084E+01	-2.91183E+02	4.94509E+02
4	1.20493E+02	-8.09580E+02	1.35881E+03	-2.58686E+02	1.73712E+03	-2.91018E+03
5	-4.33565E+01	3.00331E+02	-5.17057E+02	1.97270E+01	-1.30651E+02	2.15859E+02
6	3.70287E+01	-2.42420E+02	3.97785E+02	-9.12512E+01	5.89908E+02	-9.51112E+02

Table 7. Coefficients for the rake 1 correlated angle of attack

Probe 1	C ₀	C ₁	C ₂
a ₀	1.77666E+01	-1.27017E+02	2.13958E+02
a ₁	2.03862E+01	-4.44310E+02	7.28966E+02
c ₀₀	-1.80236E+01	1.23121E+02	-2.09761E+02
c ₁₀	-2.23746E+02	1.56540E+03	-2.73145E+03
c ₂₀	3.50499E+02	-2.68406E+03	5.02561E+03
c ₃₀	5.88464E+03	-4.08997E+04	7.06051E+04
c ₄₀	-1.48943E+04	1.15675E+05	-2.21037E+05
c ₅₀	-6.75822E+04	4.66124E+05	-7.96036E+05
c ₆₀	9.89295E+04	-8.59081E+05	1.79915E+06
c ₀₁	1.37979E+02	-9.35945E+02	1.58122E+03
c ₁₁	-1.16870E+03	8.27007E+03	-1.45655E+04
c ₂₁	-8.91116E+03	5.92819E+04	-9.79256E+04
c ₃₁	4.26743E+04	-3.07735E+05	5.50323E+05
c ₄₁	8.89552E+05	-5.96651E+06	9.92746E+06
c ₅₁	-7.02198E+05	5.08103E+06	-9.08992E+06
c ₆₁	-2.38645E+07	1.61317E+08	-2.71067E+08
c ₀₂	2.94301E+03	-2.01408E+04	3.44069E+04
c ₁₂	4.76441E+03	-3.39408E+04	5.99015E+04
c ₂₂	-1.28070E+05	8.93313E+05	-1.55456E+06
c ₃₂	-4.37405E+05	3.06056E+06	-5.33021E+06
c ₄₂	1.37338E+07	-9.45877E+07	1.62699E+08
c ₅₂	2.55397E+05	-2.29178E+06	4.91291E+06
c ₆₂	-3.29480E+08	2.26809E+09	-3.90111E+09
c ₀₃	-5.61745E+03	3.80117E+04	-6.40773E+04
c ₁₃	4.21336E+04	-2.96838E+05	5.21599E+05
c ₂₃	6.06802E+05	-4.13191E+06	7.02285E+06
c ₃₃	-4.95795E+05	3.98167E+06	-7.77464E+06
c ₄₃	-4.97491E+07	3.38620E+08	-5.74462E+08
c ₅₃	-7.41551E+06	4.11259E+07	-5.56428E+07
c ₆₃	1.36403E+09	-9.33520E+09	1.59313E+10
c ₀₄	-6.90083E+04	4.72455E+05	-8.07905E+05
c ₁₄	-8.99452E+04	6.52615E+05	-1.16858E+06
c ₂₄	3.59187E+06	-2.47245E+07	4.24603E+07
c ₃₄	1.63848E+07	-1.14463E+08	1.99334E+08
c ₄₄	-4.36435E+08	2.99302E+09	-5.12349E+09
c ₅₄	-1.65595E+08	1.16822E+09	-2.06367E+09
c ₆₄	1.18345E+10	-8.14290E+10	1.39914E+11
d ₀	-6.11746E-01	4.17411E+00	-7.14425E+00
d ₁	1.38218E+01	-9.76110E+01	1.70959E+02
d ₂	6.85118E+02	-4.69961E+03	8.05866E+03
d ₃	-4.16504E+03	2.91059E+04	-5.06277E+04
d ₄	-7.33975E+04	5.04760E+05	-8.67154E+05
d ₅	1.63255E+05	-1.13647E+06	1.97082E+06
d ₆	1.86989E+06	-1.28809E+07	2.21550E+07

Probe 2	C ₀	C ₁	C ₂
a ₀	4.92881E+00	-3.10856E+01	4.82542E+01
a ₁	6.24949E+00	-3.51916E+02	5.66447E+02
c ₀₀	-1.80307E+01	1.23958E+02	-2.13009E+02
c ₁₀	-1.40085E+02	9.89622E+02	-1.76858E+03
c ₂₀	-7.37202E+02	5.23368E+03	-9.27270E+03
c ₃₀	2.93661E+03	-2.31363E+04	4.47240E+04
c ₄₀	1.64032E+04	-1.28149E+05	2.47034E+05
c ₅₀	4.21365E+03	4.28775E+04	-1.99028E+05
c ₆₀	1.07150E+05	-3.61052E+05	-4.59045E+04
c ₀₁	2.35600E+01	-1.63770E+02	2.80435E+02
c ₁₁	-2.77321E+03	1.95657E+04	-3.43961E+04
c ₂₁	-8.20643E+03	5.87673E+04	-1.05562E+05
c ₃₁	1.83330E+05	-1.29780E+06	2.29031E+06
c ₄₁	6.96398E+05	-5.00107E+06	8.95847E+06
c ₅₁	-4.57472E+06	3.23686E+07	-5.71079E+07
c ₆₁	-2.07543E+07	1.47818E+08	-2.62544E+08
c ₀₂	2.47721E+03	-1.69893E+04	2.90669E+04
c ₁₂	-1.35873E+03	6.58621E+03	-6.53139E+03
c ₂₂	6.63495E+04	-4.68075E+05	8.18727E+05
c ₃₂	7.60885E+05	-4.92825E+06	7.91269E+06
c ₄₂	2.95438E+06	-1.90506E+07	3.06009E+07
c ₅₂	-4.47027E+07	3.01547E+08	-5.06415E+08
c ₆₂	-2.26986E+08	1.53733E+09	-2.59500E+09
c ₀₃	-1.93791E+03	1.34983E+04	-2.32278E+04
c ₁₃	1.14426E+05	-8.08601E+05	1.42435E+06
c ₂₃	5.65680E+05	-3.99968E+06	7.07936E+06
c ₃₃	-7.42673E+06	5.29421E+07	-9.40647E+07
c ₄₃	-2.84180E+07	2.03733E+08	-3.65328E+08
c ₅₃	1.57095E+08	-1.12487E+09	2.00767E+09
c ₆₃	6.28965E+08	-4.52512E+09	8.13179E+09
c ₀₄	-5.97797E+04	4.12294E+05	-7.10261E+05
c ₁₄	-3.82670E+04	3.63582E+05	-8.00610E+05
c ₂₄	-3.54272E+06	2.47365E+07	-4.29083E+07
c ₃₄	-4.61202E+06	2.05271E+07	-1.49260E+07
c ₄₄	1.24220E+08	-8.97330E+08	1.61012E+09
c ₅₄	6.46557E+08	-4.21146E+09	6.78640E+09
c ₆₄	1.58626E+09	-1.00278E+10	1.56321E+10
d ₀	-2.33342E-01	1.60568E+00	-2.73659E+00
d ₁	1.36628E+00	-1.23725E+01	2.34164E+01
d ₂	5.49594E+02	-3.82352E+03	6.63354E+03
d ₃	-1.41941E+03	1.03315E+04	-1.84556E+04
d ₄	-6.05968E+04	4.21683E+05	-7.31841E+05
d ₅	4.18487E+04	-3.03191E+05	5.39823E+05
d ₆	1.49014E+06	-1.03665E+07	1.79864E+07

Table 7. Continued

Probe 3	C ₀	C ₁	C ₂	Probe 4	C ₀	C ₁	C ₂
a ₀	2.40616E+01	-1.62561E+02	2.82064E+02	a ₀	4.60723E+01	-3.27059E+02	5.76278E+02
a ₁	-1.62133E+01	-1.88688E+02	2.87581E+02	a ₁	1.04807E+02	-1.05124E+03	1.82733E+03
c ₀₀	-1.77943E+01	1.22844E+02	-2.11275E+02	c ₀₀	-2.35286E+00	1.54251E+01	-2.49765E+01
c ₁₀	-1.66414E+02	1.16696E+03	-2.04557E+03	c ₁₀	-2.75760E+02	1.93776E+03	-3.41983E+03
c ₂₀	2.95756E+02	-2.18844E+03	4.01091E+03	c ₂₀	-1.34128E+03	9.61964E+03	-1.72101E+04
c ₃₀	-5.06702E+03	3.59801E+04	-6.35026E+04	c ₃₀	9.88801E+03	-7.16123E+04	1.29205E+05
c ₄₀	-3.87503E+04	2.75555E+05	-4.88413E+05	c ₄₀	-2.73922E+04	1.75509E+05	-2.79086E+05
c ₅₀	2.24735E+05	-1.57956E+06	2.76266E+06	c ₅₀	-1.88342E+05	1.36989E+06	-2.48406E+06
c ₆₀	1.02648E+06	-7.21146E+06	1.26243E+07	c ₆₀	1.09932E+06	-7.35676E+06	1.22855E+07
c ₀₁	3.51911E+01	-2.28382E+02	3.64864E+02	c ₀₁	1.75930E+02	-1.20482E+03	2.05846E+03
c ₁₁	-8.82941E+02	6.24721E+03	-1.10142E+04	c ₁₁	-1.44556E+03	9.88745E+03	-1.68046E+04
c ₂₁	5.26398E+03	-3.80200E+04	6.87894E+04	c ₂₁	-1.63193E+04	1.16011E+05	-2.05587E+05
c ₃₁	3.78892E+04	-2.73099E+05	4.95764E+05	c ₃₁	1.22266E+05	-8.44474E+05	1.45021E+06
c ₄₁	-7.31654E+04	5.36780E+05	-1.02062E+06	c ₄₁	1.56112E+06	-1.09987E+07	1.92863E+07
c ₅₁	-6.41153E+05	4.63797E+06	-8.52639E+06	c ₅₁	-3.13406E+06	2.17251E+07	-3.74714E+07
c ₆₁	-1.54040E+06	1.04126E+07	-1.73159E+07	c ₆₁	-3.31608E+07	2.32287E+08	-4.04933E+08
c ₀₂	1.37332E+03	-9.26976E+03	1.55041E+04	c ₀₂	-4.19018E+02	2.95615E+03	-5.23604E+03
c ₁₂	-5.10161E+03	3.64513E+04	-6.44092E+04	c ₁₂	1.33935E+04	-9.52366E+04	1.68386E+05
c ₂₂	2.05882E+04	-1.56305E+05	3.17598E+05	c ₂₂	7.74140E+04	-5.57065E+05	1.00017E+06
c ₃₂	2.24408E+06	-1.54936E+07	2.66078E+07	c ₃₂	-3.61805E+05	2.80415E+06	-5.33423E+06
c ₄₂	5.52846E+06	-3.59783E+07	5.67980E+07	c ₄₂	1.25573E+07	-8.43002E+07	1.40795E+08
c ₅₂	-8.40884E+07	5.77919E+08	-9.88497E+08	c ₅₂	-5.36242E+06	3.03487E+07	-4.10328E+07
c ₆₂	-2.69020E+08	1.80021E+09	-2.97706E+09	c ₆₂	-3.66859E+08	2.47902E+09	-4.17005E+09
c ₀₃	-2.61744E+03	1.73821E+04	-2.85857E+04	c ₀₃	-7.33012E+03	4.99560E+04	-8.49184E+04
c ₁₃	5.04598E+04	-3.57983E+05	6.34947E+05	c ₁₃	4.22705E+04	-2.86550E+05	4.82979E+05
c ₂₃	5.18790E+04	-3.26261E+05	5.24654E+05	c ₂₃	1.00608E+06	-7.12772E+06	1.26289E+07
c ₃₃	-9.62450E+05	8.14313E+06	-1.68705E+07	c ₃₃	-2.92067E+06	1.98599E+07	-3.35394E+07
c ₄₃	-5.47555E+06	4.18329E+07	-7.99687E+07	c ₄₃	-9.69705E+07	6.86382E+08	-1.21336E+09
c ₅₃	-2.88412E+07	1.58137E+08	-1.94424E+08	c ₅₃	6.91275E+07	-4.71859E+08	8.00373E+08
c ₆₃	1.77077E+07	-2.78879E+08	7.77239E+08	c ₆₃	2.13801E+09	-1.51063E+10	2.66454E+10
c ₀₄	-1.24841E+04	7.91567E+04	-1.21263E+05	c ₀₄	3.14622E+04	-2.18402E+05	3.79040E+05
c ₁₄	3.63743E+04	-2.72387E+05	4.95024E+05	c ₁₄	-3.80609E+05	2.69541E+06	-4.74589E+06
c ₂₄	-1.60696E+06	1.22151E+07	-2.37015E+07	c ₂₄	-6.62074E+06	4.69363E+07	-8.31111E+07
c ₃₄	-5.06365E+07	3.46802E+08	-5.90607E+08	c ₃₄	8.57637E+06	-6.55874E+07	1.23311E+08
c ₄₄	-5.47017E+07	2.73226E+08	-2.50579E+08	c ₄₄	2.91206E+07	-3.26149E+08	7.94493E+08
c ₅₄	2.13173E+09	-1.45731E+10	2.47948E+10	c ₅₄	1.84039E+08	-1.14444E+09	1.76215E+09
c ₆₄	5.77290E+09	-3.75432E+10	5.99926E+10	c ₆₄	2.66056E+09	-1.55474E+10	2.15160E+10
d ₀	-2.07822E+00	1.43284E+01	-2.47548E+01	d ₀	2.33744E-01	-1.70173E+00	3.01406E+00
d ₁	3.51513E+01	-2.40175E+02	4.09042E+02	d ₁	5.32156E+01	-3.56920E+02	5.95785E+02
d ₂	1.27592E+03	-8.82447E+03	1.52874E+04	d ₂	-6.39189E+01	5.38696E+02	-1.06266E+03
d ₃	-5.12250E+03	3.50433E+04	-5.97414E+04	d ₃	-9.12914E+03	6.17639E+04	-1.04314E+05
d ₄	-9.73421E+04	6.74830E+05	-1.17221E+06	d ₄	8.09710E+03	-6.58580E+04	1.27869E+05
d ₅	1.30090E+05	-8.86938E+05	1.50571E+06	d ₅	2.31528E+05	-1.56530E+06	2.64244E+06
d ₆	1.69062E+06	-1.17727E+07	2.05578E+07	d ₆	-2.34213E+05	1.84738E+06	-3.52173E+06

Table 7. Continued

Probe 5	C ₀	C ₁	C ₂
a ₀	5.21393E+01	-3.73823E+02	6.58351E+02
a ₁	6.90299E+01	-8.09177E+02	1.40907E+03
c ₀₀	3.90641E+00	-2.72675E+01	4.79400E+01
c ₁₀	-1.04965E+02	7.06064E+02	-1.21584E+03
c ₂₀	1.17570E+03	-8.07005E+03	1.38199E+04
c ₃₀	1.47589E+03	-1.12548E+04	2.11142E+04
c ₄₀	-1.01300E+05	6.94459E+05	-1.18914E+06
c ₅₀	2.27302E+03	3.56191E+03	-3.94981E+04
c ₆₀	1.90067E+06	-1.30130E+07	2.22564E+07
c ₀₁	1.40312E+02	-9.73923E+02	1.68236E+03
c ₁₁	6.41802E+02	-4.37684E+03	7.41659E+03
c ₂₁	-8.88324E+03	6.08777E+04	-1.03639E+05
c ₃₁	3.07388E+04	-2.24921E+05	4.05413E+05
c ₄₁	1.10778E+06	-7.60309E+06	1.29639E+07
c ₅₁	-1.28814E+06	9.18874E+06	-1.62348E+07
c ₆₁	-2.01712E+07	1.38176E+08	-2.35213E+08
c ₀₂	-1.15293E+03	7.90591E+03	-1.35694E+04
c ₁₂	-1.03083E+03	7.78127E+03	-1.42099E+04
c ₂₂	-2.32995E+05	1.58885E+06	-2.68901E+06
c ₃₂	1.18765E+06	-8.23240E+06	1.41944E+07
c ₄₂	2.05327E+07	-1.39303E+08	2.34948E+08
c ₅₂	-3.01604E+07	2.09064E+08	-3.60547E+08
c ₆₂	-3.66761E+08	2.47881E+09	-4.16507E+09
c ₀₃	-4.82911E+03	3.36012E+04	-5.81334E+04
c ₁₃	-3.12940E+04	2.07220E+05	-3.42689E+05
c ₂₃	7.08002E+05	-4.91357E+06	8.51482E+06
c ₃₃	-7.43167E+05	6.13338E+06	-1.20848E+07
c ₄₃	-6.15370E+07	4.25583E+08	-7.34662E+08
c ₅₃	4.63652E+07	-3.42452E+08	6.23053E+08
c ₆₃	1.06380E+09	-7.34144E+09	1.26468E+10
c ₀₄	4.37709E+04	-2.99987E+05	5.13641E+05
c ₁₄	8.14003E+03	-9.13272E+04	2.05205E+05
c ₂₄	5.66748E+06	-3.80607E+07	6.35140E+07
c ₃₄	-3.01645E+07	2.10386E+08	-3.64397E+08
c ₄₄	-5.12335E+08	3.44046E+09	-5.75132E+09
c ₅₄	8.37626E+08	-5.82982E+09	1.00842E+10
c ₆₄	9.06144E+09	-6.06238E+10	1.00978E+11
d ₀	2.41914E+00	-1.66486E+01	2.85744E+01
d ₁	4.58615E+01	-3.13708E+02	5.34432E+02
d ₂	-9.67660E+02	6.64818E+03	-1.14100E+04
d ₃	-7.07077E+03	4.82274E+04	-8.22129E+04
d ₄	6.74319E+04	-4.64253E+05	7.98178E+05
d ₅	1.81140E+05	-1.23213E+06	2.09516E+06
d ₆	-1.19557E+06	8.25249E+06	-1.42230E+07

Probe 6	C ₀	C ₁	C ₂
a ₀	1.12967E+00	-3.41928E+00	-1.12070E+00
a ₁	-3.10679E+01	-9.40324E+01	1.24684E+02
c ₀₀	1.04475E+01	-7.37995E+01	1.30516E+02
c ₁₀	-1.28509E+02	8.84337E+02	-1.53905E+03
c ₂₀	2.31311E+02	-1.52176E+03	2.49579E+03
c ₃₀	-4.23629E+03	3.07940E+04	-5.63294E+04
c ₄₀	-4.51875E+04	3.03154E+05	-5.05074E+05
c ₅₀	1.15887E+05	-8.51685E+05	1.57007E+06
c ₆₀	8.24152E+05	-5.42402E+06	8.82741E+06
c ₀₁	1.54162E+02	-1.07225E+03	1.85628E+03
c ₁₁	-1.33014E+03	9.41222E+03	-1.65439E+04
c ₂₁	2.02791E+03	-1.40022E+04	2.39016E+04
c ₃₁	8.07696E+04	-5.73653E+05	1.01347E+06
c ₄₁	8.47703E+05	-5.94274E+06	1.03595E+07
c ₅₁	-1.40955E+06	1.00861E+07	-1.79695E+07
c ₆₁	-2.52494E+07	1.76512E+08	-3.06993E+08
c ₀₂	-2.43772E+03	1.69635E+04	-2.94960E+04
c ₁₂	1.97871E+04	-1.38242E+05	2.40167E+05
c ₂₂	-1.64840E+05	1.13567E+06	-1.94069E+06
c ₃₂	-6.23183E+05	4.24347E+06	-7.11748E+06
c ₄₂	3.46673E+07	-2.40748E+08	4.16129E+08
c ₅₂	6.56606E+06	-4.16364E+07	6.29136E+07
c ₆₂	-8.07504E+08	5.60836E+09	-9.69523E+09
c ₀₃	-8.23595E+03	5.71597E+04	-9.87631E+04
c ₁₃	2.29243E+04	-1.59624E+05	2.76703E+05
c ₂₃	1.66722E+05	-1.19951E+06	2.16863E+06
c ₃₃	-1.47945E+06	1.03505E+07	-1.80391E+07
c ₄₃	-5.15618E+07	3.64986E+08	-6.44270E+08
c ₅₃	1.49828E+07	-1.06998E+08	1.91257E+08
c ₆₃	1.34824E+09	-9.51025E+09	1.67160E+10
c ₀₄	9.07303E+04	-6.29165E+05	1.08961E+06
c ₁₄	-7.83047E+05	5.49300E+06	-9.59420E+06
c ₂₄	5.14971E+06	-3.58357E+07	6.19319E+07
c ₃₄	4.20032E+07	-2.92843E+08	5.07410E+08
c ₄₄	-1.11418E+09	7.77643E+09	-1.35181E+10
c ₅₄	-7.66549E+08	5.29498E+09	-9.07228E+09
c ₆₄	2.68387E+10	-1.87297E+11	3.25570E+11
d ₀	6.04736E-01	-4.26782E+00	7.52081E+00
d ₁	4.96666E+01	-3.39431E+02	5.77565E+02
d ₂	-4.94999E+01	3.80141E+02	-7.27714E+02
d ₃	-8.68325E+03	5.94970E+04	-1.01766E+05
d ₄	4.74720E+03	-3.42602E+04	6.22346E+04
d ₅	2.41833E+05	-1.65413E+06	2.82444E+06
d ₆	-2.86378E+05	1.99239E+06	-3.47539E+06

Table 7. Concluded

Probe 7	C ₀	C ₁	C ₂	Probe 8	C ₀	C ₁	C ₂
a ₀	2.10456E+01	-1.46244E+02	2.58571E+02	a ₀	7.97842E+01	-5.65377E+02	1.00925E+03
a ₁	-9.11643E+01	3.35856E+02	-6.52497E+02	a ₁	-3.16444E+02	1.96568E+03	-3.58031E+03
c ₀₀	4.52289E+00	-3.24961E+01	5.80080E+01	c ₀₀	1.23771E+01	-8.65075E+01	1.51564E+02
c ₁₀	-1.45448E+02	1.03820E+03	-1.90563E+03	c ₁₀	6.22554E+01	-4.51747E+02	7.77662E+02
c ₂₀	2.19345E+03	-1.56776E+04	2.79915E+04	c ₂₀	1.17204E+03	-8.07828E+03	1.39742E+04
c ₃₀	-8.43125E+03	5.76295E+04	-9.78710E+04	c ₃₀	-2.11635E+04	1.50550E+05	-2.67154E+05
c ₄₀	-1.81859E+05	1.29689E+06	-2.31038E+06	c ₄₀	-8.93176E+04	6.26477E+05	-1.10416E+06
c ₅₀	2.39071E+05	-1.64803E+06	2.82179E+06	c ₅₀	3.70714E+05	-2.65271E+06	4.72910E+06
c ₆₀	3.91827E+06	-2.79008E+07	4.96139E+07	c ₆₀	1.55030E+06	-1.09554E+07	1.94769E+07
c ₀₁	8.11130E+01	-5.83785E+02	1.04615E+03	c ₀₁	-2.77968E+00	1.18561E+01	-7.59392E+00
c ₁₁	1.18499E+03	-8.13372E+03	1.39913E+04	c ₁₁	-6.96554E+01	5.11446E+02	-9.30671E+02
c ₂₁	-1.69211E+03	1.43717E+04	-3.10188E+04	c ₂₁	1.46181E+04	-1.01422E+05	1.74583E+05
c ₃₁	1.71921E+04	-1.36060E+05	2.67643E+05	c ₃₁	4.04037E+04	-2.89956E+05	5.20722E+05
c ₄₁	5.51197E+05	-4.12497E+06	7.76653E+06	c ₄₁	-2.20139E+05	1.57596E+06	-2.78326E+06
c ₅₁	-1.21969E+06	8.94165E+06	-1.64376E+07	c ₅₁	-1.05470E+06	7.59279E+06	-1.36904E+07
c ₆₁	-1.32643E+07	9.88649E+07	-1.85362E+08	c ₆₁	-3.15225E+05	4.89466E+05	1.63668E+06
c ₀₂	-2.18076E+03	1.52844E+04	-2.67650E+04	c ₀₂	-2.93569E+03	2.04238E+04	-3.55319E+04
c ₁₂	-1.51266E+04	1.04877E+05	-1.81080E+05	c ₁₂	-1.19038E+03	1.14842E+04	-2.57176E+04
c ₂₂	-2.48758E+05	1.75614E+06	-3.09702E+06	c ₂₂	-3.11627E+05	2.18708E+06	-3.82594E+06
c ₃₂	3.18380E+06	-2.22635E+07	3.88189E+07	c ₃₂	1.06064E+06	-7.78226E+06	1.42167E+07
c ₄₂	3.09633E+07	-2.18236E+08	3.83966E+08	c ₄₂	3.18309E+07	-2.23828E+08	3.92525E+08
c ₅₂	-7.89492E+07	5.51859E+08	-9.61586E+08	c ₅₂	-2.18713E+07	1.61336E+08	-2.95817E+08
c ₆₂	-7.26656E+08	5.11757E+09	-8.99356E+09	c ₆₂	-6.31227E+08	4.44326E+09	-7.80096E+09
c ₀₃	-5.56069E+03	3.99320E+04	-7.13327E+04	c ₀₃	-2.09778E+03	1.52905E+04	-2.77625E+04
c ₁₃	-8.69975E+04	6.03446E+05	-1.04273E+06	c ₁₃	1.04200E+04	-7.96882E+04	1.52400E+05
c ₂₃	1.21039E+05	-9.78537E+05	1.97680E+06	c ₂₃	-5.89331E+05	4.00944E+06	-6.76300E+06
c ₃₃	2.72748E+05	-6.13455E+05	-1.35415E+06	c ₃₃	-3.06013E+06	2.21064E+07	-3.99560E+07
c ₄₃	-2.93647E+07	2.19259E+08	-4.09808E+08	c ₄₃	-2.22567E+06	2.07110E+07	-4.71473E+07
c ₅₃	4.95223E+07	-3.83925E+08	7.40612E+08	c ₅₃	5.95627E+07	-4.32628E+08	7.86439E+08
c ₆₃	6.77528E+08	-5.04788E+09	9.41324E+09	c ₆₃	2.30925E+08	-1.66081E+09	3.01242E+09
c ₀₄	9.71914E+04	-6.83211E+05	1.19911E+06	c ₀₄	9.65094E+04	-6.71810E+05	1.16844E+06
c ₁₄	6.29201E+05	-4.36752E+06	7.55626E+06	c ₁₄	-1.87451E+05	1.25830E+06	-2.10700E+06
c ₂₄	6.47825E+06	-4.53379E+07	7.91964E+07	c ₂₄	7.12800E+06	-4.95336E+07	8.56498E+07
c ₃₄	-8.83272E+07	6.14539E+08	-1.06593E+09	c ₃₄	-2.42058E+06	2.24824E+07	-4.79177E+07
c ₄₄	-8.27538E+08	5.80039E+09	-1.01467E+10	c ₄₄	-7.44730E+08	5.21267E+09	-9.09131E+09
c ₅₄	2.08662E+09	-1.44974E+10	2.51019E+10	c ₅₄	1.13056E+08	-9.20698E+08	1.80259E+09
c ₆₄	1.92421E+10	-1.34796E+11	2.35619E+11	c ₆₄	1.51490E+10	-1.06320E+11	1.85991E+11
d ₀	2.17391E+00	-1.53870E+01	2.72973E+01	d ₀	1.80358E+00	-1.25749E+01	2.19897E+01
d ₁	-5.66568E+01	4.03650E+02	-7.24606E+02	d ₁	-3.70341E+01	2.59022E+02	-4.55083E+02
d ₂	-2.58905E+02	1.90062E+03	-3.49718E+03	d ₂	2.08859E+02	-1.52163E+03	2.74024E+03
d ₃	4.67842E+03	-3.35294E+04	6.01238E+04	d ₃	5.75557E+03	-4.03657E+04	7.07063E+04
d ₄	8.83268E+03	-6.84088E+04	1.33281E+05	d ₄	-3.33222E+04	2.37091E+05	-4.19402E+05
d ₅	-1.32039E+05	9.49138E+05	-1.70639E+06	d ₅	-2.06513E+05	1.45528E+06	-2.56119E+06
d ₆	-5.57838E+04	5.07468E+05	-1.13402E+06	d ₆	1.04844E+06	-7.43420E+06	1.31307E+07

Table 8. Coefficients for the rake 2 correlated angle of attack

Probe 1	C ₀	C ₁	C ₂
a ₀	-8.54957E+01	6.31049E+02	-1.14357E+03
a ₁	5.44635E+01	-6.91347E+02	1.17290E+03
c ₀₀	-2.26873E+01	1.56601E+02	-2.69057E+02
c ₁₀	-1.90647E+02	1.32807E+03	-2.28194E+03
c ₂₀	1.77681E+03	-1.23344E+04	2.13600E+04
c ₃₀	2.00653E+04	-1.36349E+05	2.31374E+05
c ₄₀	-6.35810E+04	4.45511E+05	-7.77803E+05
c ₅₀	-8.13834E+05	5.57587E+06	-9.53940E+06
c ₆₀	-1.24342E+06	8.43976E+06	-1.43290E+07
c ₀₁	-2.22935E+02	1.54795E+03	-2.68629E+03
c ₁₁	-3.50079E+03	2.44560E+04	-4.26357E+04
c ₂₁	-1.28533E+04	8.67709E+04	-1.46093E+05
c ₃₁	5.44566E+05	-3.78802E+06	6.57216E+06
c ₄₁	2.46958E+06	-1.70951E+07	2.94919E+07
c ₅₁	-1.84597E+07	1.28420E+08	-2.22831E+08
c ₆₁	-8.81709E+07	6.12500E+08	-1.06084E+09
c ₀₂	2.13599E+03	-1.44583E+04	2.44294E+04
c ₁₂	2.05006E+04	-1.39493E+05	2.36755E+05
c ₂₂	-4.63757E+04	3.11357E+05	-5.18450E+05
c ₃₂	-5.94253E+06	4.10150E+07	-7.06495E+07
c ₄₂	-1.62946E+07	1.13798E+08	-1.98598E+08
c ₅₂	2.23375E+08	-1.54404E+09	2.66363E+09
c ₆₂	8.54377E+08	-5.92996E+09	1.02763E+10
c ₀₃	1.00576E+04	-7.02437E+04	1.22546E+05
c ₁₃	1.90096E+05	-1.31893E+06	2.28270E+06
c ₂₃	1.39821E+06	-9.63061E+06	1.65841E+07
c ₃₃	-3.43261E+07	2.37686E+08	-4.10703E+08
c ₄₃	-1.82322E+08	1.26384E+09	-2.18698E+09
c ₅₃	1.17879E+09	-8.16516E+09	1.41143E+10
c ₆₃	5.98193E+09	-4.14944E+10	7.18317E+10
c ₀₄	-5.98263E+04	4.11066E+05	-7.04927E+05
c ₁₄	-9.60018E+05	6.59877E+06	-1.13079E+07
c ₂₄	-4.09010E+06	2.87057E+07	-5.04610E+07
c ₃₄	2.55200E+08	-1.76602E+09	3.04907E+09
c ₄₄	1.06927E+09	-7.46035E+09	1.29994E+10
c ₅₄	-9.17344E+09	6.35165E+10	-1.09730E+11
c ₆₄	-4.10060E+10	2.85046E+11	-4.94575E+11
d ₀	2.33907E+00	-1.61422E+01	2.78757E+01
d ₁	-5.86083E+01	4.08989E+02	-7.13456E+02
d ₂	-1.15378E+03	8.03650E+03	-1.39892E+04
d ₃	1.08654E+04	-7.61243E+04	1.33035E+05
d ₄	6.26389E+04	-4.38092E+05	7.66290E+05
d ₅	-3.86303E+05	2.69985E+06	-4.70663E+06
d ₆	-1.85099E+05	1.35243E+06	-2.49650E+06

Probe 2	C ₀	C ₁	C ₂
a ₀	9.16962E+00	-5.97379E+01	9.54523E+01
a ₁	3.71945E+01	-5.26660E+02	8.39499E+02
c ₀₀	-1.01429E+01	6.48273E+01	-1.03145E+02
c ₁₀	-1.66862E+02	1.10493E+03	-1.85792E+03
c ₂₀	-1.82166E+03	1.22555E+04	-2.05619E+04
c ₃₀	1.44416E+04	-9.55825E+04	1.57611E+05
c ₄₀	1.45737E+05	-9.78965E+05	1.64142E+06
c ₅₀	-3.97798E+05	2.63817E+06	-4.36113E+06
c ₆₀	-3.05521E+06	2.05060E+07	-3.43646E+07
c ₀₁	1.02081E+01	-6.66145E+01	1.03745E+02
c ₁₁	-1.95658E+03	1.32605E+04	-2.24457E+04
c ₂₁	-5.85121E+03	4.03306E+04	-6.87705E+04
c ₃₁	2.42255E+04	-1.72699E+05	3.06158E+05
c ₄₁	2.66982E+05	-1.87581E+06	3.23724E+06
c ₅₁	2.58112E+05	-1.50684E+06	2.13293E+06
c ₆₁	-7.14935E+06	4.95418E+07	-8.47791E+07
c ₀₂	1.91237E+03	-1.24674E+04	2.02867E+04
c ₁₂	7.70037E+02	-5.07295E+03	8.38413E+03
c ₂₂	4.49107E+05	-3.01726E+06	5.05471E+06
c ₃₂	-1.16735E+06	7.81868E+06	-1.30544E+07
c ₄₂	-4.05321E+07	2.71520E+08	-4.53798E+08
c ₅₂	3.17799E+07	-2.12775E+08	3.55122E+08
c ₆₂	8.43132E+08	-5.63891E+09	9.41057E+09
c ₀₃	-1.96656E+01	-3.88633E+01	5.82688E+02
c ₁₃	6.47374E+04	-4.38143E+05	7.38747E+05
c ₂₃	-6.67902E+04	4.43737E+05	-7.28571E+05
c ₃₃	-5.86729E+05	4.19163E+06	-7.44553E+06
c ₄₃	2.35627E+07	-1.57712E+08	2.63261E+08
c ₅₃	-1.74707E+07	1.11825E+08	-1.77484E+08
c ₆₃	-4.34848E+08	2.90764E+09	-4.85210E+09
c ₀₄	-4.57082E+04	3.00906E+05	-4.95123E+05
c ₁₄	3.19003E+03	-1.29673E+04	4.61669E+02
c ₂₄	-1.41864E+07	9.52862E+07	-1.59571E+08
c ₃₄	2.97091E+07	-1.99895E+08	3.35700E+08
c ₄₄	1.33083E+09	-8.91815E+09	1.49087E+10
c ₅₄	-8.66299E+08	5.82052E+09	-9.75598E+09
c ₆₄	-2.74459E+10	1.83670E+11	-3.06667E+11
d ₀	-1.76209E-01	1.44074E+00	-2.80495E+00
d ₁	-9.59133E+01	6.41021E+02	-1.07305E+03
d ₂	3.12819E+02	-2.18275E+03	3.77618E+03
d ₃	1.03553E+04	-6.92156E+04	1.15531E+05
d ₄	-3.24511E+04	2.23370E+05	-3.82440E+05
d ₅	-2.67577E+05	1.79072E+06	-2.99263E+06
d ₆	7.16138E+05	-4.90323E+06	8.35673E+06

Table 8. Continued

Probe 3	C ₀	C ₁	C ₂
a ₀	3.19434E+01	-2.22542E+02	3.85438E+02
a ₁	-2.39431E+00	-2.89602E+02	4.68707E+02
c ₀₀	-3.54604E-01	2.02814E+00	-2.77872E+00
c ₁₀	-2.84907E+02	2.00401E+03	-3.49613E+03
c ₂₀	-2.15942E+03	1.47031E+04	-2.50100E+04
c ₃₀	1.68061E+04	-1.15966E+05	1.99844E+05
c ₄₀	1.59150E+05	-1.08555E+06	1.85064E+06
c ₅₀	-3.47429E+05	2.39443E+06	-4.11999E+06
c ₆₀	-3.35694E+06	2.29646E+07	-3.92675E+07
c ₀₁	1.46300E+02	-1.00458E+03	1.71766E+03
c ₁₁	4.09570E+02	-2.62109E+03	4.14175E+03
c ₂₁	9.53516E+03	-6.48419E+04	1.10122E+05
c ₃₁	-1.57045E+05	1.06995E+06	-1.81674E+06
c ₄₁	4.00617E+04	-4.13944E+05	9.40096E+05
c ₅₁	5.10757E+06	-3.50129E+07	5.98421E+07
c ₆₁	-1.01105E+07	7.27132E+07	-1.30199E+08
c ₀₂	-6.06841E+02	4.17341E+03	-7.19007E+03
c ₁₂	1.20246E+04	-8.32096E+04	1.44015E+05
c ₂₂	5.84065E+05	-4.00309E+06	6.85154E+06
c ₃₂	-1.28607E+05	8.71142E+05	-1.52839E+06
c ₄₂	-4.86836E+07	3.34160E+08	-5.72420E+08
c ₅₂	-2.13271E+07	1.47509E+08	-2.53139E+08
c ₆₂	1.10002E+09	-7.55690E+09	1.29531E+10
c ₀₃	-6.80005E+03	4.65739E+04	-7.93882E+04
c ₁₃	-4.08112E+04	2.76058E+05	-4.64825E+05
c ₂₃	-5.93303E+05	4.07409E+06	-6.97410E+06
c ₃₃	9.14218E+06	-6.25710E+07	1.06734E+08
c ₄₃	2.58412E+07	-1.75645E+08	2.97219E+08
c ₅₃	-2.62934E+08	1.80278E+09	-3.08147E+09
c ₆₃	-1.41173E+08	9.26217E+08	-1.50112E+09
c ₀₄	2.29156E+04	-1.55051E+05	2.62257E+05
c ₁₄	-2.97956E+05	2.03964E+06	-3.49028E+06
c ₂₄	-1.86418E+07	1.27983E+08	-2.19274E+08
c ₃₄	-2.59935E+06	1.97495E+07	-3.55038E+07
c ₄₄	1.61264E+09	-1.10841E+10	1.90019E+10
c ₅₄	9.04591E+08	-6.28030E+09	1.08325E+10
c ₆₄	-3.62926E+10	2.49590E+11	-4.28055E+11
d ₀	-8.62893E-01	5.93706E+00	-1.02134E+01
d ₁	3.66053E+01	-2.47902E+02	4.19234E+02
d ₂	5.35623E+02	-3.67839E+03	6.31684E+03
d ₃	-3.65234E+03	2.42847E+04	-4.04138E+04
d ₄	-4.23630E+04	2.90762E+05	-4.99328E+05
d ₅	9.19296E+04	-6.09292E+05	1.01128E+06
d ₆	8.25171E+05	-5.66498E+06	9.73510E+06

Probe 4	C ₀	C ₁	C ₂
a ₀	2.04811E+01	-1.49536E+02	2.49857E+02
a ₁	-1.47543E+01	-1.82111E+02	2.62818E+02
c ₀₀	-2.05319E+00	1.07338E+01	-1.63340E+01
c ₁₀	-3.02483E+02	2.00595E+03	-3.39597E+03
c ₂₀	9.61942E+02	-6.33729E+03	1.04176E+04
c ₃₀	2.59979E+04	-1.73696E+05	2.89402E+05
c ₄₀	-1.28619E+04	8.39700E+04	-1.36579E+05
c ₅₀	-1.26124E+06	8.43904E+06	-1.40886E+07
c ₆₀	-3.61283E+06	2.42127E+07	-4.04887E+07
c ₀₁	8.10686E+01	-5.23050E+02	8.33744E+02
c ₁₁	2.17725E+03	-1.44192E+04	2.37382E+04
c ₂₁	8.54198E+03	-6.09196E+04	1.08385E+05
c ₃₁	-2.59494E+05	1.68924E+06	-2.72894E+06
c ₄₁	-4.94138E+05	3.36451E+06	-5.72114E+06
c ₅₁	8.59557E+06	-5.55324E+07	8.89599E+07
c ₆₁	2.80187E+07	-1.82414E+08	2.94984E+08
c ₀₂	-4.17376E+02	2.79052E+03	-4.66137E+03
c ₁₂	3.14743E+04	-2.10284E+05	3.50038E+05
c ₂₂	-4.44635E+04	2.86392E+05	-4.61008E+05
c ₃₂	-3.28359E+06	2.17228E+07	-3.57715E+07
c ₄₂	-1.27759E+06	8.34199E+06	-1.32931E+07
c ₅₂	1.54397E+08	-1.02270E+09	1.68773E+09
c ₆₂	4.90624E+08	-3.24836E+09	5.35586E+09
c ₀₃	-4.25240E+03	2.78958E+04	-4.53863E+04
c ₁₃	-1.53939E+05	1.02703E+06	-1.70725E+06
c ₂₃	-1.02055E+05	8.26953E+05	-1.63600E+06
c ₃₃	2.22951E+07	-1.47837E+08	2.44319E+08
c ₄₃	3.26150E+07	-2.21480E+08	3.75915E+08
c ₅₃	-7.88686E+08	5.21544E+09	-8.59579E+09
c ₆₃	-2.56544E+09	1.70327E+10	-2.82037E+10
c ₀₄	3.61498E+03	-2.34469E+04	3.82852E+04
c ₁₄	-1.12497E+06	7.52004E+06	-1.25294E+07
c ₂₄	1.46092E+06	-9.21816E+06	1.44076E+07
c ₃₄	1.49028E+08	-9.90270E+08	1.64033E+09
c ₄₄	1.09935E+08	-7.45160E+08	1.26010E+09
c ₅₄	-6.17674E+09	4.10255E+10	-6.79420E+10
c ₆₄	-1.94793E+10	1.29599E+11	-2.15024E+11
d ₀	1.45549E+00	-9.43688E+00	1.47732E+01
d ₁	-7.19318E+01	4.83173E+02	-8.21695E+02
d ₂	-6.81969E+02	4.53712E+03	-7.53430E+03
d ₃	6.31764E+03	-4.31265E+04	7.33683E+04
d ₄	4.37736E+04	-2.94342E+05	4.93960E+05
d ₅	-2.13046E+05	1.46089E+06	-2.49422E+06
d ₆	-1.09086E+06	7.42222E+06	-1.25887E+07

Table 8. Concluded

Probe 5	C ₀	C ₁	C ₂
a ₀	-6.46899E+00	4.44996E+01	-8.47579E+01
a ₁	-9.13391E+01	3.36424E+02	-6.41976E+02
c ₀₀	-5.64650E-01	2.33763E+00	-4.04088E+00
c ₁₀	-1.52075E+02	1.03592E+03	-1.80956E+03
c ₂₀	1.65698E+03	-1.13191E+04	1.93261E+04
c ₃₀	1.71982E+04	-1.15841E+05	1.94695E+05
c ₄₀	-7.47923E+04	5.17362E+05	-8.94032E+05
c ₅₀	-1.13952E+06	7.75444E+06	-1.31759E+07
c ₆₀	-2.65708E+06	1.80159E+07	-3.04981E+07
c ₀₁	6.43833E+01	-4.52689E+02	7.90731E+02
c ₁₁	1.69289E+03	-1.16538E+04	2.00159E+04
c ₂₁	-5.19308E+03	3.43932E+04	-5.69242E+04
c ₃₁	-9.96130E+04	6.57276E+05	-1.07347E+06
c ₄₁	3.24917E+05	-2.23402E+06	3.82977E+06
c ₅₁	5.26605E+06	-3.48257E+07	5.70854E+07
c ₆₁	1.27234E+07	-8.33303E+07	1.35099E+08
c ₀₂	-2.32528E+03	1.61159E+04	-2.78291E+04
c ₁₂	1.34451E+04	-9.16974E+04	1.56143E+05
c ₂₂	-1.74162E+05	1.19743E+06	-2.05707E+06
c ₃₂	-4.20933E+06	2.86802E+07	-4.87218E+07
c ₄₂	5.73659E+06	-4.03772E+07	7.10163E+07
c ₅₂	2.64420E+08	-1.81052E+09	3.09222E+09
c ₆₂	7.73417E+08	-5.28755E+09	9.01588E+09
c ₀₃	-3.56413E+03	2.53869E+04	-4.49311E+04
c ₁₃	-1.18244E+05	8.20251E+05	-1.42029E+06
c ₂₃	4.62397E+05	-3.17633E+06	5.44777E+06
c ₃₃	1.18827E+07	-8.16866E+07	1.40077E+08
c ₄₃	-1.03766E+07	7.16911E+07	-1.23686E+08
c ₅₃	-5.21319E+08	3.57451E+09	-6.11394E+09
c ₆₃	-1.42787E+09	9.78150E+09	-1.67166E+10
c ₀₄	7.33078E+04	-5.06466E+05	8.71969E+05
c ₁₄	-4.05386E+05	2.77238E+06	-4.73209E+06
c ₂₄	7.54806E+06	-5.20749E+07	8.97165E+07
c ₃₄	1.53407E+08	-1.05091E+09	1.79507E+09
c ₄₄	-2.57221E+08	1.79858E+09	-3.14189E+09
c ₅₄	-9.35187E+09	6.42538E+10	-1.10107E+11
c ₆₄	-2.65644E+10	1.82259E+11	-3.11848E+11
d ₀	7.46026E-01	-4.90252E+00	8.00906E+00
d ₁	-8.42795E+01	5.87125E+02	-1.02685E+03
d ₂	-1.04290E+02	6.71986E+02	-1.09965E+03
d ₃	1.01090E+04	-7.07033E+04	1.23702E+05
d ₄	2.21960E+04	-1.51422E+05	2.60563E+05
d ₅	-3.09008E+05	2.16517E+06	-3.79520E+06
d ₆	-9.43920E+05	6.54602E+06	-1.14018E+07

Probe 6	C ₀	C ₁	C ₂
a ₀	9.28387E+00	-6.06612E+01	1.05057E+02
a ₁	-3.91913E+01	-3.08247E+01	8.80932E+00
c ₀₀	1.77255E+01	-1.23979E+02	2.16309E+02
c ₁₀	-1.52900E+02	9.98181E+02	-1.70179E+03
c ₂₀	-2.18784E+03	1.50500E+04	-2.58616E+04
c ₃₀	1.23454E+04	-8.22339E+04	1.36214E+05
c ₄₀	2.46934E+05	-1.69545E+06	2.90453E+06
c ₅₀	-4.70011E+05	3.17153E+06	-5.33063E+06
c ₆₀	-6.27698E+06	4.31141E+07	-7.38700E+07
c ₀₁	2.28307E+01	-1.60777E+02	2.81355E+02
c ₁₁	6.27430E+02	-4.22756E+03	7.15087E+03
c ₂₁	1.75017E+04	-1.22700E+05	2.14350E+05
c ₃₁	1.53518E+04	-1.13773E+05	2.11539E+05
c ₄₁	-1.08400E+03	2.19041E+05	-7.57307E+05
c ₅₁	-1.61320E+06	1.13390E+07	-1.99594E+07
c ₆₁	-1.41856E+07	9.28399E+07	-1.50845E+08
c ₀₂	-3.12445E+03	2.15445E+04	-3.70946E+04
c ₁₂	1.52488E+04	-1.00724E+05	1.65826E+05
c ₂₂	4.11795E+05	-2.81777E+06	4.80882E+06
c ₃₂	-1.82203E+06	1.20745E+07	-1.99382E+07
c ₄₂	-4.23545E+07	2.88455E+08	-4.89693E+08
c ₅₂	6.14823E+07	-4.12422E+08	6.89866E+08
c ₆₂	1.08047E+09	-7.35559E+09	1.24819E+10
c ₀₃	-1.54053E+03	1.06717E+04	-1.83857E+04
c ₁₃	-5.28442E+04	3.67145E+05	-6.34947E+05
c ₂₃	-1.24116E+06	8.73608E+06	-1.53110E+07
c ₃₃	-2.25929E+06	1.51993E+07	-2.56503E+07
c ₄₃	2.60493E+07	-1.96916E+08	3.67267E+08
c ₅₃	1.28570E+08	-8.78081E+08	1.50033E+09
c ₆₃	2.41257E+08	-1.26951E+09	1.52862E+09
c ₀₄	9.19683E+04	-6.31741E+05	1.08324E+06
c ₁₄	-3.67365E+05	2.38901E+06	-3.86685E+06
c ₂₄	-9.60873E+06	6.52024E+07	-1.10379E+08
c ₃₄	6.70484E+07	-4.47198E+08	7.44039E+08
c ₄₄	1.13933E+09	-7.71379E+09	1.30201E+10
c ₅₄	-2.13979E+09	1.43954E+10	-2.41645E+10
c ₆₄	-3.03713E+10	2.05874E+11	-3.47909E+11
d ₀	3.92899E+00	-2.65850E+01	4.51060E+01
d ₁	-6.10299E+01	4.20077E+02	-7.33304E+02
d ₂	-8.41850E+02	5.73028E+03	-9.75869E+03
d ₃	6.01242E+03	-4.19079E+04	7.26575E+04
d ₄	3.76582E+04	-2.55733E+05	4.36568E+05
d ₅	-1.68045E+05	1.17150E+06	-2.02938E+06
d ₆	-4.66813E+05	3.14688E+06	-5.36874E+06

Table 9. Coefficients for the rake 1 correlated angle of sideslip

Probe 1	C ₀	C ₁	C ₂
e ₀	-5.36193E+00	3.72986E+01	-6.48241E+01
e ₁	-2.76115E+02	1.60358E+03	-2.77893E+03
g ₀₀	-6.42556E+00	4.43749E+01	-7.61645E+01
g ₁₀	7.91999E+01	-5.57427E+02	9.84746E+02
g ₂₀	1.05746E+03	-7.33840E+03	1.27453E+04
g ₃₀	-7.79919E+03	5.46670E+04	-9.62057E+04
g ₄₀	-1.15449E+05	8.06098E+05	-1.40751E+06
g ₅₀	3.48479E+05	-2.44812E+06	4.30698E+06
g ₆₀	3.03204E+06	-2.11796E+07	3.69901E+07
g ₀₁	-1.01488E+02	7.02206E+02	-1.21641E+03
g ₁₁	7.45104E+00	-5.08174E+01	6.35958E+01
g ₂₁	3.59331E+03	-2.56514E+04	4.48605E+04
g ₃₁	-4.03962E+04	2.65775E+05	-4.32985E+05
g ₄₁	1.18899E+05	-8.44950E+05	1.49948E+06
g ₅₁	-6.39064E+04	1.04309E+06	-2.86858E+06
g ₆₁	-3.72793E+06	2.73023E+07	-4.97009E+07
g ₀₂	-4.92505E+02	3.42216E+03	-5.93261E+03
g ₁₂	2.63954E+03	-1.87541E+04	3.25514E+04
g ₂₂	-7.78921E+03	6.71483E+04	-1.41315E+05
g ₃₂	-2.52891E+04	1.58290E+03	3.97743E+05
g ₄₂	1.16785E+07	-8.26060E+07	1.46068E+08
g ₅₂	-2.29108E+07	1.65212E+08	-2.99553E+08
g ₆₂	-3.13906E+08	2.21691E+09	-3.91621E+09
g ₀₃	3.99236E+03	-2.76109E+04	4.78163E+04
g ₁₃	1.05410E+03	-4.27769E+03	3.31641E+03
g ₂₃	-3.32527E+05	2.32065E+06	-4.02288E+06
g ₃₃	2.39013E+06	-1.65806E+07	2.85206E+07
g ₄₃	2.46295E+05	-3.44185E+06	8.38242E+06
g ₅₃	-1.55134E+07	1.02903E+08	-1.66452E+08
g ₆₃	-4.52294E+05	2.26629E+07	-6.47194E+07
g ₀₄	4.82804E+04	-3.34782E+05	5.78485E+05
g ₁₄	-1.96197E+04	1.52768E+05	-2.74810E+05
g ₂₄	-1.95455E+06	1.32058E+07	-2.21282E+07
g ₃₄	1.03315E+07	-6.71191E+07	1.05356E+08
g ₄₄	-2.18484E+08	1.55495E+09	-2.77092E+09
g ₅₄	2.93488E+08	-2.19166E+09	4.14270E+09
g ₆₄	5.58187E+09	-3.96936E+10	7.07343E+10
h ₀	4.90321E-01	-3.30614E+00	5.55541E+00
h ₁	-5.65226E+00	3.56122E+01	-5.57156E+01
h ₂	-3.46184E+02	2.27617E+03	-3.72209E+03
h ₃	8.31244E+02	-5.26822E+03	8.28833E+03
h ₄	2.97434E+04	-1.94481E+05	3.16057E+05
h ₅	-2.63484E+04	1.70542E+05	-2.74734E+05
h ₆	-6.01478E+05	3.91779E+06	-6.33982E+06

Probe 2	C ₀	C ₁	C ₂
e ₀	-3.37098E+01	2.37414E+02	-4.29011E+02
e ₁	-6.37780E+01	1.08941E+02	-1.60891E+02
g ₀₀	-9.96927E+00	6.84981E+01	-1.17599E+02
g ₁₀	4.00577E+01	-2.68281E+02	4.72042E+02
g ₂₀	-9.64923E+02	6.78370E+03	-1.18517E+04
g ₃₀	-1.38613E+04	9.60527E+04	-1.66007E+05
g ₄₀	1.20756E+05	-8.45632E+05	1.47525E+06
g ₅₀	4.57711E+05	-3.18623E+06	5.53087E+06
g ₆₀	-2.61776E+06	1.82954E+07	-3.18652E+07
g ₀₁	-1.52991E+01	9.08285E+01	-1.34856E+02
g ₁₁	-6.98646E+02	5.18675E+03	-9.55310E+03
g ₂₁	-1.11565E+04	7.80407E+04	-1.37098E+05
g ₃₁	1.31937E+05	-9.40600E+05	1.66831E+06
g ₄₁	1.53382E+05	-1.12543E+06	2.07680E+06
g ₅₁	-4.04389E+06	2.85624E+07	-5.02045E+07
g ₆₁	5.31019E+06	-3.51994E+07	5.73920E+07
g ₀₂	1.22740E+03	-8.42320E+03	1.44546E+04
g ₁₂	-5.55985E+03	3.84334E+04	-6.63585E+04
g ₂₂	2.59827E+05	-1.84043E+06	3.24006E+06
g ₃₂	3.39920E+06	-2.36462E+07	4.10156E+07
g ₄₂	-3.33083E+07	2.33943E+08	-4.09154E+08
g ₅₂	-1.08075E+08	7.52598E+08	-1.30666E+09
g ₆₂	8.21504E+08	-5.75464E+09	1.00424E+10
g ₀₃	1.25820E+03	-8.18665E+03	1.34066E+04
g ₁₃	2.81878E+04	-2.11555E+05	3.93220E+05
g ₂₃	7.62509E+05	-5.36479E+06	9.45168E+06
g ₃₃	-8.35218E+06	5.94561E+07	-1.05314E+08
g ₄₃	-3.20778E+07	2.27467E+08	-4.05294E+08
g ₅₃	2.57188E+08	-1.81784E+09	3.19805E+09
g ₆₃	3.43380E+08	-2.50317E+09	4.61718E+09
g ₀₄	-2.14410E+04	1.45375E+05	-2.46359E+05
g ₁₄	2.74184E+05	-1.93489E+06	3.40988E+06
g ₂₄	-5.55680E+06	3.92715E+07	-6.89447E+07
g ₃₄	-1.23958E+08	8.66195E+08	-1.50938E+09
g ₄₄	8.82336E+08	-6.18738E+09	1.08024E+10
g ₅₄	3.71758E+09	-2.59760E+10	4.52583E+10
g ₆₄	-2.26500E+10	1.58535E+11	-2.76371E+11
h ₀	3.27687E-01	-2.23234E+00	3.75699E+00
h ₁	4.96909E+01	-3.47853E+02	6.04772E+02
h ₂	1.90364E+02	-1.37115E+03	2.45500E+03
h ₃	-8.38331E+03	5.88481E+04	-1.02788E+05
h ₄	-3.69757E+04	2.62084E+05	-4.62231E+05
h ₅	2.44980E+05	-1.72116E+06	3.00842E+06
h ₆	1.14725E+06	-8.10491E+06	1.42472E+07

Table 9. Continued

Probe 3	C ₀	C ₁	C ₂	Probe 4	C ₀	C ₁	C ₂
e ₀	-1.64297E+01	1.04089E+02	-1.78062E+02	e ₀	-8.93998E+00	6.42614E+01	-1.17114E+02
e ₁	-2.53592E+02	1.46207E+03	-2.56190E+03	e ₁	-2.48747E+02	1.43173E+03	-2.51770E+03
g ₀₀	-1.32659E+01	9.18201E+01	-1.58429E+02	g ₀₀	-1.54453E+01	1.06402E+02	-1.82814E+02
g ₁₀	-4.48084E+00	2.57922E+01	-2.39774E+01	g ₁₀	-8.00191E+01	5.80807E+02	-1.01700E+03
g ₂₀	6.73395E+02	-4.56485E+03	7.70469E+03	g ₂₀	-1.08424E+03	7.69968E+03	-1.36075E+04
g ₃₀	4.51716E+03	-3.03547E+04	5.14181E+04	g ₃₀	2.93399E+03	-2.18828E+04	4.03700E+04
g ₄₀	-7.35220E+04	5.02918E+05	-8.59568E+05	g ₄₀	1.47957E+05	-1.03710E+06	1.81016E+06
g ₅₀	-1.20374E+05	7.88832E+05	-1.30404E+06	g ₅₀	2.10913E+04	-1.15919E+05	1.50500E+05
g ₆₀	1.81708E+06	-1.23890E+07	2.11381E+07	g ₆₀	-3.32085E+06	2.32445E+07	-4.05240E+07
g ₀₁	-9.14861E+01	6.31569E+02	-1.09711E+03	g ₀₁	-1.14034E+02	7.79439E+02	-1.33220E+03
g ₁₁	1.19217E+03	-8.30906E+03	1.44699E+04	g ₁₁	5.63446E+01	-1.51803E+02	-1.40722E+02
g ₂₁	4.59707E+03	-3.25371E+04	5.70315E+04	g ₂₁	3.45452E+03	-2.67822E+04	5.00046E+04
g ₃₁	-2.84661E+05	1.97317E+06	-3.40987E+06	g ₃₁	-3.14673E+04	2.08841E+05	-3.46867E+05
g ₄₁	9.25033E+05	-6.43509E+06	1.11452E+07	g ₄₁	-5.97429E+05	4.36618E+06	-7.90760E+06
g ₅₁	6.92229E+06	-4.76125E+07	8.16958E+07	g ₅₁	1.03835E+06	-7.13337E+06	1.22827E+07
g ₆₁	-2.97399E+07	2.05486E+08	-3.54047E+08	g ₆₁	1.67907E+07	-1.20716E+08	2.15693E+08
g ₀₂	2.83020E+02	-1.90412E+03	3.18232E+03	g ₀₂	1.84296E+03	-1.26530E+04	2.16995E+04
g ₁₂	3.14761E+03	-2.34954E+04	4.40944E+04	g ₁₂	5.62245E+03	-3.89676E+04	6.69478E+04
g ₂₂	-2.28184E+04	1.51113E+05	-2.55473E+05	g ₂₂	1.31002E+05	-9.05809E+05	1.55258E+06
g ₃₂	-1.16591E+06	8.23503E+06	-1.45832E+07	g ₃₂	1.14078E+06	-7.80542E+06	1.33535E+07
g ₄₂	9.64683E+06	-6.78984E+07	1.19862E+08	g ₄₂	-2.70783E+07	1.87443E+08	-3.23006E+08
g ₅₂	3.11066E+07	-2.19343E+08	3.88339E+08	g ₅₂	-3.73667E+07	2.56359E+08	-4.39520E+08
g ₆₂	-2.51008E+08	1.77322E+09	-3.14228E+09	g ₆₂	6.66840E+08	-4.62010E+09	7.97229E+09
g ₀₃	6.13303E+03	-4.25387E+04	7.38510E+04	g ₀₃	4.77055E+03	-3.26474E+04	5.58627E+04
g ₁₃	1.01855E+04	-6.54492E+04	1.03049E+05	g ₁₃	4.79018E+03	-4.16670E+04	8.64340E+04
g ₂₃	-4.96757E+05	3.46040E+06	-5.98698E+06	g ₂₃	9.49370E+03	-1.93490E+03	-8.63900E+04
g ₃₃	1.07243E+07	-7.46748E+07	1.29767E+08	g ₃₃	-9.32690E+04	1.00744E+06	-2.31055E+06
g ₄₃	-4.19358E+07	2.93302E+08	-5.13312E+08	g ₄₃	8.38899E+06	-6.50124E+07	1.23289E+08
g ₅₃	-2.51573E+08	1.74325E+09	-3.01784E+09	g ₅₃	9.54230E+06	-6.89346E+07	1.22783E+08
g ₆₃	1.25729E+09	-8.76811E+09	1.52982E+10	g ₆₃	-3.59275E+08	2.63199E+09	-4.77916E+09
g ₀₄	2.86989E+04	-2.01457E+05	3.52166E+05	g ₀₄	-4.27460E+04	2.93548E+05	-5.03830E+05
g ₁₄	1.79985E+05	-1.18802E+06	1.92896E+06	g ₁₄	-1.47420E+05	1.00825E+06	-1.71125E+06
g ₂₄	-1.75209E+06	1.22438E+07	-2.10047E+07	g ₂₄	-5.12436E+06	3.53795E+07	-6.07106E+07
g ₃₄	3.63646E+07	-2.58230E+08	4.59567E+08	g ₃₄	-3.97431E+07	2.74524E+08	-4.73744E+08
g ₄₄	-2.52346E+08	1.79259E+09	-3.20182E+09	g ₄₄	8.91541E+08	-6.17935E+09	1.06672E+10
g ₅₄	-8.04798E+08	5.73434E+09	-1.02652E+10	g ₅₄	1.15509E+09	-7.98142E+09	1.37792E+10
g ₆₄	6.20493E+09	-4.43350E+10	7.96224E+10	g ₆₄	-2.12202E+10	1.47317E+11	-2.54785E+11
h ₀	1.76570E-02	-2.29972E-01	5.88874E-01	h ₀	-3.84745E-01	2.67907E+00	-4.65132E+00
h ₁	-5.14300E+01	3.50358E+02	-5.94881E+02	h ₁	1.75249E+01	-1.14040E+02	1.81130E+02
h ₂	-4.35070E+02	3.04310E+03	-5.31267E+03	h ₂	4.36109E+02	-3.03384E+03	5.24908E+03
h ₃	9.11675E+03	-6.20757E+04	1.05320E+05	h ₃	-2.89600E+03	1.92011E+04	-3.14326E+04
h ₄	5.39111E+04	-3.72673E+05	6.42652E+05	h ₄	-4.00697E+04	2.78484E+05	-4.81482E+05
h ₅	-3.13646E+05	2.13864E+06	-3.63397E+06	h ₅	5.82415E+04	-3.81513E+05	6.14702E+05
h ₆	-1.61357E+06	1.10854E+07	-1.89924E+07	h ₆	7.48707E+05	-5.19192E+06	8.95180E+06

Table 9. Continued

Probe 5	C ₀	C ₁	C ₂	Probe 6	C ₀	C ₁	C ₂
e ₀	-7.58893E+00	5.21403E+01	-8.84899E+01	e ₀	1.88494E+01	-1.30341E+02	2.29114E+02
e ₁	-2.38266E+02	1.34723E+03	-2.33361E+03	e ₁	-2.00591E+02	1.09473E+03	-1.93565E+03
g ₀₀	-1.43798E+01	9.93393E+01	-1.70566E+02	g ₀₀	-1.25572E+01	8.63865E+01	-1.48374E+02
g ₁₀	3.58359E+01	-2.23727E+02	3.73569E+02	g ₁₀	-8.26091E+01	5.71569E+02	-9.49025E+02
g ₂₀	9.99352E+02	-6.86792E+03	1.18025E+04	g ₂₀	2.58160E+03	-1.78748E+04	3.09113E+04
g ₃₀	-1.19075E+03	7.71276E+03	-1.23314E+04	g ₃₀	7.59168E+02	-3.69452E+03	3.35359E+03
g ₄₀	-7.38645E+04	5.09813E+05	-8.79998E+05	g ₄₀	-8.56115E+04	5.76801E+05	-9.70239E+05
g ₅₀	1.11740E+05	-7.80120E+05	1.35835E+06	g ₅₀	1.16187E+05	-8.61133E+05	1.59096E+06
g ₆₀	1.55877E+06	-1.07984E+07	1.87166E+07	g ₆₀	1.03483E+06	-6.69588E+06	1.07840E+07
g ₀₁	-4.82183E+01	3.18870E+02	-5.28083E+02	g ₀₁	-2.44007E+02	1.69444E+03	-2.94499E+03
g ₁₁	5.56140E+02	-3.80700E+03	6.57192E+03	g ₁₁	2.31122E+02	-1.35537E+03	1.99747E+03
g ₂₁	-2.51646E+04	1.73193E+05	-2.97353E+05	g ₂₁	6.39156E+03	-4.56956E+04	8.08018E+04
g ₃₁	-6.01002E+04	4.13774E+05	-7.11307E+05	g ₃₁	-8.77472E+04	6.04732E+05	-1.04218E+06
g ₄₁	1.77666E+06	-1.21816E+07	2.07840E+07	g ₄₁	1.04886E+05	-6.60505E+05	1.03171E+06
g ₅₁	9.93443E+05	-6.78904E+06	1.15847E+07	g ₅₁	2.05509E+06	-1.42725E+07	2.48042E+07
g ₆₁	-3.02195E+07	2.06232E+08	-3.50204E+08	g ₆₁	-4.31076E+06	2.85756E+07	-4.73775E+07
g ₀₂	-5.10645E+00	5.98974E+01	-1.39674E+02	g ₀₂	2.52482E+03	-1.74772E+04	3.01932E+04
g ₁₂	-6.95895E+03	4.54752E+04	-7.37580E+04	g ₁₂	1.46927E+04	-9.95600E+04	1.67769E+05
g ₂₂	8.99915E+04	-6.22696E+05	1.07220E+06	g ₂₂	-3.16404E+05	2.18892E+06	-3.77505E+06
g ₃₂	8.99449E+04	-5.74576E+05	9.02948E+05	g ₃₂	8.81921E+05	-6.43293E+06	1.16886E+07
g ₄₂	-2.19728E+06	1.44466E+07	-2.33919E+07	g ₄₂	6.63421E+06	-4.33899E+07	7.02244E+07
g ₅₂	-2.14262E+06	1.67220E+07	-3.21282E+07	g ₅₂	-4.27599E+07	3.04952E+08	-5.42039E+08
g ₆₂	6.57040E+07	-4.26447E+08	6.80966E+08	g ₆₂	-8.80642E+06	-2.22934E+07	1.90389E+08
g ₀₃	1.88317E+03	-1.24557E+04	2.06773E+04	g ₀₃	1.09054E+04	-7.58863E+04	1.32188E+05
g ₁₃	-4.84742E+03	3.32946E+04	-5.77255E+04	g ₁₃	-3.90714E+03	2.33496E+04	-3.46012E+04
g ₂₃	7.30514E+05	-5.04525E+06	8.70248E+06	g ₂₃	-3.37442E+05	2.43342E+06	-4.37673E+06
g ₃₃	2.74687E+06	-1.90262E+07	3.28425E+07	g ₃₃	2.49406E+06	-1.73504E+07	3.02275E+07
g ₄₃	-6.60524E+07	4.52758E+08	-7.74342E+08	g ₄₃	-3.82314E+06	2.04542E+07	-2.44095E+07
g ₅₃	-5.45888E+07	3.79413E+08	-6.56655E+08	g ₅₃	-3.62471E+07	2.56883E+08	-4.57598E+08
g ₆₃	1.23127E+09	-8.39929E+09	1.42961E+10	g ₆₃	1.31328E+08	-7.89905E+08	1.14667E+09
g ₀₄	3.27481E+04	-2.26745E+05	3.91065E+05	g ₀₄	-7.19724E+04	4.97928E+05	-8.59274E+05
g ₁₄	2.75136E+05	-1.83396E+06	3.04524E+06	g ₁₄	-4.21469E+05	2.84379E+06	-4.77398E+06
g ₂₄	-6.10697E+06	4.21889E+07	-7.26135E+07	g ₂₄	5.97034E+06	-4.09680E+07	6.99835E+07
g ₃₄	-1.60883E+06	1.00142E+07	-1.59152E+07	g ₃₄	-2.99230E+07	2.18469E+08	-3.97067E+08
g ₄₄	2.82945E+08	-1.92984E+09	3.27505E+09	g ₄₄	4.71562E+07	-4.23054E+08	9.06726E+08
g ₅₄	-7.61622E+07	4.72509E+08	-7.01938E+08	g ₅₄	1.21472E+09	-8.71020E+09	1.55608E+10
g ₆₄	-6.64617E+09	4.50067E+10	-7.57732E+10	g ₆₄	-3.57967E+09	2.76418E+10	-5.28686E+10
h ₀	6.20854E-01	-4.27609E+00	7.29507E+00	h ₀	-9.95764E-01	7.04315E+00	-1.24299E+01
h ₁	-9.82474E+00	6.07864E+01	-9.54089E+01	h ₁	-1.59227E+01	1.21480E+02	-2.33115E+02
h ₂	-8.74863E+02	6.05575E+03	-1.04243E+04	h ₂	8.98016E+02	-6.36004E+03	1.12331E+04
h ₃	9.51151E+02	-5.77012E+03	8.71087E+03	h ₃	2.01637E+03	-1.54906E+04	2.97348E+04
h ₄	7.31359E+04	-5.06440E+05	8.71801E+05	h ₄	-8.17224E+04	5.79684E+05	-1.02590E+06
h ₅	-3.84031E+04	2.47104E+05	-3.98127E+05	h ₅	-7.25620E+04	5.46768E+05	-1.03005E+06
h ₆	-1.41976E+06	9.82773E+06	-1.69098E+07	h ₆	1.72105E+06	-1.22442E+07	2.17375E+07

Table 9. Concluded

Probe 7	C ₀	C ₁	C ₂	Probe 8	C ₀	C ₁	C ₂
e ₀	-2.12000E+01	1.46699E+02	-2.57895E+02	e ₀	5.40305E+00	-3.27632E+01	5.23908E+01
e ₁	-2.68825E+02	1.59565E+03	-2.85526E+03	e ₁	-2.57717E+02	1.51149E+03	-2.68576E+03
g ₀₀	-1.65041E+01	1.15411E+02	-2.01710E+02	g ₀₀	-1.71932E+01	1.19514E+02	-2.07672E+02
g ₁₀	1.25020E+02	-8.53189E+02	1.51258E+03	g ₁₀	-3.69378E+01	2.47179E+02	-3.73840E+02
g ₂₀	6.44569E+02	-4.51063E+03	7.88941E+03	g ₂₀	3.76754E+03	-2.62673E+04	4.57127E+04
g ₃₀	-1.89425E+03	1.27694E+04	-2.14655E+04	g ₃₀	-1.39833E+03	1.11524E+04	-2.16313E+04
g ₄₀	-4.20841E+04	2.95235E+05	-5.18377E+05	g ₄₀	-1.67099E+05	1.16216E+06	-2.01911E+06
g ₅₀	4.69318E+04	-3.40585E+05	6.14904E+05	g ₅₀	2.40042E+05	-1.72731E+06	3.08963E+06
g ₆₀	8.84867E+05	-6.19482E+06	1.08715E+07	g ₆₀	1.86434E+06	-1.28406E+07	2.21326E+07
g ₀₁	-3.37281E+01	2.25640E+02	-3.84842E+02	g ₀₁	-2.71856E+02	1.88810E+03	-3.27596E+03
g ₁₁	7.43156E+02	-5.23723E+03	9.22523E+03	g ₁₁	7.31147E+02	-4.83174E+03	7.86765E+03
g ₂₁	-2.67948E+04	1.90015E+05	-3.36334E+05	g ₂₁	1.30027E+04	-9.20615E+04	1.62008E+05
g ₃₁	-1.62591E+05	1.14301E+06	-2.00619E+06	g ₃₁	-1.36977E+05	9.27431E+05	-1.55717E+06
g ₄₁	2.19438E+06	-1.54688E+07	2.71598E+07	g ₄₁	-3.60943E+04	4.10803E+05	-1.01801E+06
g ₅₁	4.77502E+06	-3.33065E+07	5.79988E+07	g ₅₁	2.76224E+06	-1.82980E+07	2.99446E+07
g ₆₁	-4.52570E+07	3.16983E+08	-5.53190E+08	g ₆₁	-4.46144E+06	2.56506E+07	-3.42584E+07
g ₀₂	1.70424E+02	-1.23723E+03	2.22448E+03	g ₀₂	2.23971E+03	-1.54150E+04	2.64504E+04
g ₁₂	-2.42798E+04	1.70142E+05	-2.97270E+05	g ₁₂	1.84299E+04	-1.26954E+05	2.18001E+05
g ₂₂	2.40584E+05	-1.71490E+06	3.05115E+06	g ₂₂	-5.17267E+05	3.61174E+06	-6.28847E+06
g ₃₂	2.15128E+06	-1.52503E+07	2.69491E+07	g ₃₂	1.26002E+06	-8.97946E+06	1.59477E+07
g ₄₂	-1.63870E+07	1.17130E+08	-2.08920E+08	g ₄₂	2.04529E+07	-1.42831E+08	2.48718E+08
g ₅₂	-6.87146E+07	4.90013E+08	-8.71209E+08	g ₅₂	-6.41988E+07	4.52208E+08	-7.94039E+08
g ₆₂	4.71509E+08	-3.36881E+09	6.00394E+09	g ₆₂	-1.78857E+08	1.24390E+09	-2.15744E+09
g ₀₃	2.42948E+03	-1.65682E+04	2.86220E+04	g ₀₃	1.18854E+04	-8.24339E+04	1.42864E+05
g ₁₃	9.39154E+03	-6.79798E+04	1.20265E+05	g ₁₃	-2.77833E+04	1.84070E+05	-3.01788E+05
g ₂₃	6.91308E+05	-4.89160E+06	8.61102E+06	g ₂₃	-5.88781E+05	4.14832E+06	-7.27701E+06
g ₃₃	7.89613E+06	-5.52030E+07	9.64933E+07	g ₃₃	6.79541E+06	-4.63021E+07	7.84414E+07
g ₄₃	-8.51345E+07	5.95341E+08	-1.03696E+09	g ₄₃	-8.11797E+06	4.99906E+07	-7.54196E+07
g ₅₃	-2.92030E+08	2.03590E+09	-3.54780E+09	g ₅₃	-1.17690E+08	7.80266E+08	-1.28058E+09
g ₆₃	2.09116E+09	-1.45326E+10	2.51795E+10	g ₆₃	3.56674E+08	-2.24908E+09	3.48056E+09
g ₀₄	3.93001E+04	-2.77735E+05	4.90044E+05	g ₀₄	-6.55875E+04	4.51112E+05	-7.74279E+05
g ₁₄	9.20904E+05	-6.46473E+06	1.13089E+07	g ₁₄	-4.51194E+05	3.10883E+06	-5.34411E+06
g ₂₄	-1.19280E+07	8.48641E+07	-1.50648E+08	g ₂₄	1.12151E+07	-7.81910E+07	1.35931E+08
g ₃₄	-7.75274E+07	5.48189E+08	-9.66848E+08	g ₃₄	-5.24949E+07	3.70919E+08	-6.52844E+08
g ₄₄	8.19722E+08	-5.84389E+09	1.03953E+10	g ₄₄	-2.34407E+08	1.62910E+09	-2.82256E+09
g ₅₄	2.66879E+09	-1.89482E+10	3.35721E+10	g ₅₄	2.09020E+09	-1.46772E+10	2.56814E+10
g ₆₄	-2.29761E+10	1.63641E+11	-2.90814E+11	g ₆₄	-1.24221E+09	8.93449E+09	-1.59987E+10
h ₀	1.66709E-01	-8.75511E-01	9.23253E-01	h ₀	-1.34655E+00	9.39065E+00	-1.63307E+01
h ₁	-2.34065E+01	1.65997E+02	-2.98513E+02	h ₁	-3.07352E+01	2.23851E+02	-4.11001E+02
h ₂	-1.85854E+03	1.30764E+04	-2.29602E+04	h ₂	9.87095E+02	-6.84763E+03	1.18504E+04
h ₃	4.16490E+03	-2.93414E+04	5.15683E+04	h ₃	3.24787E+03	-2.34539E+04	4.25092E+04
h ₄	1.84053E+05	-1.29627E+06	2.27875E+06	h ₄	-8.91924E+04	6.19363E+05	-1.07309E+06
h ₅	-1.99711E+05	1.40626E+06	-2.47157E+06	h ₅	-9.73567E+04	6.97184E+05	-1.25246E+06
h ₆	-4.11299E+06	2.89786E+07	-5.09639E+07	h ₆	1.82448E+06	-1.26788E+07	2.19884E+07

Table 10. Coefficients for the rake 2 correlated angle of sideslip

Probe 1	C ₀	C ₁	C ₂
e ₀	1.63664E+01	-1.31007E+02	2.40566E+02
e ₁	-2.47966E+02	1.42271E+03	-2.49662E+03
g ₀₀	-1.11270E+01	8.01469E+01	-1.42998E+02
g ₁₀	-4.43511E+01	2.92770E+02	-5.03135E+02
g ₂₀	2.58802E+02	-1.80624E+03	3.11768E+03
g ₃₀	1.21942E+04	-8.69778E+04	1.54477E+05
g ₄₀	-4.76179E+04	3.39857E+05	-6.04621E+05
g ₅₀	-5.55601E+05	3.93142E+06	-6.93070E+06
g ₆₀	2.50199E+06	-1.77161E+07	3.12674E+07
g ₀₁	-1.50989E+02	1.06805E+03	-1.88804E+03
g ₁₁	-1.52208E+03	1.03384E+04	-1.75657E+04
g ₂₁	3.03350E+04	-2.15229E+05	3.79829E+05
g ₃₁	-1.03459E+05	7.86447E+05	-1.47186E+06
g ₄₁	-4.85488E+05	3.30300E+06	-5.62040E+06
g ₅₁	3.39007E+06	-2.59446E+07	4.87894E+07
g ₆₁	-7.54753E+06	6.06857E+07	-1.18181E+08
g ₀₂	3.38913E+02	-2.27826E+03	3.82433E+03
g ₁₂	-4.45860E+02	7.30856E+02	2.49588E+03
g ₂₂	-6.91074E+04	4.93970E+05	-8.87026E+05
g ₃₂	-2.24608E+06	1.62671E+07	-2.92811E+07
g ₄₂	1.51384E+07	-1.09028E+08	1.96019E+08
g ₅₂	1.07674E+08	-7.73350E+08	1.38209E+09
g ₆₂	-5.99415E+08	4.30344E+09	-7.70075E+09
g ₀₃	1.17880E+04	-8.30981E+04	1.46215E+05
g ₁₃	7.44955E+04	-5.03508E+05	8.49550E+05
g ₂₃	-2.00756E+06	1.41663E+07	-2.48682E+07
g ₃₃	1.36147E+07	-9.87002E+07	1.77586E+08
g ₄₃	-7.29606E+06	5.56880E+07	-1.06122E+08
g ₅₃	-3.30207E+08	2.45125E+09	-4.49873E+09
g ₆₃	1.17882E+09	-8.75654E+09	1.61064E+10
g ₀₄	3.98470E+04	-2.82557E+05	4.98666E+05
g ₁₄	1.81109E+05	-1.17290E+06	1.89543E+06
g ₂₄	-3.42488E+06	2.38751E+07	-4.11400E+07
g ₃₄	1.15774E+08	-8.31112E+08	1.48407E+09
g ₄₄	-5.18995E+08	3.72248E+09	-6.66796E+09
g ₅₄	-3.97087E+09	2.86319E+10	-5.13362E+10
g ₆₄	2.02542E+10	-1.45812E+11	2.61509E+11
h ₀	-1.53649E+00	1.05675E+01	-1.82287E+01
h ₁	-1.89951E+01	1.28331E+02	-2.18135E+02
h ₂	6.87560E+02	-4.78866E+03	8.34260E+03
h ₃	5.02645E+03	-3.46466E+04	5.96679E+04
h ₄	-2.84345E+04	2.00034E+05	-3.52566E+05
h ₅	-1.45333E+05	9.97888E+05	-1.71208E+06
h ₆	1.52780E+05	-1.15306E+06	2.17583E+06

Probe 2	C ₀	C ₁	C ₂
e ₀	-2.12385E+00	1.48199E+01	-2.47838E+01
e ₁	-2.34235E+02	1.28717E+03	-2.17611E+03
g ₀₀	-1.52993E+01	1.00481E+02	-1.64659E+02
g ₁₀	5.06475E+01	-3.23116E+02	5.58472E+02
g ₂₀	-1.26924E+03	8.66393E+03	-1.46856E+04
g ₃₀	-2.85418E+03	1.85579E+04	-2.97934E+04
g ₄₀	1.46655E+05	-9.93188E+05	1.67603E+06
g ₅₀	9.34860E+04	-6.15960E+05	1.00531E+06
g ₆₀	-2.95568E+06	2.00357E+07	-3.38730E+07
g ₀₁	-7.04598E+01	4.49736E+02	-7.20840E+02
g ₁₁	1.13104E+02	-5.90941E+02	7.30974E+02
g ₂₁	-5.50253E+02	4.51649E+03	-9.28398E+03
g ₃₁	-1.01498E+04	5.46222E+04	-7.17123E+04
g ₄₁	-4.52460E+04	2.84739E+05	-4.45613E+05
g ₅₁	2.02007E+05	-1.12985E+06	1.60088E+06
g ₆₁	3.19634E+06	-2.15154E+07	3.59531E+07
g ₀₂	2.05911E+03	-1.36784E+04	2.27003E+04
g ₁₂	-1.06155E+04	7.15377E+04	-1.20190E+05
g ₂₂	-1.16784E+04	7.69833E+04	-1.23955E+05
g ₃₂	2.21818E+06	-1.47551E+07	2.44374E+07
g ₄₂	-1.33794E+07	9.05328E+07	-1.53300E+08
g ₅₂	-5.09009E+07	3.37252E+08	-5.55978E+08
g ₆₂	3.58683E+08	-2.43202E+09	4.12668E+09
g ₀₃	3.03731E+03	-1.94336E+04	3.12230E+04
g ₁₃	-1.81280E+04	1.17024E+05	-1.89139E+05
g ₂₃	-1.31861E+05	7.89951E+05	-1.15024E+06
g ₃₃	9.79969E+05	-6.26474E+06	1.01429E+07
g ₄₃	-1.69257E+06	1.73464E+07	-3.99601E+07
g ₅₃	-1.76643E+06	8.61800E+06	-1.40709E+07
g ₆₃	3.85812E+07	-3.69507E+08	8.23009E+08
g ₀₄	-4.88009E+04	3.25176E+05	-5.41061E+05
g ₁₄	4.33145E+05	-2.92300E+06	4.92133E+06
g ₂₄	-1.44237E+06	9.78142E+06	-1.66610E+07
g ₃₄	-8.20237E+07	5.47950E+08	-9.12339E+08
g ₄₄	5.11994E+08	-3.46514E+09	5.86630E+09
g ₅₄	1.78228E+09	-1.18602E+10	1.96615E+10
g ₆₄	-1.25740E+10	8.52932E+10	-1.44745E+11
h ₀	-1.61603E+00	1.10300E+01	-1.88116E+01
h ₁	5.00632E+00	-3.31428E+01	4.94988E+01
h ₂	5.94578E+02	-3.96579E+03	6.59711E+03
h ₃	-1.94868E+03	1.31955E+04	-2.20309E+04
h ₄	-4.62310E+04	3.07959E+05	-5.11761E+05
h ₅	3.12068E+04	-2.12805E+05	3.55713E+05
h ₆	8.38561E+05	-5.58389E+06	9.27910E+06

Table 10. Continued

Probe 3	C ₀	C ₁	C ₂
e ₀	7.50908E-01	-3.39968E+00	8.74067E+00
e ₁	-2.85366E+02	1.67965E+03	-2.93561E+03
g ₀₀	-7.37971E+00	5.12938E+01	-8.85241E+01
g ₁₀	8.28284E+00	-6.44275E+01	1.11613E+02
g ₂₀	9.33676E+02	-6.72200E+03	1.20260E+04
g ₃₀	8.04358E+03	-5.71969E+04	1.01312E+05
g ₄₀	-1.04970E+05	7.54292E+05	-1.34861E+06
g ₅₀	-1.66025E+05	1.17203E+06	-2.06290E+06
g ₆₀	2.48009E+06	-1.77613E+07	3.16740E+07
g ₀₁	-1.85757E+02	1.26449E+03	-2.15075E+03
g ₁₁	2.03847E+03	-1.41914E+04	2.46775E+04
g ₂₁	4.18036E+03	-2.68325E+04	4.24606E+04
g ₃₁	-1.57415E+05	1.09101E+06	-1.88336E+06
g ₄₁	-2.47490E+05	1.59349E+06	-2.57668E+06
g ₅₁	1.99192E+06	-1.37025E+07	2.34516E+07
g ₆₁	8.04187E+06	-5.43748E+07	9.23178E+07
g ₀₂	1.02881E+01	5.86389E+01	-3.52207E+02
g ₁₂	-1.05591E+04	7.08167E+04	-1.18603E+05
g ₂₂	-2.38150E+05	1.69560E+06	-3.00298E+06
g ₃₂	-4.43514E+05	3.35208E+06	-6.23499E+06
g ₄₂	2.75662E+07	-1.95958E+08	3.46665E+08
g ₅₂	8.13516E+06	-6.25137E+07	1.17987E+08
g ₆₂	-5.84586E+08	4.16386E+09	-7.38029E+09
g ₀₃	6.61996E+03	-4.48690E+04	7.60556E+04
g ₁₃	-9.41046E+04	6.55655E+05	-1.13859E+06
g ₂₃	-9.69985E+05	6.60408E+06	-1.12135E+07
g ₃₃	7.35671E+06	-5.09548E+07	8.78627E+07
g ₄₃	6.80984E+07	-4.66950E+08	7.99073E+08
g ₅₃	-9.34091E+07	6.43400E+08	-1.10120E+09
g ₆₃	-1.49087E+09	1.02744E+10	-1.76734E+10
g ₀₄	2.52562E+04	-1.80356E+05	3.20233E+05
g ₁₄	5.57573E+05	-3.80772E+06	6.49247E+06
g ₂₄	7.23939E+06	-5.08154E+07	8.87677E+07
g ₃₄	-4.62460E+05	-5.15166E+06	2.25424E+07
g ₄₄	-8.20831E+08	5.78304E+09	-1.01398E+10
g ₅₄	1.16092E+08	-5.92066E+08	6.66500E+08
g ₆₄	1.61221E+10	-1.14063E+11	2.00748E+11
h ₀	-2.48774E-01	1.88198E+00	-3.52794E+00
h ₁	3.52020E+00	-3.46097E+01	7.49116E+01
h ₂	1.51755E+02	-1.13900E+03	2.14369E+03
h ₃	4.86351E+02	-2.42007E+03	2.85363E+03
h ₄	-1.83168E+04	1.33833E+05	-2.45753E+05
h ₅	-1.68984E+04	9.91873E+04	-1.49400E+05
h ₆	5.29429E+05	-3.80171E+06	6.86362E+06

Probe 4	C ₀	C ₁	C ₂
e ₀	-1.50631E+01	8.74240E+01	-1.45353E+02
e ₁	-2.04670E+02	1.09721E+03	-1.87859E+03
g ₀₀	-1.67334E+01	1.11498E+02	-1.82093E+02
g ₁₀	1.06160E+02	-6.66512E+02	1.12162E+03
g ₂₀	2.56669E+03	-1.72719E+04	2.90257E+04
g ₃₀	8.92419E+03	-6.24780E+04	1.08607E+05
g ₄₀	-6.04859E+04	4.00154E+05	-6.62767E+05
g ₅₀	-5.09403E+05	3.50093E+06	-5.98472E+06
g ₆₀	-1.11864E+06	7.83705E+06	-1.35956E+07
g ₀₁	-2.62614E+01	1.83064E+02	-3.24900E+02
g ₁₁	1.03725E+03	-6.36492E+03	9.61288E+03
g ₂₁	1.32183E+04	-8.86328E+04	1.47809E+05
g ₃₁	-1.69494E+05	1.08565E+06	-1.72600E+06
g ₄₁	-1.81978E+06	1.20850E+07	-2.00089E+07
g ₅₁	5.36782E+06	-3.47203E+07	5.58059E+07
g ₆₁	4.26055E+07	-2.81168E+08	4.62234E+08
g ₀₂	1.57761E+03	-1.05040E+04	1.74801E+04
g ₁₂	-1.77895E+04	1.20448E+05	-2.03907E+05
g ₂₂	-1.10622E+05	7.51540E+05	-1.28013E+06
g ₃₂	1.03765E+06	-6.97335E+06	1.17667E+07
g ₄₂	-6.94407E+05	4.37731E+06	-6.31212E+06
g ₅₂	8.88152E+06	-6.15715E+07	1.03525E+08
g ₆₂	1.33980E+08	-9.06109E+08	1.51352E+09
g ₀₃	1.05815E+03	-7.72425E+03	1.42805E+04
g ₁₃	-9.24158E+04	5.79002E+05	-8.96257E+05
g ₂₃	-1.65012E+06	1.10830E+07	-1.85309E+07
g ₃₃	1.12470E+07	-7.15830E+07	1.12891E+08
g ₄₃	1.62189E+08	-1.08029E+09	1.79180E+09
g ₅₃	-2.58950E+08	1.63530E+09	-2.55570E+09
g ₆₃	-2.94302E+09	1.94004E+10	-3.18295E+10
g ₀₄	-2.85096E+04	1.87354E+05	-3.07508E+05
g ₁₄	4.29124E+04	-4.50049E+05	1.04750E+06
g ₂₄	-4.80055E+06	3.20564E+07	-5.31529E+07
g ₃₄	1.38259E+07	-7.75629E+07	1.01119E+08
g ₄₄	6.10468E+08	-4.05999E+09	6.71462E+09
g ₅₄	-8.76320E+08	5.50103E+09	-8.47199E+09
g ₆₄	-1.22579E+10	8.09756E+10	-1.32886E+11
h ₀	-4.80525E+00	3.28337E+01	-5.66965E+01
h ₁	1.22257E+01	-8.84939E+01	1.47631E+02
h ₂	2.27932E+02	-1.51378E+03	2.52120E+03
h ₃	-5.97843E+03	4.11857E+04	-7.08001E+04
h ₄	-3.76619E+04	2.54281E+05	-4.29506E+05
h ₅	1.45435E+05	-1.00829E+06	1.74236E+06
h ₆	8.25279E+05	-5.63157E+06	9.60147E+06

Table 10. Concluded

Probe 5	C ₀	C ₁	C ₂
e ₀	-4.58248E+01	3.07207E+02	-5.40818E+02
e ₁	-2.17802E+02	1.21103E+03	-2.12292E+03
g ₀₀	-1.77364E+01	1.22086E+02	-2.08973E+02
g ₁₀	1.04396E+02	-6.98710E+02	1.22160E+03
g ₂₀	-5.90234E+02	4.13545E+03	-7.17180E+03
g ₃₀	1.14460E+03	-8.98283E+03	1.72297E+04
g ₄₀	6.94575E+04	-4.82139E+05	8.30749E+05
g ₅₀	-6.46435E+04	4.64166E+05	-8.25035E+05
g ₆₀	-1.23247E+06	8.49221E+06	-1.45267E+07
g ₀₁	-6.67305E+01	4.52584E+02	-7.63337E+02
g ₁₁	-1.69692E+03	1.17138E+04	-2.01563E+04
g ₂₁	-1.75880E+04	1.25951E+05	-2.23914E+05
g ₃₁	1.87860E+05	-1.30458E+06	2.26217E+06
g ₄₁	1.69360E+06	-1.19915E+07	2.10390E+07
g ₅₁	-4.62681E+06	3.22970E+07	-5.62756E+07
g ₆₁	-2.76294E+07	1.95396E+08	-3.42093E+08
g ₀₂	1.22506E+03	-8.45984E+03	1.46101E+04
g ₁₂	-2.12141E+04	1.46520E+05	-2.52779E+05
g ₂₂	1.02353E+05	-7.18744E+05	1.26552E+06
g ₃₂	2.30122E+06	-1.59244E+07	2.75012E+07
g ₄₂	-4.27637E+06	3.00547E+07	-5.33905E+07
g ₅₂	-5.36509E+07	3.71788E+08	-6.42822E+08
g ₆₂	3.81472E+07	-2.67582E+08	4.83514E+08
g ₀₃	1.30332E+04	-8.99137E+04	1.54486E+05
g ₁₃	1.19323E+05	-8.25782E+05	1.42618E+06
g ₂₃	3.54122E+05	-2.77679E+06	5.33236E+06
g ₃₃	-4.52551E+06	3.11337E+07	-5.36627E+07
g ₄₃	-6.54453E+07	4.76536E+08	-8.59265E+08
g ₅₃	7.19894E+07	-4.98323E+08	8.64492E+08
g ₆₃	7.10788E+08	-5.35285E+09	9.89494E+09
g ₀₄	4.09865E+04	-2.84079E+05	4.89344E+05
g ₁₄	7.67131E+05	-5.30614E+06	9.16437E+06
g ₂₄	-1.50719E+06	9.66759E+06	-1.55352E+07
g ₃₄	-5.07657E+07	3.49885E+08	-6.02802E+08
g ₄₄	-9.91367E+07	7.53778E+08	-1.39568E+09
g ₅₄	1.10224E+09	-7.60747E+09	1.31203E+10
g ₆₄	6.42946E+08	-5.88006E+09	1.21152E+10
h ₀	-2.40896E+00	1.64565E+01	-2.83287E+01
h ₁	-7.43476E+01	5.12282E+02	-8.84093E+02
h ₂	6.28721E+02	-4.26246E+03	7.22893E+03
h ₃	1.62608E+04	-1.11636E+05	1.90995E+05
h ₄	-6.14412E+03	3.91100E+04	-6.36991E+04
h ₅	-7.82438E+05	5.36648E+06	-9.17604E+06
h ₆	-2.23393E+06	1.53526E+07	-2.62804E+07

Probe 6	C ₀	C ₁	C ₂
e ₀	9.41113E+00	-6.45826E+01	1.09388E+02
e ₁	-3.31112E+01	-8.71018E+01	1.37952E+02
g ₀₀	-1.21460E+01	8.11549E+01	-1.36367E+02
g ₁₀	-9.91595E+01	7.19567E+02	-1.21142E+03
g ₂₀	2.23993E+03	-1.53570E+04	2.62963E+04
g ₃₀	6.93066E+03	-4.74954E+04	8.14523E+04
g ₄₀	-7.09375E+04	4.89834E+05	-8.46702E+05
g ₅₀	1.21156E+04	-9.63864E+04	1.77771E+05
g ₆₀	2.12227E+05	-1.47580E+06	2.64168E+06
g ₀₁	-2.95726E+02	2.02598E+03	-3.46773E+03
g ₁₁	1.09766E+03	-7.48383E+03	1.26968E+04
g ₂₁	4.00358E+04	-2.74638E+05	4.69443E+05
g ₃₁	-4.40562E+04	3.11180E+05	-5.43532E+05
g ₄₁	-1.77974E+06	1.20908E+07	-2.05298E+07
g ₅₁	-9.00395E+05	5.78695E+06	-9.34054E+06
g ₆₁	2.83380E+07	-1.91013E+08	3.22223E+08
g ₀₂	1.50115E+03	-1.01490E+04	1.71251E+04
g ₁₂	9.85623E+03	-6.42635E+04	1.04024E+05
g ₂₂	-4.64180E+05	3.21362E+06	-5.54939E+06
g ₃₂	1.34186E+06	-9.46407E+06	1.65943E+07
g ₄₂	1.96424E+07	-1.37153E+08	2.39050E+08
g ₅₂	-5.26100E+07	3.64661E+08	-6.28794E+08
g ₆₂	-2.13313E+08	1.51423E+09	-2.68673E+09
g ₀₃	1.35031E+04	-9.25091E+04	1.58366E+05
g ₁₃	-3.69536E+04	2.47836E+05	-4.13616E+05
g ₂₃	-2.07435E+06	1.42360E+07	-2.43663E+07
g ₃₃	1.24228E+06	-8.57302E+06	1.47038E+07
g ₄₃	1.02243E+08	-6.99009E+08	1.19290E+09
g ₅₃	1.03915E+08	-7.07414E+08	1.20193E+09
g ₆₃	-1.78469E+09	1.21694E+10	-2.07259E+10
g ₀₄	-4.53724E+04	3.08269E+05	-5.22752E+05
g ₁₄	-1.05503E+04	-5.48919E+04	3.21084E+05
g ₂₄	1.11114E+07	-7.73051E+07	1.34133E+08
g ₃₄	-8.20677E+07	5.74757E+08	-1.00314E+09
g ₄₄	-2.67376E+08	1.90725E+09	-3.39369E+09
g ₅₄	2.61737E+09	-1.81667E+10	3.14234E+10
g ₆₄	-1.33672E+08	-4.85091E+08	3.38576E+09
h ₀	1.50066E-01	-1.17572E+00	2.24643E+00
h ₁	-7.20377E+01	4.94718E+02	-8.60175E+02
h ₂	3.39921E+02	-2.41537E+03	4.27383E+03
h ₃	7.17691E+03	-4.94679E+04	8.51710E+04
h ₄	-3.03414E+04	2.14445E+05	-3.77257E+05
h ₅	-1.81374E+05	1.24771E+06	-2.14549E+06
h ₆	5.29298E+05	-3.74625E+06	6.59437E+06

Figure 1. Mach number error due to total pressure recovery.

Figure 2. 10° wedge probe design.

Figure 3. 4 X 4 cone-probe rake assembly.

Figure 4. 2 X 4 cone-probe rake assembly.

Figure 5. 2 X 3 cone-probe rake assembly.

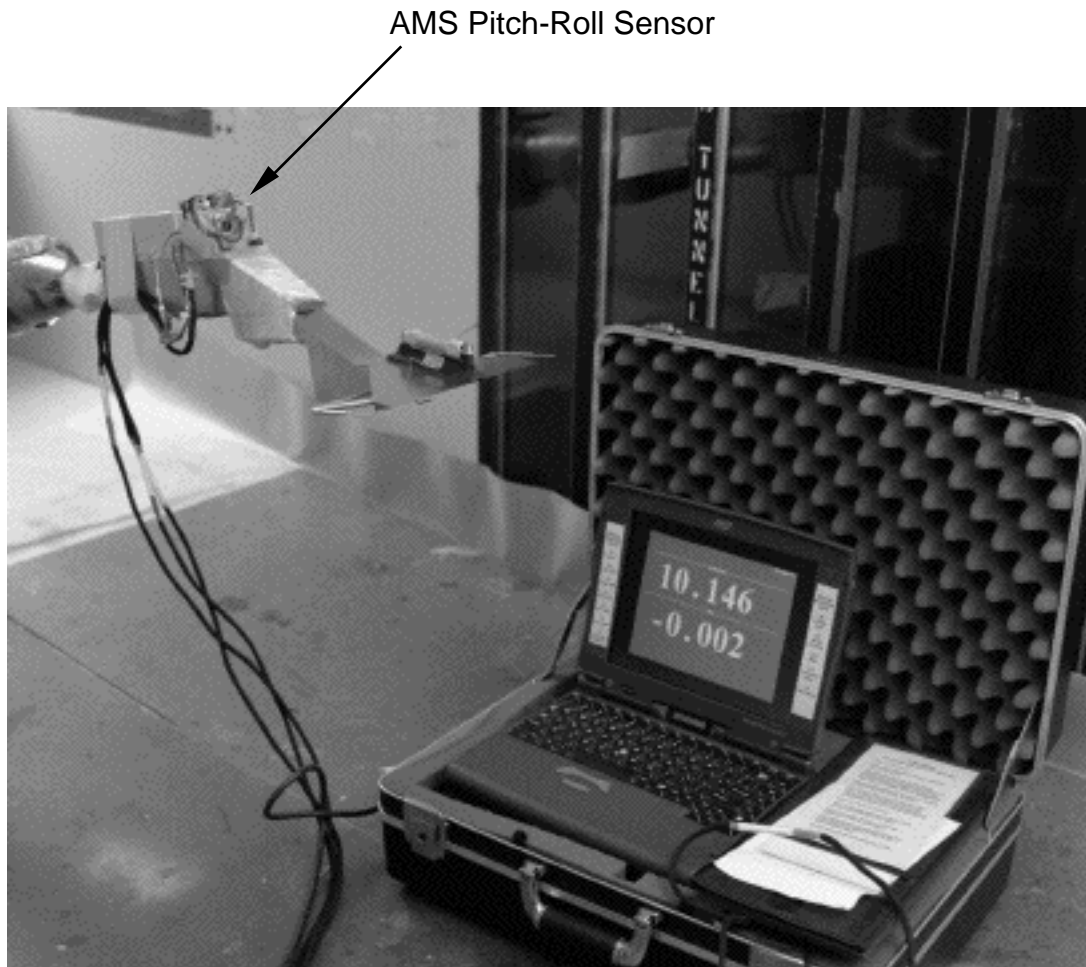
Figure 6. Wedge installation.

Figure 7. Wedge orientations relative to the test section.

Figure 8. Cone-probe rake installation.

Figure 9. Wedge positioning for cone-probe calibration.

Figure 10. Measured sting adapter to model pitch angle relationship.



Laptop Computer and Signal Conditioning Equipment

Figure 11. Langley angle measurement system.

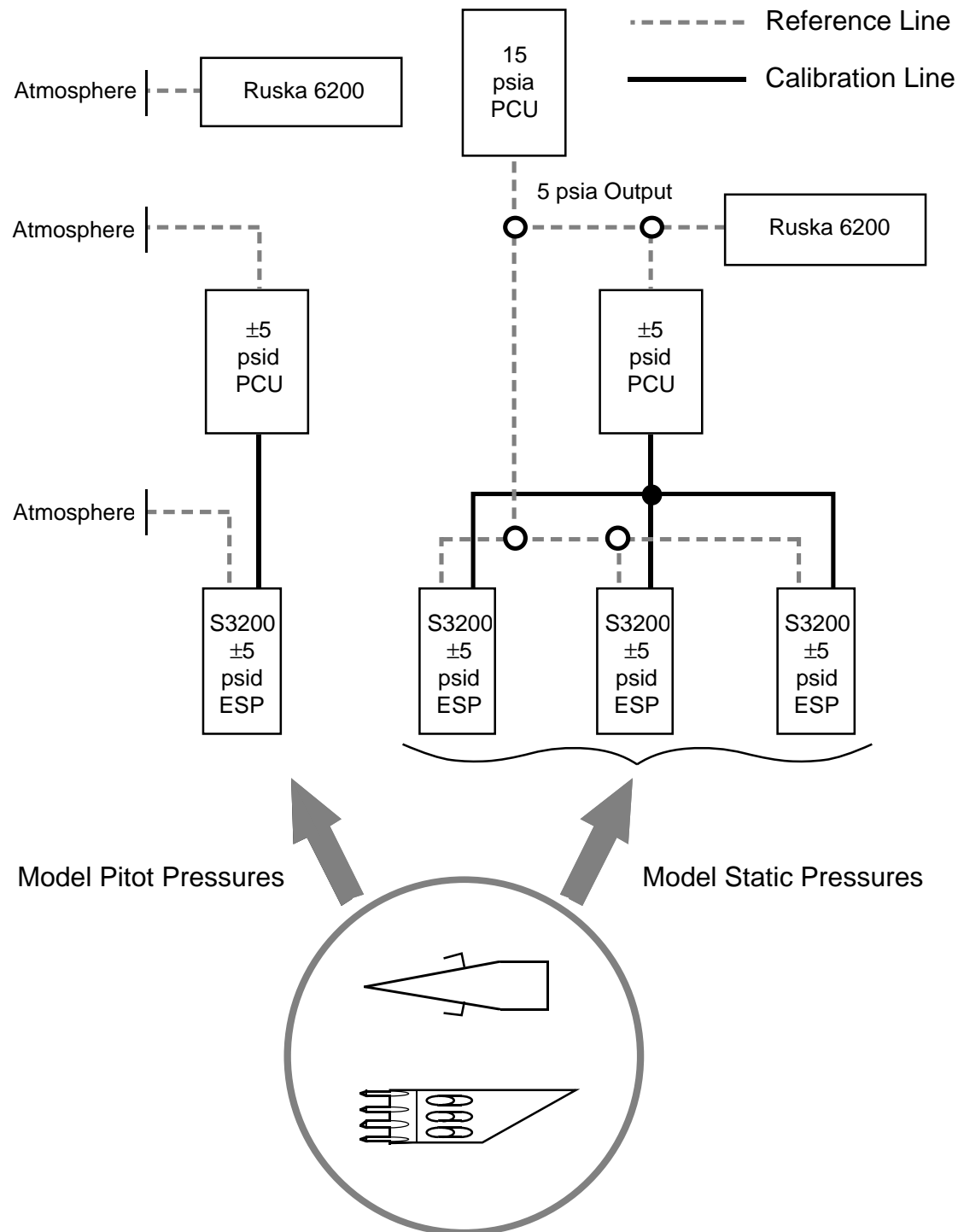


Figure 12. ESP scanner reference pressure arrangement.

Figure 13. General wedge flow relationship.

Figure 14. Complementary wedge pressure and geometric variables.

Figure 15. Boundary layer displacement effect on oblique shock.

Figure 16. Freestream Mach number variation with calculation method for 10° wedge.

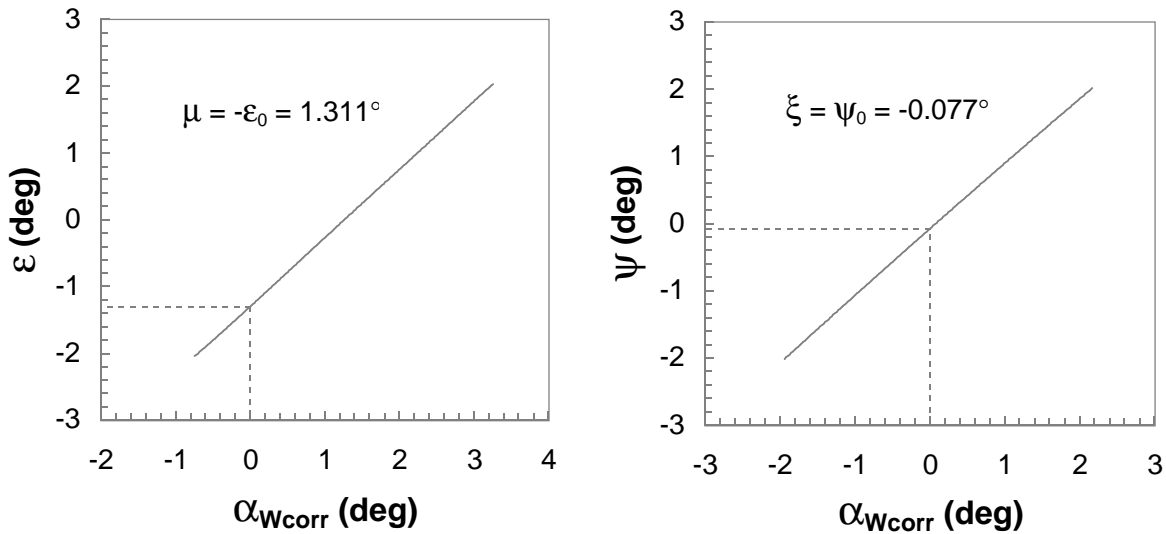
Figure 17. Freestream normal shock recovery distribution.

Figure 18. Wedge angle of attack sensitivity to static pressure ratio.

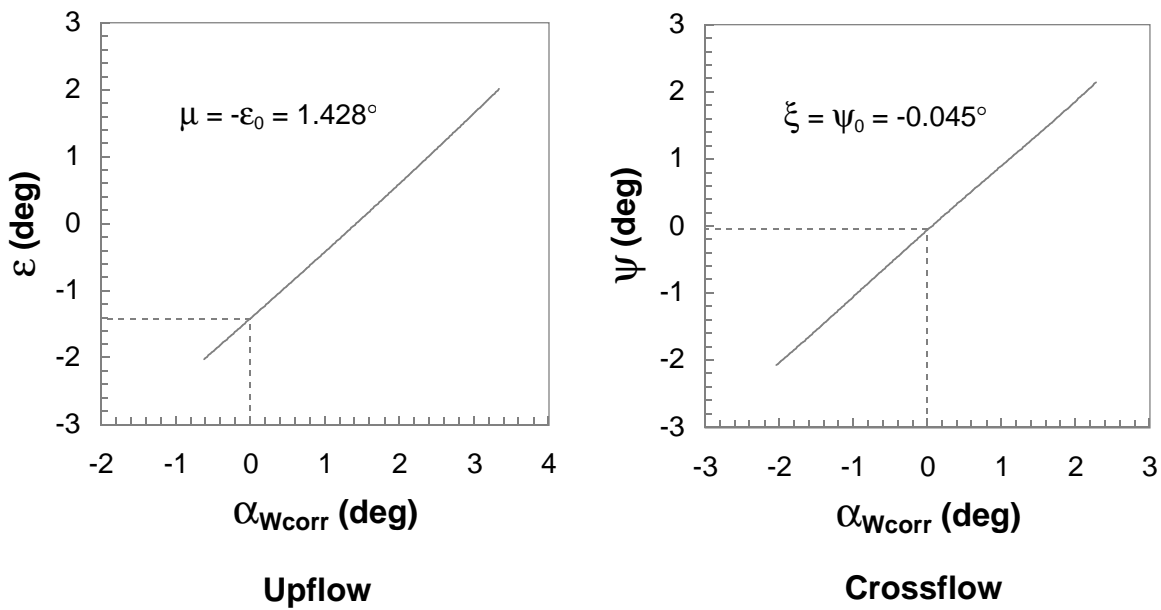
Figure 18. Continued.

Figure 18. Concluded.

$z = 16.24$ in



$z = 19.73$ in



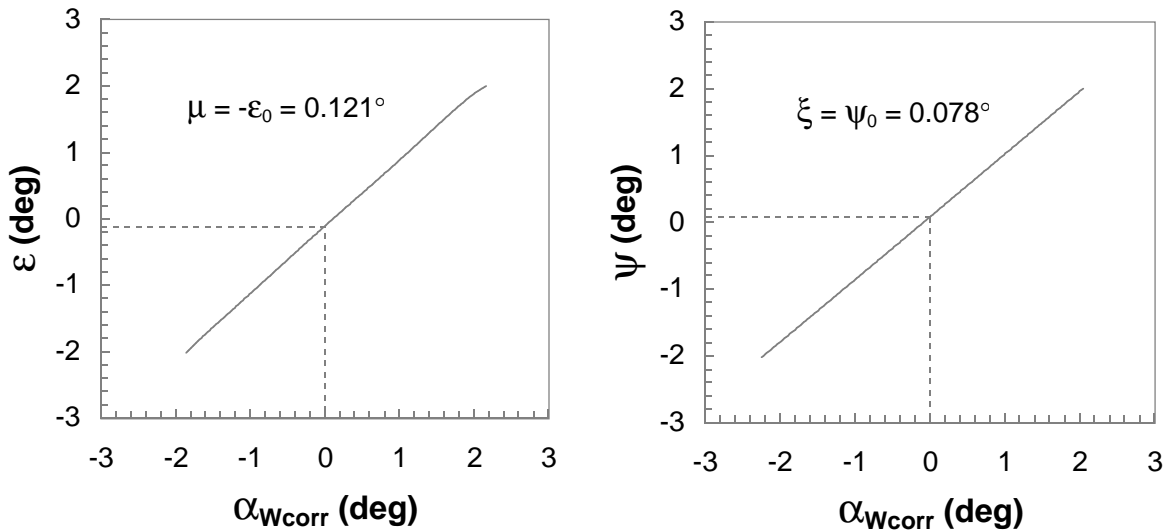
Upflow

Crossflow

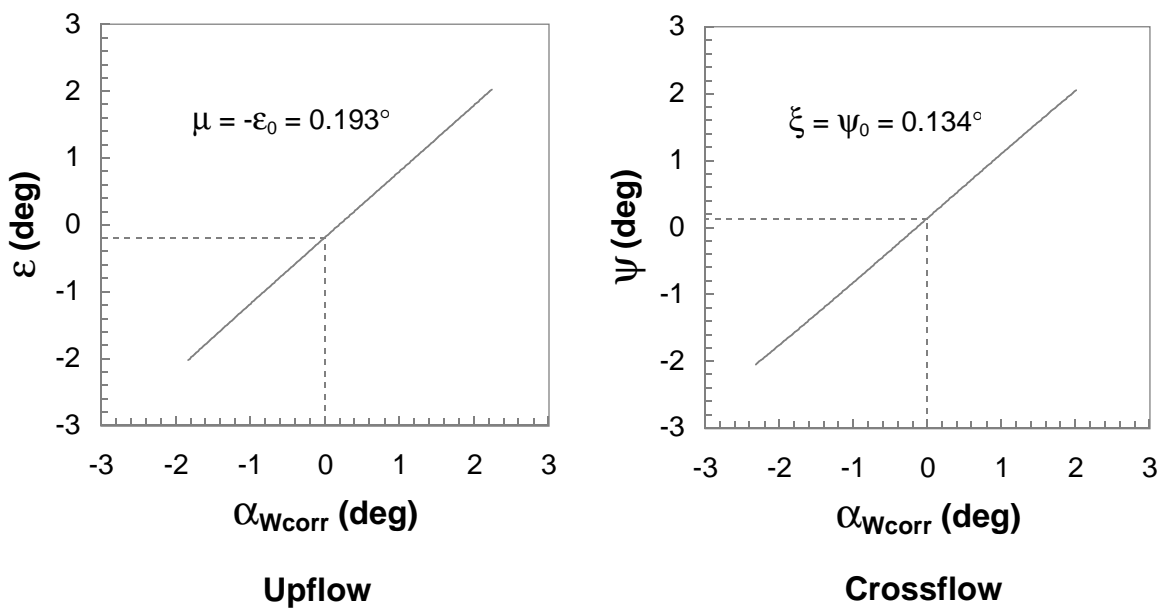
UPWT Test Section 1, $M_{\text{set}} = 2.15$

Figure 19. Tunnel upflow and crossflow derivation.

$$\underline{z = 16.24 \text{ in}}$$



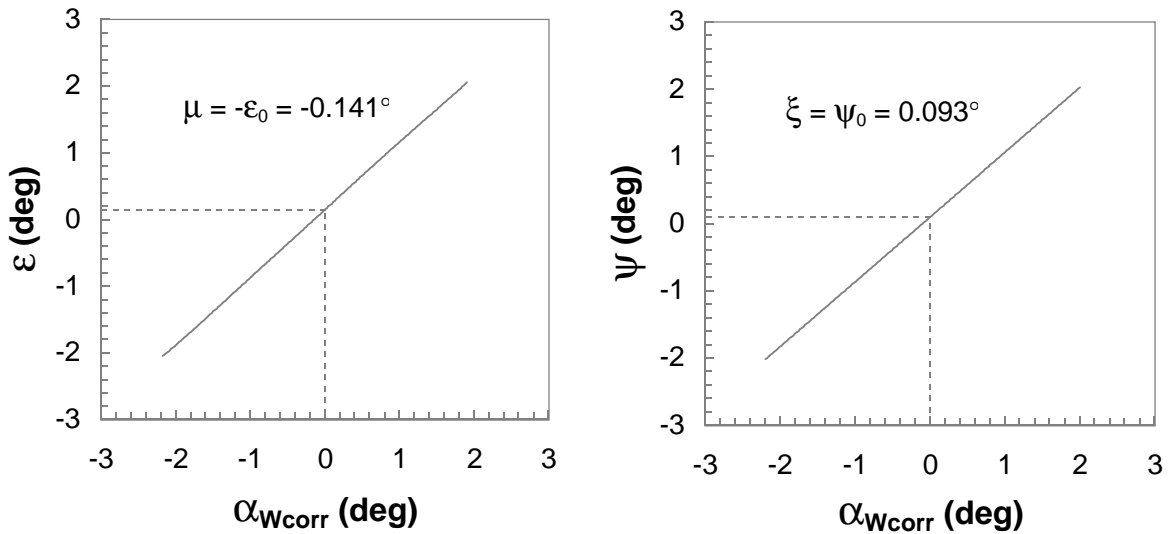
$$\underline{z = 19.73 \text{ in}}$$



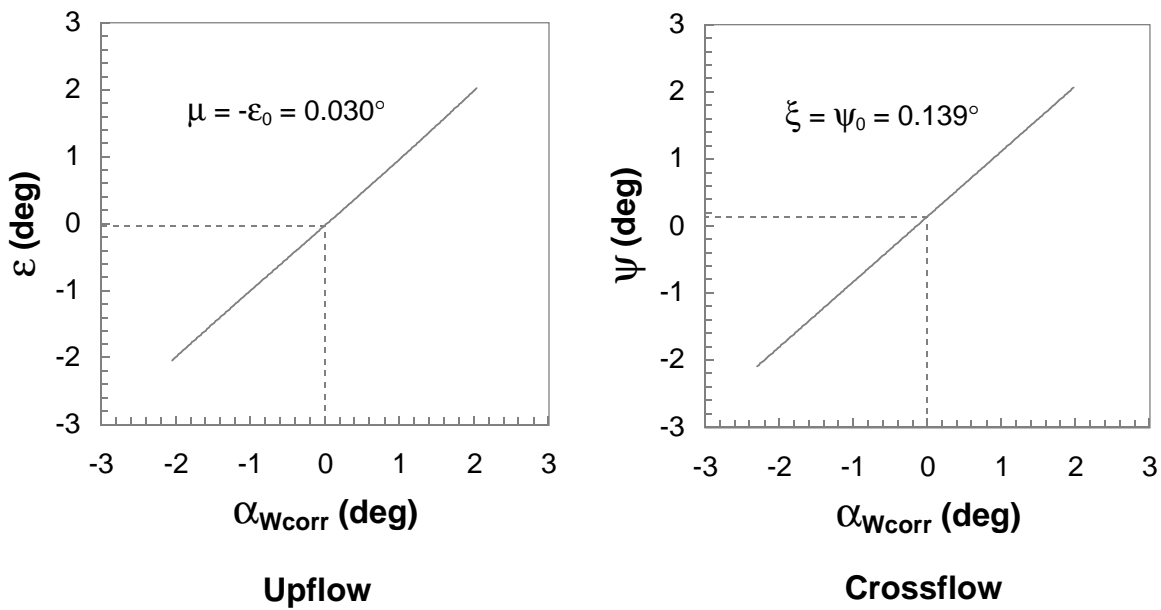
UPWT Test Section 2, M_{set} = 2.29

Figure 19. Continued.

$z = 16.24$ in



$z = 19.73$ in



UPWT Test Section 2, $M_{\text{set}} = 2.40$

Figure 19. Concluded.

Figure 20. Linear test section flow upflow distribution (z-direction).

Figure 21. Linear test section flow crossflow distribution (z-direction).

Figure 22. Wedge outboard pitot survey locations.

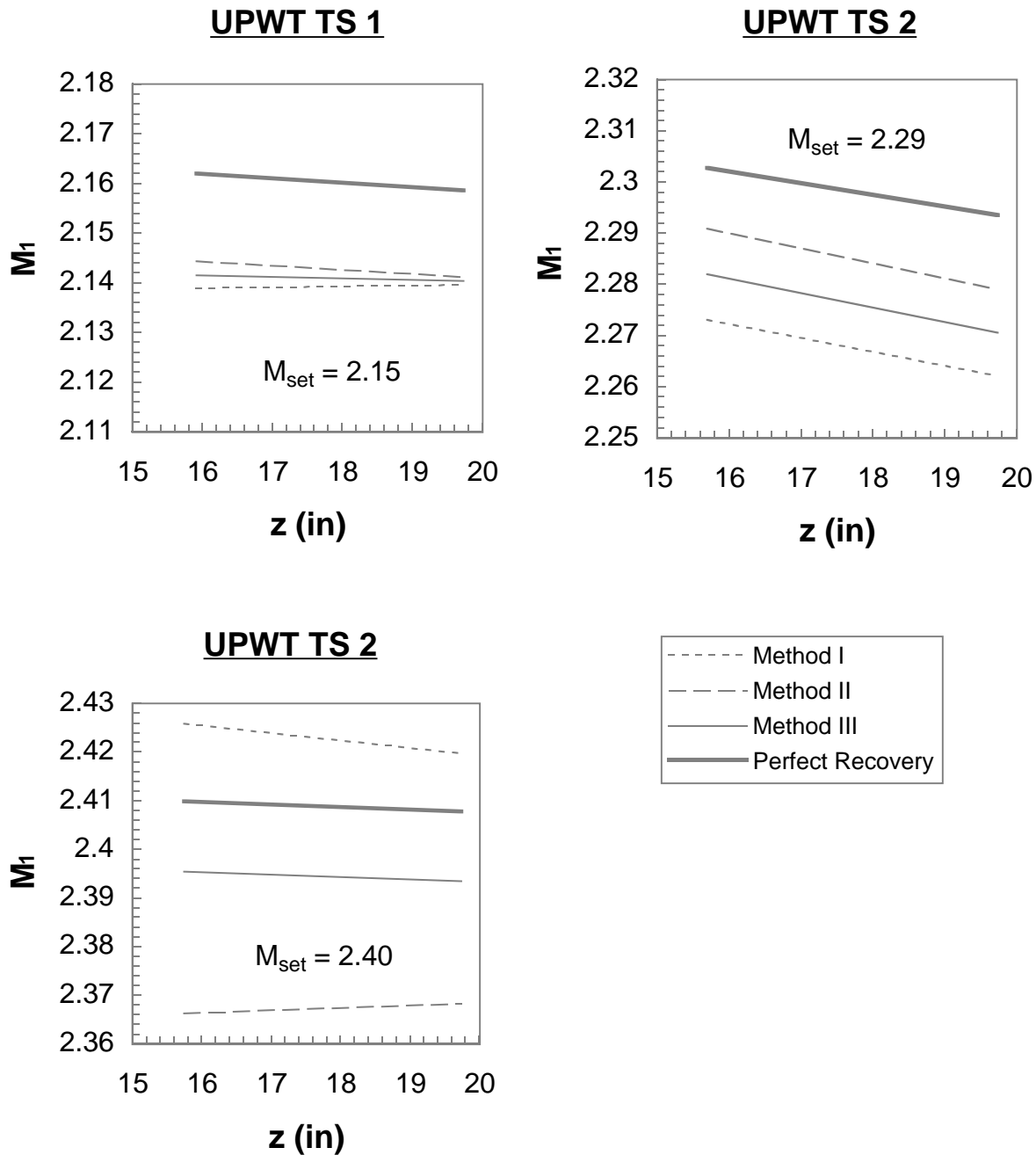


Figure 23. Linear test section Mach number distribution (z -cirection) for various calculation methods.

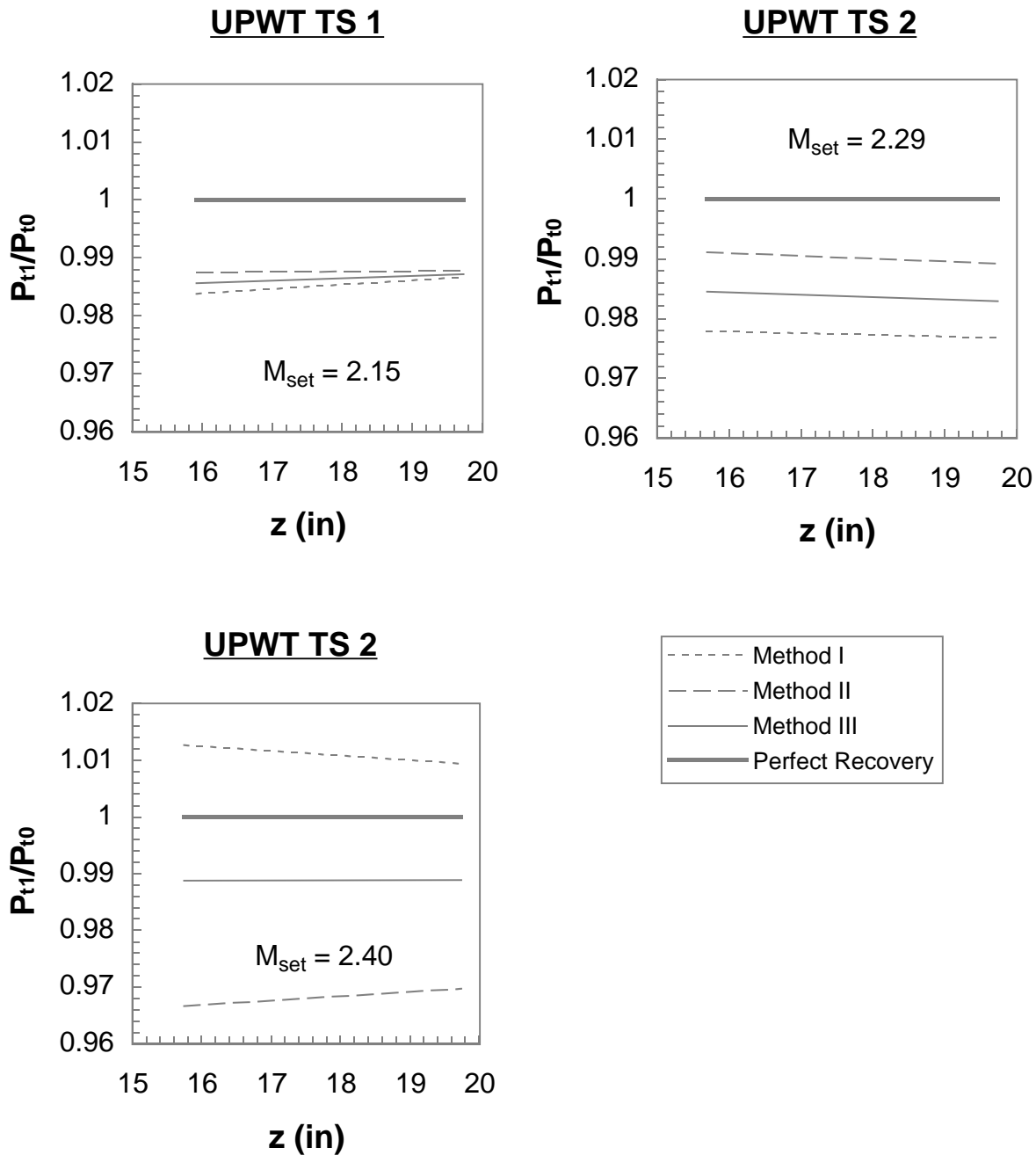


Figure 24. Linear test section total pressure recovery distribution (z -direction) for various calculation methods.

Figure 25. Calculated viscous flow deflection increment from Method III.

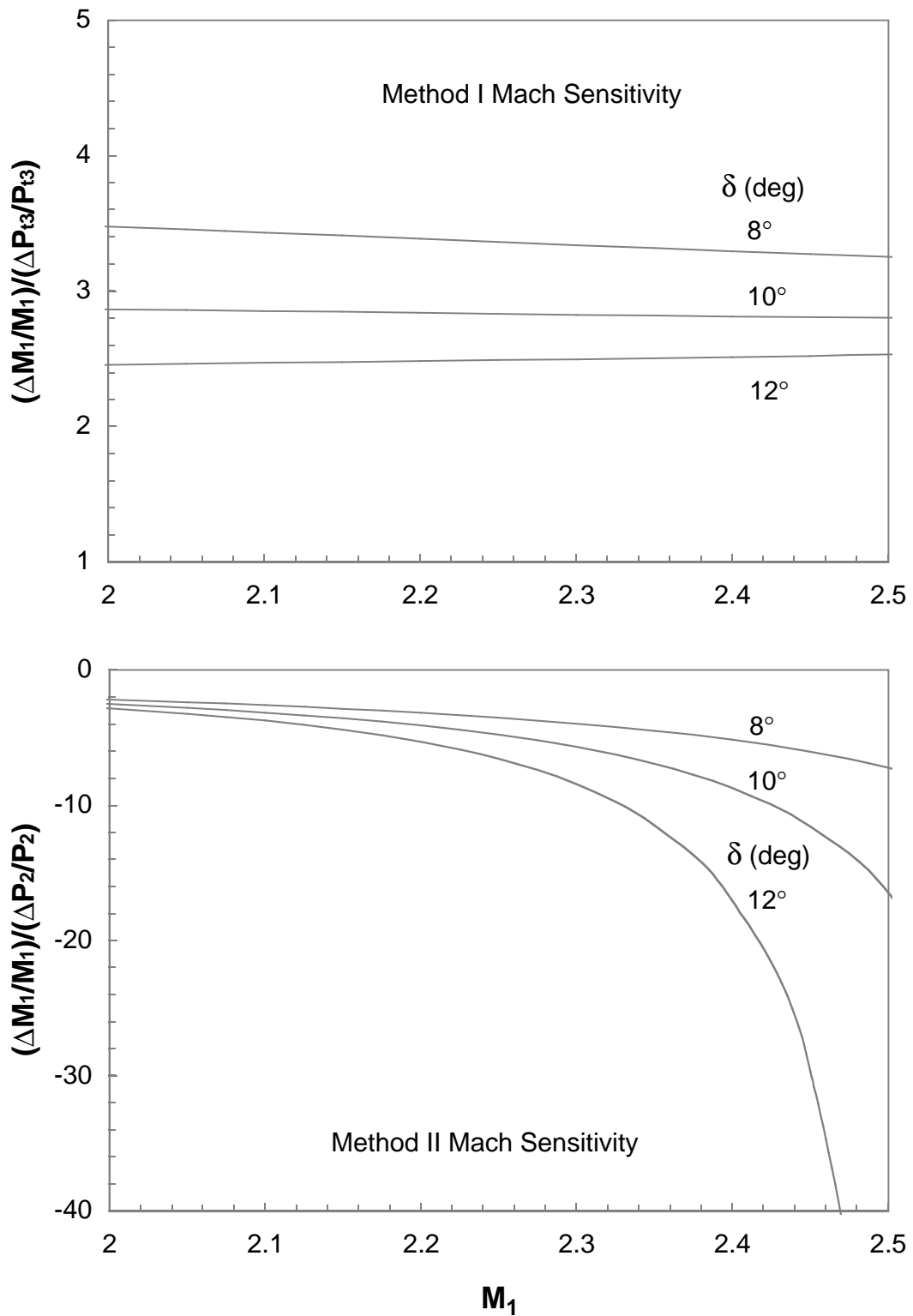
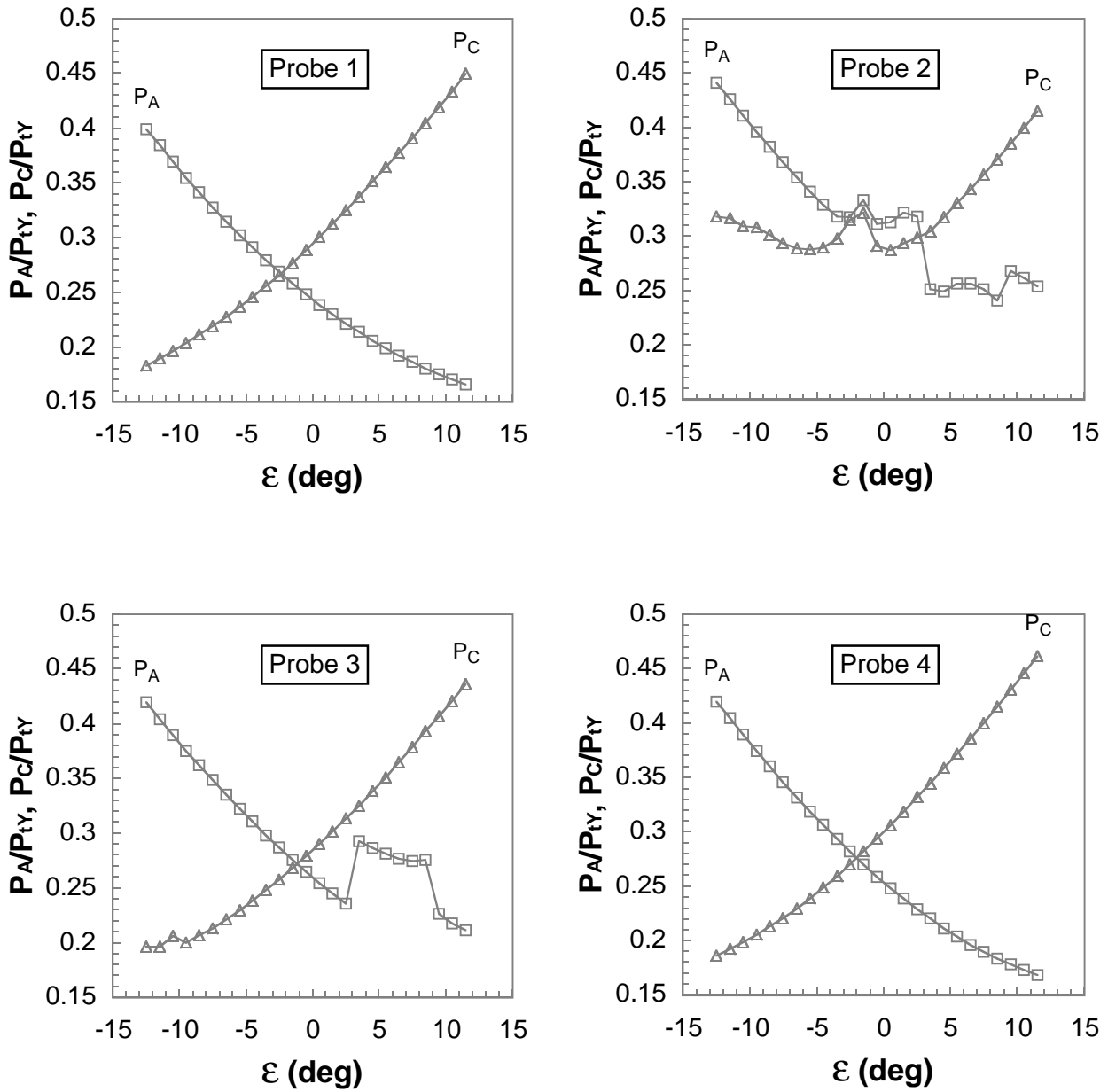
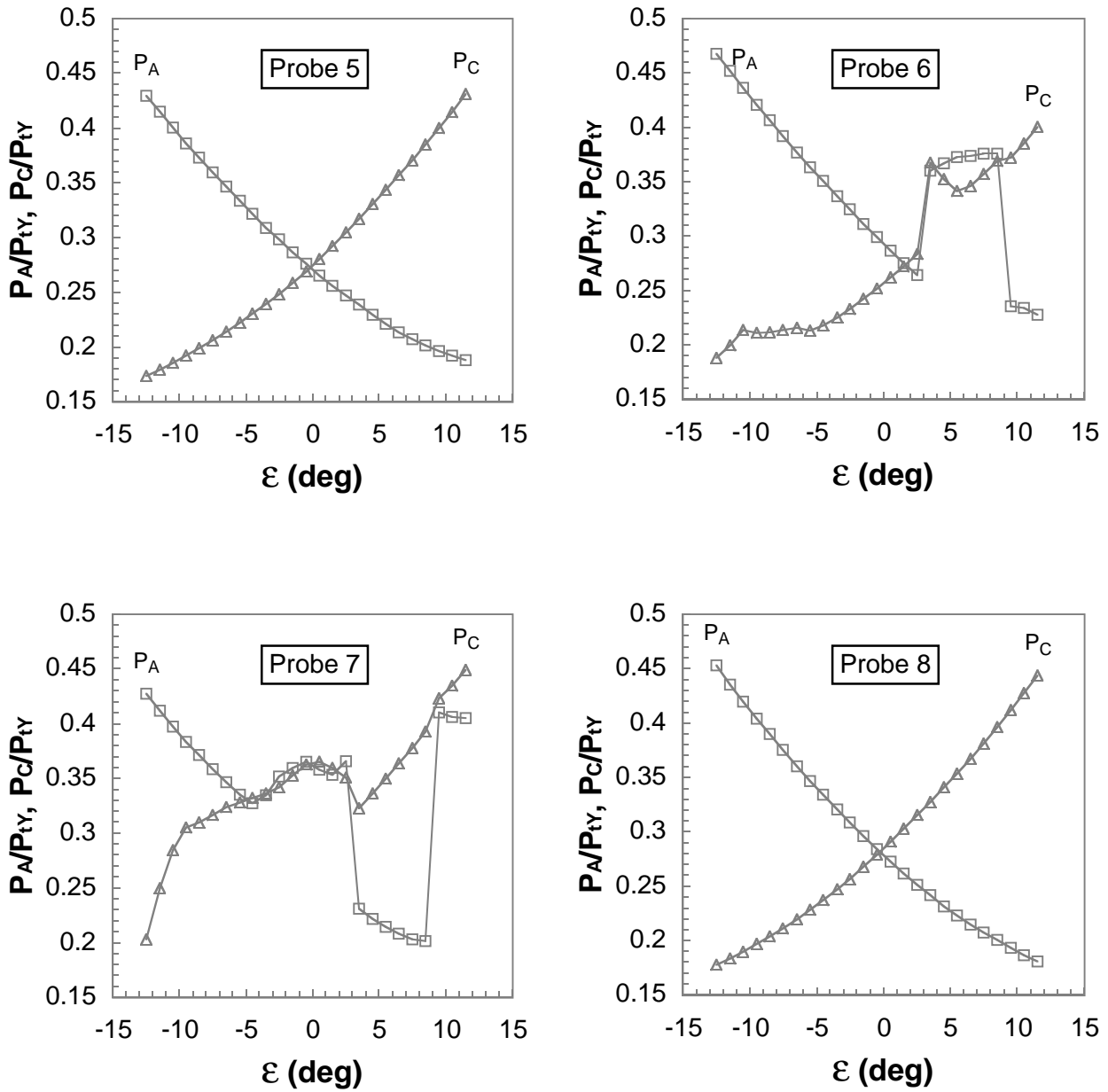


Figure 26. Comparison of Mach number sensitivity to wedge inclination.



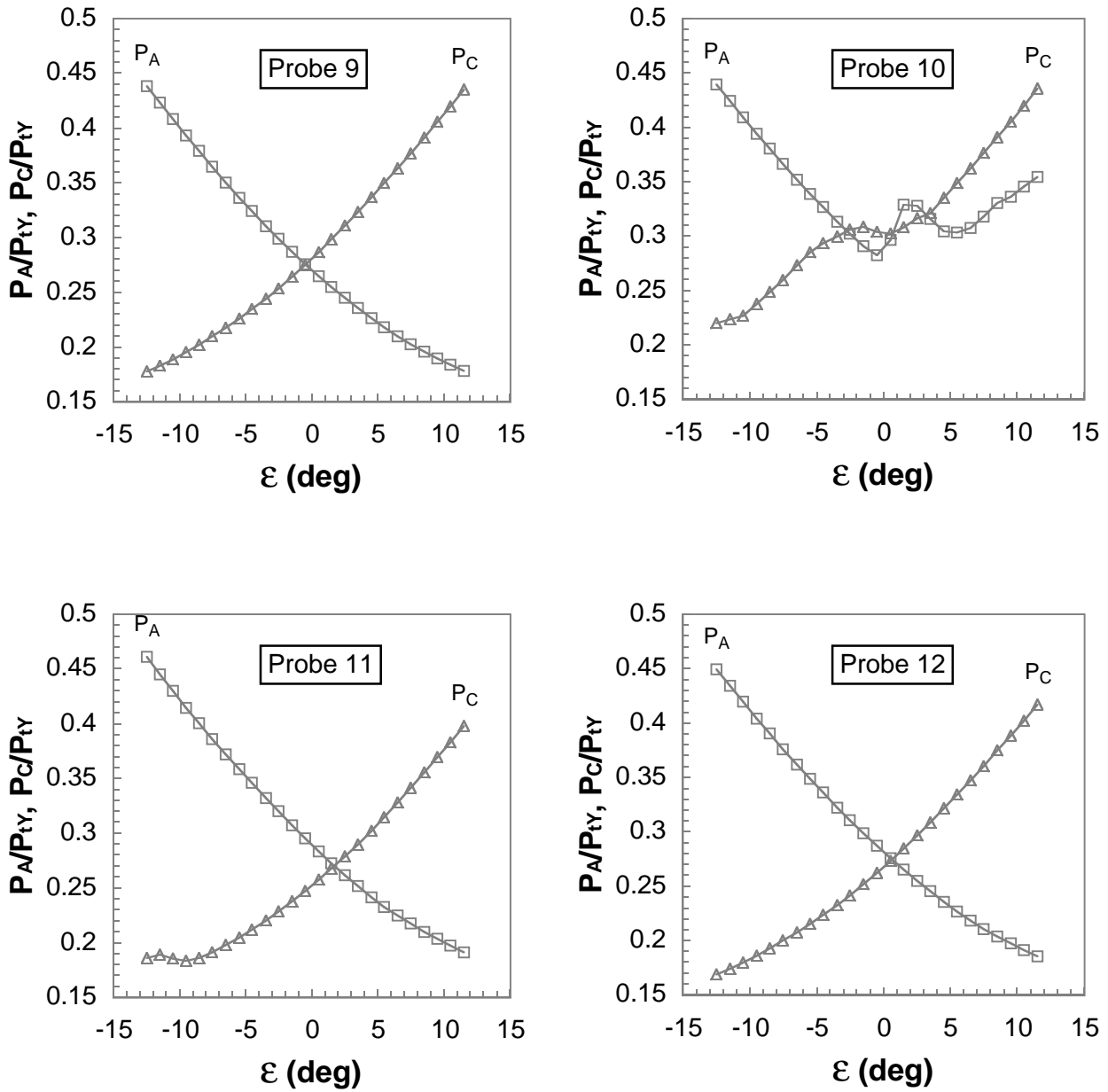
UPWT TS 2, $M_{\text{set}} = 2.40, \Psi = 0^\circ$

Figure 27. 16-probe rake static pressure polars for taps A and C.



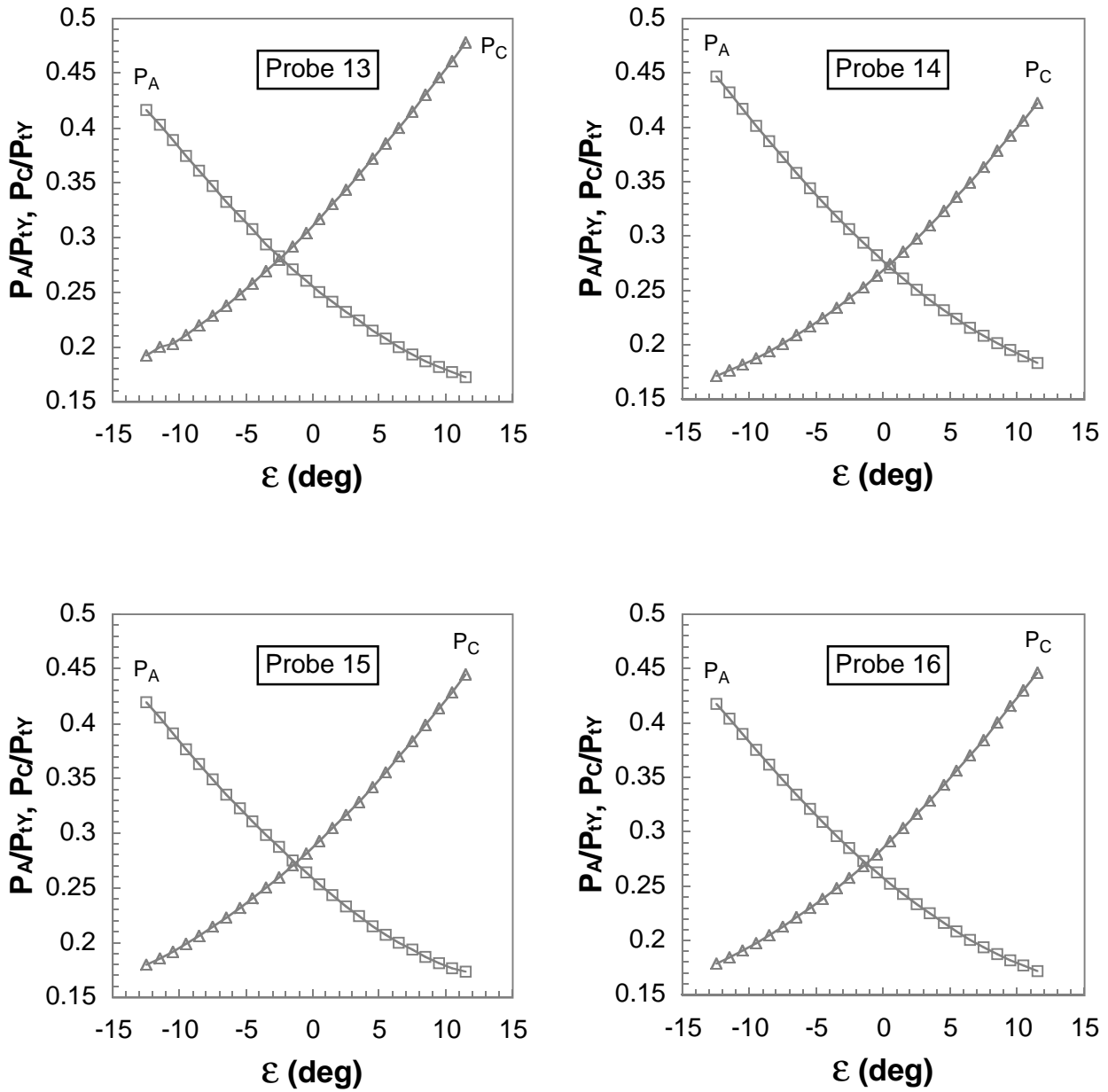
UPWT TS 2, $M_{set} = 2.40, \Psi = 0^\circ$

Figure 27. Continued.



UPWT TS 2, $M_{set} = 2.40, \Psi = 0^\circ$

Figure 27. Continued.



UPWT TS 2, $M_{set} = 2.40$, $\psi = 0^\circ$

Figure 27. Concluded.



Probes Affected by Flow Disturbances

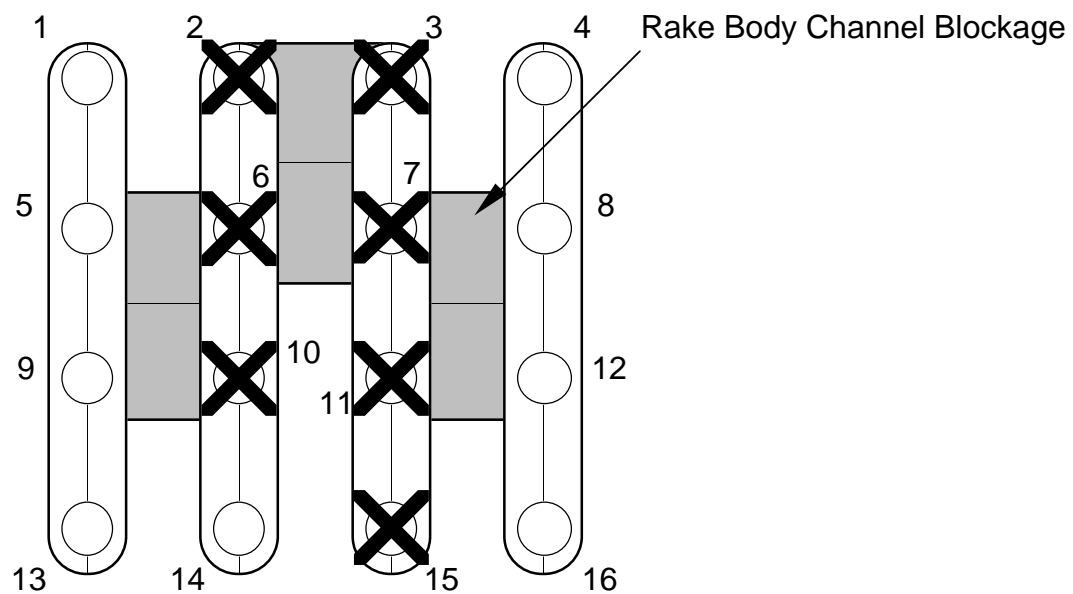
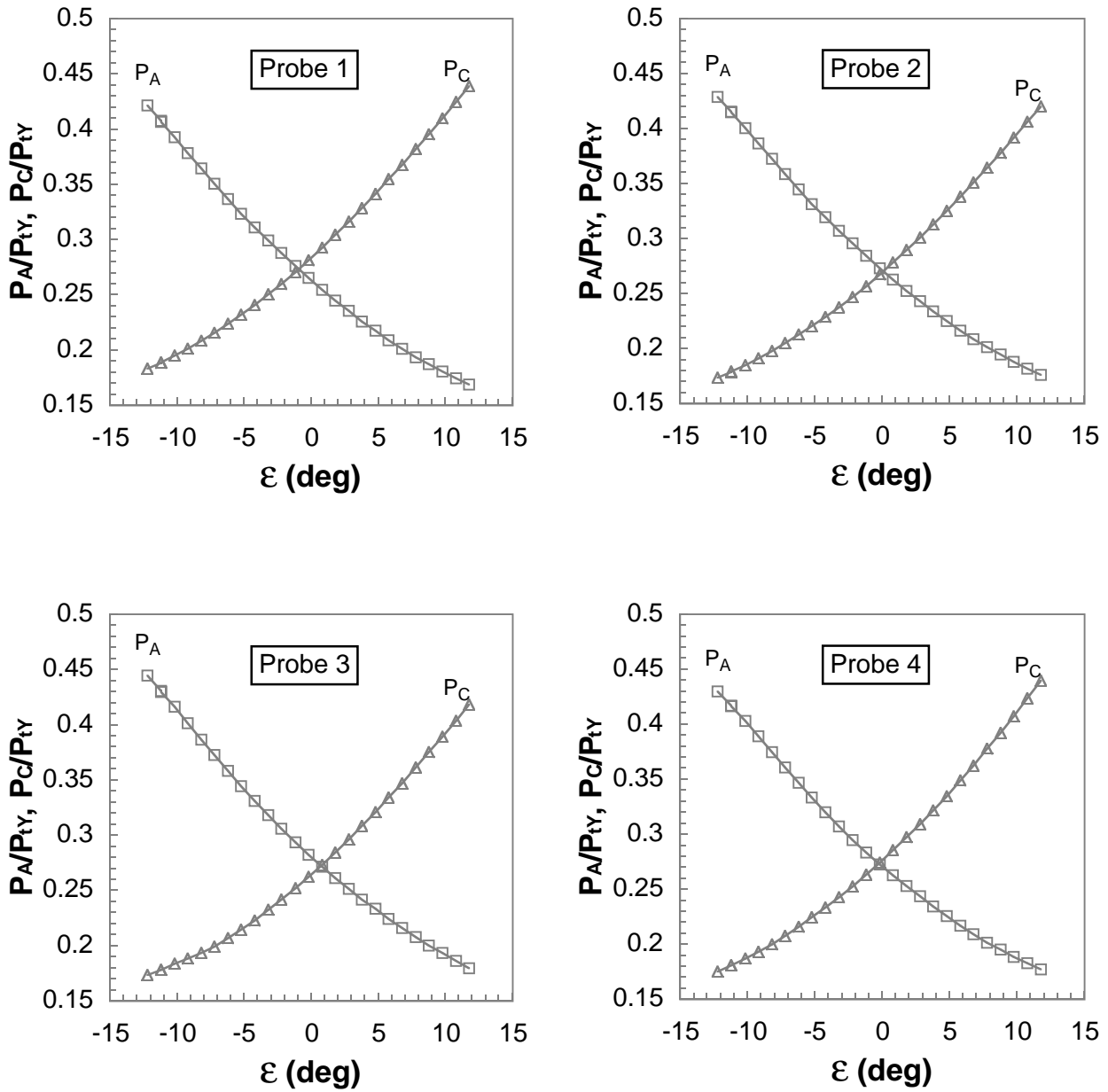
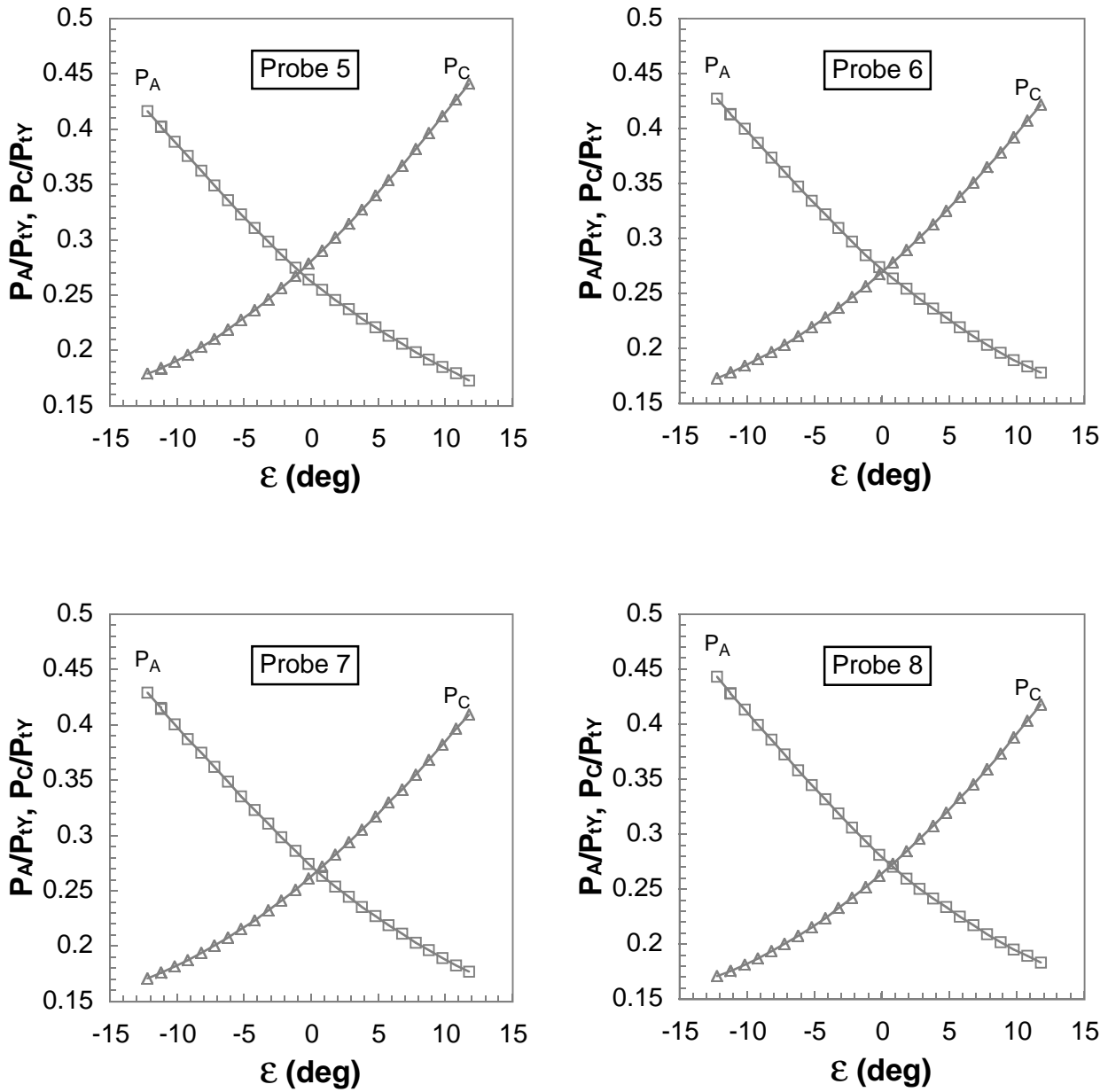


Figure 28. Location of affected probes relative to rake blockage areas.



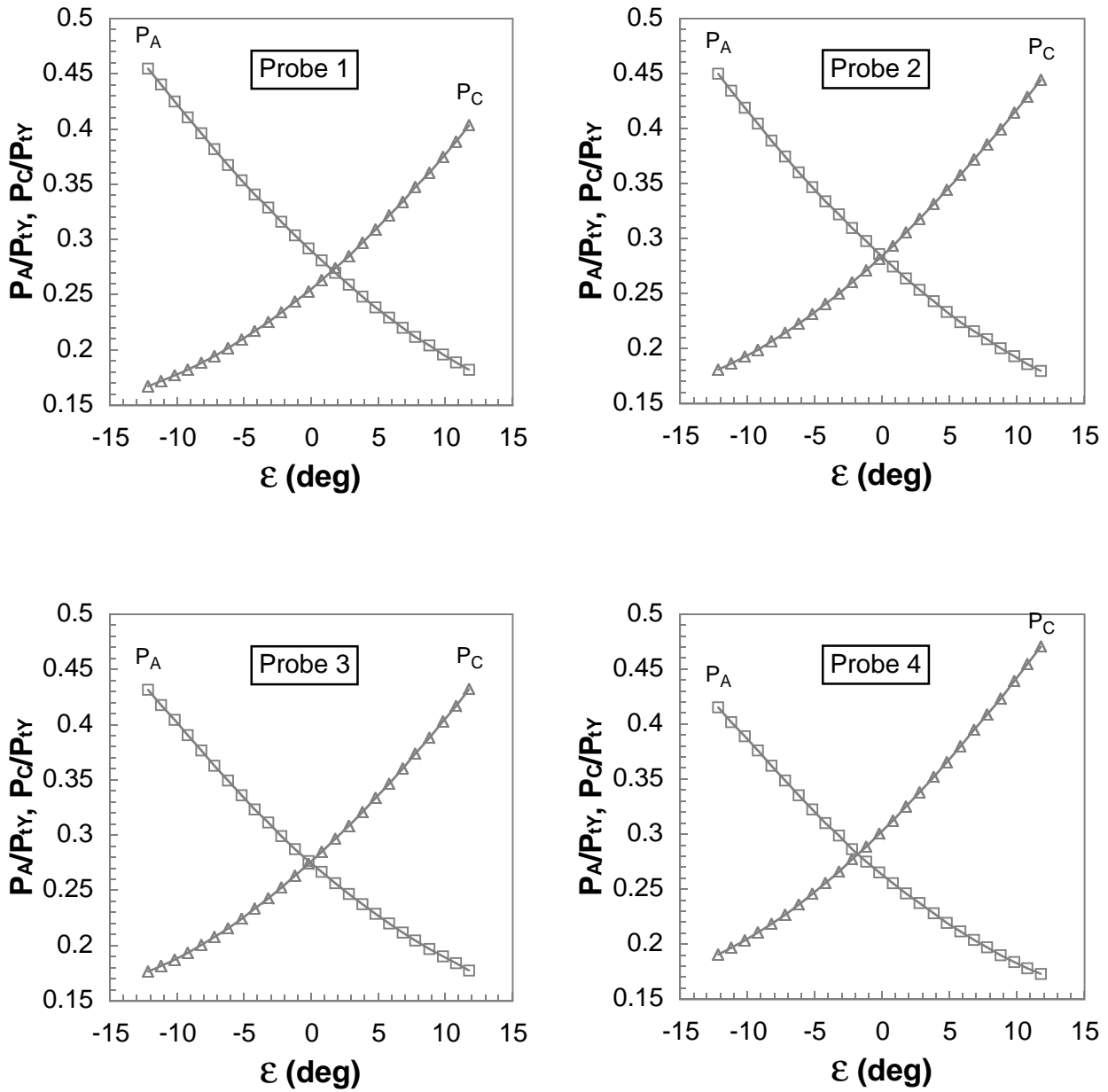
UPWT TS 2, $M_{\text{set}} = 2.40, \Psi = 0^\circ$

Figure 29. Rake 1 static pressure polars for taps A and C.



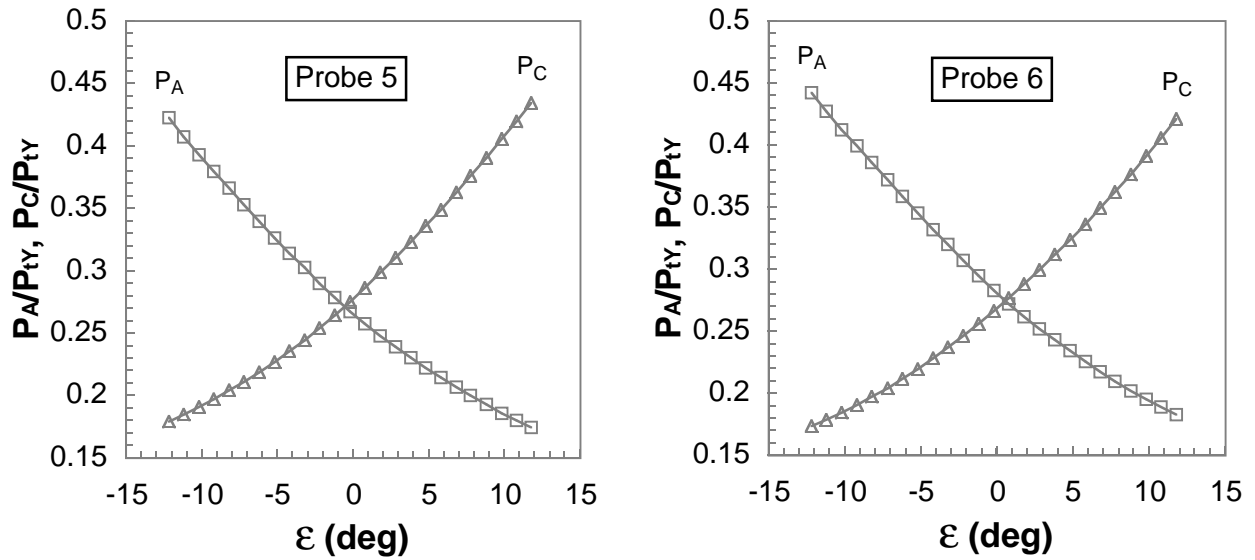
UPWT TS 2, $M_{set} = 2.40$, $\Psi = 0^\circ$

Figure 29. Concluded.



UPWT TS 2, $M_{set} = 2.40$, $\Psi = 0^\circ$

Figure 30. Rake 2 static pressure polars for taps A and C.



UPWT TS 2, $M_{set} = 2.40, \psi = 0^\circ$

Figure 30. Concluded.



16-Probe Rake
Mset = 2.15

8-Probe Rake
Mset = 2.40

6-Probe Rake
Mset = 2.29

Figure 31. Shadowgraph of cone-probe flow structure.

Figure 32. Cone-probe orientation angles.

View Facing Into Cone-Probe

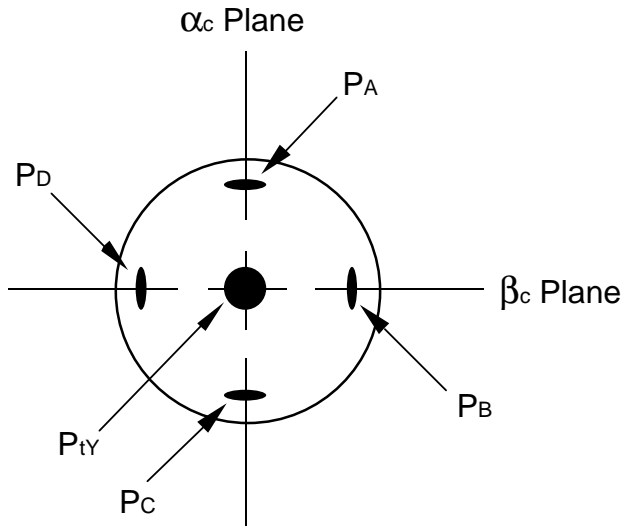


Figure 33. Cone-probe pressure tap identification.

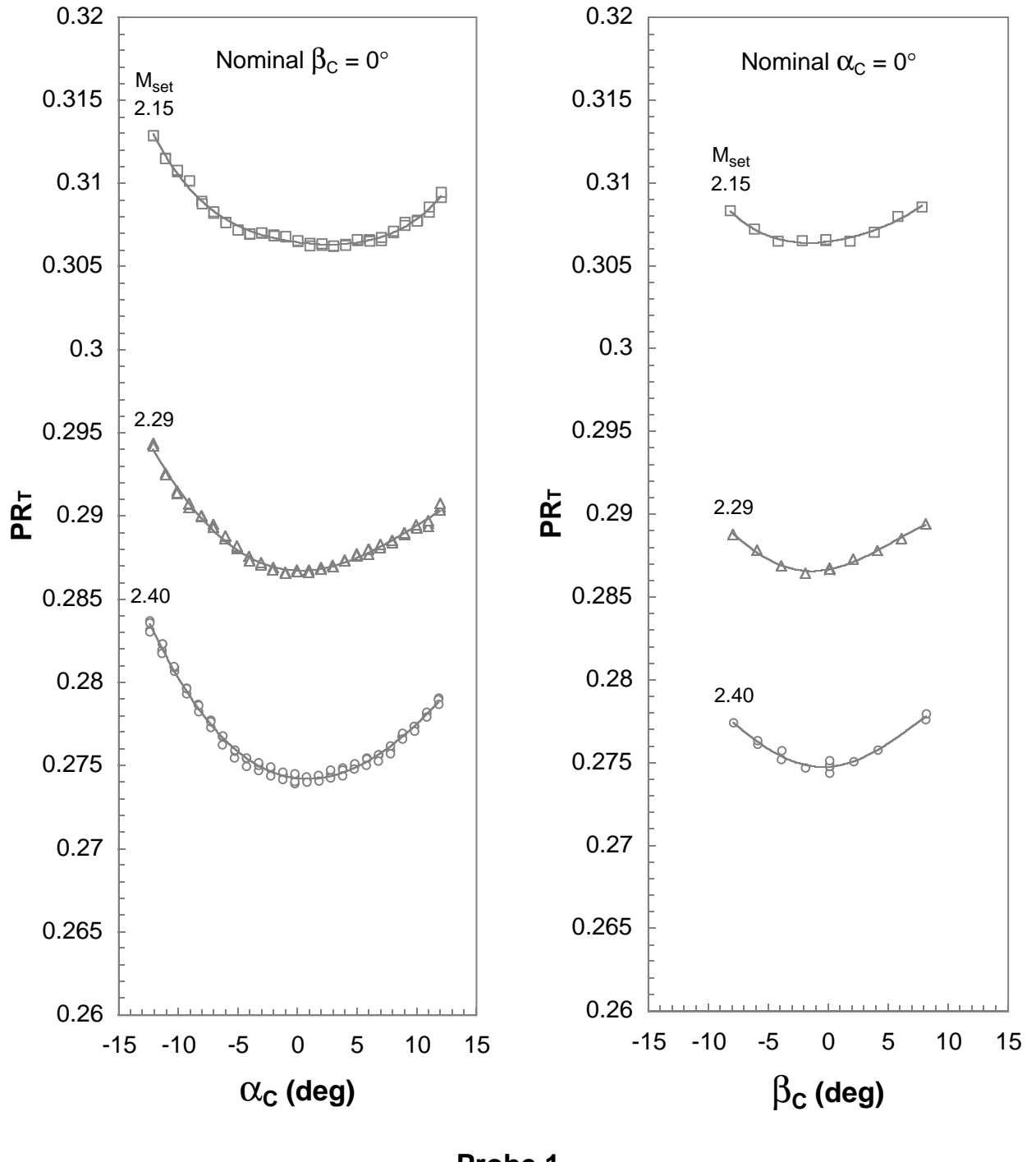


Figure 34. Compressibility parameter variation with flow angle for rake 1.

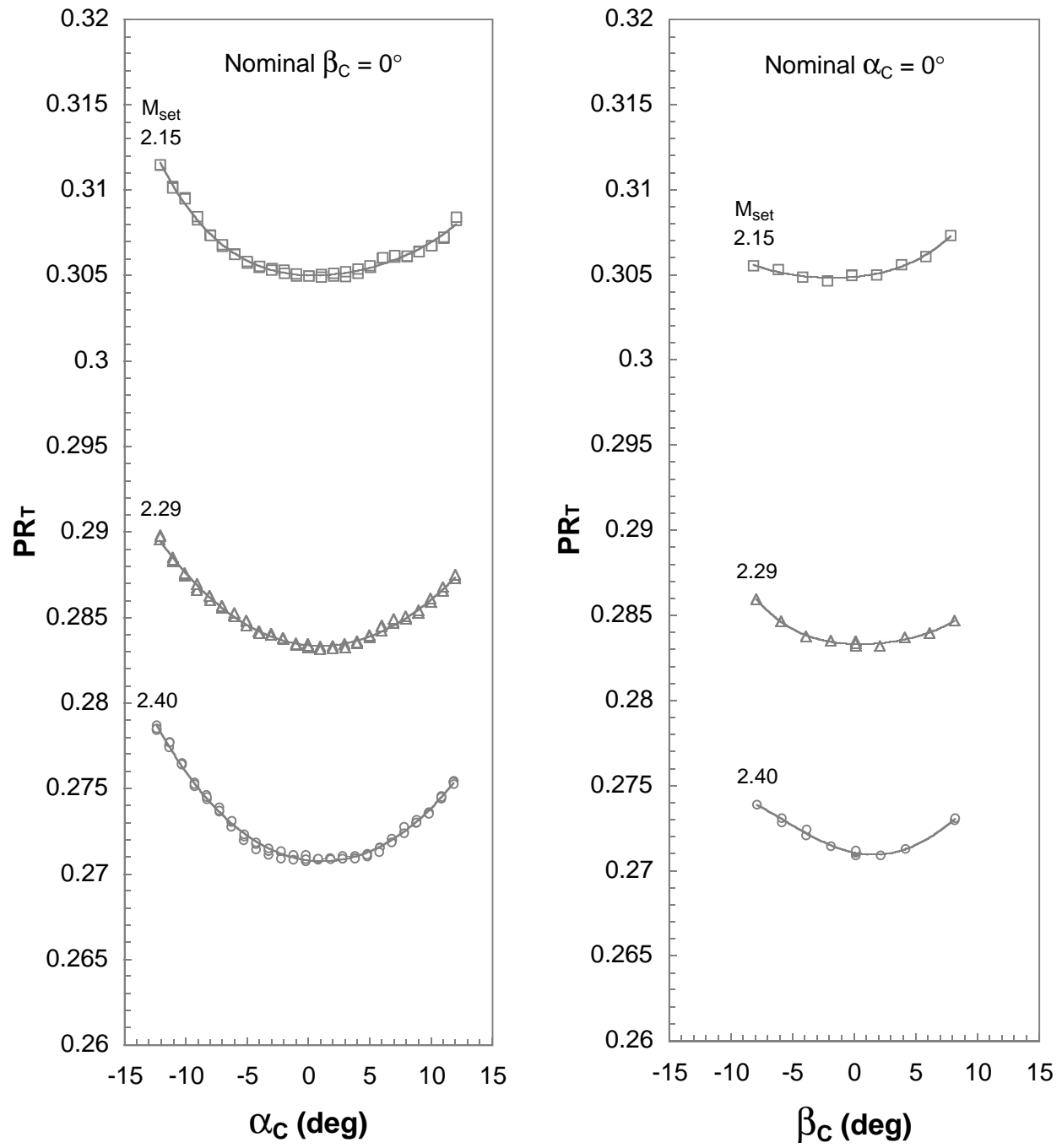
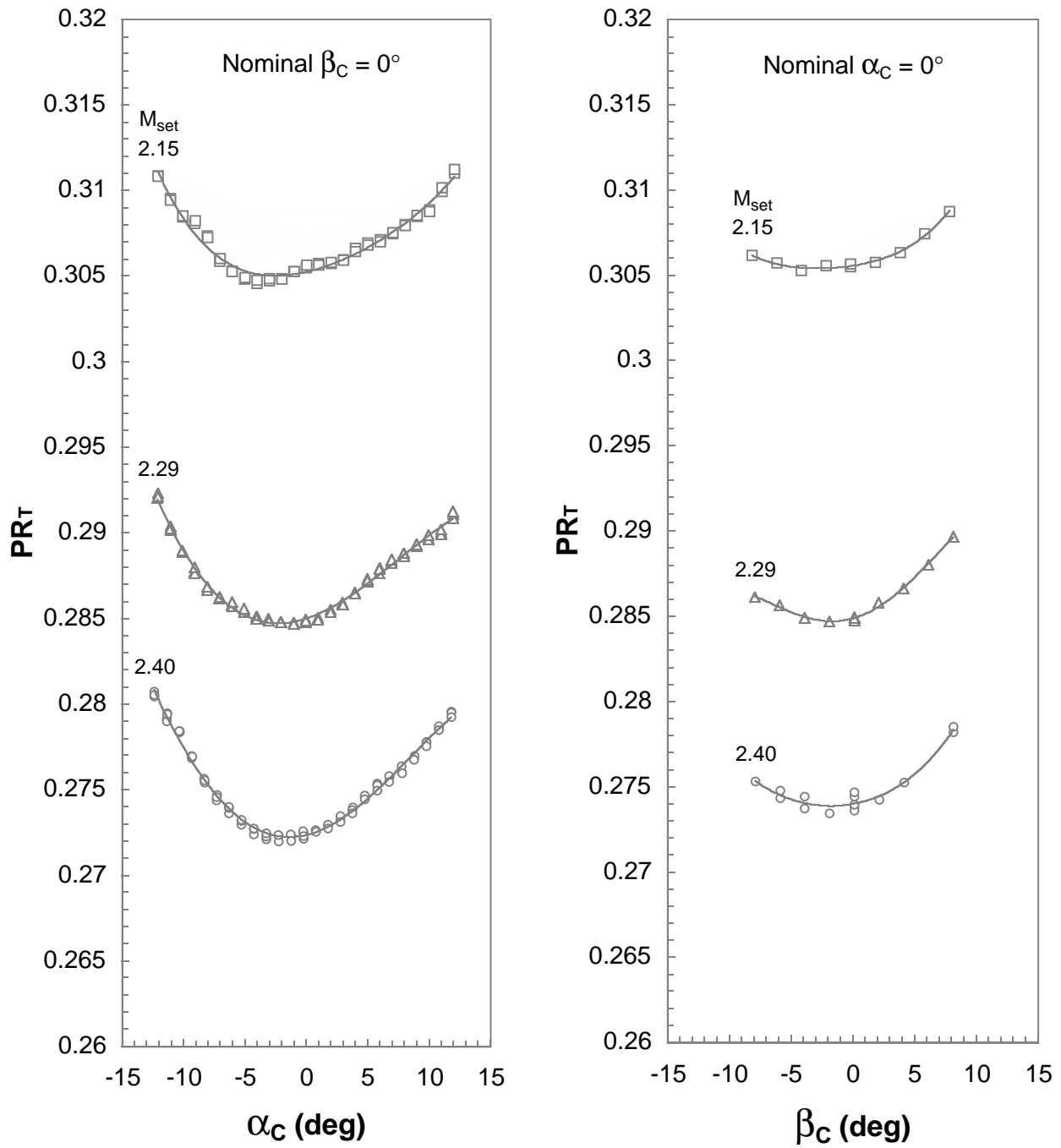
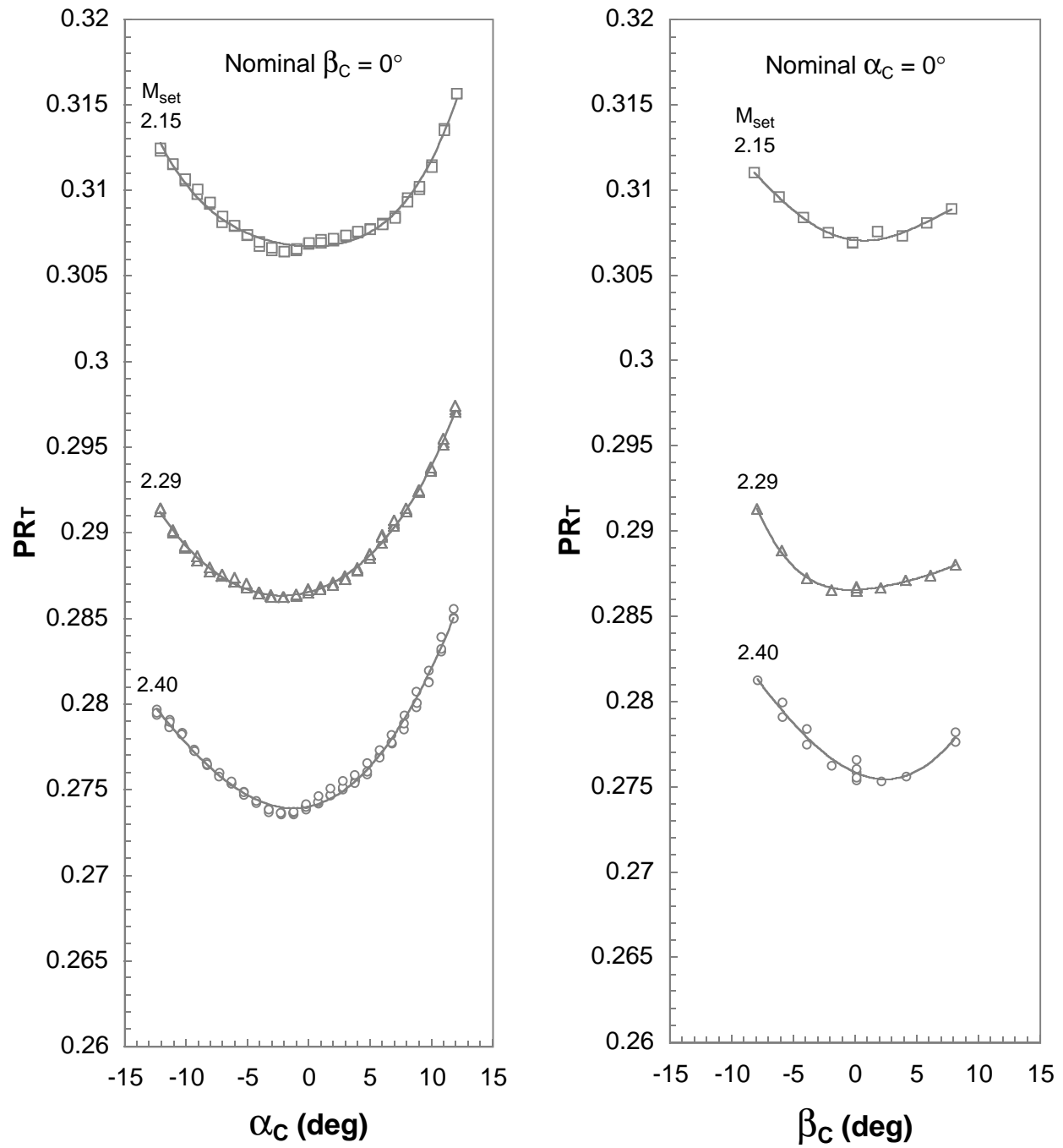


Figure 34. Continued.



Probe 3

Figure 34. Continued.



Probe 4

Figure 34. Continued.

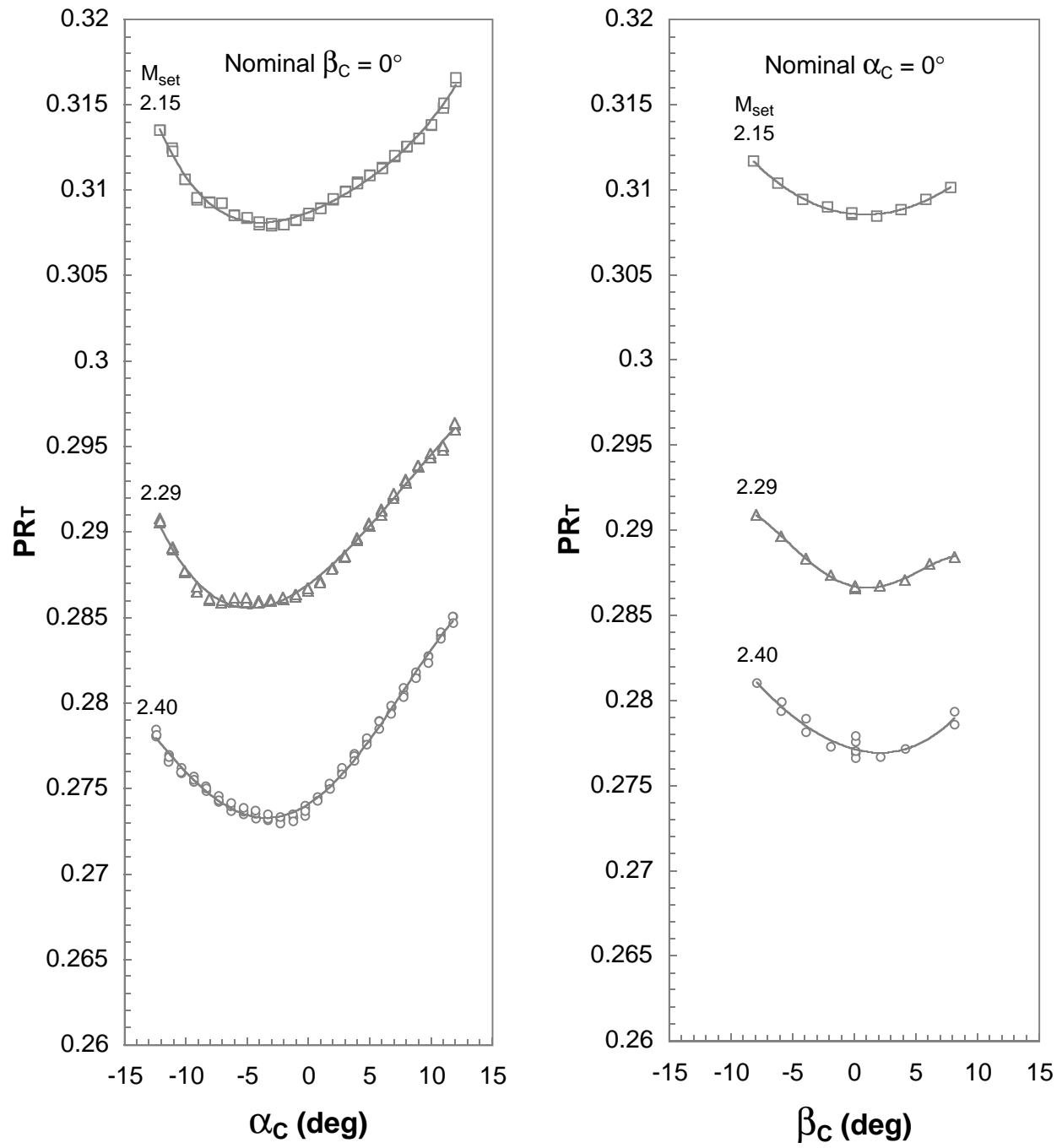


Figure 34. Continued.

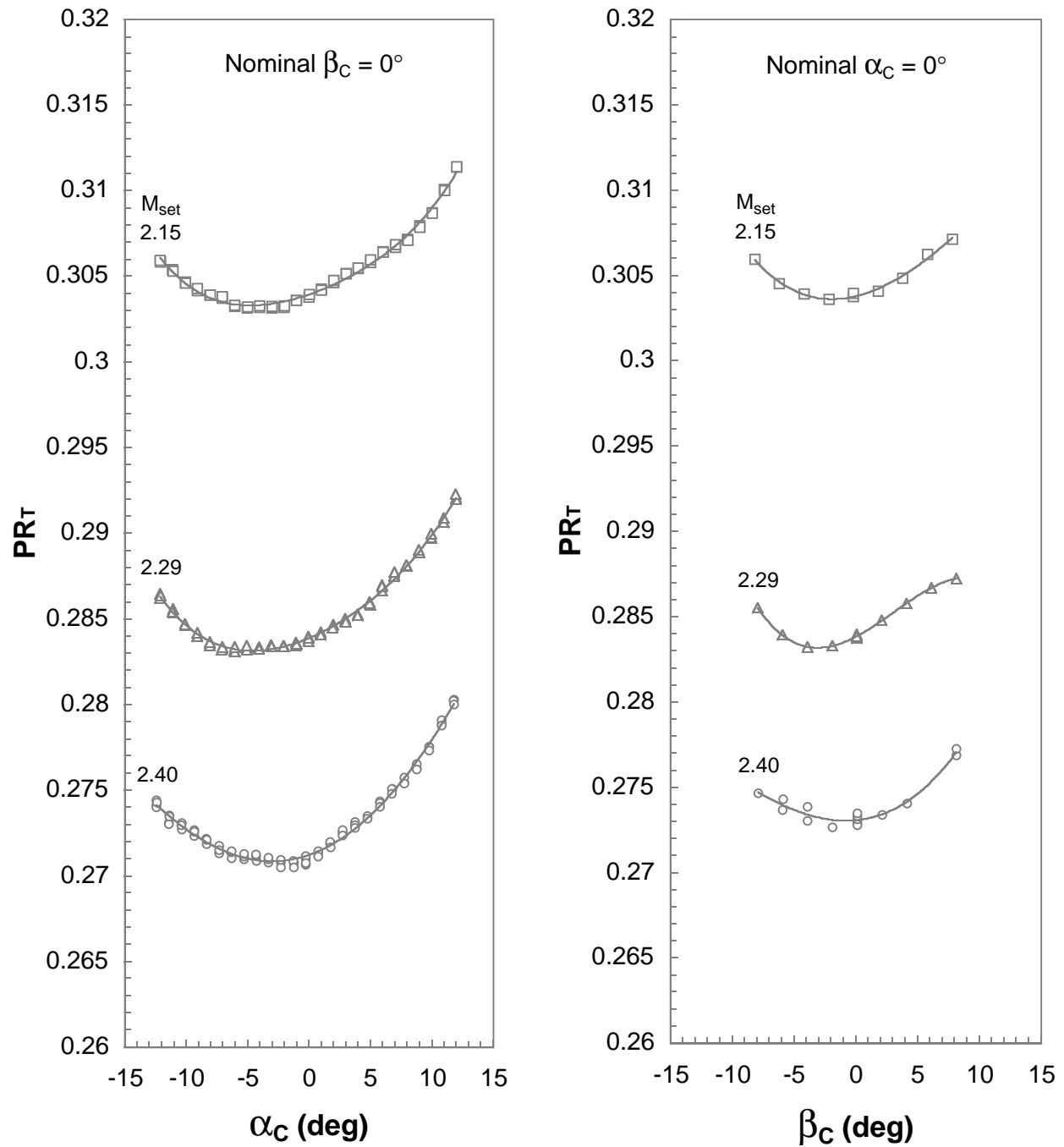


Figure 34. Continued.

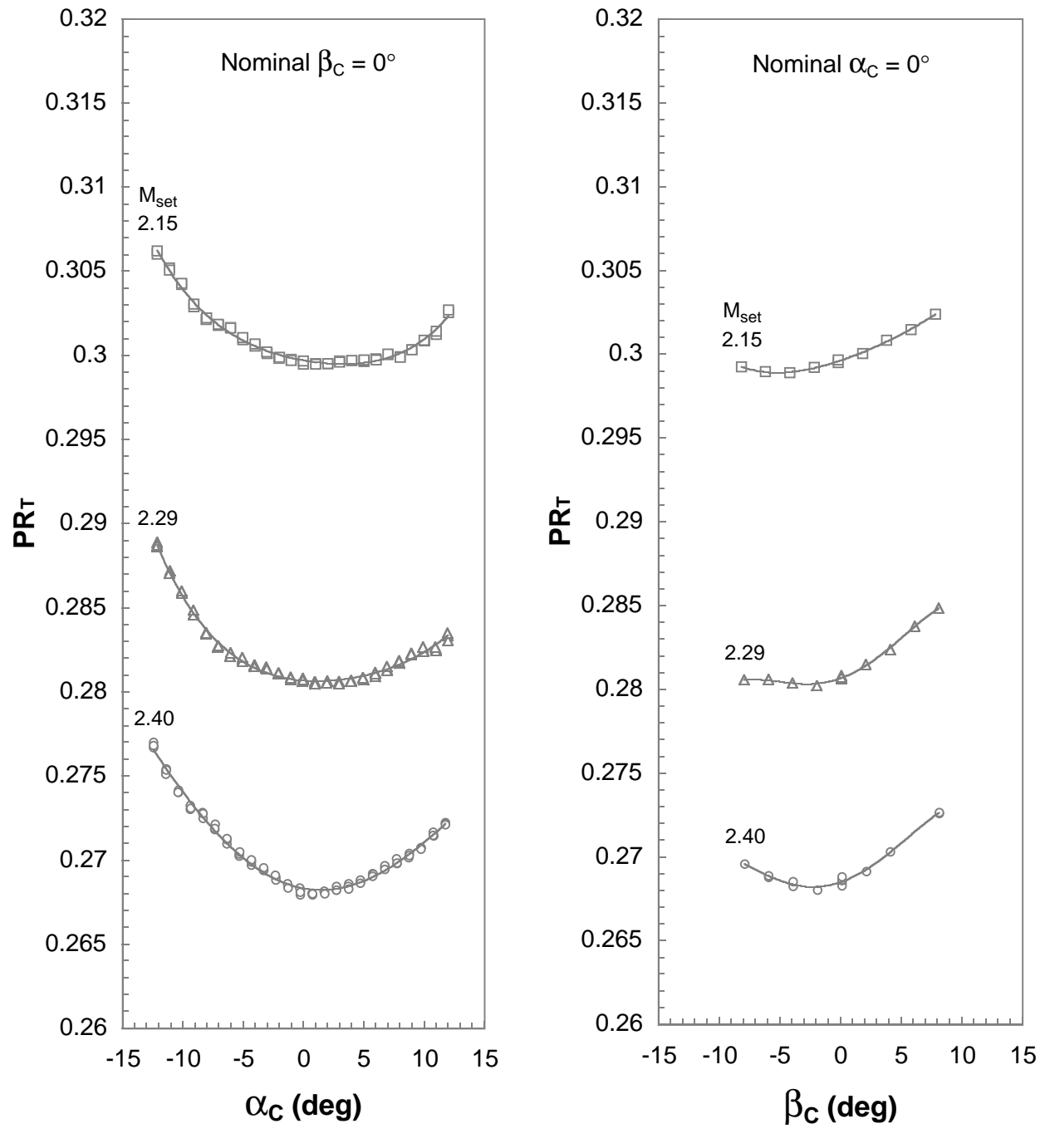


Figure 34. Continued.

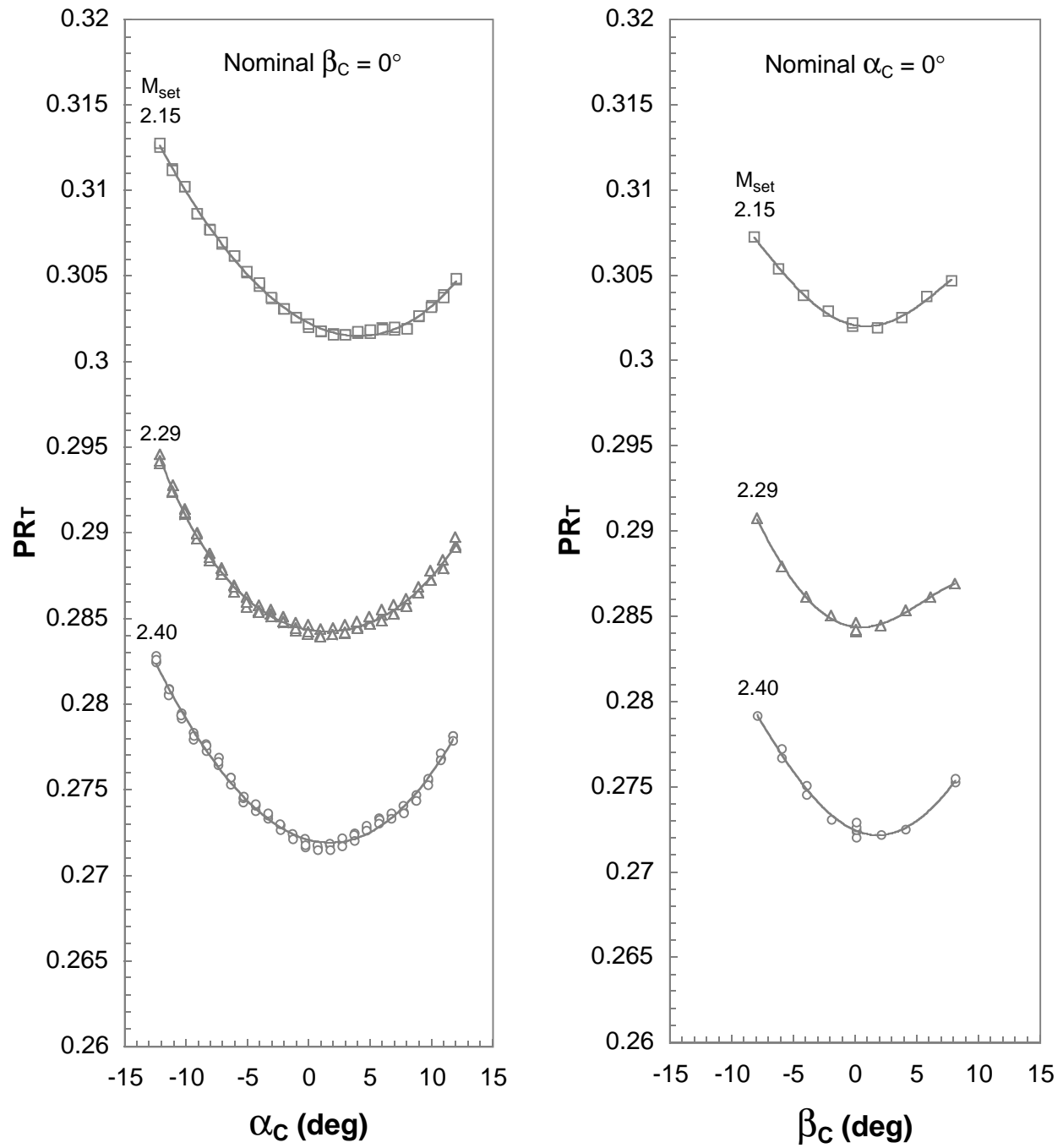


Figure 34. Concluded.

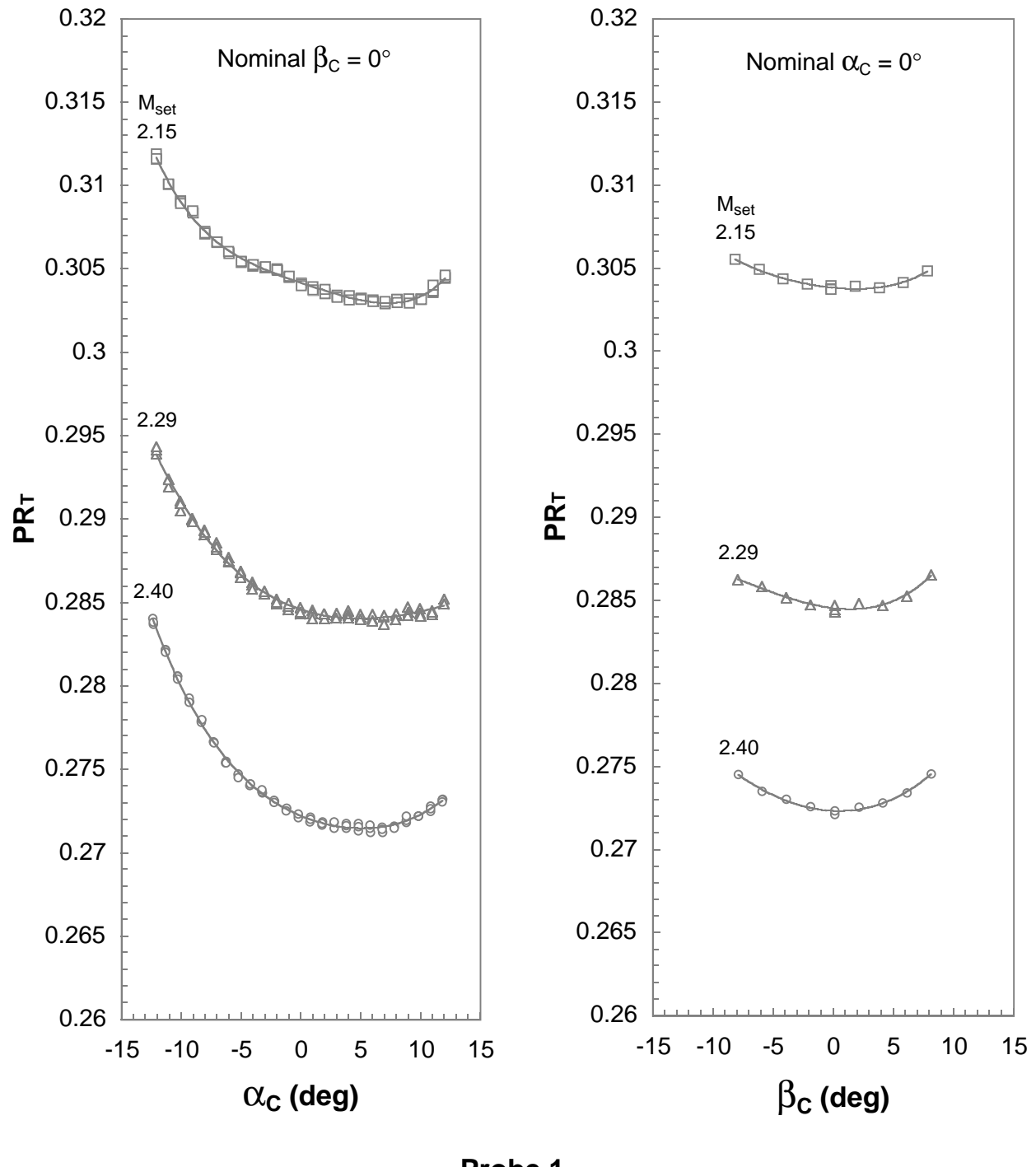


Figure 35. Compressibility parameter variation with flow angle for rake 2.

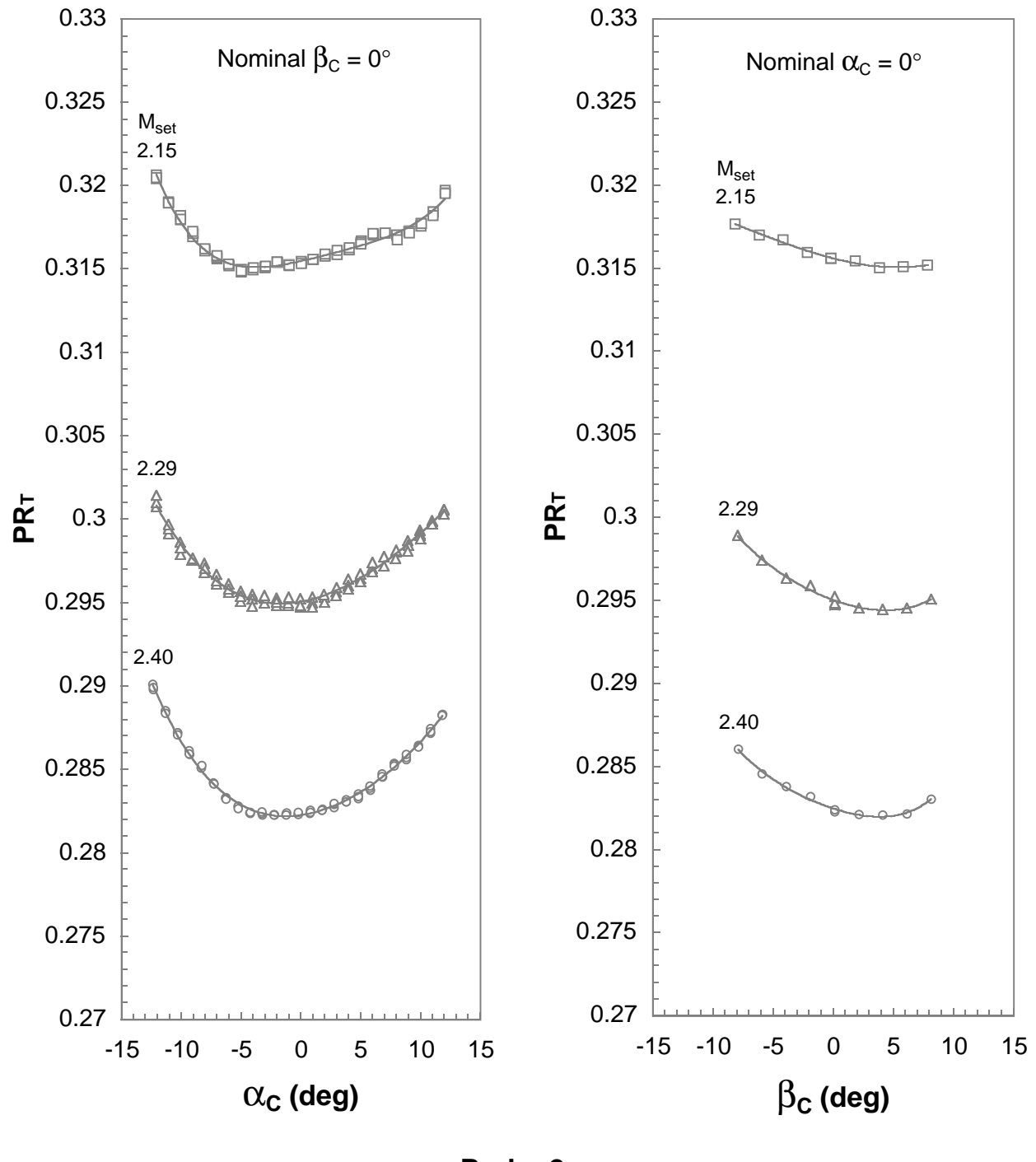
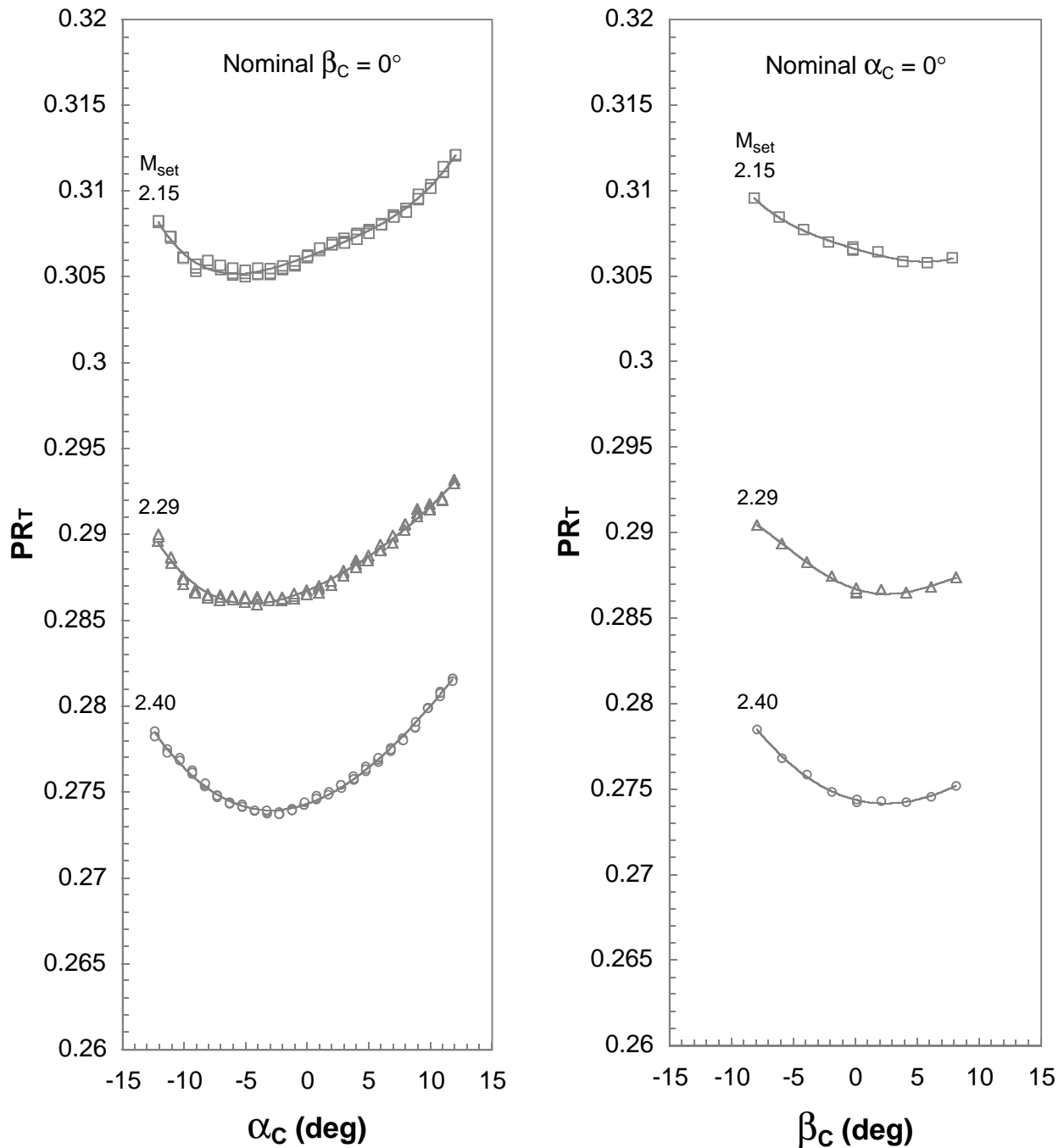
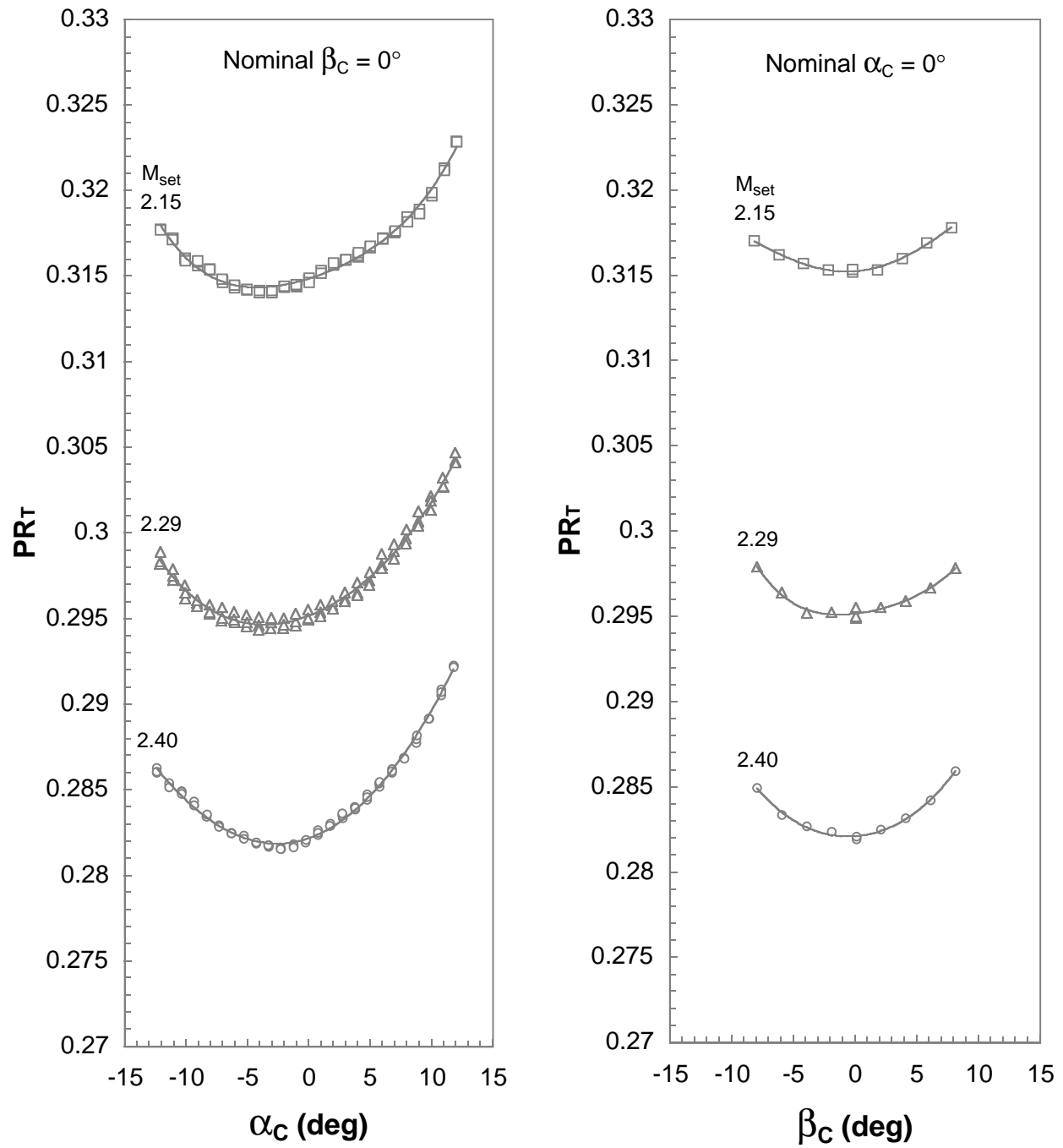


Figure 35. Continued.



Probe 3

Figure 35. Continued.



Probe 4

Figure 35. Continued.

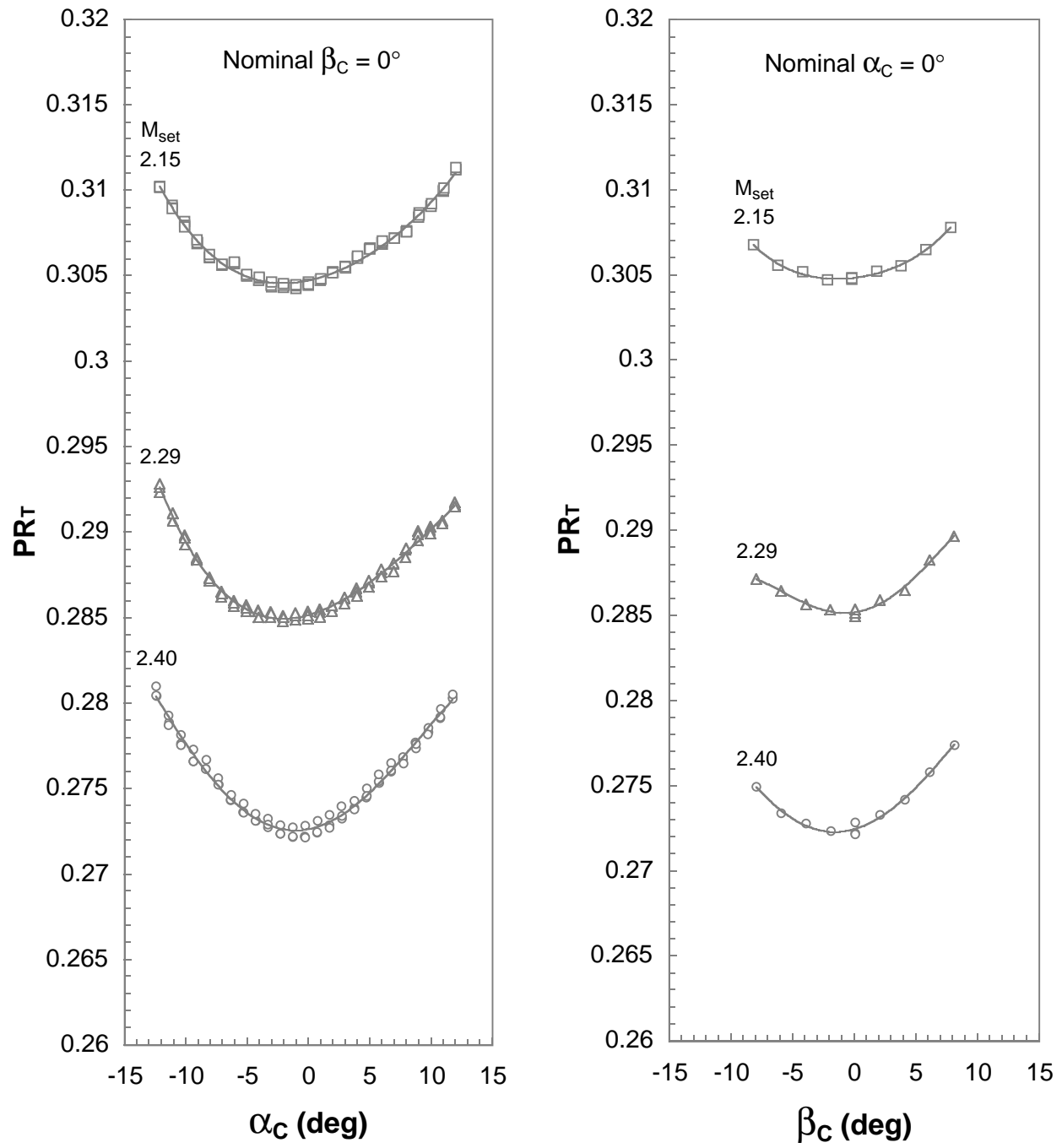


Figure 35. Continued.

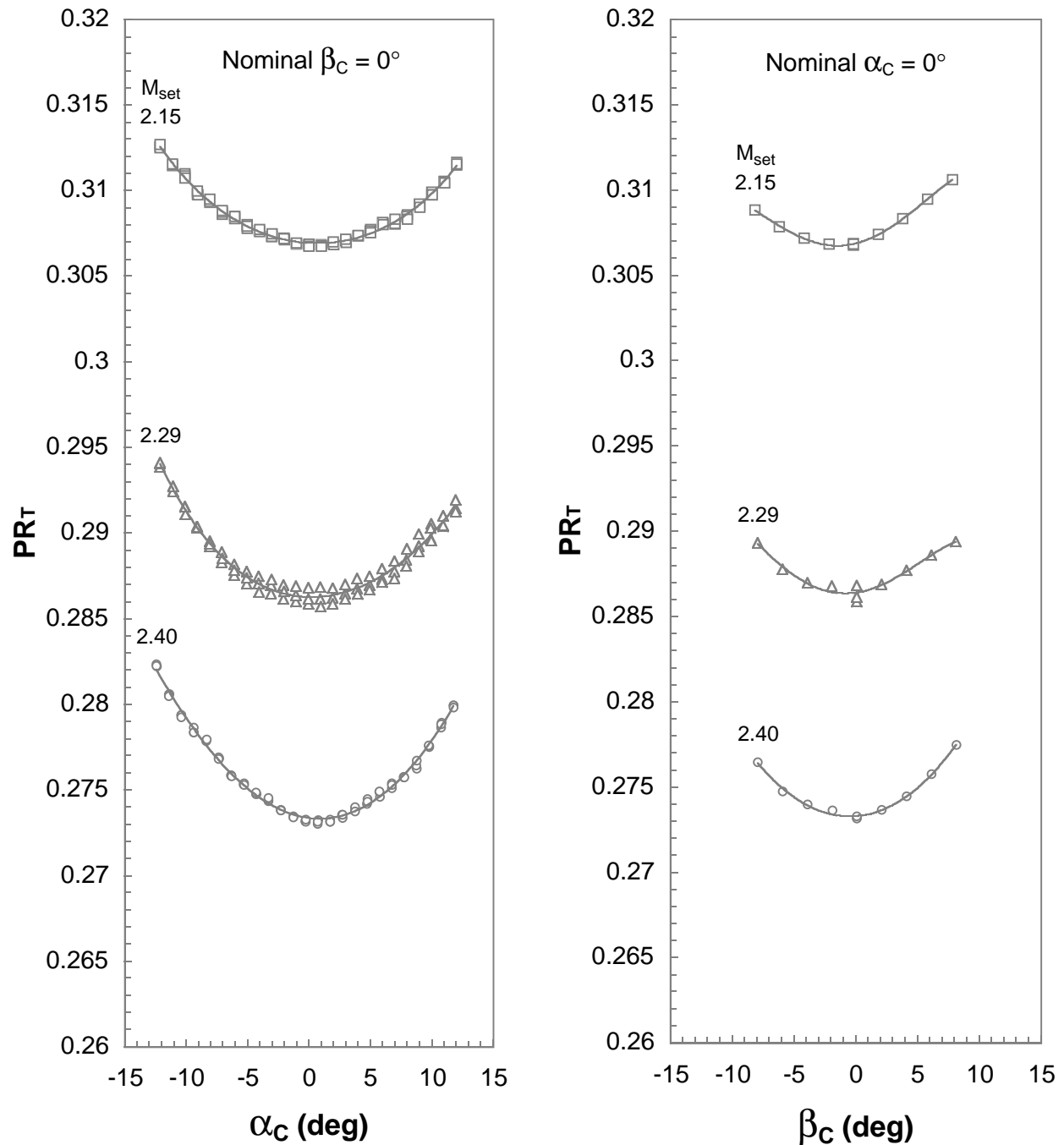
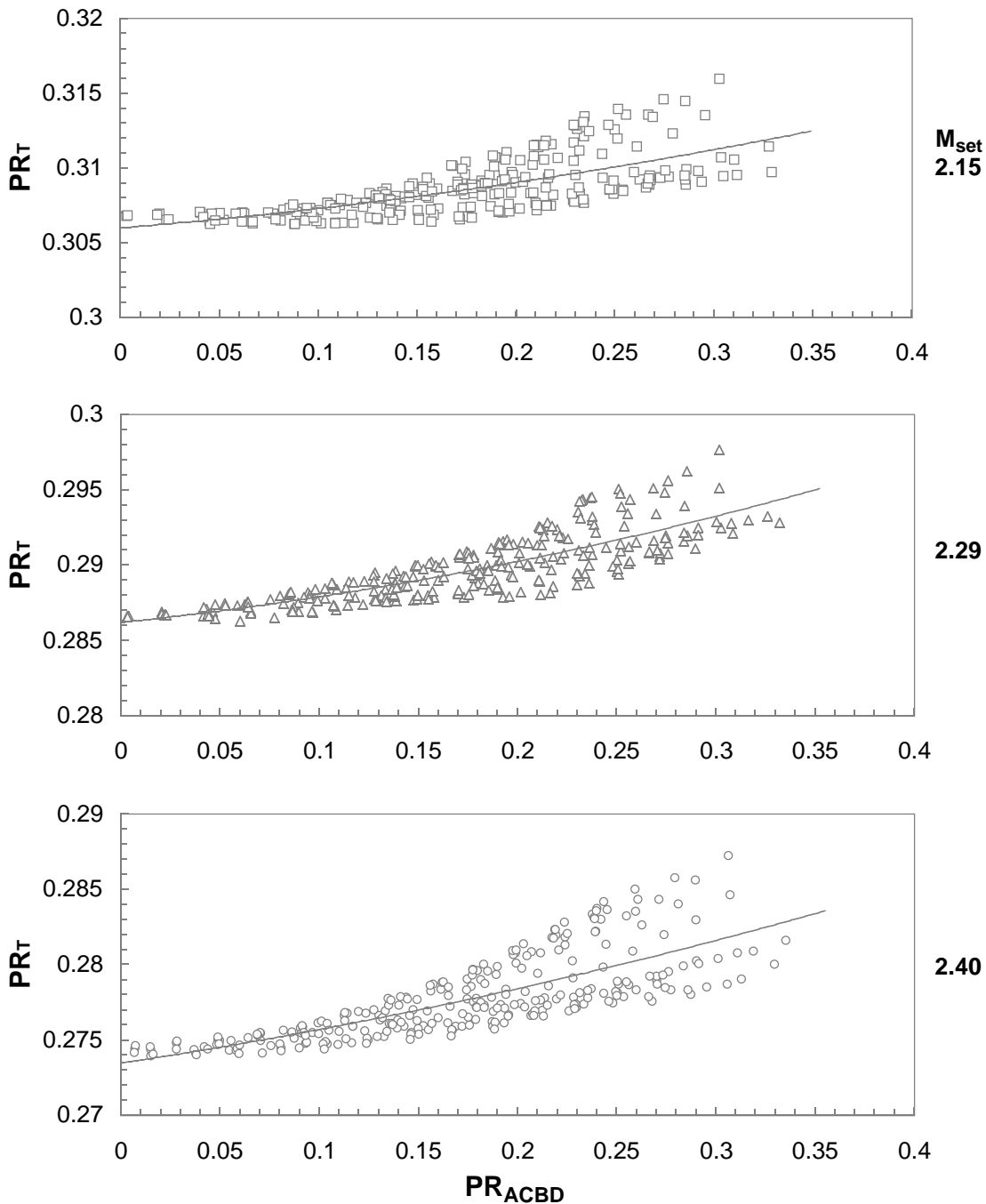


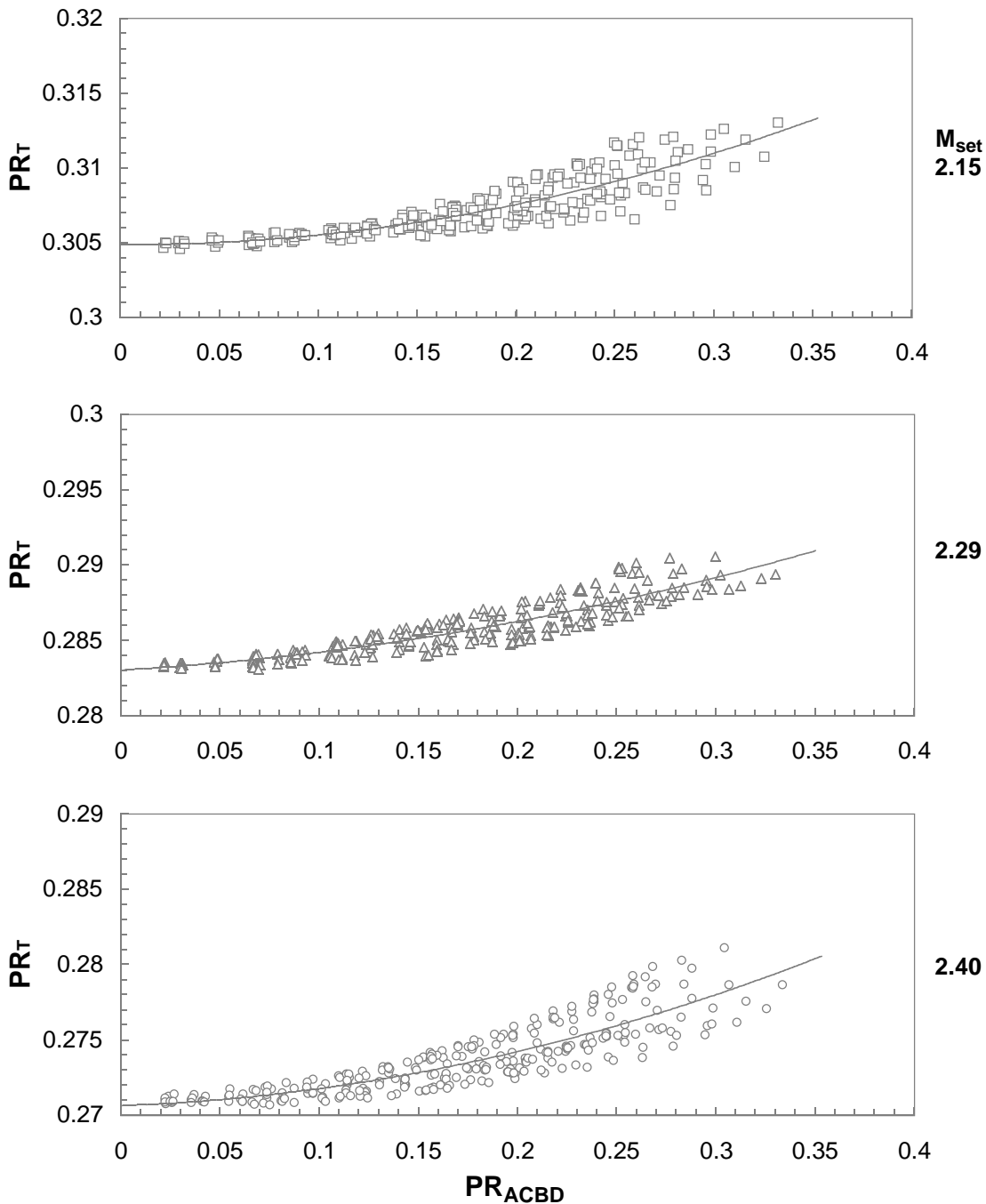
Figure 35. Concluded.



Probe 1

$-12^\circ \leq \alpha_C \leq 12^\circ$
 $-8^\circ \leq \beta_C \leq 8^\circ$

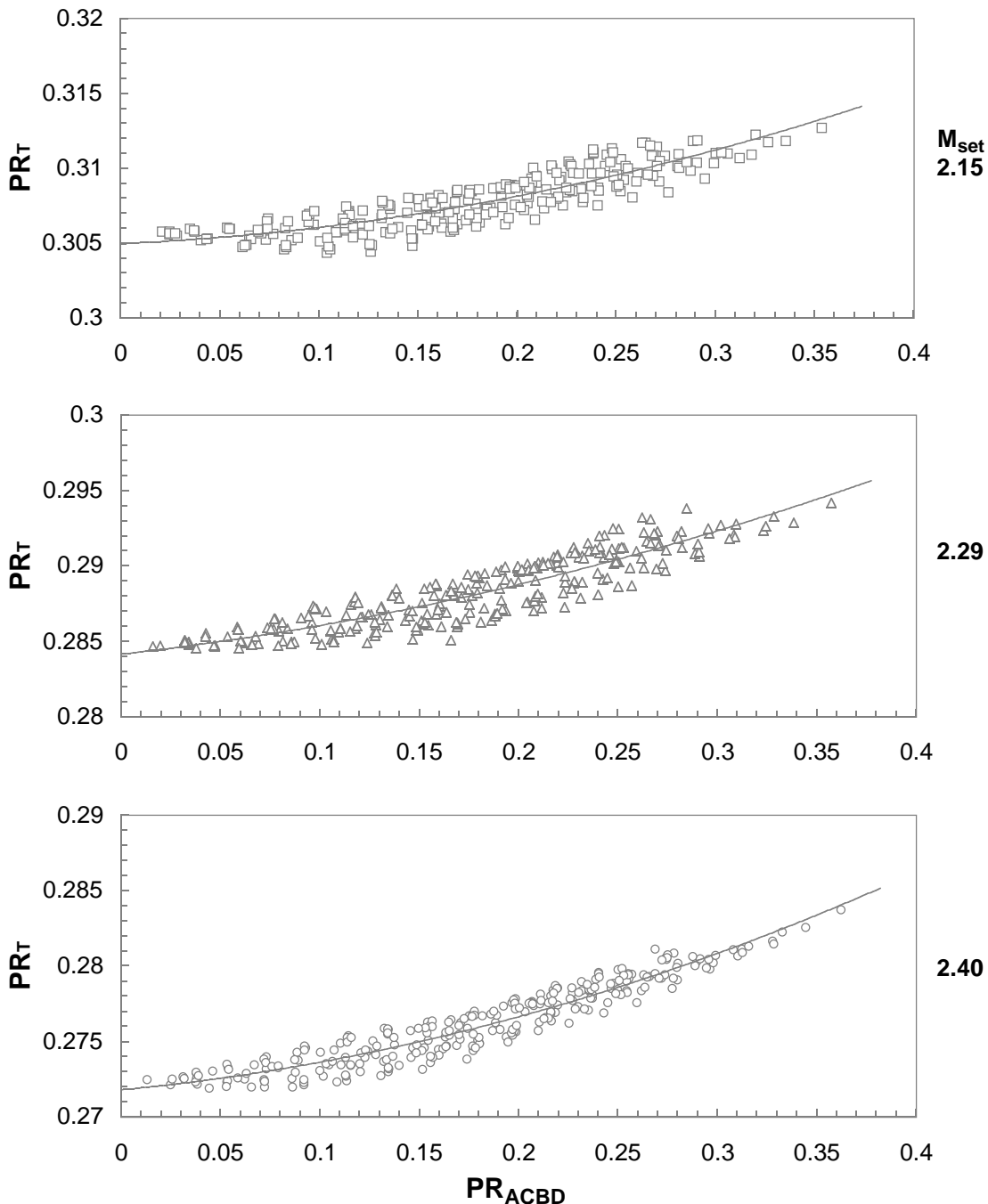
Figure 36. Compressibility parameter variation with inclination parameter for rake 1.



Probe 2

$-12^\circ \leq \alpha_C \leq 12^\circ$
 $-8^\circ \leq \beta_C \leq 8^\circ$

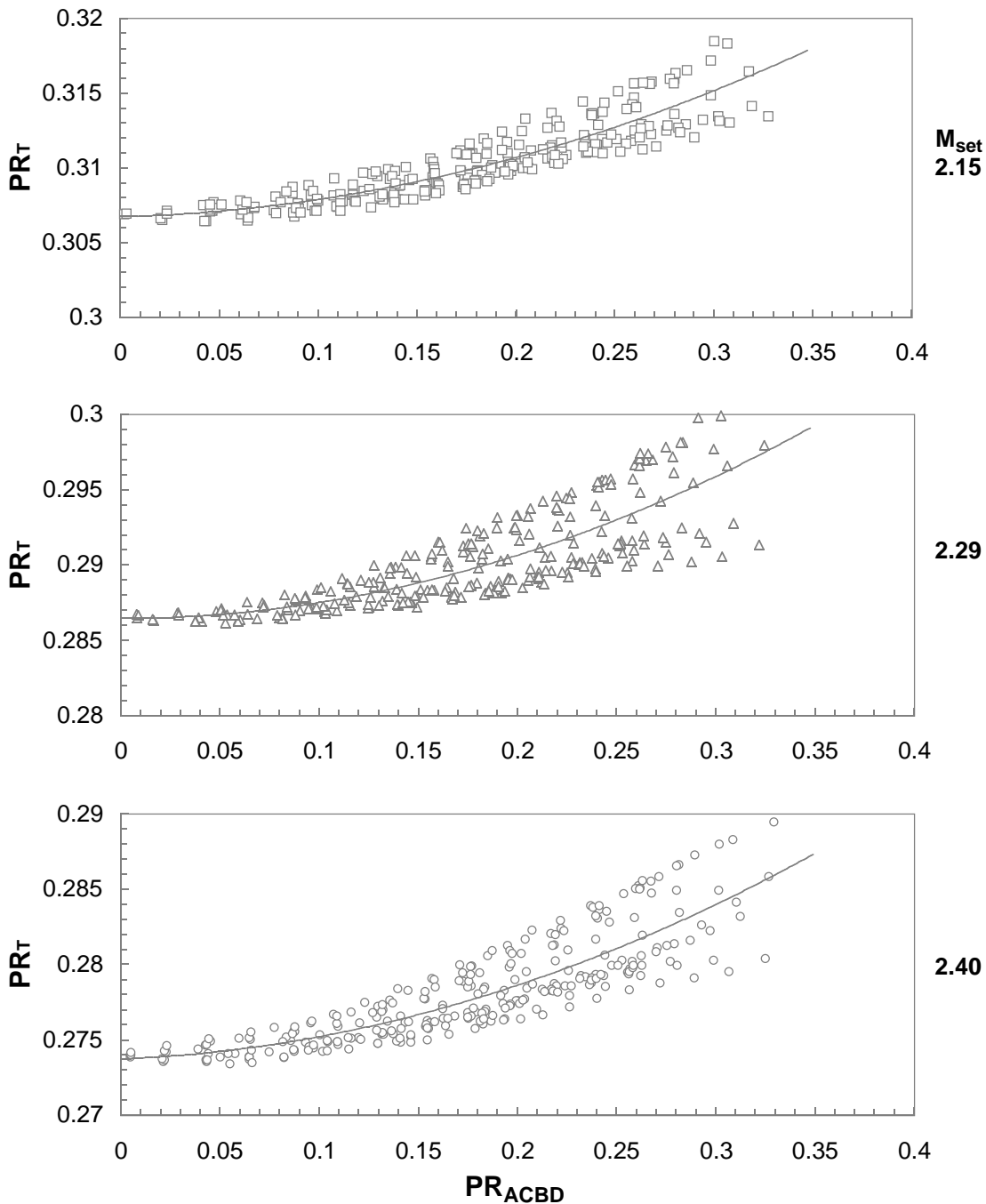
Figure 36. Continued.



Probe 3

$-12^\circ \leq \alpha_C \leq 12^\circ$
 $-8^\circ \leq \beta_C \leq 8^\circ$

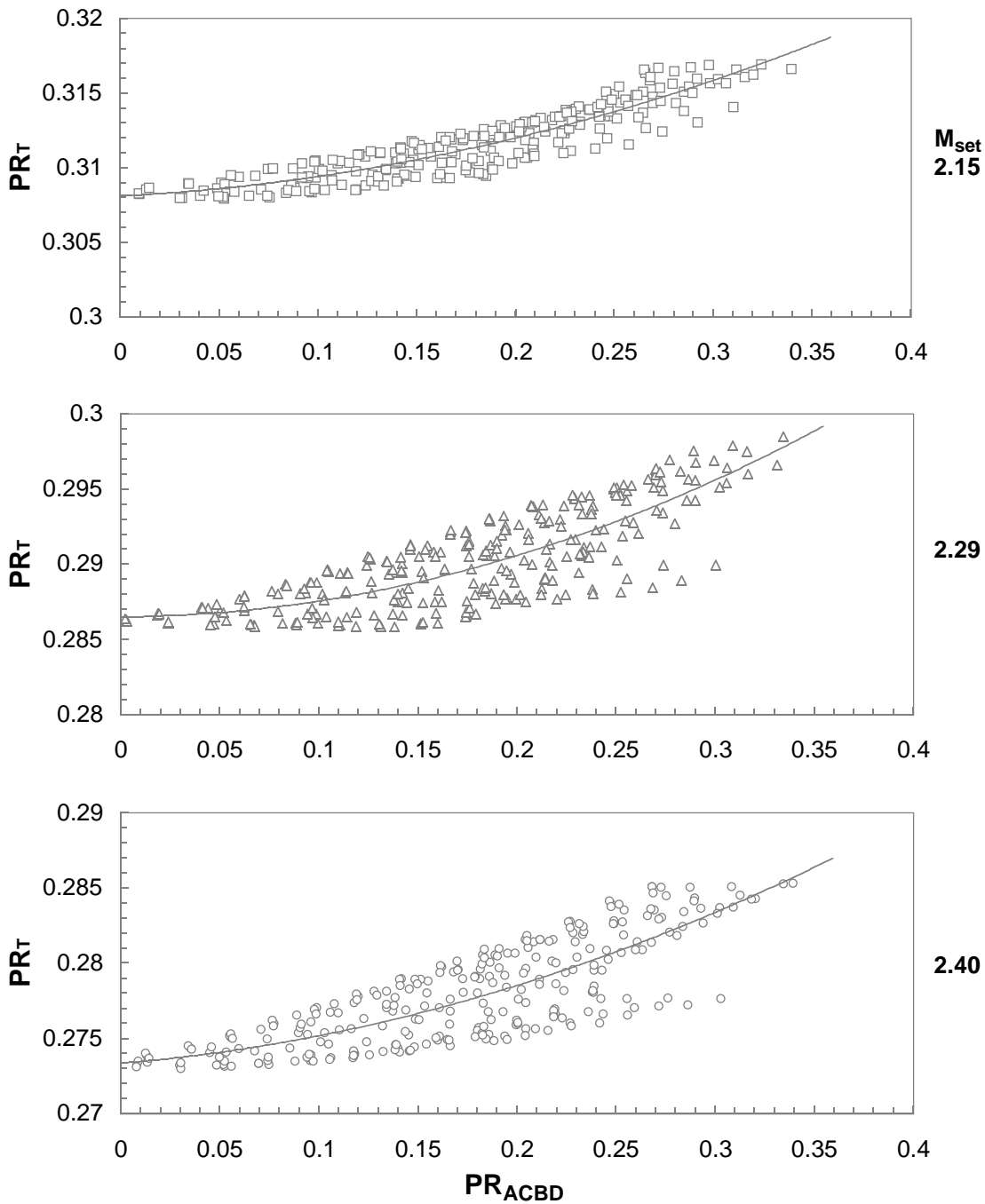
Figure 36. Continued.



Probe 4

$-12^\circ \leq \alpha_C \leq 12^\circ$
 $-8^\circ \leq \beta_C \leq 8^\circ$

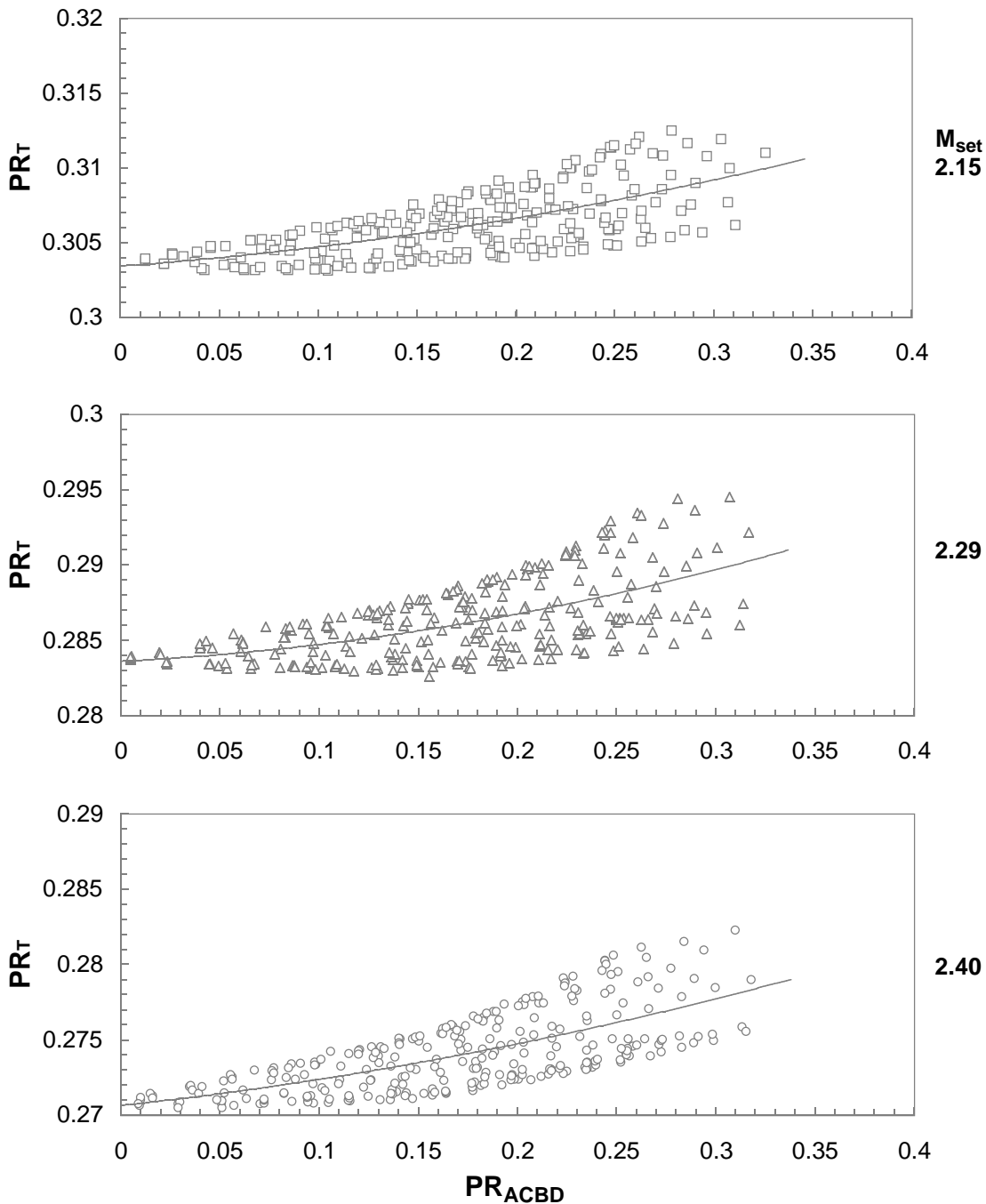
Figure 36. Continued.



Probe 5

$-12^\circ \leq \alpha_C \leq 12^\circ$
 $-8^\circ \leq \beta_C \leq 8^\circ$

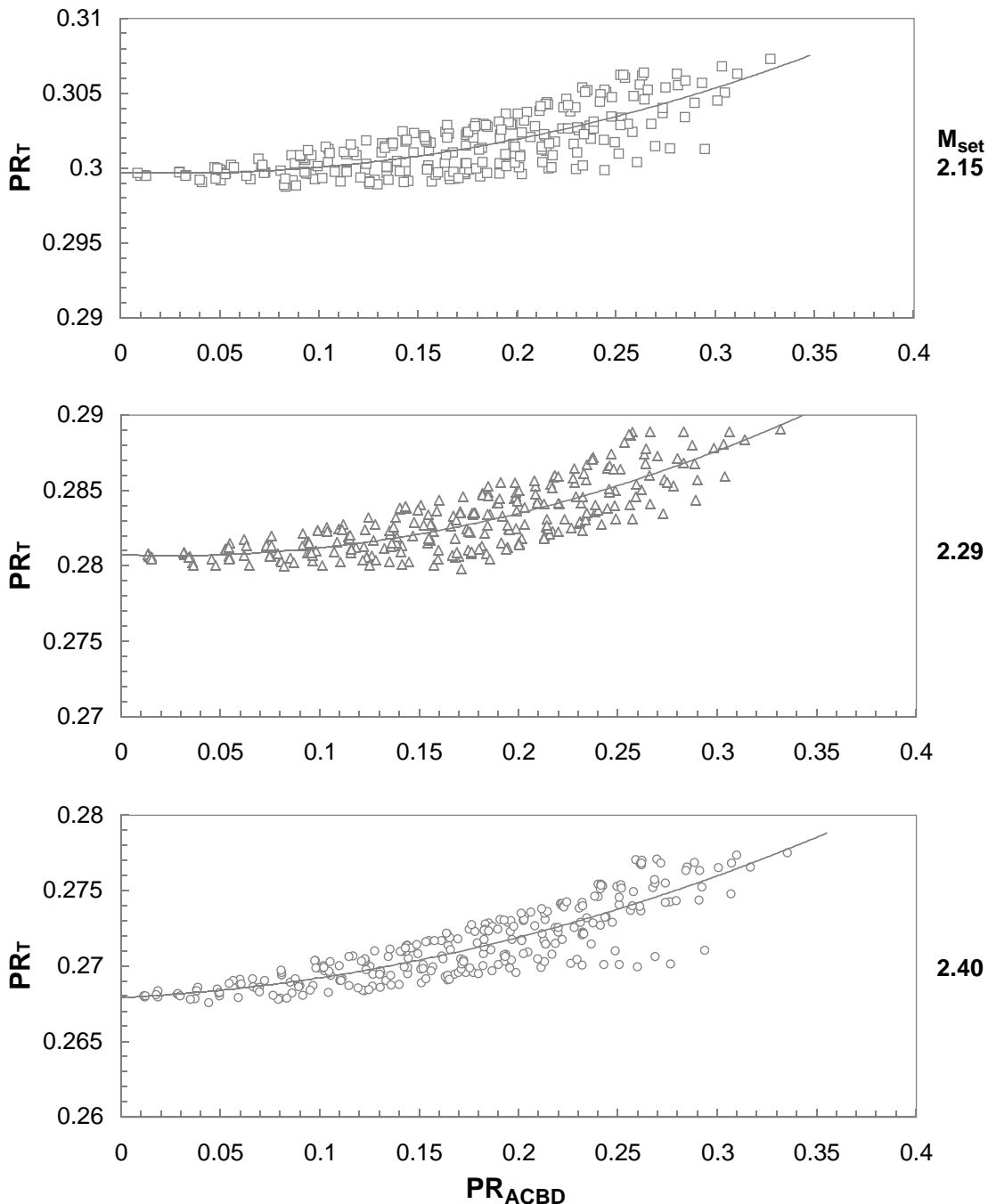
Figure 36. Continued.



Probe 6

$-12^\circ \leq \alpha_C \leq 12^\circ$
 $-8^\circ \leq \beta_C \leq 8^\circ$

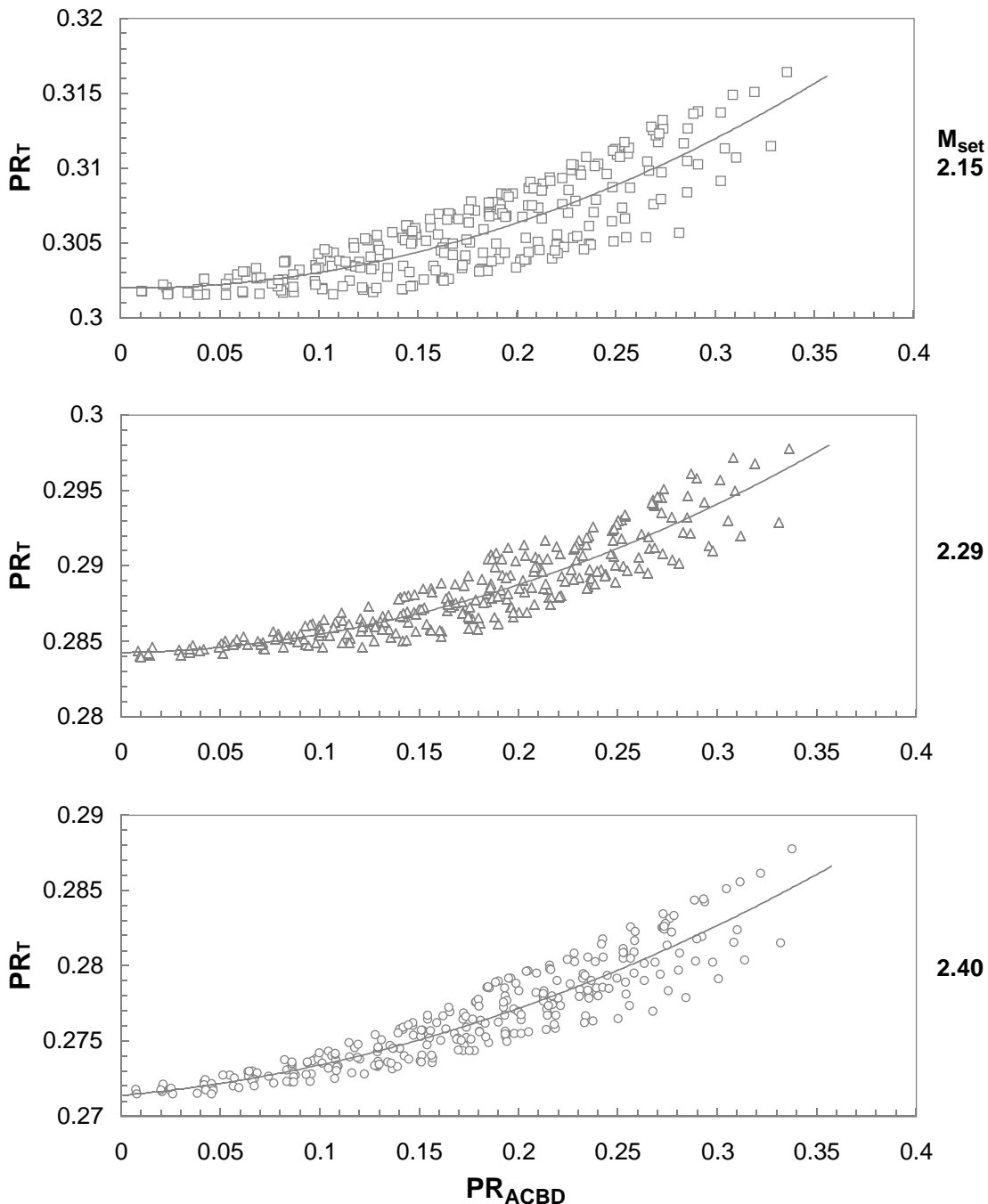
Figure 36. Continued.



Probe 7

$-12^\circ \leq \alpha_C \leq 12^\circ$
 $-8^\circ \leq \beta_C \leq 8^\circ$

Figure 36. Continued.



Probe 8

$-12^\circ \leq \alpha_C \leq 12^\circ$
 $-8^\circ \leq \beta_C \leq 8^\circ$

Figure 36. Concluded.

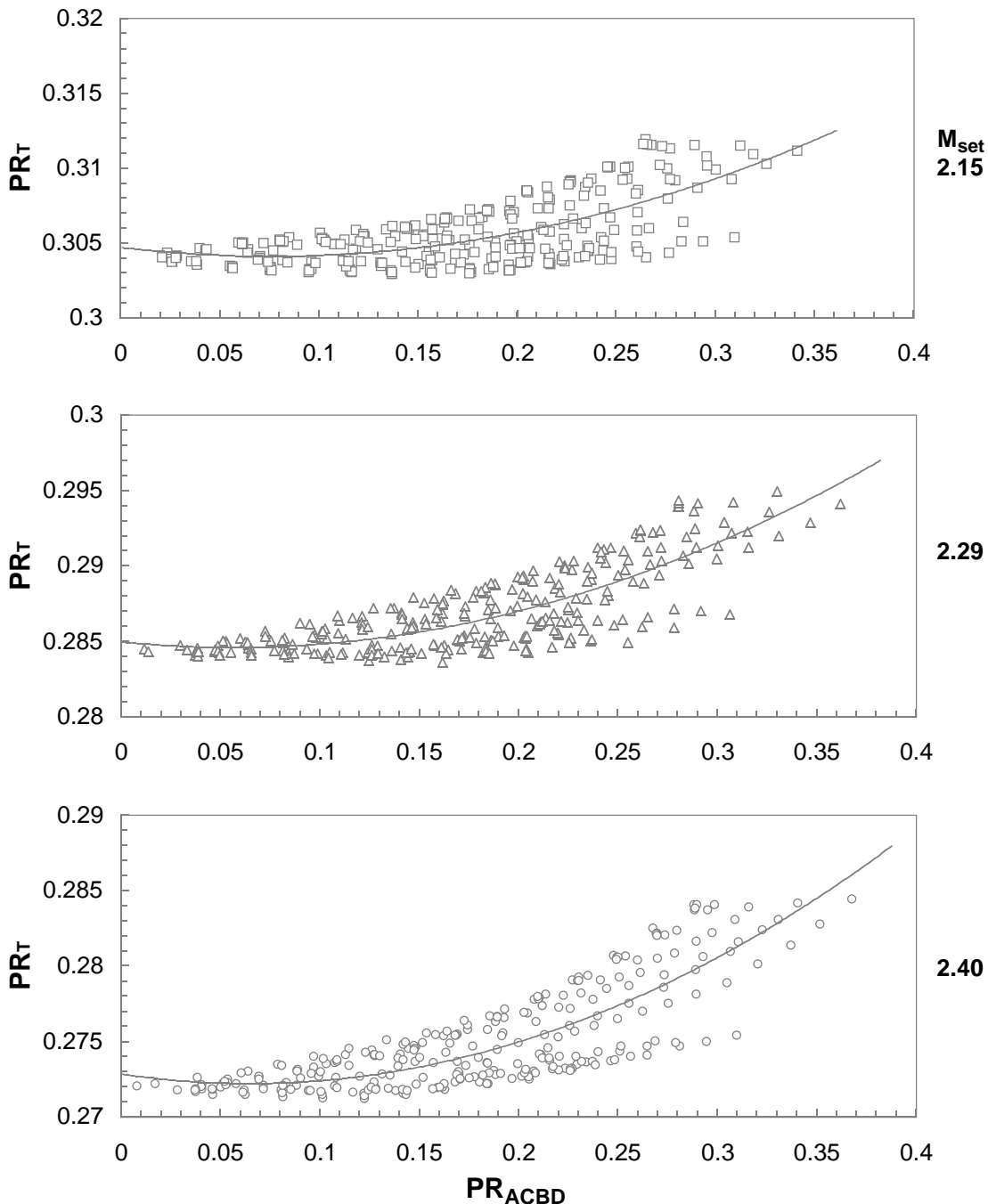
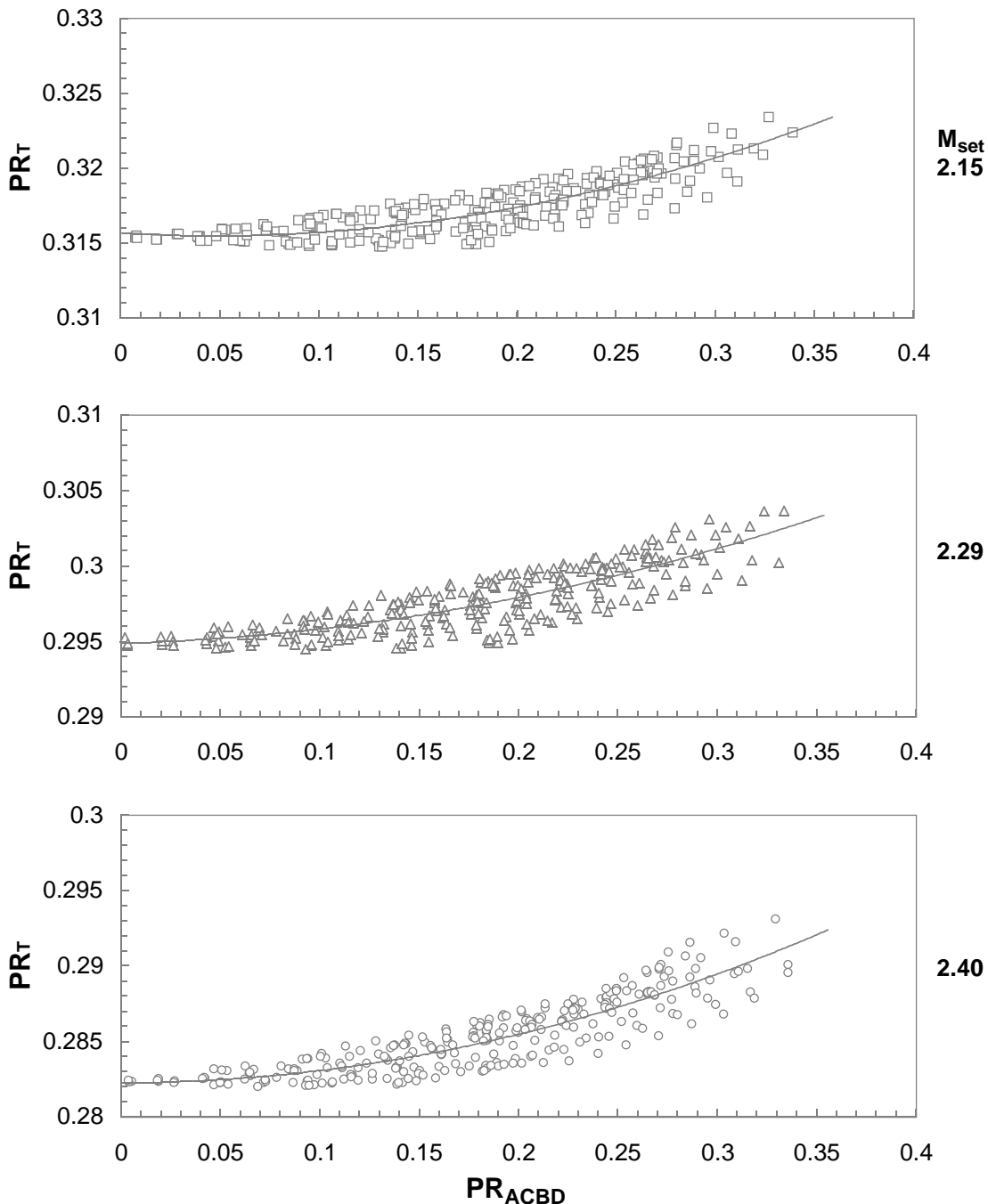


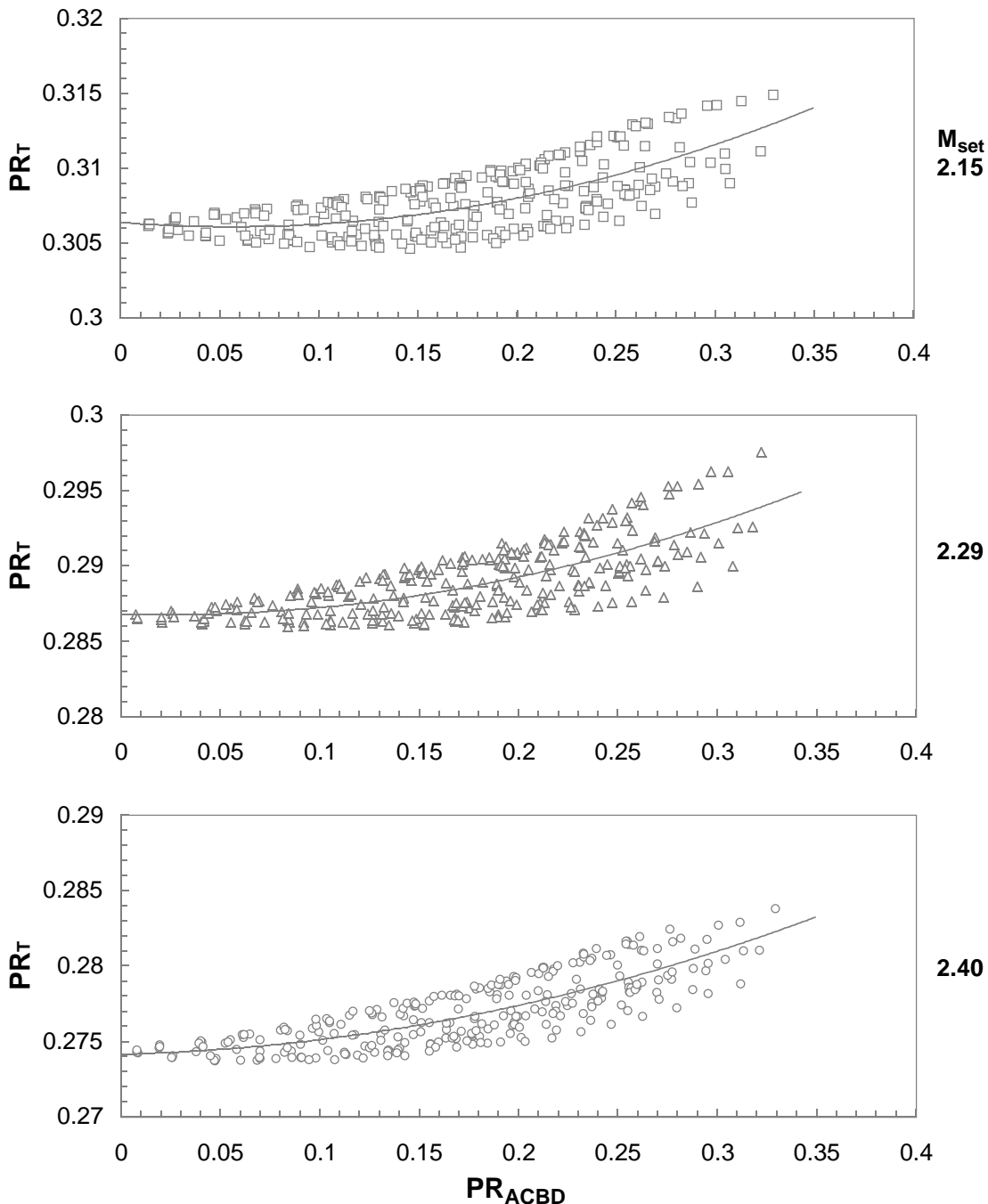
Figure 37. Compressibility parameter variation with inclination parameter for rake 2.



Probe 2

$-12^\circ \leq \alpha_C \leq 12^\circ$
 $-8^\circ \leq \beta_C \leq 8^\circ$

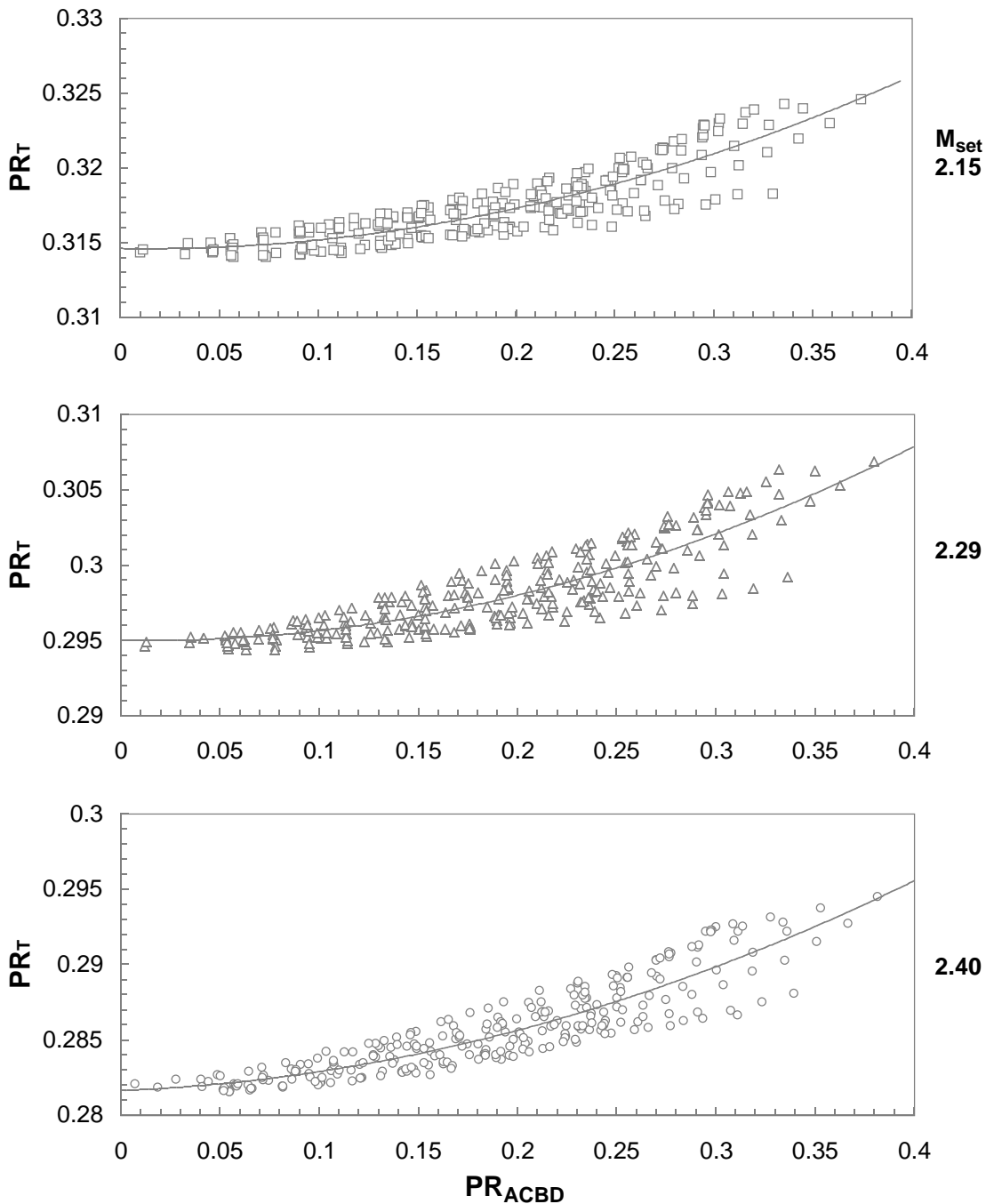
Figure 37. Continued.



Probe 3

$-12^\circ \leq \alpha_C \leq 12^\circ$
 $-8^\circ \leq \beta_C \leq 8^\circ$

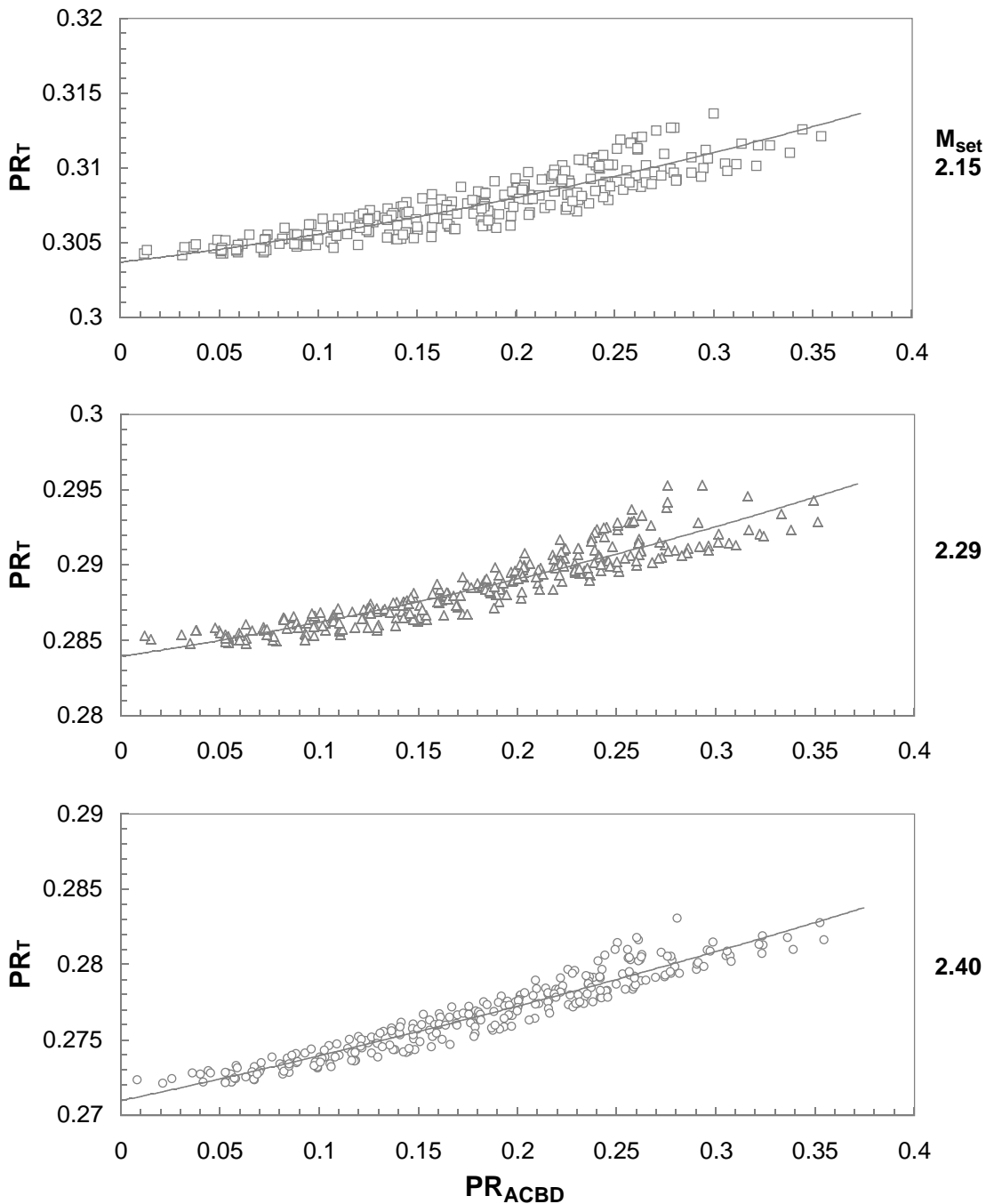
Figure 37. Continued.



Probe 4

$-12^\circ \leq \alpha_C \leq 12^\circ$
 $-8^\circ \leq \beta_C \leq 8^\circ$

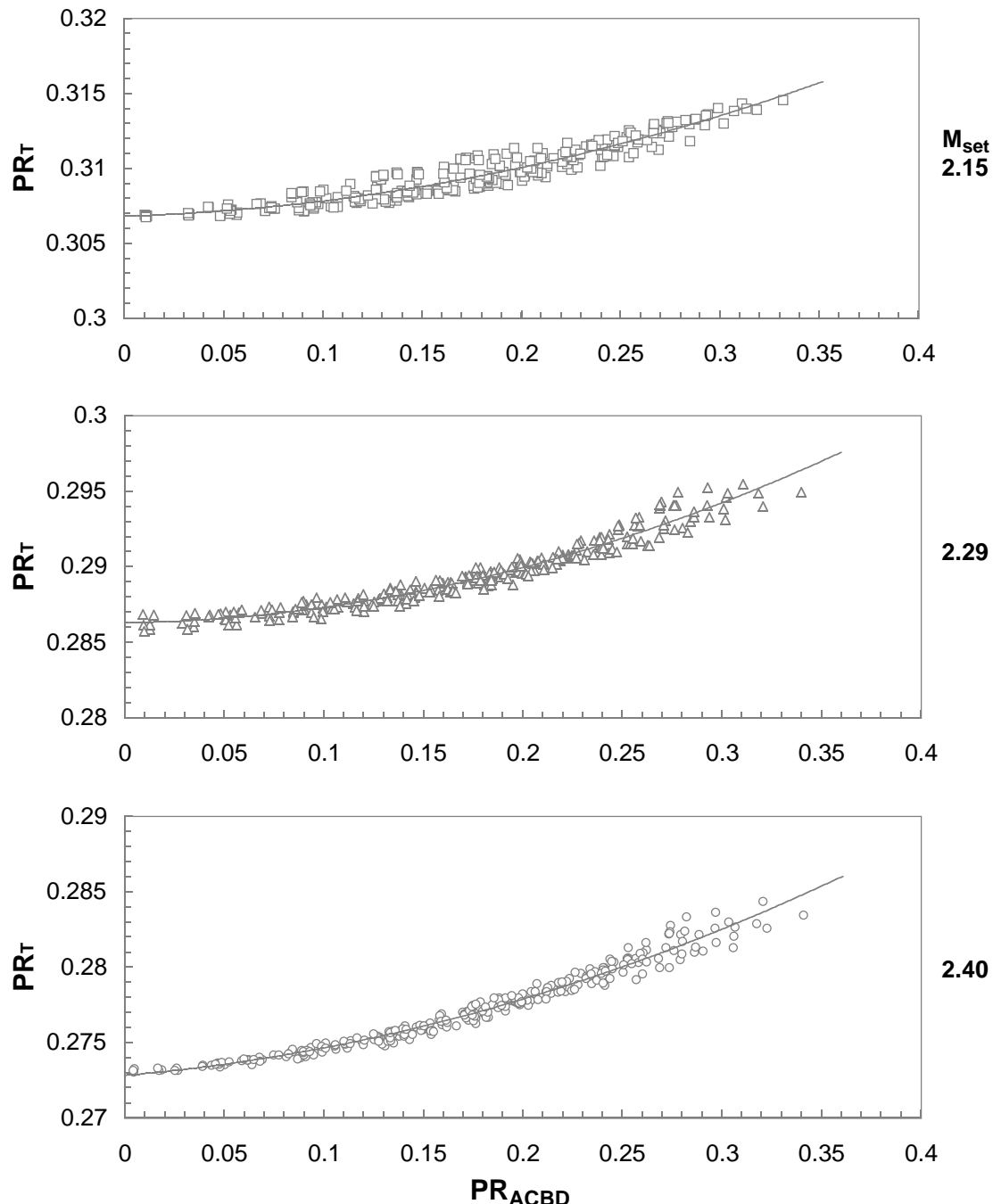
Figure 37. Continued.



Probe 5

$-12^\circ \leq \alpha_C \leq 12^\circ$
 $-8^\circ \leq \beta_C \leq 8^\circ$

Figure 37. Continued.



Probe 6

$-12^\circ \leq \alpha_C \leq 12^\circ$
 $-8^\circ \leq \beta_C \leq 8^\circ$

Figure 37. Concluded.

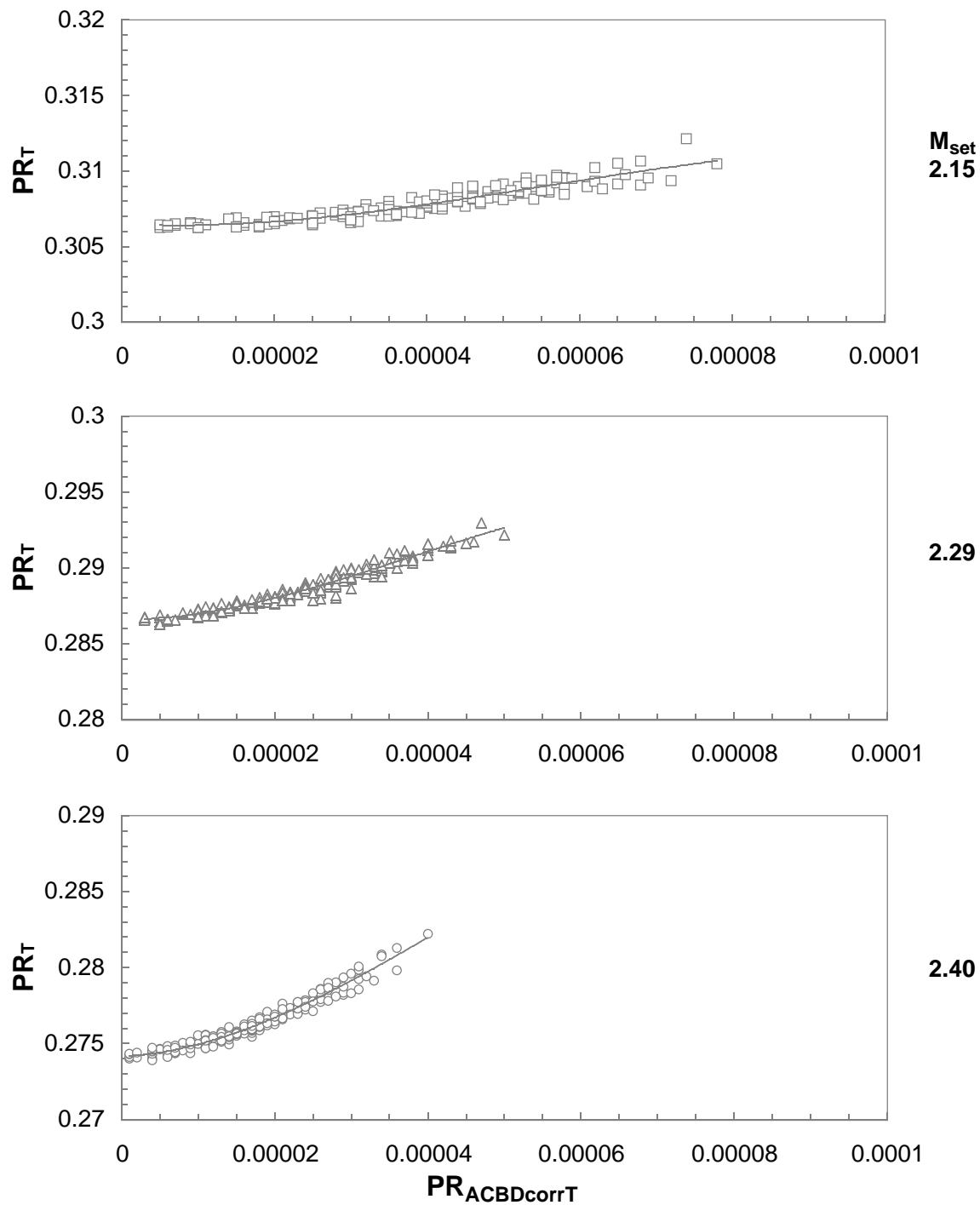
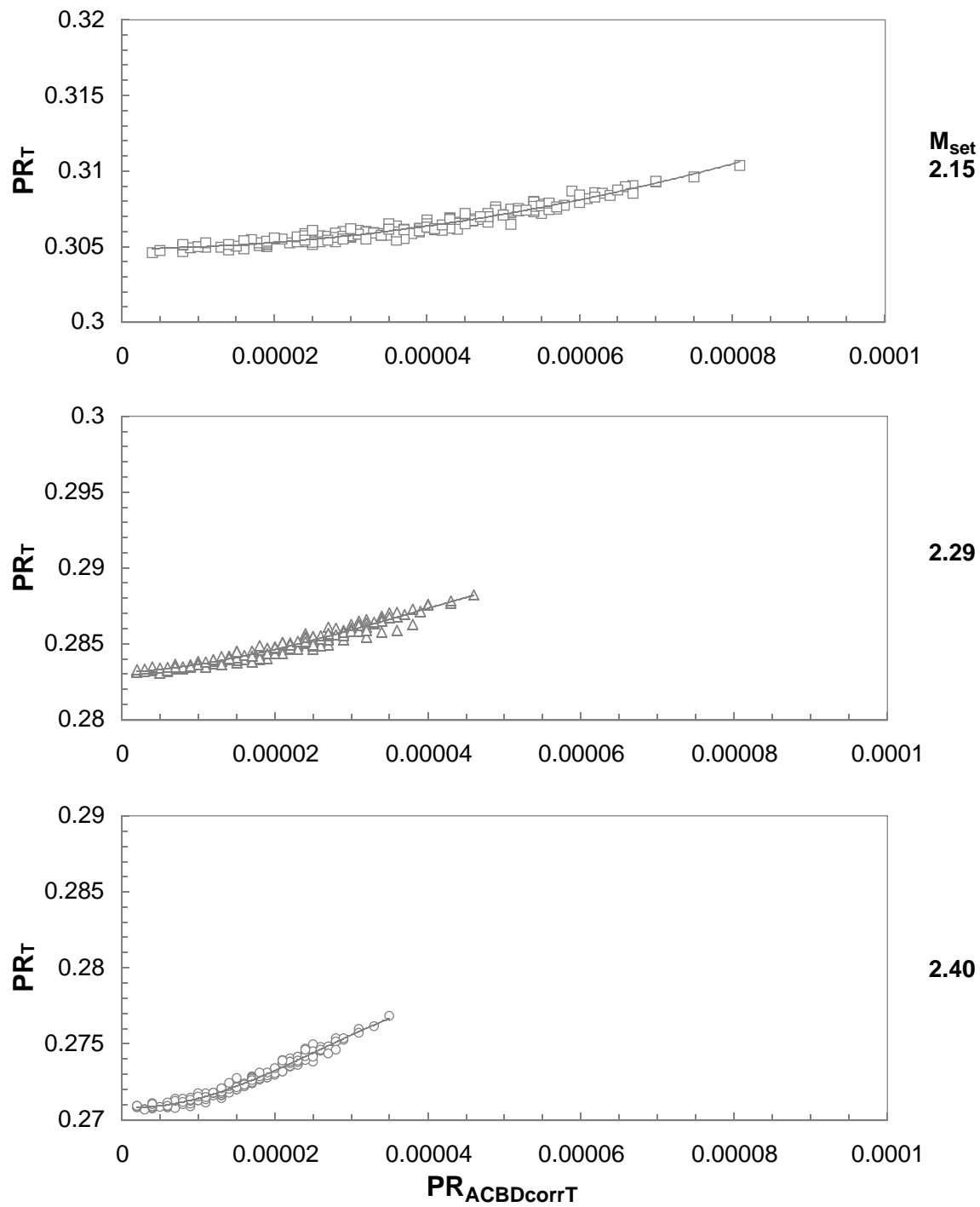


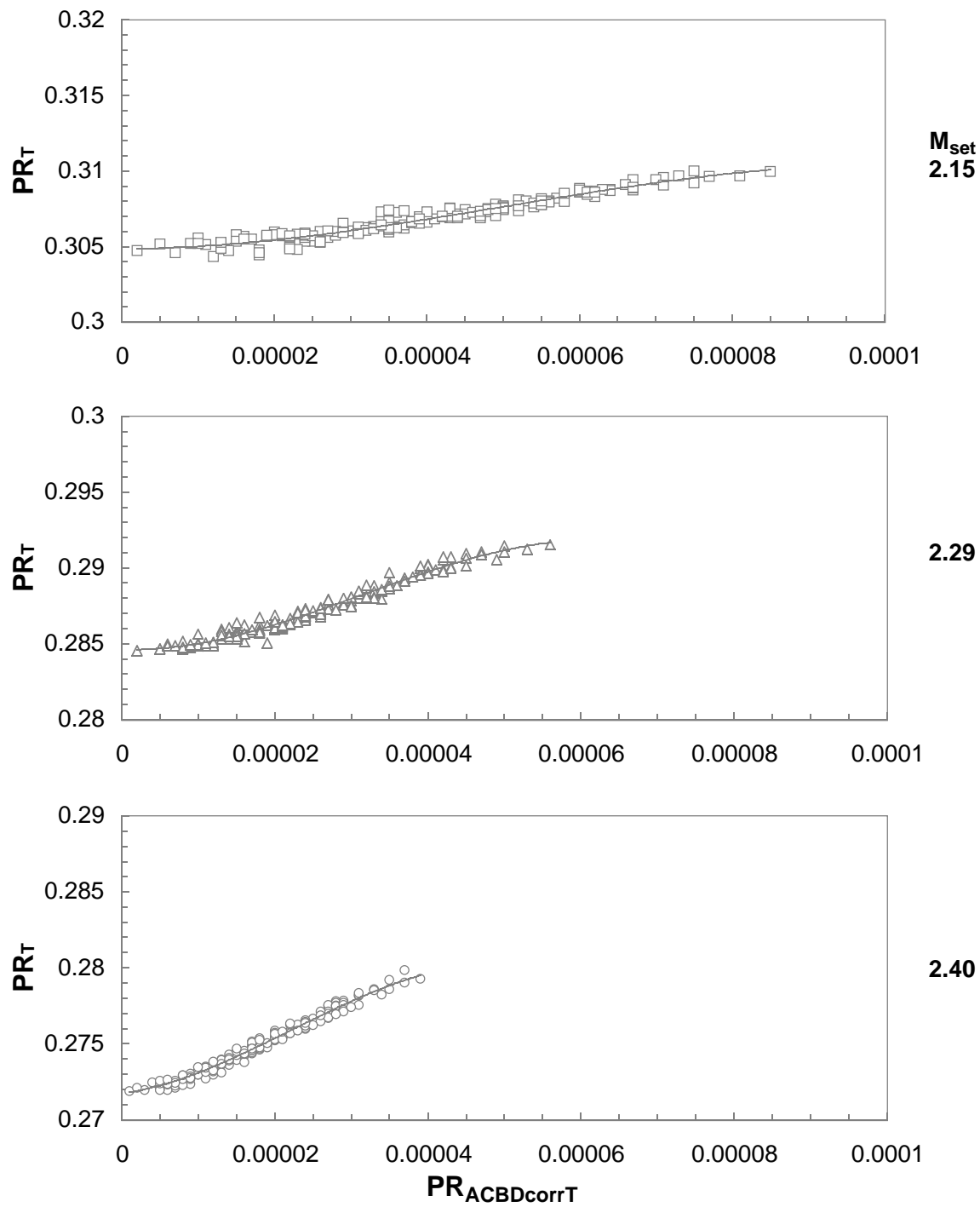
Figure 38. Compressibility parameter variation with corrected inclination parameter for rake 1.



Probe 2

$$-8^\circ \leq \alpha_C, \beta_C \leq 8^\circ$$

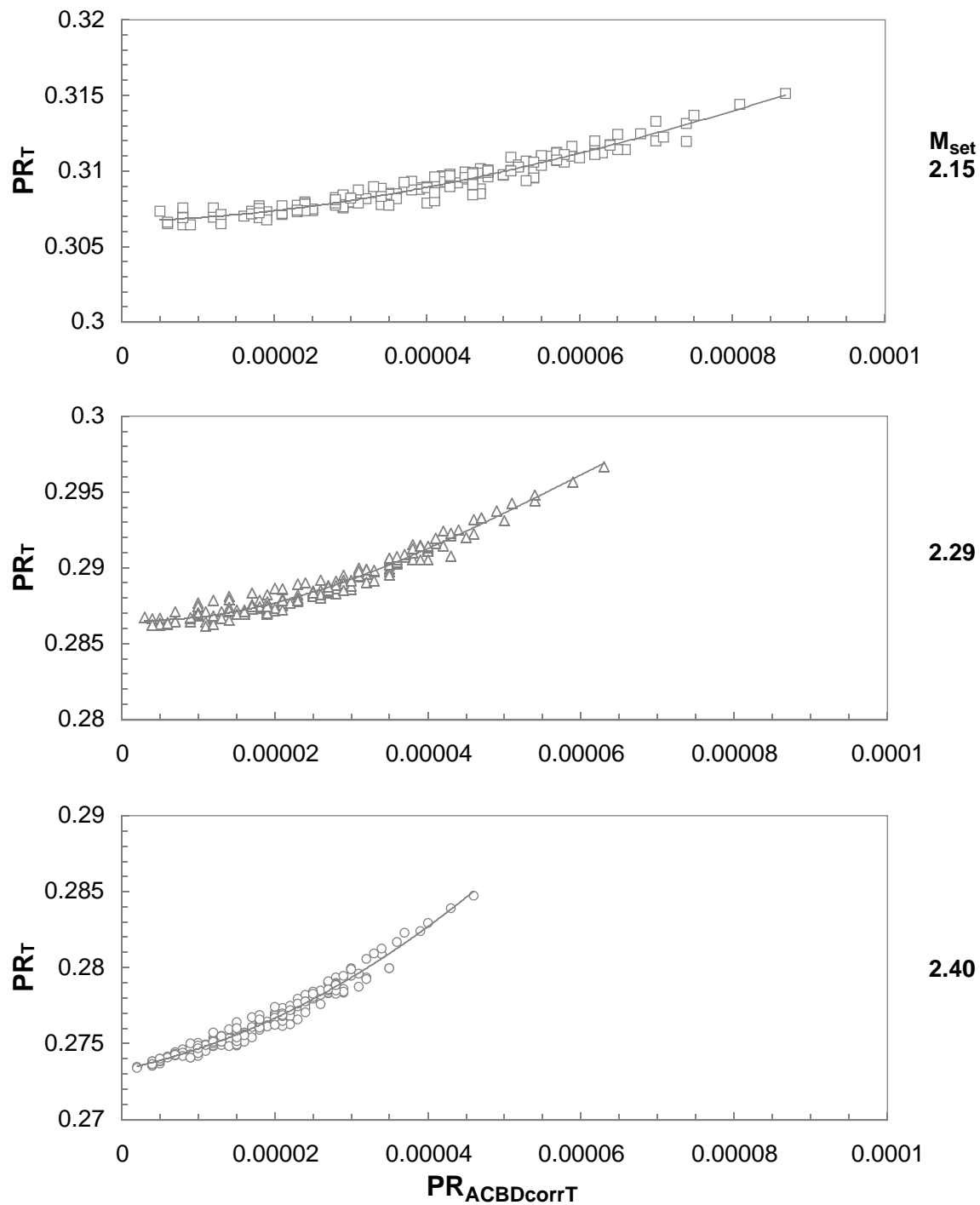
Figure 38. Continued.



Probe 3

$$-8^\circ \leq \alpha_C, \beta_C \leq 8^\circ$$

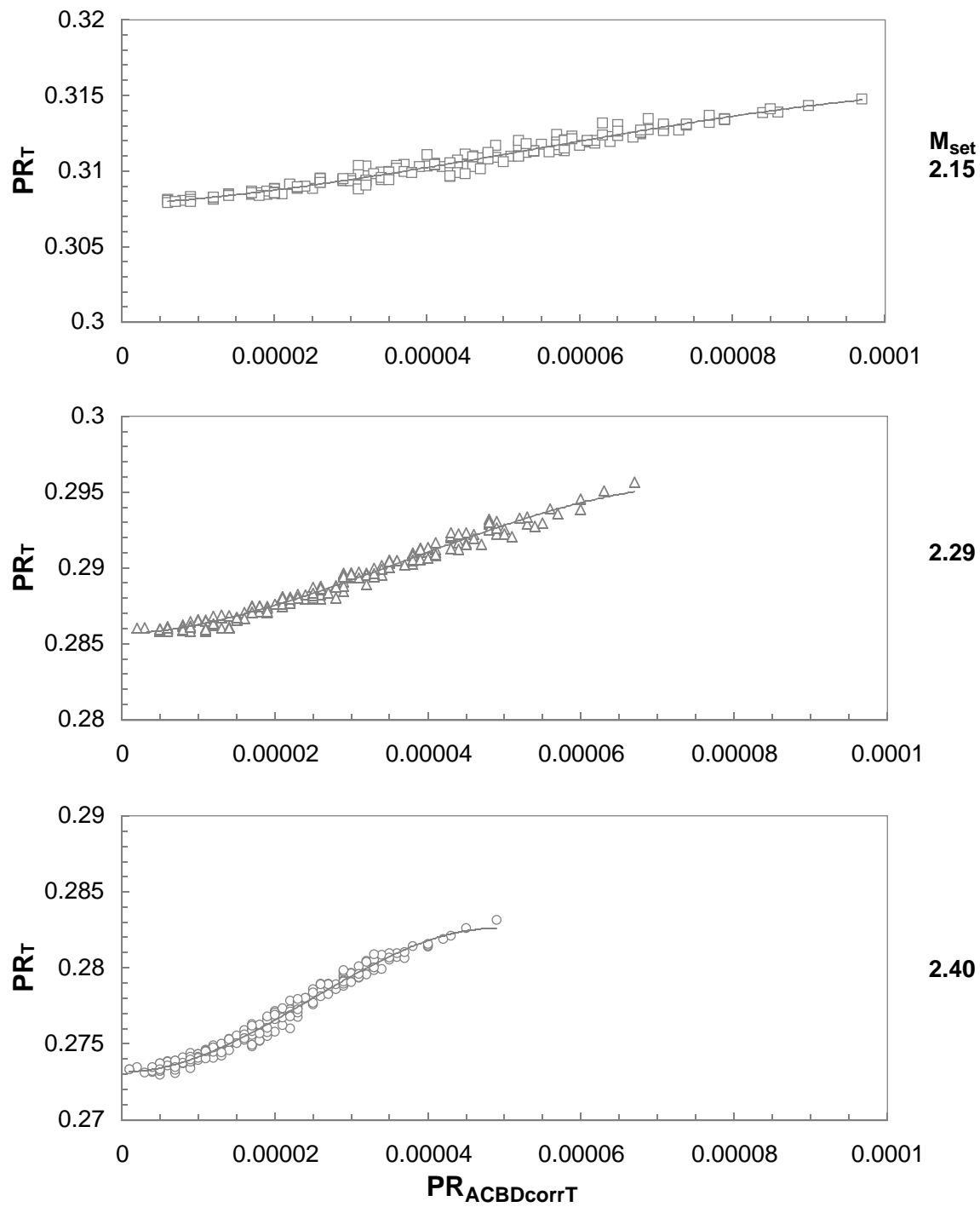
Figure 38. Continued.



Probe 4

$$-8^\circ \leq \alpha_C, \beta_C \leq 8^\circ$$

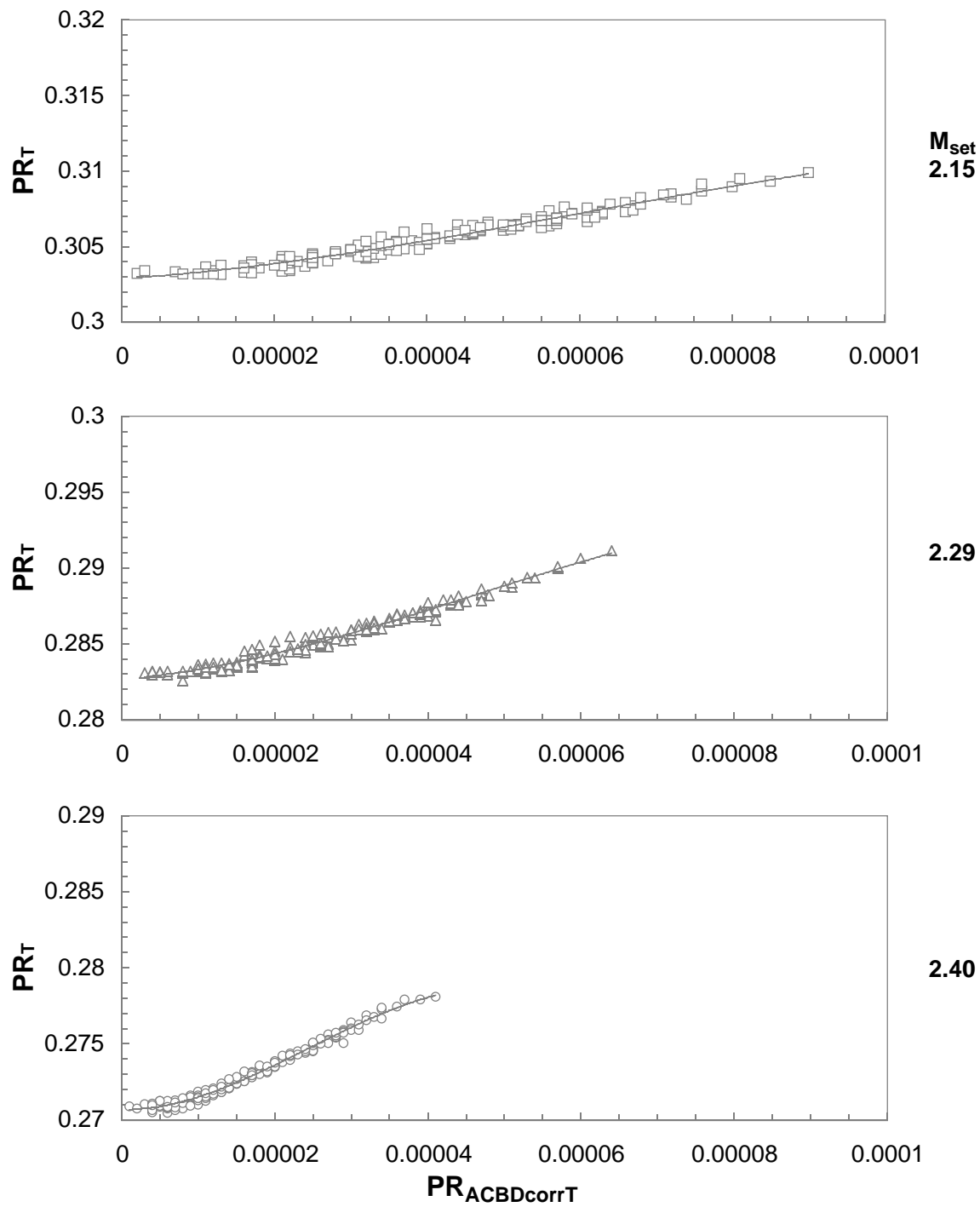
Figure 38. Continued.



Probe 5

$$-8^\circ \leq \alpha_C, \beta_C \leq 8^\circ$$

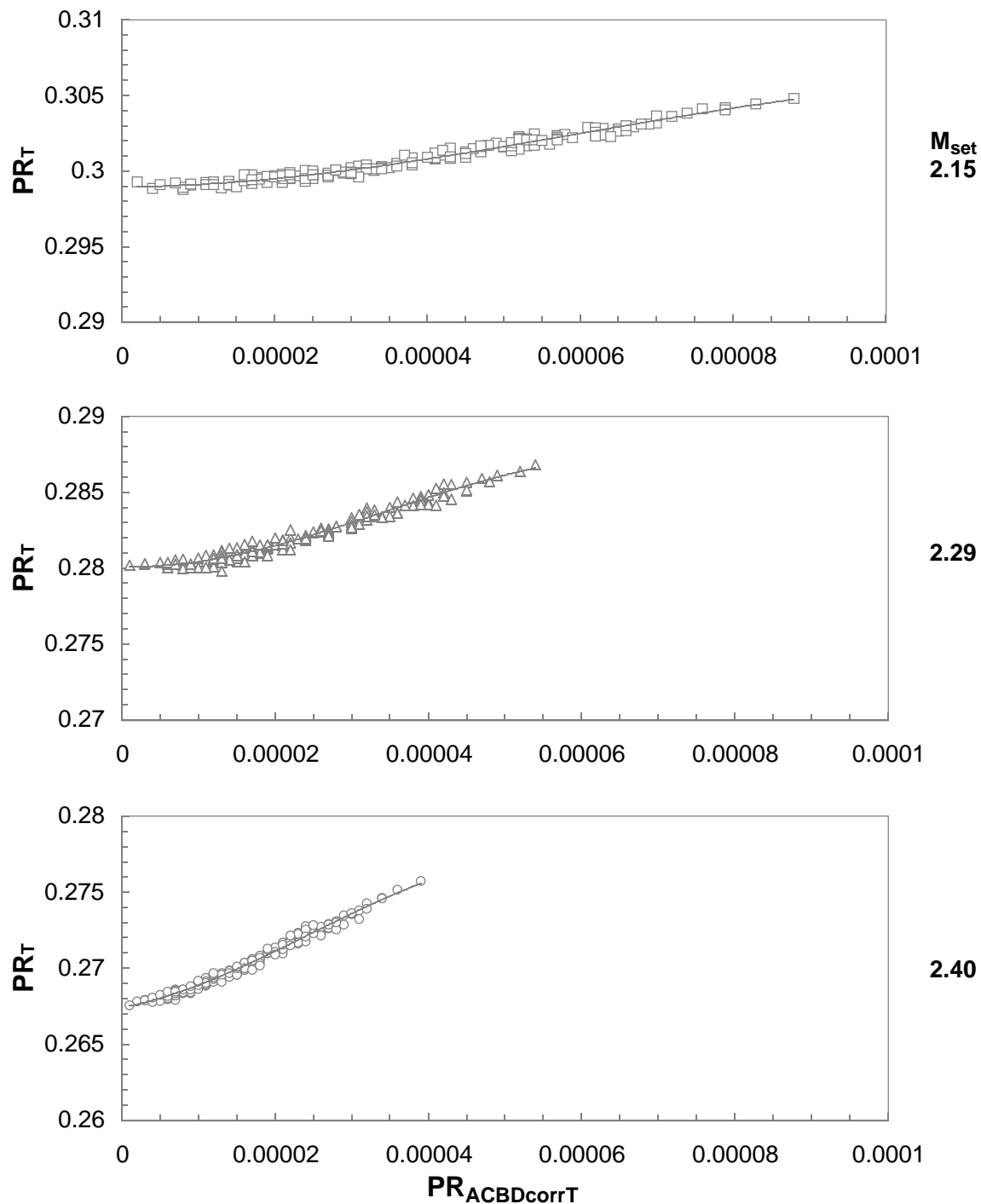
Figure 38. Continued.



Probe 6

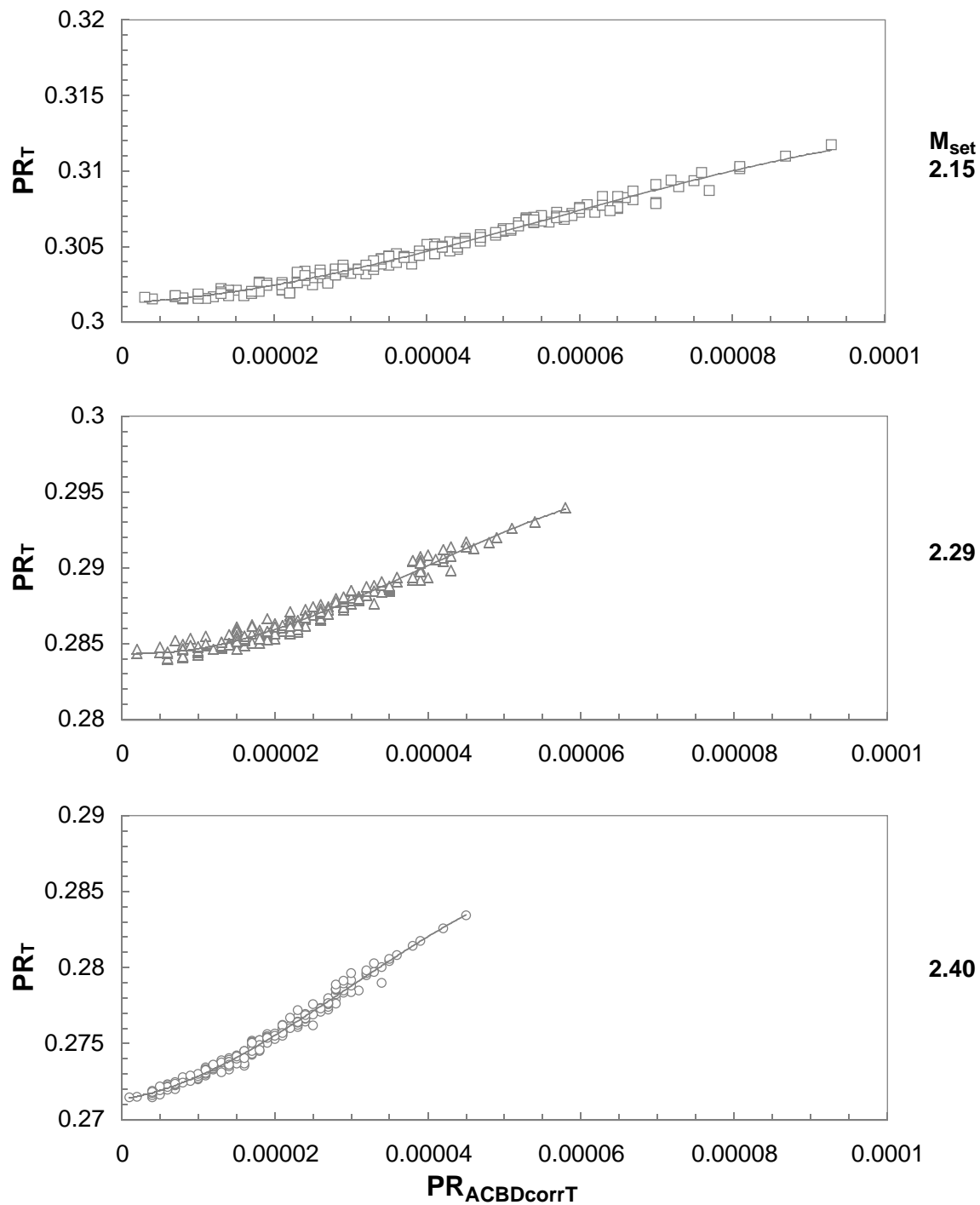
$$-8^\circ \leq \alpha_C, \beta_C \leq 8^\circ$$

Figure 38. Continued.



Probe 7
 $-8^\circ \leq \alpha_C, \beta_C \leq 8^\circ$

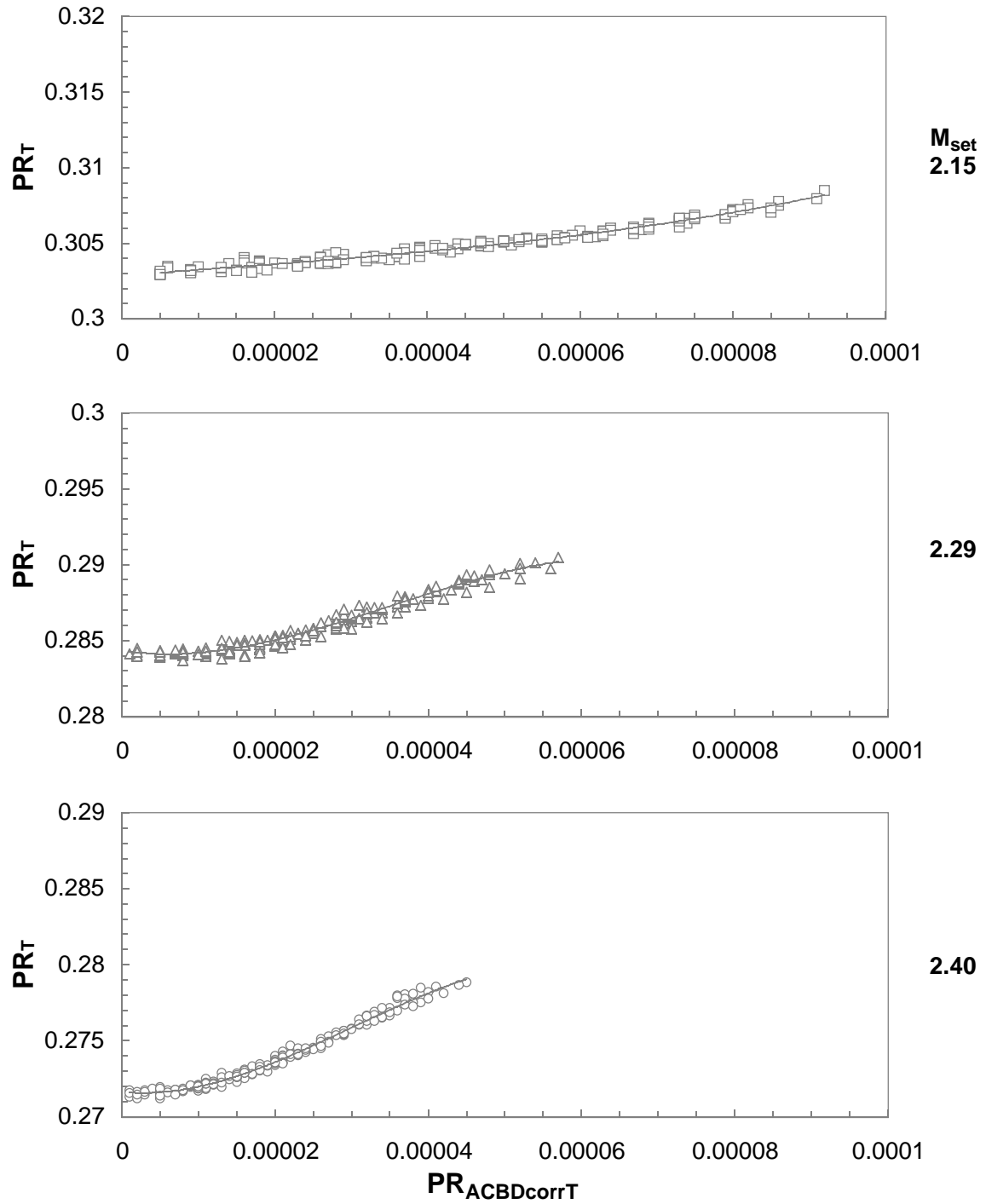
Figure 38. Continued.



Probe 8

$$-8^\circ \leq \alpha_C, \beta_C \leq 8^\circ$$

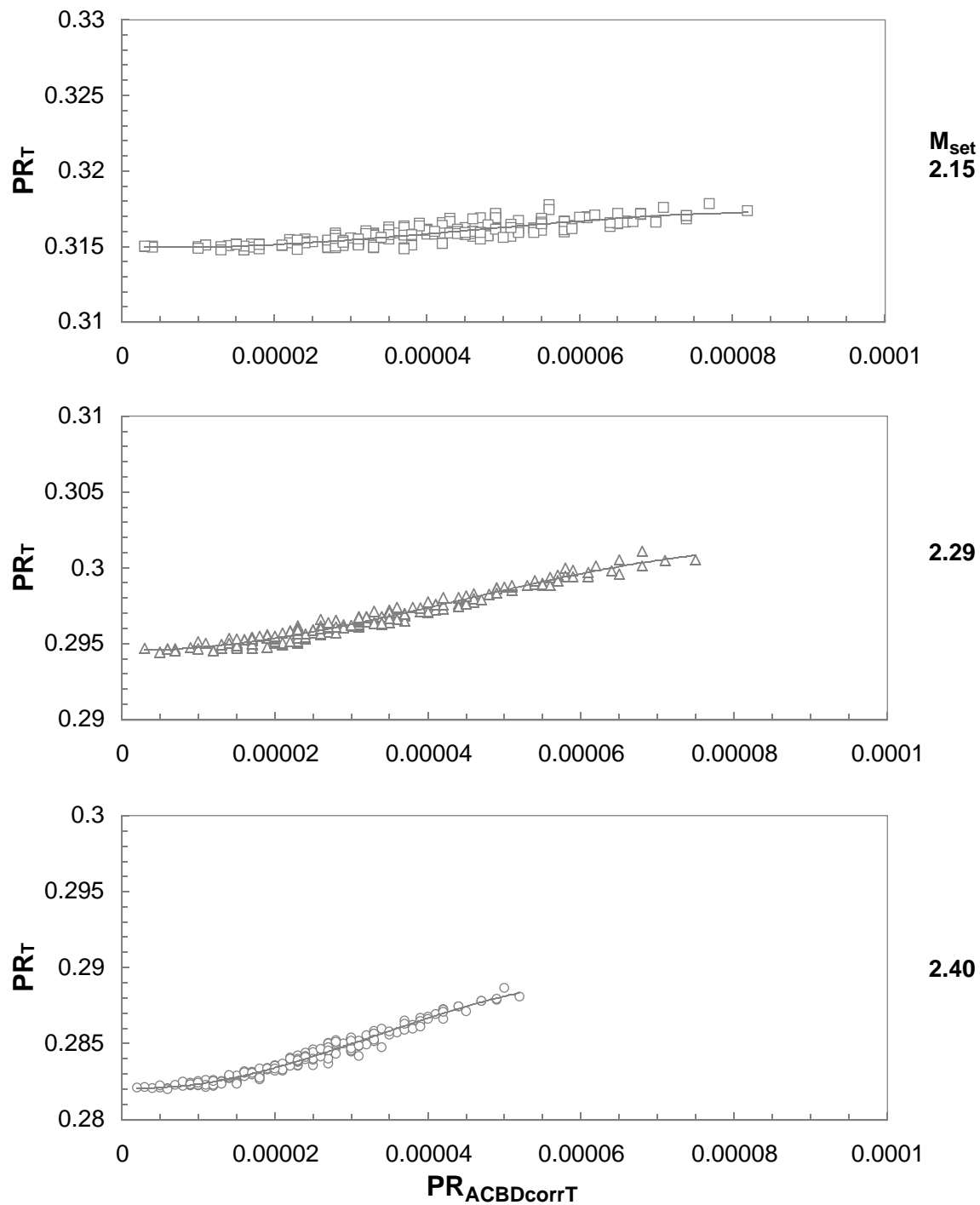
Figure 38. Concluded.



Probe 1

$$-8^\circ \leq \alpha_C, \beta_C \leq 8^\circ$$

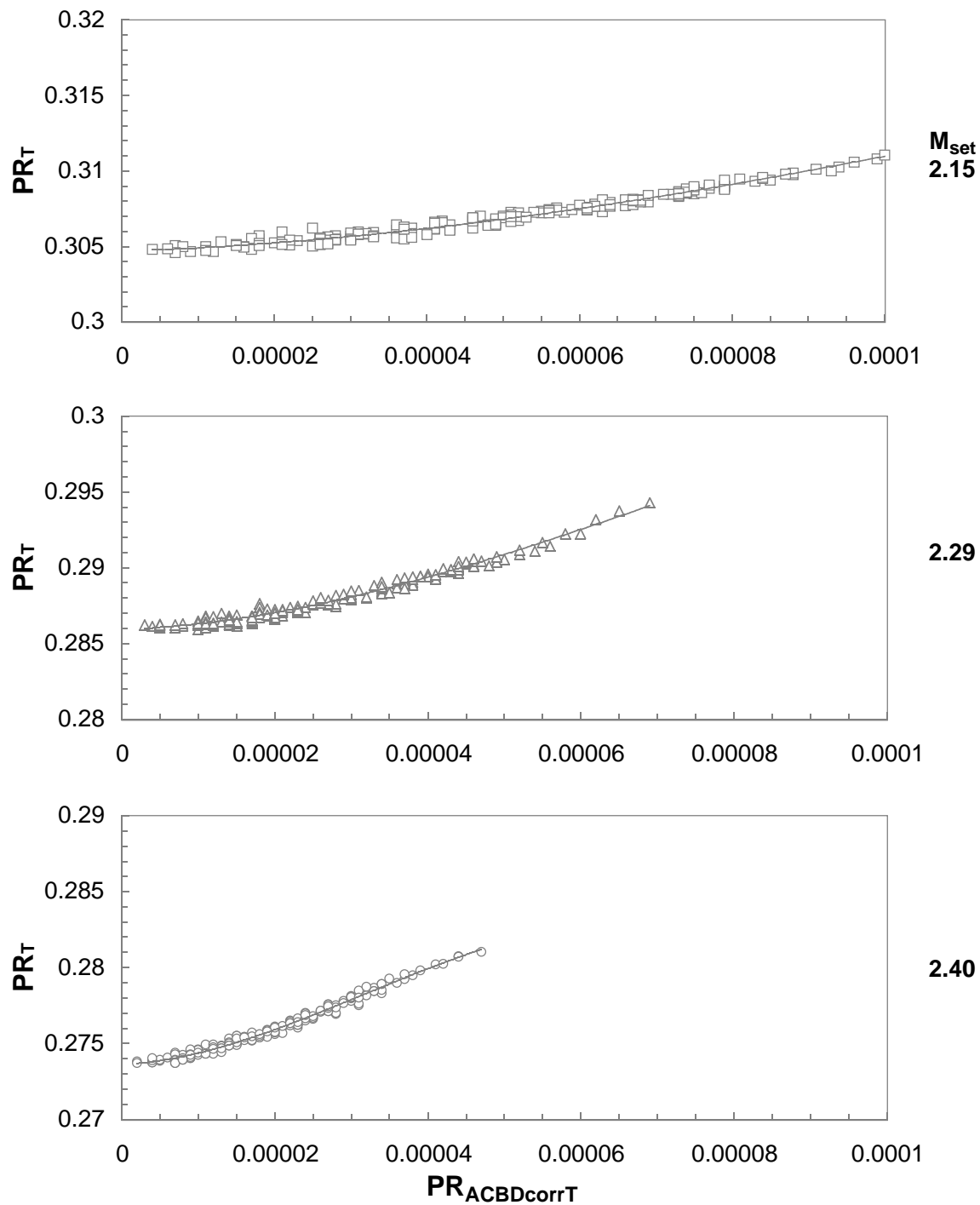
Figure 39. Compressibility parameter variation with corrected inclination parameter for rake 2.



Probe 2

$$-8^\circ \leq \alpha_C, \beta_C \leq 8^\circ$$

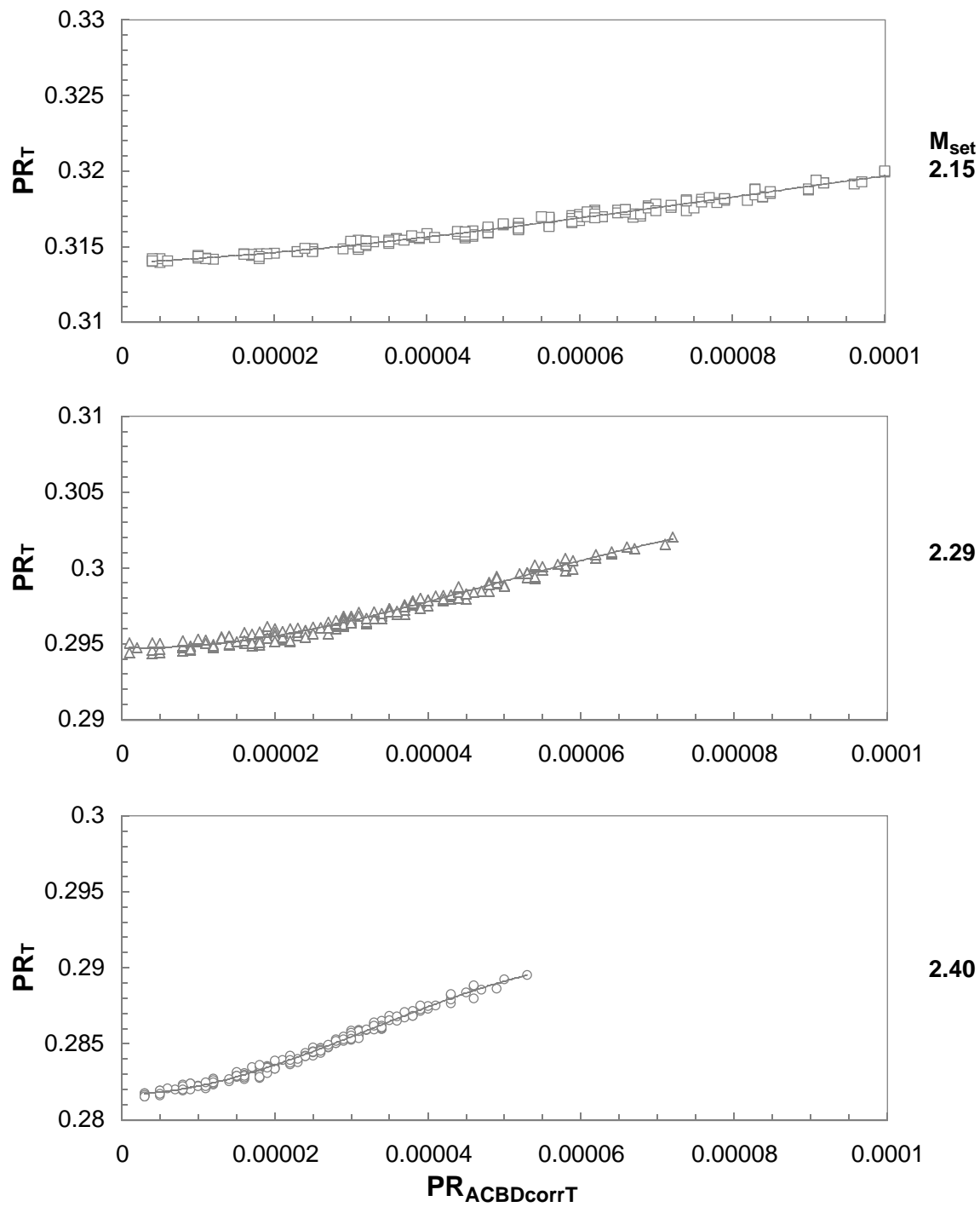
Figure 39. Continued.



Probe 3

$$-8^\circ \leq \alpha_C, \beta_C \leq 8^\circ$$

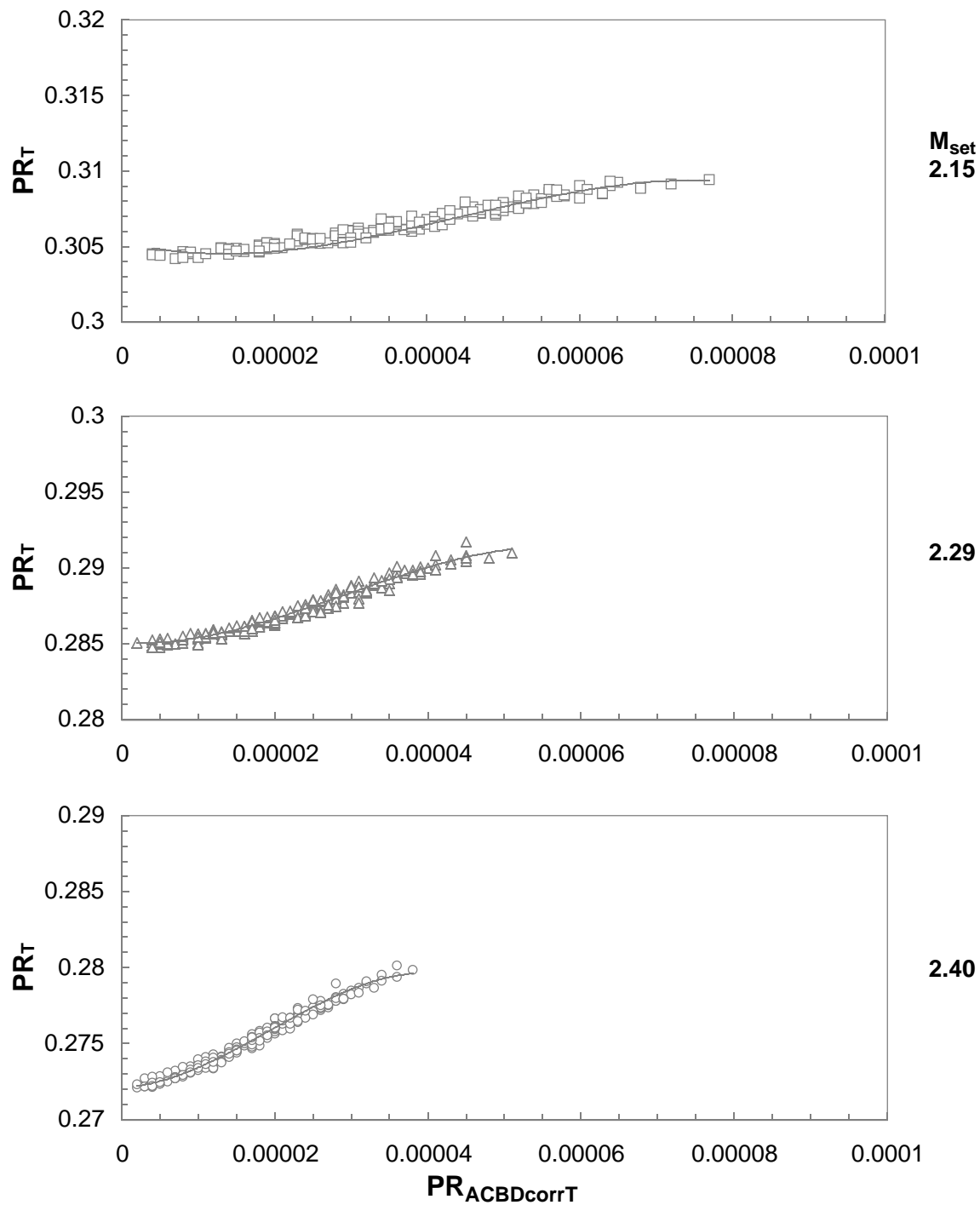
Figure 39. Continued.



Probe 4

$$-8^\circ \leq \alpha_C, \beta_C \leq 8^\circ$$

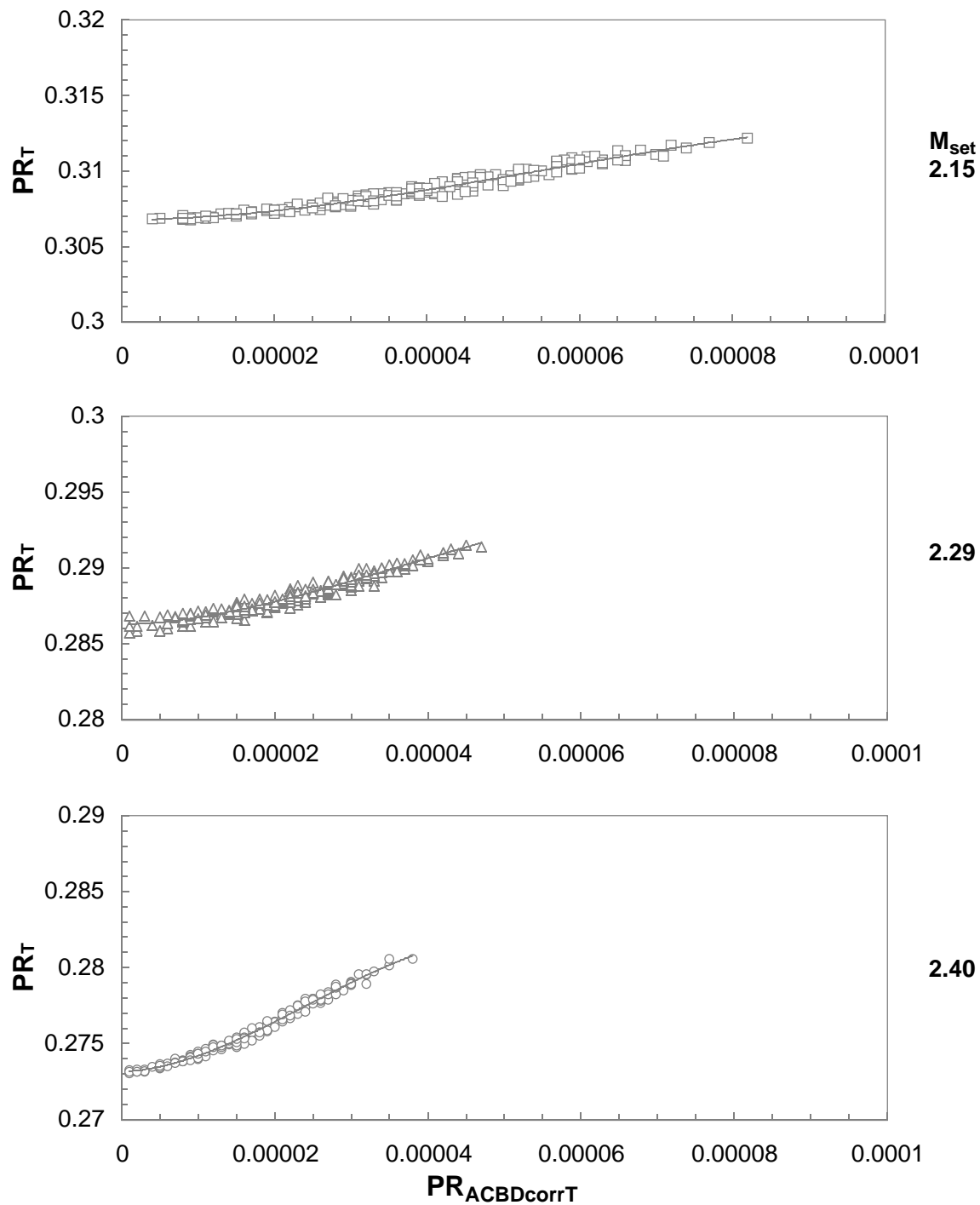
Figure 39. Continued.



Probe 5

$$-8^\circ \leq \alpha_C, \beta_C \leq 8^\circ$$

Figure 39. Continued.

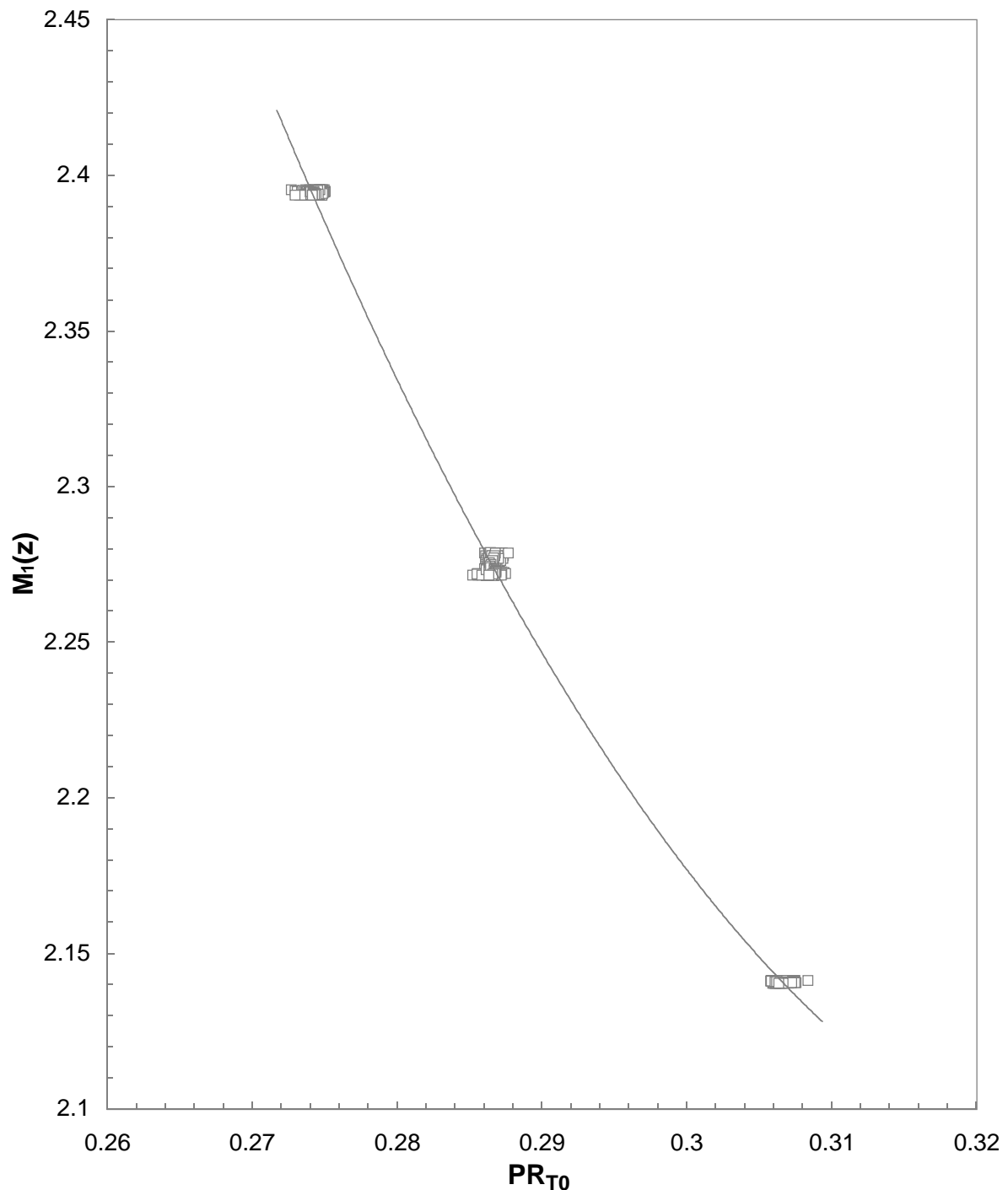


Probe 6

$$-8^\circ \leq \alpha_C, \beta_C \leq 8^\circ$$

Figure 39. Concluded.

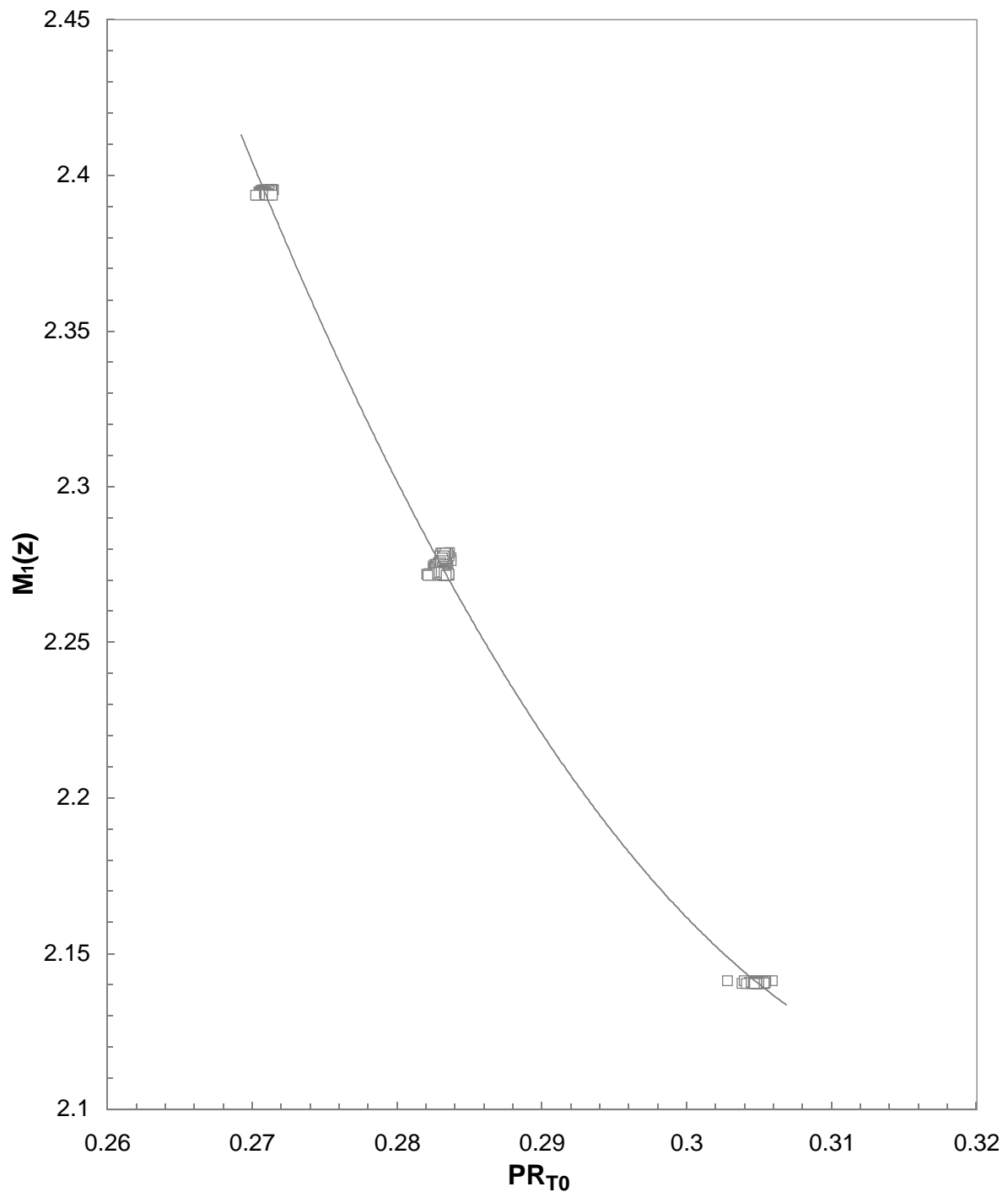
Figure 40. Fundamental cone-probe compressibility parameter model.



Probe 1

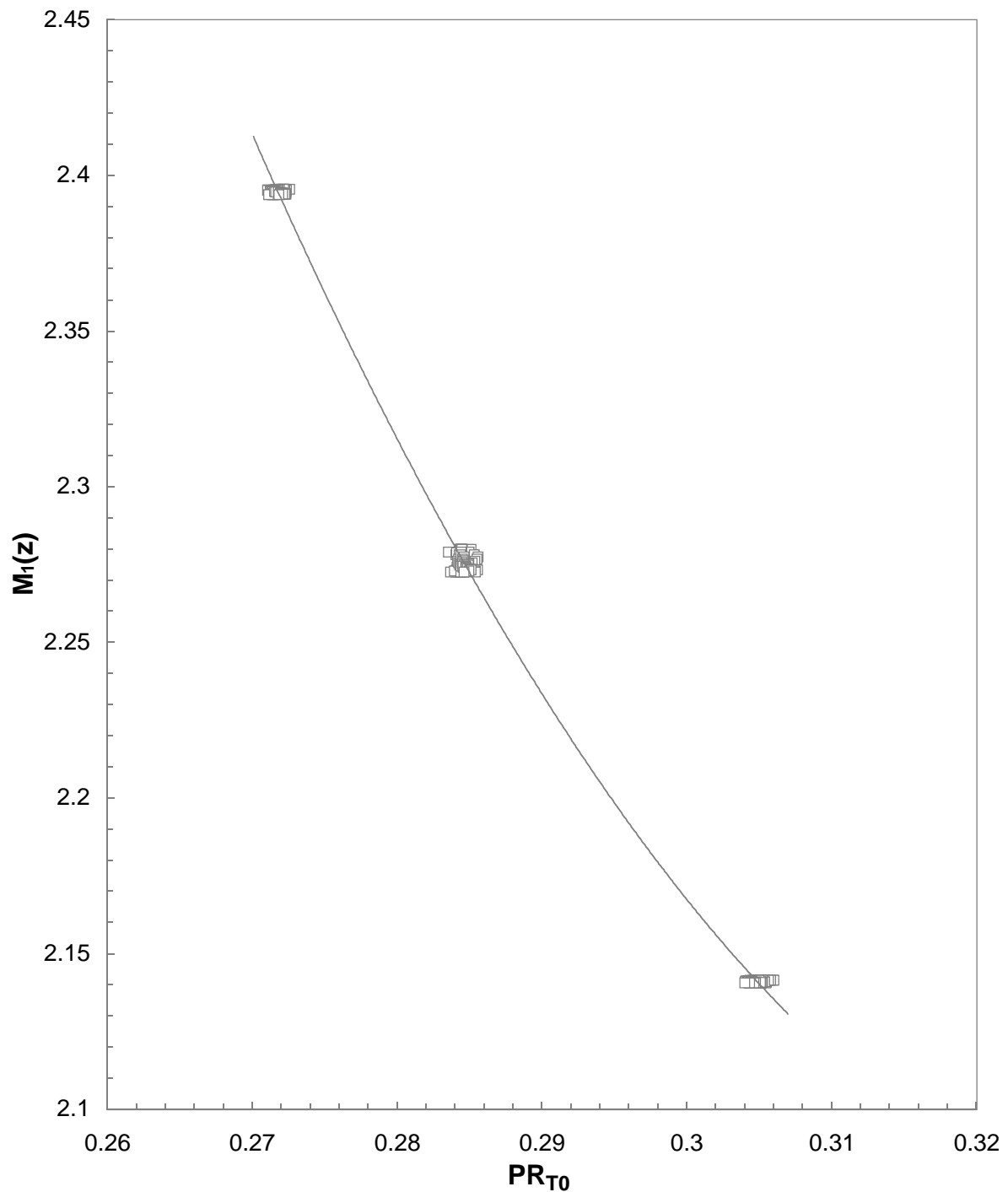
$$-8^\circ \leq \alpha_c, \beta_c \leq 8^\circ$$

Figure 41. Mach number dependency on fundamental compressibility parameter for rake 1.



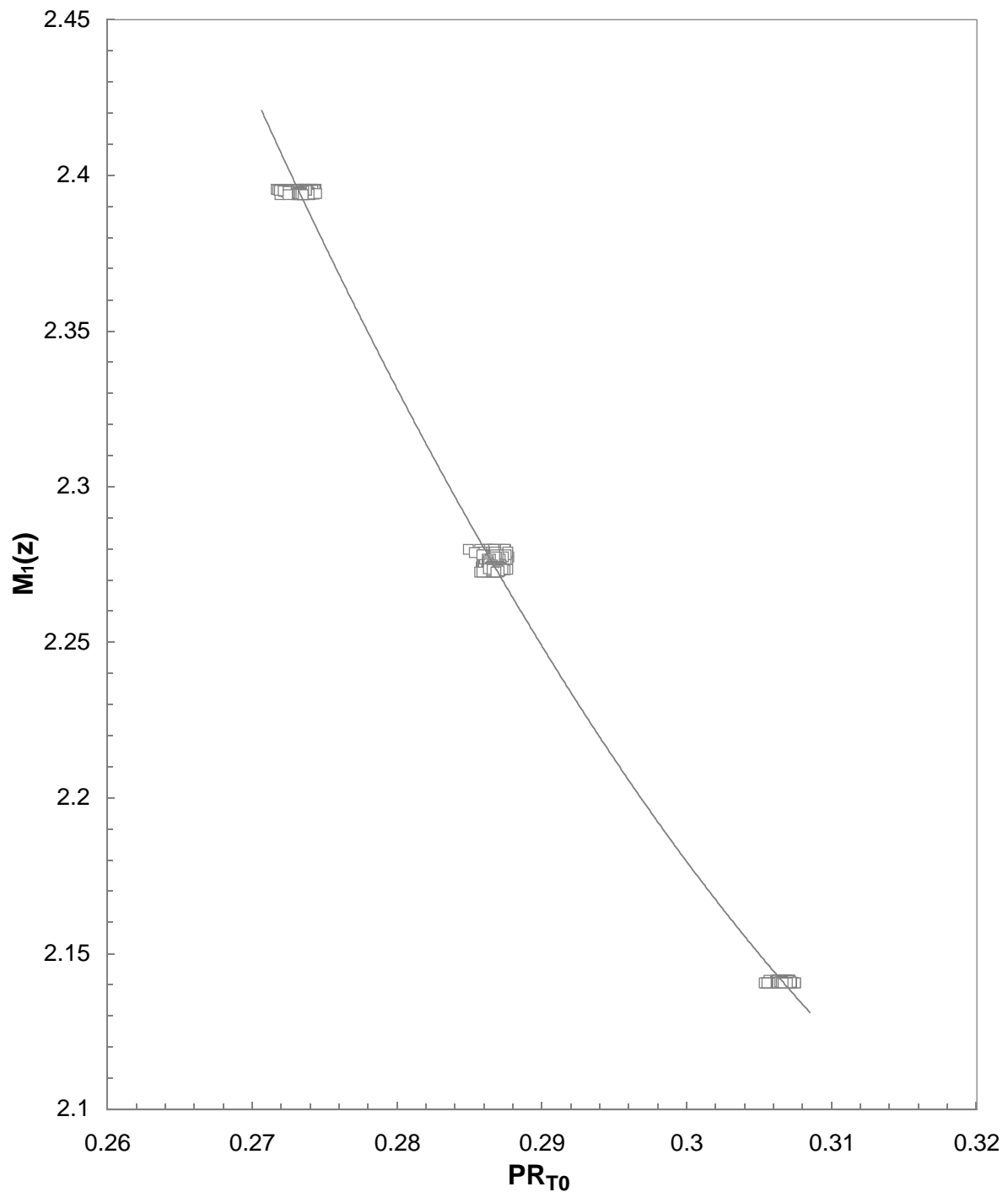
Probe 2
 $-8^\circ \leq \alpha_C, \beta_C \leq 8^\circ$

Figure 41. Continued.



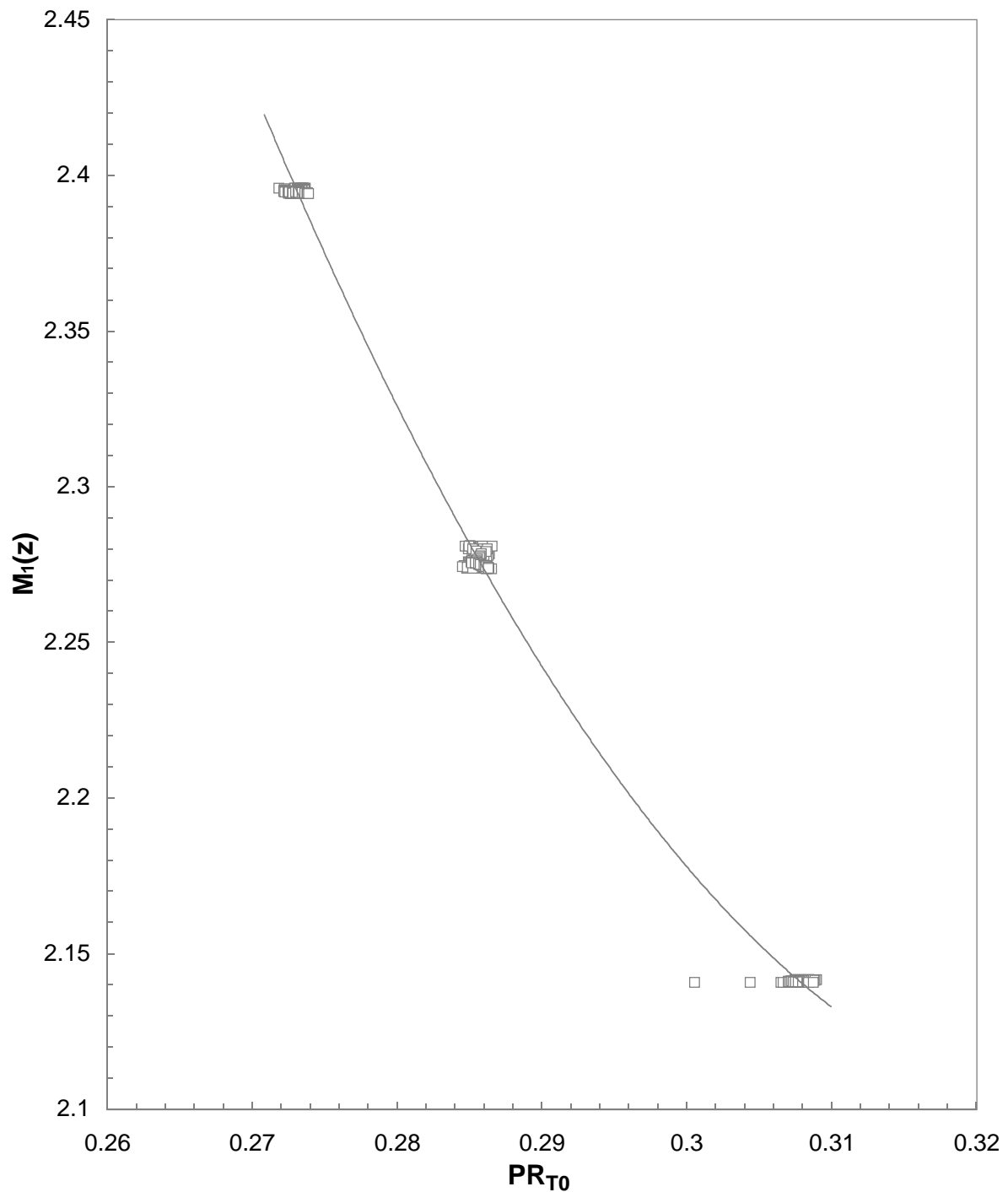
Probe 3
 $-8^\circ \leq \alpha_C, \beta_C \leq 8^\circ$

Figure 41. Continued.



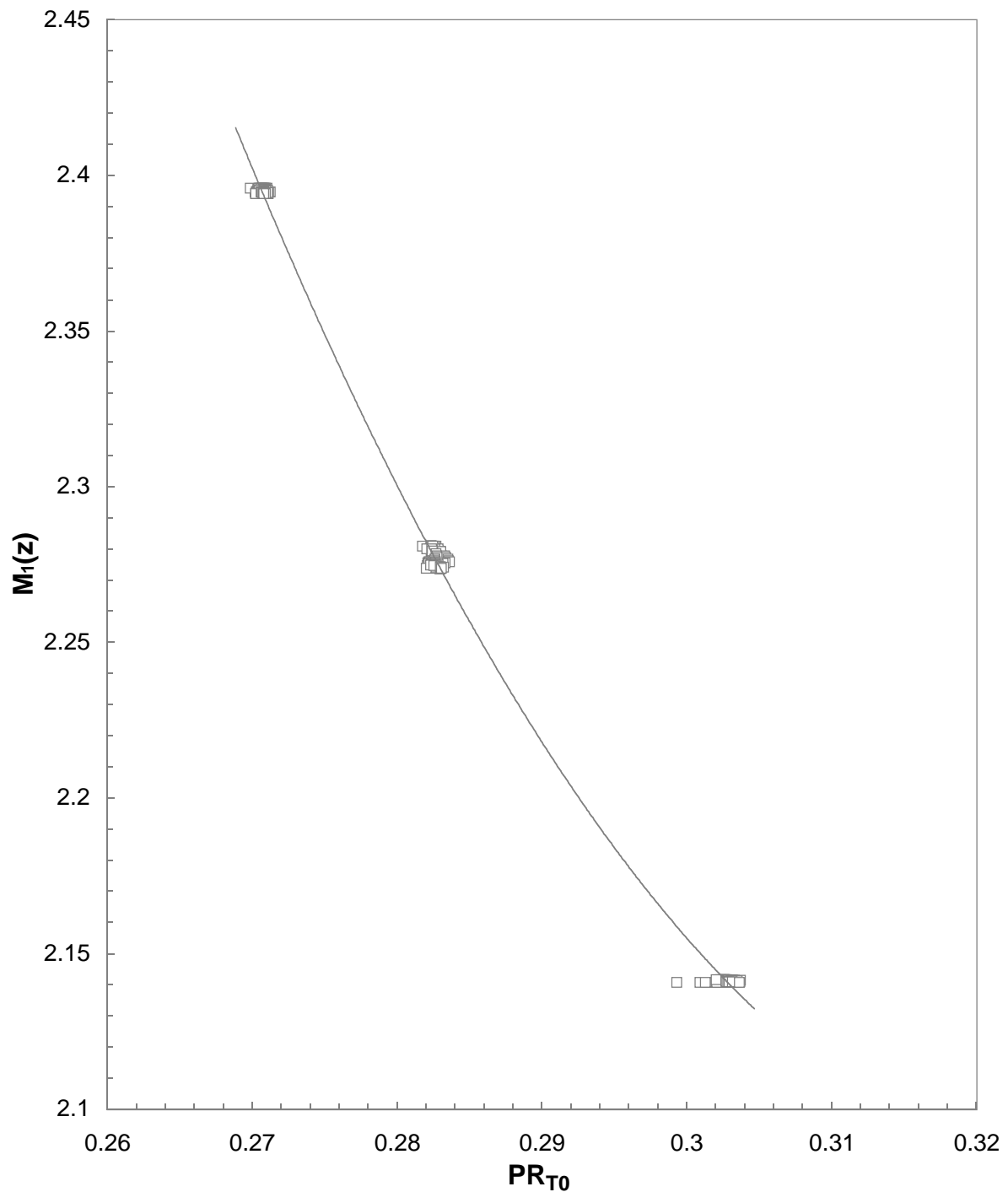
Probe 4
 $-8^\circ \leq \alpha_C, \beta_C \leq 8^\circ$

Figure 41. Continued.



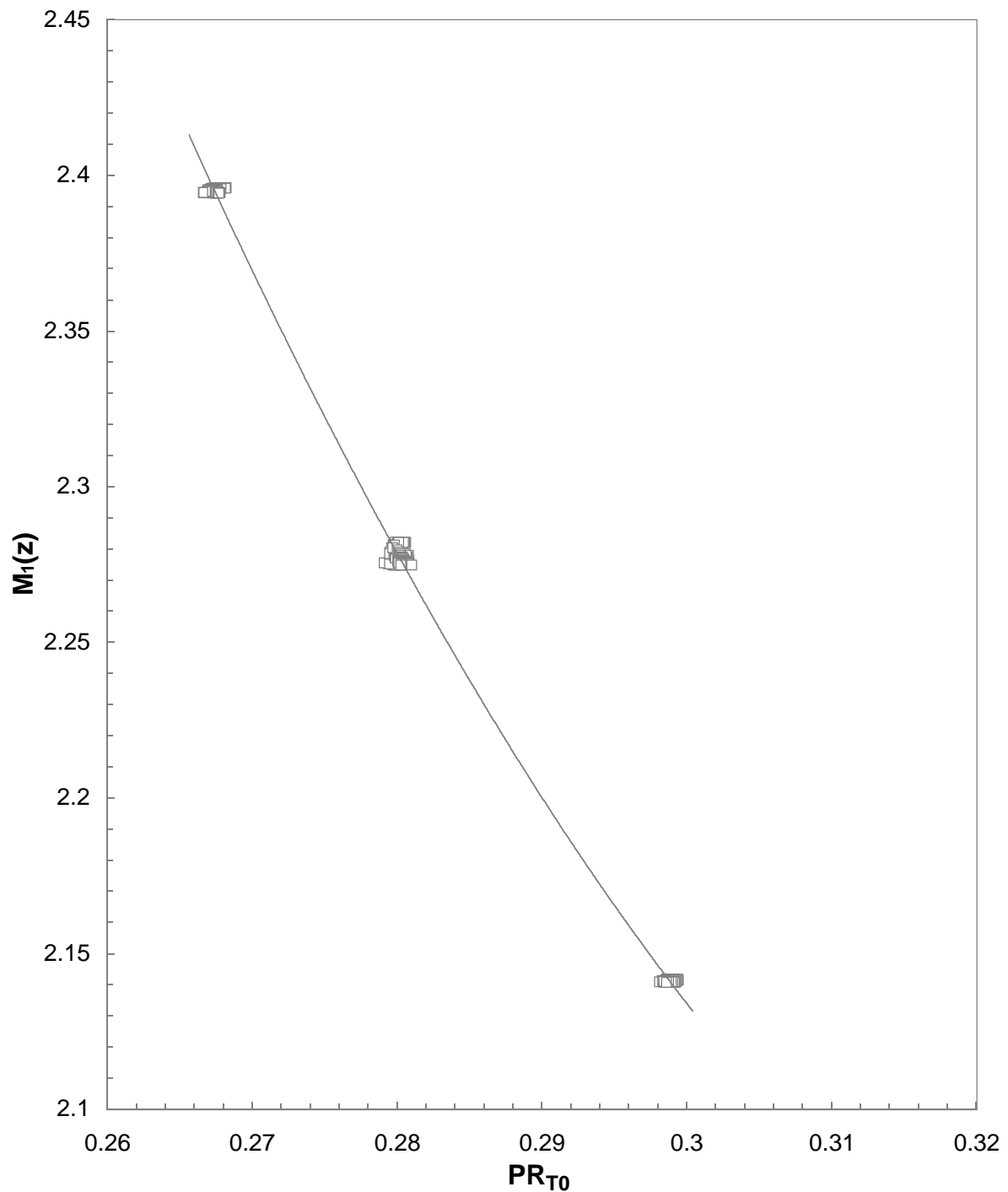
Probe 5
 $-8^\circ \leq \alpha_C, \beta_C \leq 8^\circ$

Figure 41. Continued.



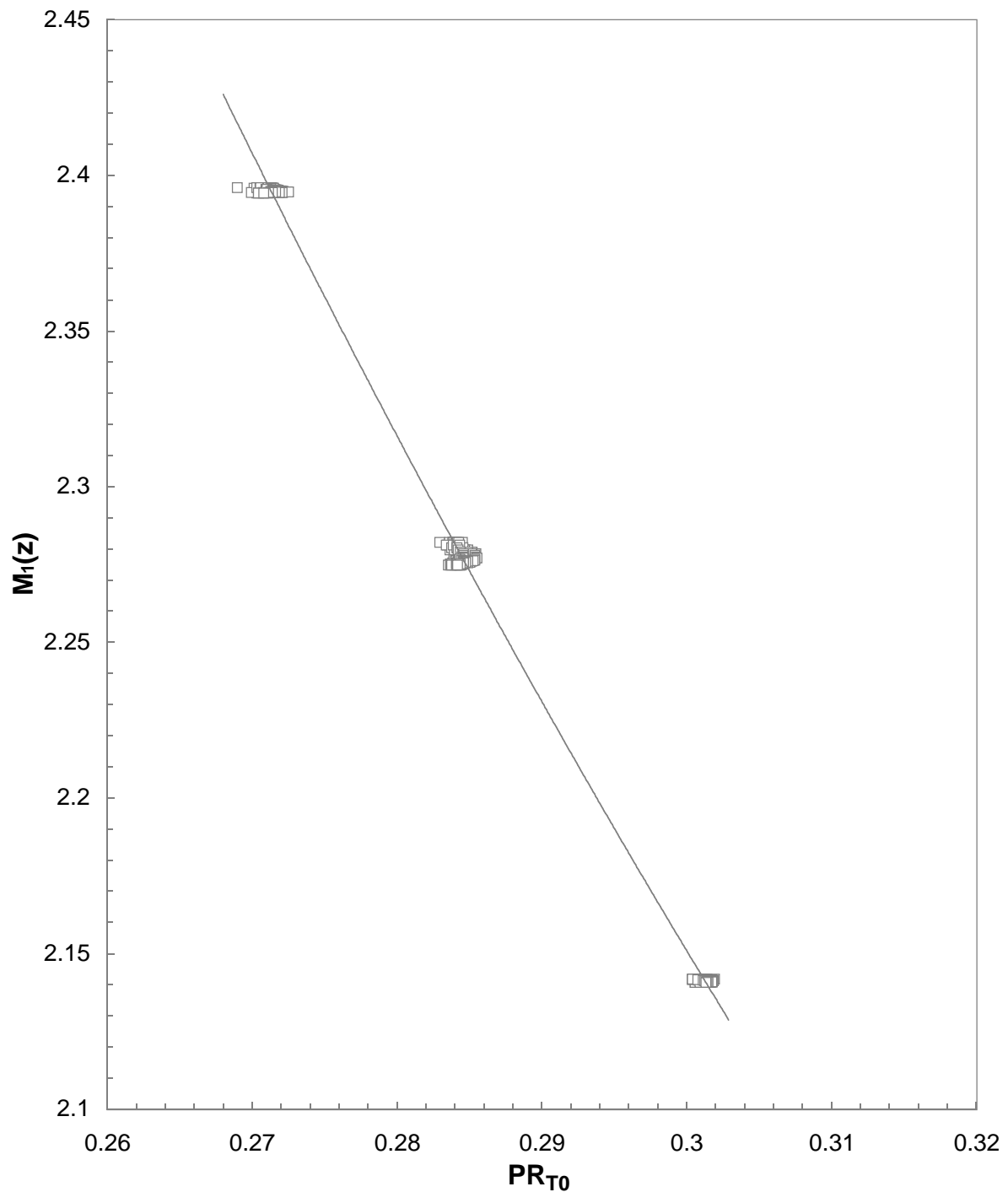
Probe 6
 $-8^\circ \leq \alpha_C, \beta_C \leq 8^\circ$

Figure 41. Continued.



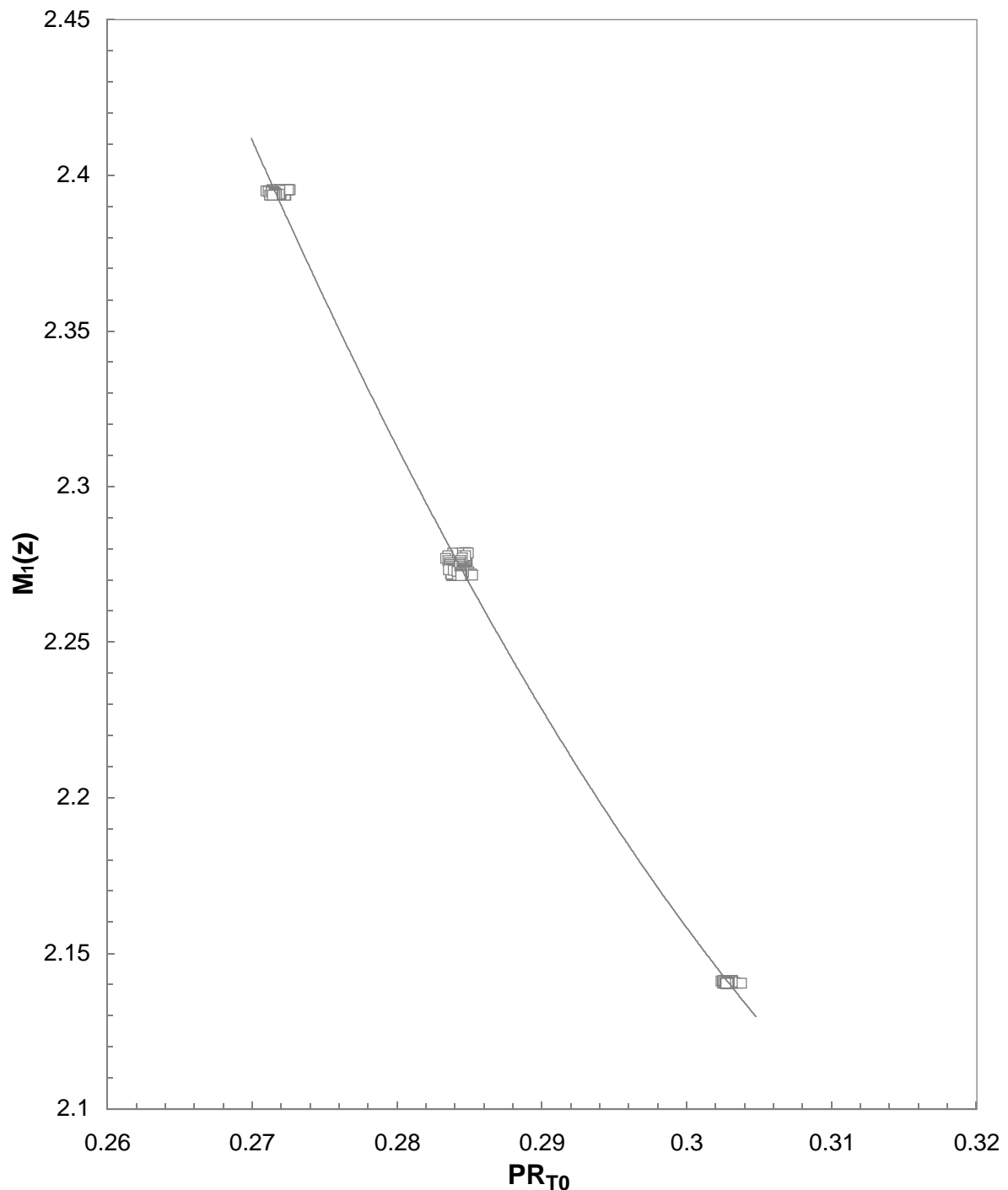
Probe 7
 $-8^\circ \leq \alpha_C, \beta_C \leq 8^\circ$

Figure 41. Continued.



Probe 8
 $-8^\circ \leq \alpha_C, \beta_C \leq 8^\circ$

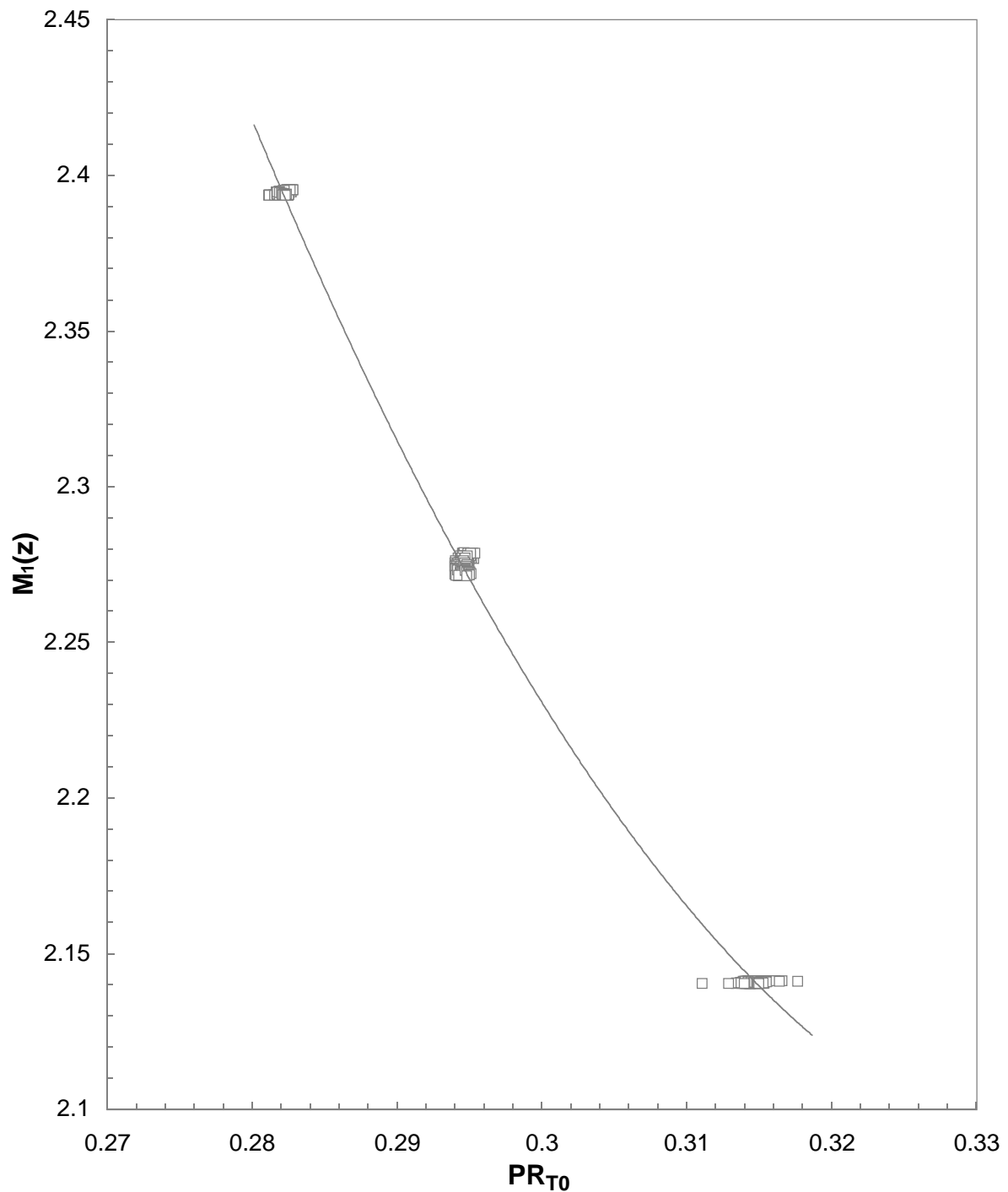
Figure 41. Concluded.



Probe 1

$$-8^\circ \leq \alpha_C, \beta_C \leq 8^\circ$$

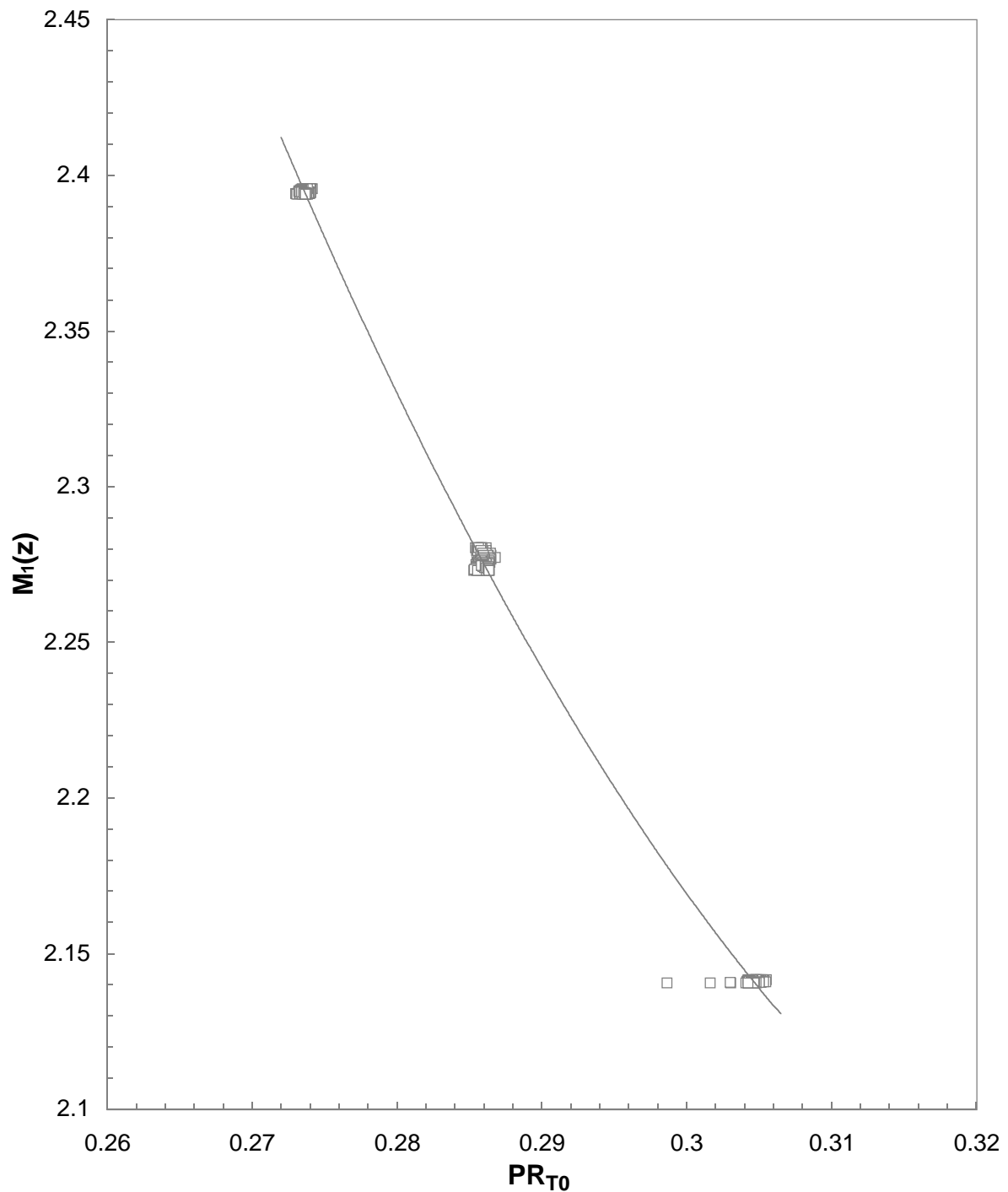
Figure 42. Mach number dependency on fundamental compressibility parameter for rake 2.



Probe 2

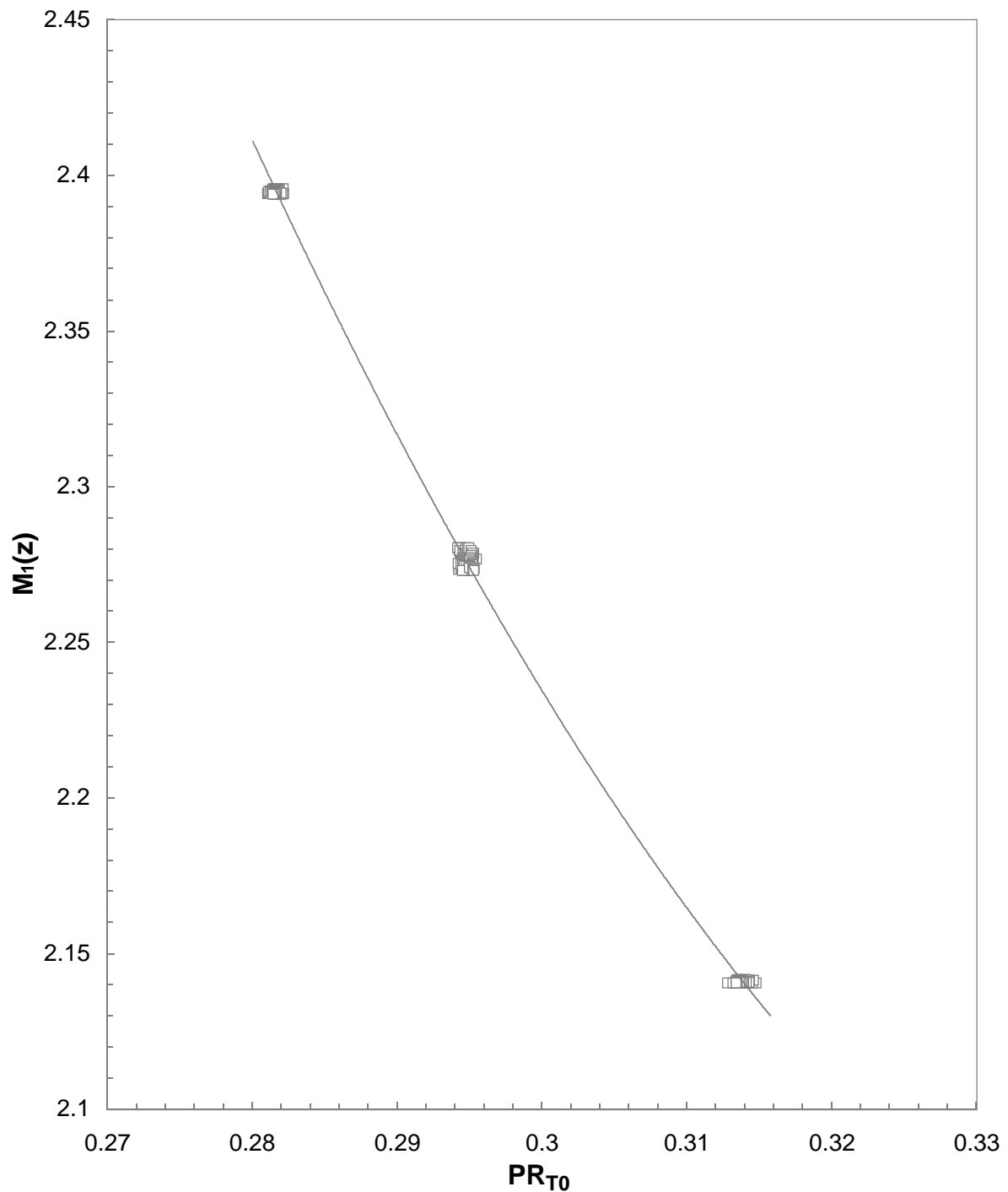
$-8^\circ \leq \alpha_C, \beta_C \leq 8^\circ$

Figure 42. Continued.



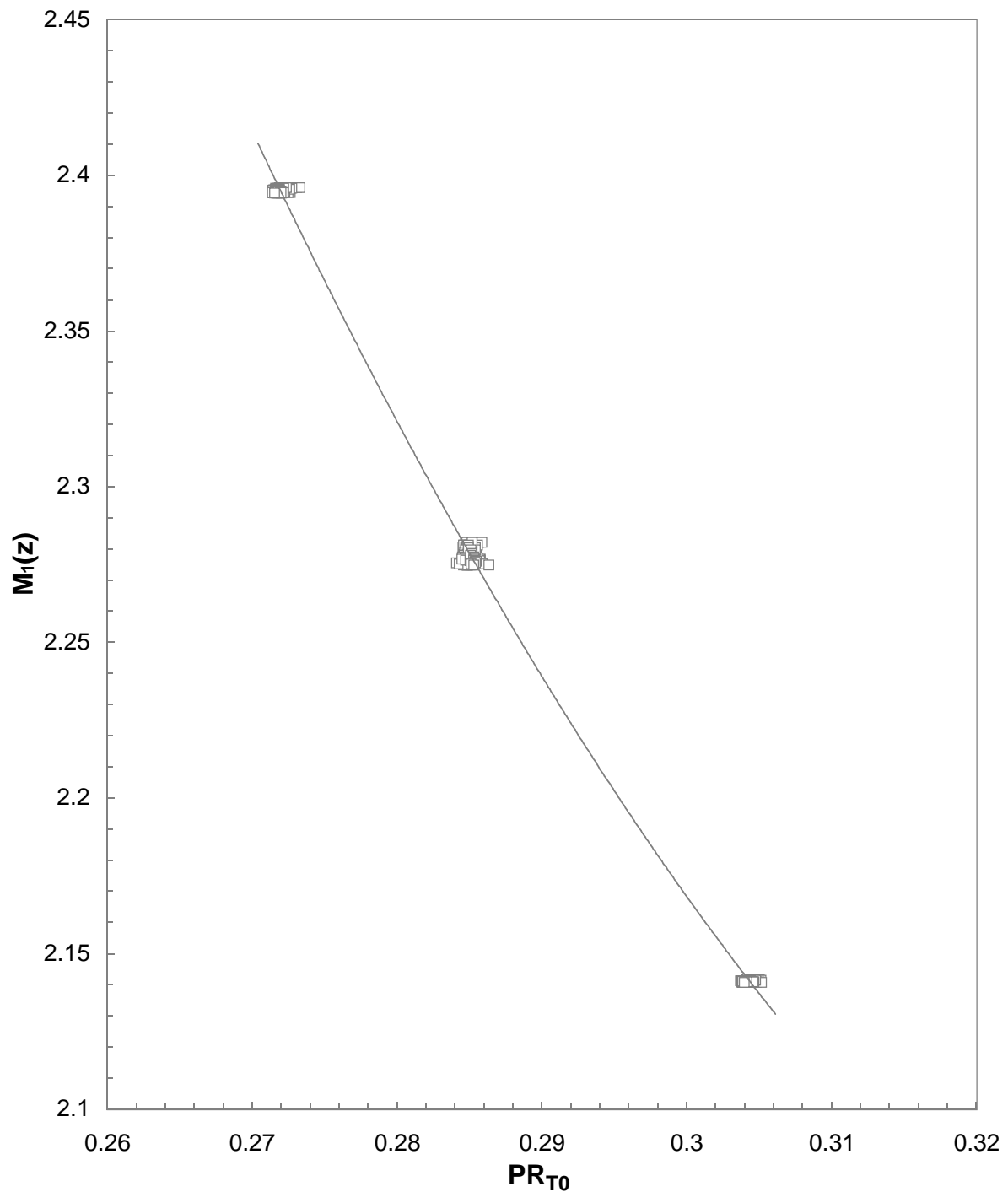
Probe 3

Figure 42. Continued.



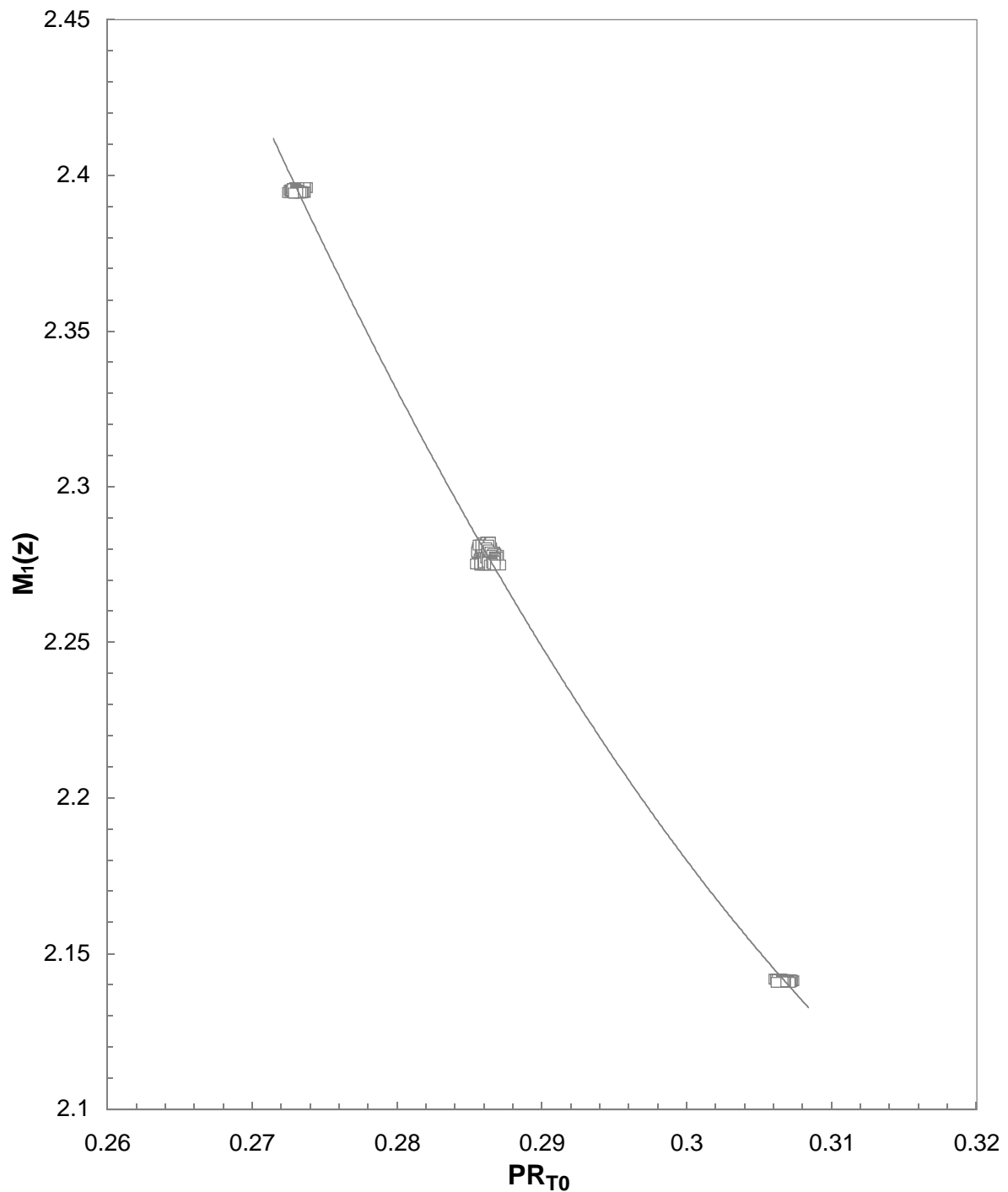
Probe 4
 $-8^\circ \leq \alpha_C, \beta_C \leq 8^\circ$

Figure 42. Continued.



Probe 5
 $-8^\circ \leq \alpha_C, \beta_C \leq 8^\circ$

Figure 42. Continued.



Probe 6
 $-8^\circ \leq \alpha_C, \beta_C \leq 8^\circ$

Figure 42. Concluded.

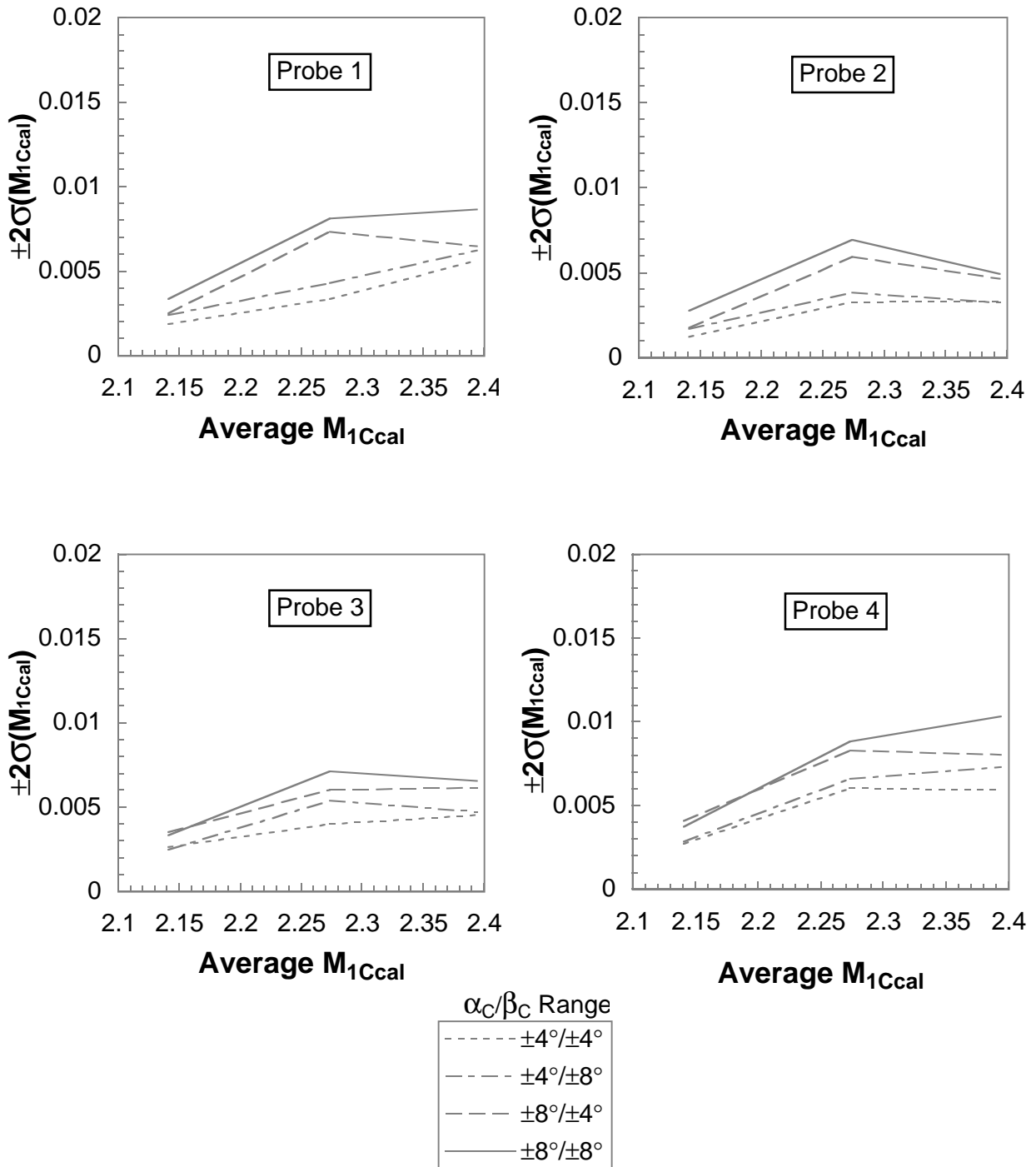


Figure 43. Mach number correlation residual for rake 1.

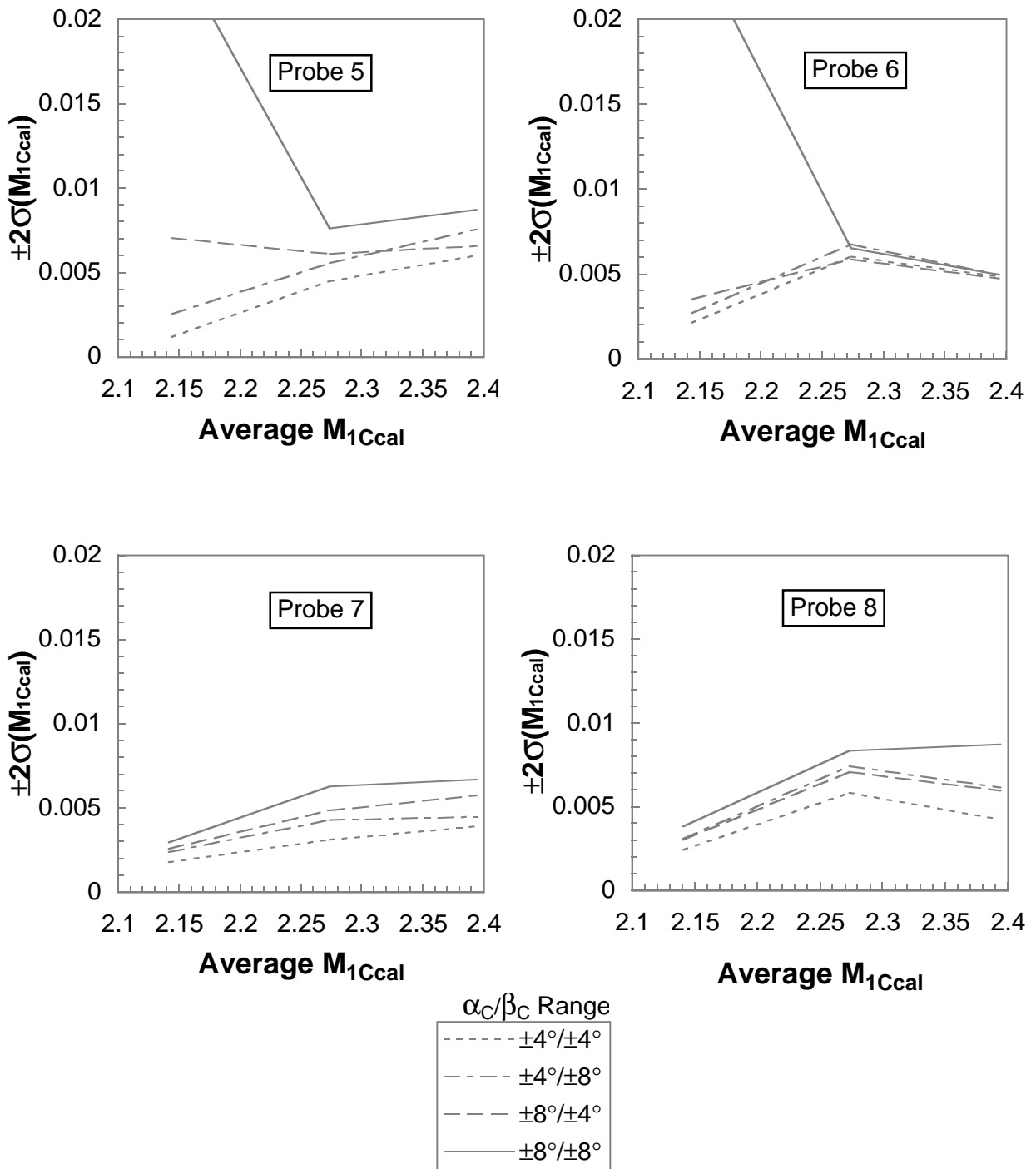


Figure 43. Concluded.

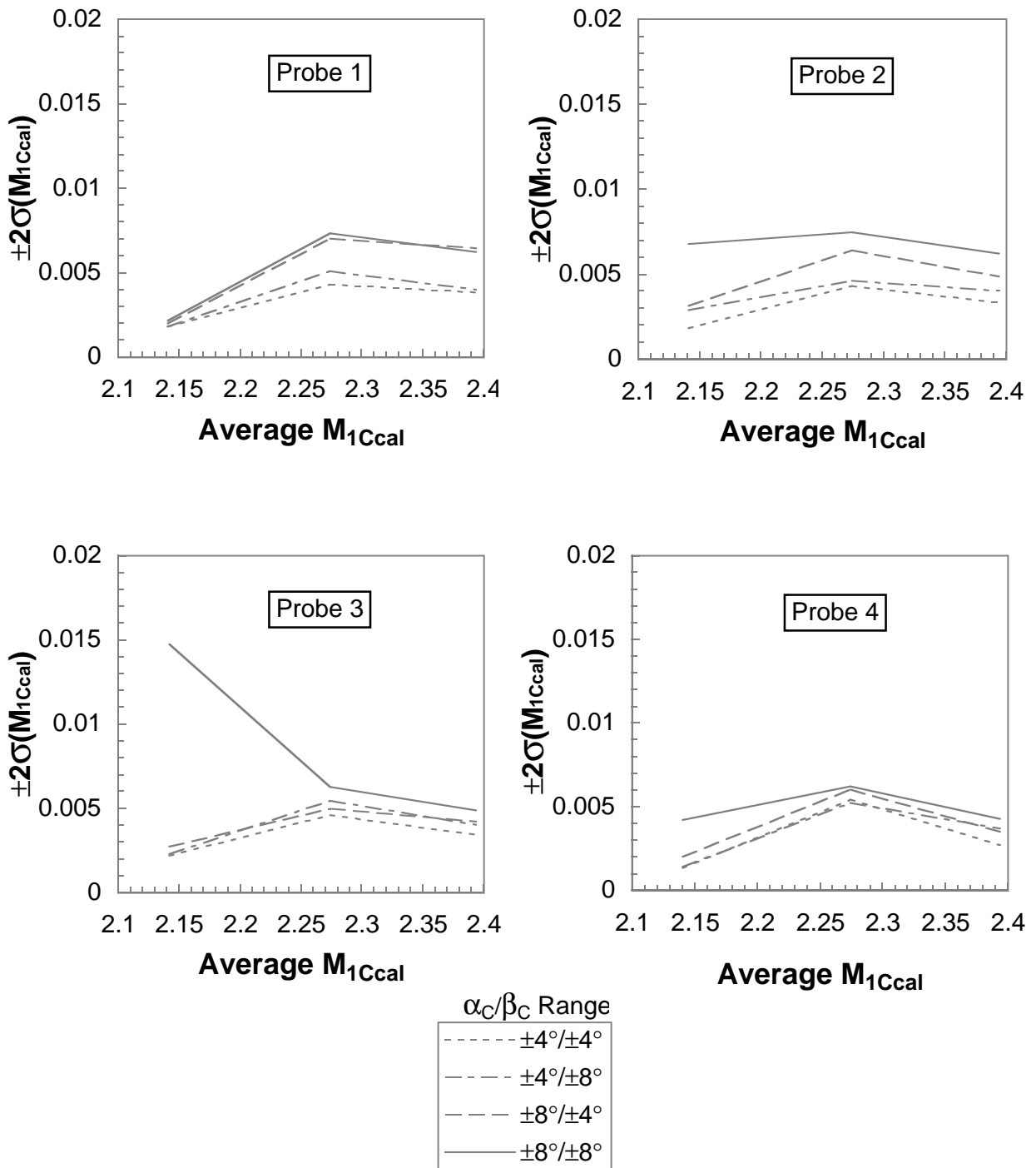


Figure 44. Mach number correlation residual for rake 2.

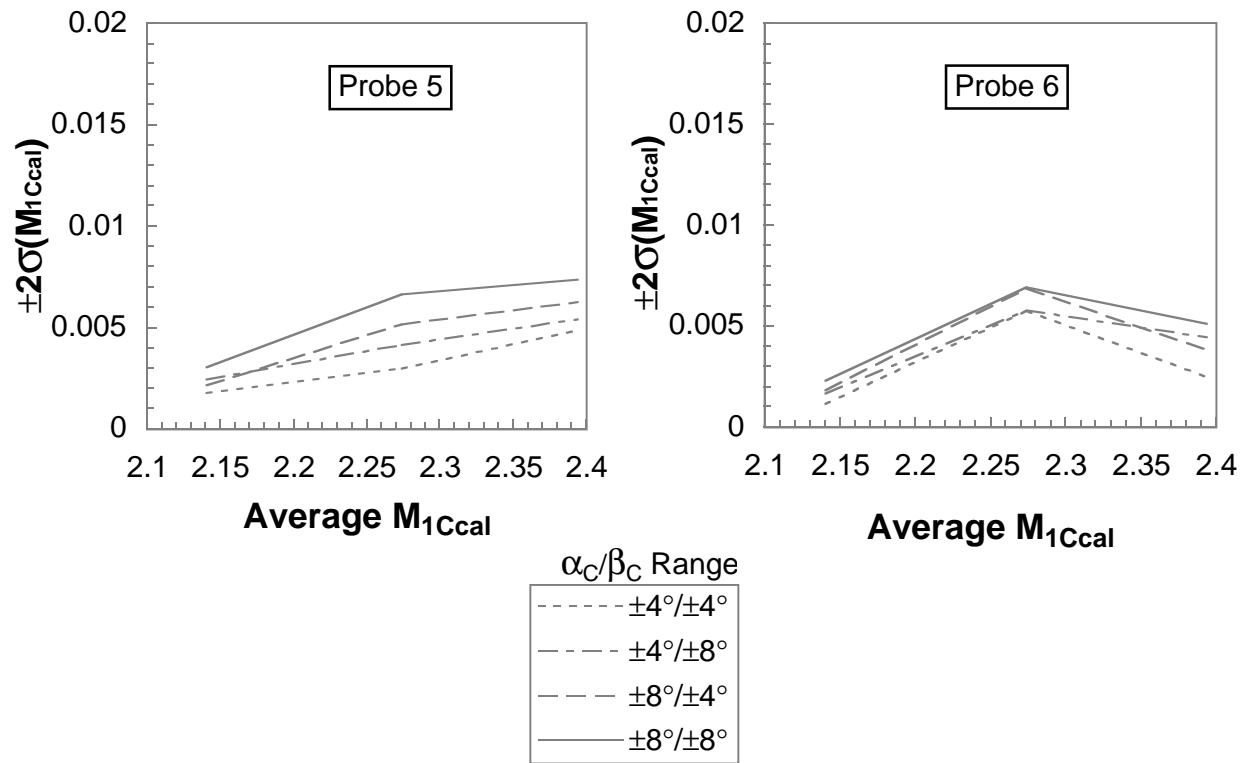


Figure 44. Concluded.

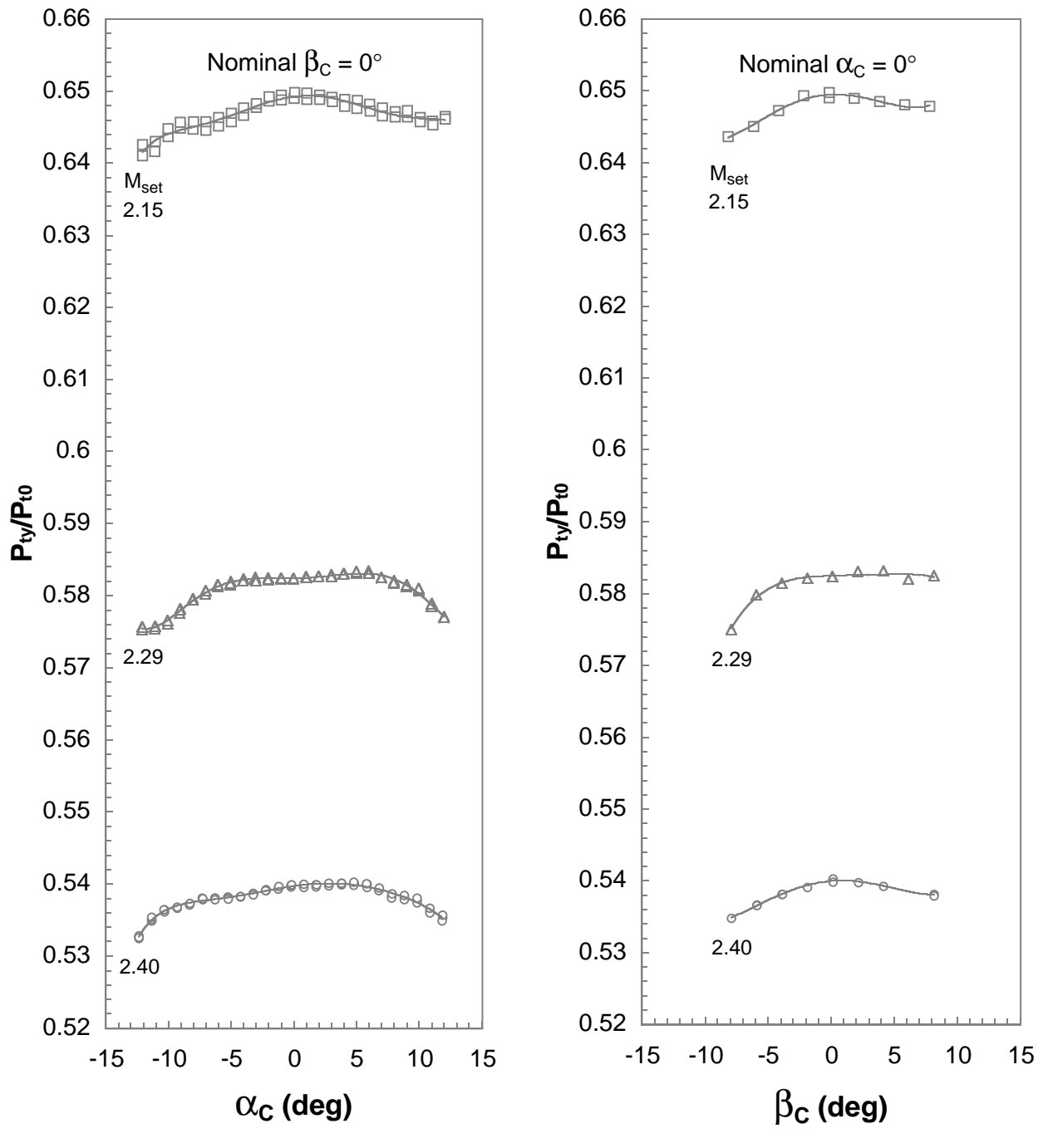


Figure 45. Pitot pressure variation with flow angle for rake 1.

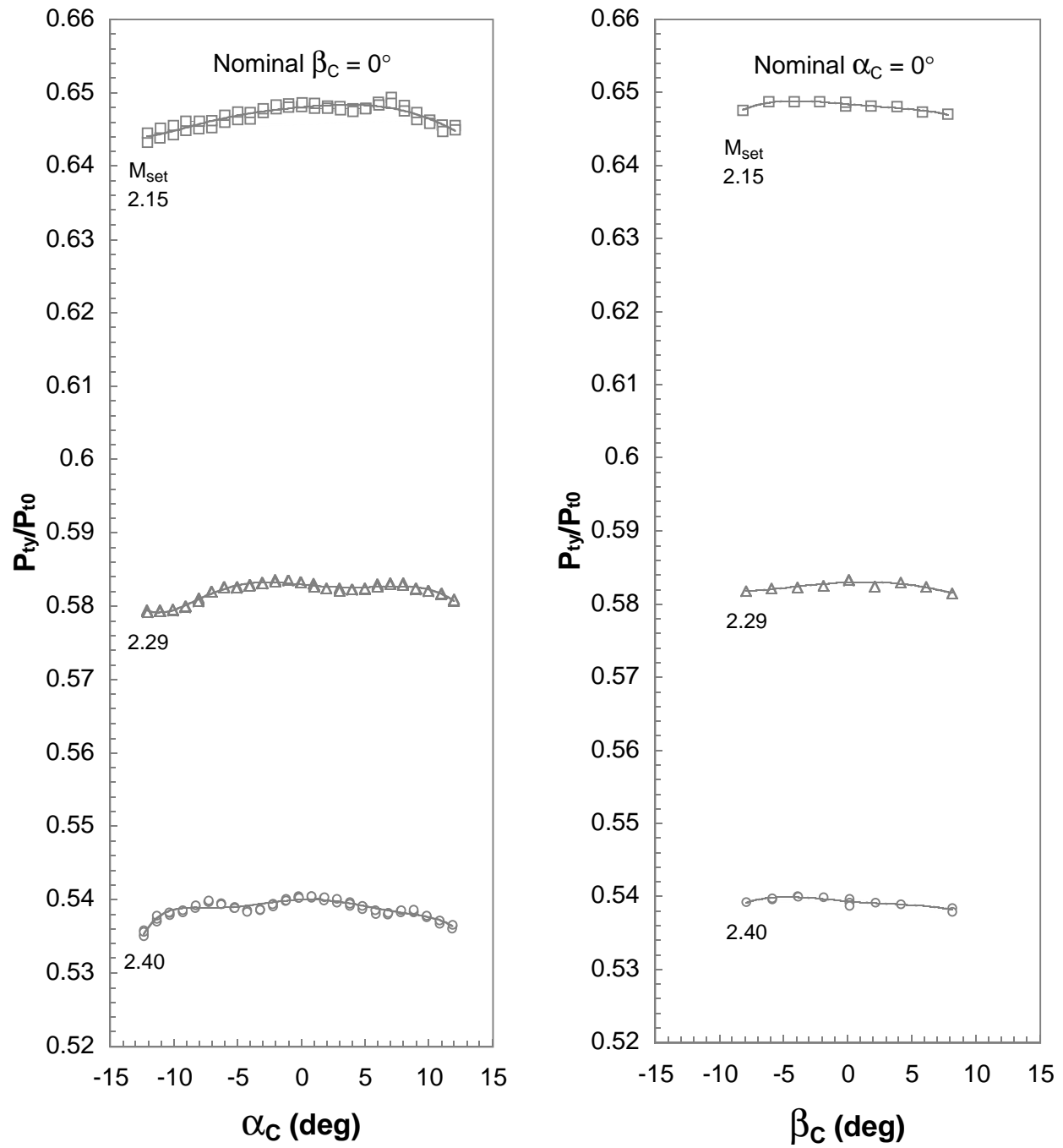
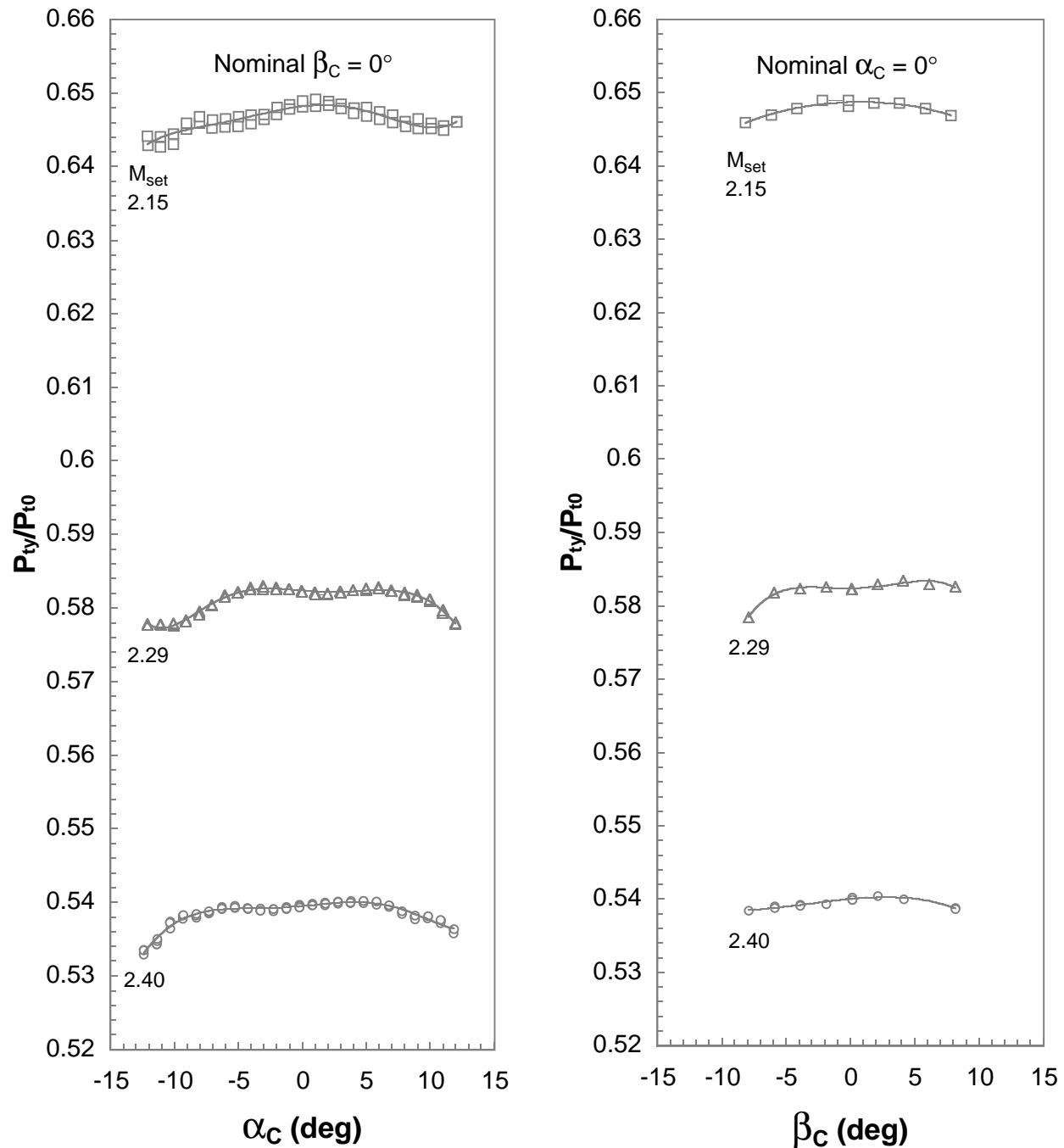
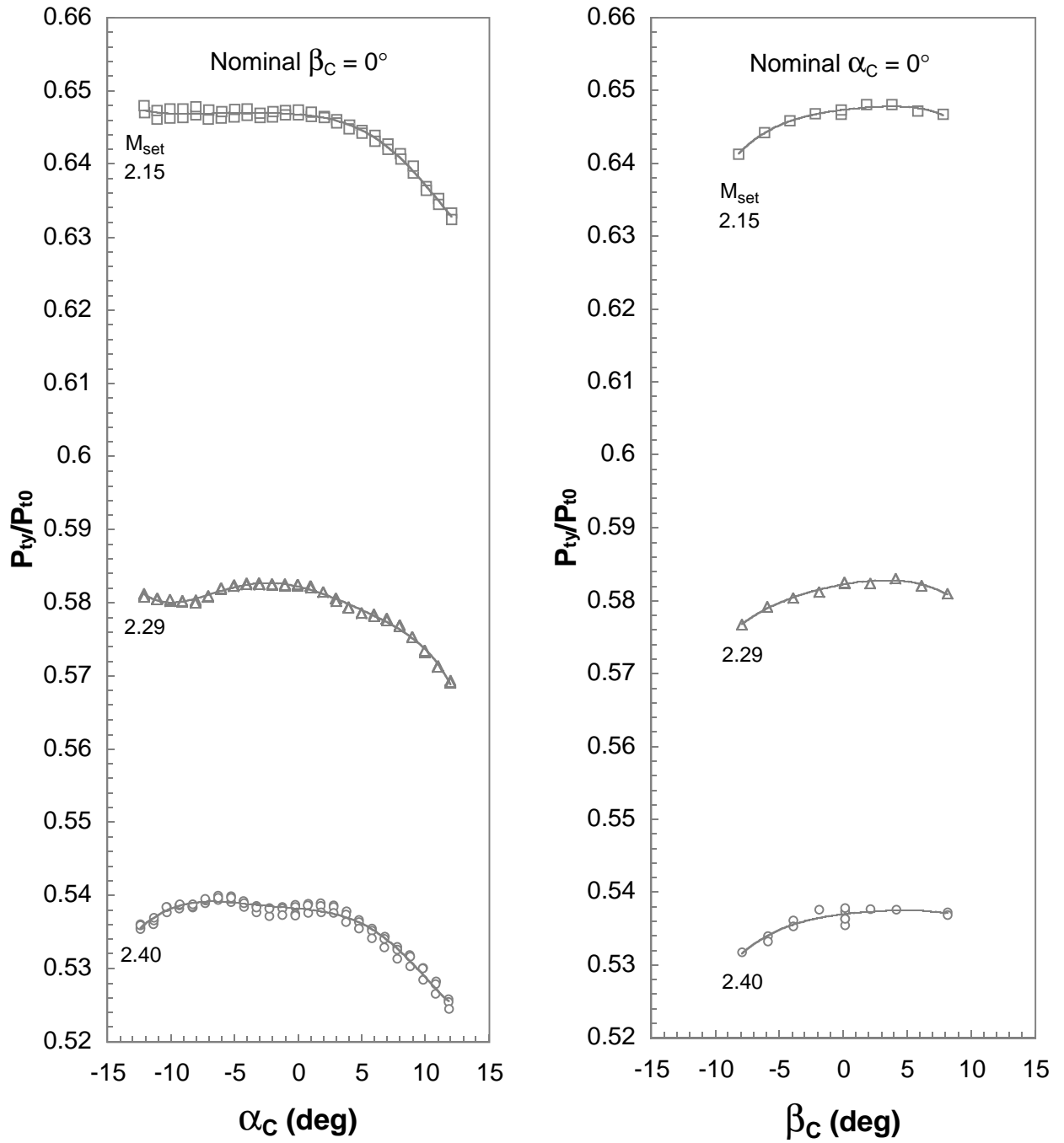


Figure 45. Continued.



Probe 3

Figure 45. Continued.



Probe 4

Figure 45. Continued.

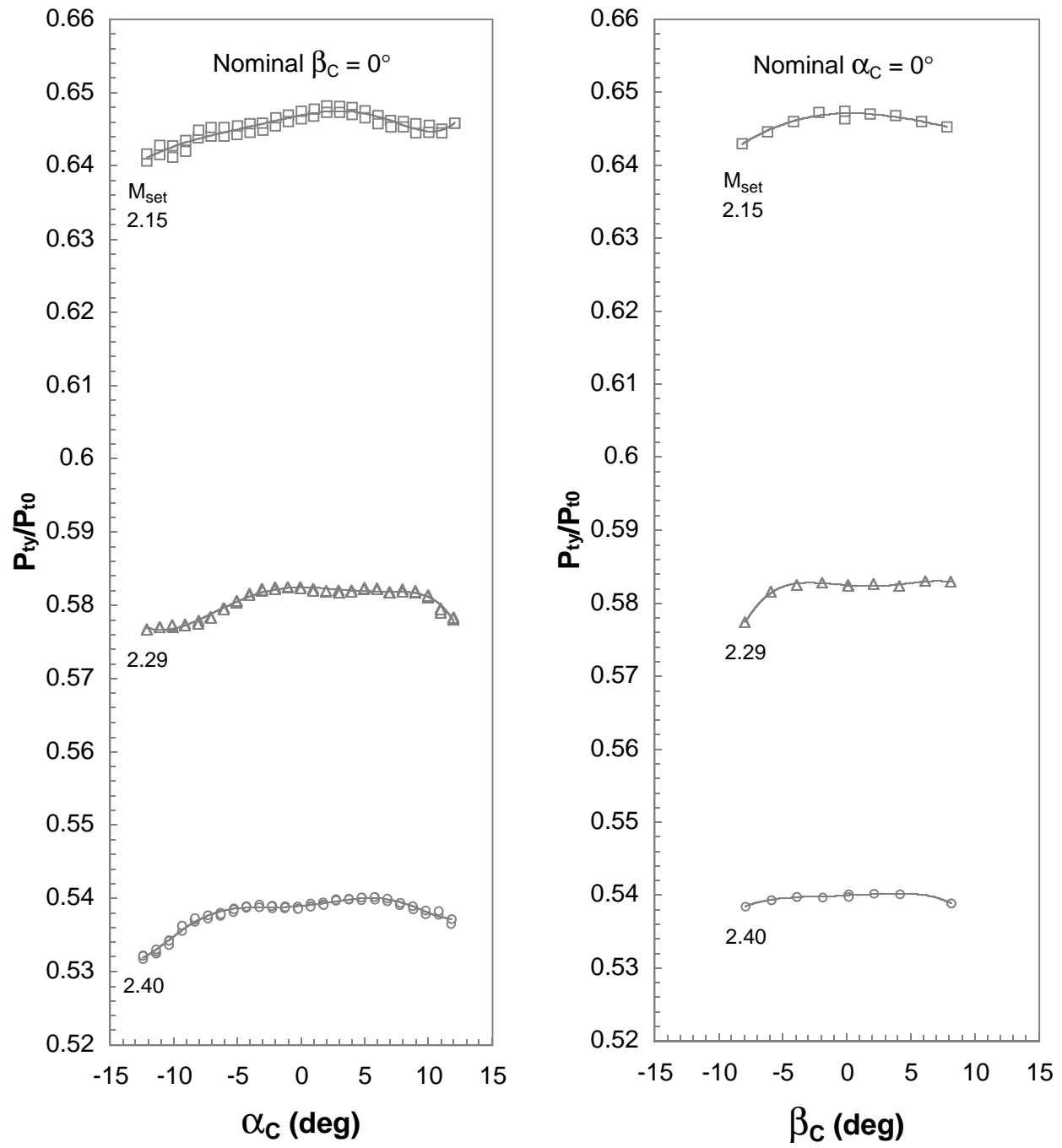


Figure 45. Continued.

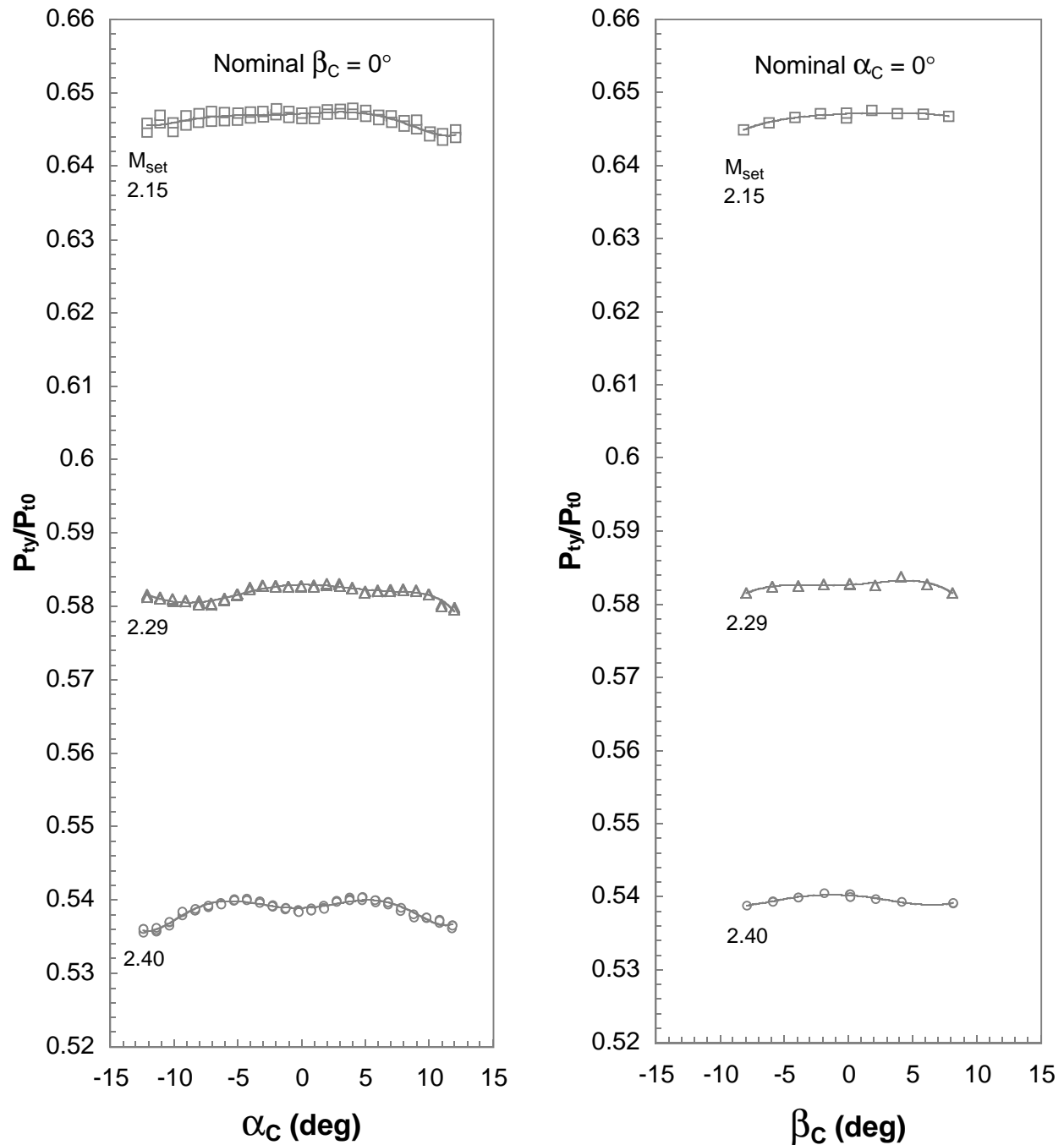


Figure 45. Continued.

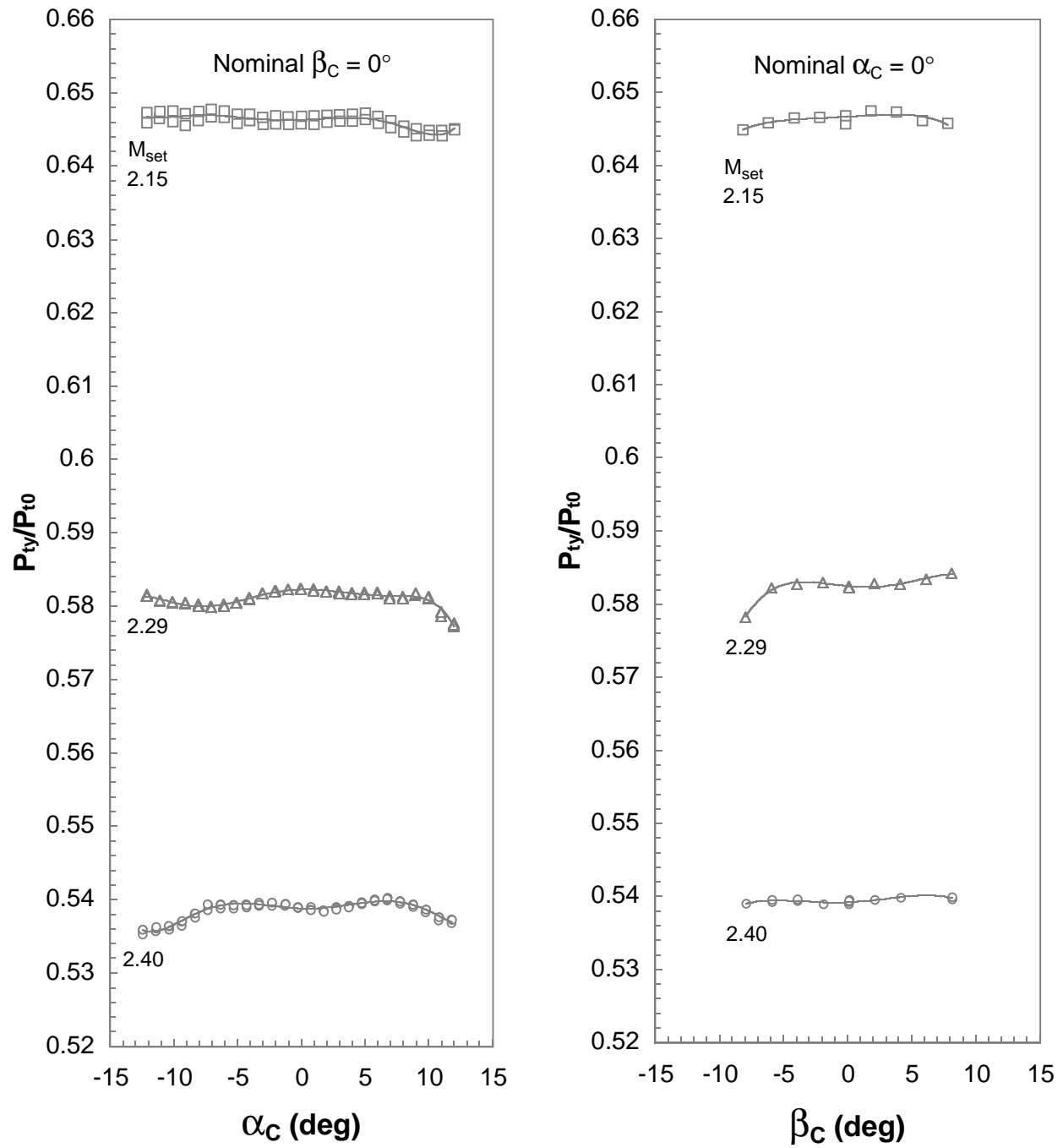
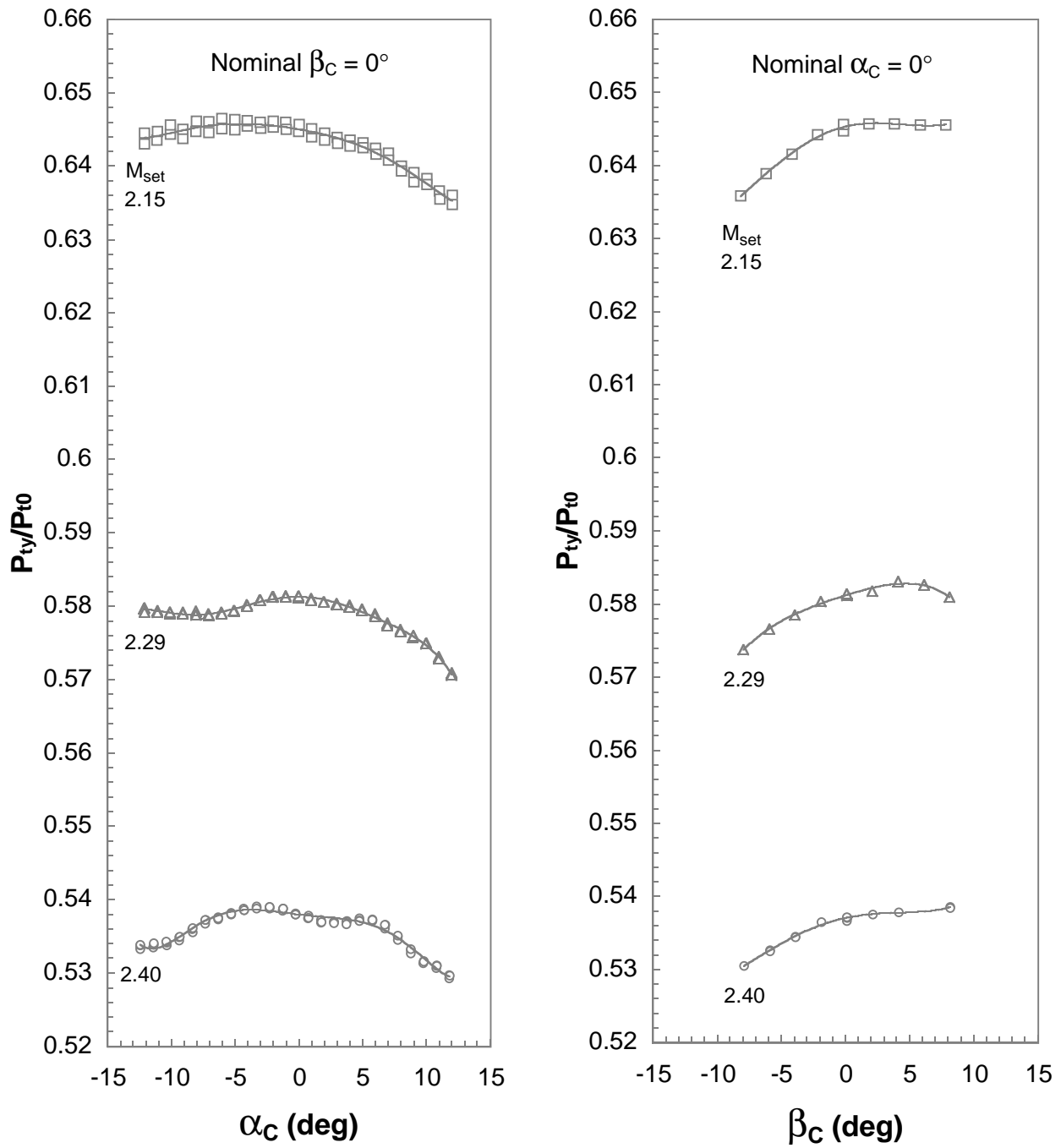


Figure 45. Continued.



Probe 8

Figure 45. Concluded.

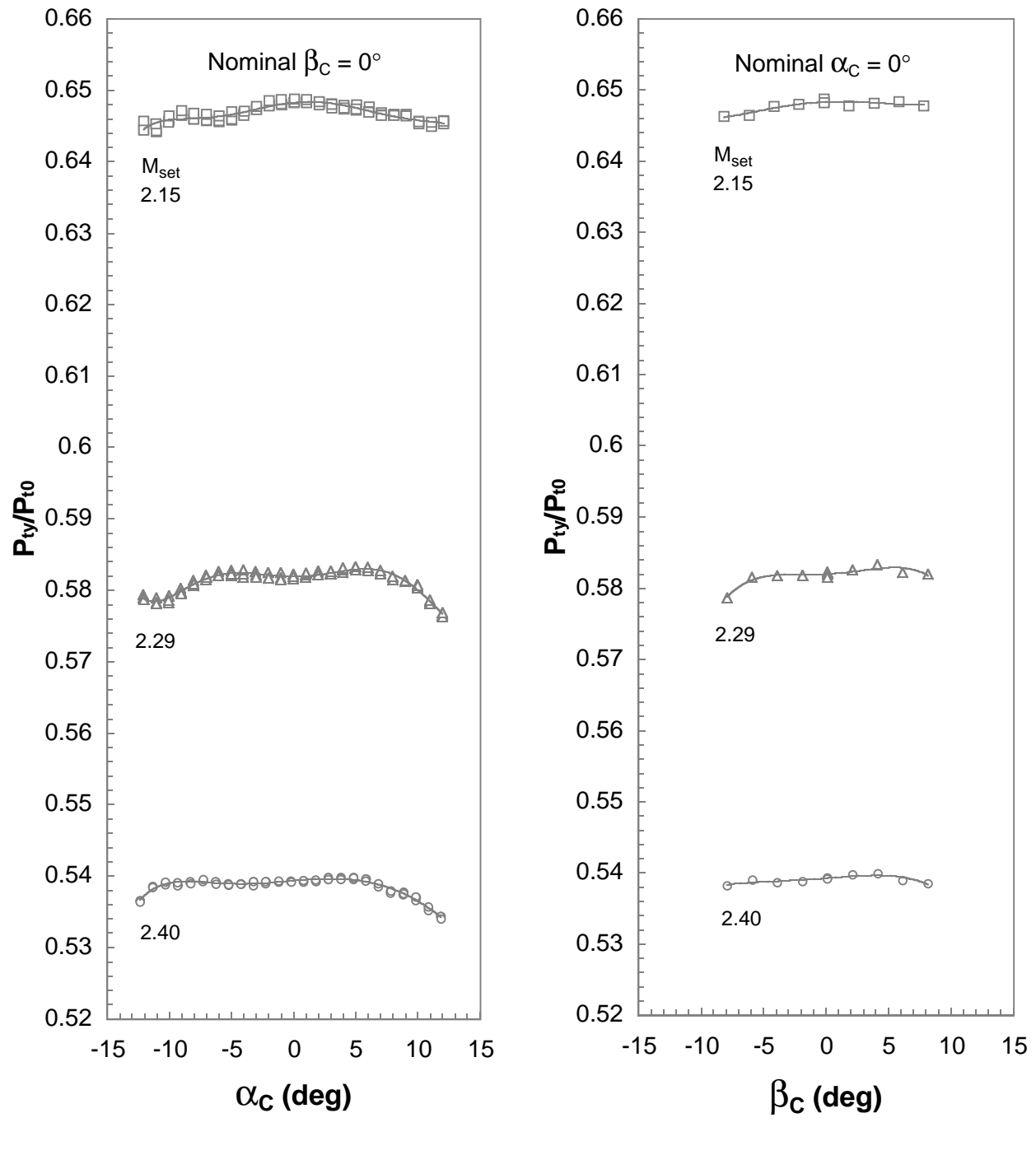
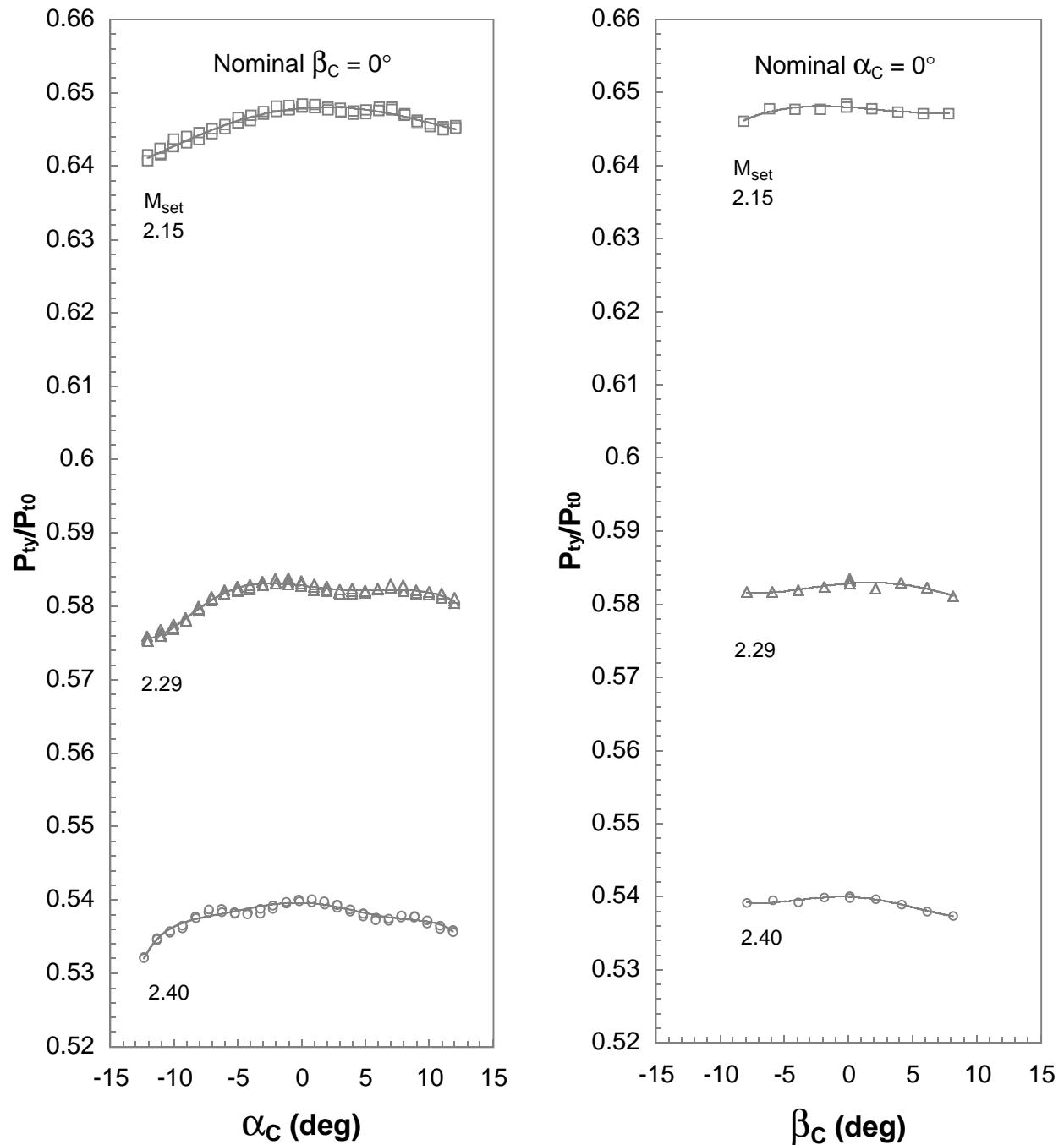
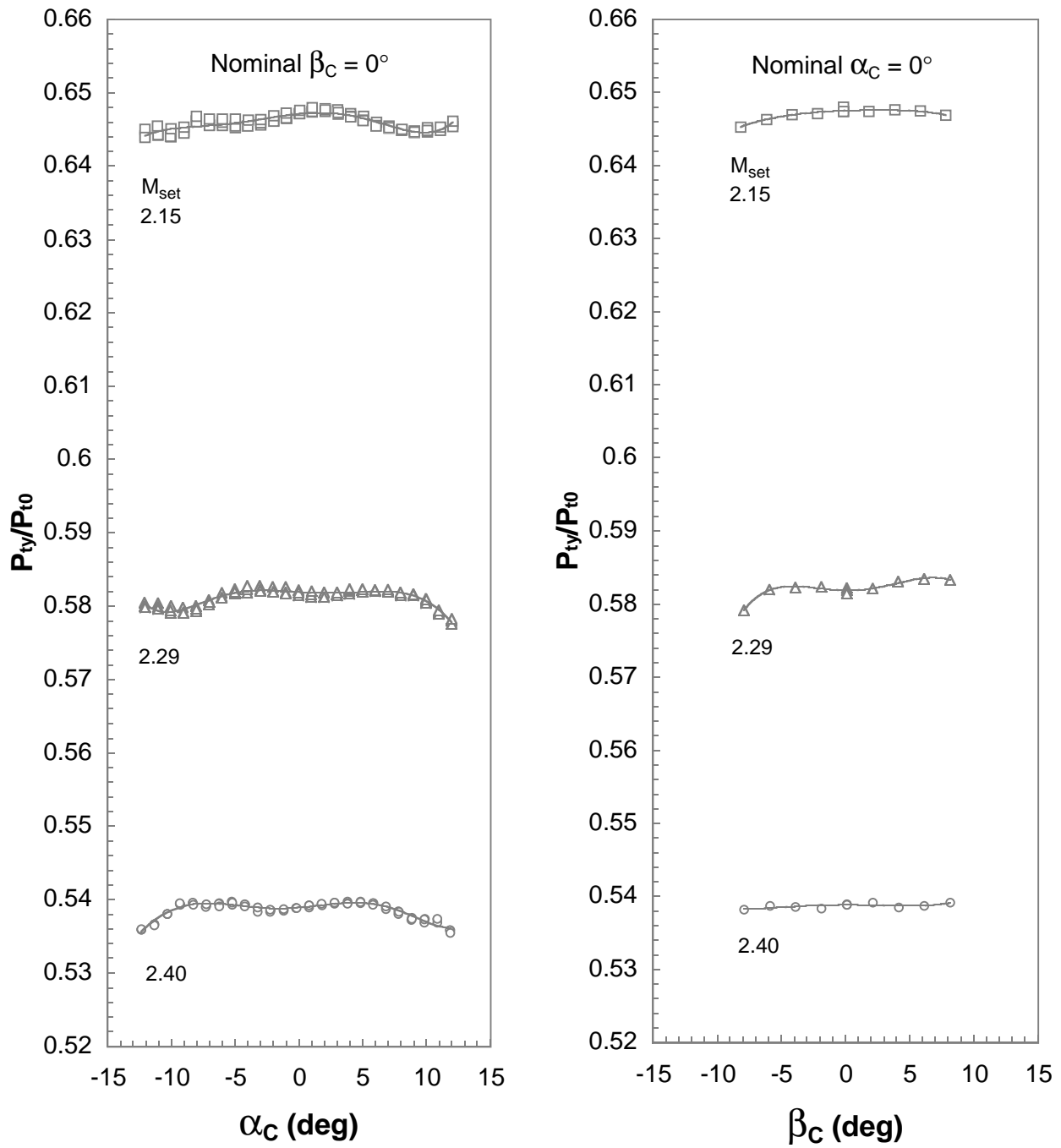


Figure 46. Pitot pressure variation with flow angle for rake 2.



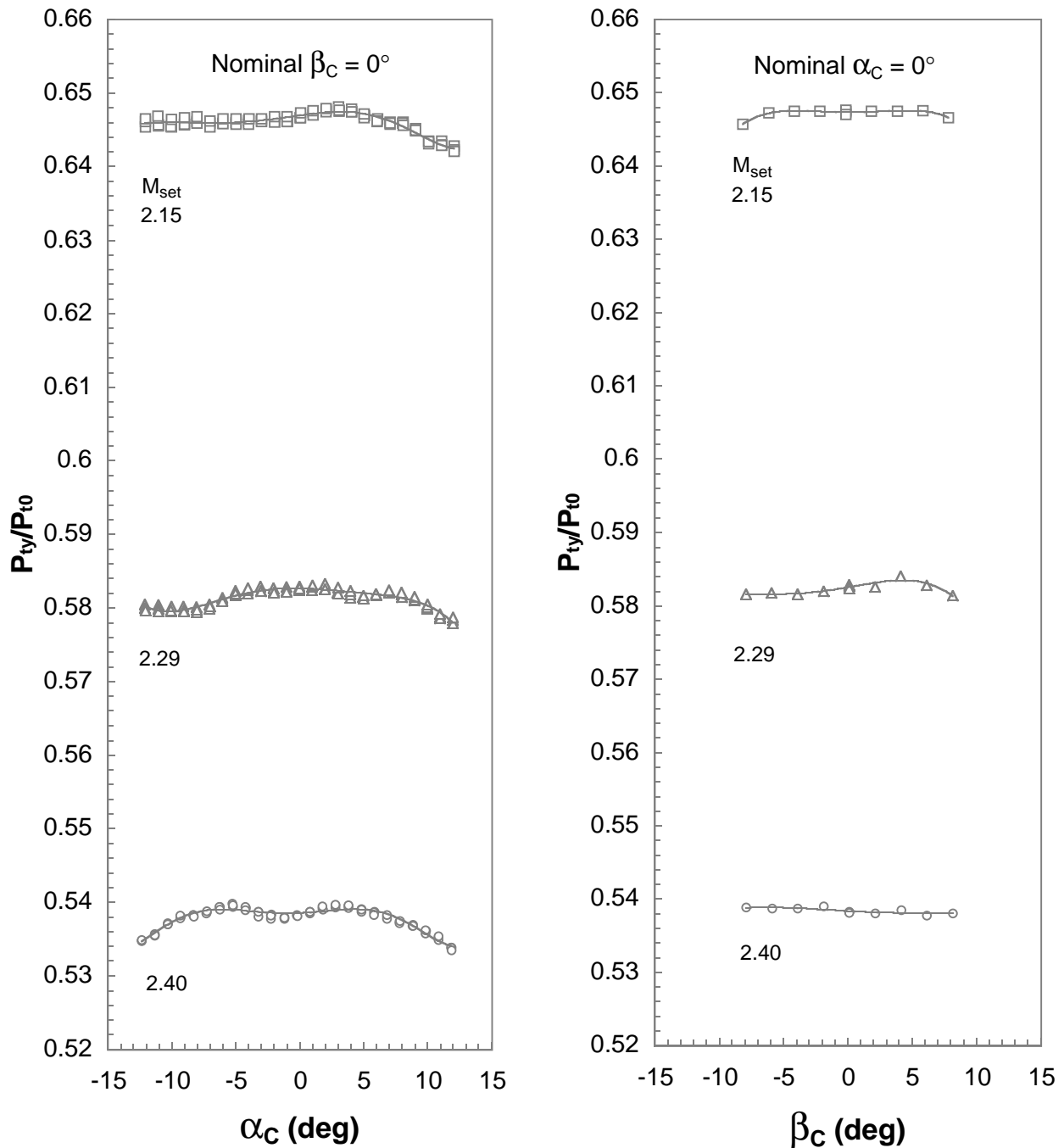
Probe 2

Figure 46. Continued.



Probe 3

Figure 46. Continued.



Probe 4

Figure 46. Continued.

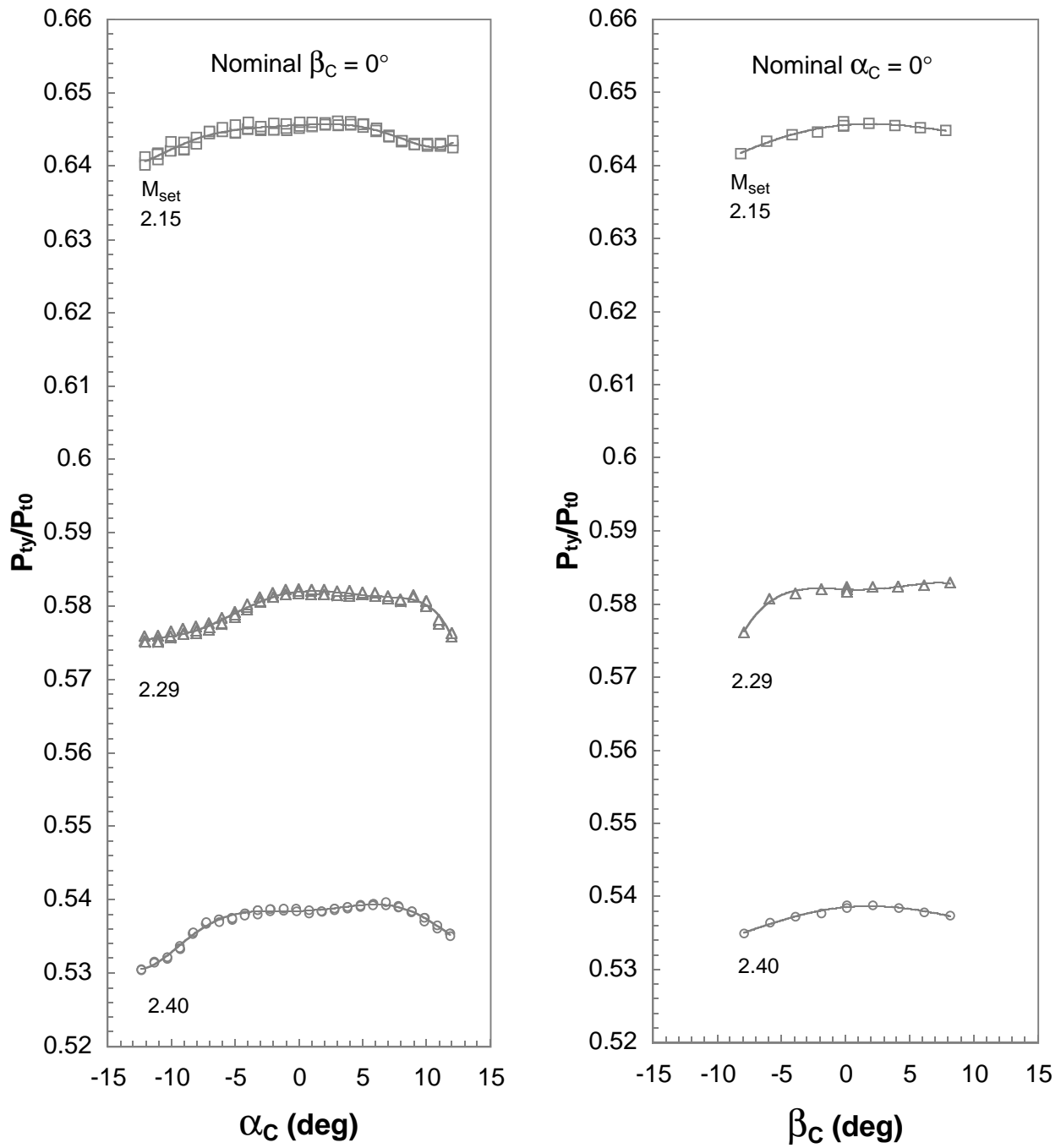


Figure 46. Continued.

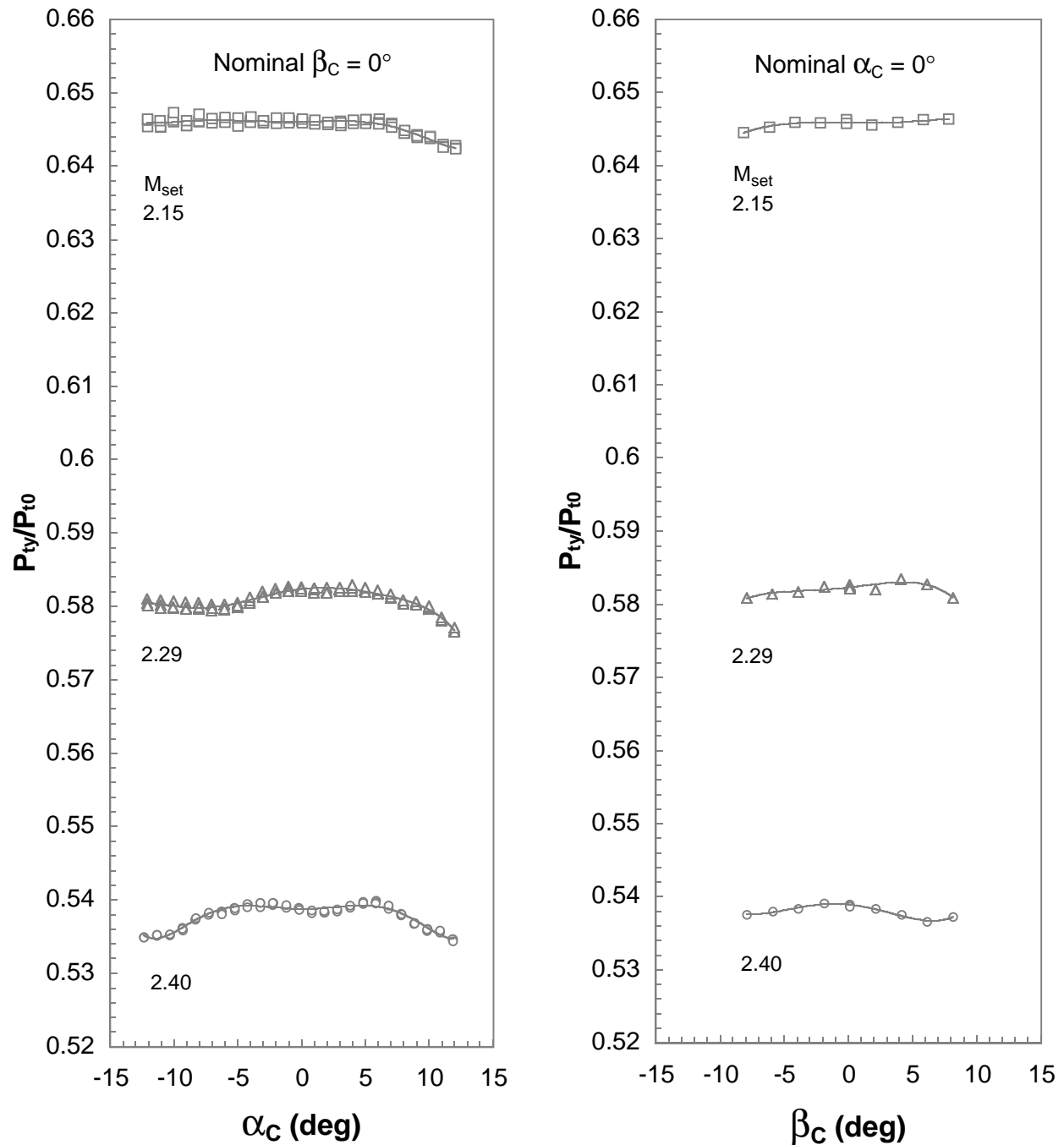
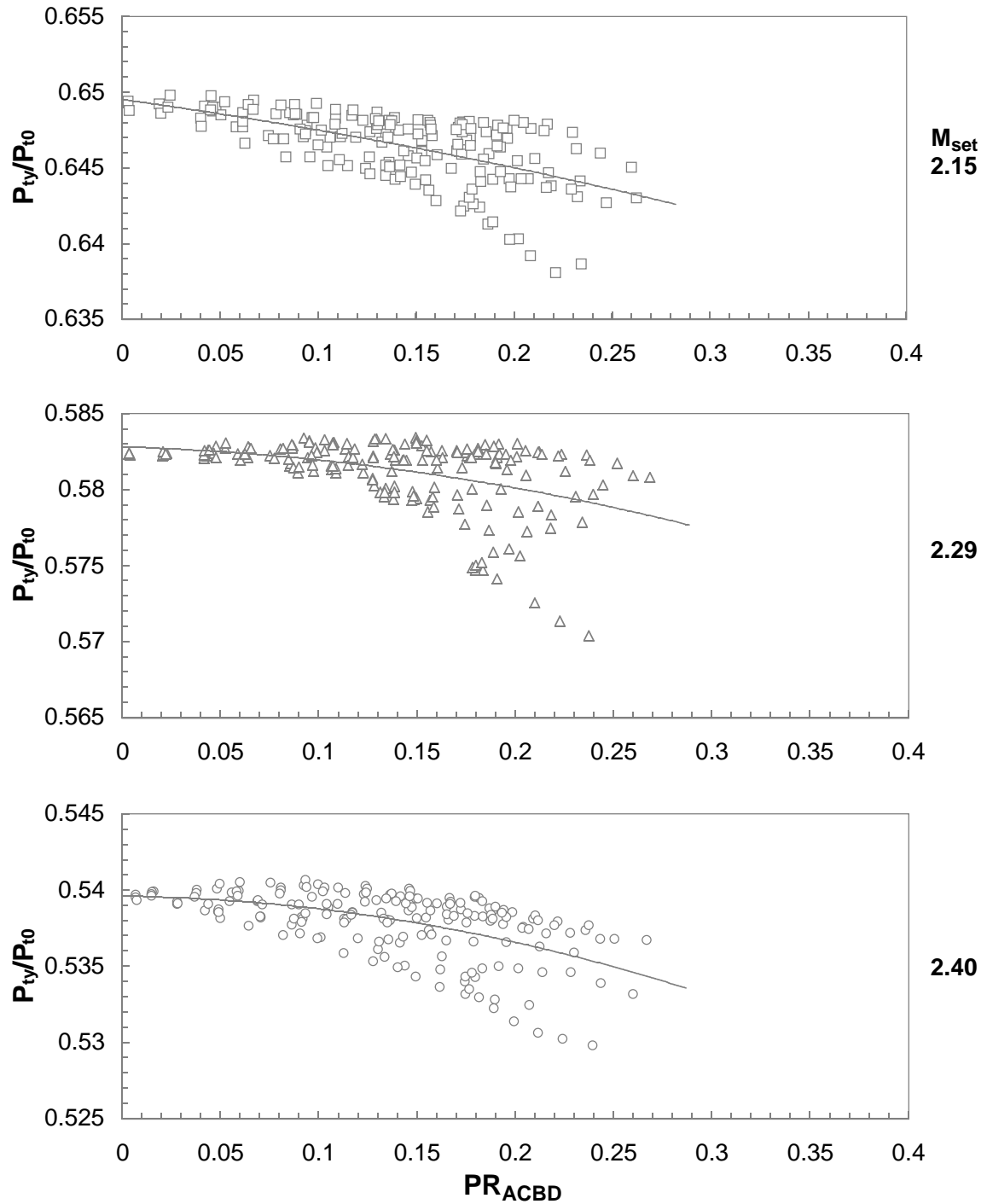


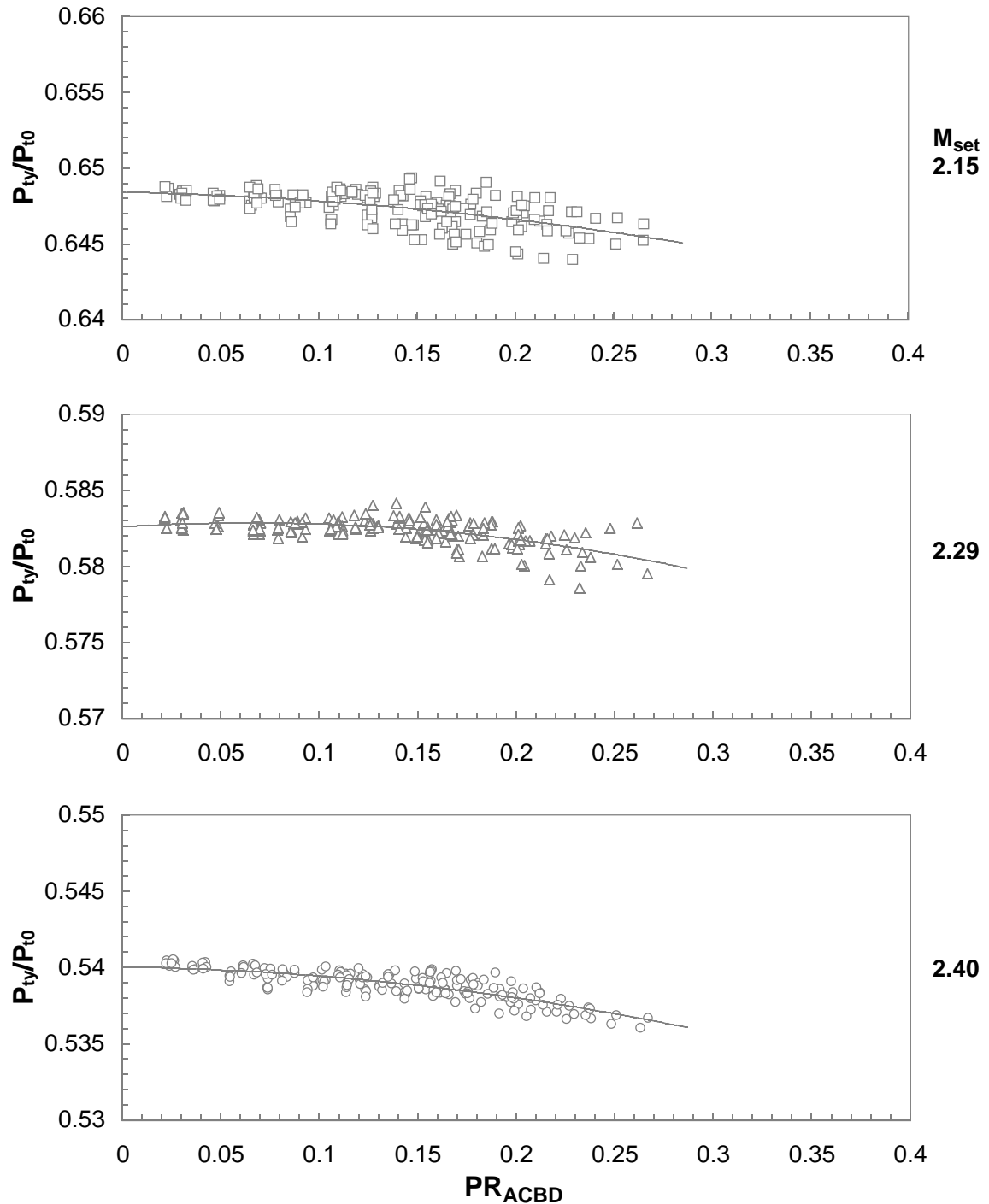
Figure 46. Concluded.



Probe 1

$$-8^\circ \leq \alpha_C, \beta_C \leq 8^\circ$$

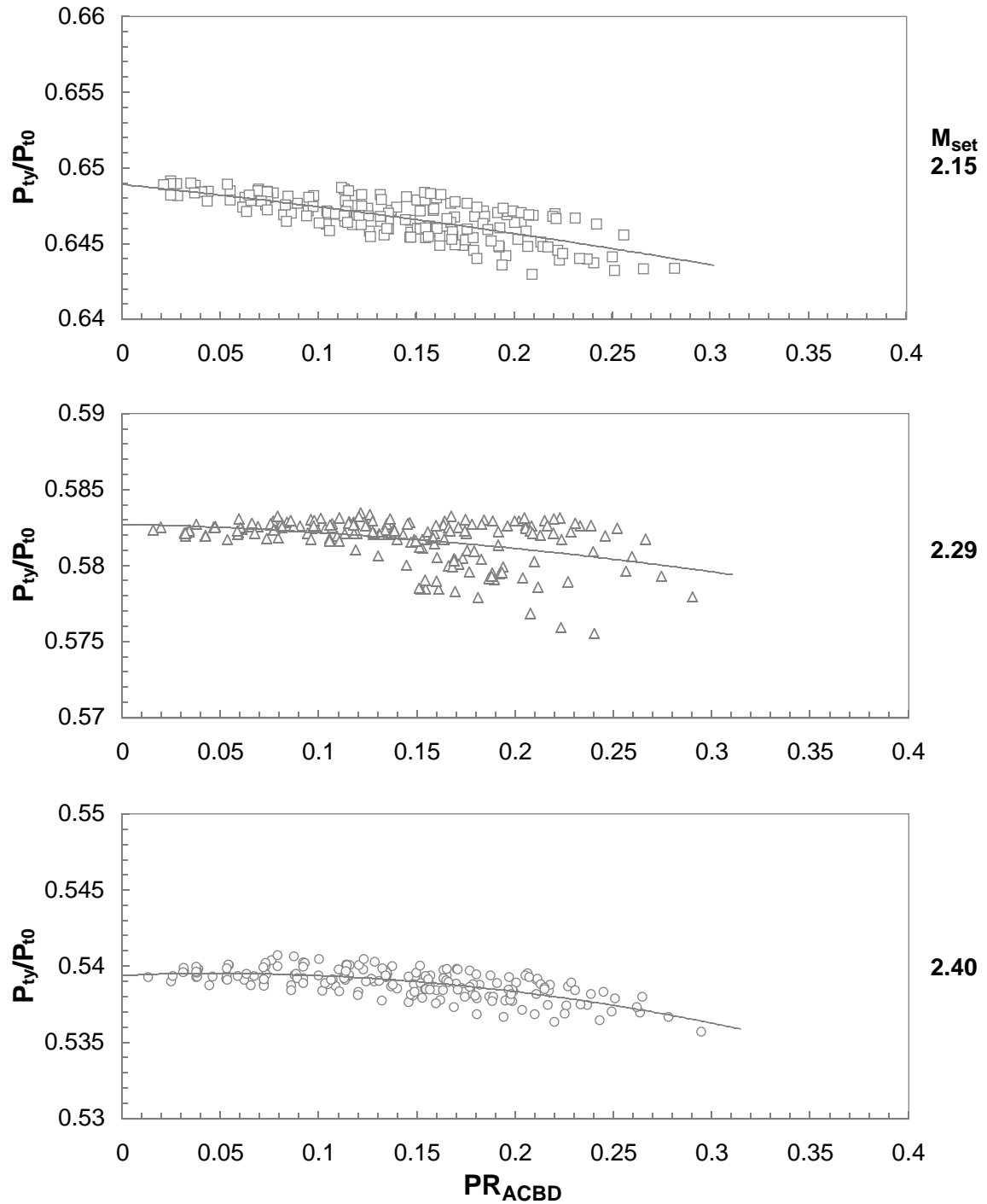
Figure 47. Pitot pressure variation with inclination parameter for rake 1.



Probe 2

$$-8^\circ \leq \alpha_C, \beta_C \leq 8^\circ$$

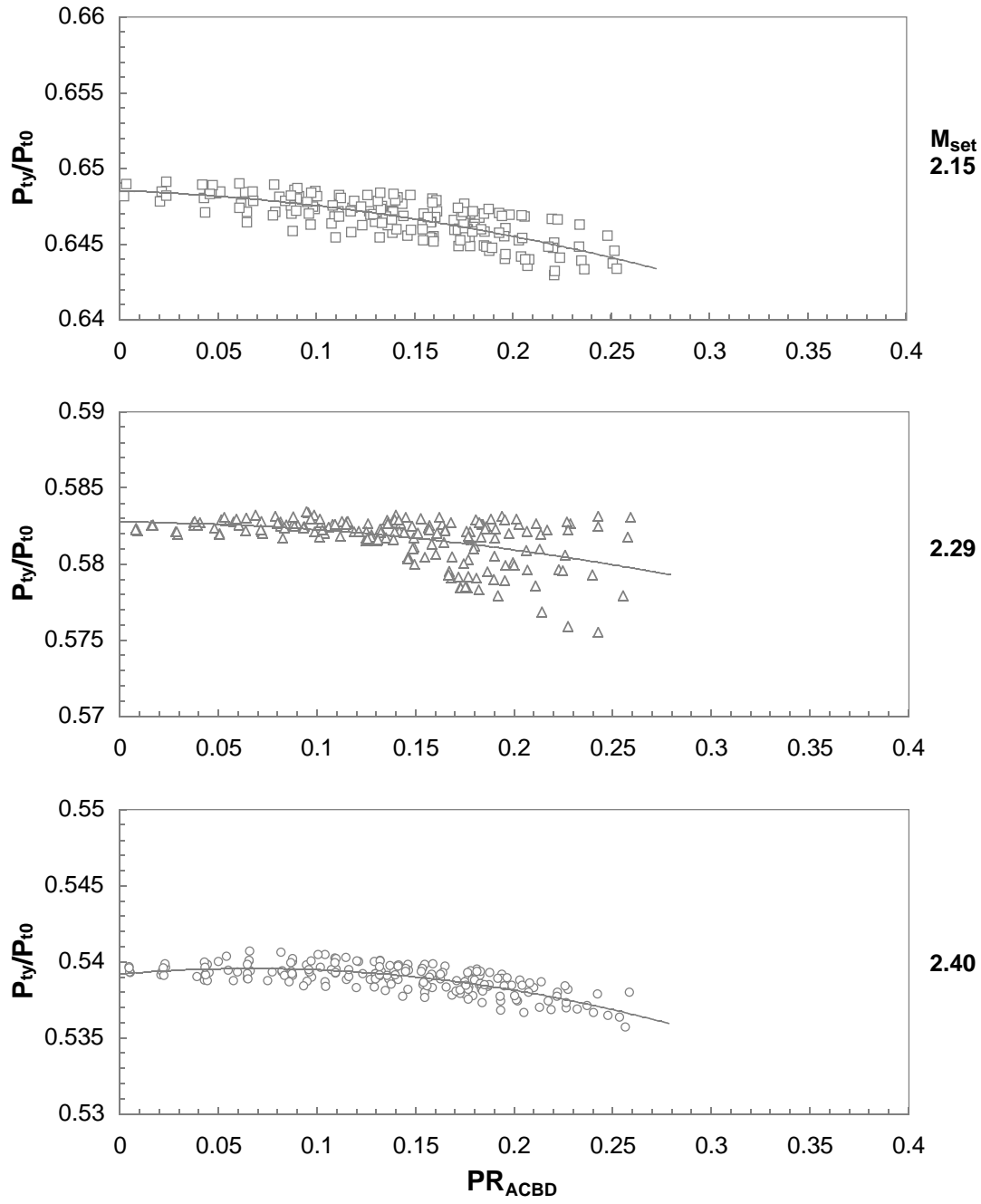
Figure 47. Continued.



Probe 3

$$-8^\circ \leq \alpha_C, \beta_C \leq 8^\circ$$

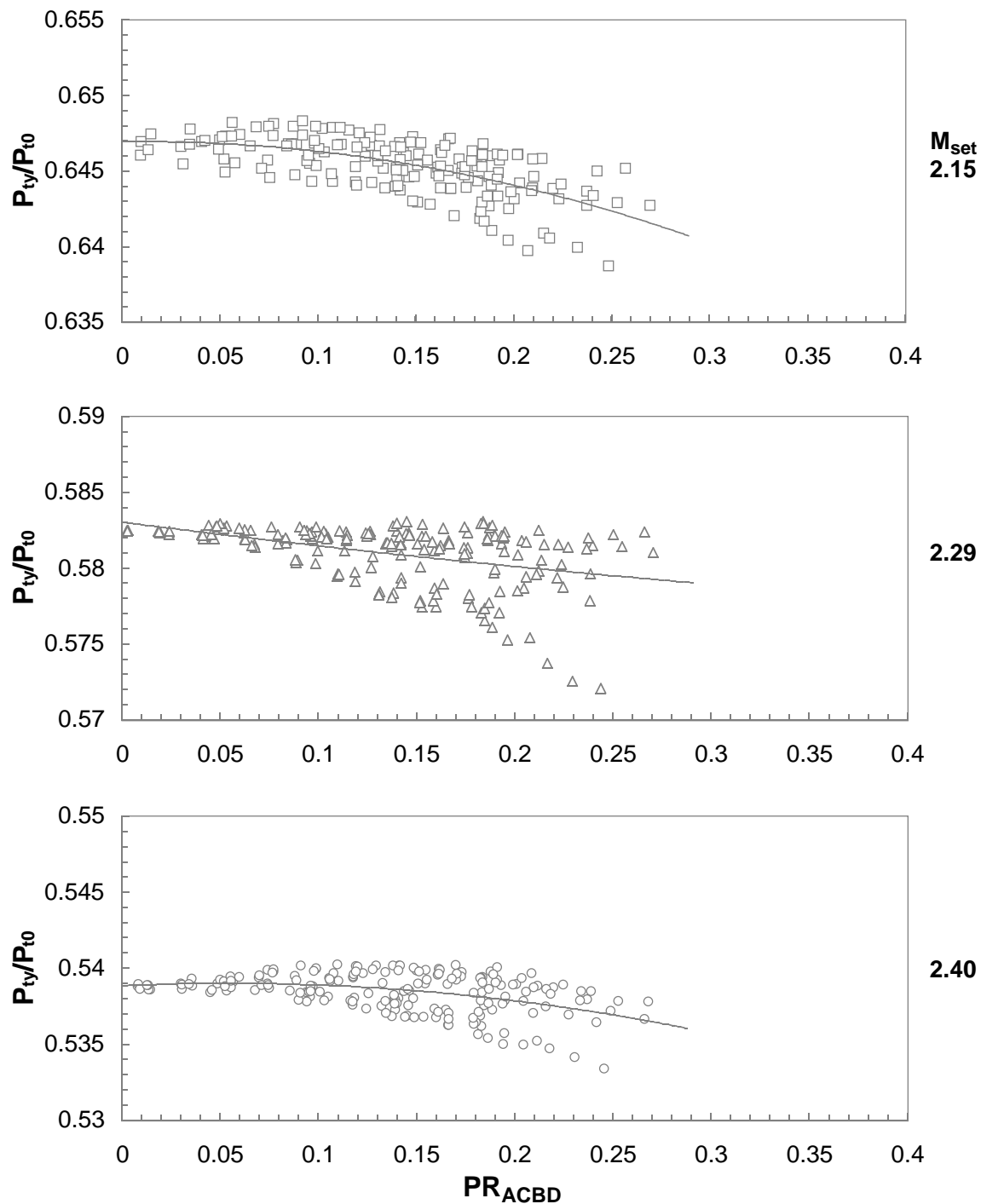
Figure 47. Continued.



Probe 4

$$-8^\circ \leq \alpha_C, \beta_C \leq 8^\circ$$

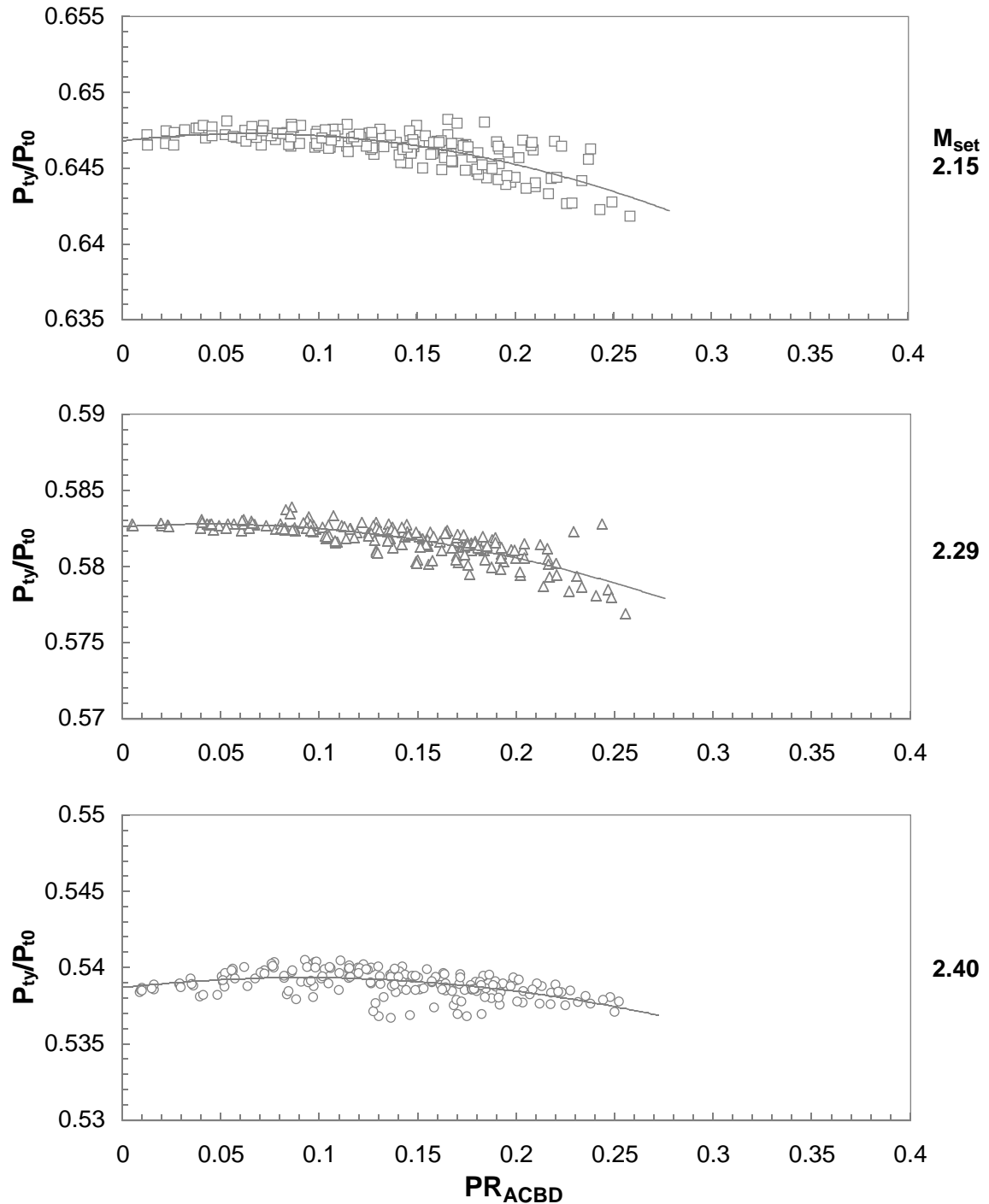
Figure 47. Continued.



Probe 5

$$-8^\circ \leq \alpha_C, \beta_C \leq 8^\circ$$

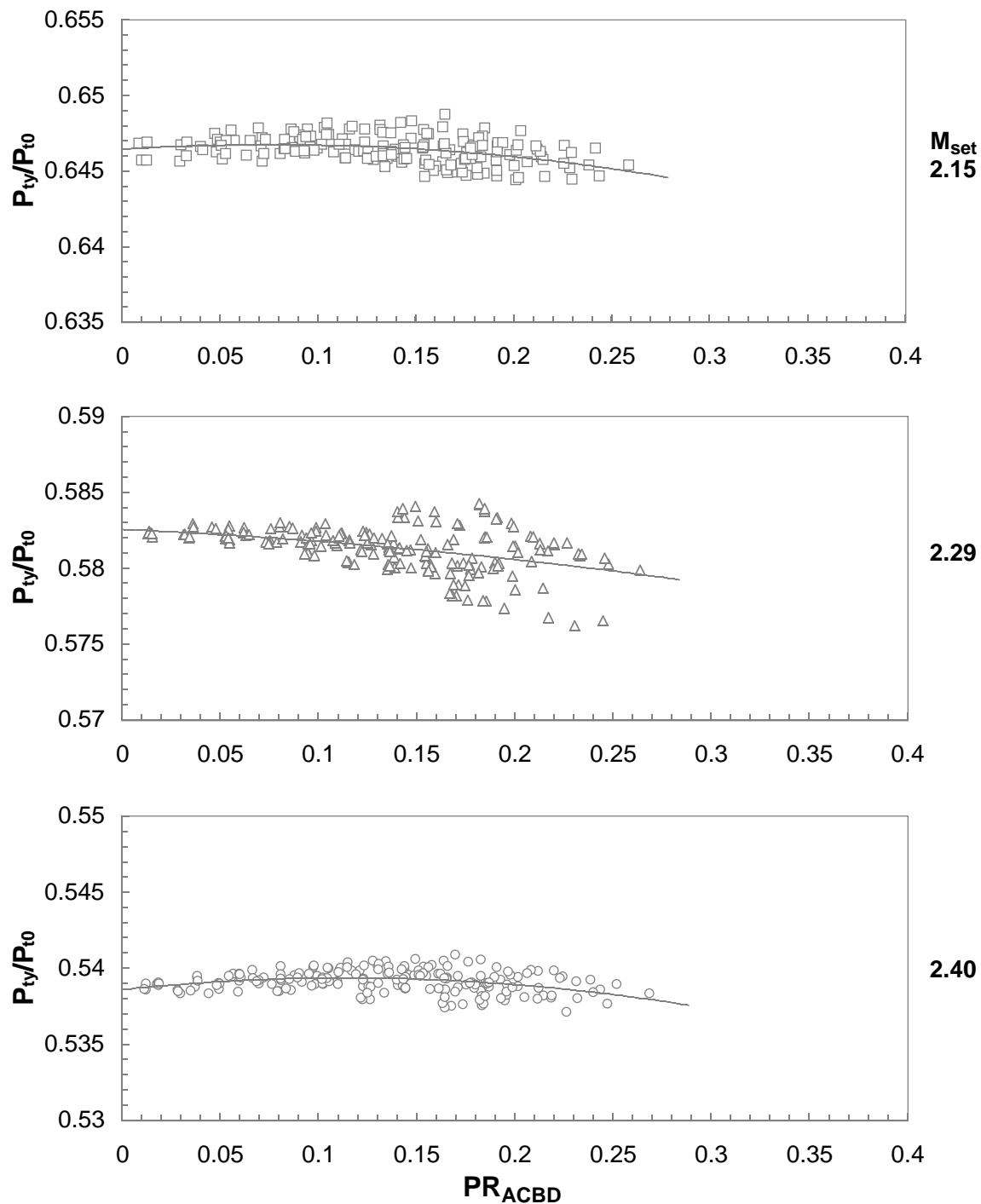
Figure 47. Continued.



Probe 6

$$-8^\circ \leq \alpha_C, \beta_C \leq 8^\circ$$

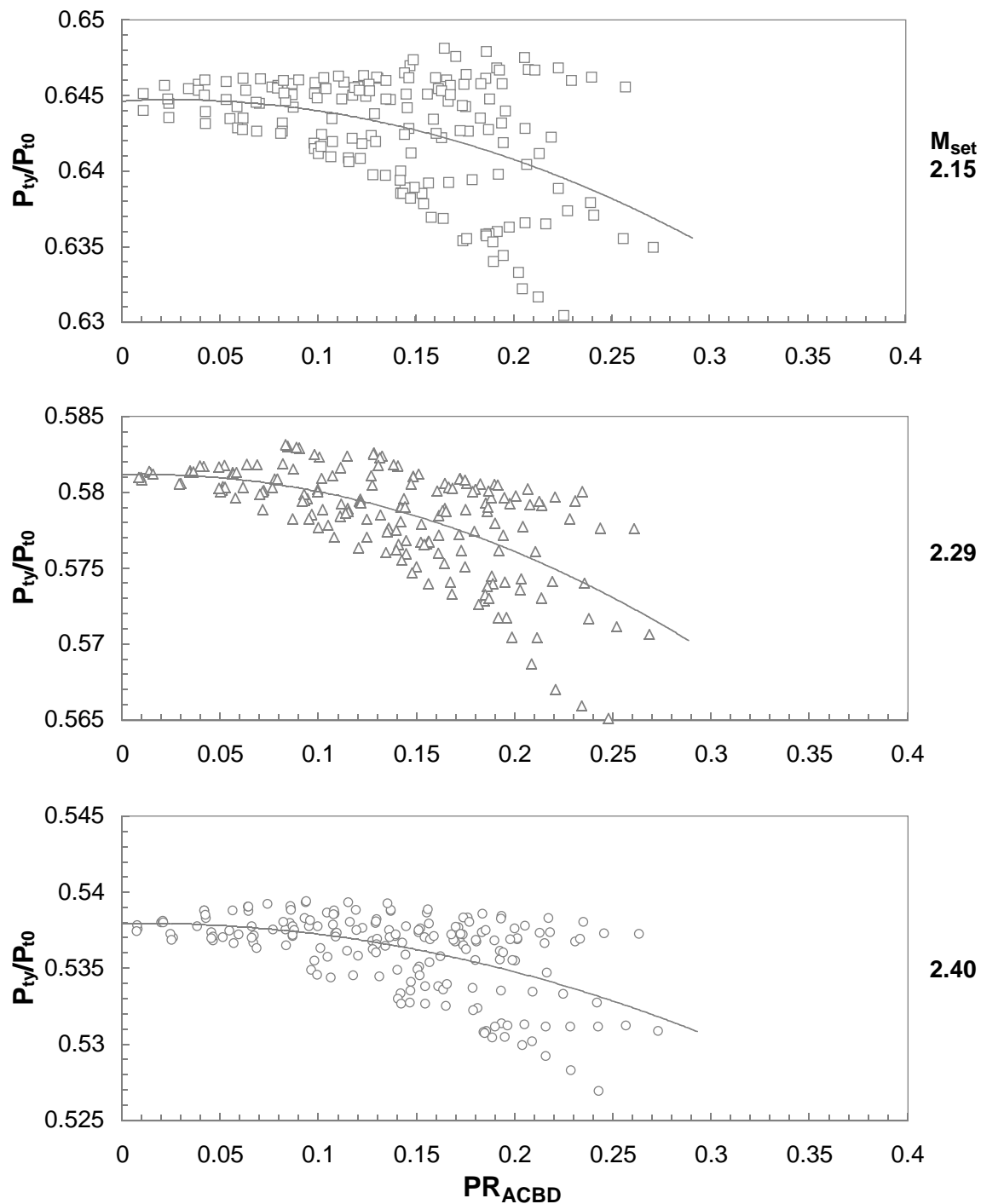
Figure 47. Continued.



Probe 7

$$-8^\circ \leq \alpha_C, \beta_C \leq 8^\circ$$

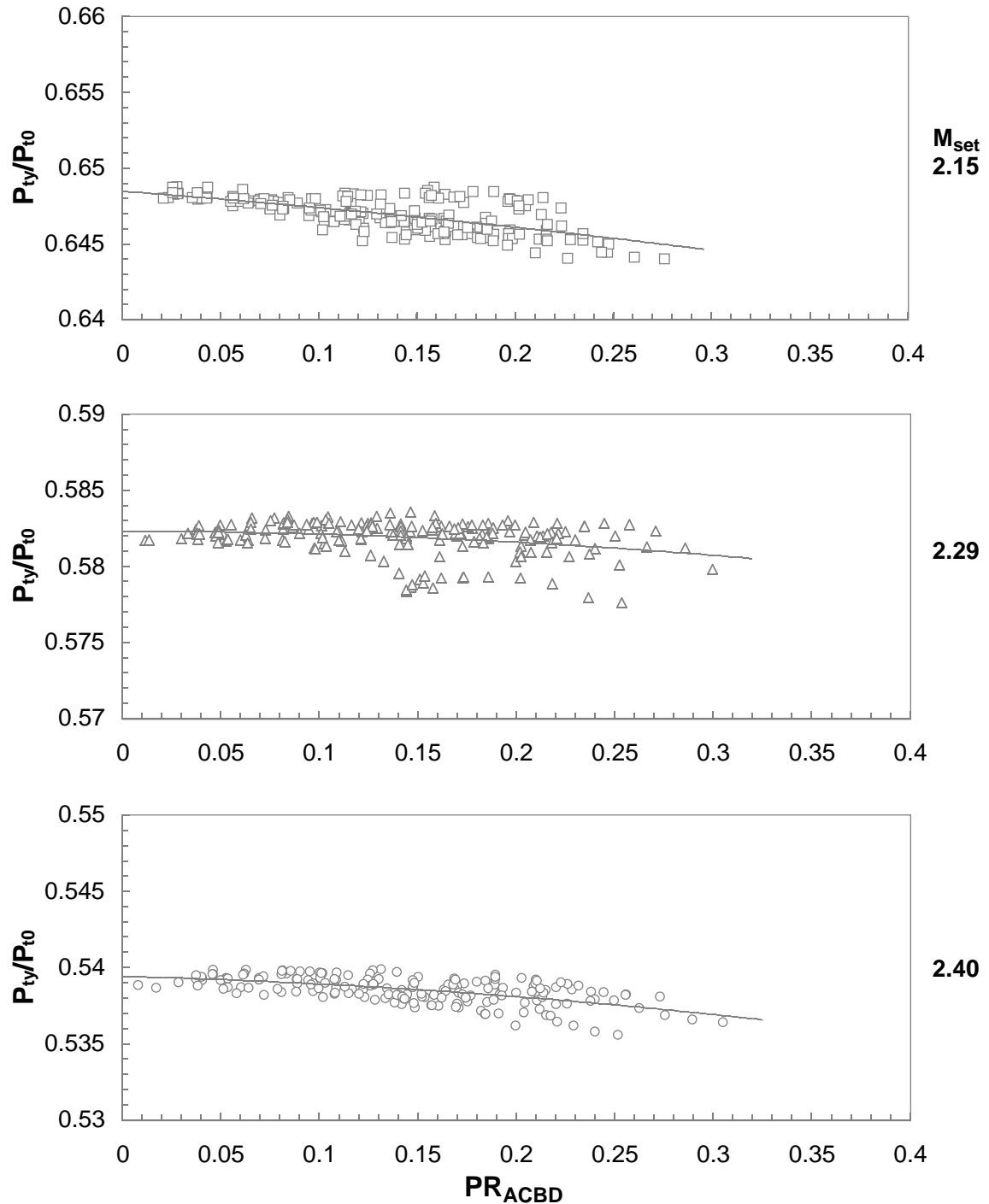
Figure 47. Continued.



Probe 8

$$-8^\circ \leq \alpha_C, \beta_C \leq 8^\circ$$

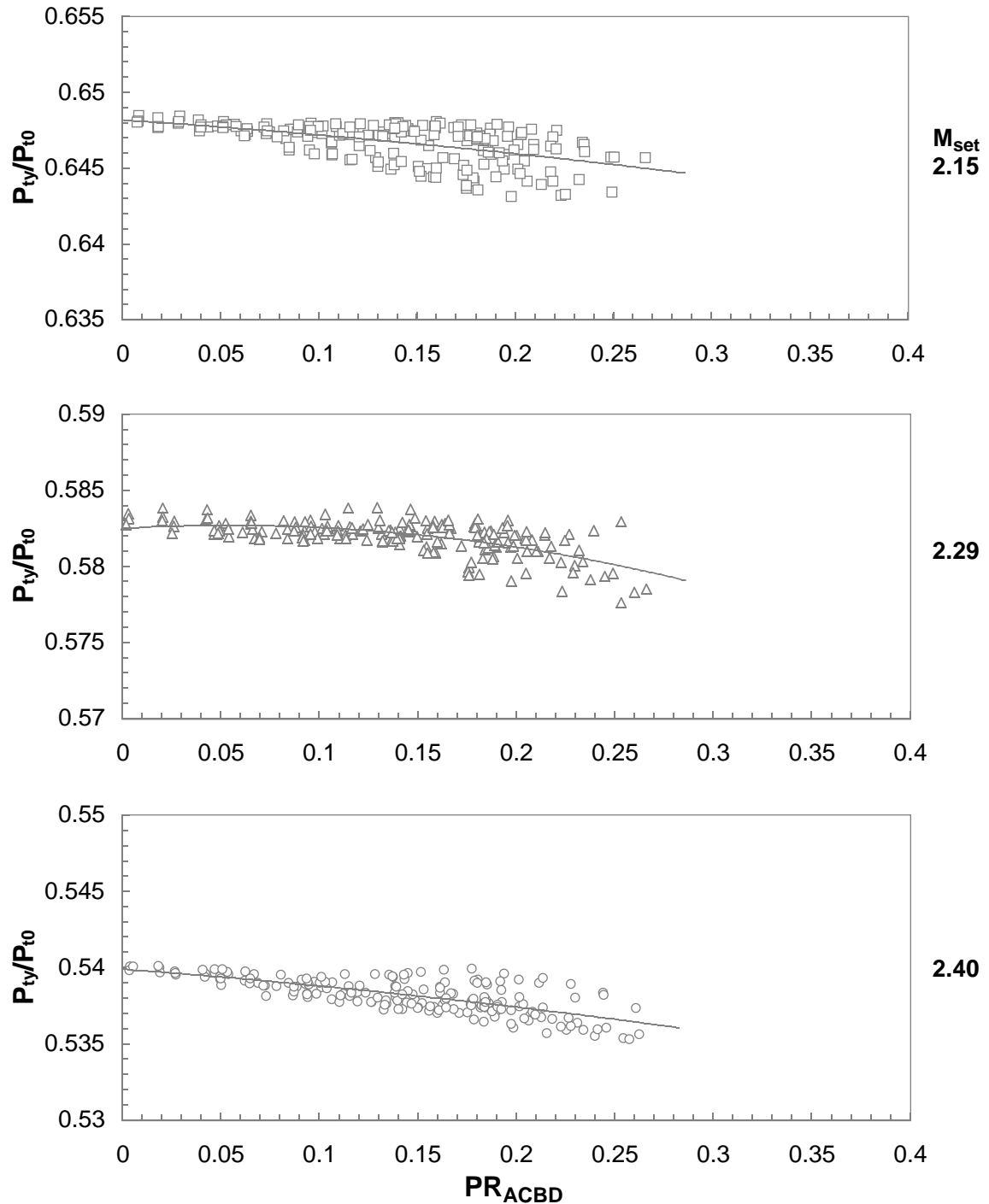
Figure 47. Concluded.



Probe 1

$$-8^\circ \leq \alpha_C, \beta_C \leq 8^\circ$$

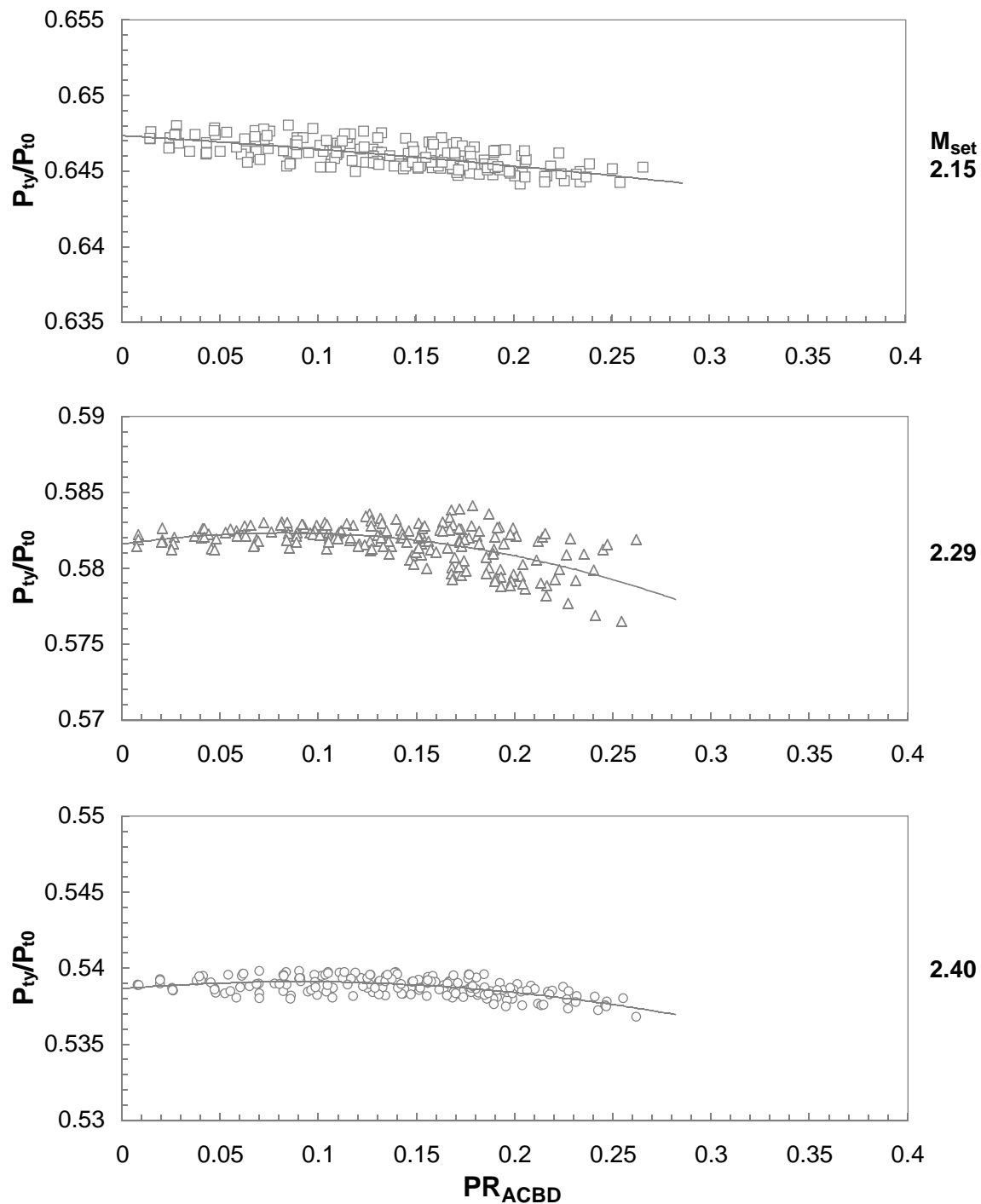
Figure 48. Pitot pressure variation with inclination parameter for rake 2.



Probe 2

$$-8^\circ \leq \alpha_C, \beta_C \leq 8^\circ$$

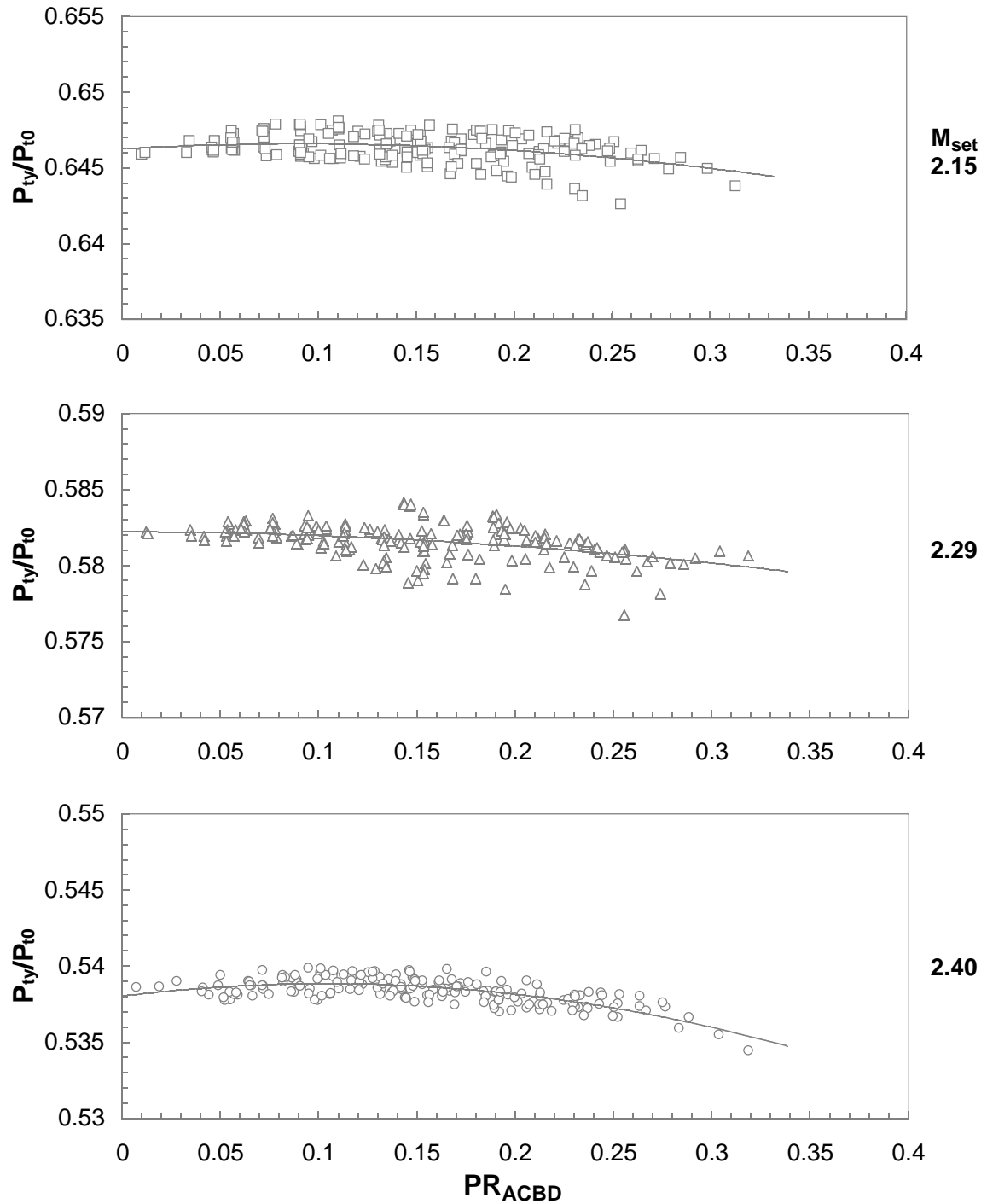
Figure 48. Continued.



Probe 3

$$-8^\circ \leq \alpha_C, \beta_C \leq 8^\circ$$

Figure 48. Continued.



Probe 4

$$-8^\circ \leq \alpha_C, \beta_C \leq 8^\circ$$

Figure 48. Continued.

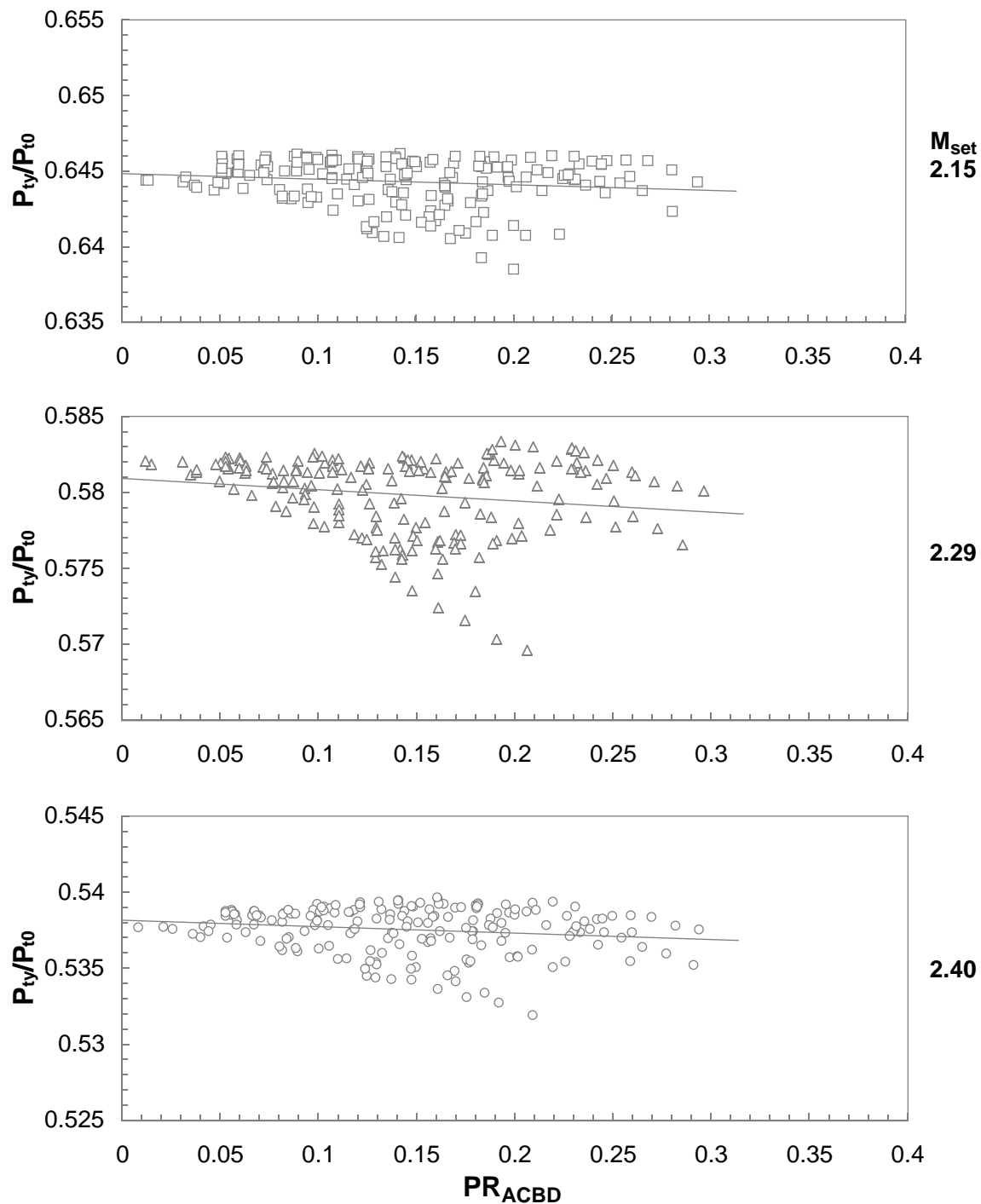
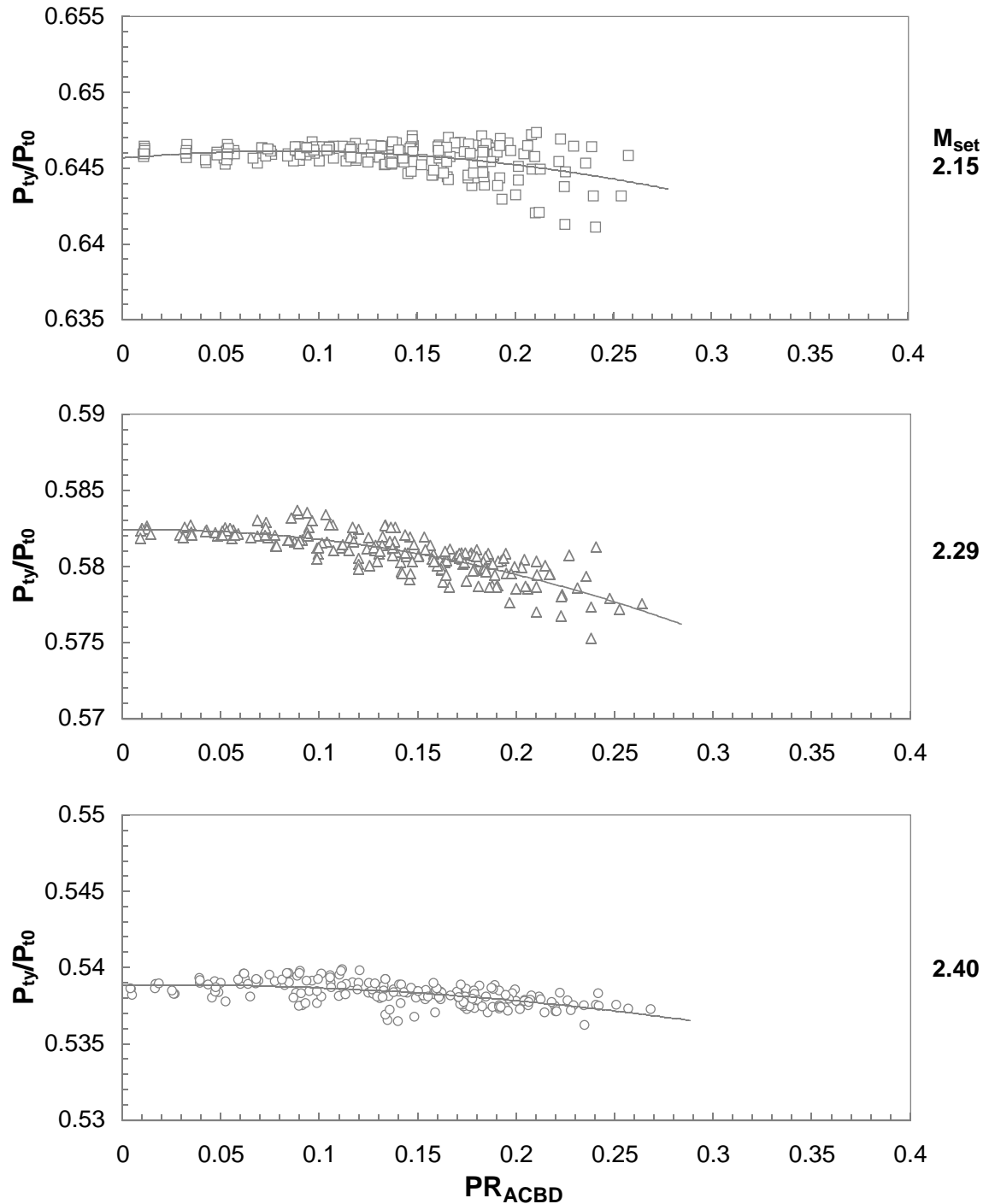


Figure 48. Continued.

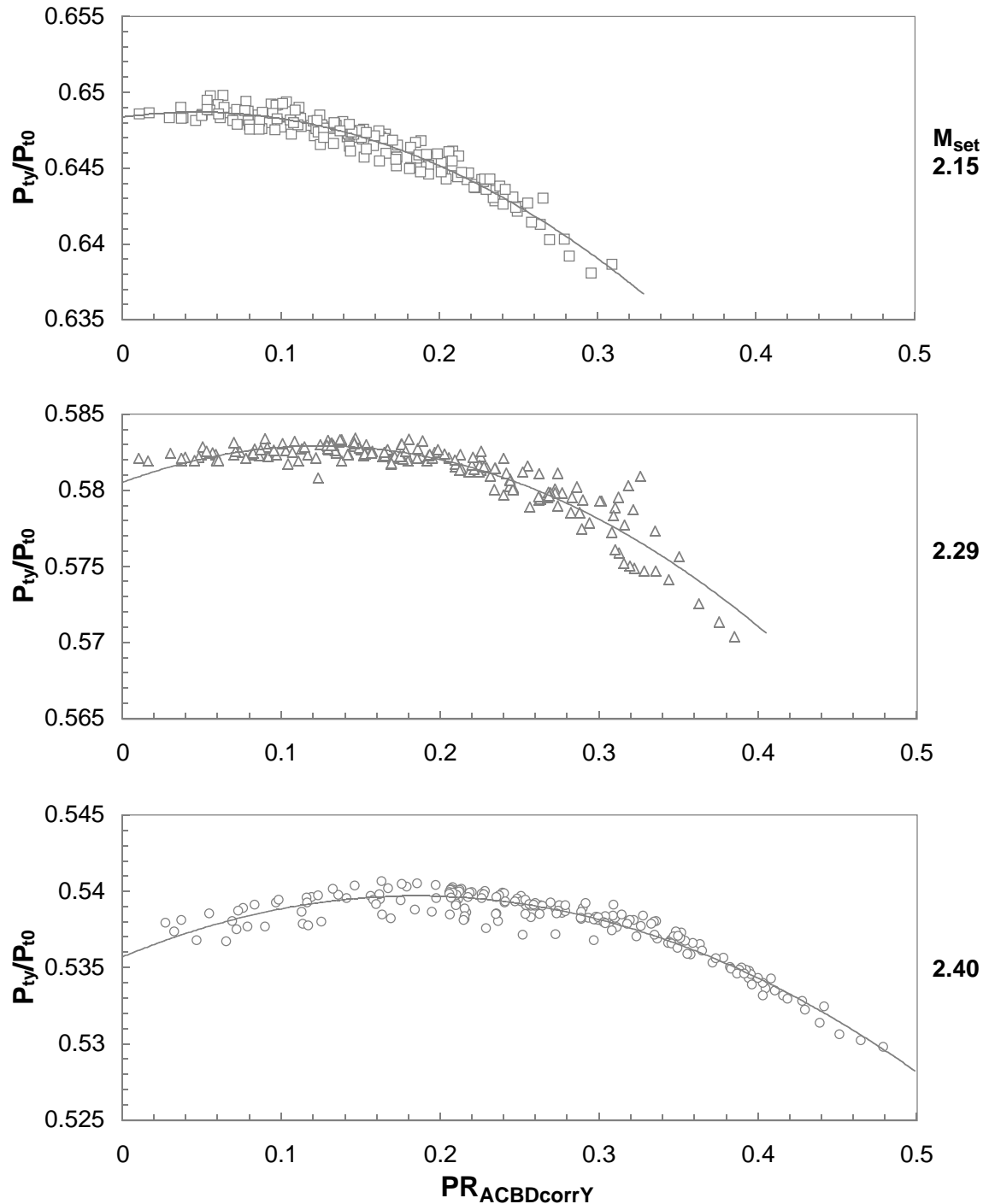


Probe 6

$$-8^\circ \leq \alpha_C, \beta_C \leq 8^\circ$$

Figure 48. Concluded.

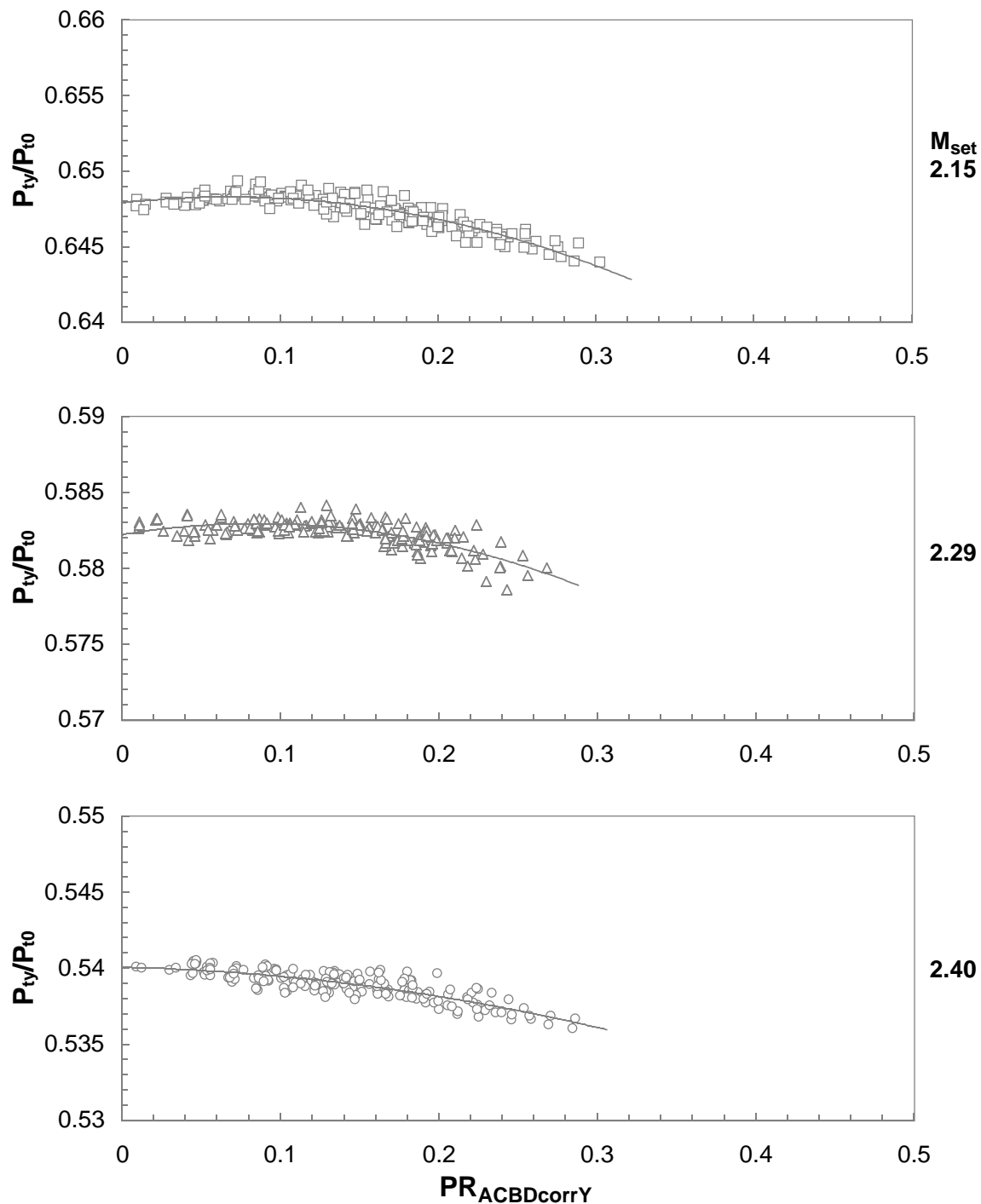
Figure 49. Cone-probe pitot pressure model.



Probe 1

$$-8^\circ \leq \alpha_C, \beta_C \leq 8^\circ$$

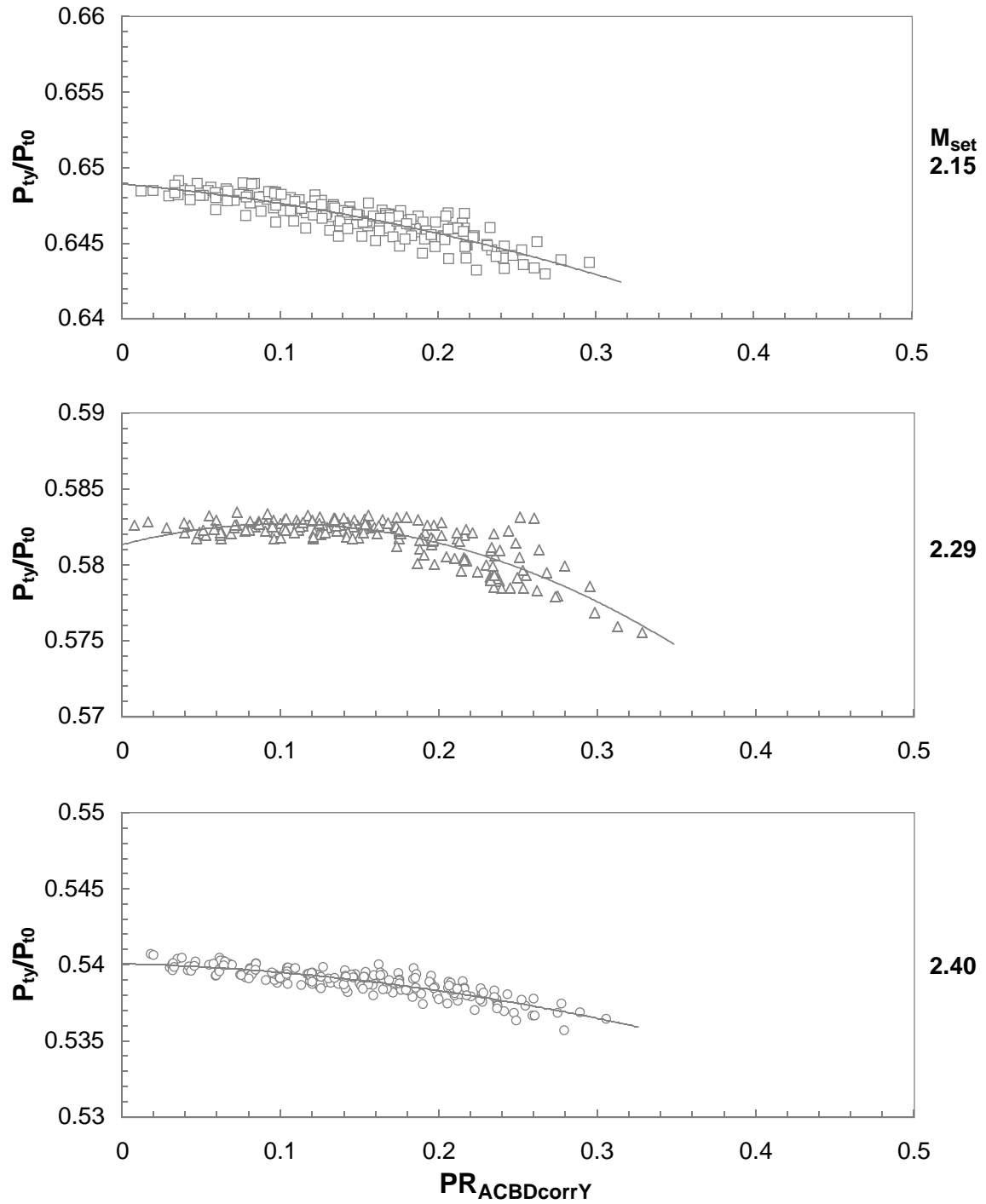
Figure 50. Converged solution of pitot pressure deviation for rake 1.



Probe 2

$$-8^\circ \leq \alpha_C, \beta_C \leq 8^\circ$$

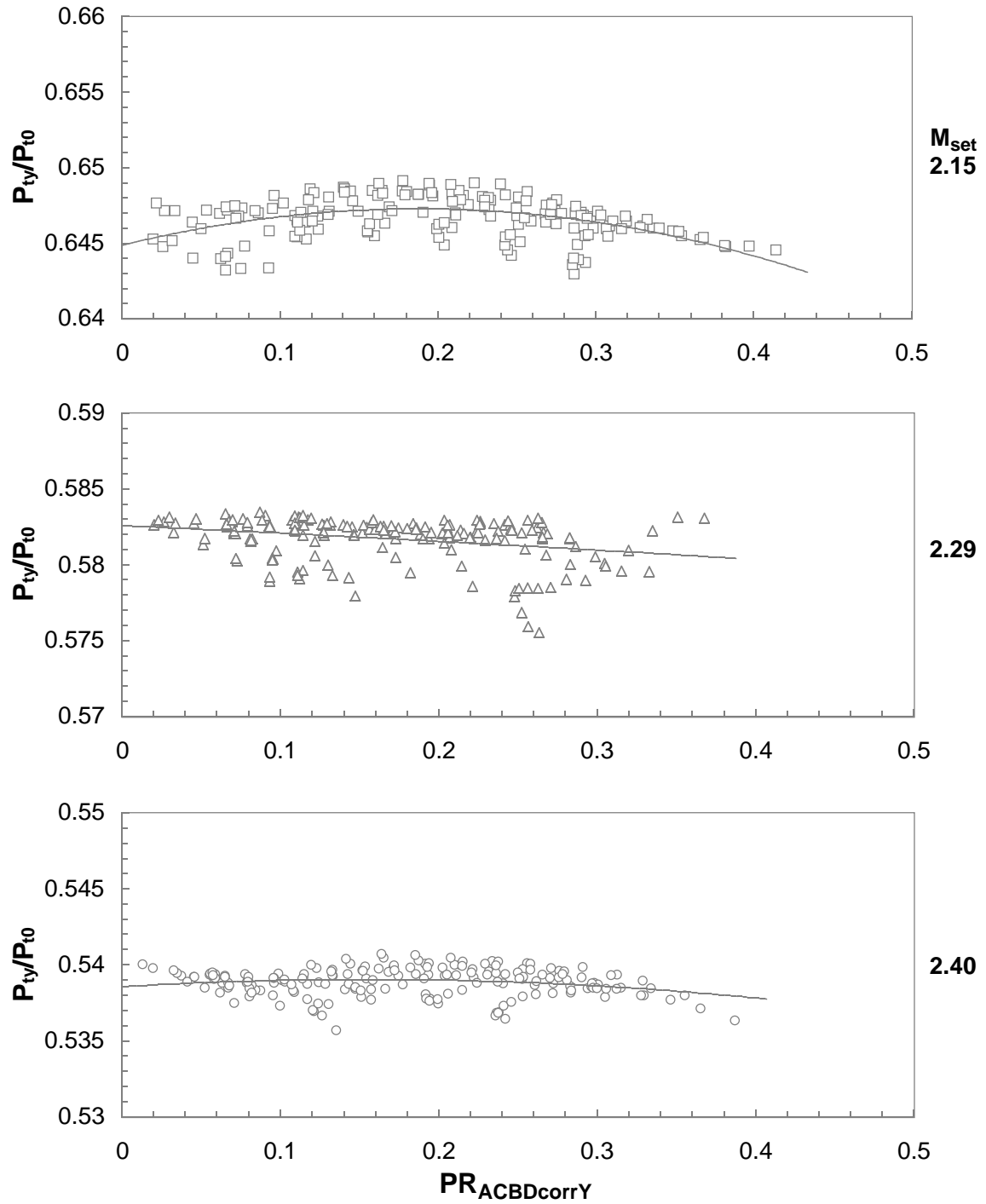
Figure 50. Continued.



Probe 3

$$-8^\circ \leq \alpha_C, \beta_C \leq 8^\circ$$

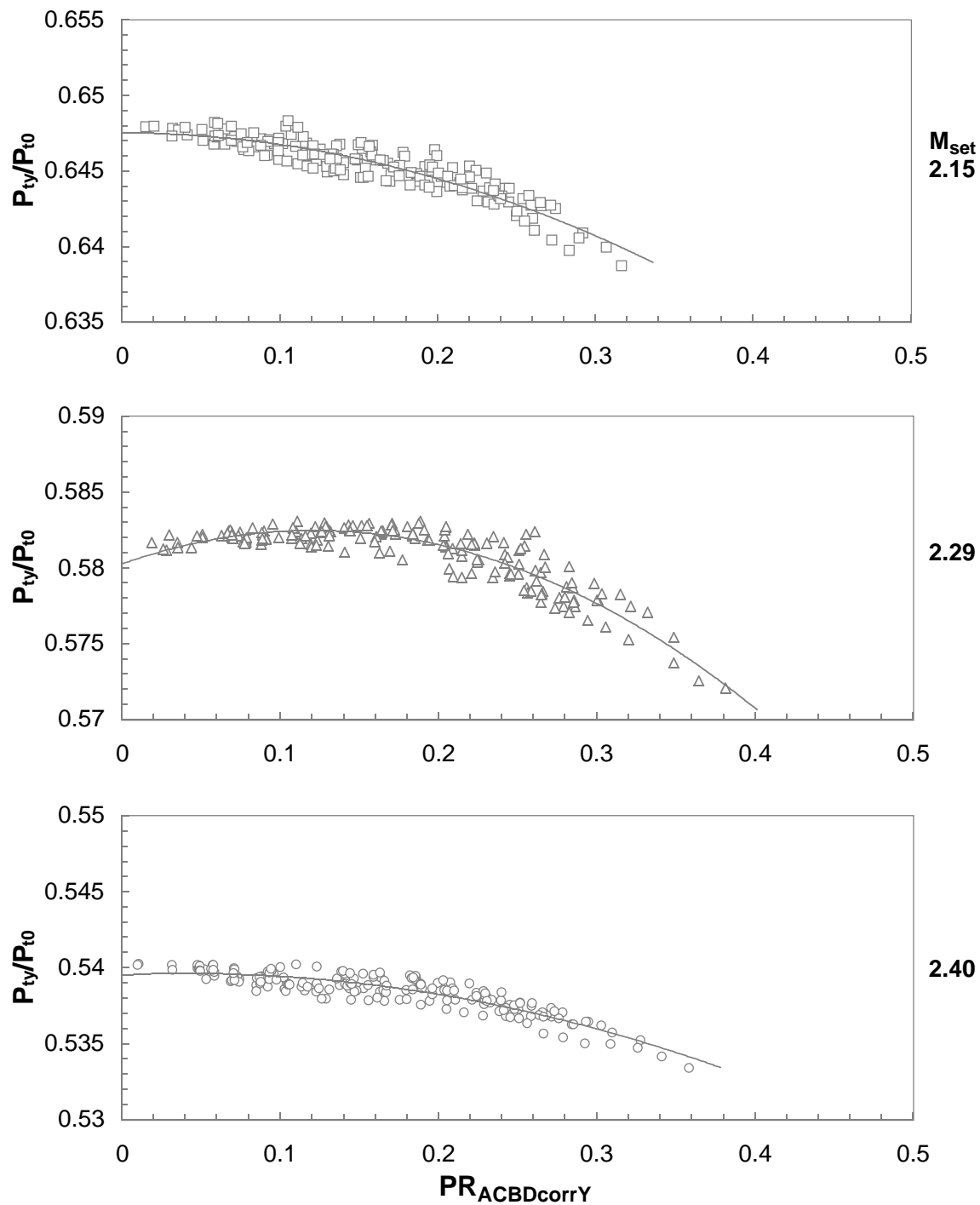
Figure 50. Continued.



Probe 4

$$-8^\circ \leq \alpha_C, \beta_C \leq 8^\circ$$

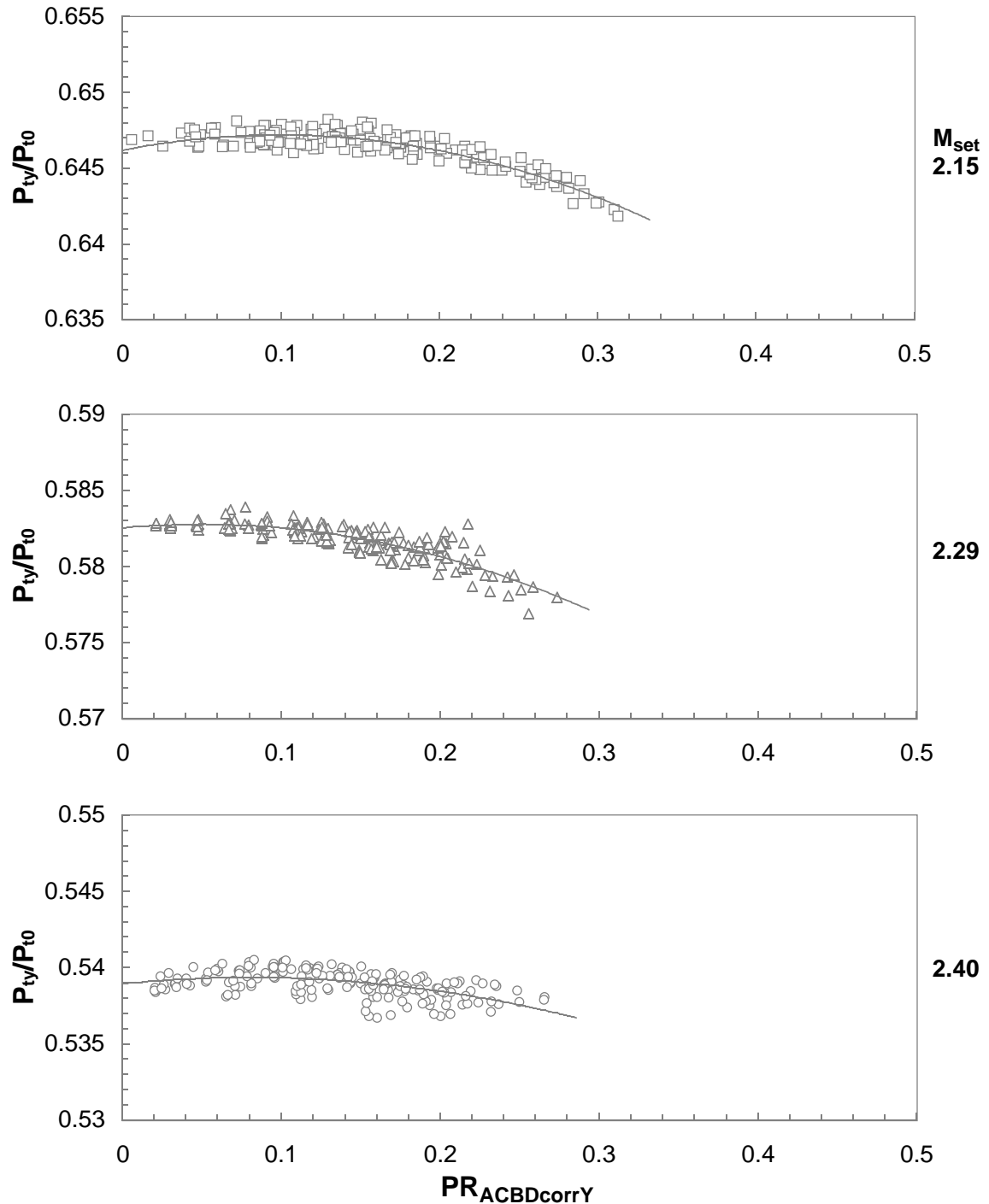
Figure 50. Continued.



Probe 5

$$-8^\circ \leq \alpha_C, \beta_C \leq 8^\circ$$

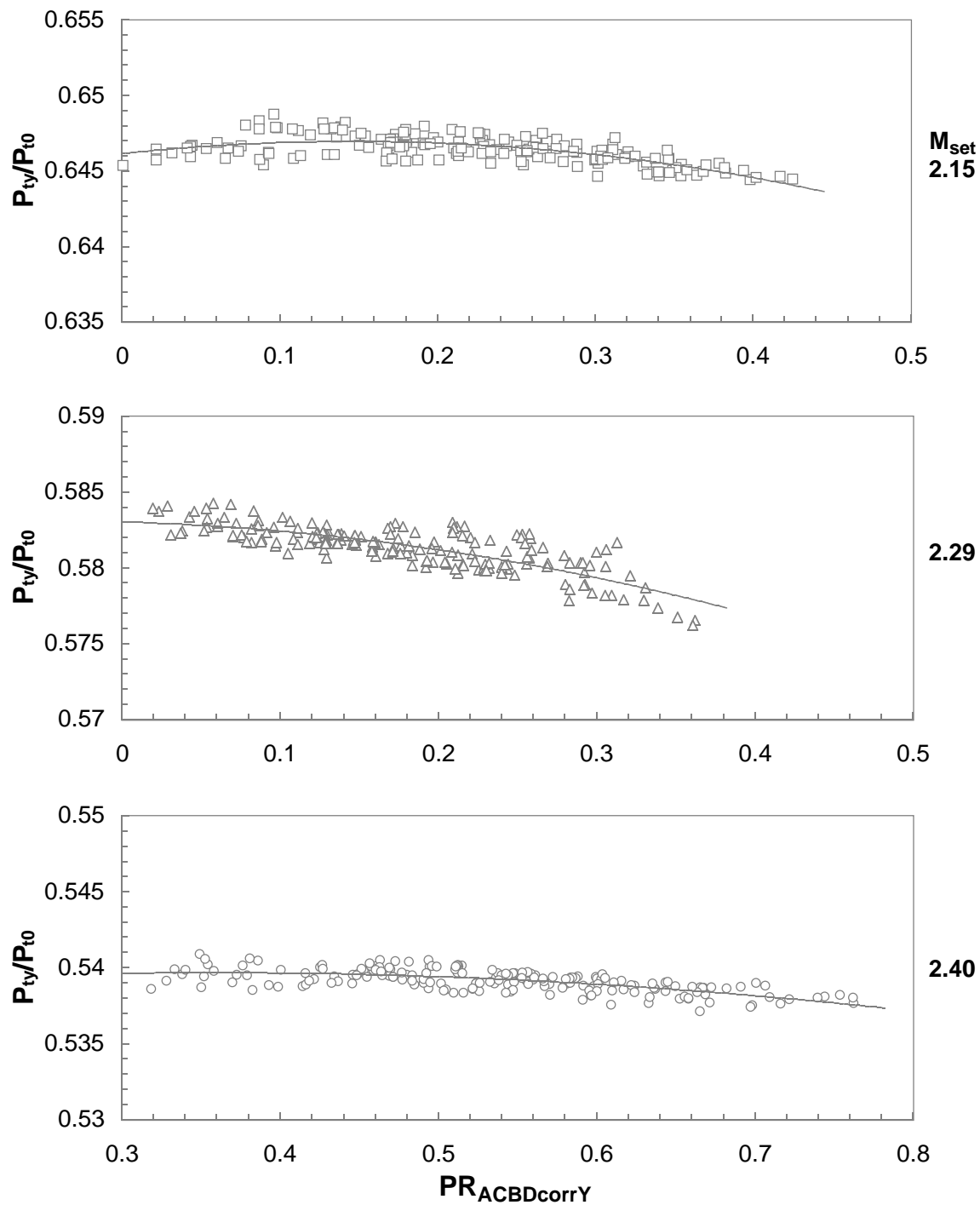
Figure 50. Continued.



Probe 6

$$-8^\circ \leq \alpha_C, \beta_C \leq 8^\circ$$

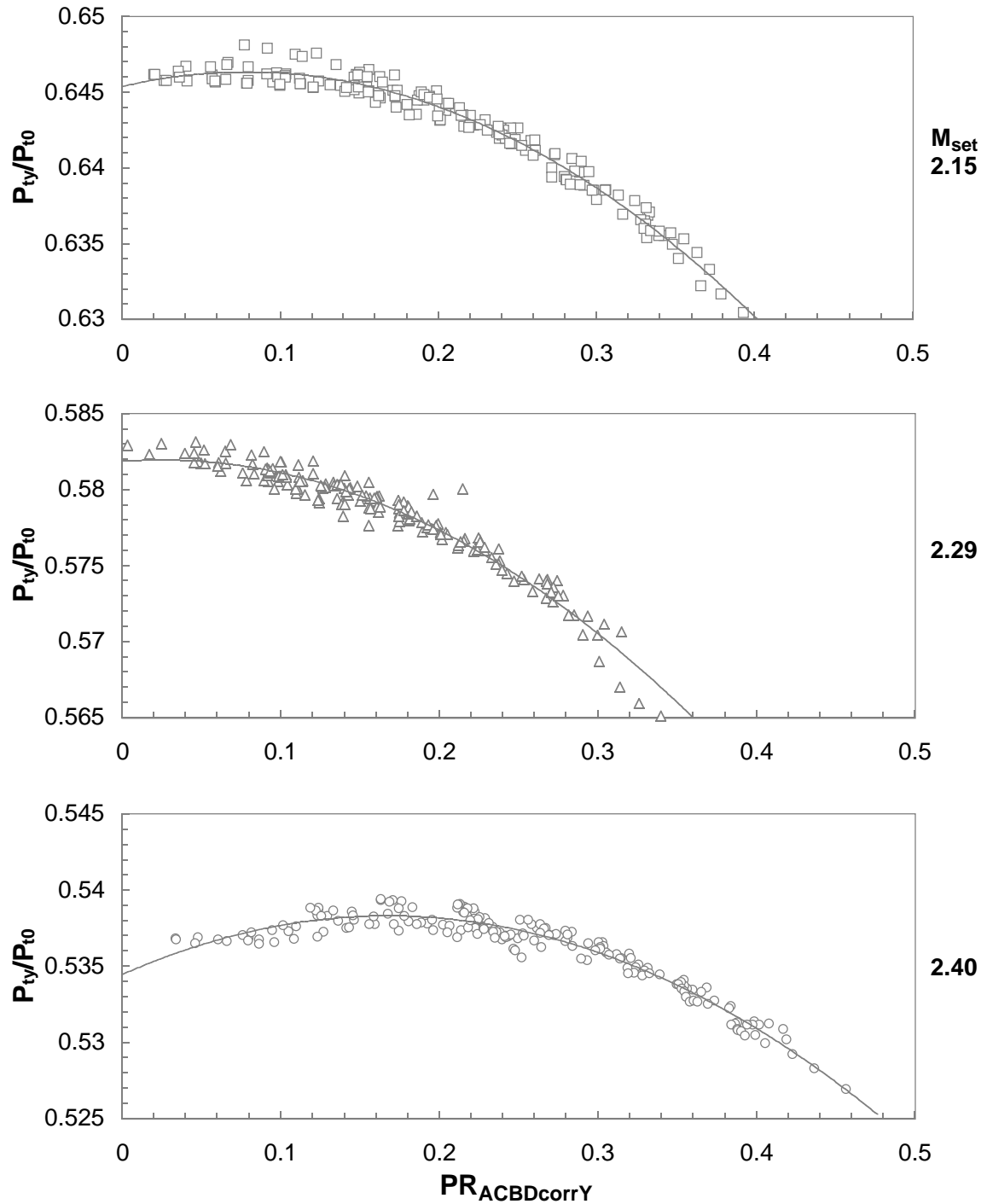
Figure 50. Continued.



Probe 7

$$-8^\circ \leq \alpha_C, \beta_C \leq 8^\circ$$

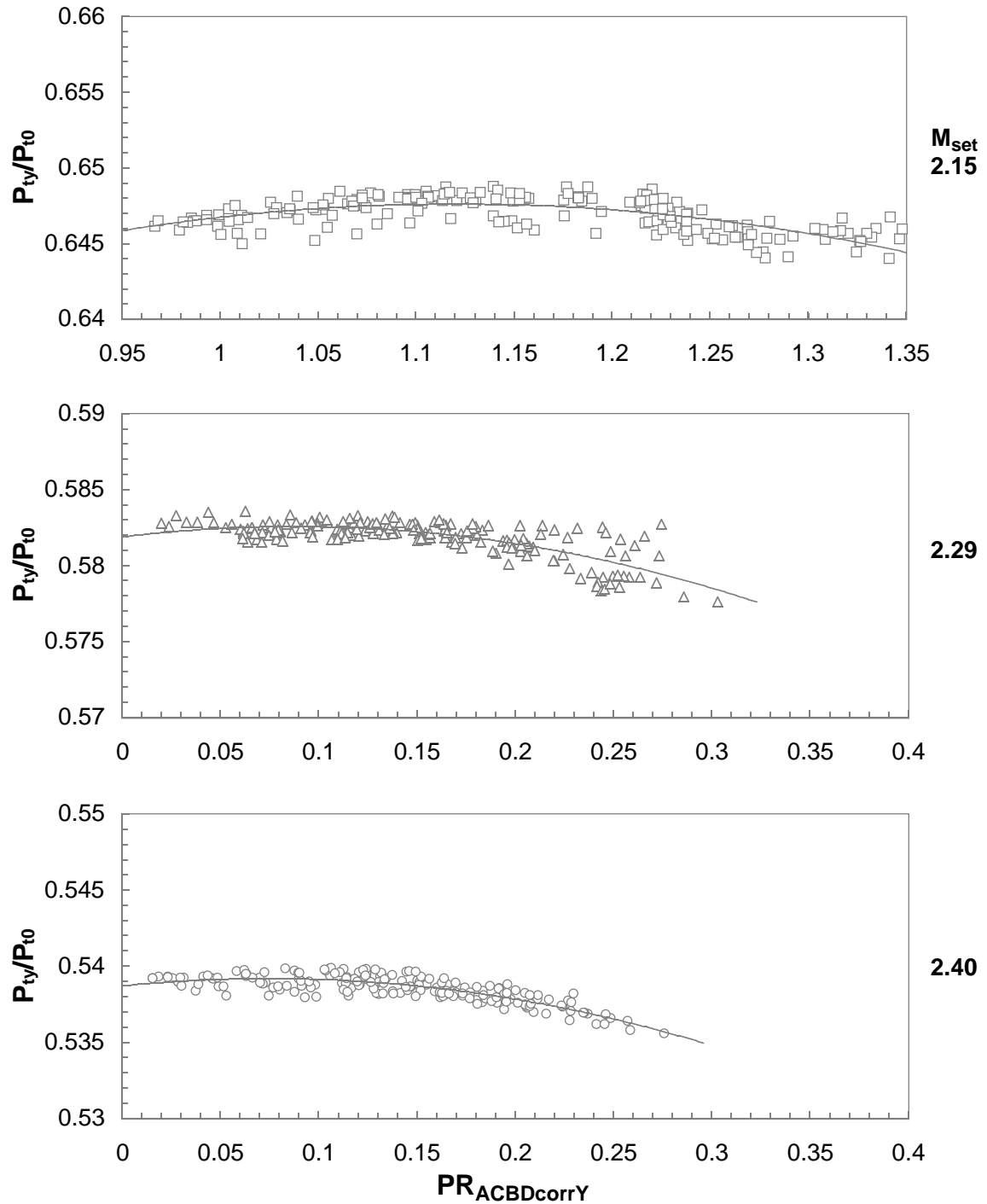
Figure 50. Continued.



Probe 8

$$-8^\circ \leq \alpha_C, \beta_C \leq 8^\circ$$

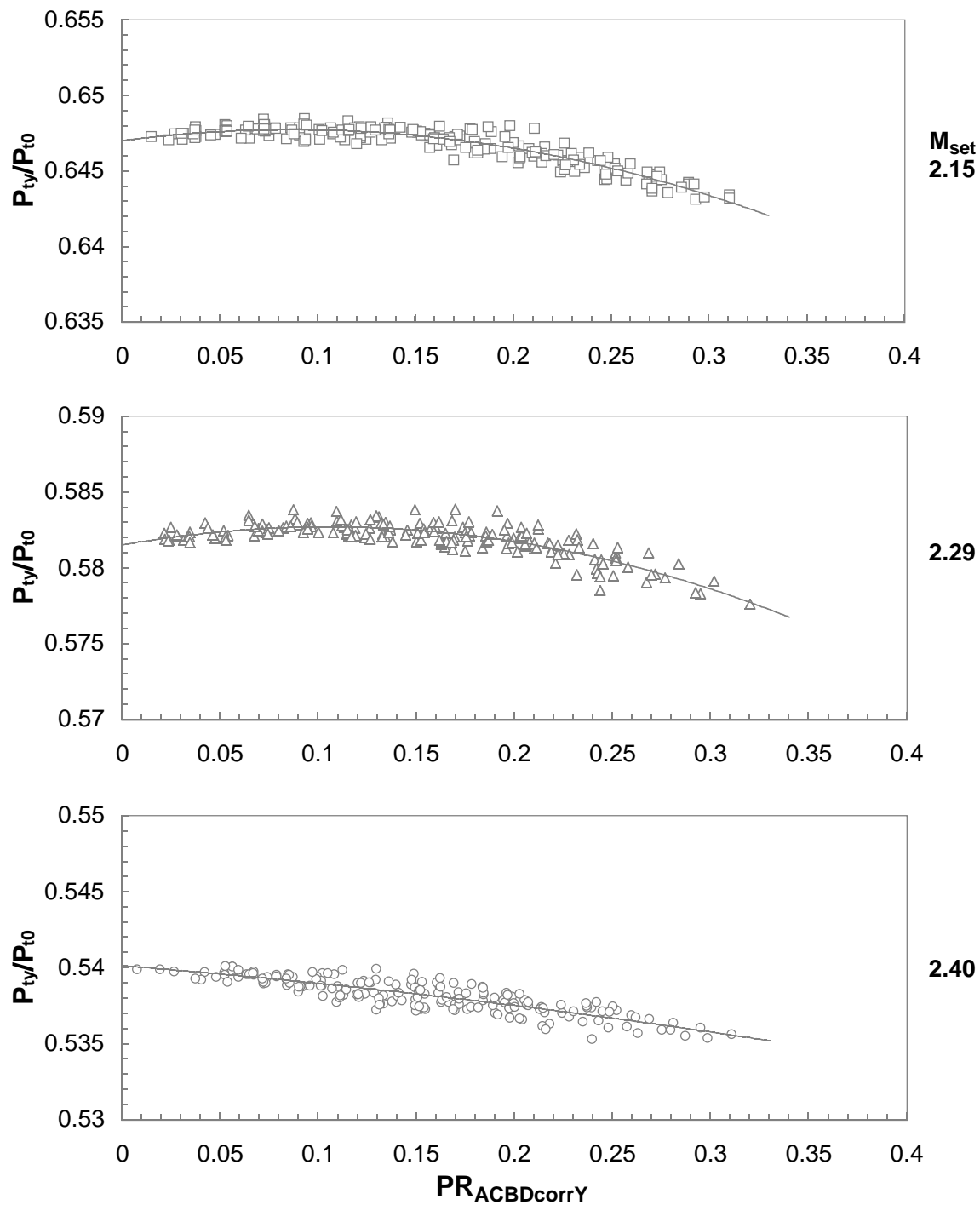
Figure 50. Concluded.



Probe 1

$$-8^\circ \leq \alpha_C, \beta_C \leq 8^\circ$$

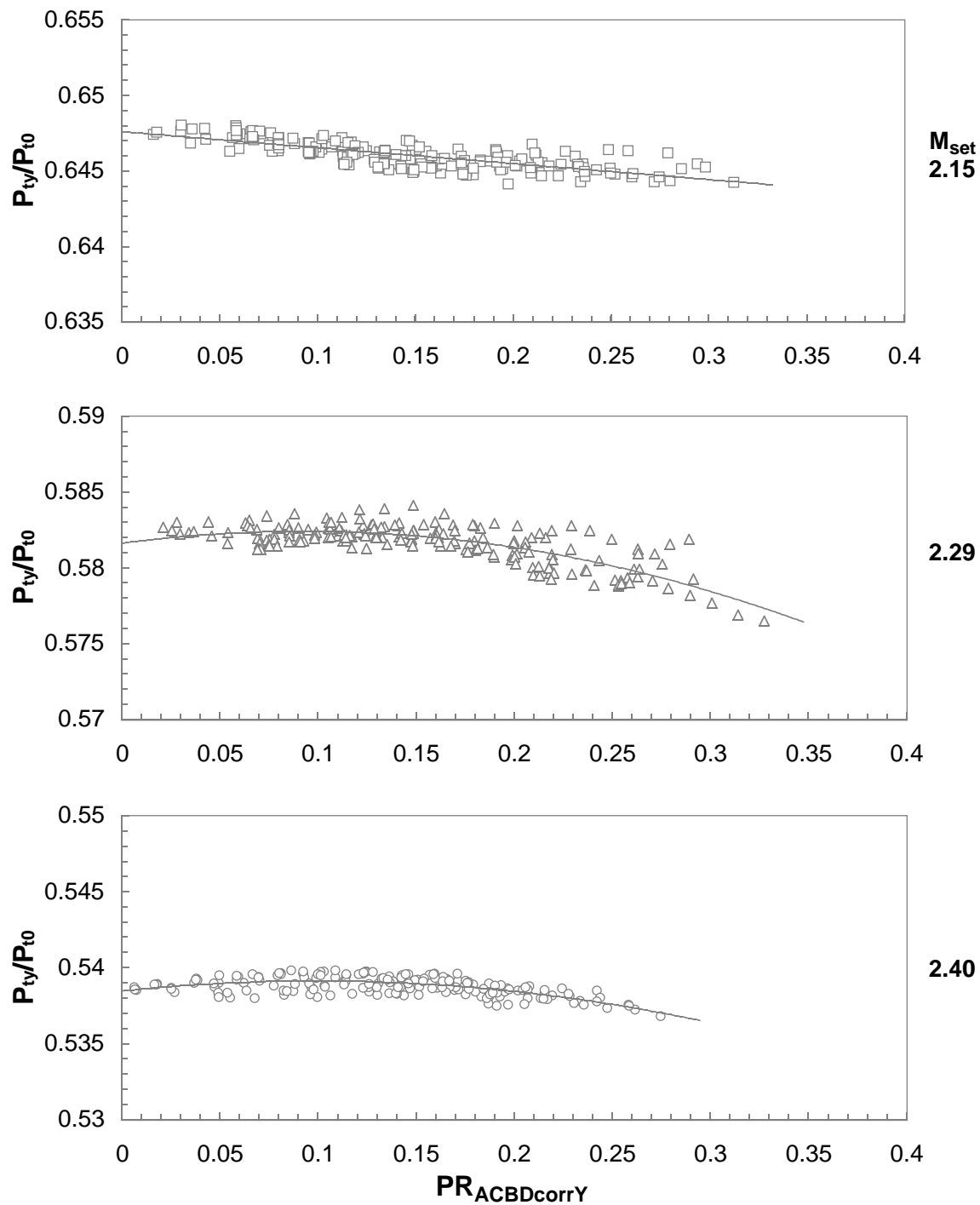
Figure 51. Converged solution of pitot pressure deviation for rake 2.



Probe 2

$$-8^\circ \leq \alpha_C, \beta_C \leq 8^\circ$$

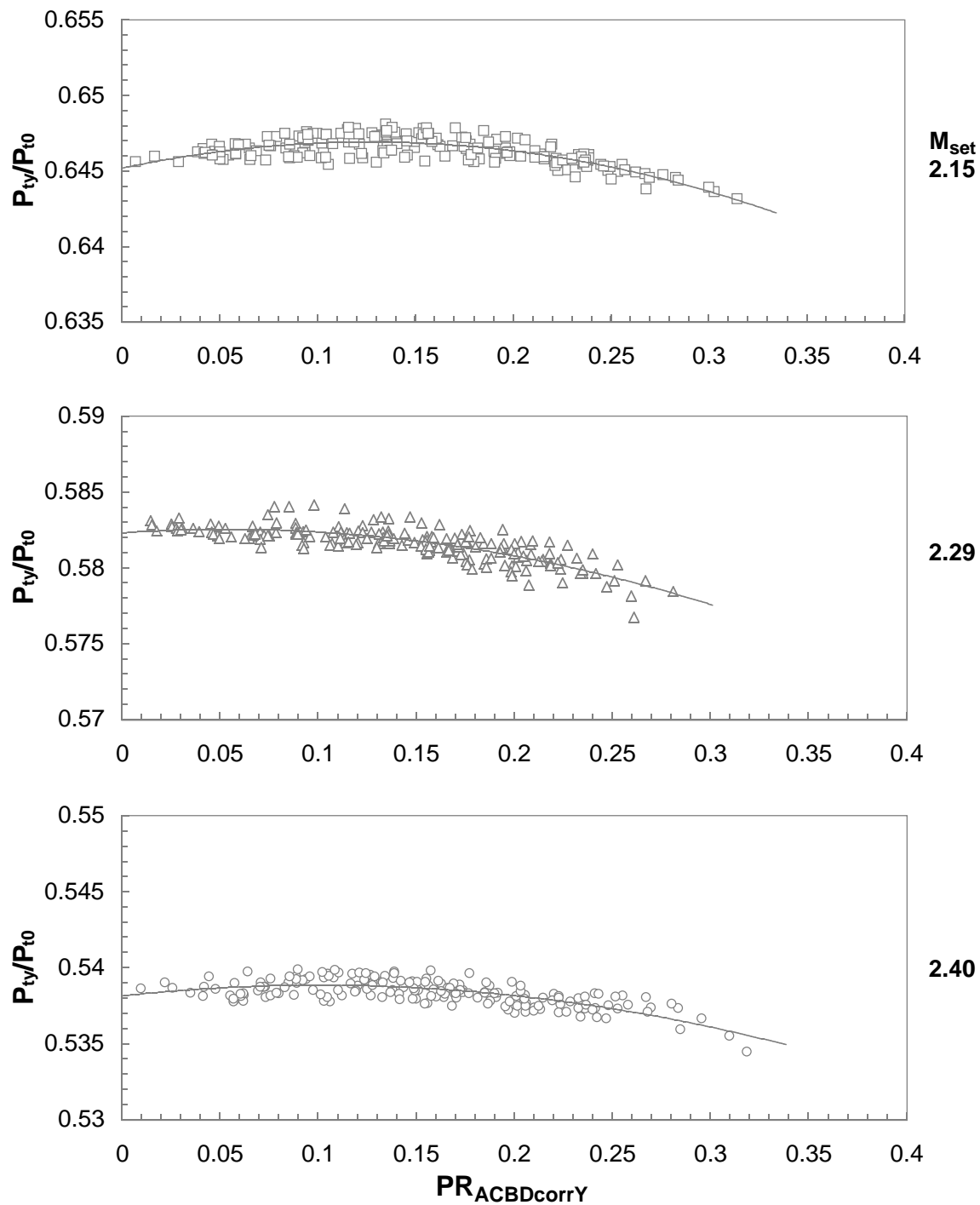
Figure 51. Continued.



Probe 3

$$-8^\circ \leq \alpha_C, \beta_C \leq 8^\circ$$

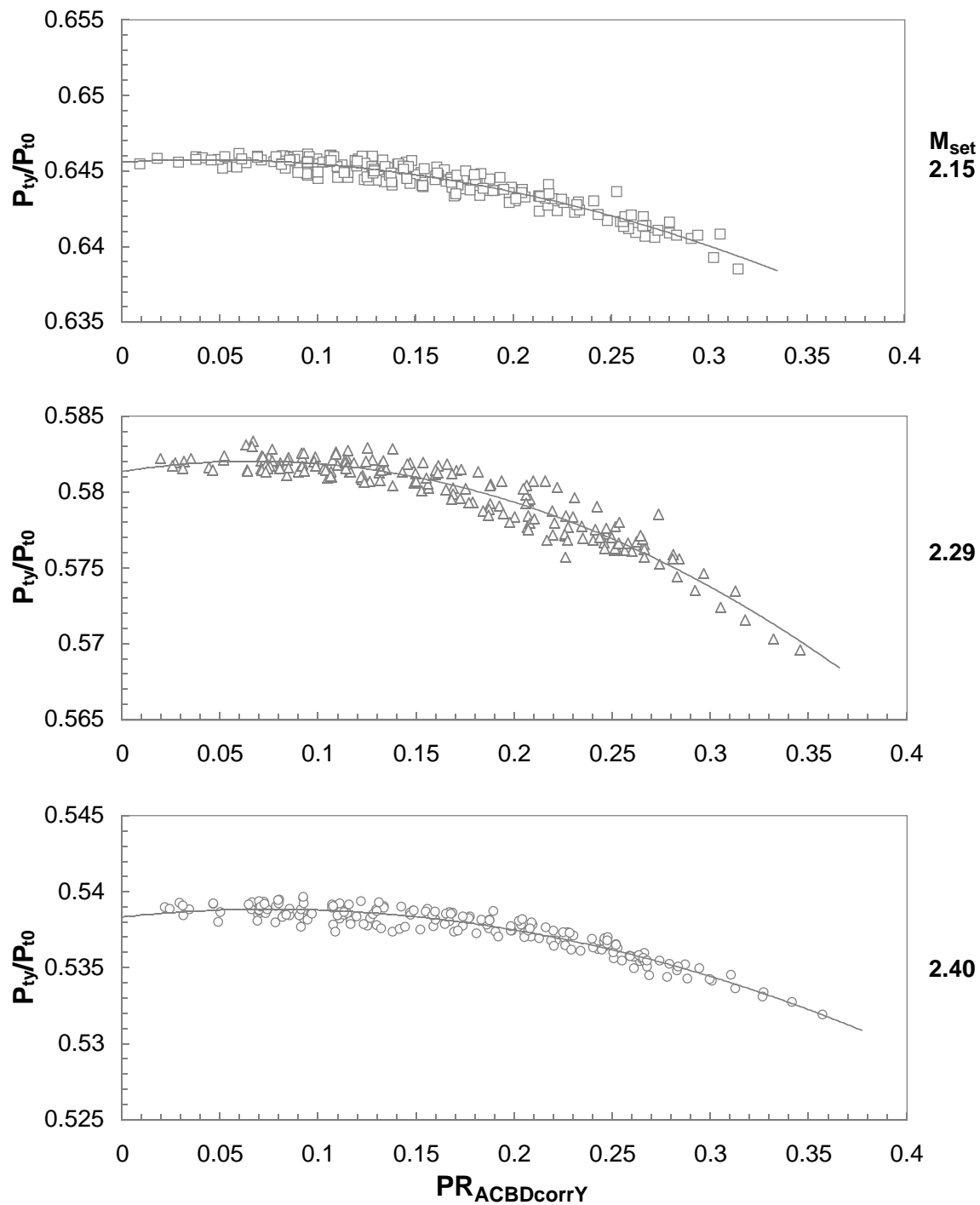
Figure 51. Continued.



Probe 4

$$-8^\circ \leq \alpha_C, \beta_C \leq 8^\circ$$

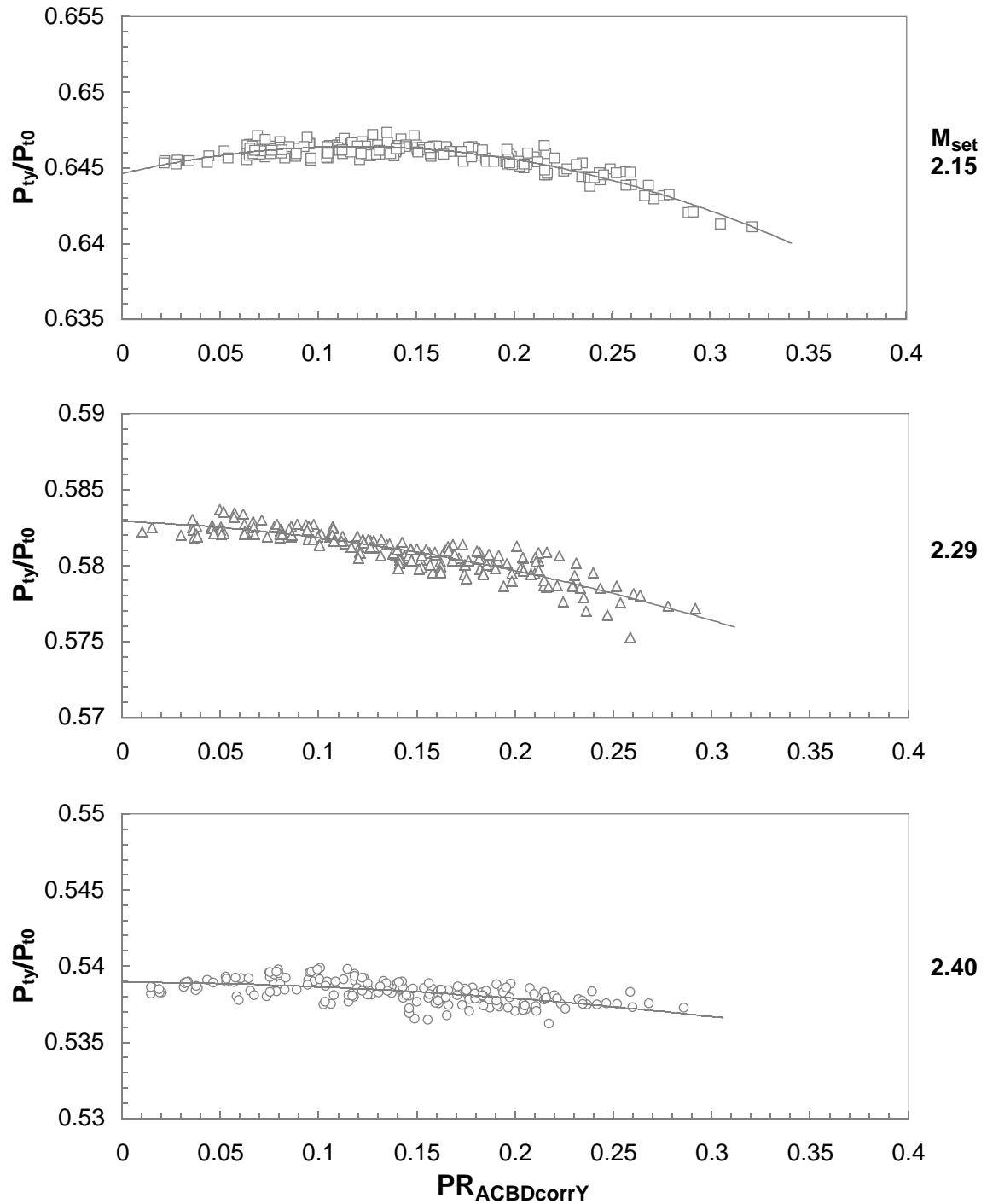
Figure 51. Continued.



Probe 5

$$-8^\circ \leq \alpha_C, \beta_C \leq 8^\circ$$

Figure 51. Continued.



Probe 6

$$-8^\circ \leq \alpha_C, \beta_C \leq 8^\circ$$

Figure 51. Concluded.

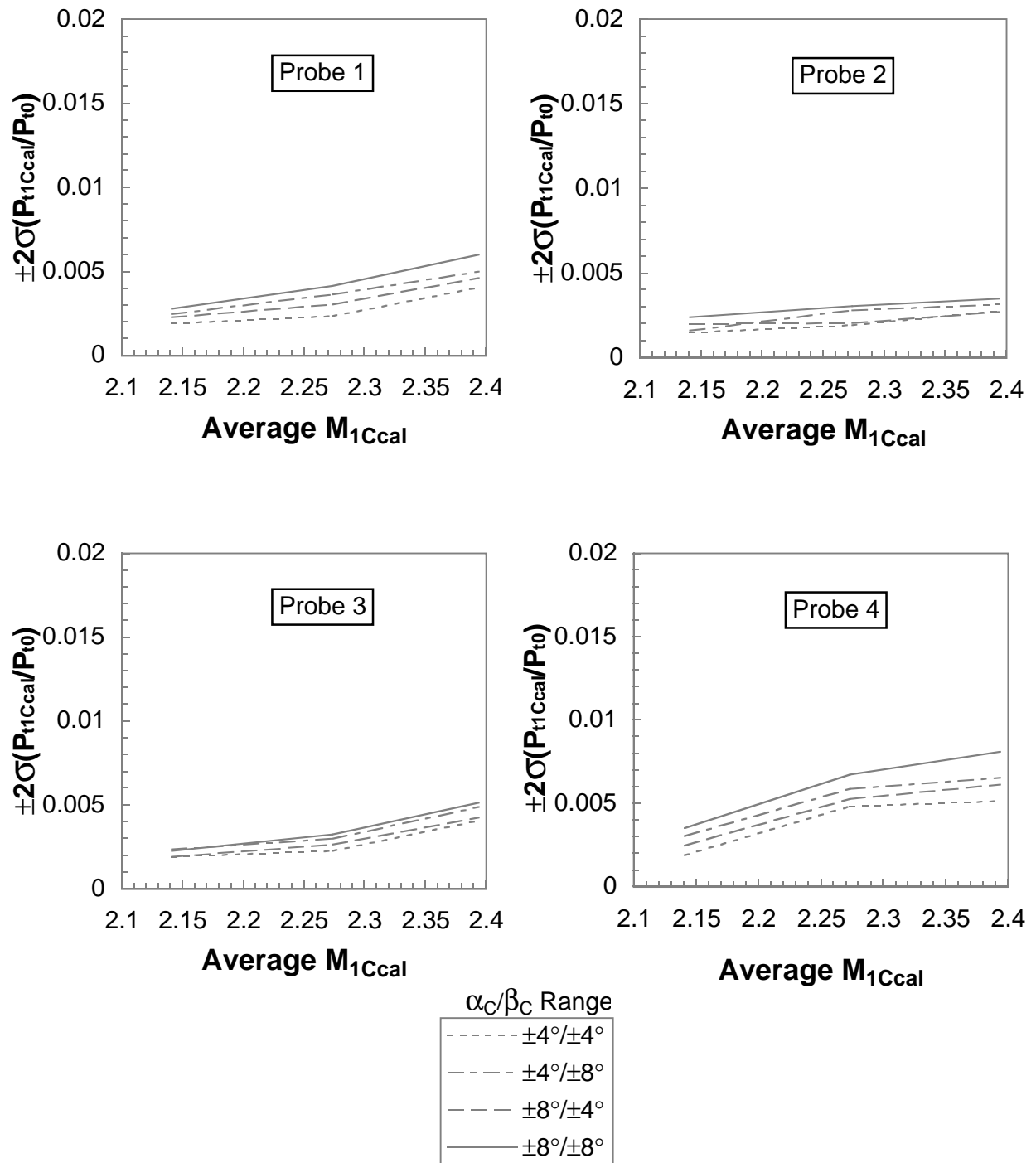


Figure 52. Total pressure recovery correlation residual for rake 1.

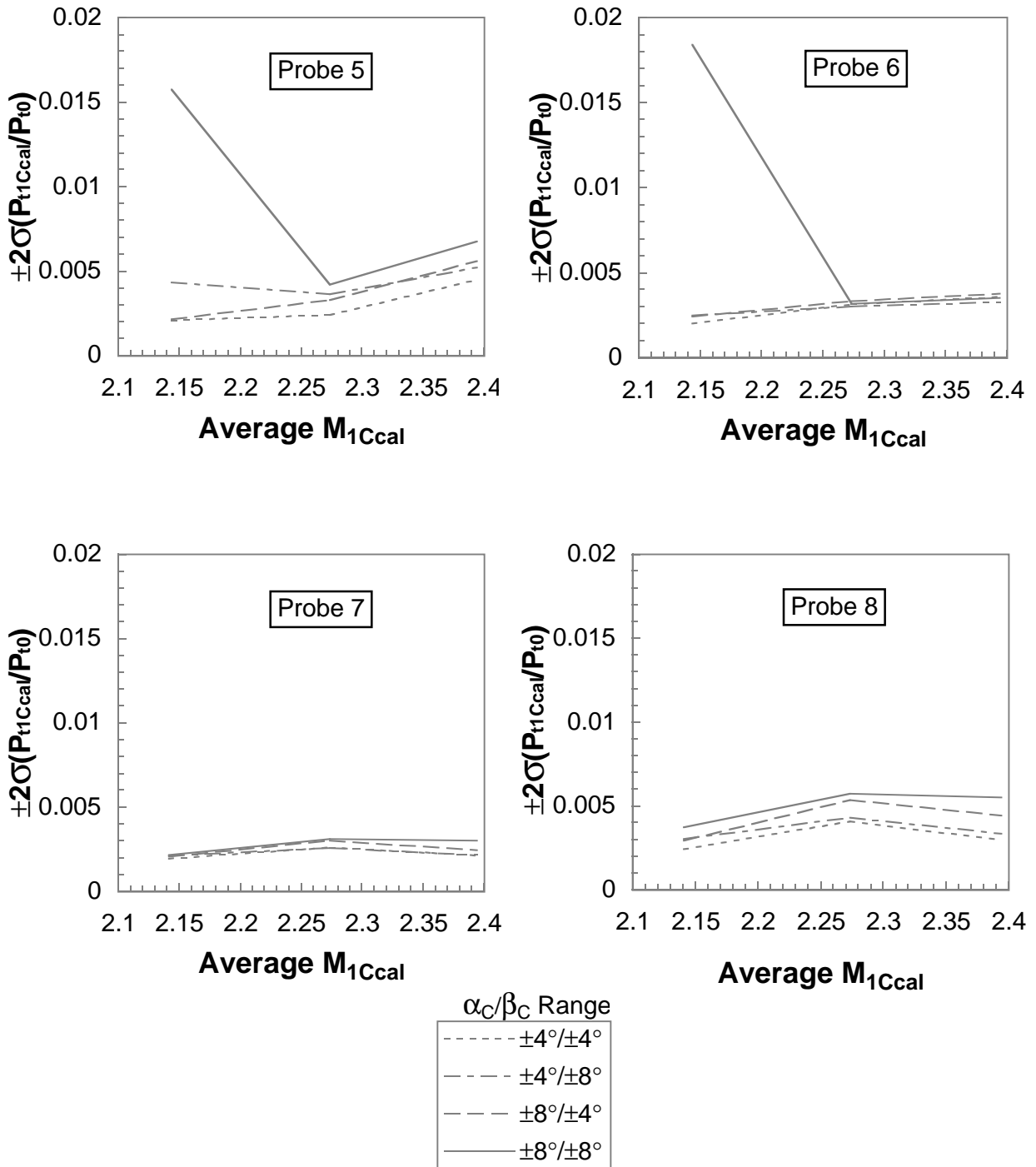


Figure 52. Concluded.

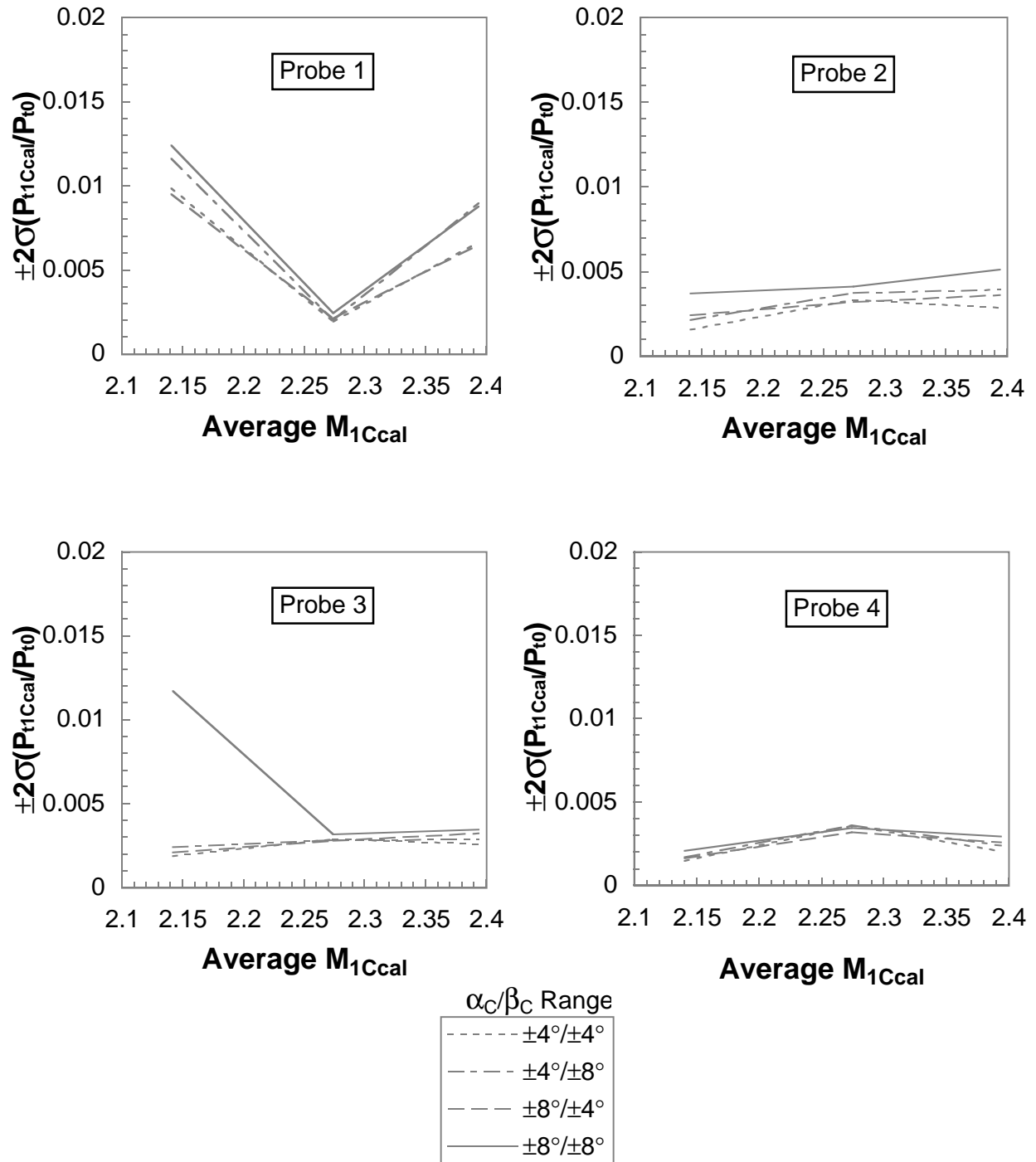


Figure 53. Total pressure recovery correlation residual for rake 2.

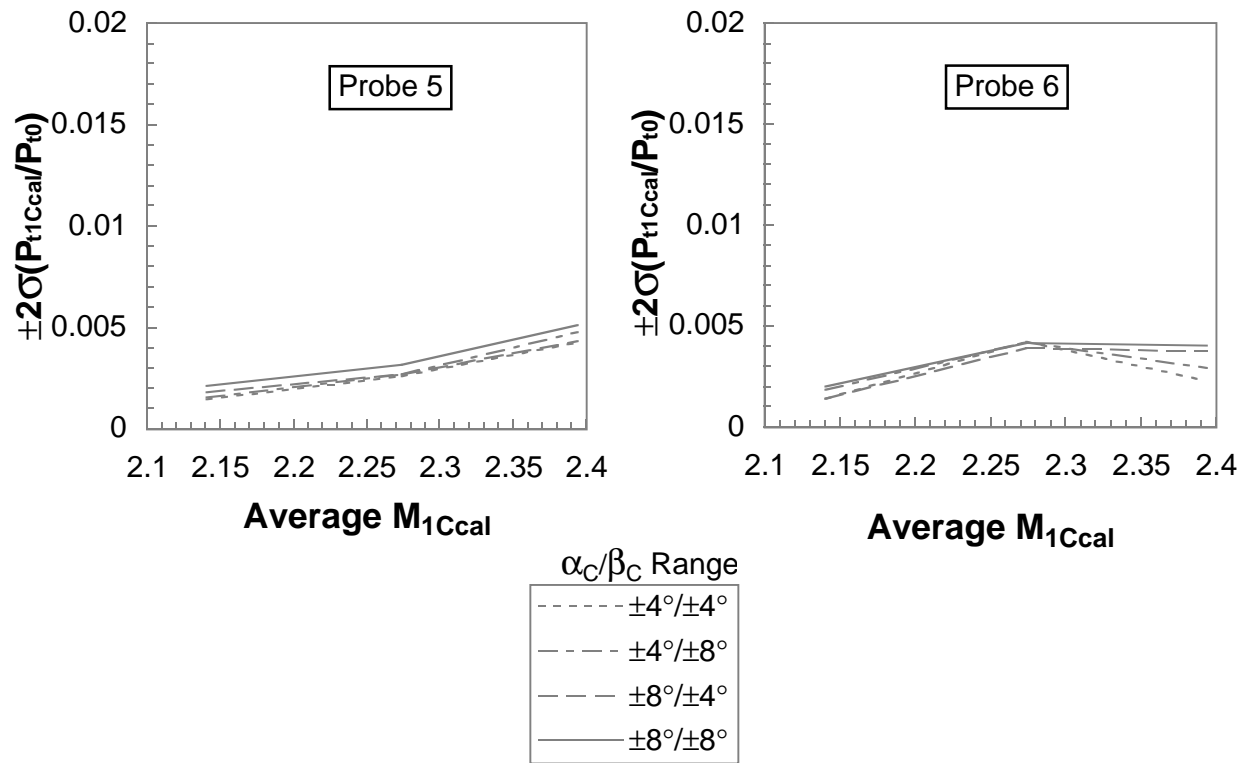
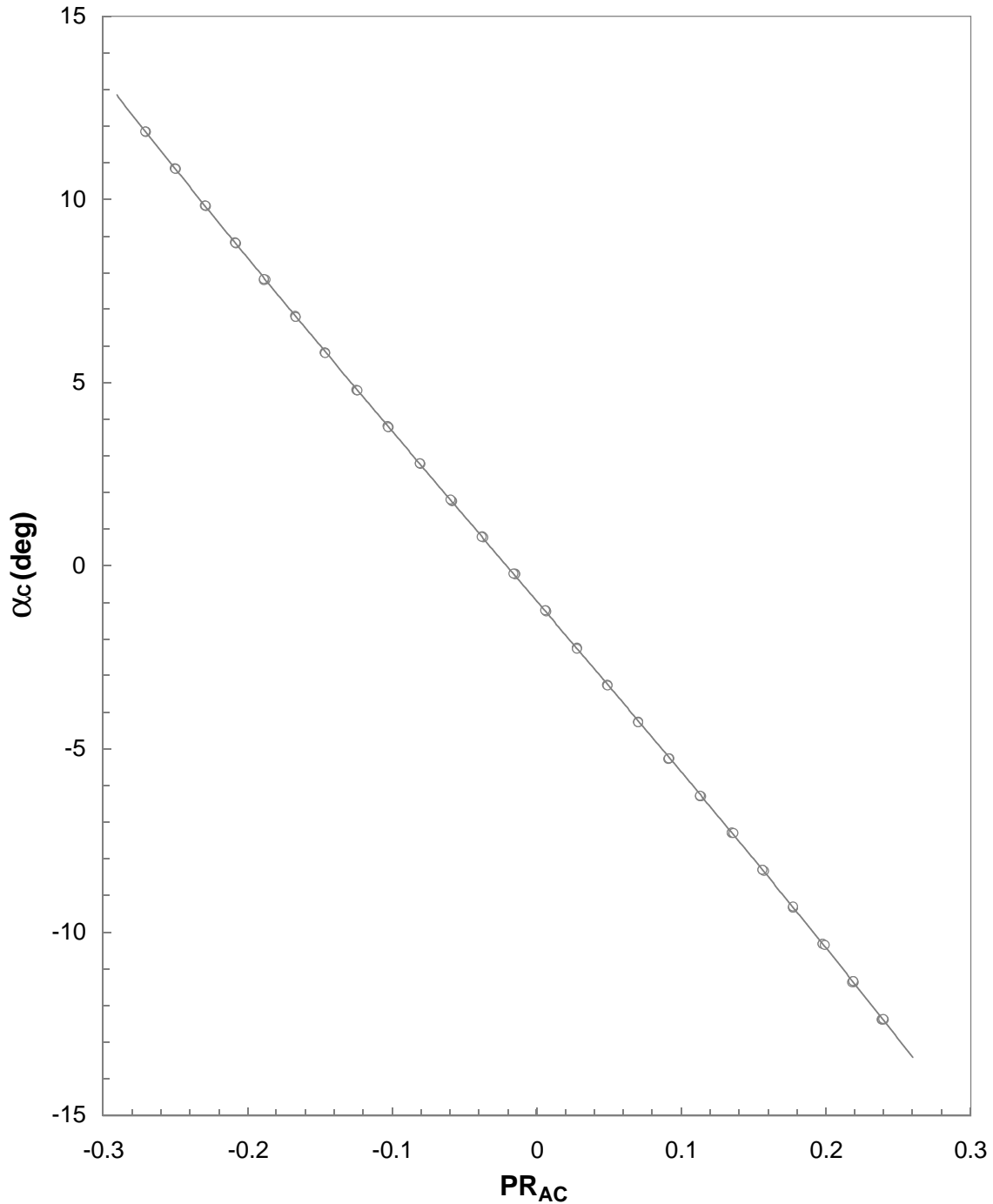
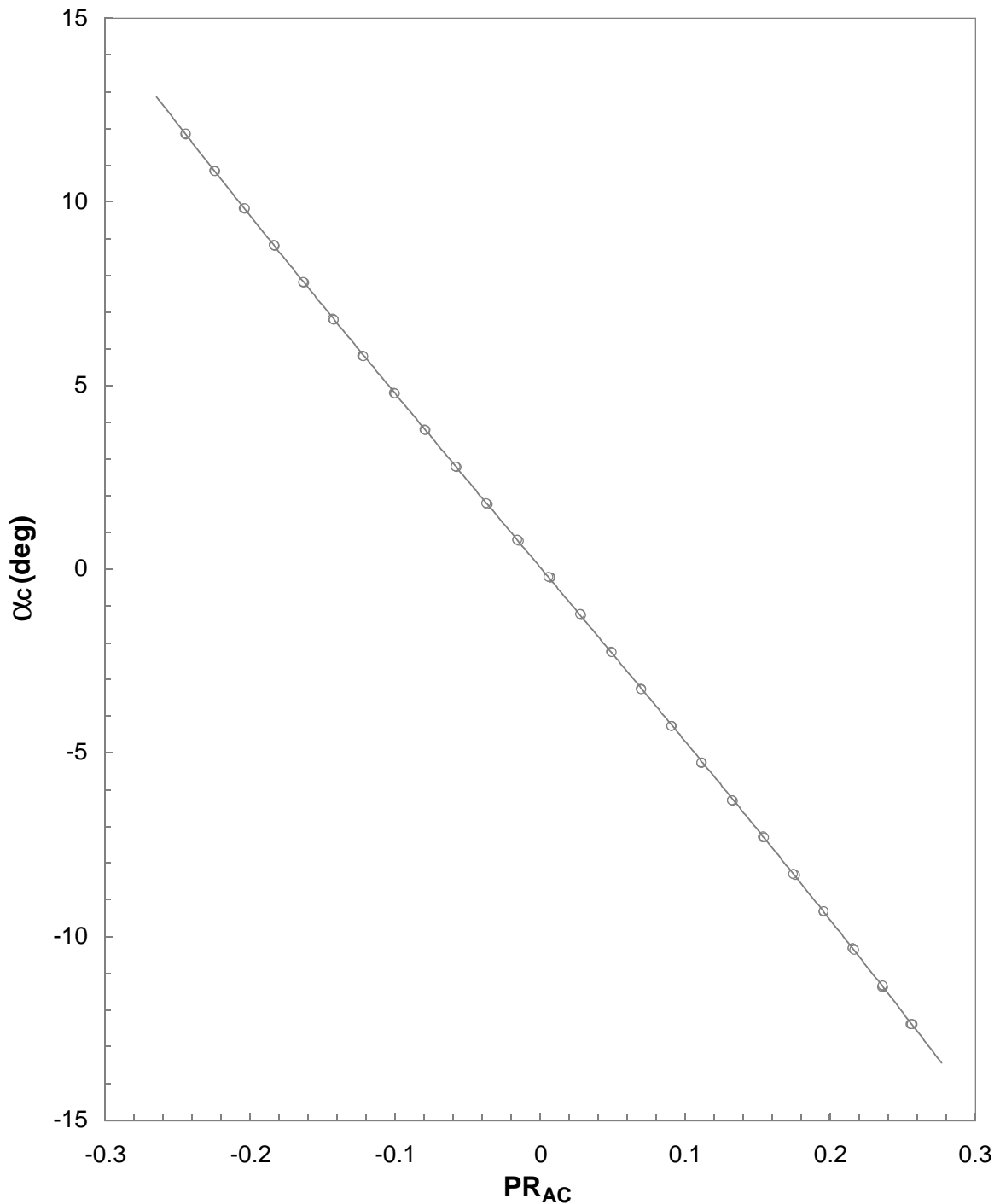


Figure 53. Concluded.



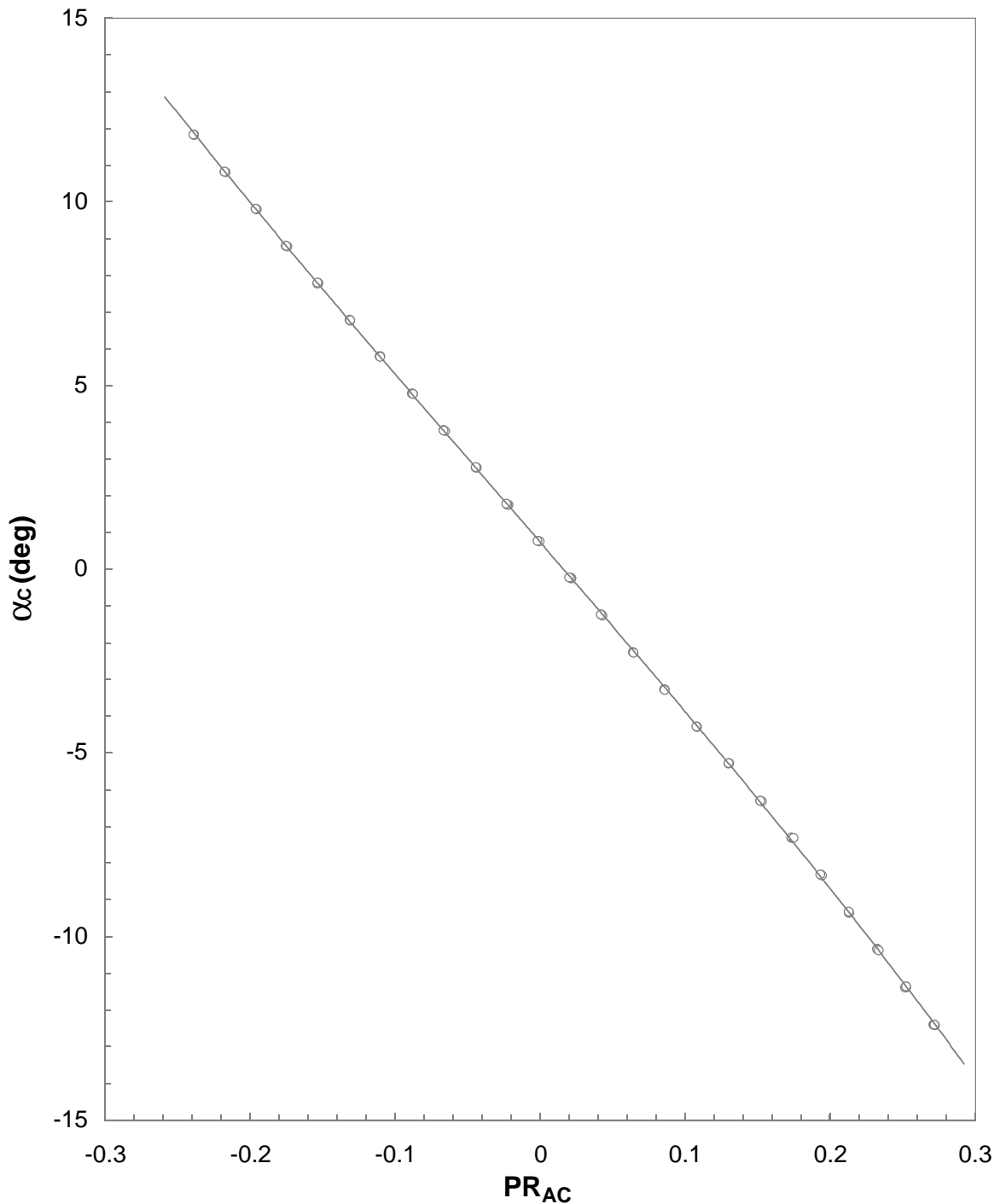
Probe 1
Mset = 2.40, Nominal $\beta_C = 0^\circ$

Figure 54. Cone-probe angle of attack variation for rake 1 at $M_{\text{set}} = 2.40$.



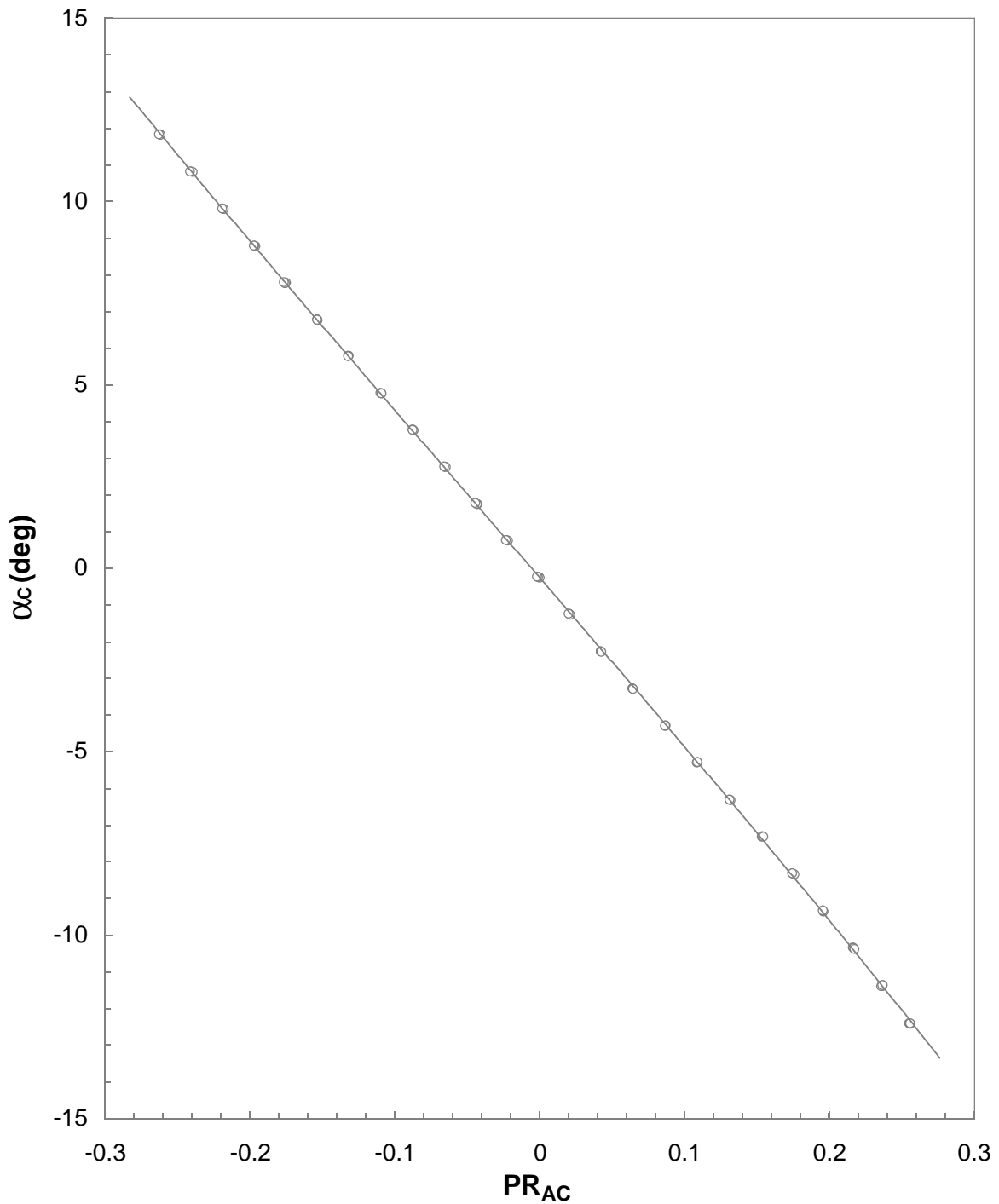
Probe 2
Mset = 2.40, Nominal $\beta_C = 0^\circ$

Figure 54. Continued.



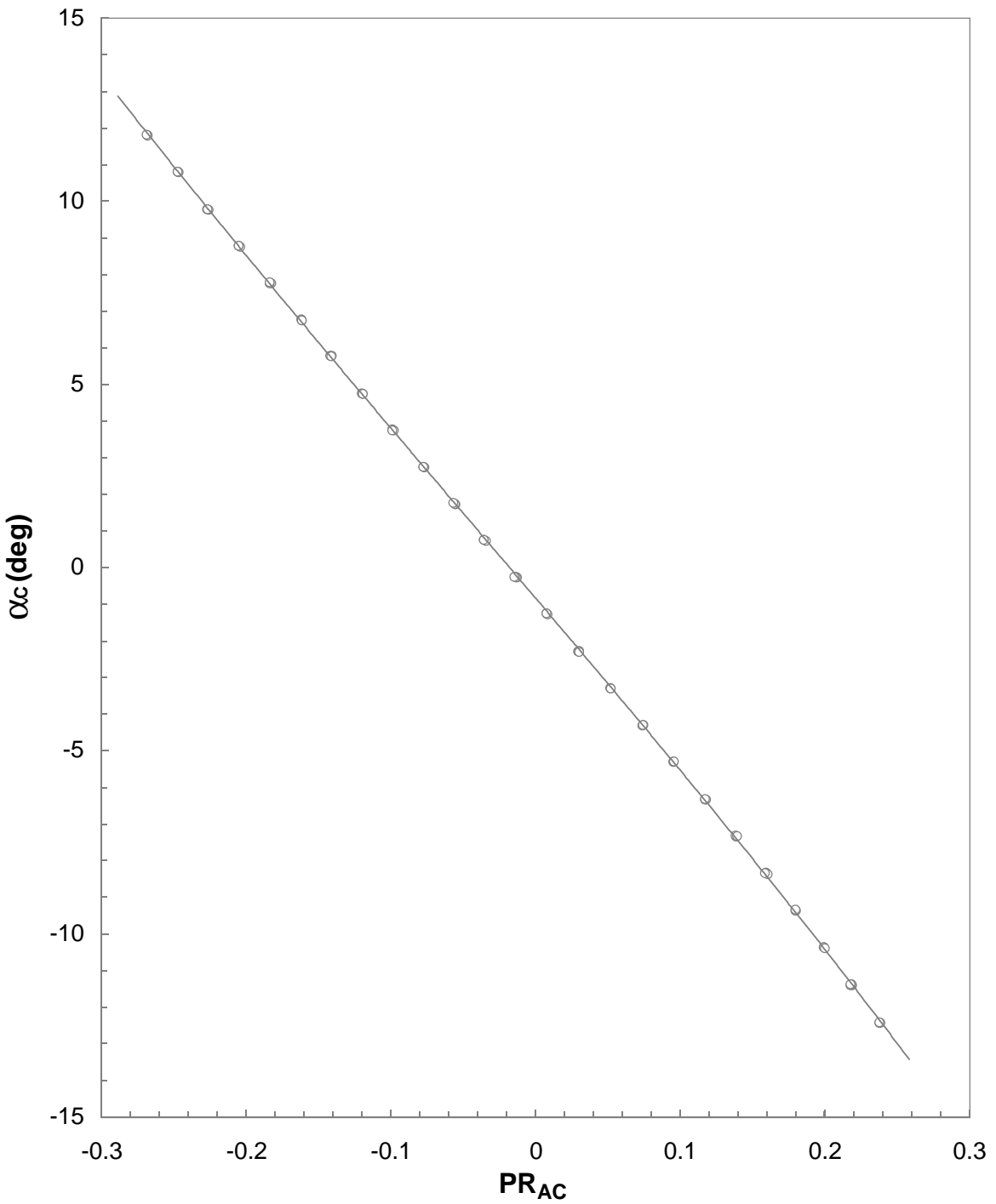
Probe 3
Mset = 2.40, Nominal $\beta_C = 0^\circ$

Figure 54. Continued.



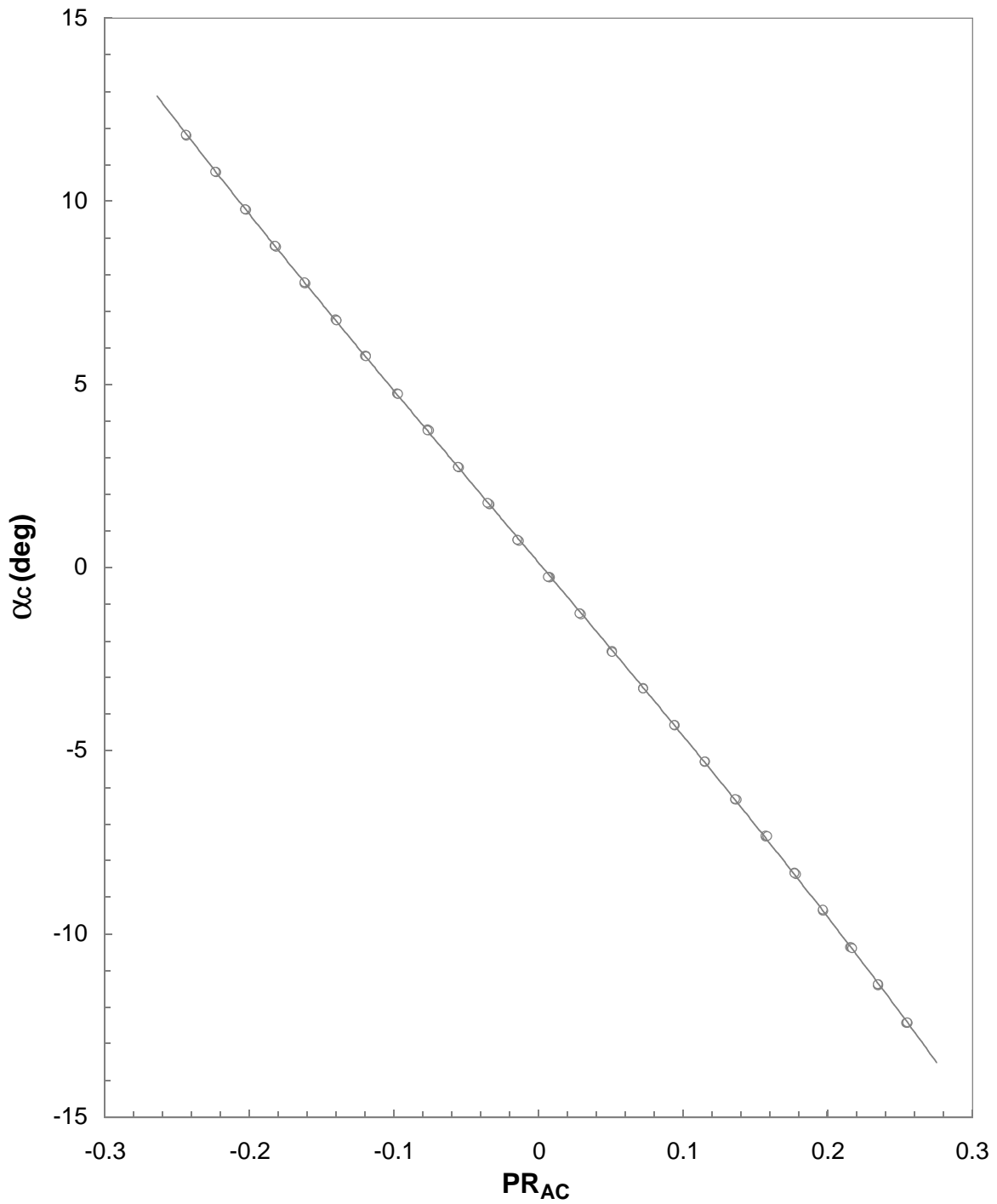
Probe 4
Mset = 2.40, Nominal $\beta_C = 0^\circ$

Figure 54. Continued.



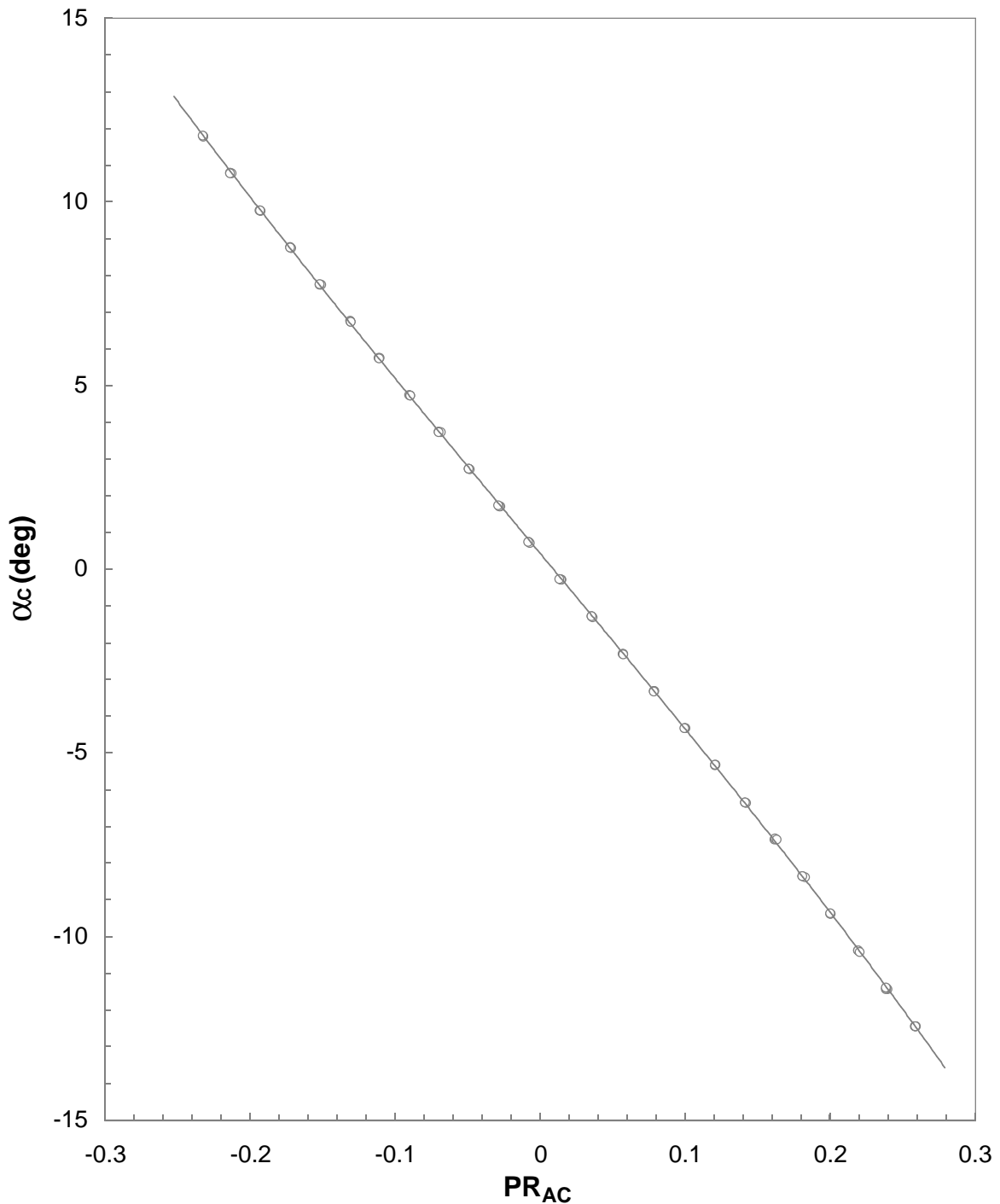
Probe 5
Mset = 2.40, Nominal $\beta_C = 0^\circ$

Figure 54. Continued.



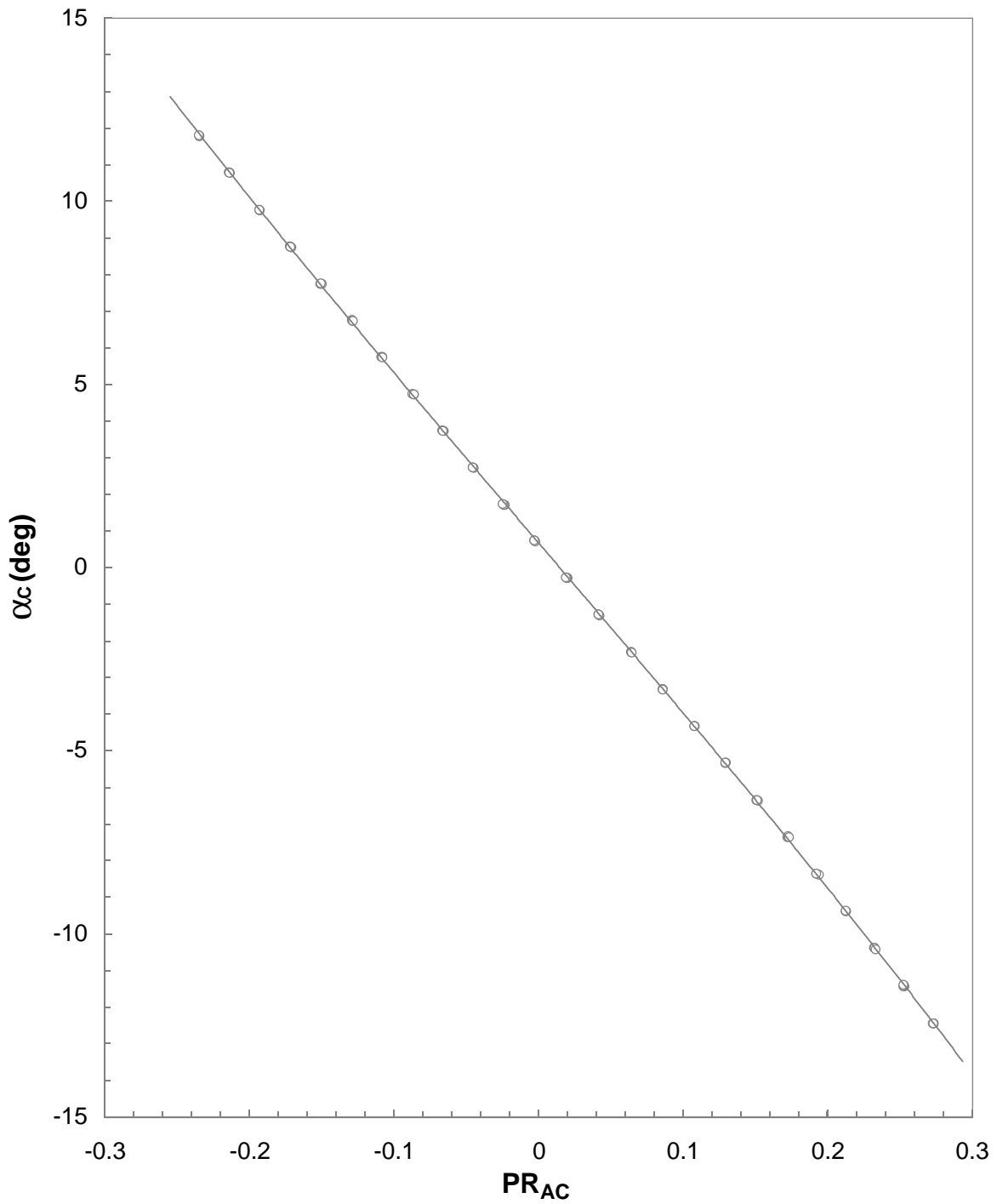
Probe 6
Mset = 2.40, Nominal $\beta_C = 0^\circ$

Figure 54. Continued.



Probe 7
Mset = 2.40, Nominal $\beta_C = 0^\circ$

Figure 54. Continued.



Probe 8
Mset = 2.40, Nominal $\beta_C = 0^\circ$

Figure 54. Concluded.

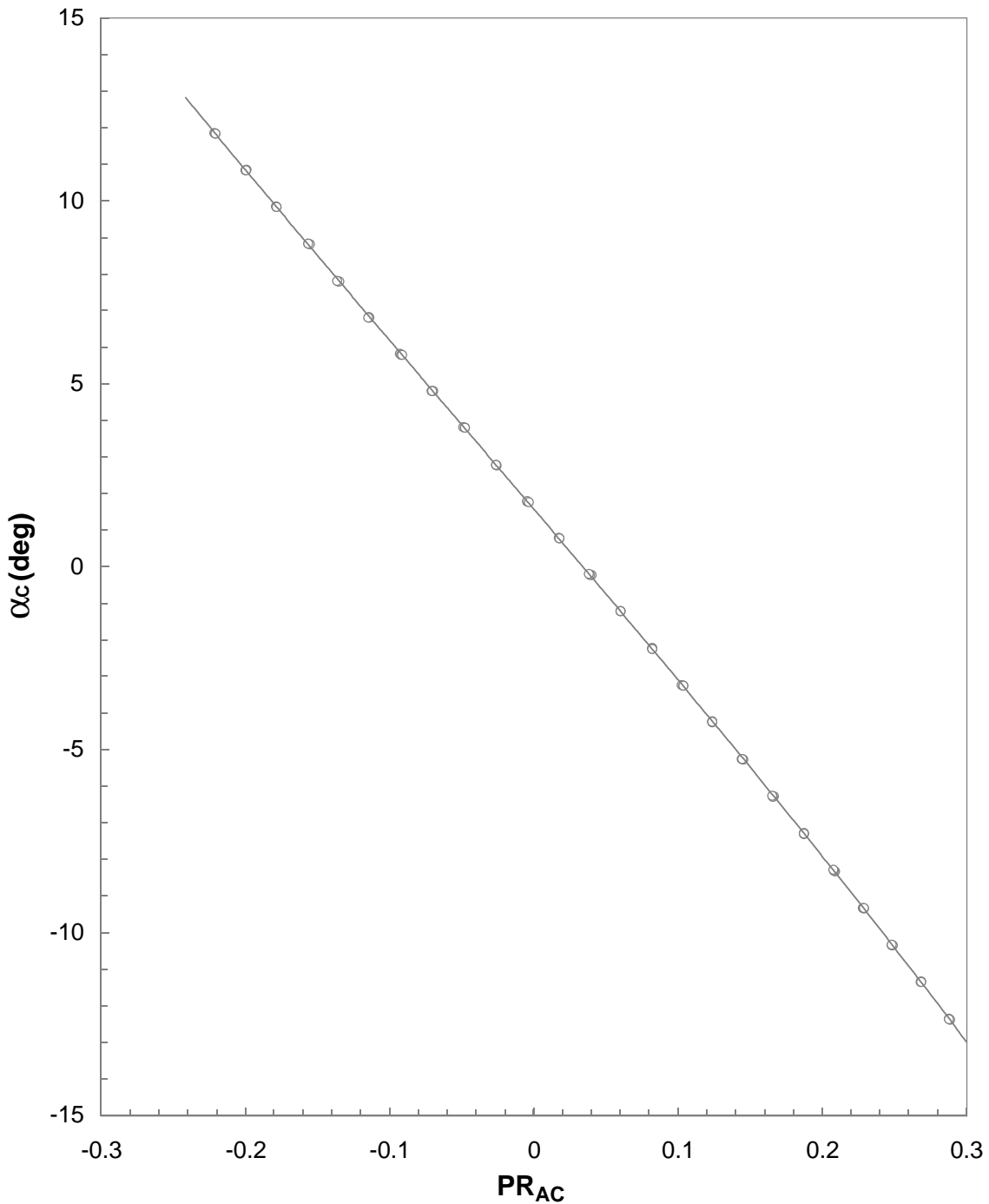
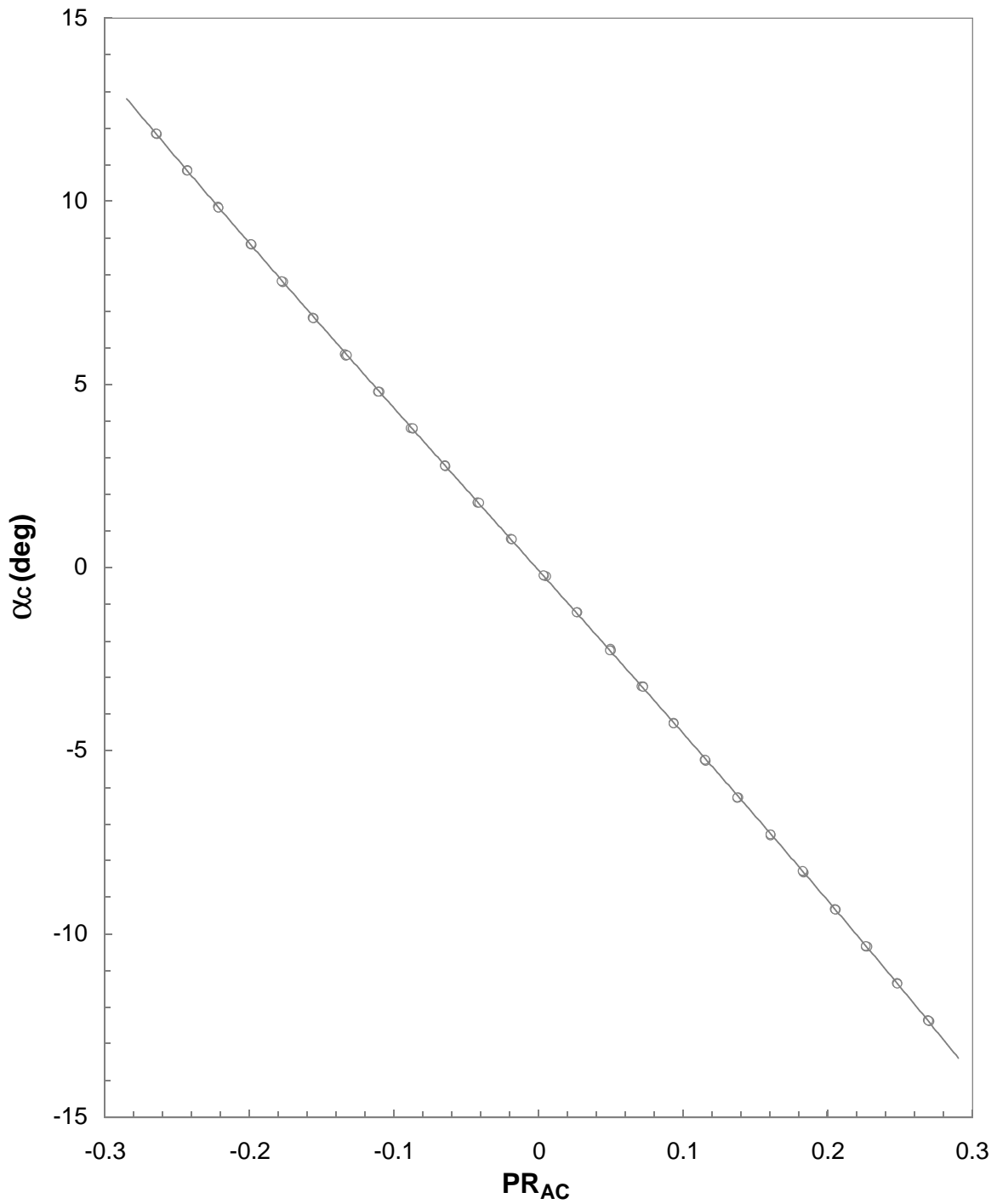
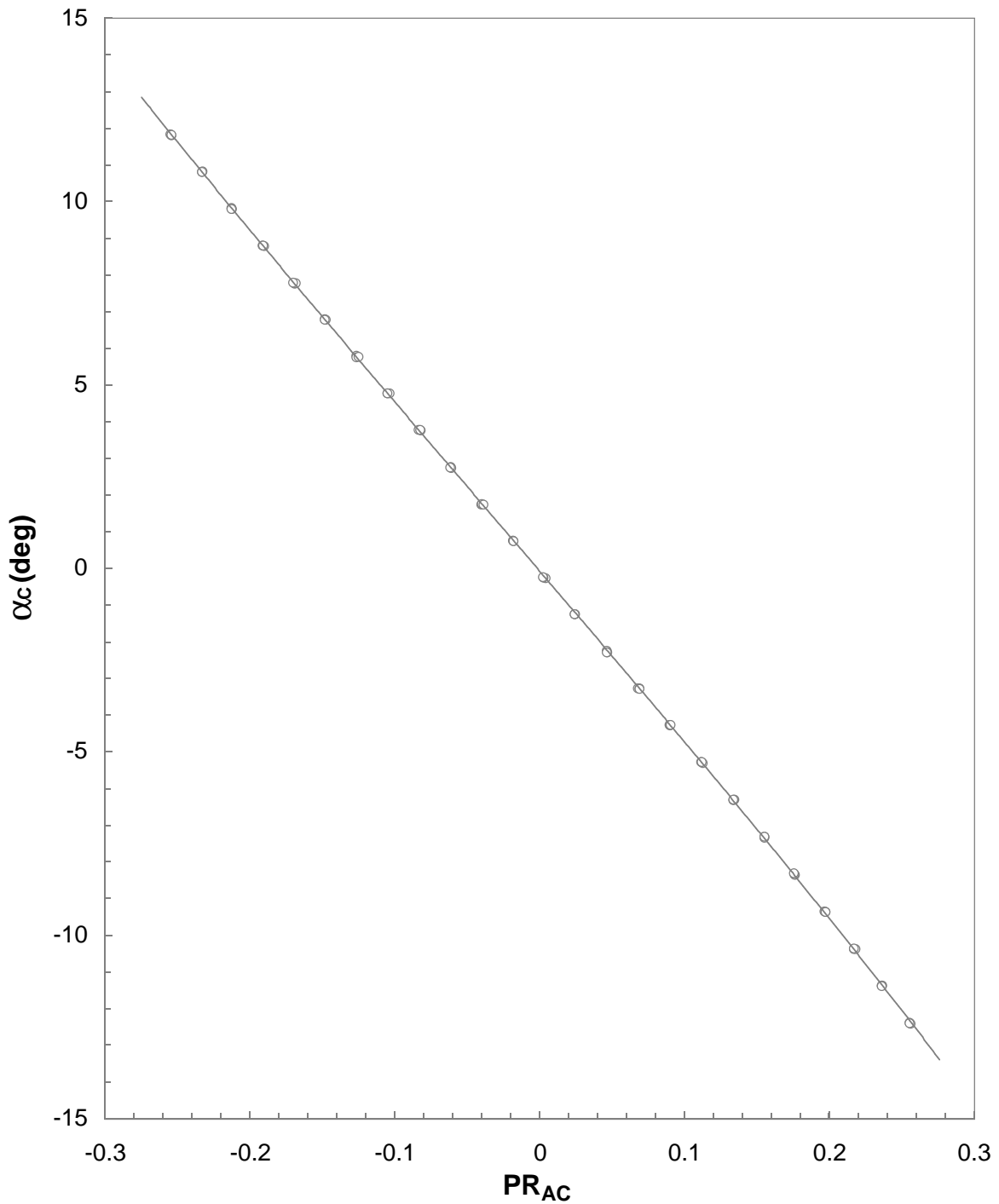


Figure 55. Cone-probe angle of attack variation for rake 2 at $M_{set} = 2.40$.



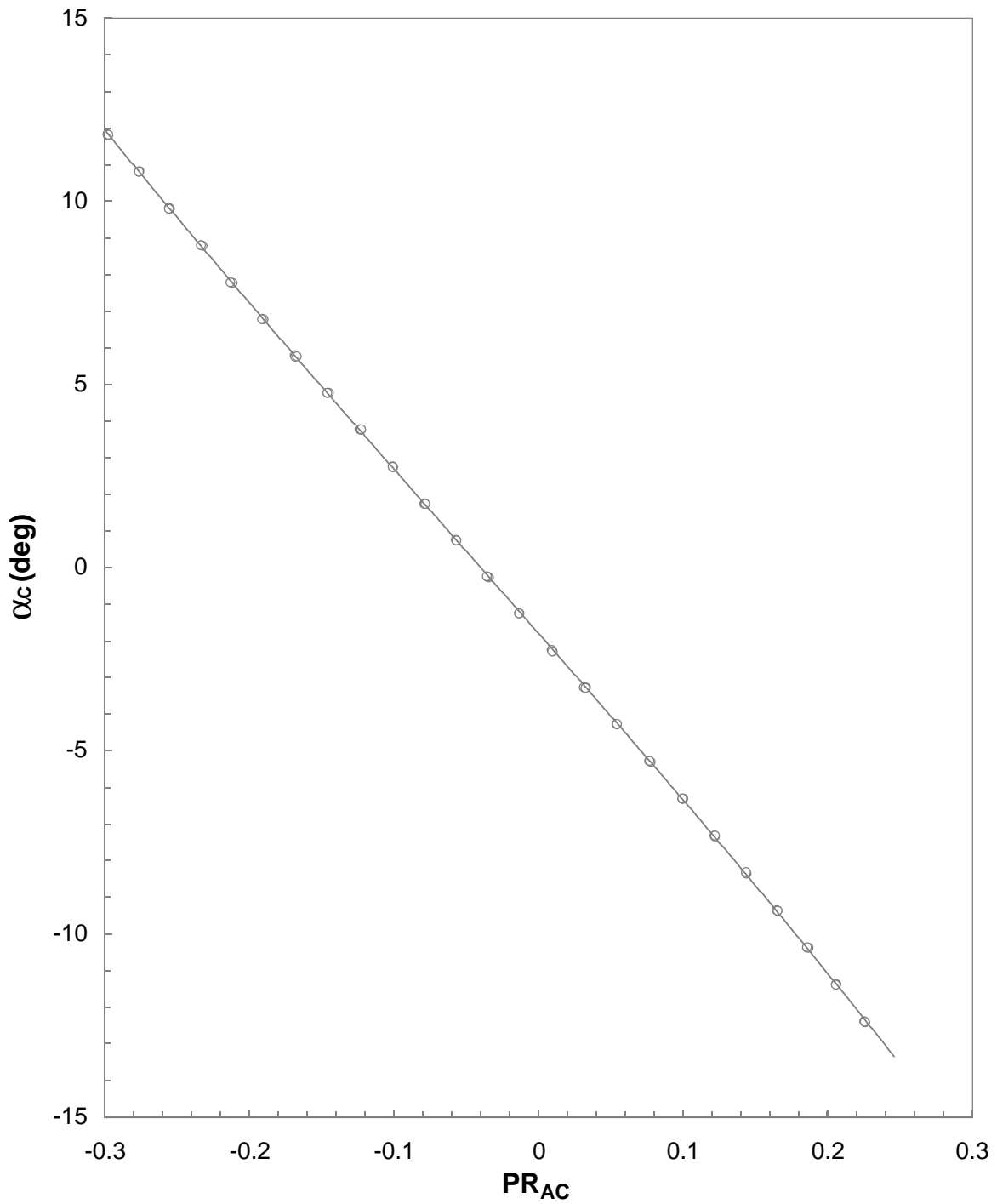
Probe 2
Mset = 2.40, Nominal $\beta_C = 0^\circ$

Figure 55. Continued.



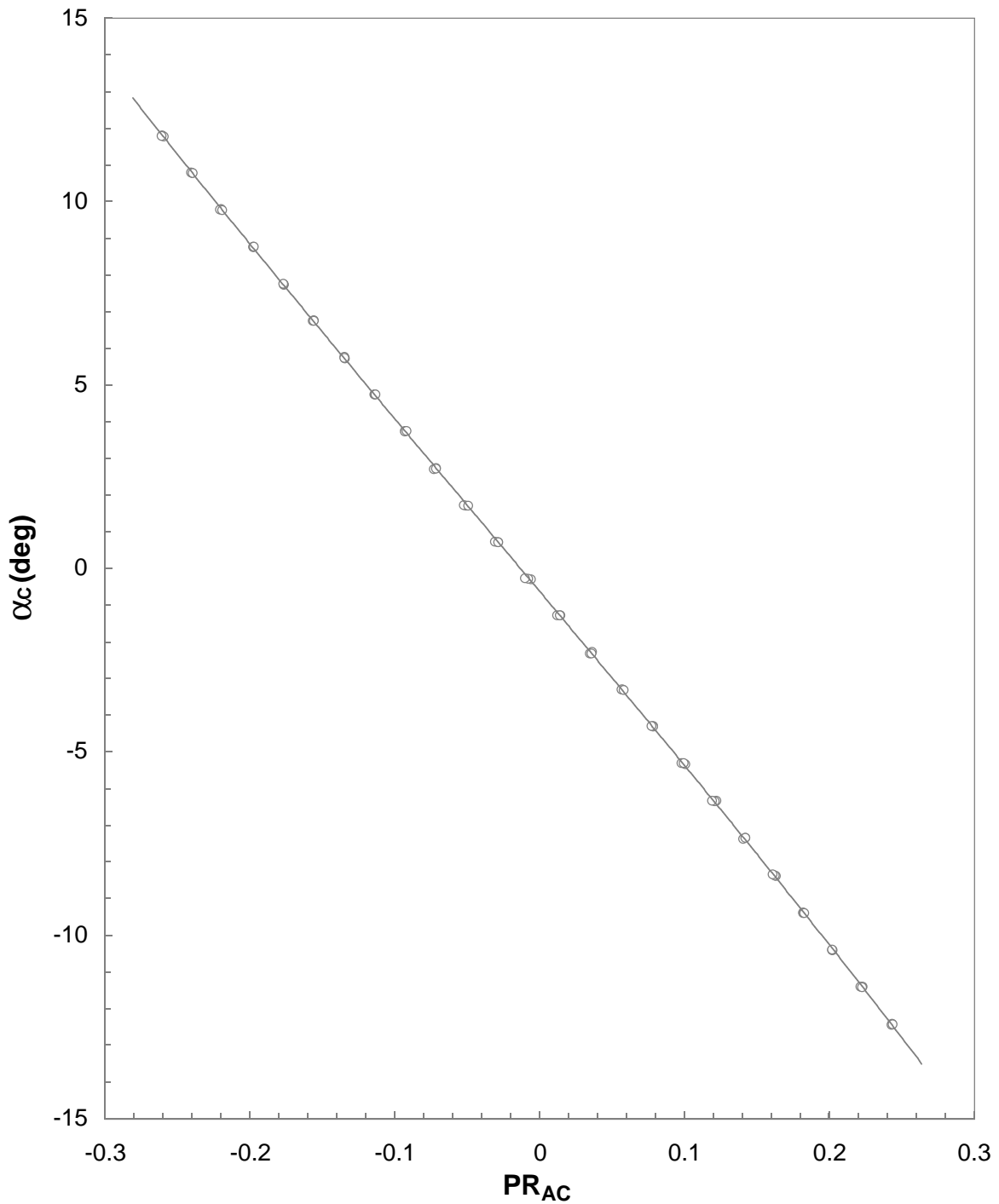
Probe 3
Mset = 2.40, Nominal $\beta_C = 0^\circ$

Figure 55. Continued.



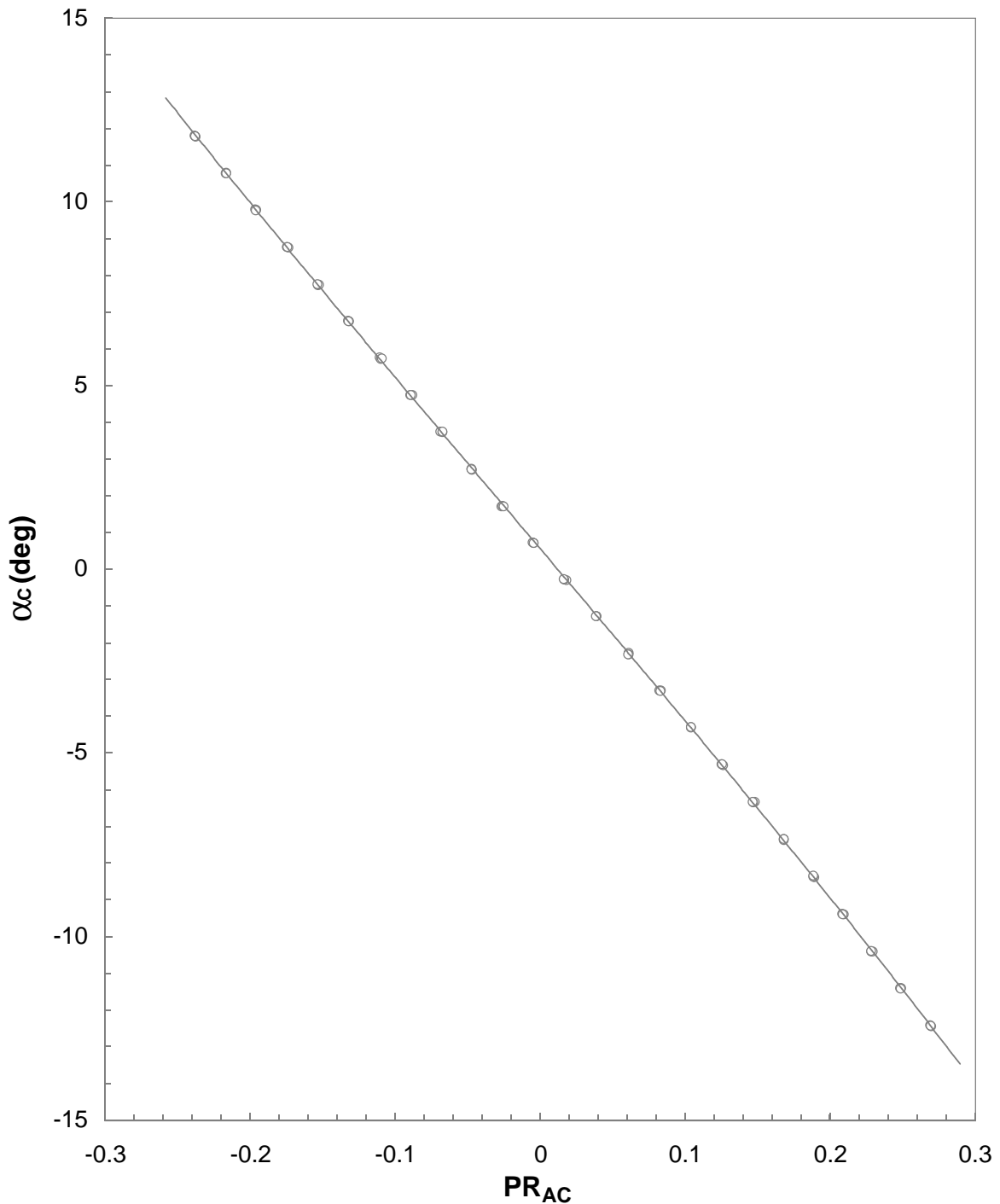
Probe 4
Mset = 2.40, Nominal $\beta_C = 0^\circ$

Figure 55. Continued.



Probe 5
Mset = 2.40, Nominal $\beta_C = 0^\circ$

Figure 55. Continued.



Probe 6
Mset = 2.40, Nominal $\beta_C = 0^\circ$

Figure 55. Concluded.

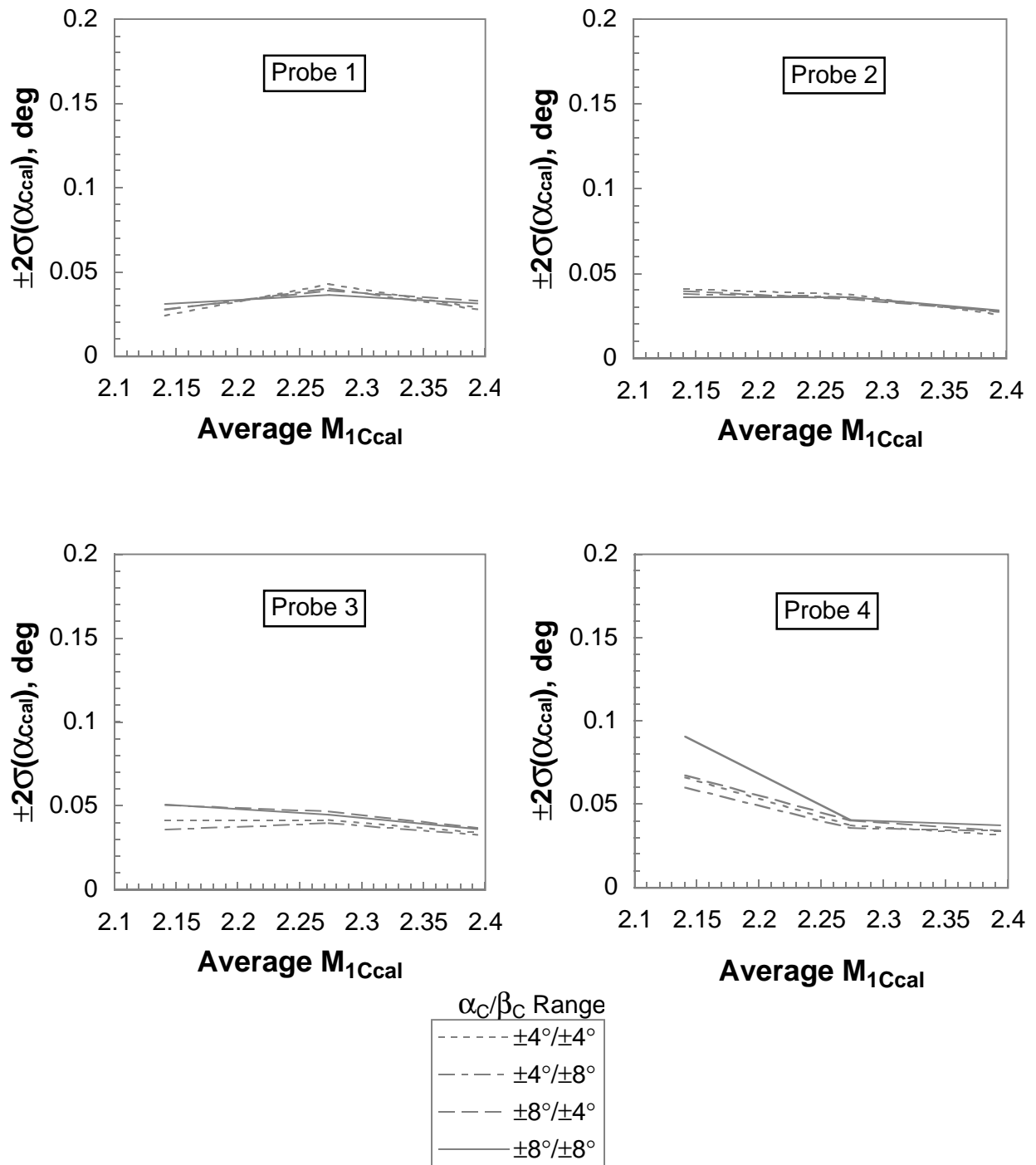


Figure 56. Angle of attack correlation residual for rake 1.

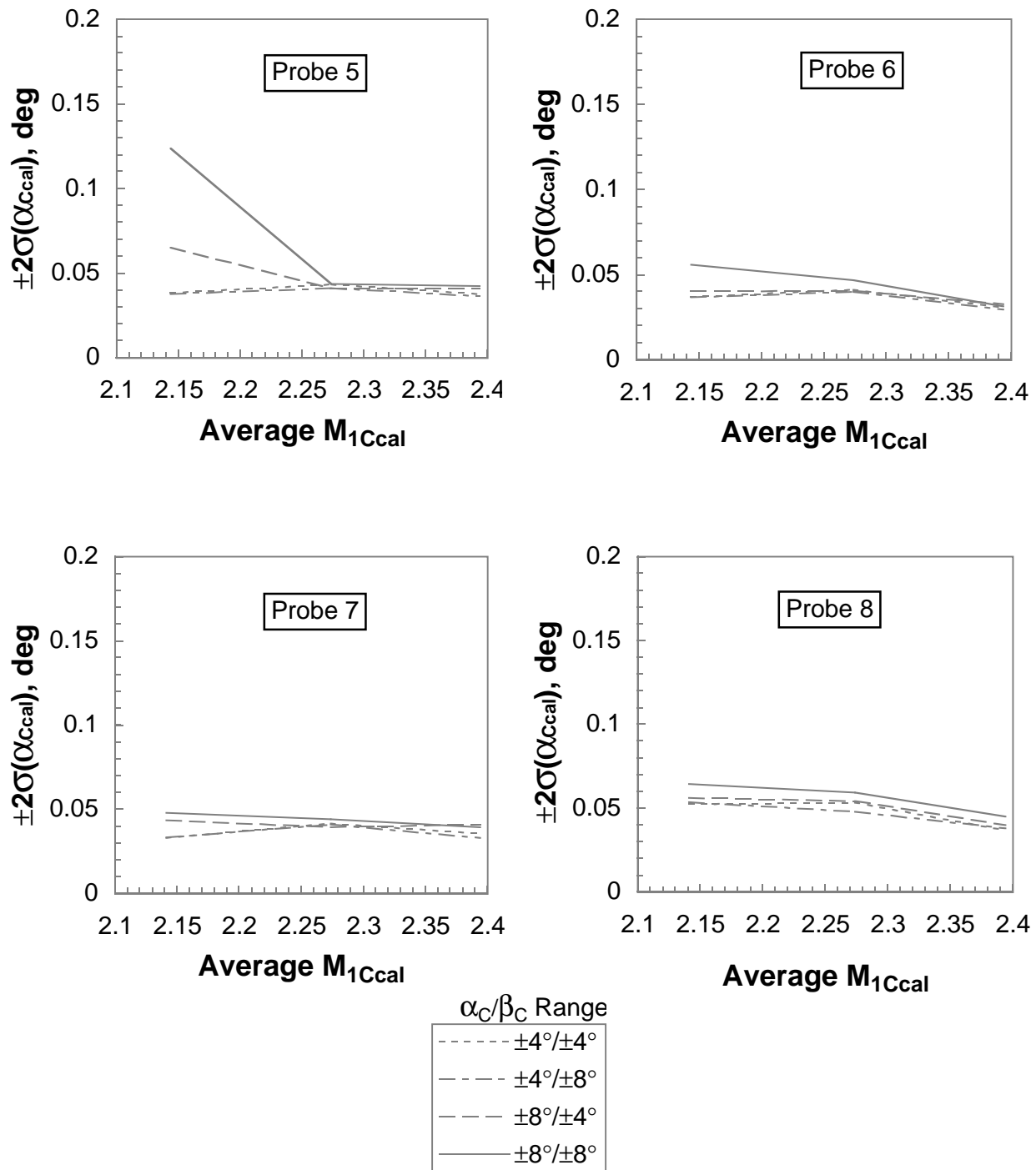


Figure 56. Concluded.

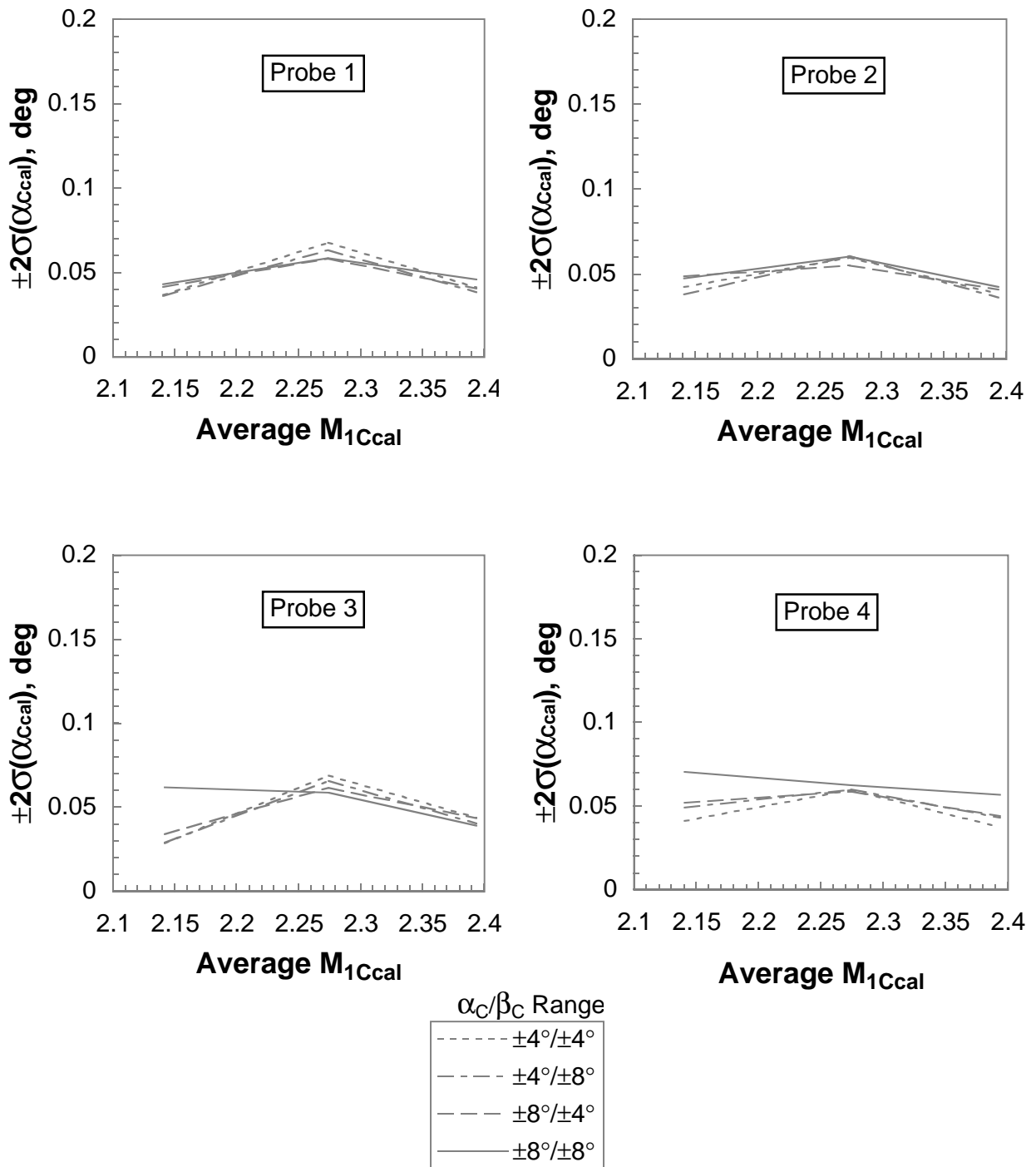


Figure 57. Angle of attack correlation residual for rake 2.

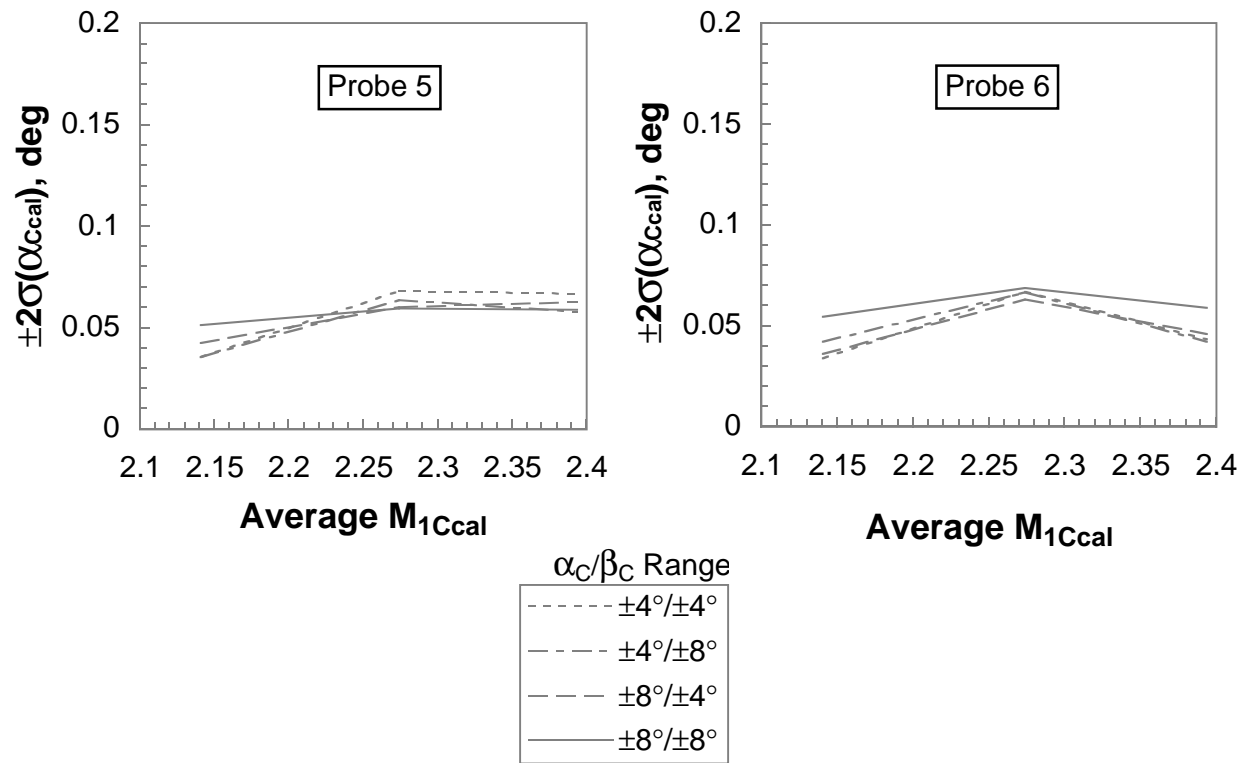
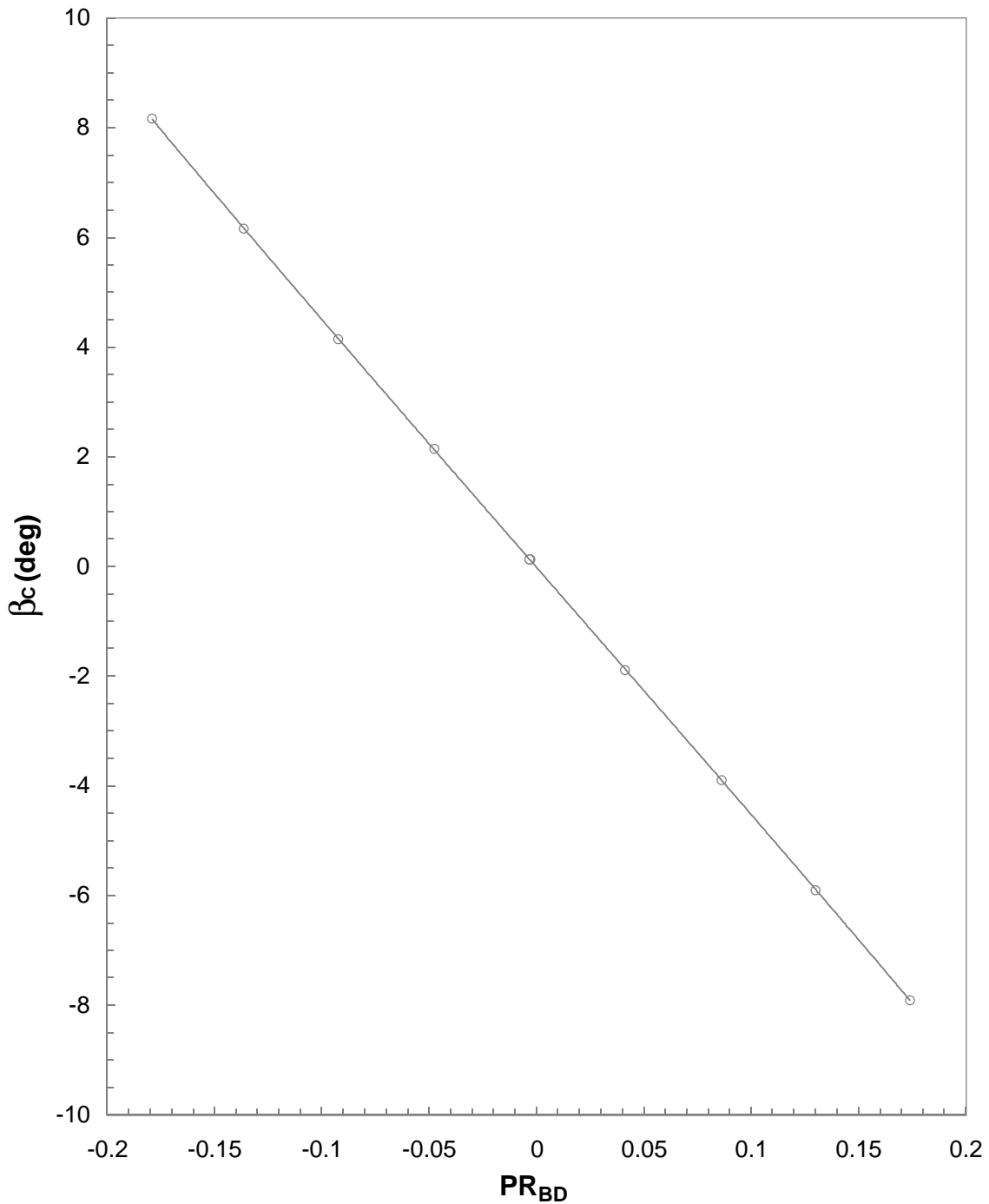
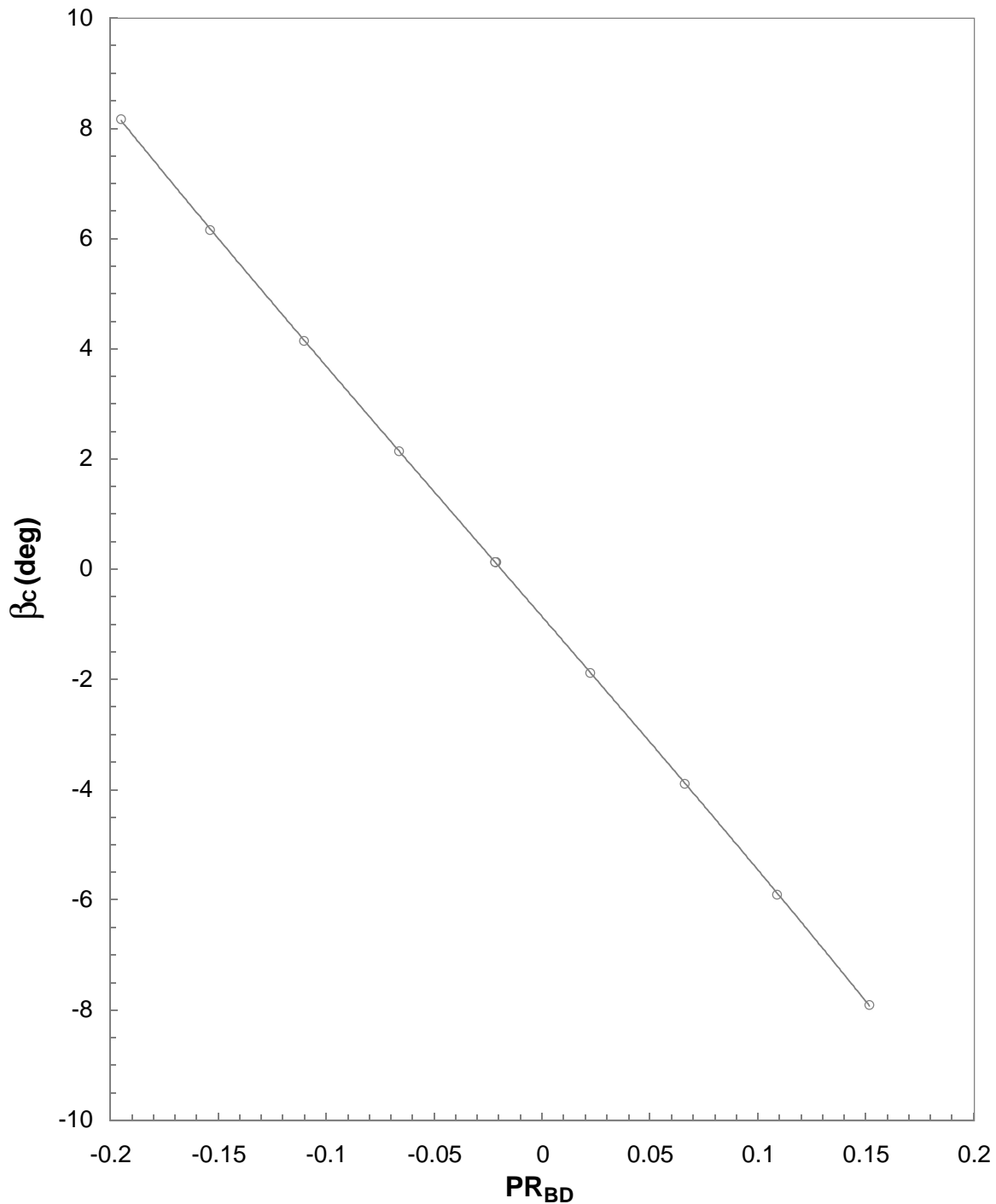


Figure 57. Concluded.



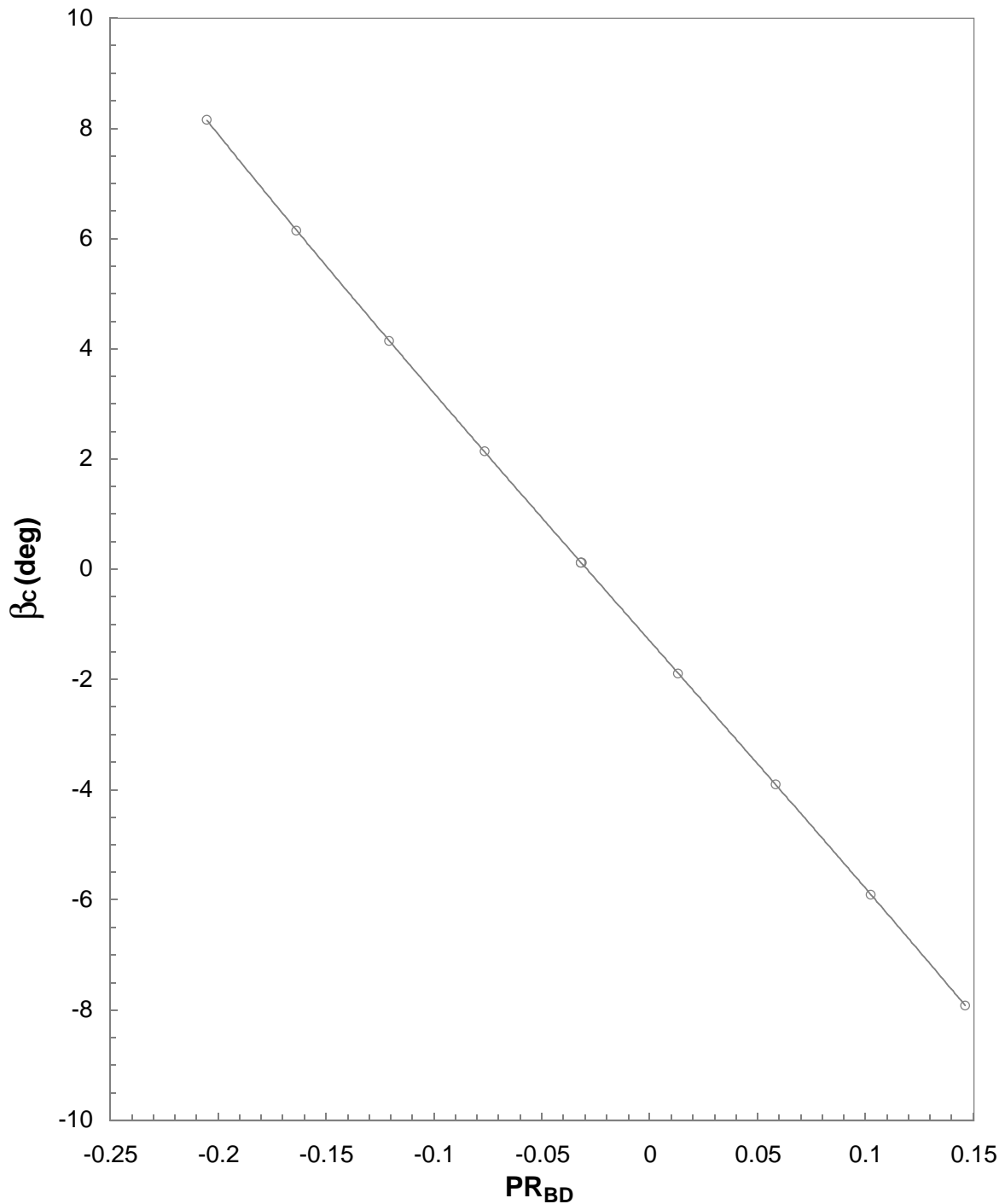
Probe 1
Mset = 2.40, Nominal $\alpha_C = 0^\circ$

Figure 58. Cone-probe angle of sideslip variation for rake 1 at $M_{\text{set}} = 2.40$.



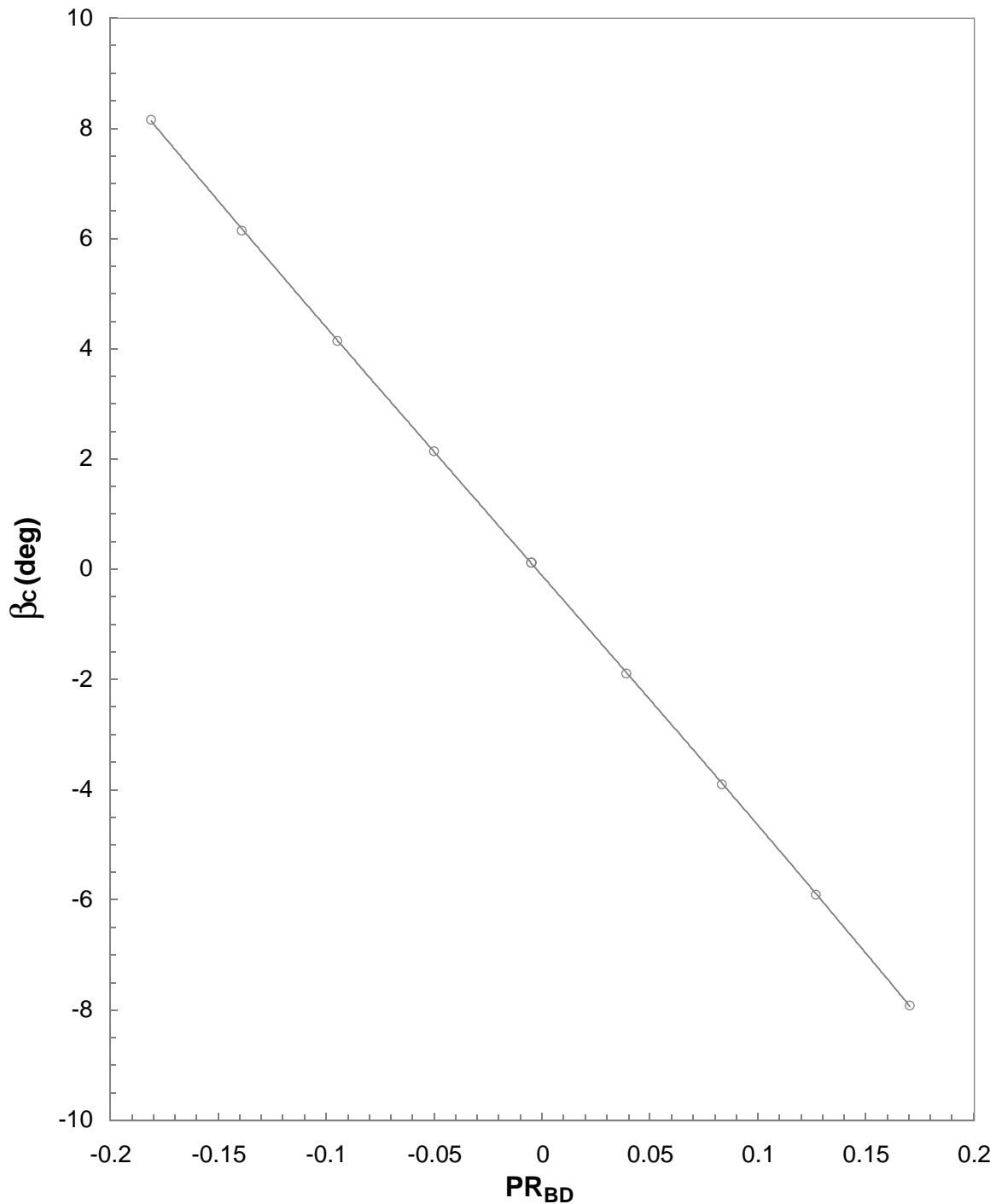
Probe 2
Mset = 2.40, Nominal $\alpha_C = 0^\circ$

Figure 58. Continued.



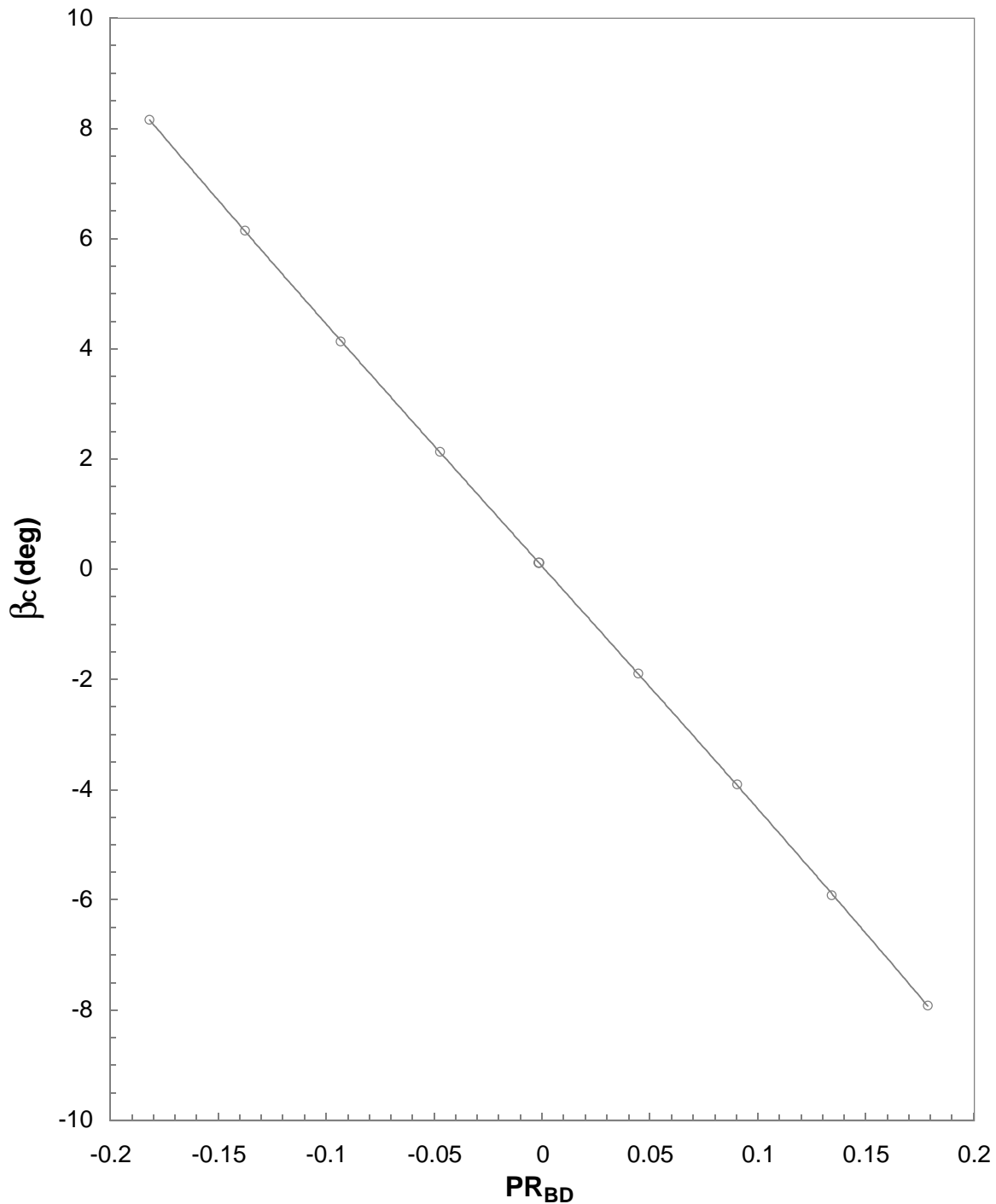
Probe 3
Mset = 2.40, Nominal $\alpha_C = 0^\circ$

Figure 58. Continued.



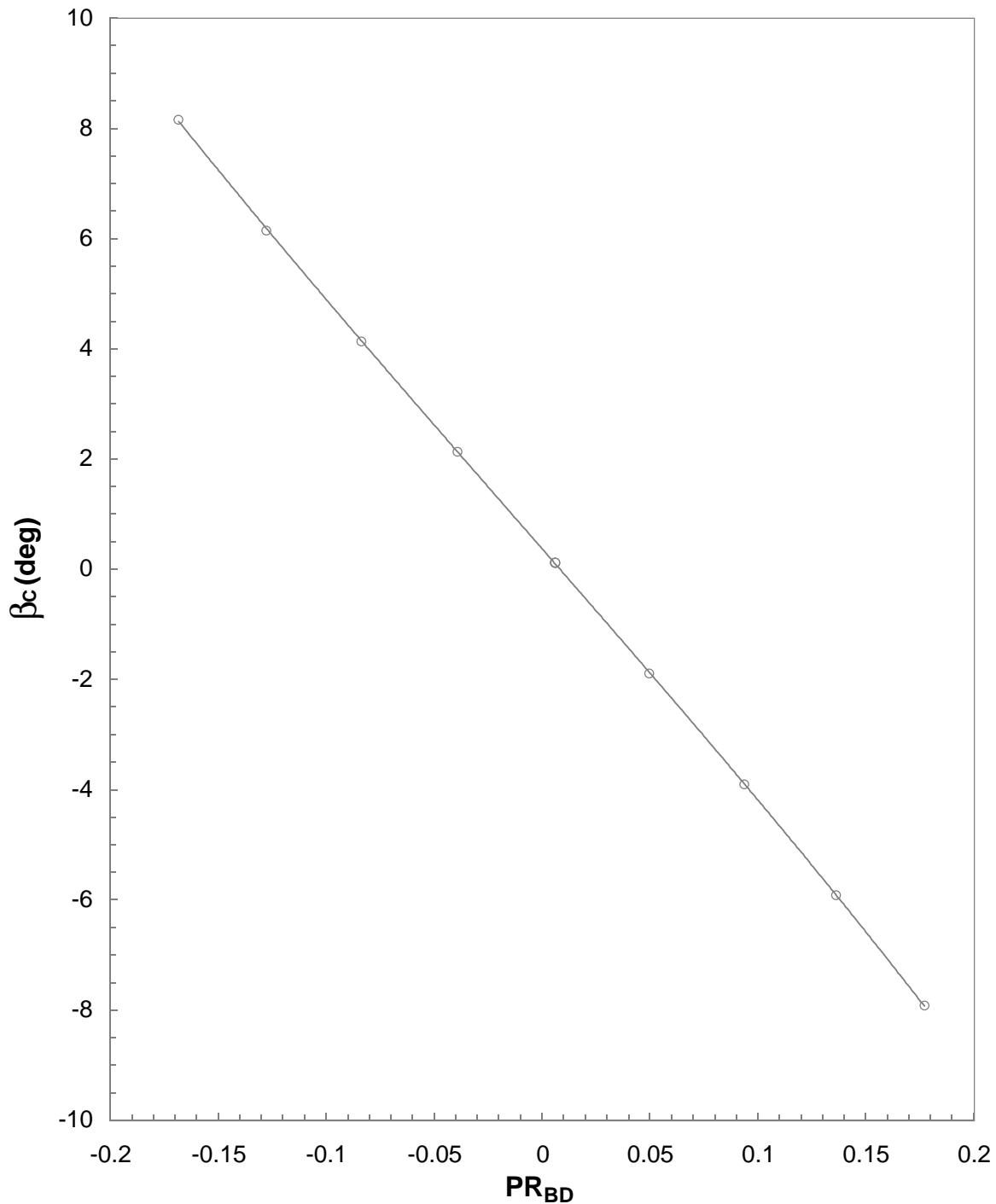
Probe 4
Mset = 2.40, Nominal $\alpha_C = 0^\circ$

Figure 58. Continued.



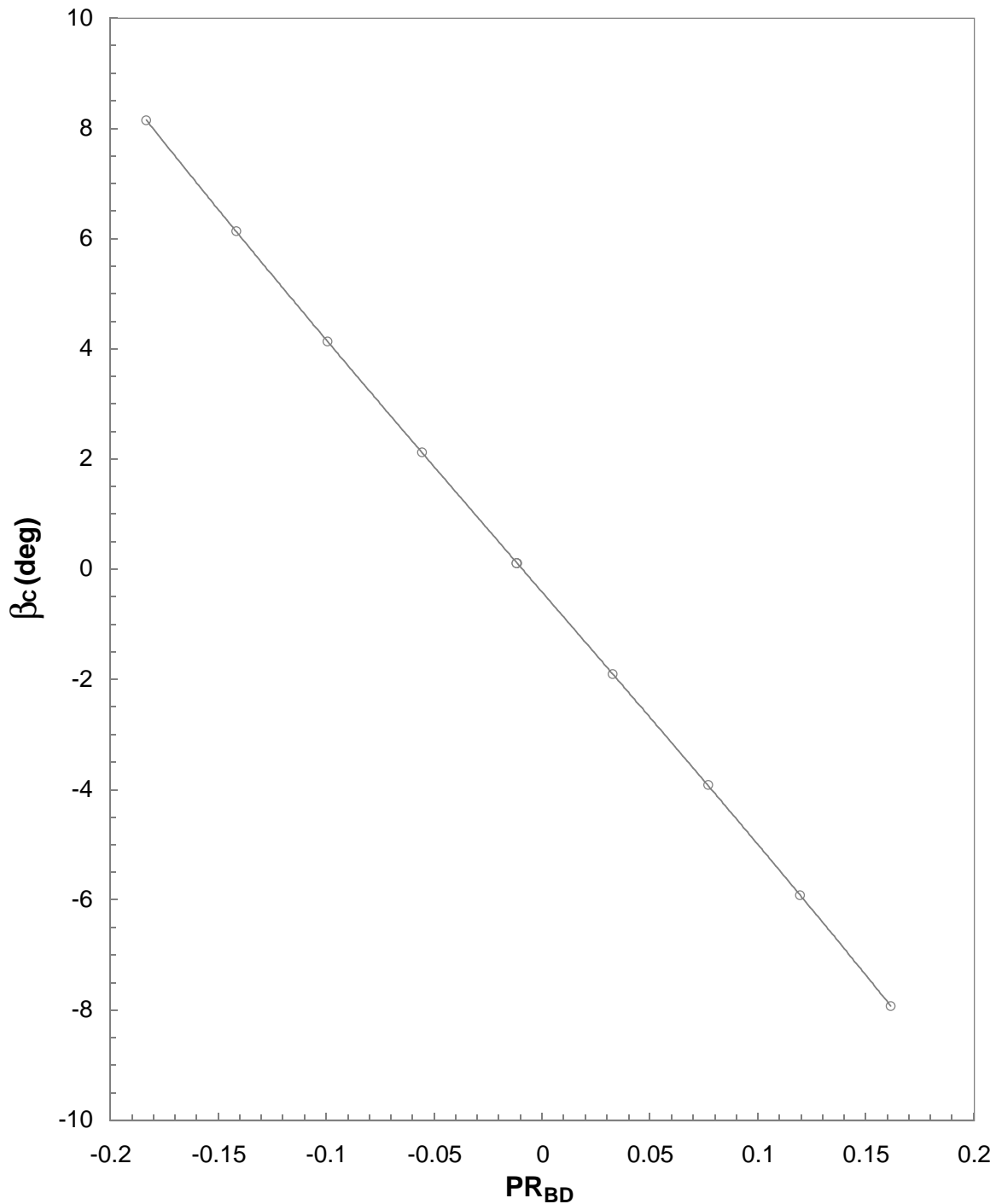
Probe 5
Mset = 2.40, Nominal $\alpha_C = 0^\circ$

Figure 58. Continued.



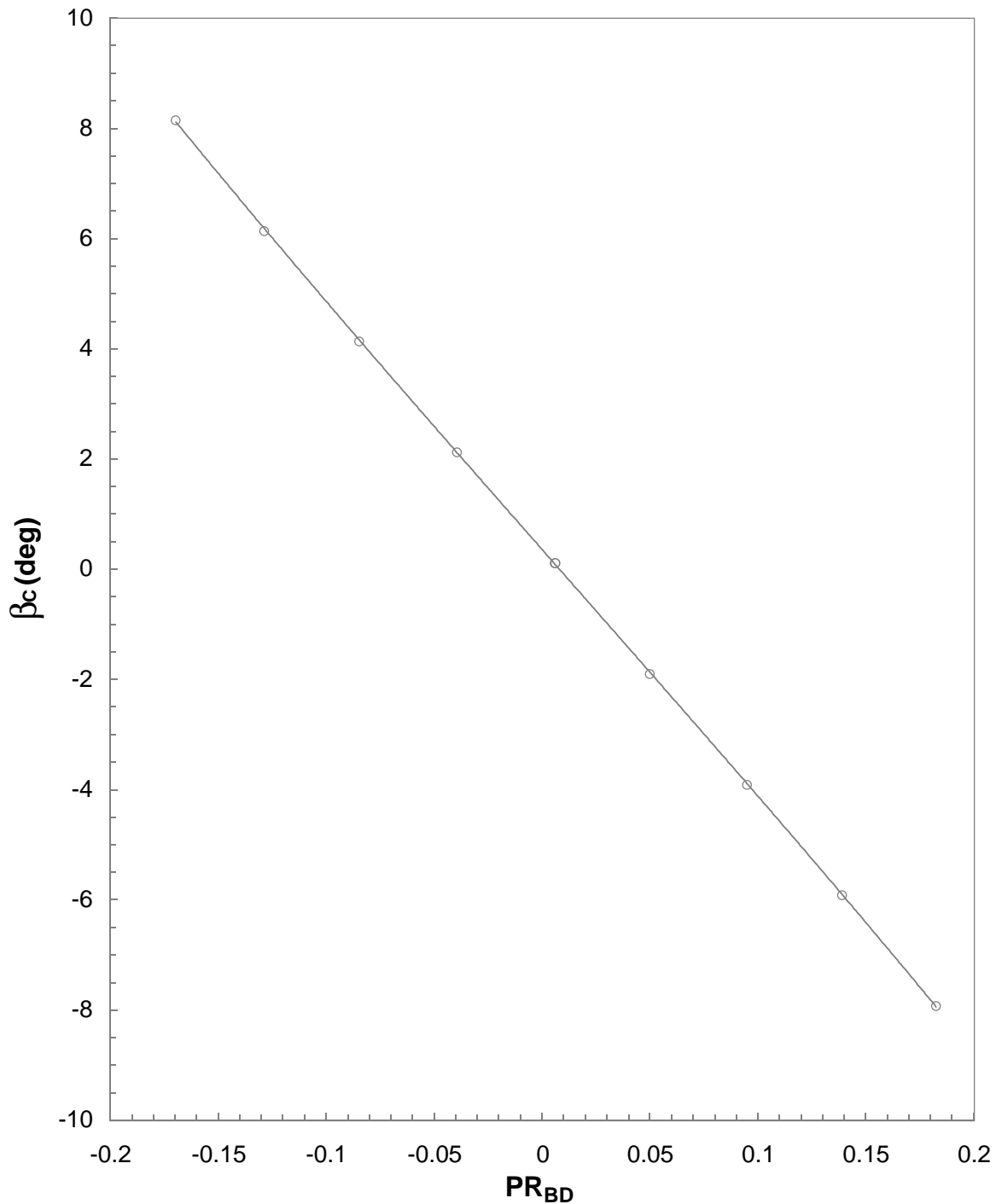
Probe 6
Mset = 2.40, Nominal $\alpha_C = 0^\circ$

Figure 58. Continued.



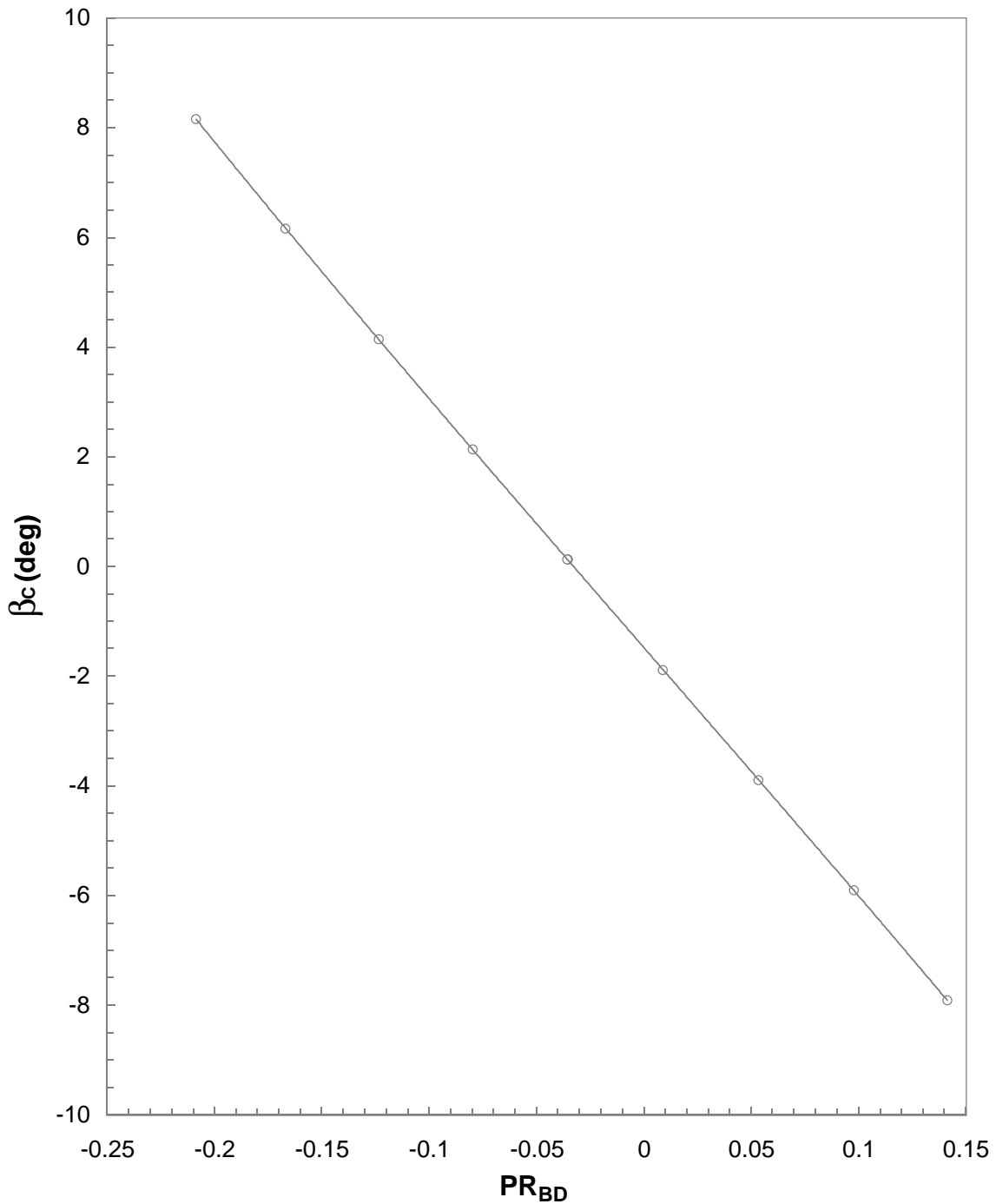
Probe 7
Mset = 2.40, Nominal $\alpha_C = 0^\circ$

Figure 58. Continued.



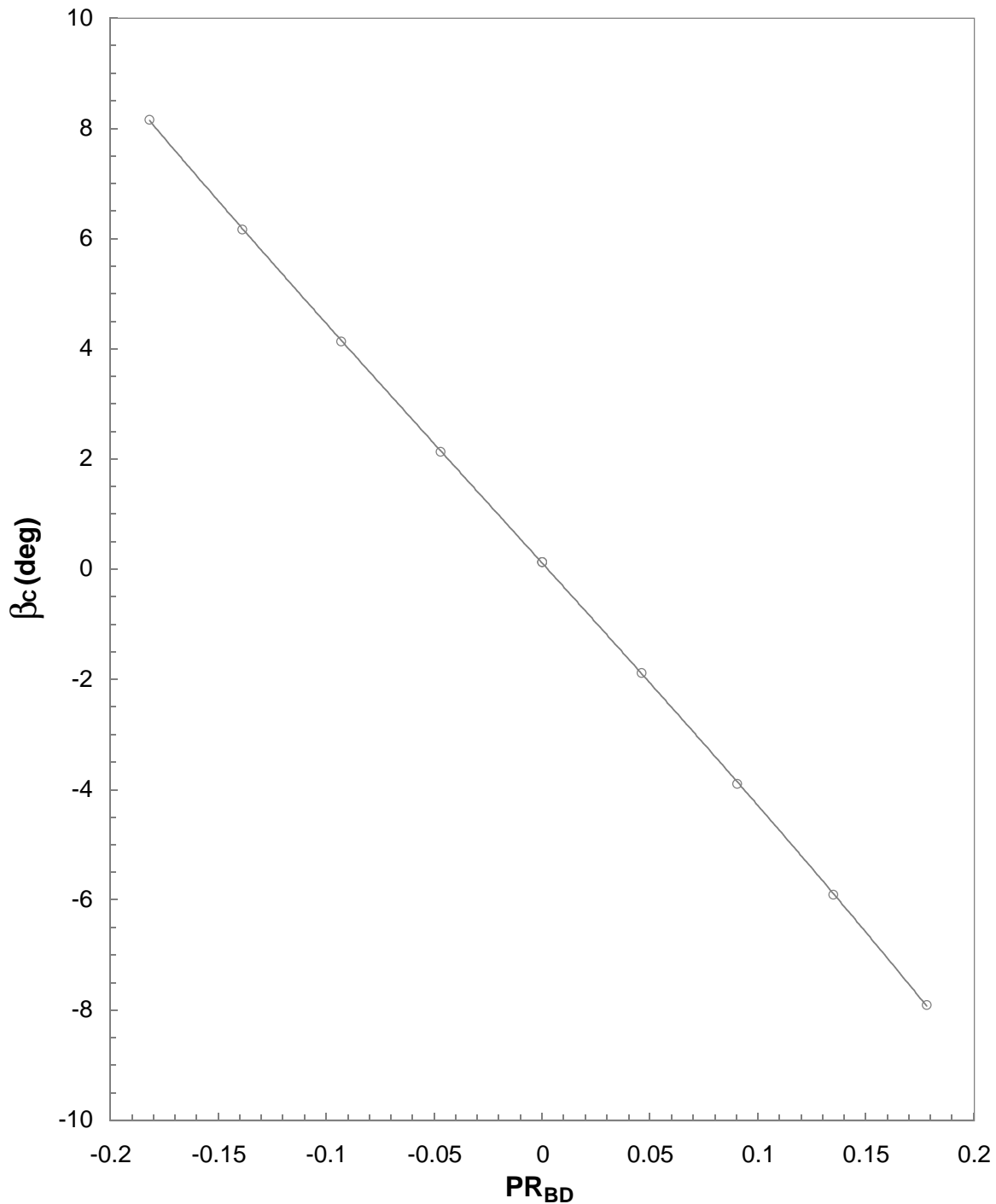
Probe 8
Mset = 2.40, Nominal $\alpha_C = 0^\circ$

Figure 58. Concluded.



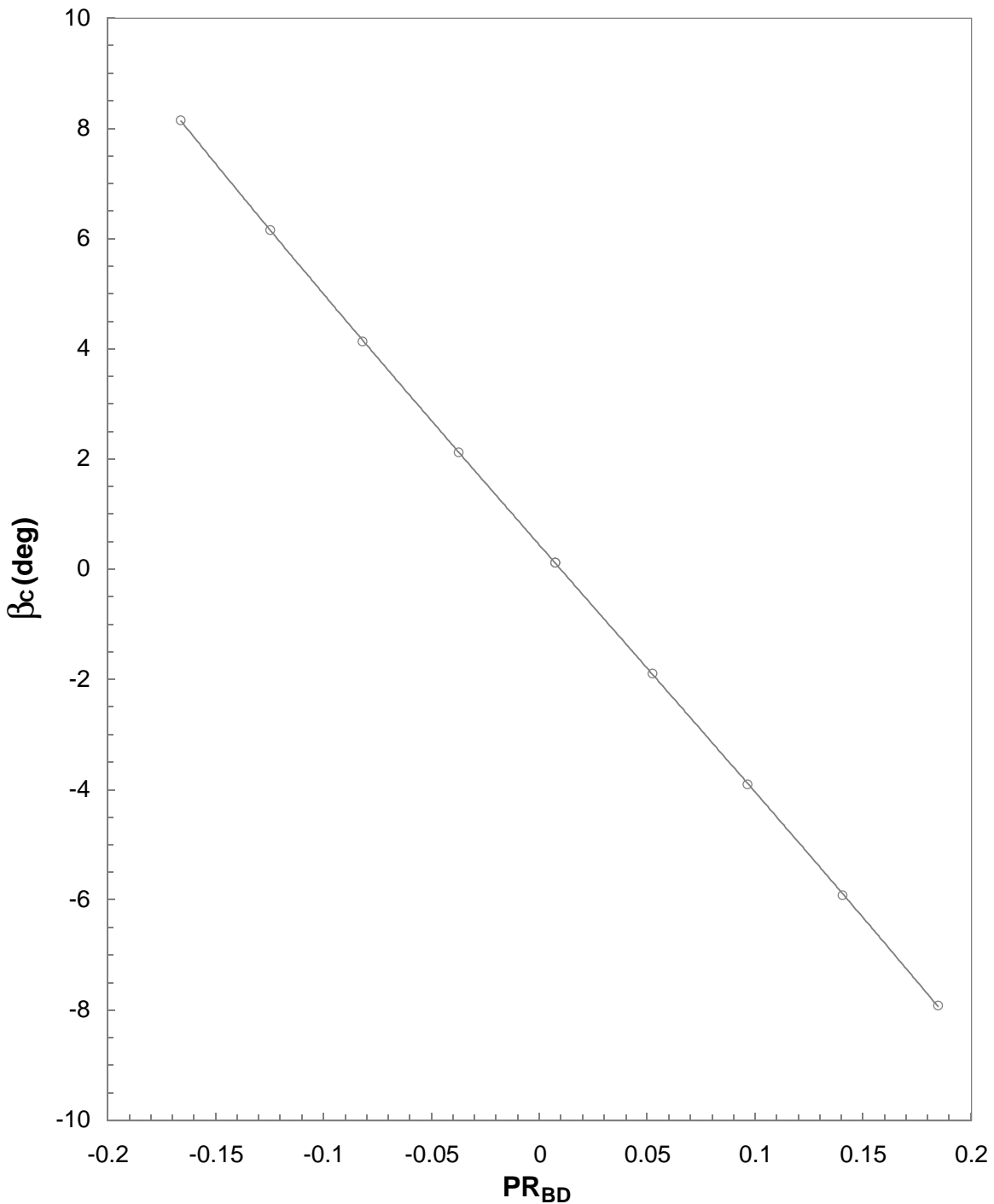
Probe 1
Mset = 2.40, Nominal $\alpha_C = 0^\circ$

Figure 59. Cone-probe angle of sideslip variation for rake 2 at $M_{set} = 2.40$.



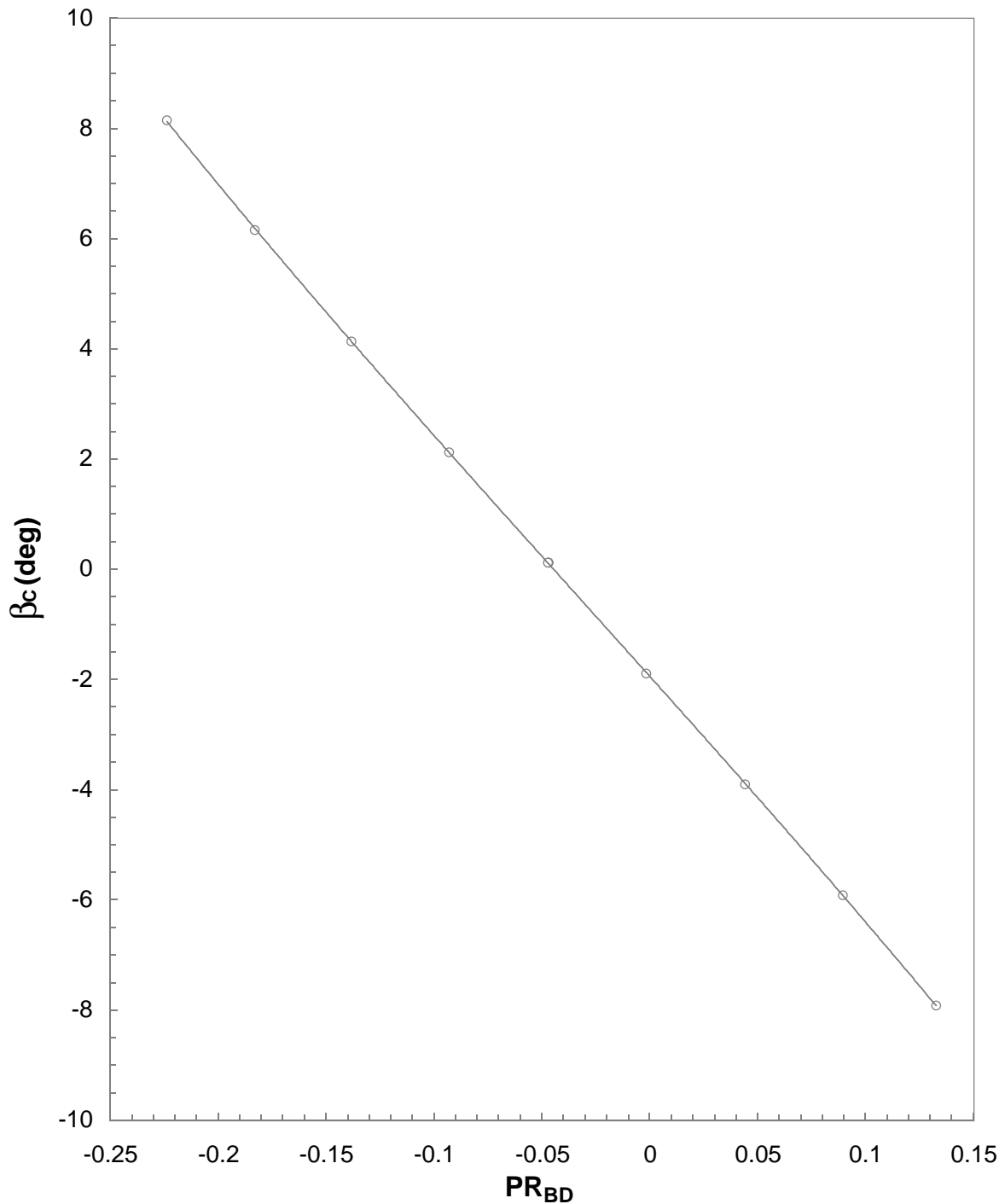
Probe 2
Mset = 2.40, Nominal $\alpha_C = 0^\circ$

Figure 59. Continued.



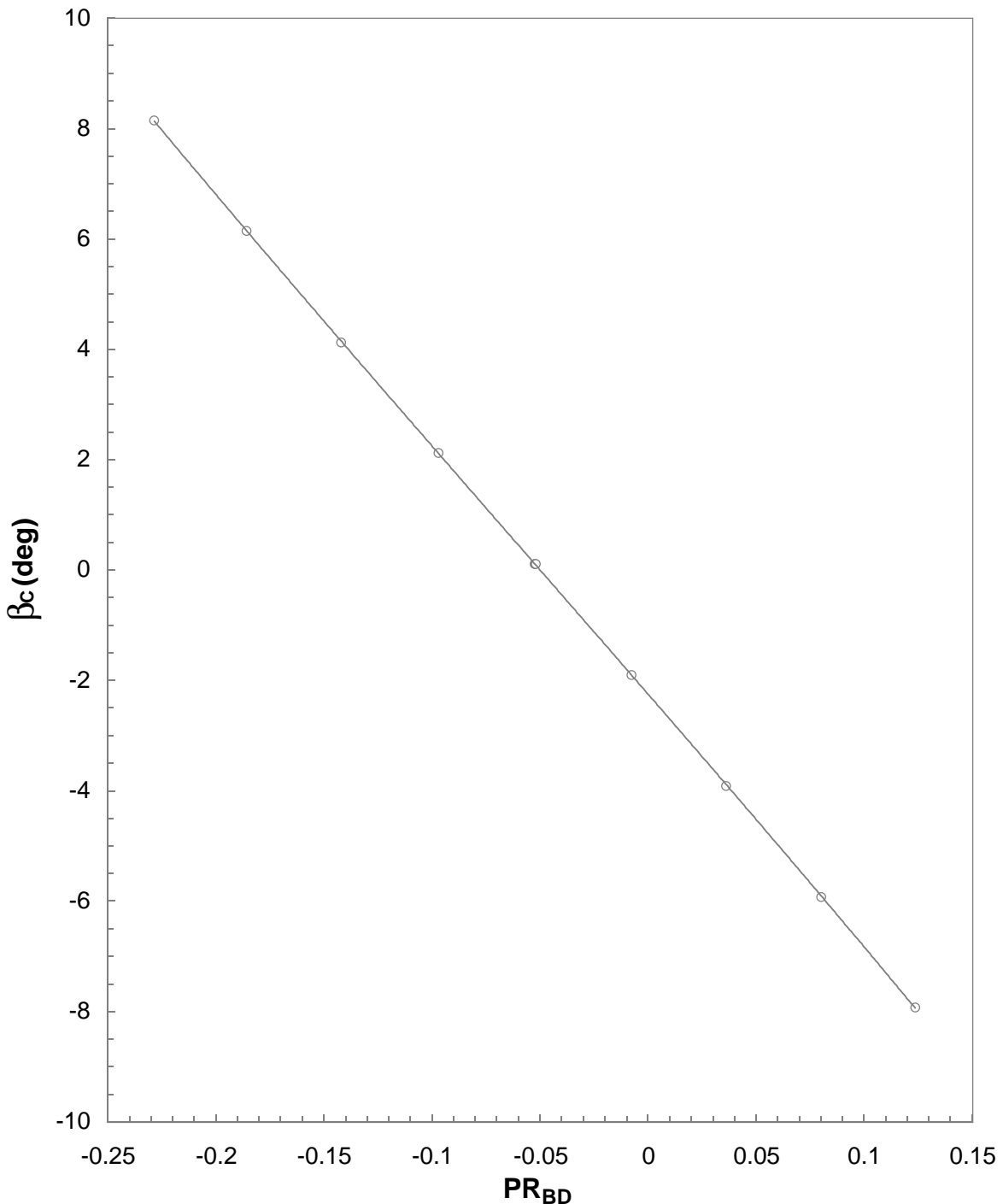
Probe 3
Mset = 2.40, Nominal $\alpha_C = 0^\circ$

Figure 59. Continued.



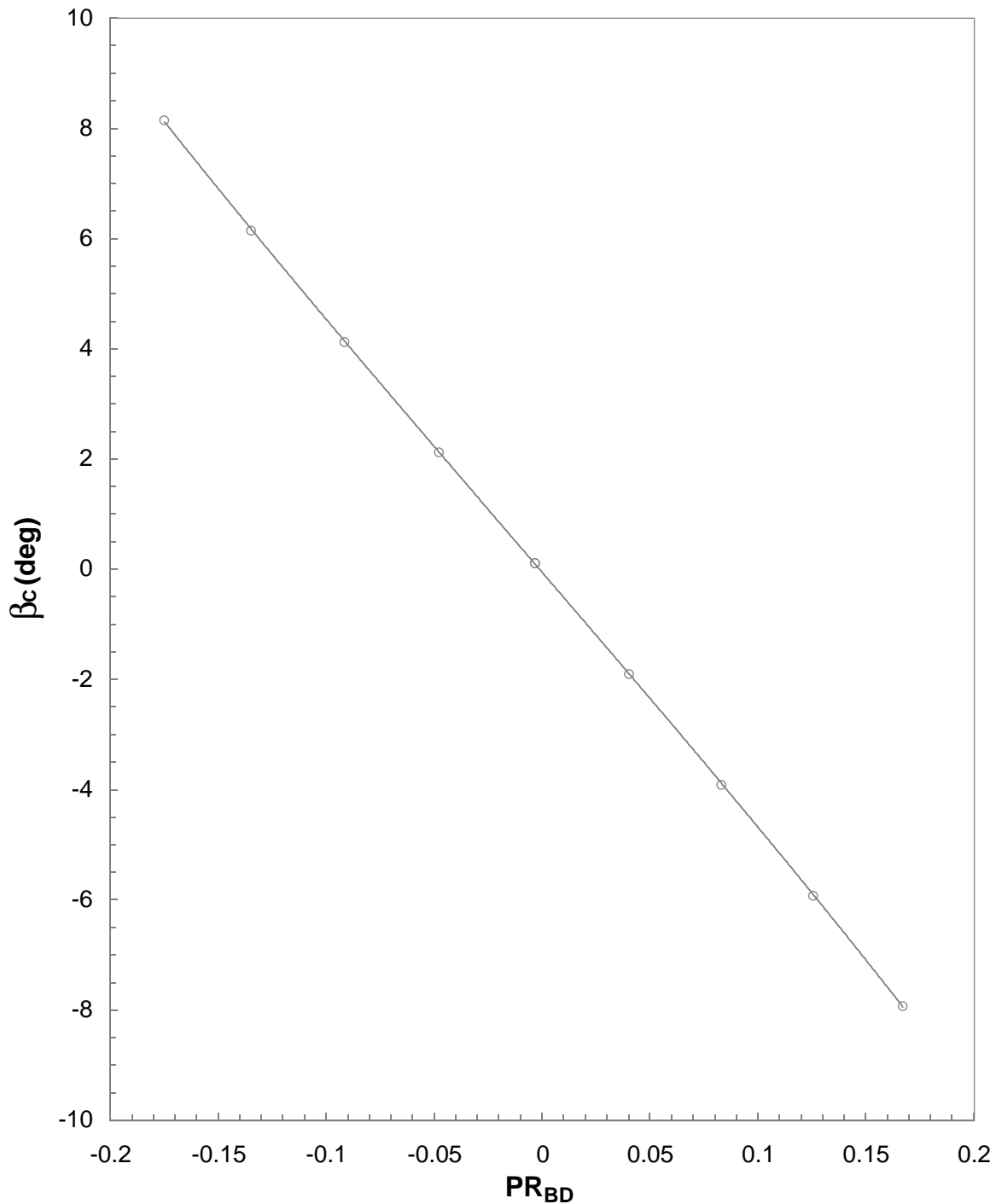
Probe 4
Mset = 2.40, Nominal $\alpha_C = 0^\circ$

Figure 59. Continued.



Probe 5
Mset = 2.40, Nominal $\alpha_C = 0^\circ$

Figure 59. Continued.



Probe 6
Mset = 2.40, Nominal $\alpha_C = 0^\circ$

Figure 59. Concluded.

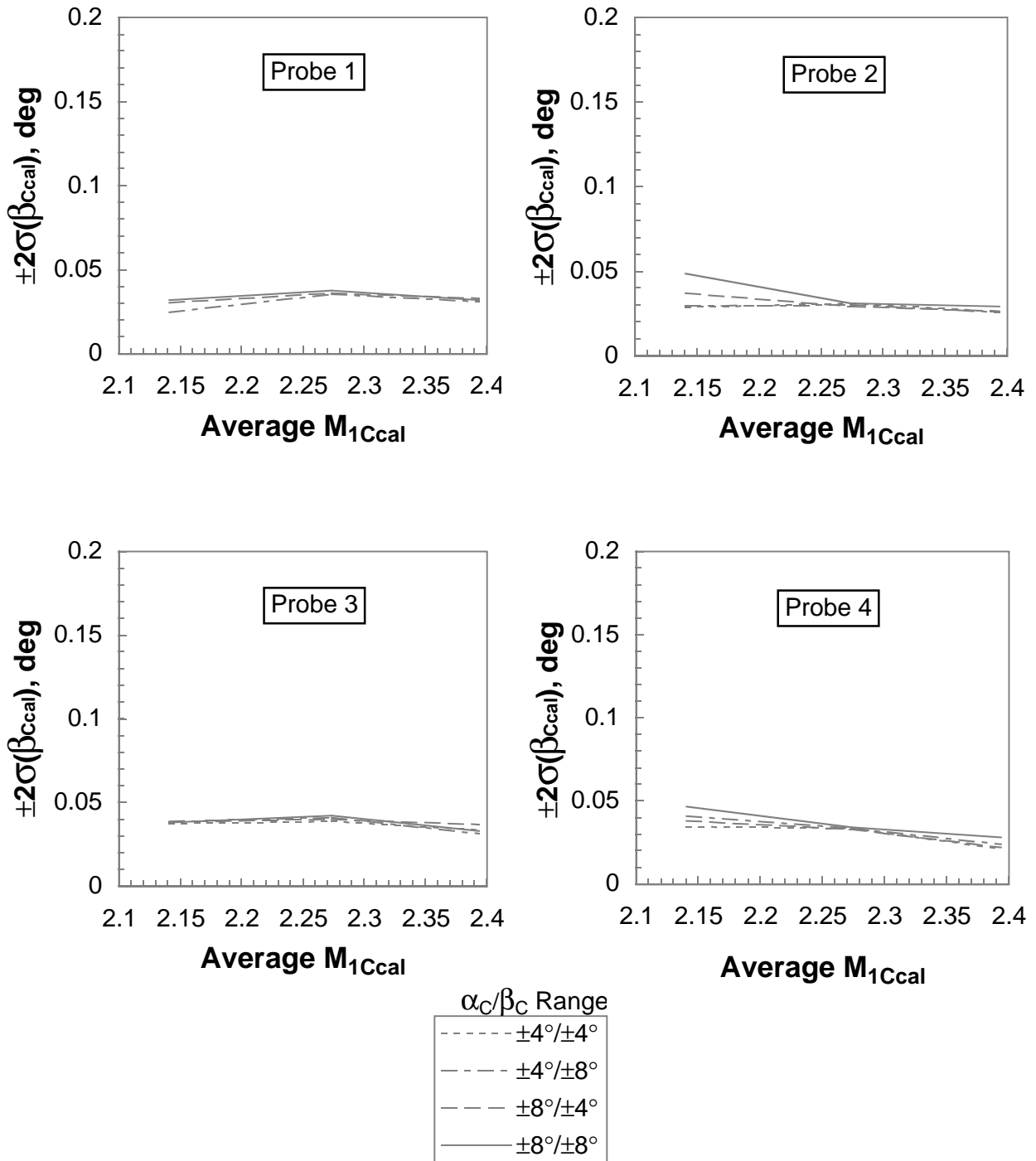


Figure 60. Angle of sideslip correlation residual for rake 1.

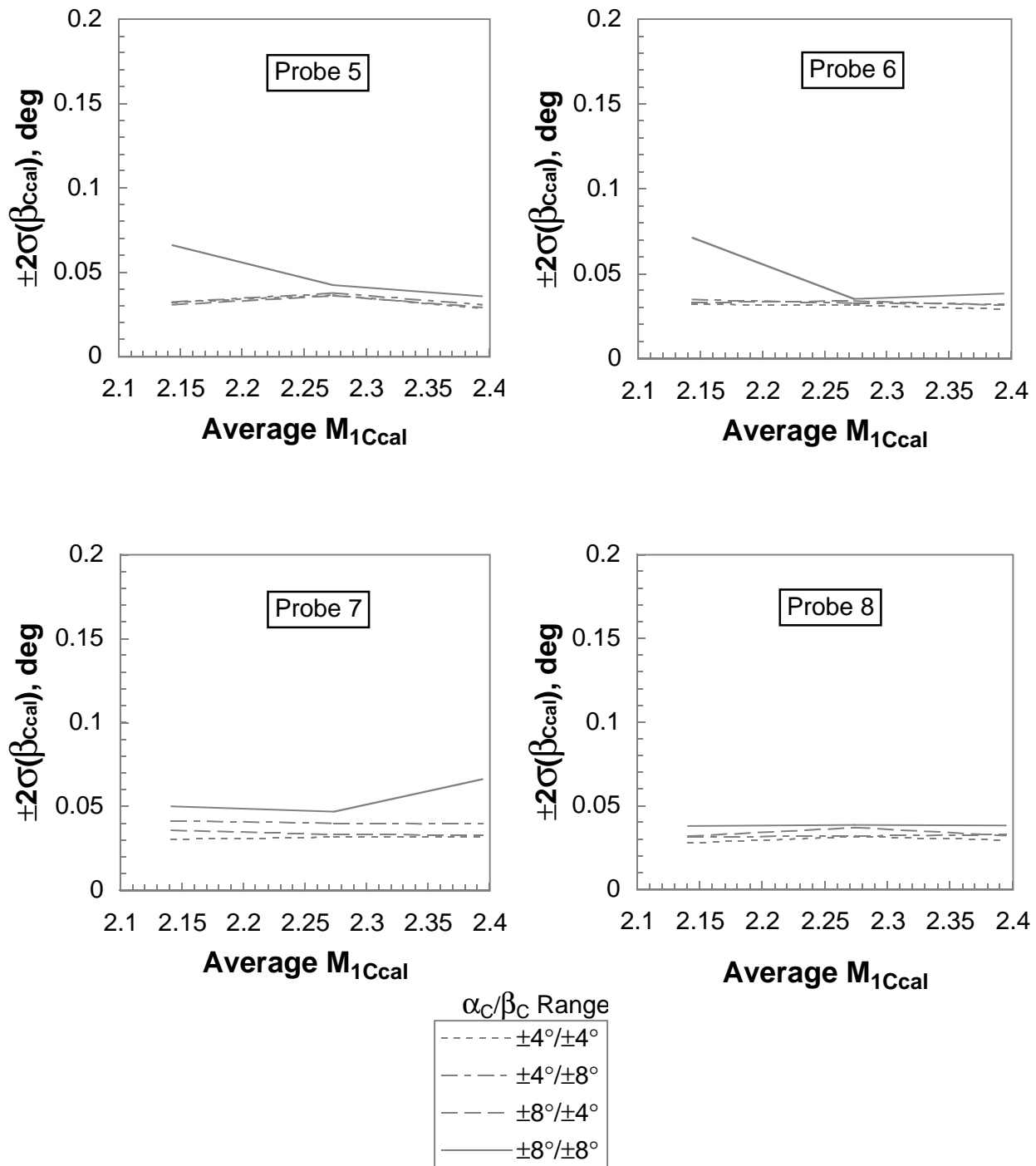


Figure 60. Concluded.

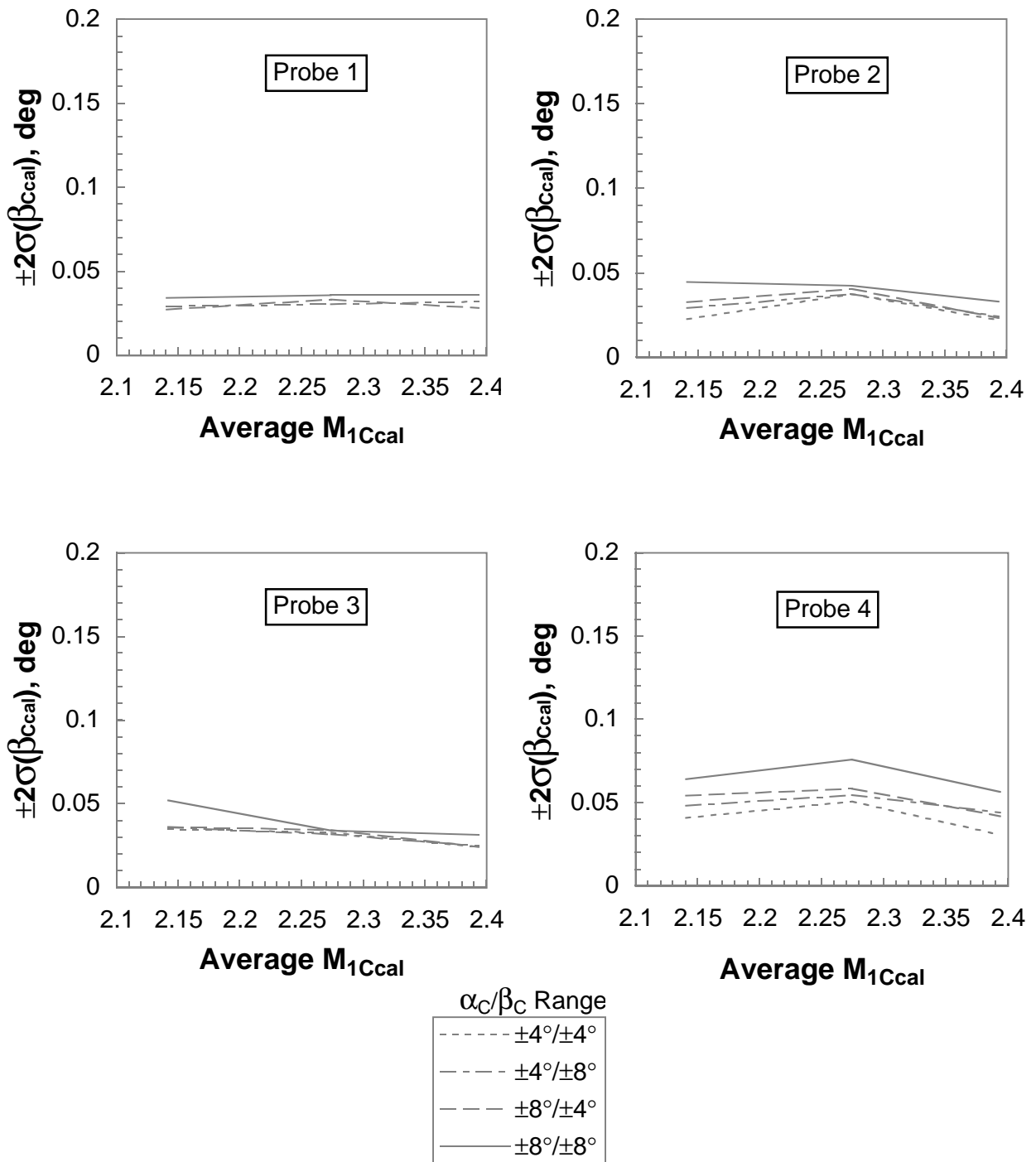


Figure 61. Angle of sideslip correlation residual for rake 2.

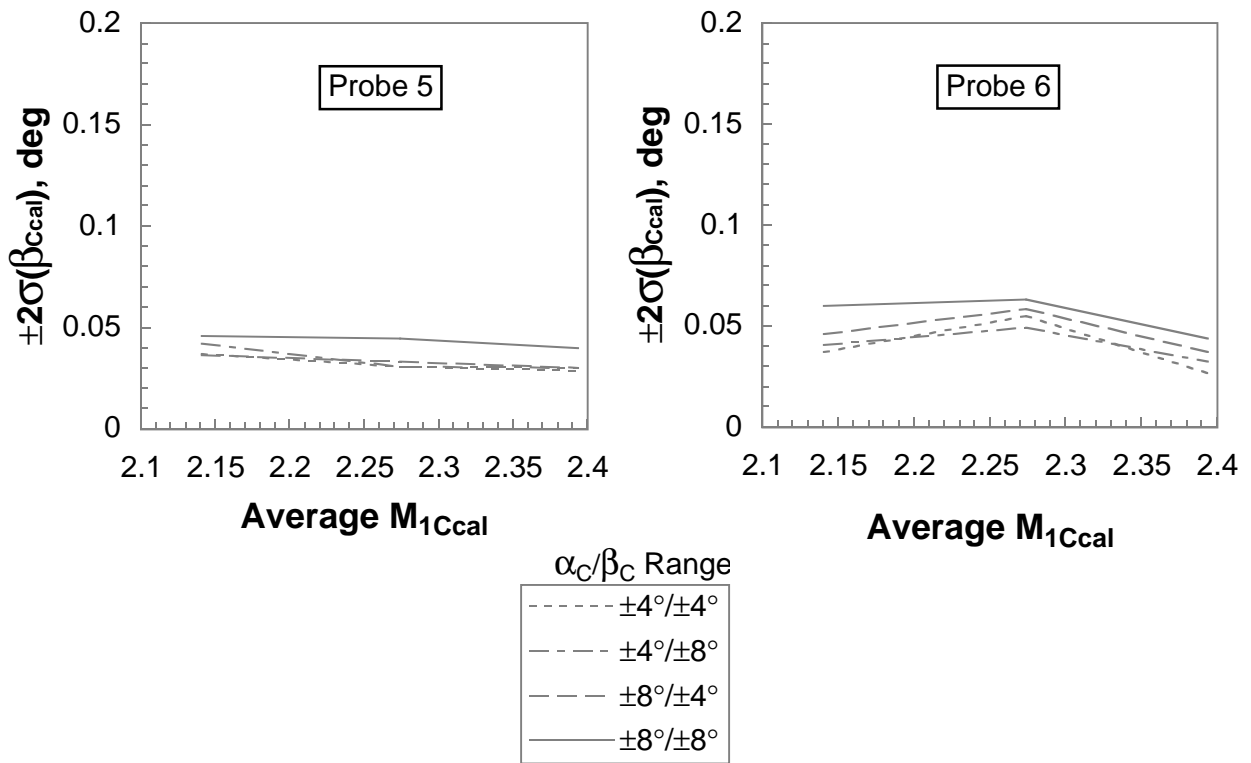
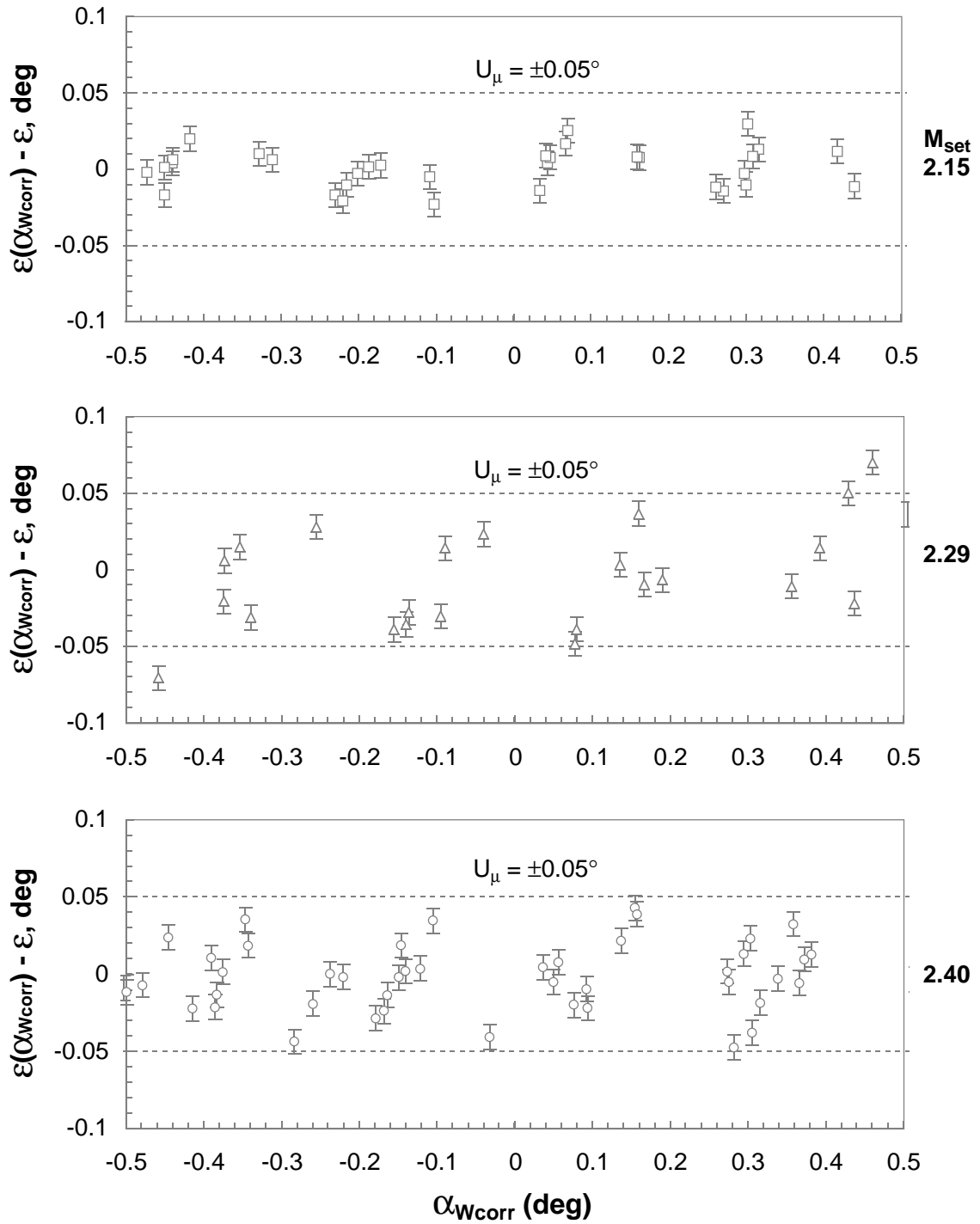


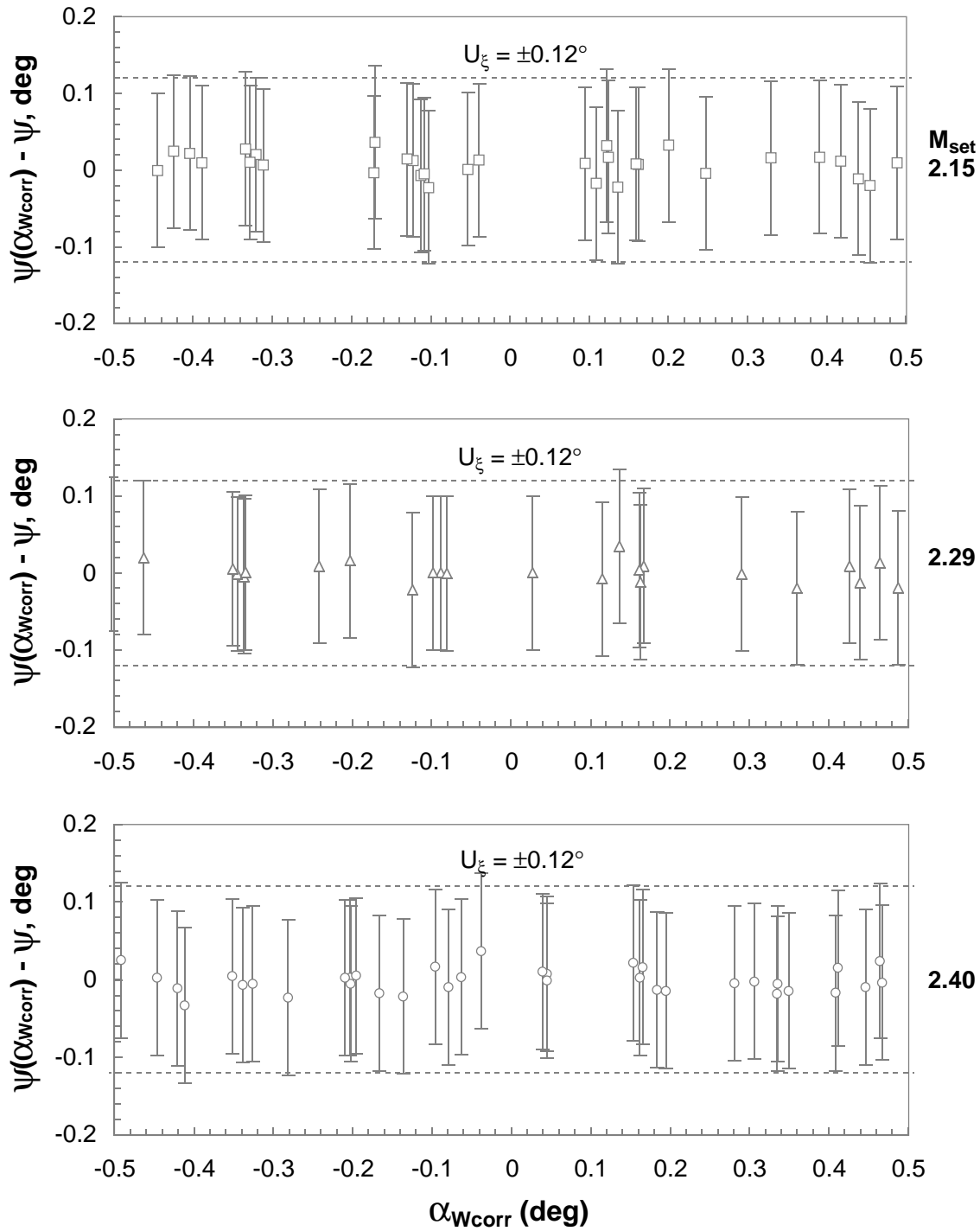
Figure 61. Concluded.



Upright/Inverted Wedge Runs at $z = 16.24, 19.73$ in.

Nominal $\phi_M = 0^\circ, 180^\circ, \psi = 0^\circ$

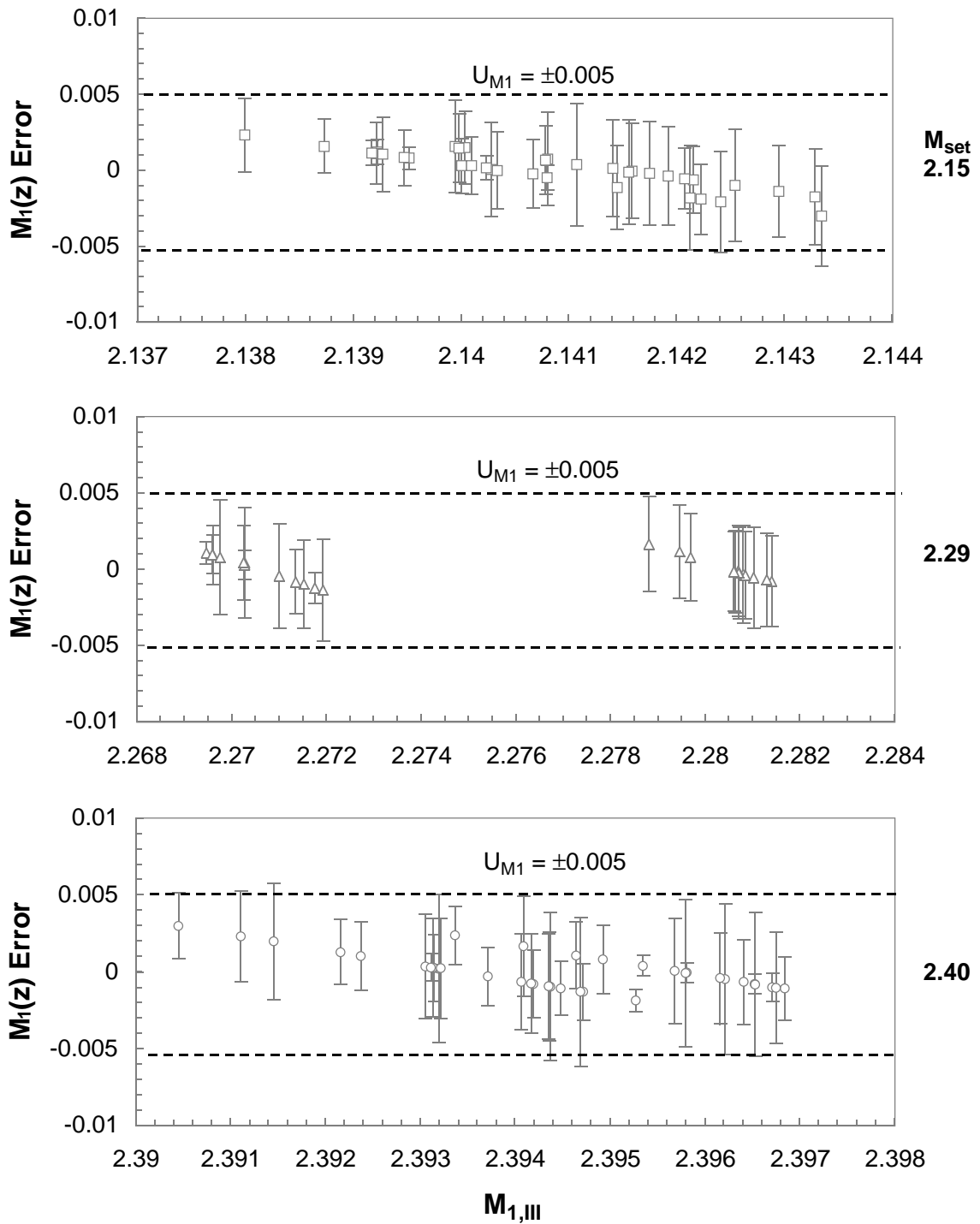
Figure 62. Test section upflow uncertainty.



Upright/Inverted Wedge Runs at $z = 16.24, 19.73$ in.

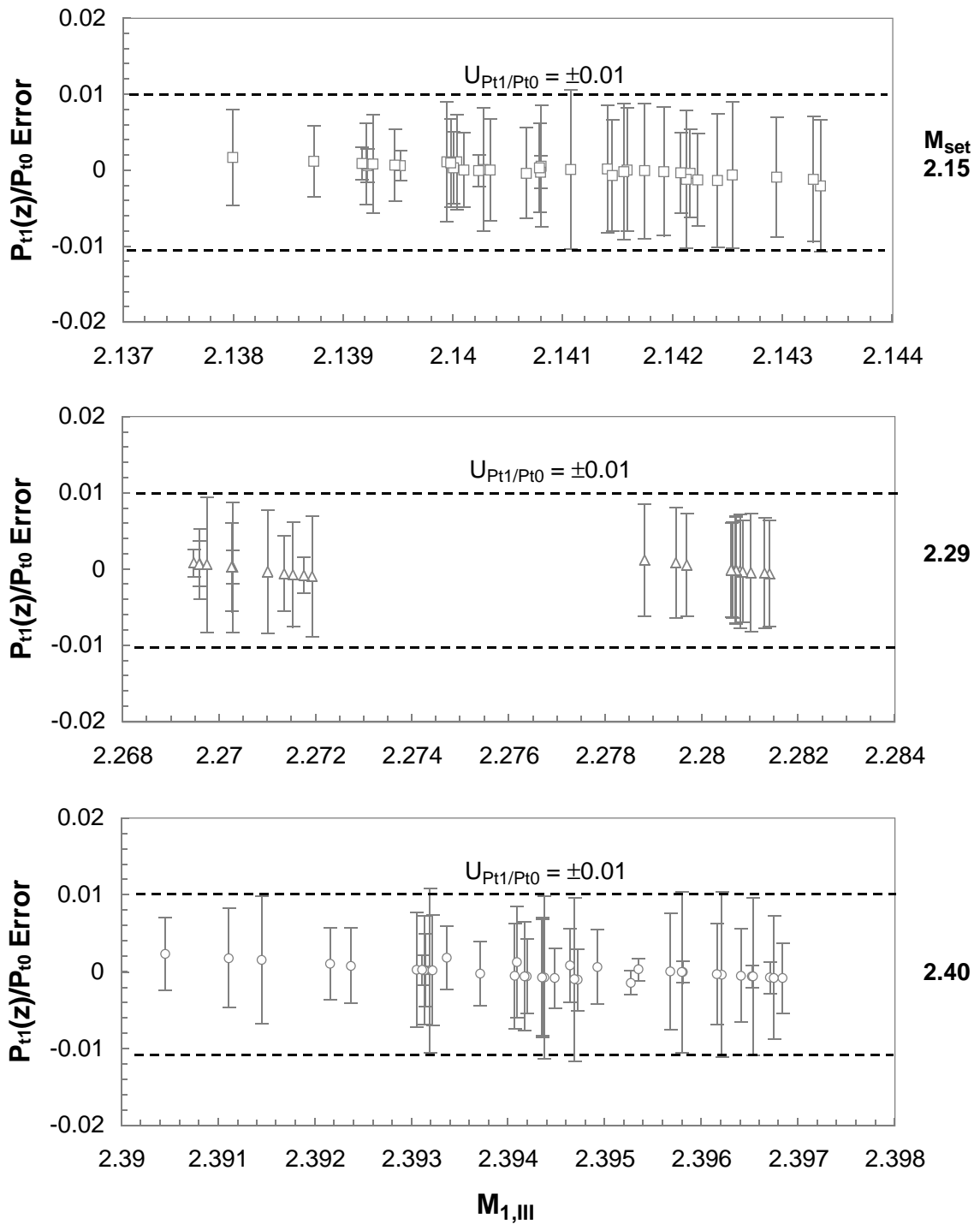
Nominal $\phi_M = \pm 90^\circ, \varepsilon = 0^\circ$

Figure 63. Test section crossflow uncertainty.



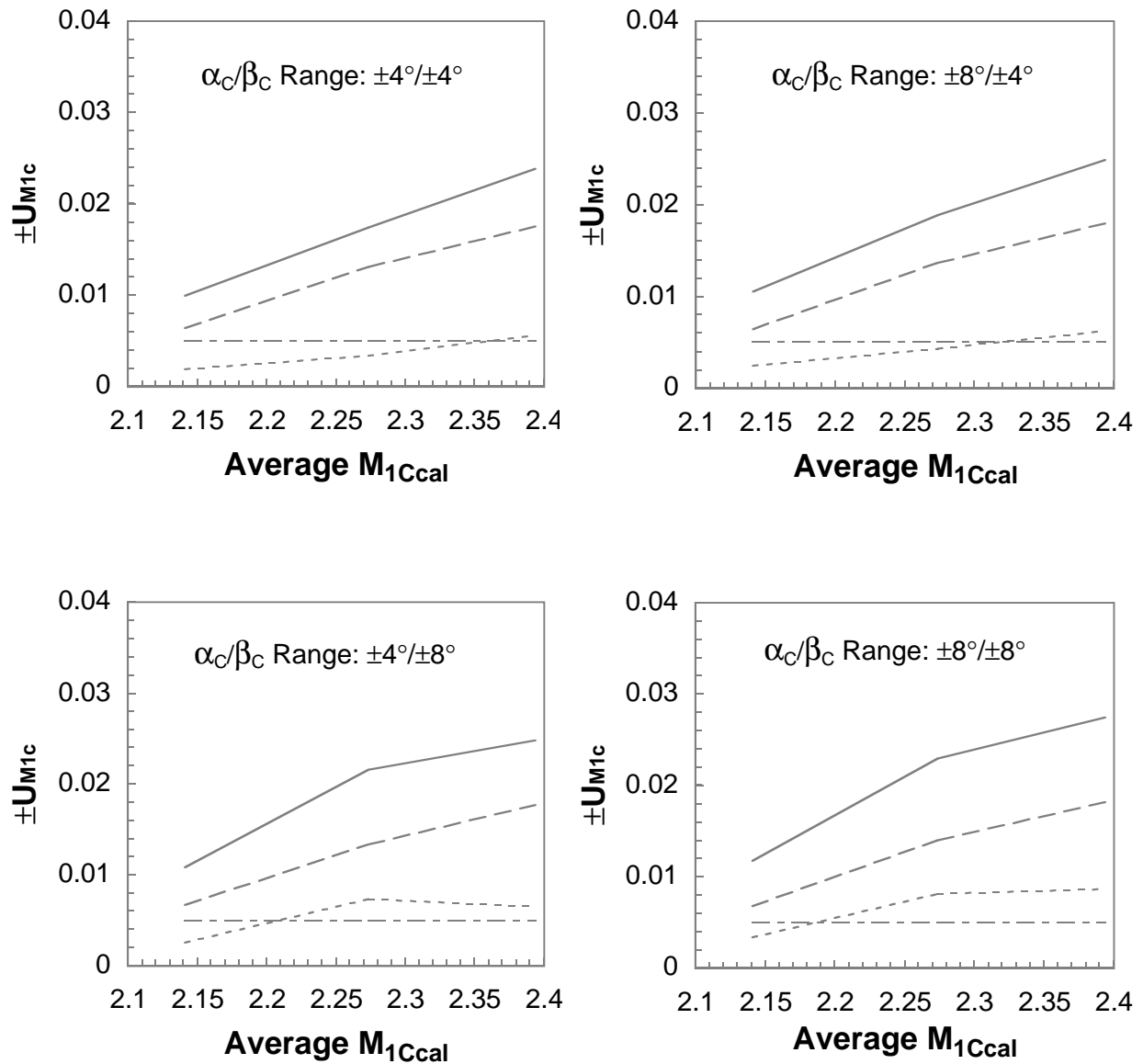
**Upright/Inverted Wedge Runs at $z = 16.24, 19.73$ in.
Nominal ε, ψ within $\pm 0.25^\circ$ of stream angle**

Figure 64. Test section Mach number uncertainty for Method III calculation.



**Upright/Inverted Wedge Runs at $z = 16.24, 19.73$ in.
Nominal ε, ψ within $\pm 0.25^\circ$ of stream angle**

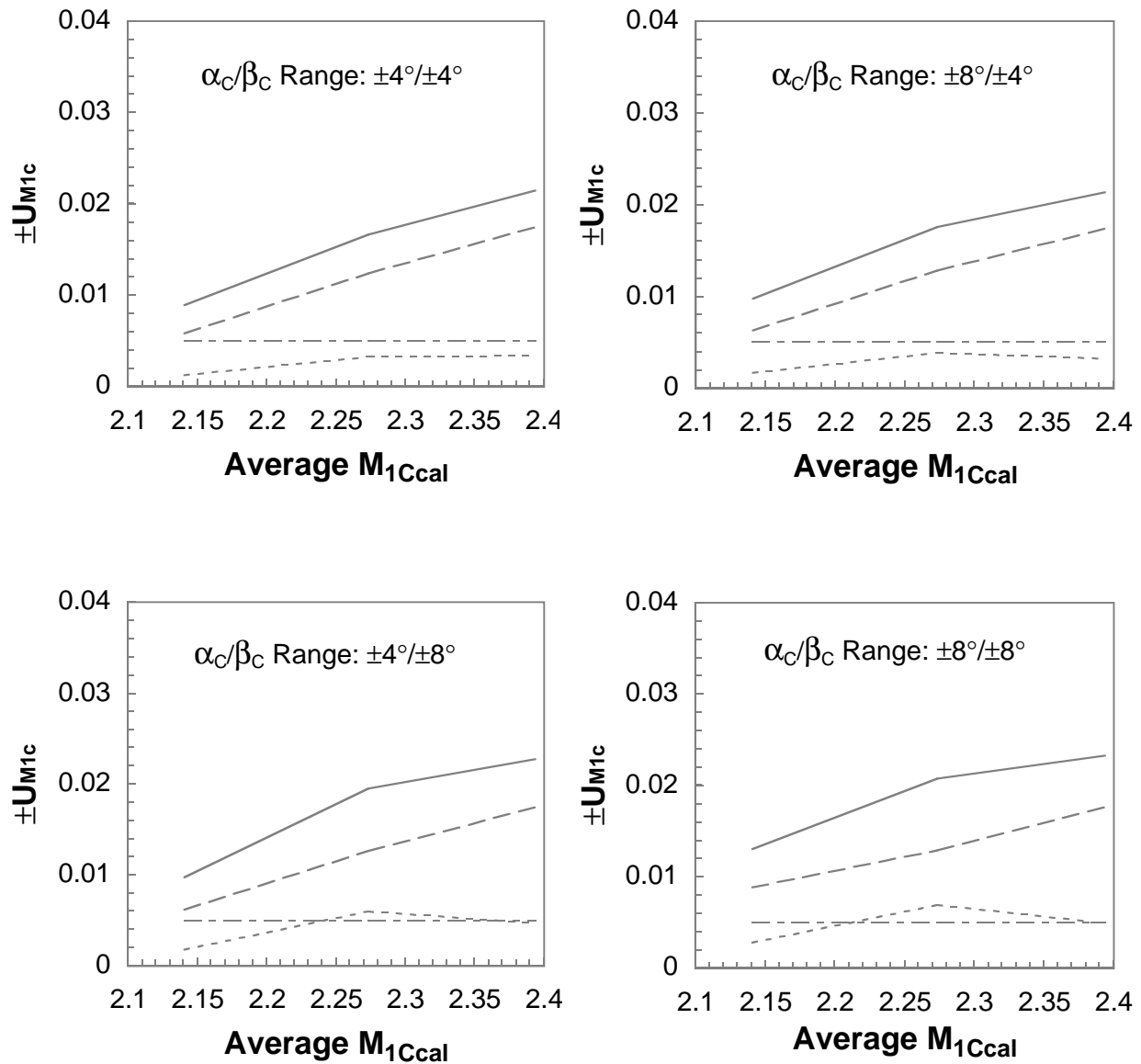
Figure 65. Test section total pressure recovery uncertainty for Method III calculation.



Probe 1

- 2σ of correlation residuals
- - - Calculation uncertainty
- · - Reference uncertainty
- Absolute uncertainty

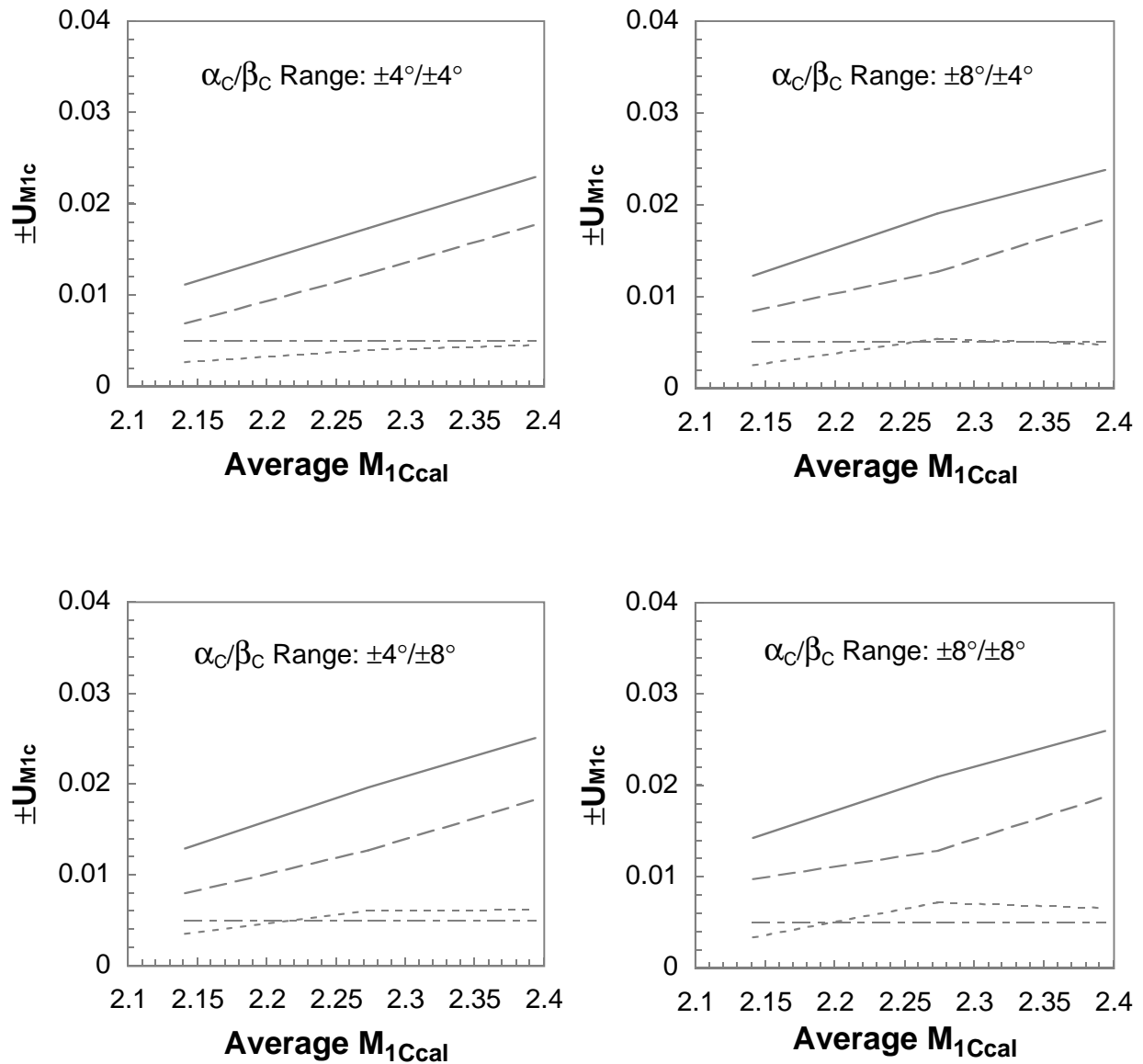
Figure 66. Calibrated Mach number uncertainty for rake 1.



Probe 2

- 2σ of correlation residuals
- - - Calculation uncertainty
- · - Reference uncertainty
- Absolute uncertainty

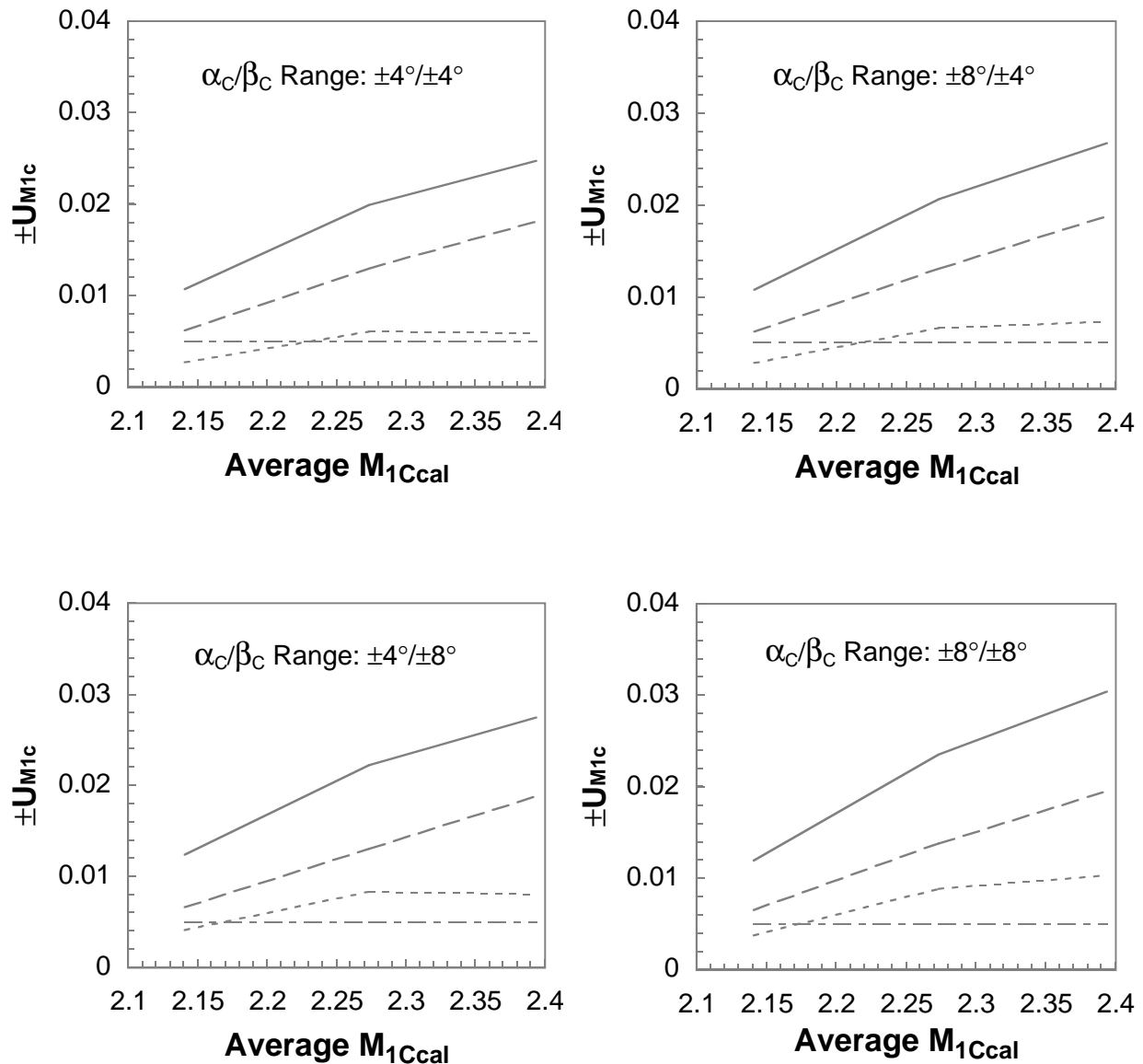
Figure 66. Continued.



Probe 3

- 2σ of correlation residuals
- - - Calculation uncertainty
- · - Reference uncertainty
- Absolute uncertainty

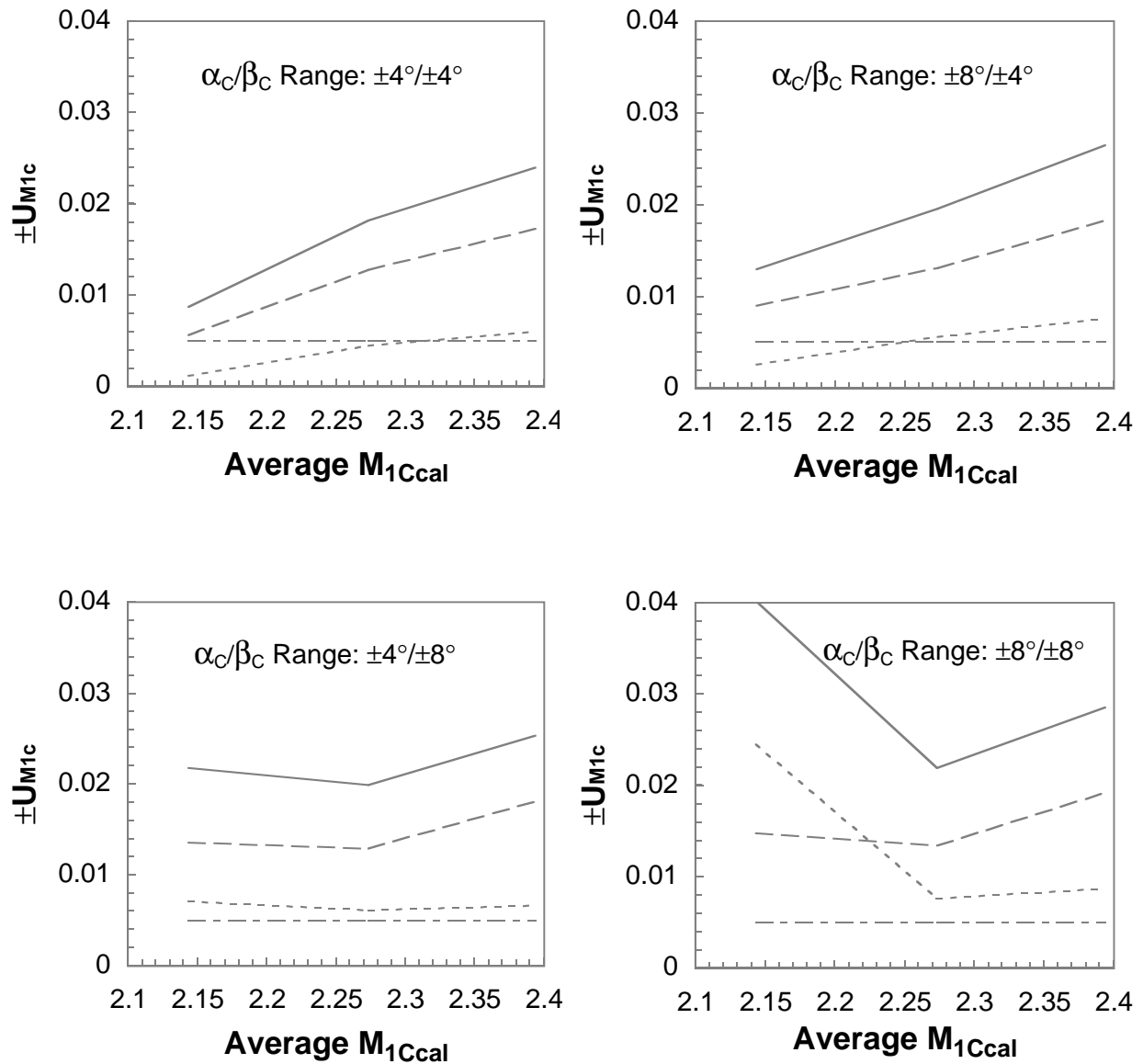
Figure 66. Continued.



Probe 4

- 2σ of correlation residuals
- - - Calculation uncertainty
- · - Reference uncertainty
- Absolute uncertainty

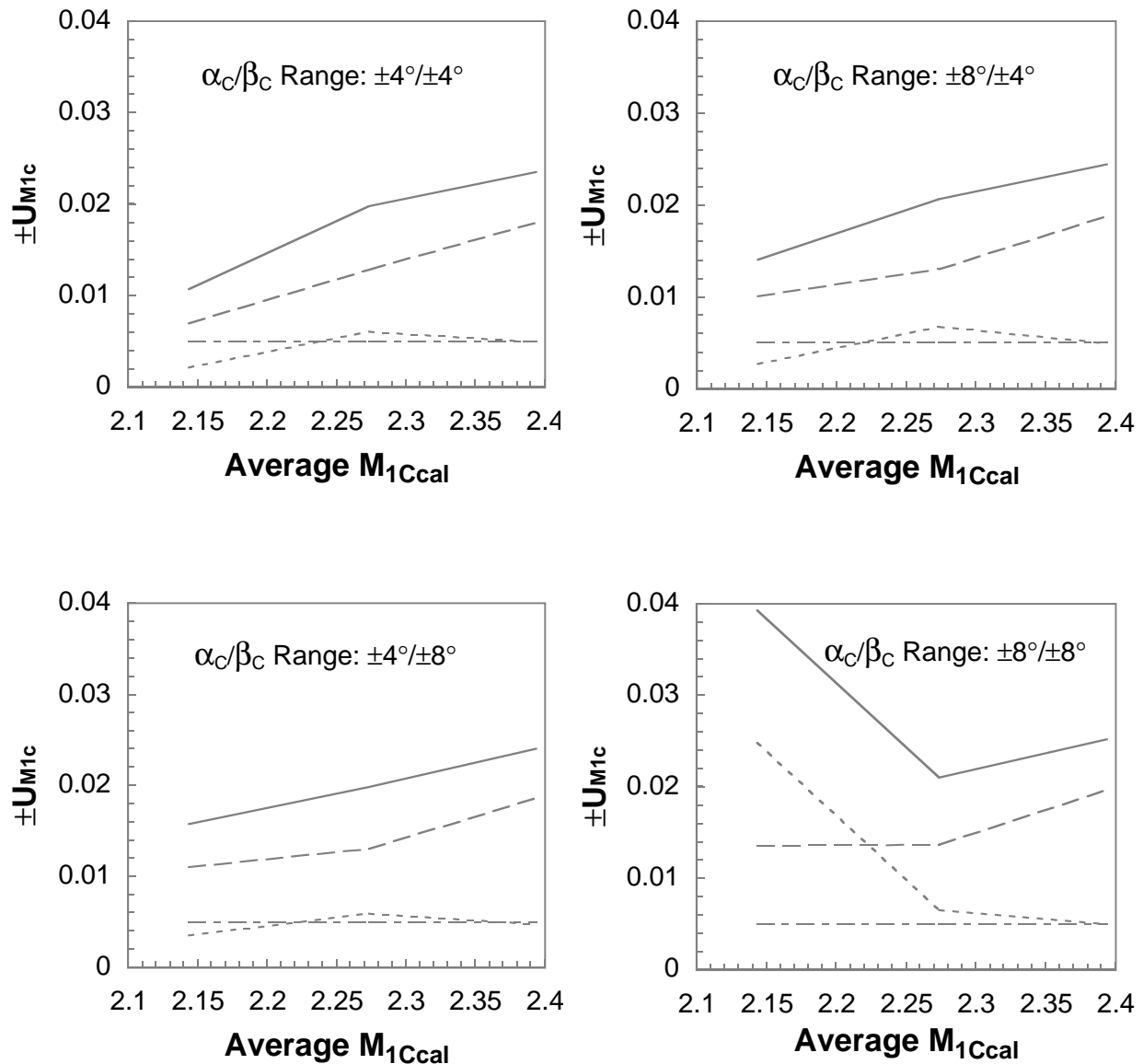
Figure 66. Continued.



Probe 5

- 2σ of correlation residuals
- - - Calculation uncertainty
- · - Reference uncertainty
- Absolute uncertainty

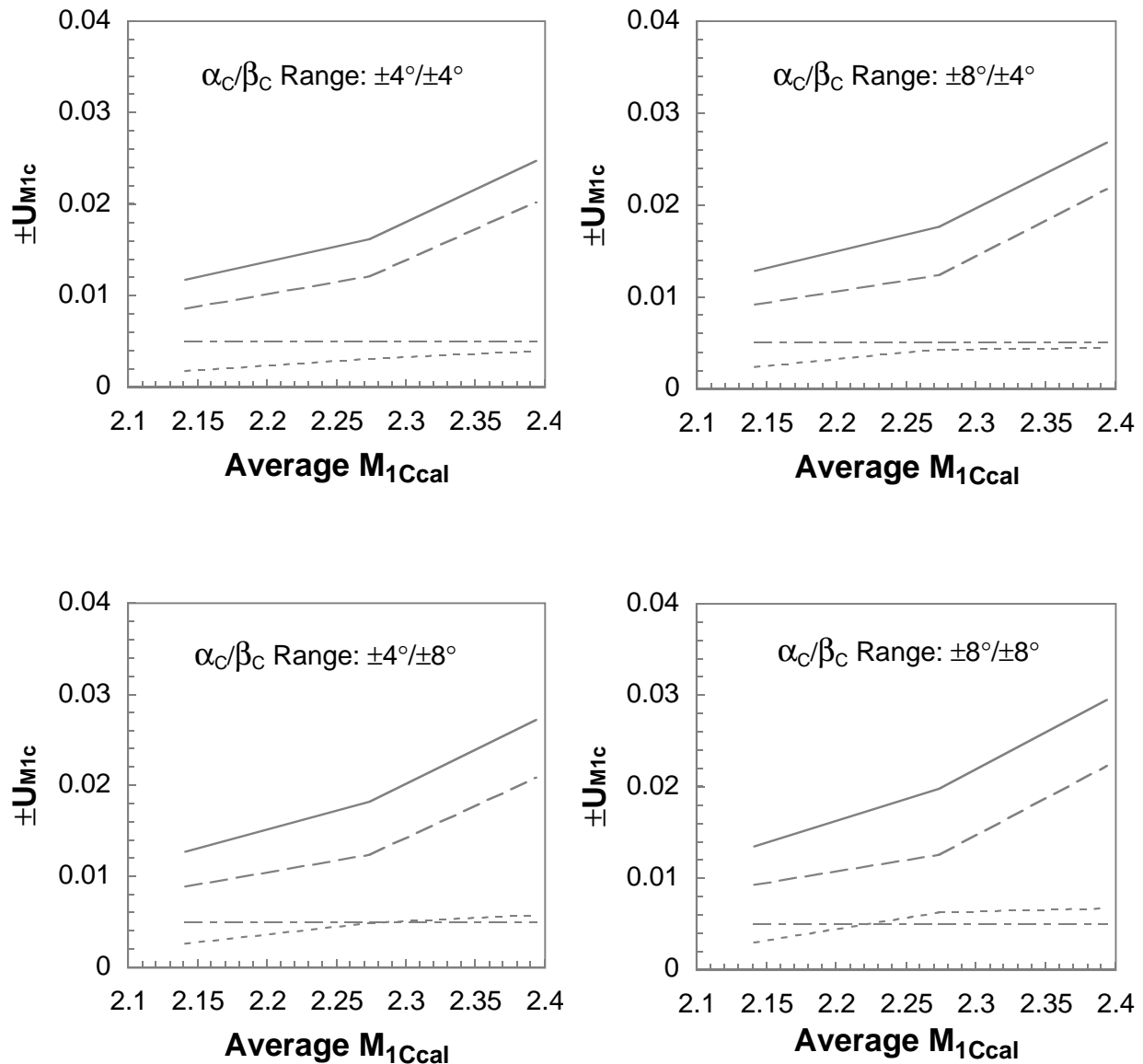
Figure 66. Continued.



Probe 6

- 2σ of correlation residuals
- - - Calculation uncertainty
- · - Reference uncertainty
- Absolute uncertainty

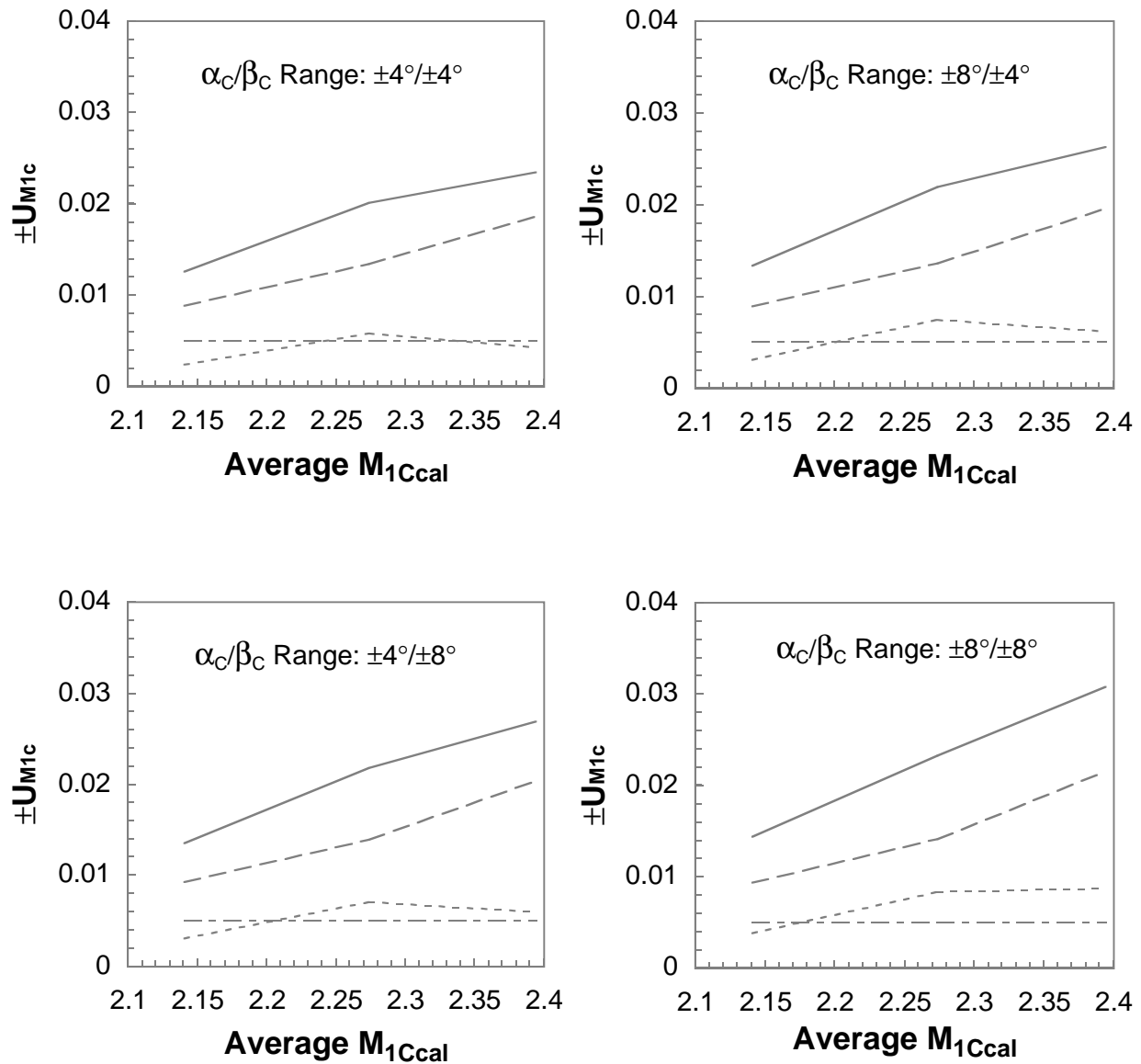
Figure 66. Continued.



Probe 7

- 2σ of correlation residuals
- - - Calculation uncertainty
- · - Reference uncertainty
- Absolute uncertainty

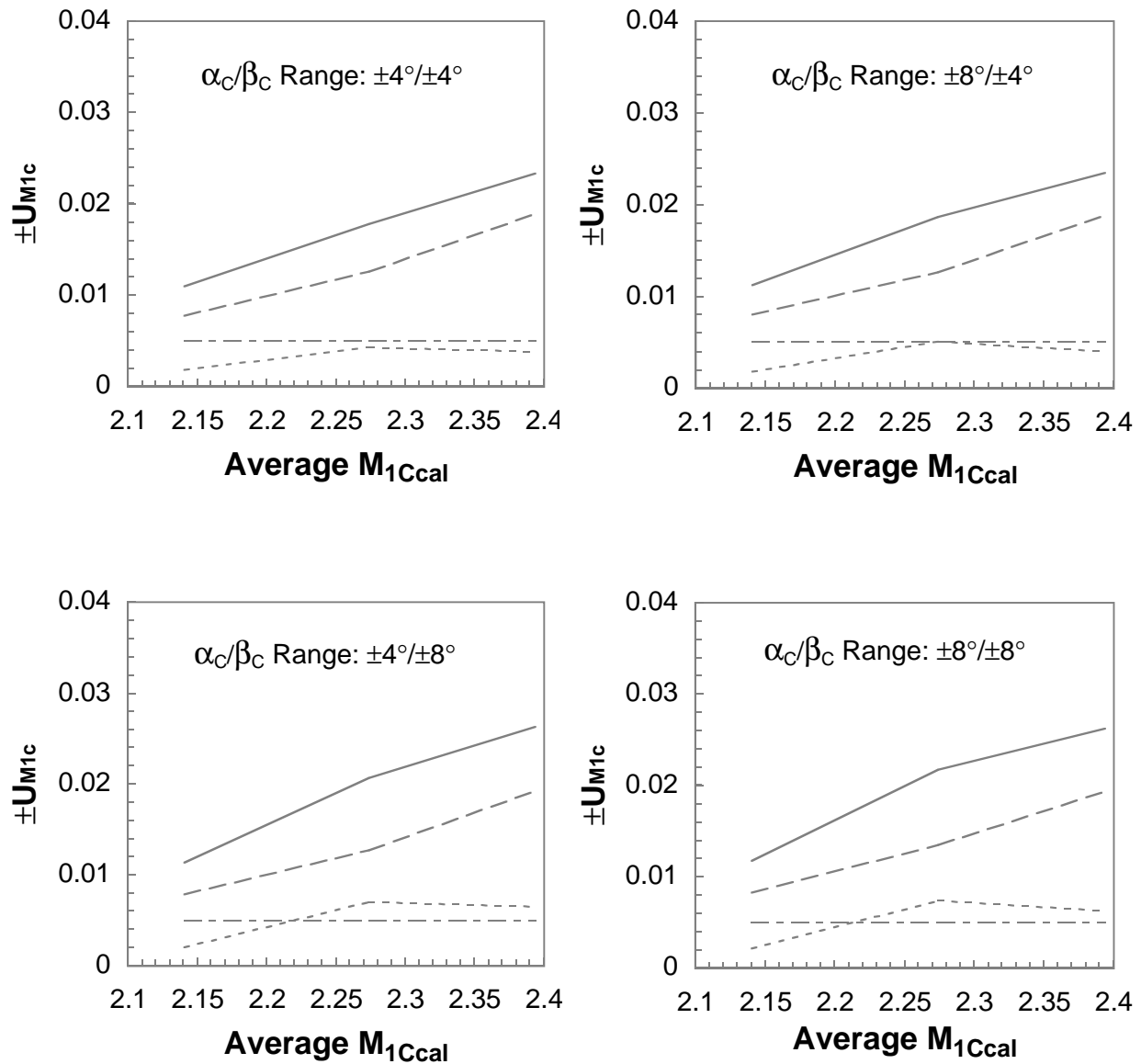
Figure 66. Continued.



Probe 8

- 2σ of correlation residuals
- - - Calculation uncertainty
- · - Reference uncertainty
- Absolute uncertainty

Figure 66. Concluded.



Probe 1

- 2σ of correlation residuals
- - - Calculation uncertainty
- · - Reference uncertainty
- Absolute uncertainty

Figure 67. Calibrated Mach number uncertainty for rake 2.

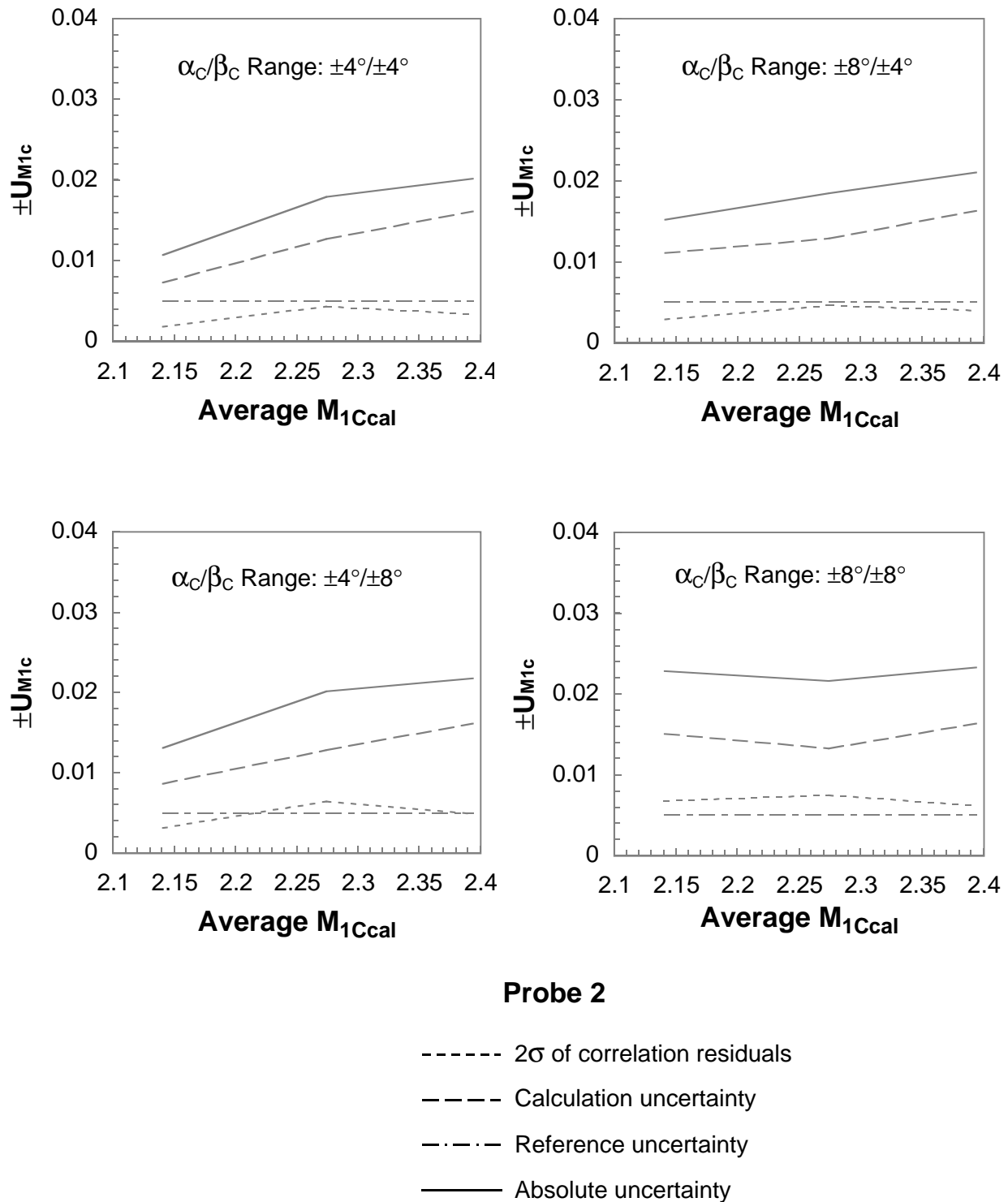
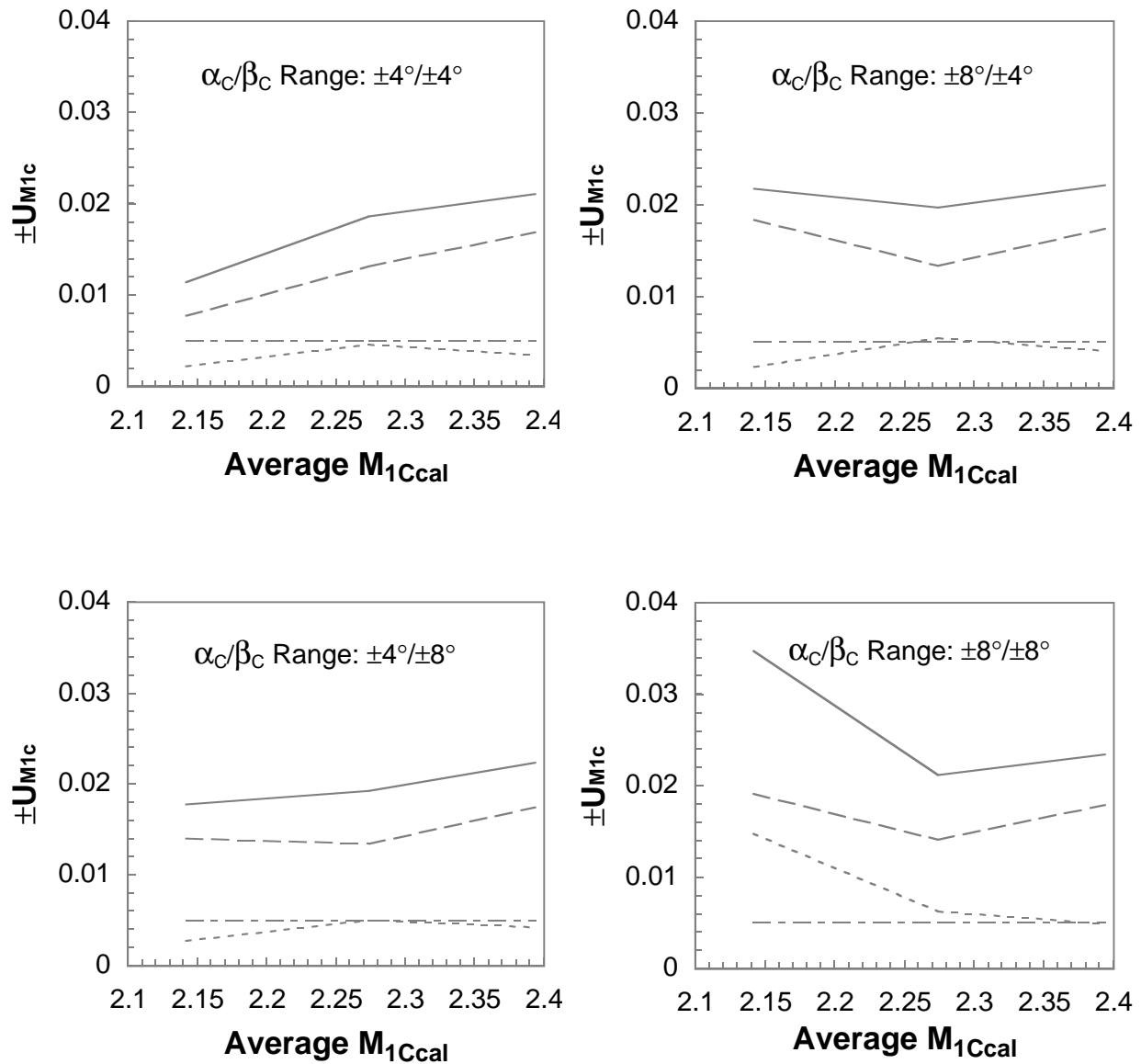


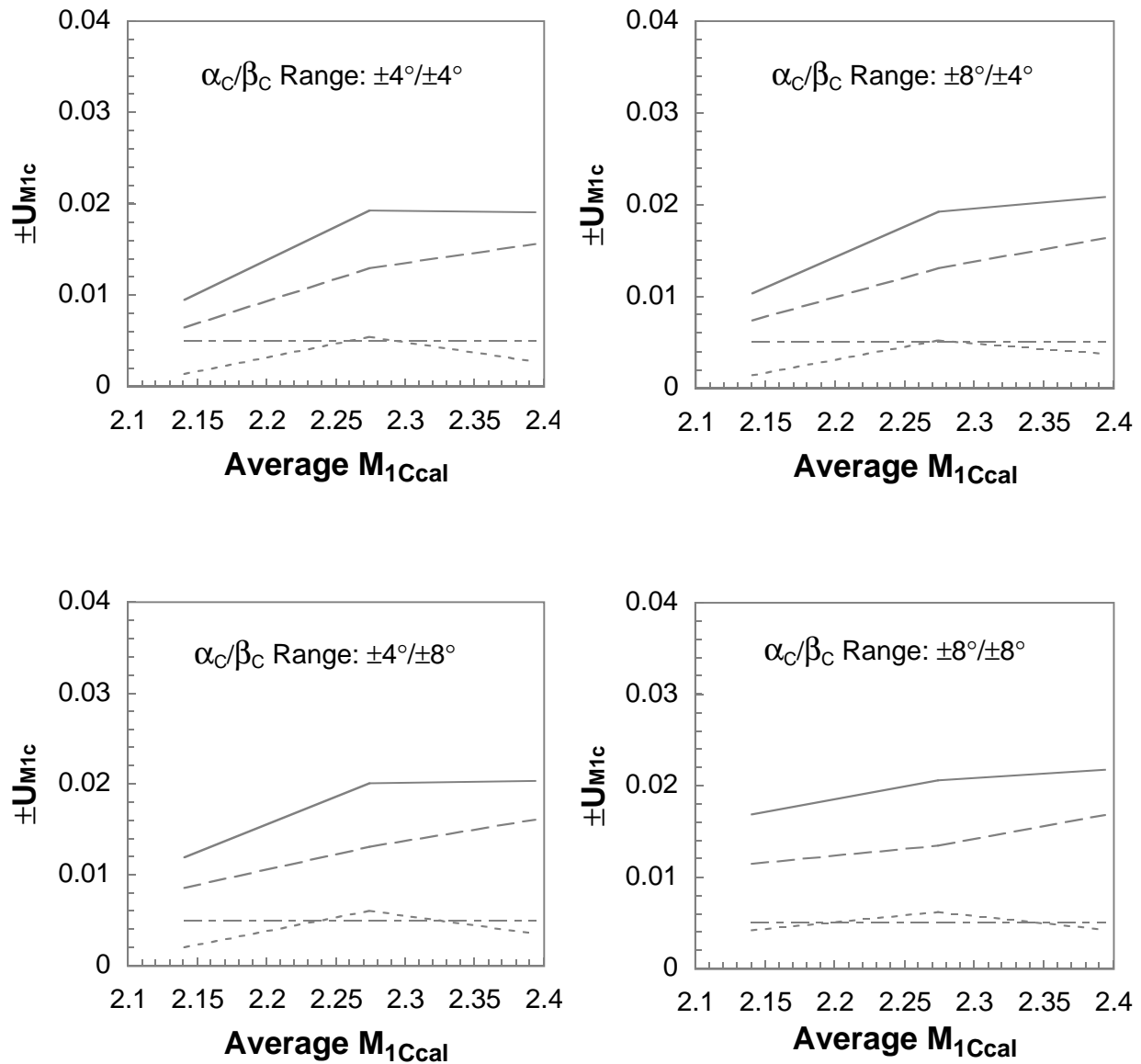
Figure 67. Continued.



Probe 3

- 2σ of correlation residuals
- - - Calculation uncertainty
- · - Reference uncertainty
- Absolute uncertainty

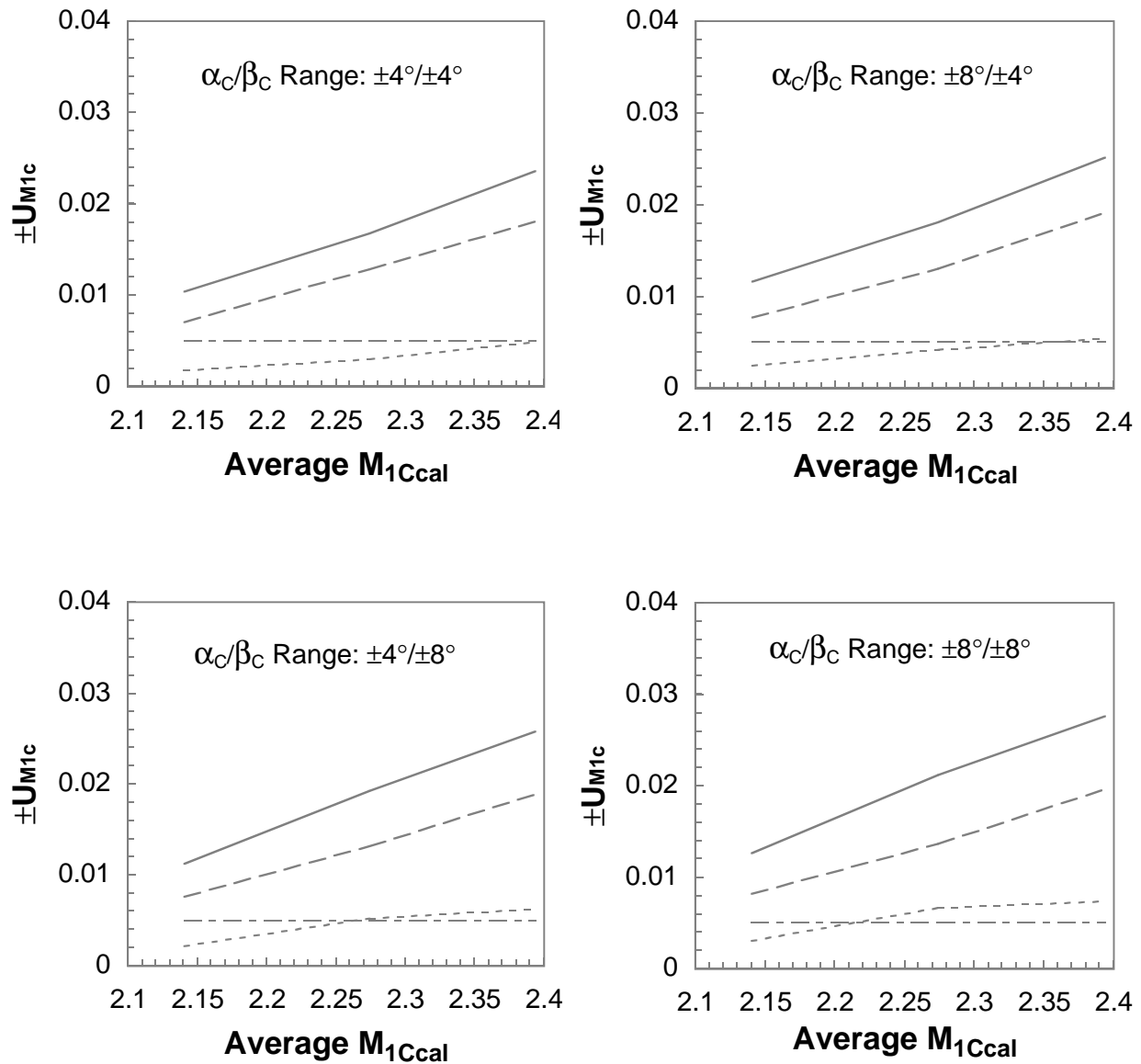
Figure 67. Continued.



Probe 4

- 2σ of correlation residuals
- - - Calculation uncertainty
- · - Reference uncertainty
- Absolute uncertainty

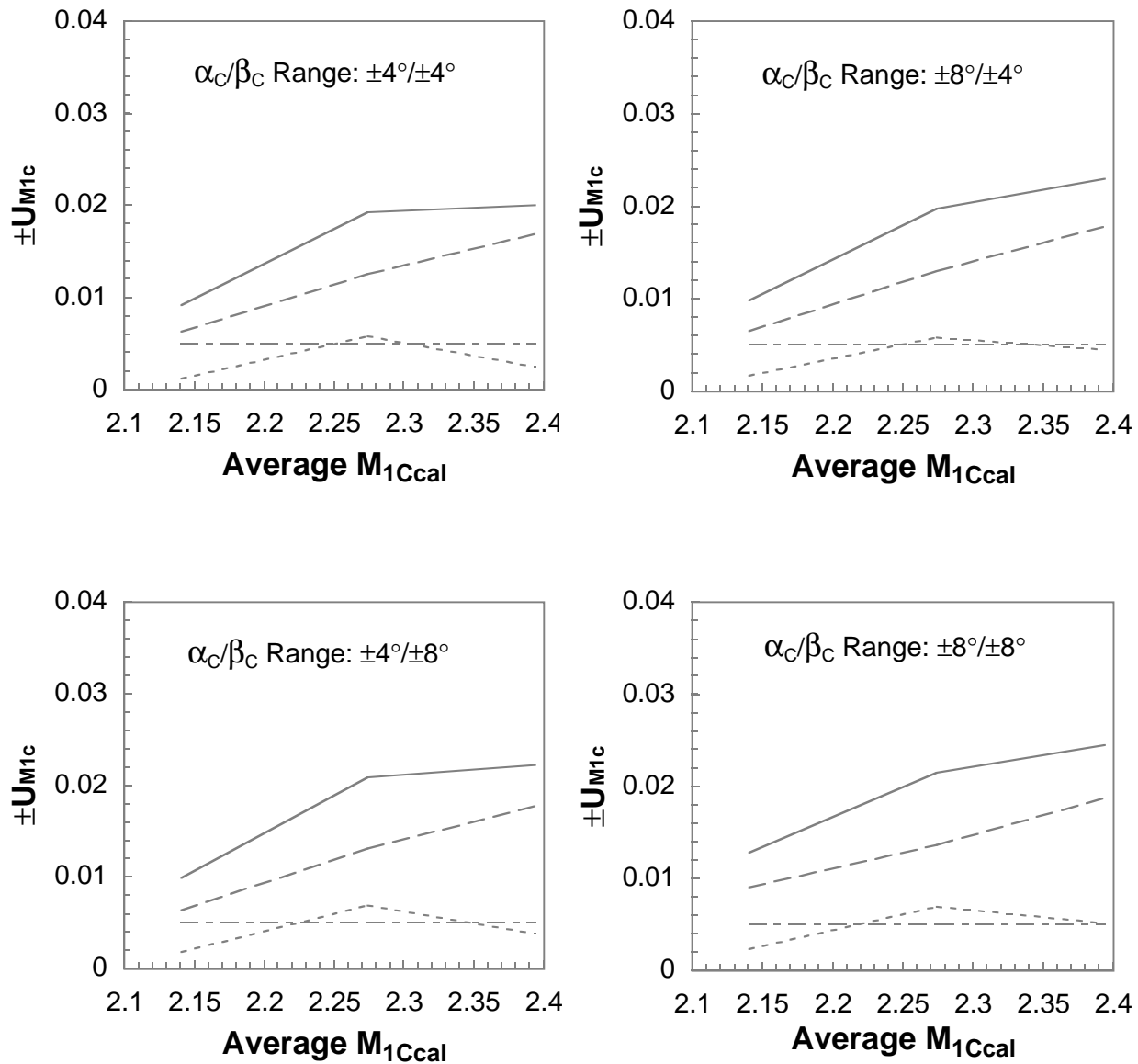
Figure 67. Continued.



Probe 5

- 2σ of correlation residuals
- - - Calculation uncertainty
- · - Reference uncertainty
- Absolute uncertainty

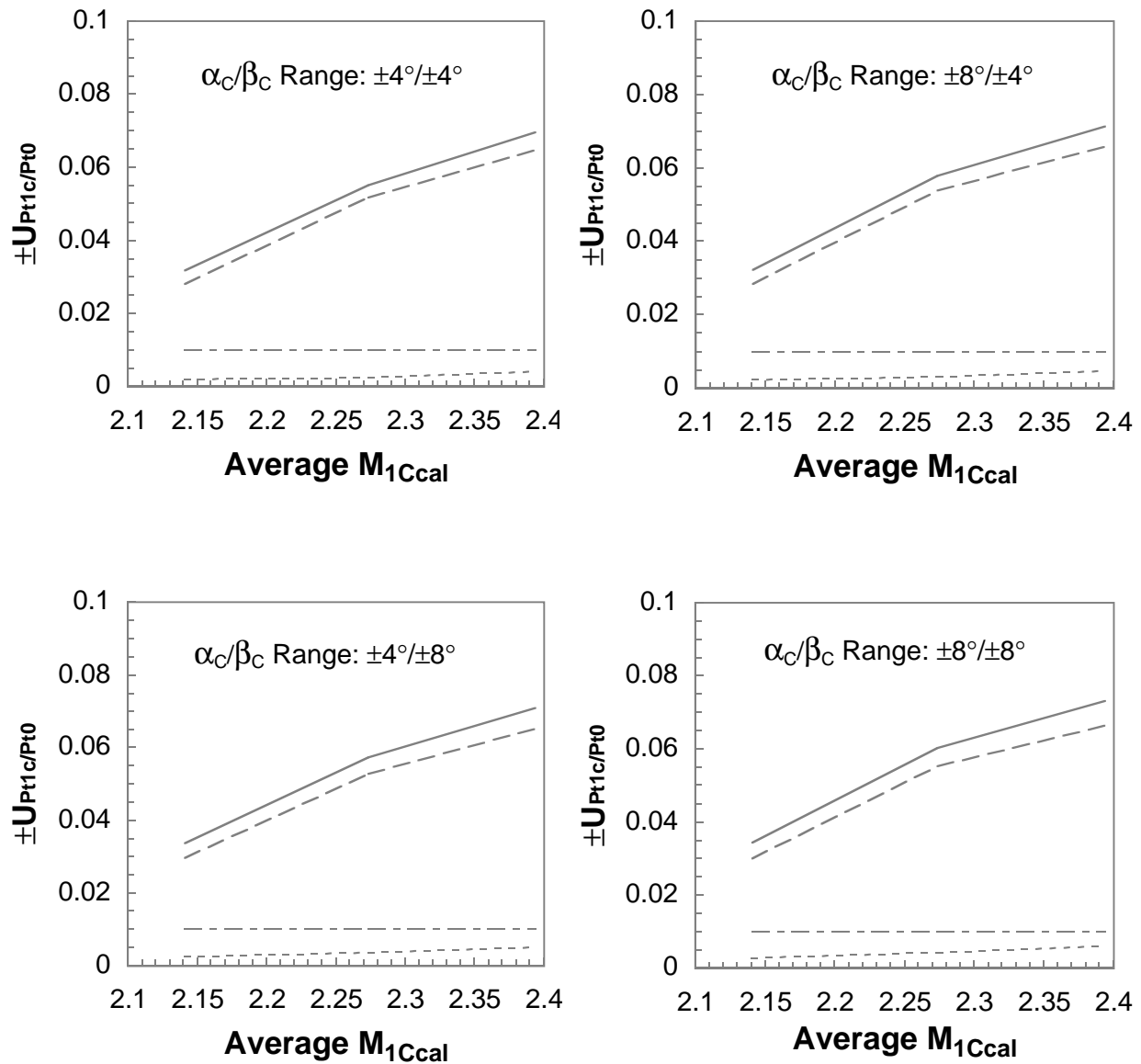
Figure 67. Continued.



Probe 6

- 2σ of correlation residuals
- - - Calculation uncertainty
- · - Reference uncertainty
- Absolute uncertainty

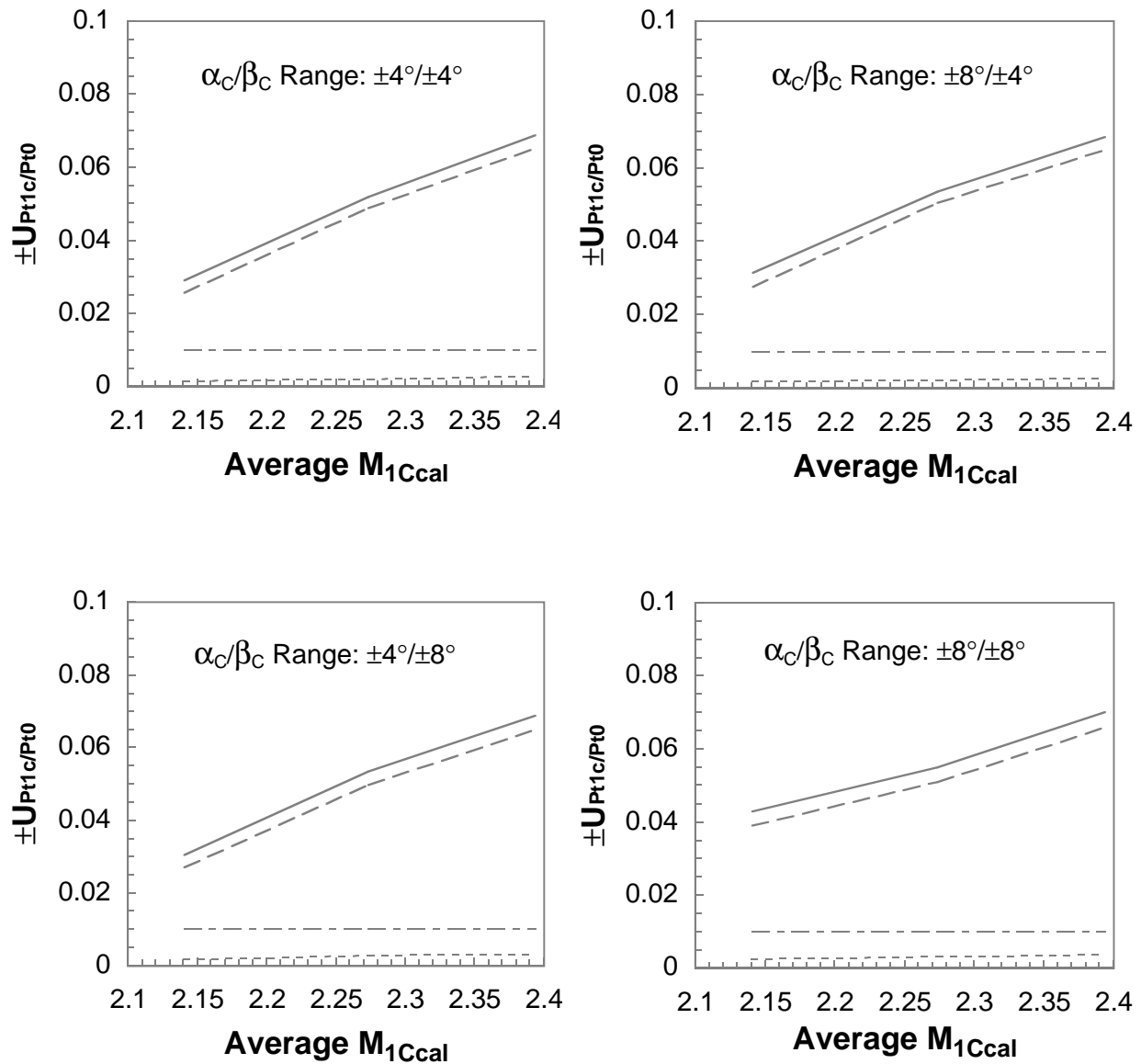
Figure 67. Concluded.



Probe 1

- 2σ of correlation residuals
- - - Calculation uncertainty
- · - Reference uncertainty
- Absolute uncertainty

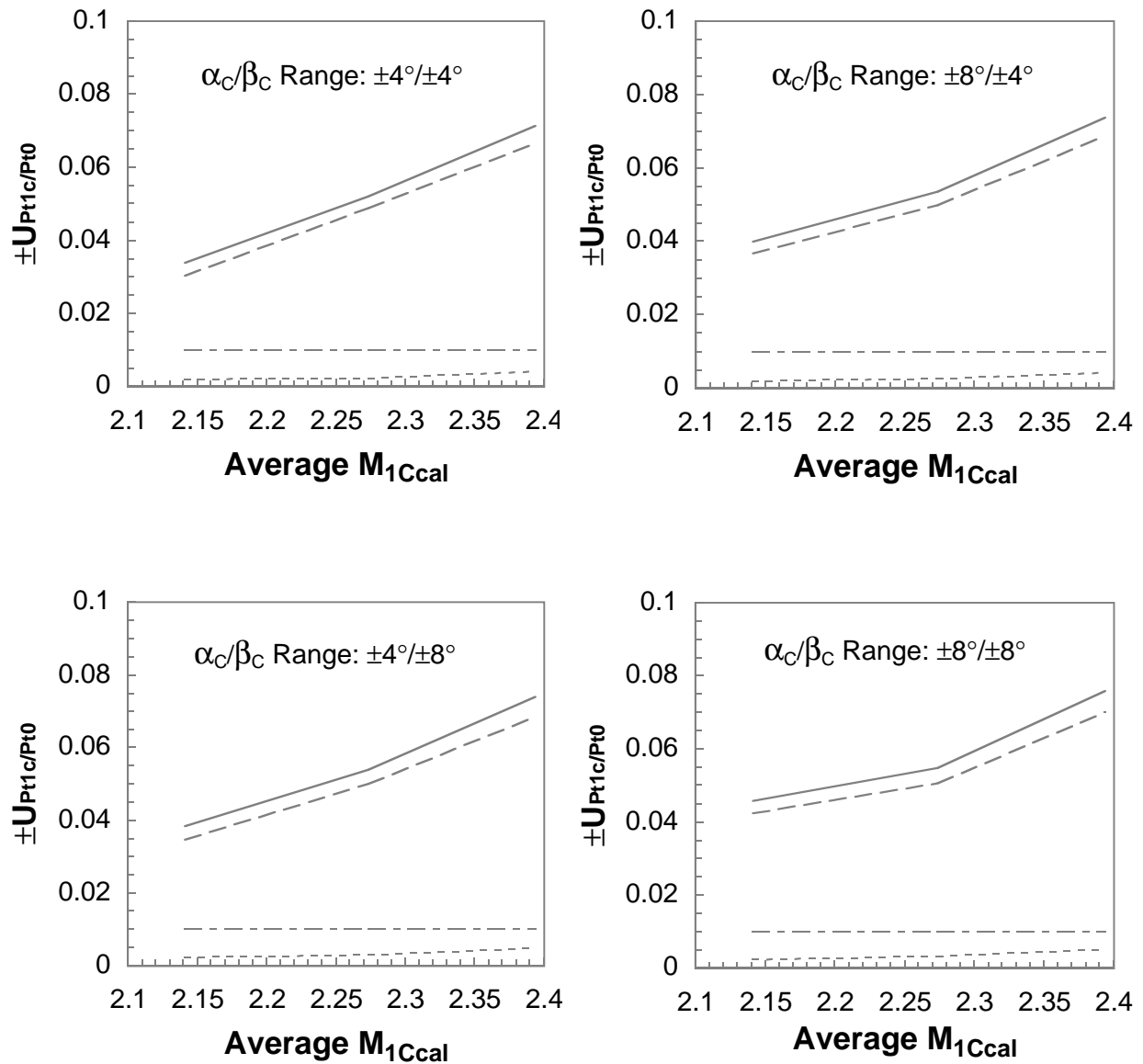
Figure 68. Calibrated total pressure uncertainty for rake 1.



Probe 2

- 2σ of correlation residuals
- - - Calculation uncertainty
- · - Reference uncertainty
- Absolute uncertainty

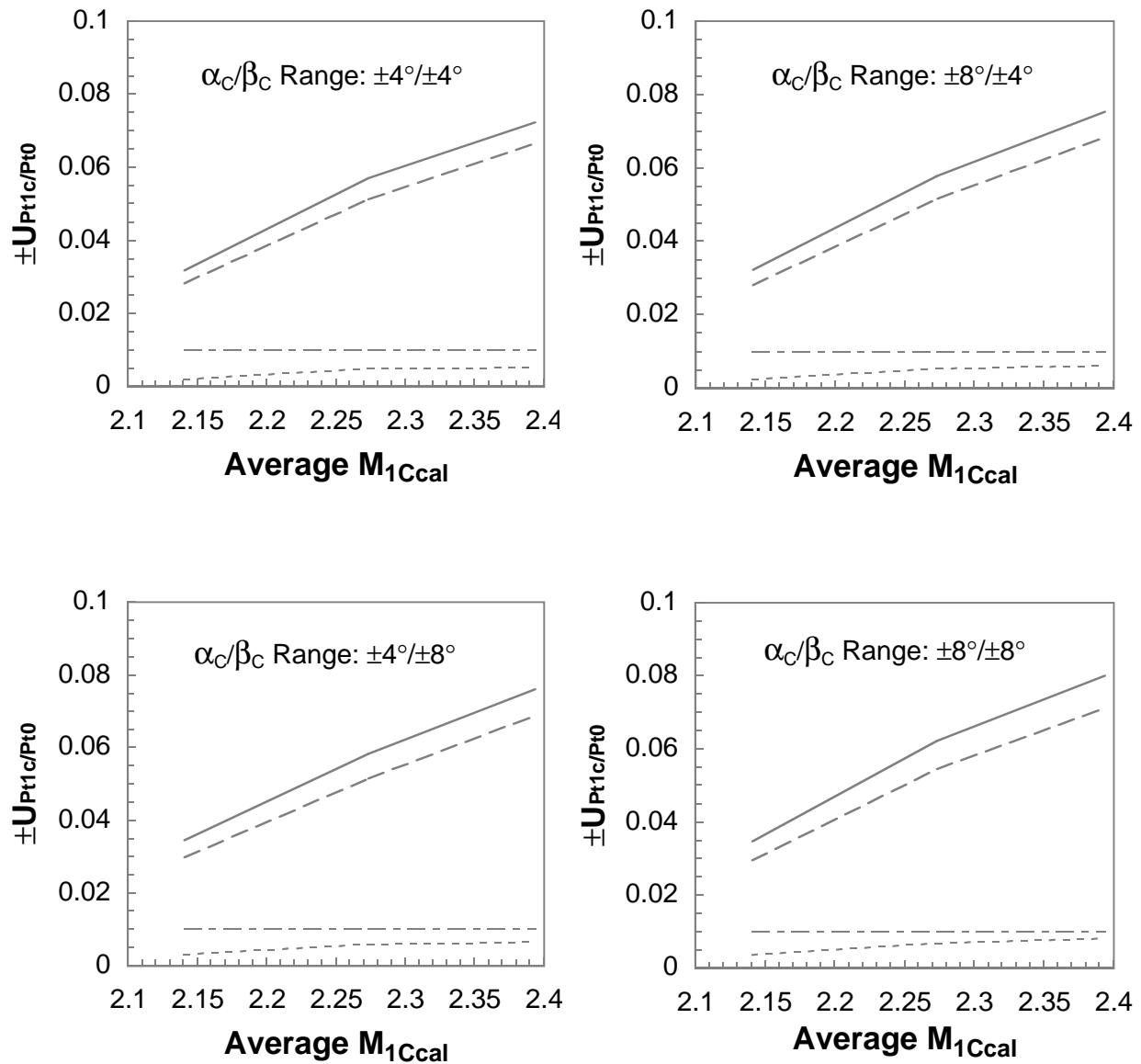
Figure 68. Continued.



Probe 3

- 2σ of correlation residuals
- - - Calculation uncertainty
- · - Reference uncertainty
- Absolute uncertainty

Figure 68. Continued.



Probe 4

- 2σ of correlation residuals
- - - Calculation uncertainty
- · - Reference uncertainty
- Absolute uncertainty

Figure 68. Continued.

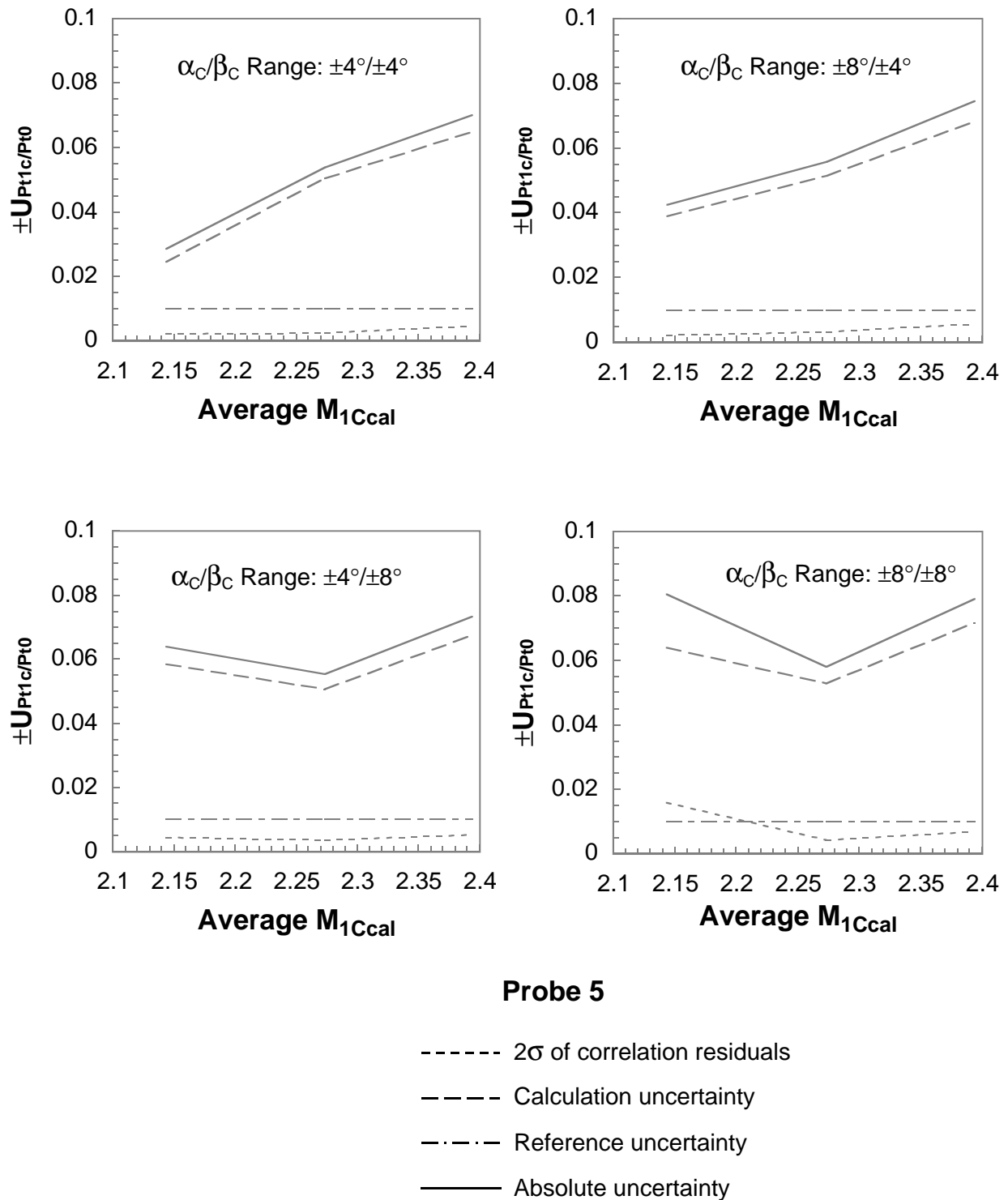
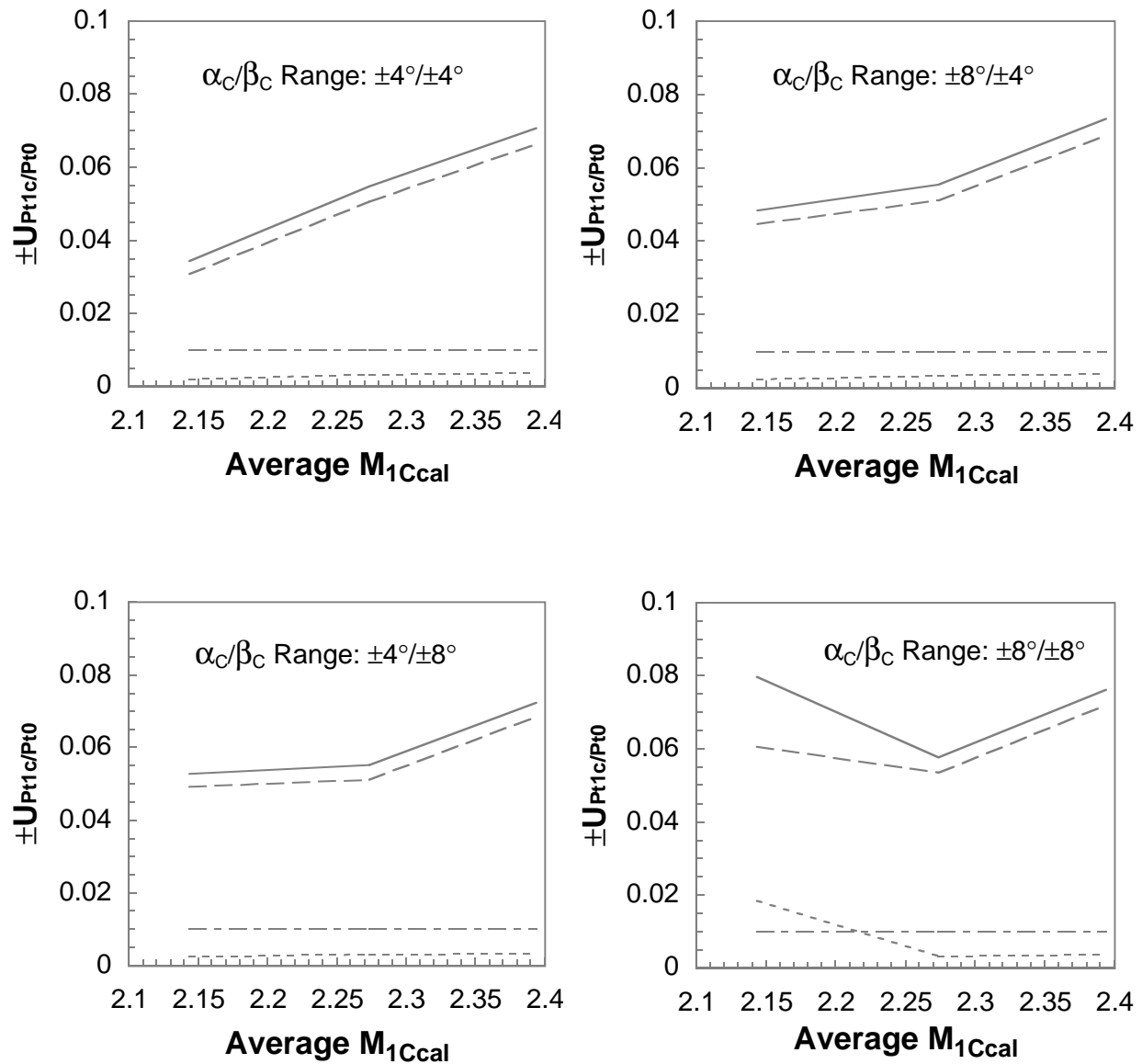


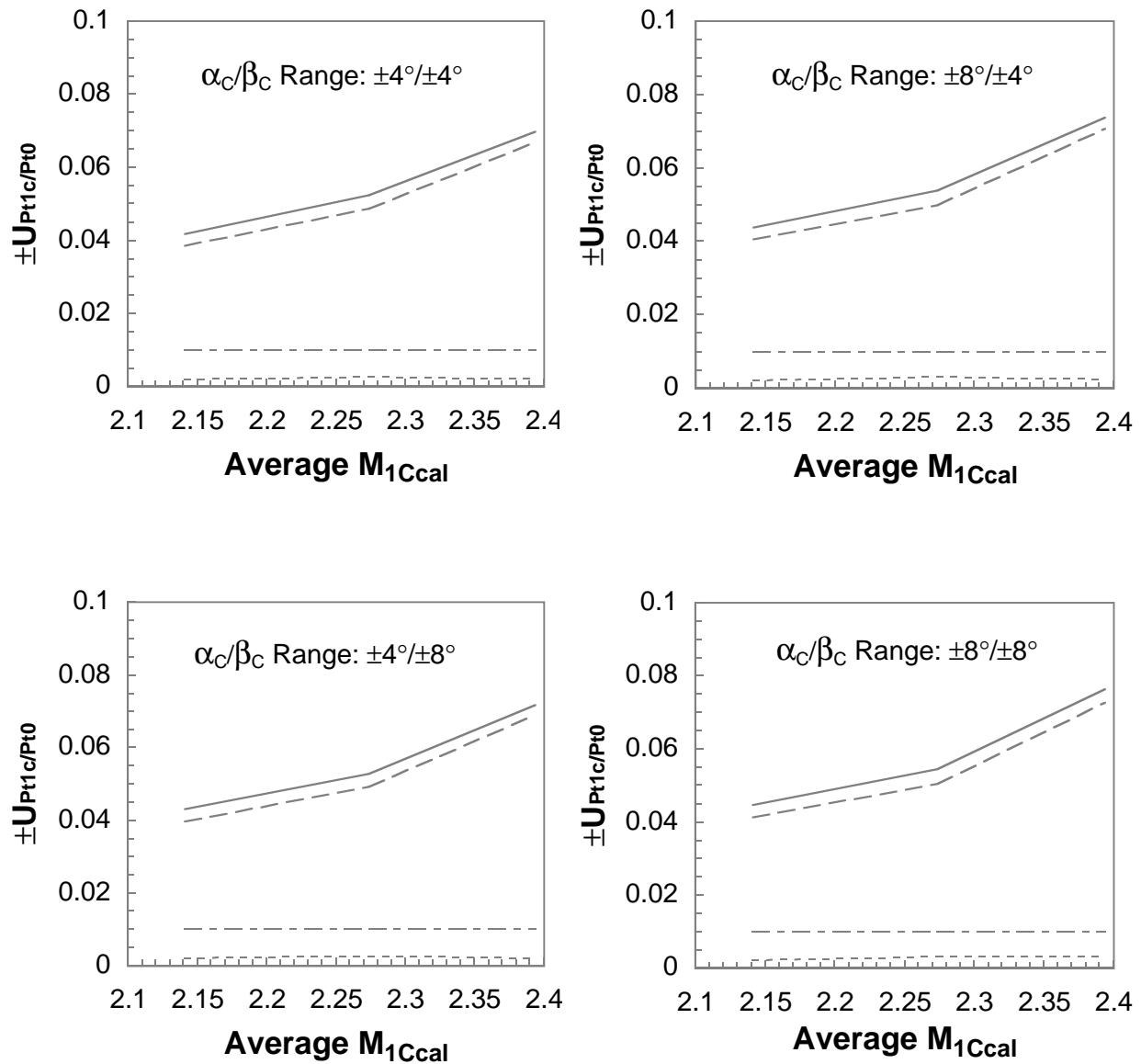
Figure 68. Continued.



Probe 6

- 2σ of correlation residuals
- - - Calculation uncertainty
- · - Reference uncertainty
- Absolute uncertainty

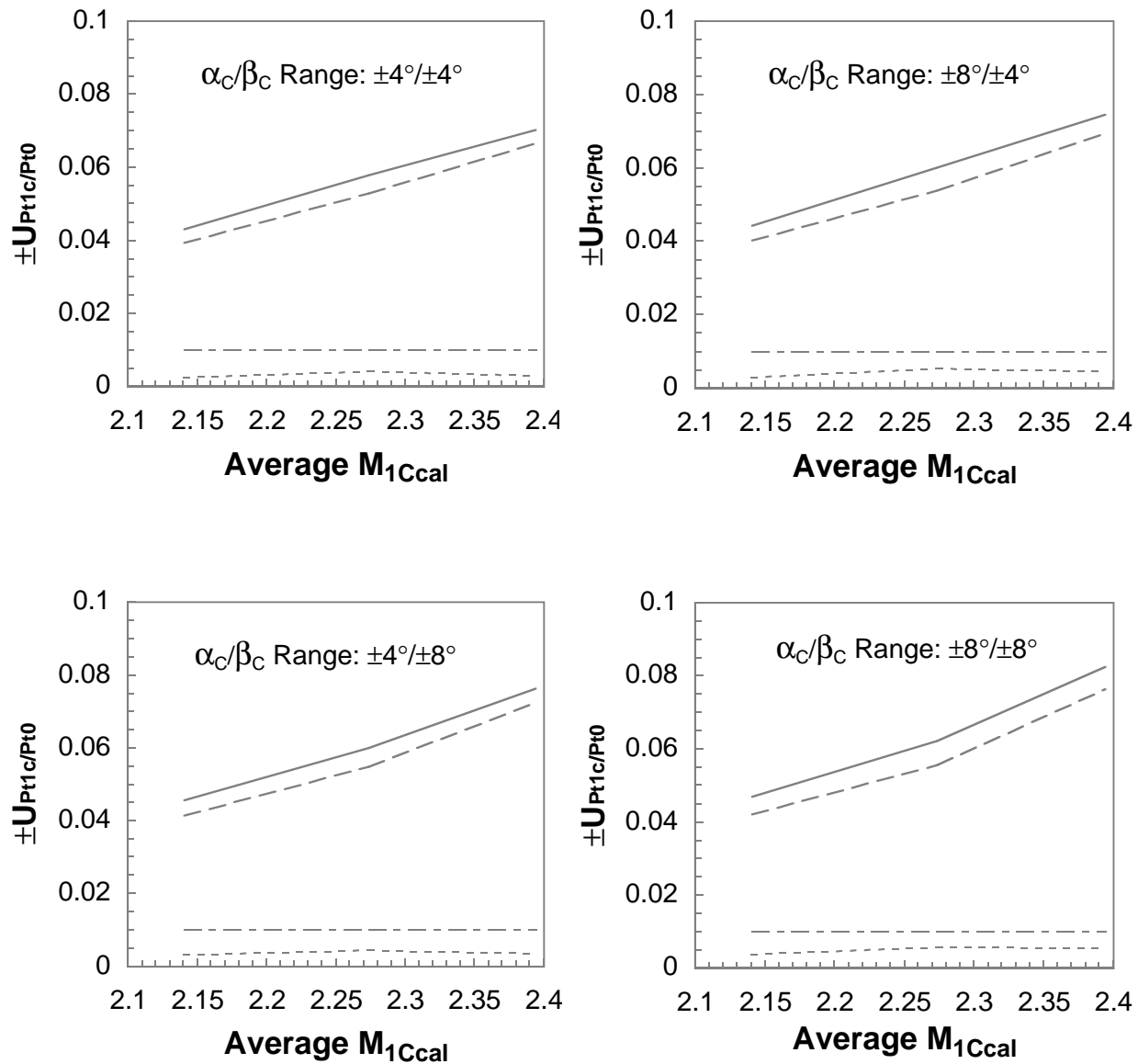
Figure 68. Continued.



Probe 7

- 2σ of correlation residuals
- - - Calculation uncertainty
- · - Reference uncertainty
- Absolute uncertainty

Figure 68. Continued.



Probe 8

- 2σ of correlation residuals
- - - Calculation uncertainty
- · - Reference uncertainty
- Absolute uncertainty

Figure 68. Concluded.

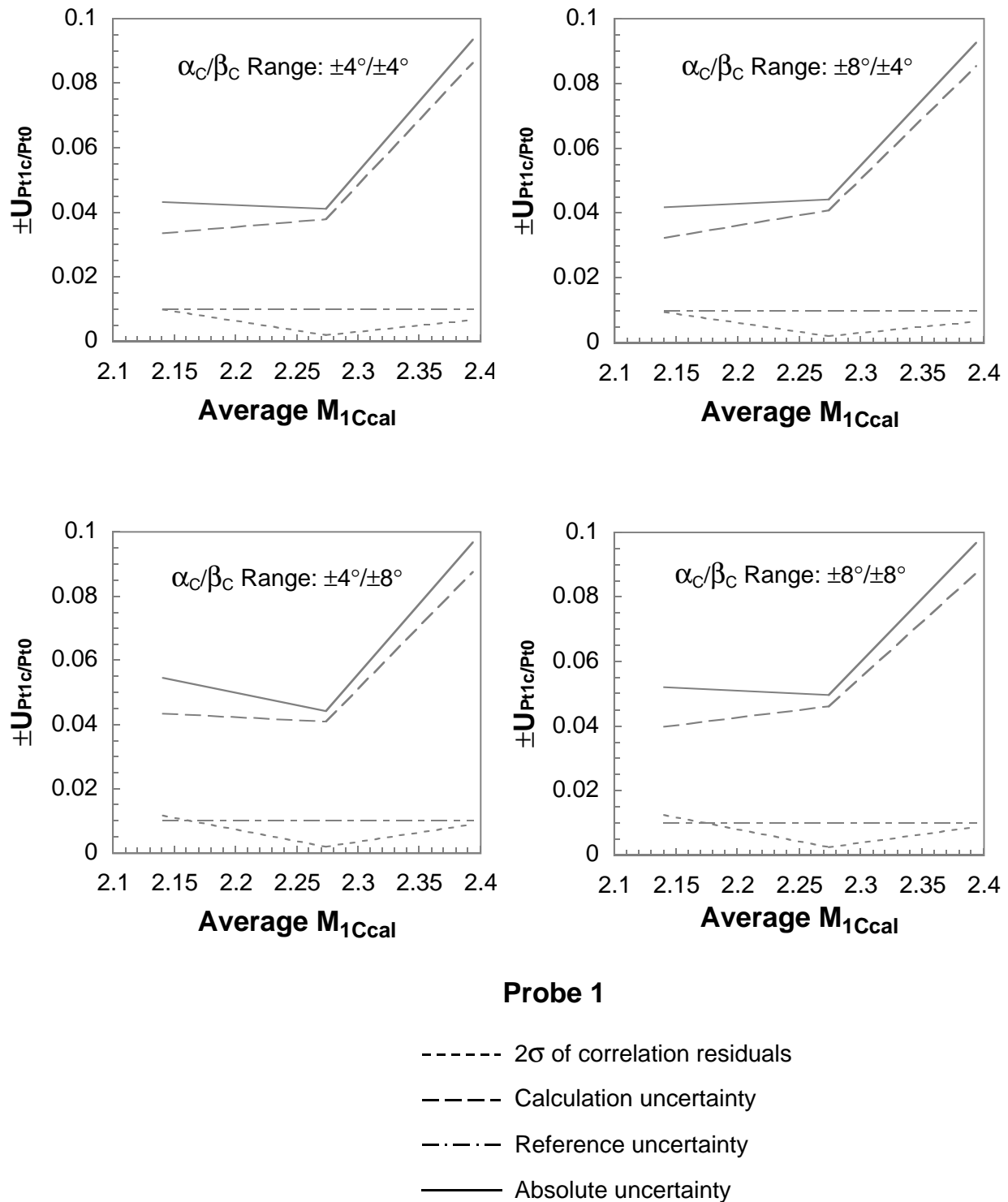
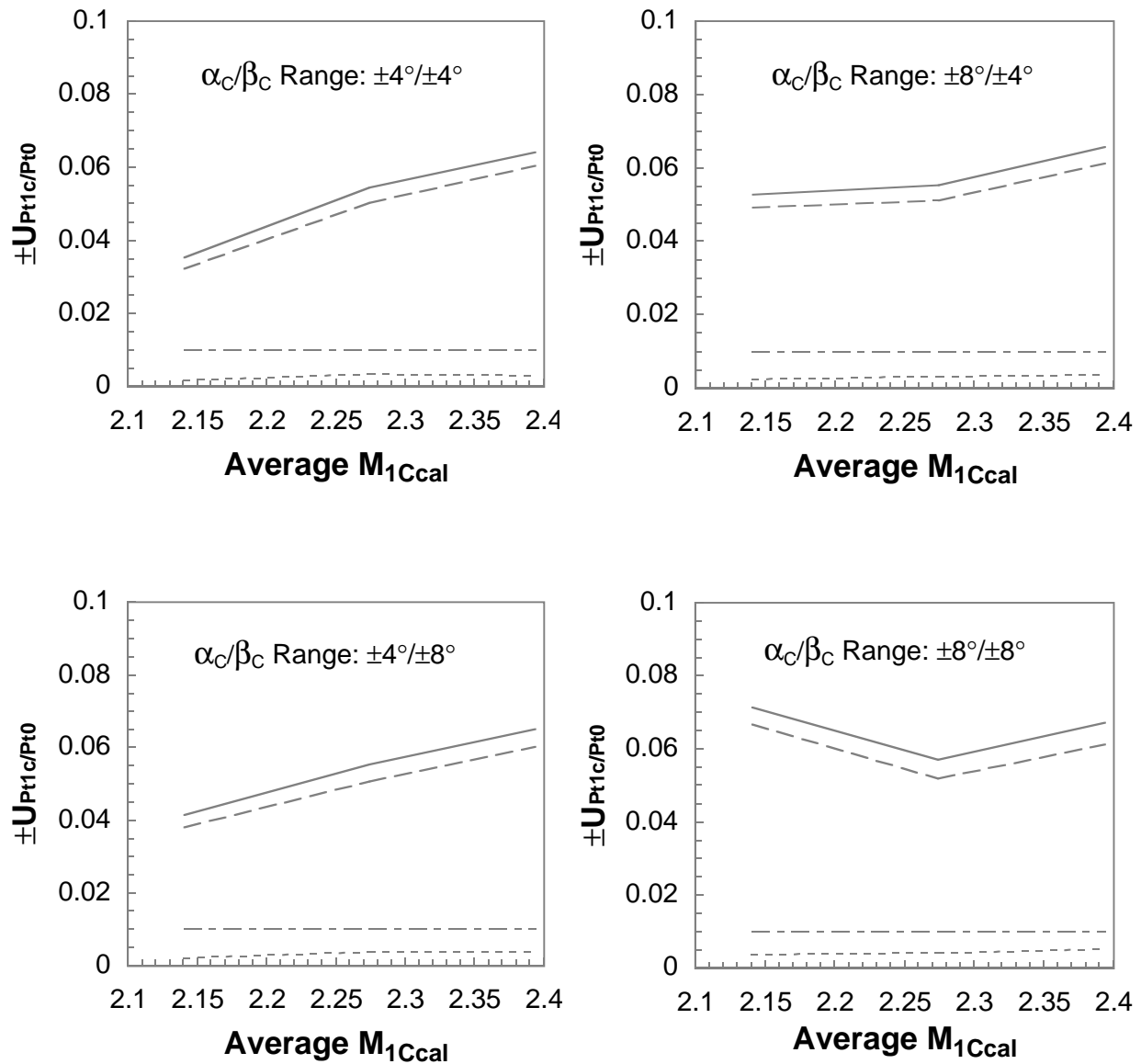


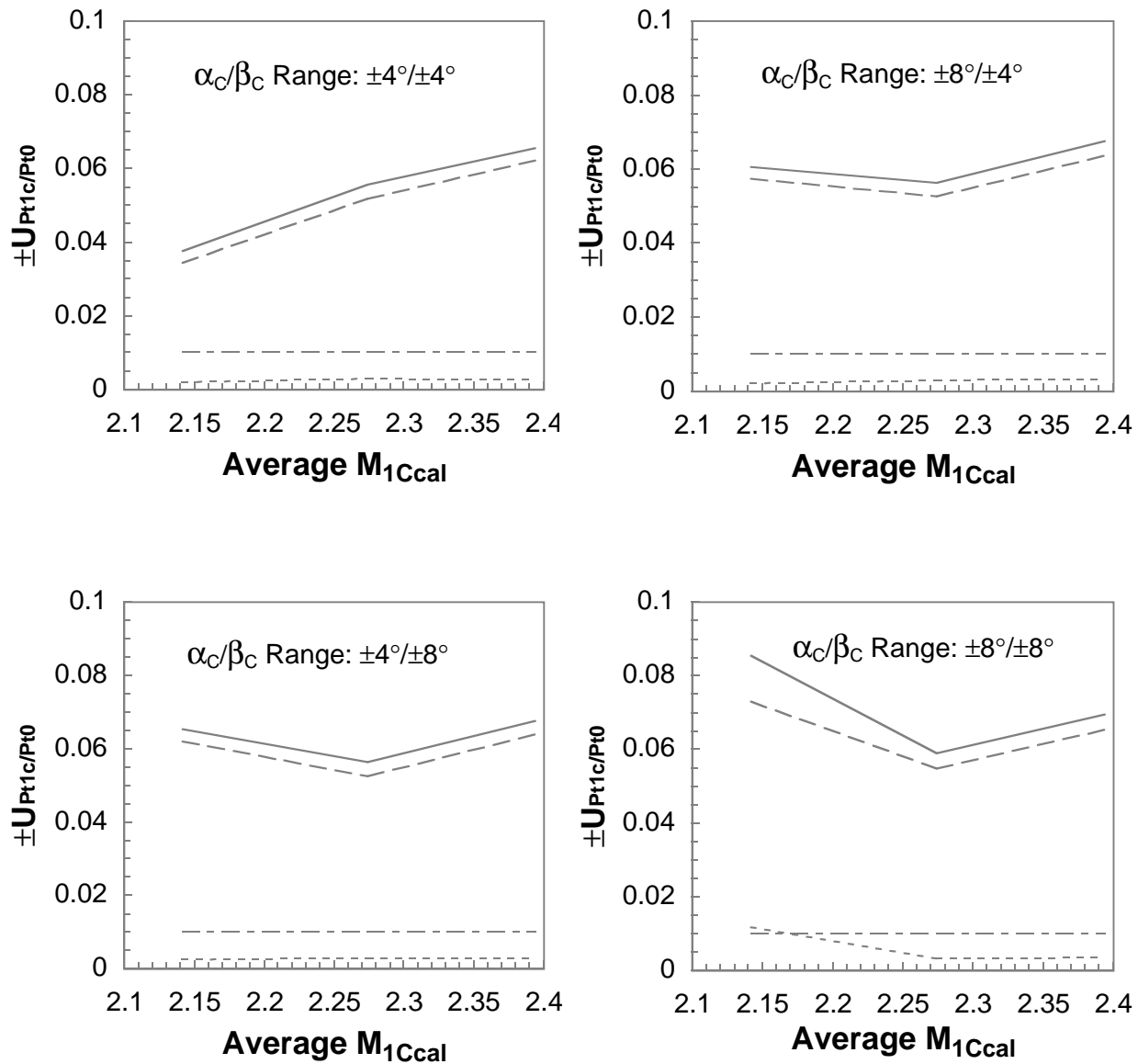
Figure 69. Calibrated total pressure uncertainty for rake 2.



Probe 2

- 2σ of correlation residuals
- - - Calculation uncertainty
- · - Reference uncertainty
- Absolute uncertainty

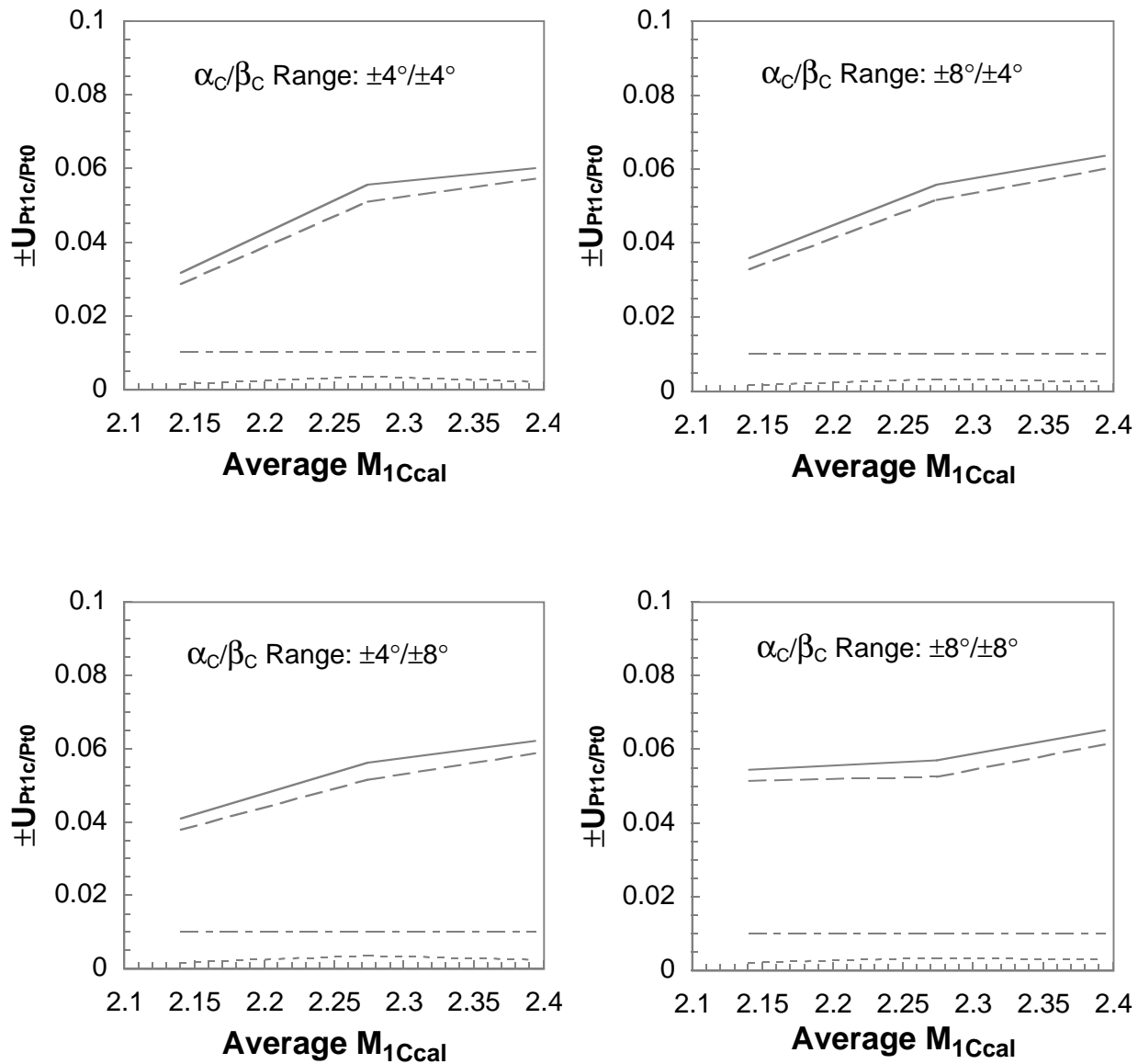
Figure 69. Continued.



Probe 3

- 2σ of correlation residuals
- - - Calculation uncertainty
- · - Reference uncertainty
- Absolute uncertainty

Figure 69. Continued.



Probe 4

- 2σ of correlation residuals
- - - Calculation uncertainty
- · - Reference uncertainty
- Absolute uncertainty

Figure 69. Continued.

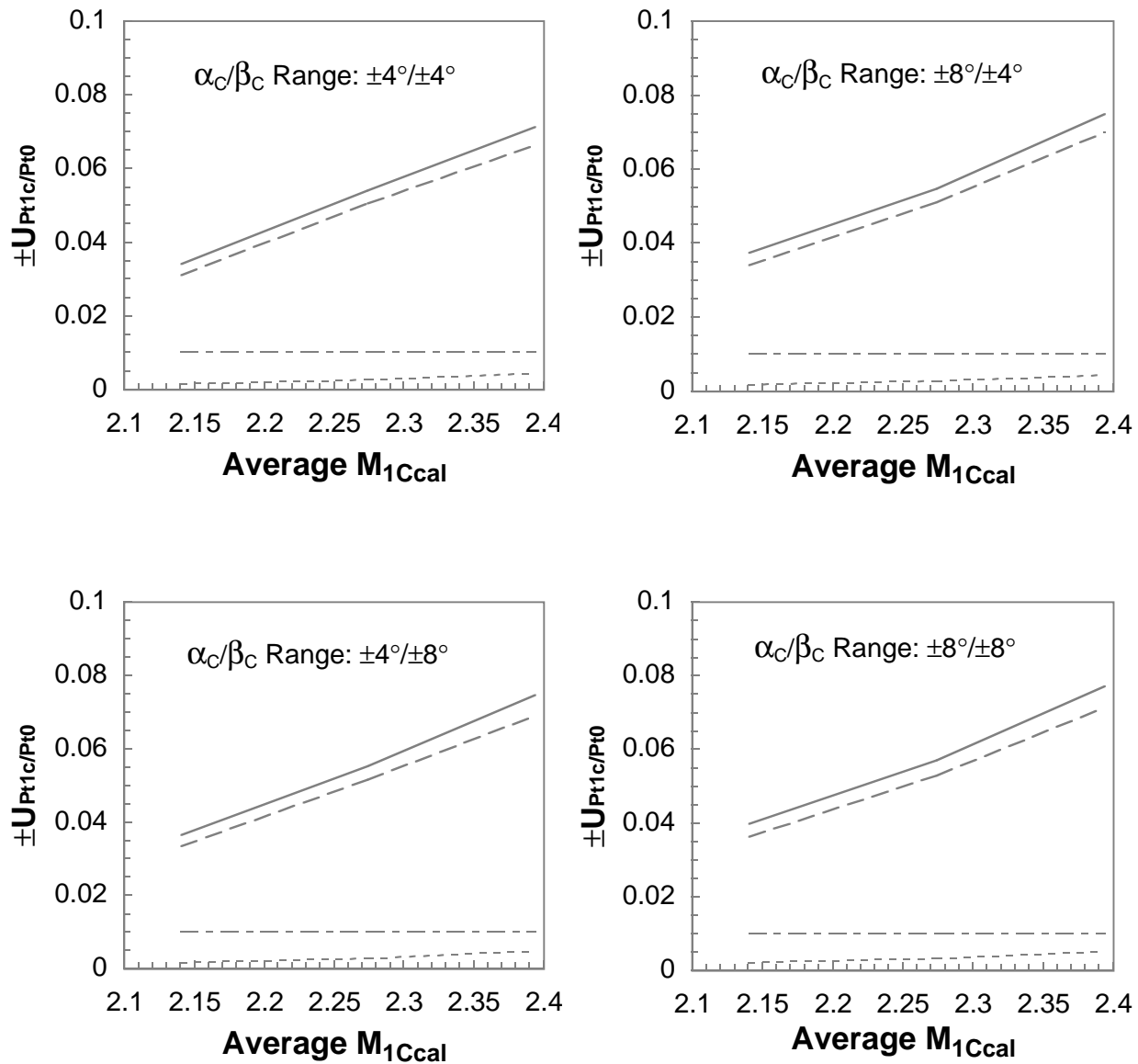
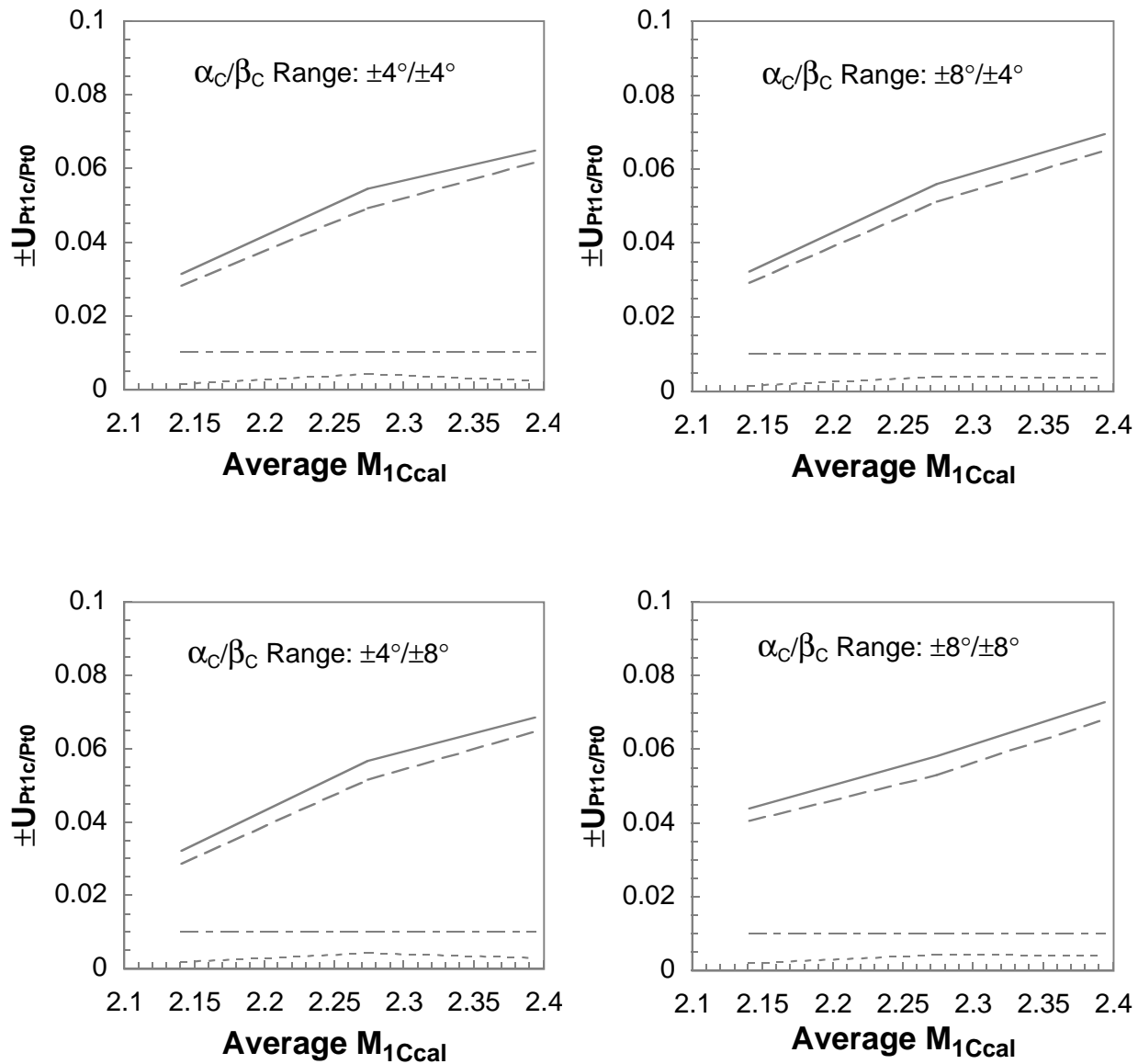


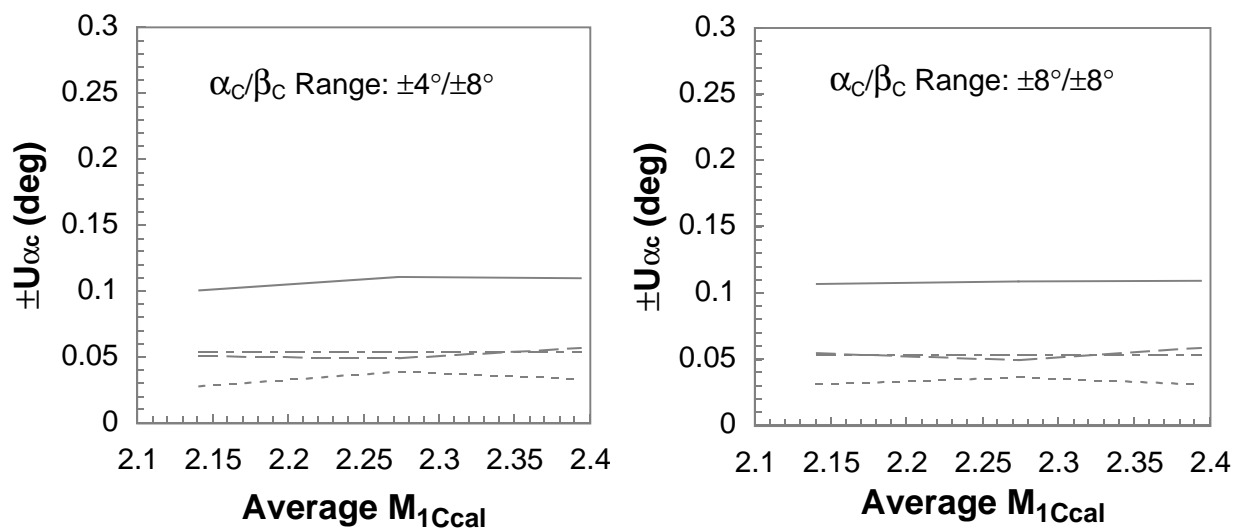
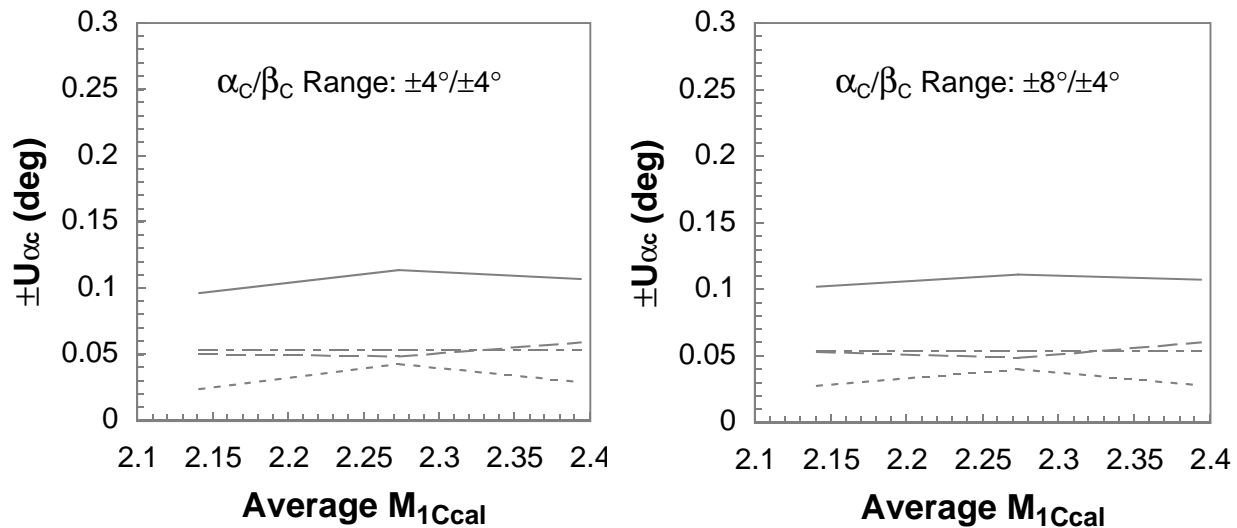
Figure 69. Continued.



Probe 6

- 2σ of correlation residuals
- - - Calculation uncertainty
- · - Reference uncertainty
- Absolute uncertainty

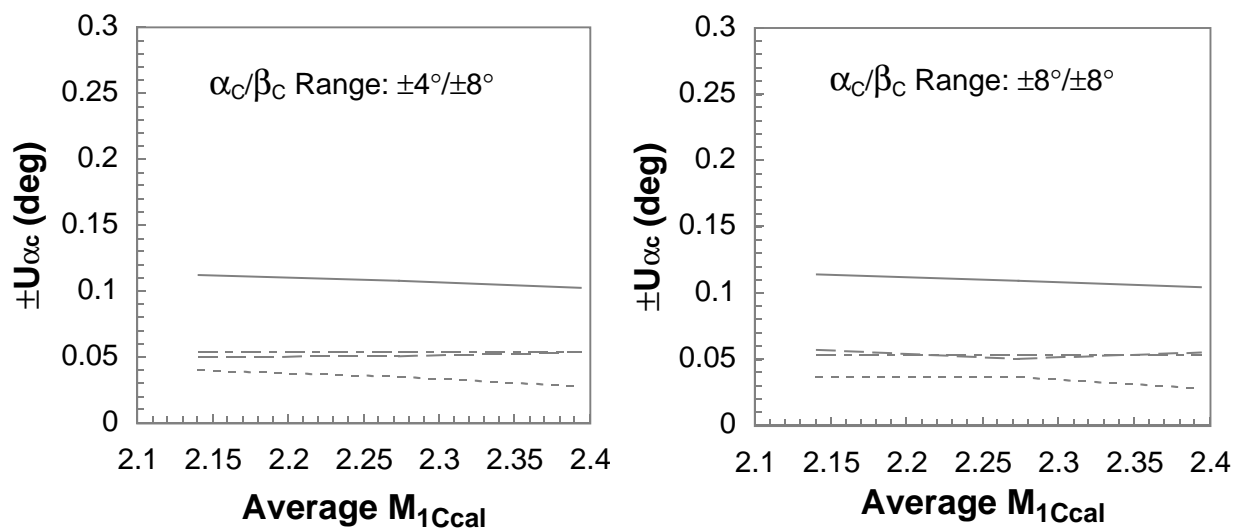
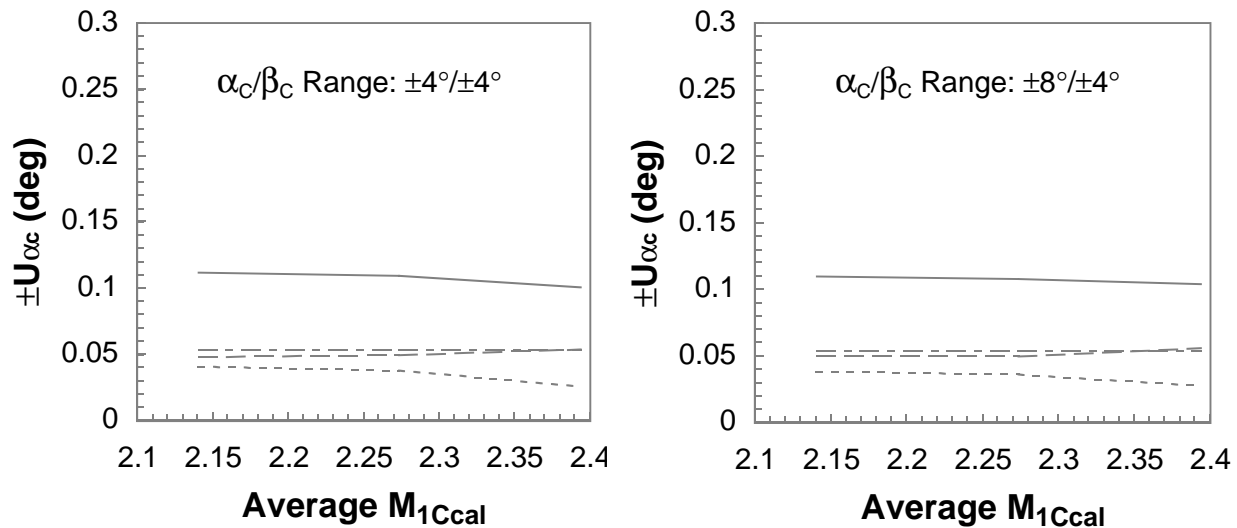
Figure 69. Concluded.



Probe 1

- 2σ of correlation residuals
- - - Calculation uncertainty
- · - Reference uncertainty
- Absolute uncertainty

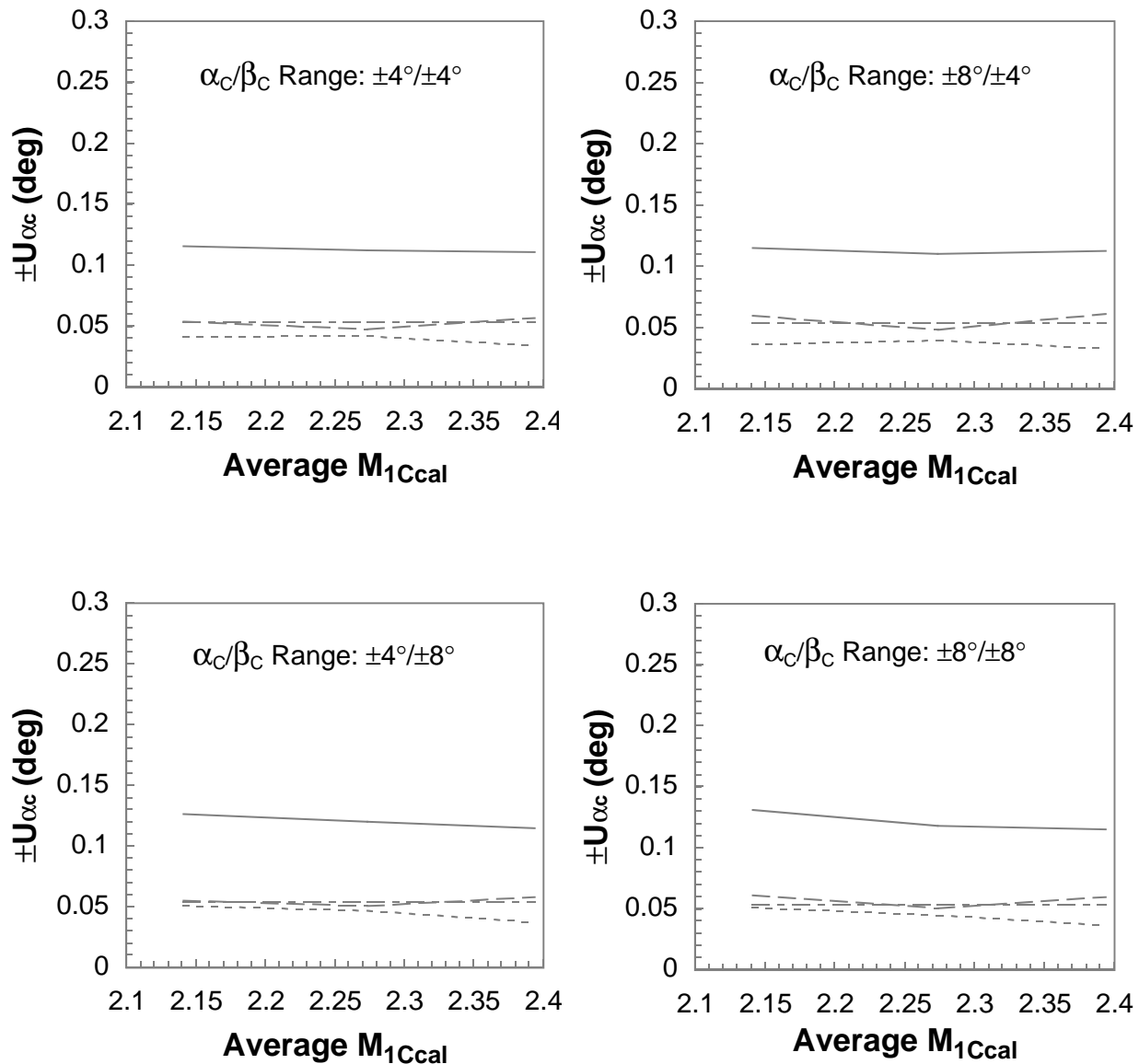
Figure 70. Calibrated angle of attack uncertainty for rake 1.



Probe 2

- 2σ of correlation residuals
- - - Calculation uncertainty
- · - Reference uncertainty
- Absolute uncertainty

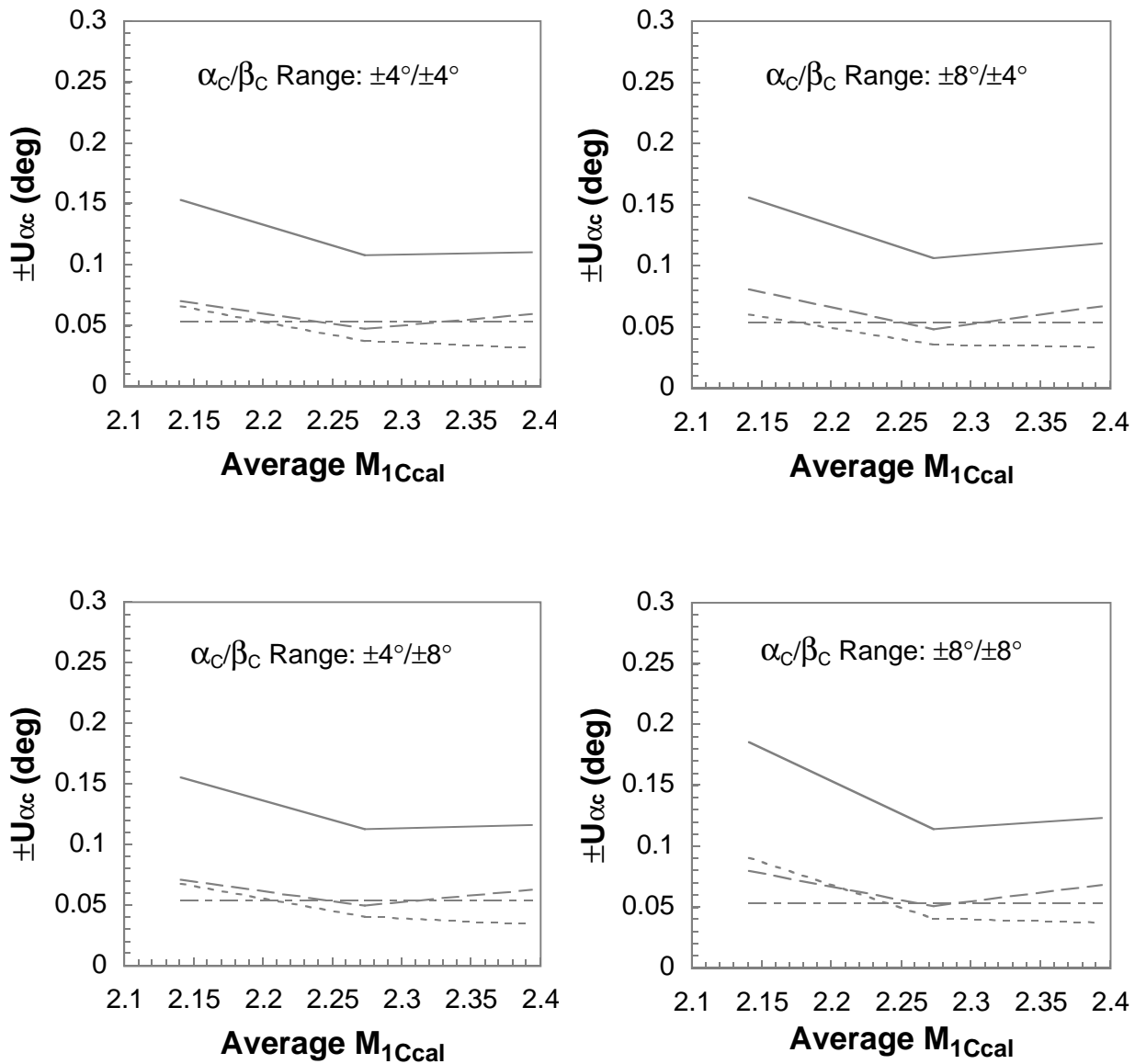
Figure 70. Continued.



Probe 3

- 2σ of correlation residuals
- - - Calculation uncertainty
- · - Reference uncertainty
- Absolute uncertainty

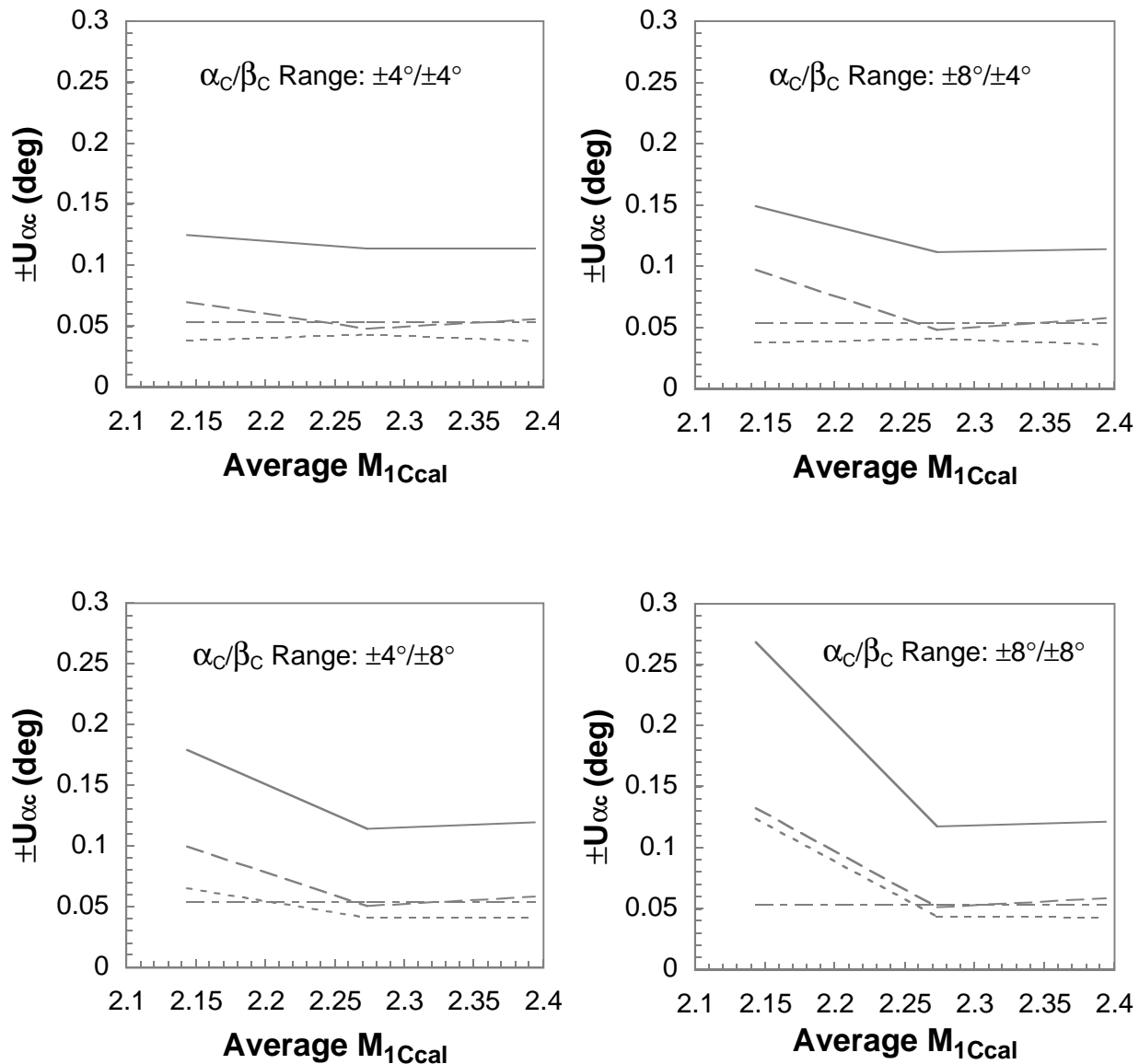
Figure 70. Continued.



Probe 4

- 2σ of correlation residuals
- - - Calculation uncertainty
- · - Reference uncertainty
- Absolute uncertainty

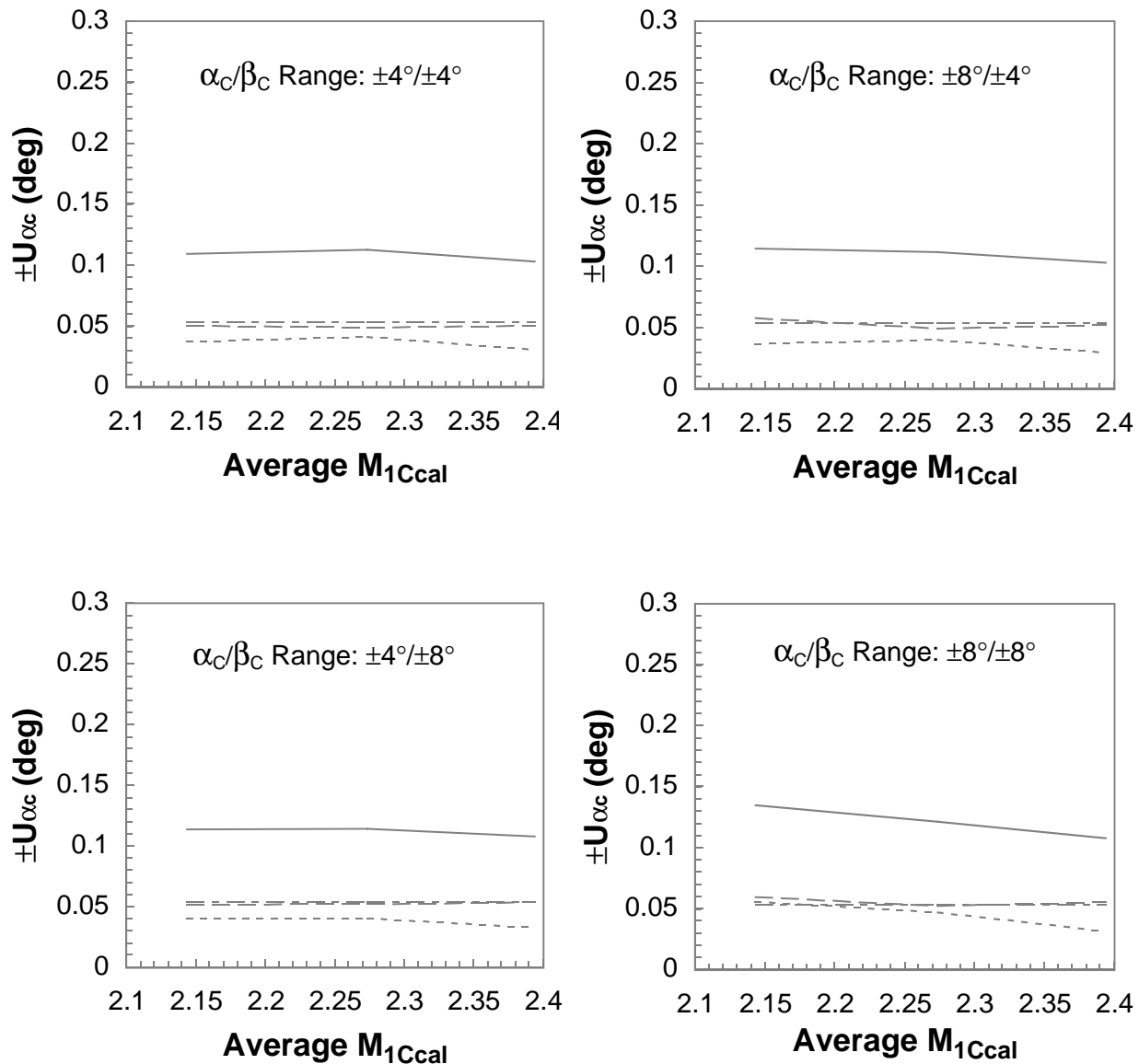
Figure 70. Continued.



Probe 5

- 2σ of correlation residuals
- - - Calculation uncertainty
- · - Reference uncertainty
- Absolute uncertainty

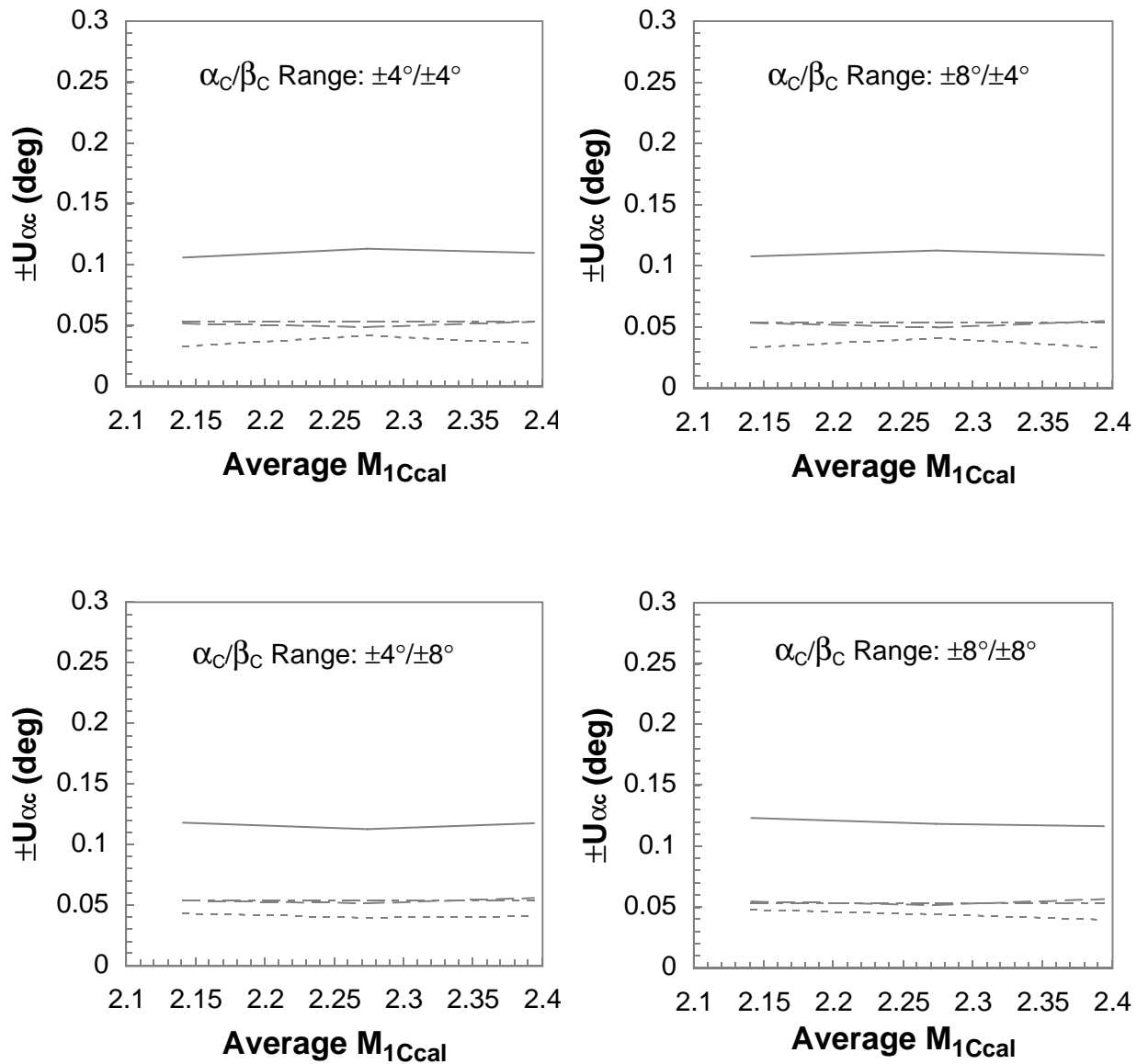
Figure 70. Continued.



Probe 6

- 2σ of correlation residuals
- - - Calculation uncertainty
- · - Reference uncertainty
- Absolute uncertainty

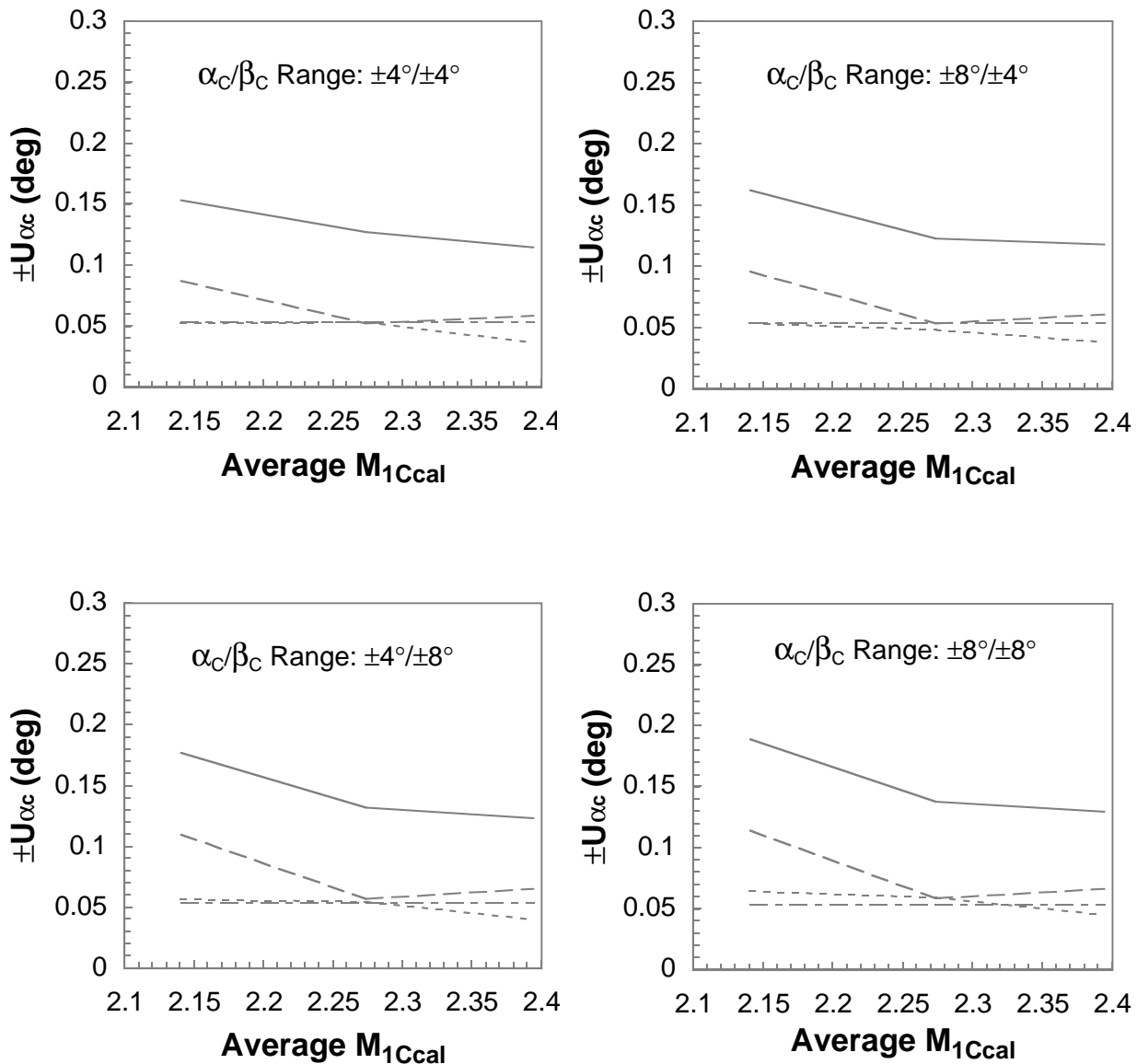
Figure 70. Continued.



Probe 7

- 2σ of correlation residuals
- - - Calculation uncertainty
- · - Reference uncertainty
- Absolute uncertainty

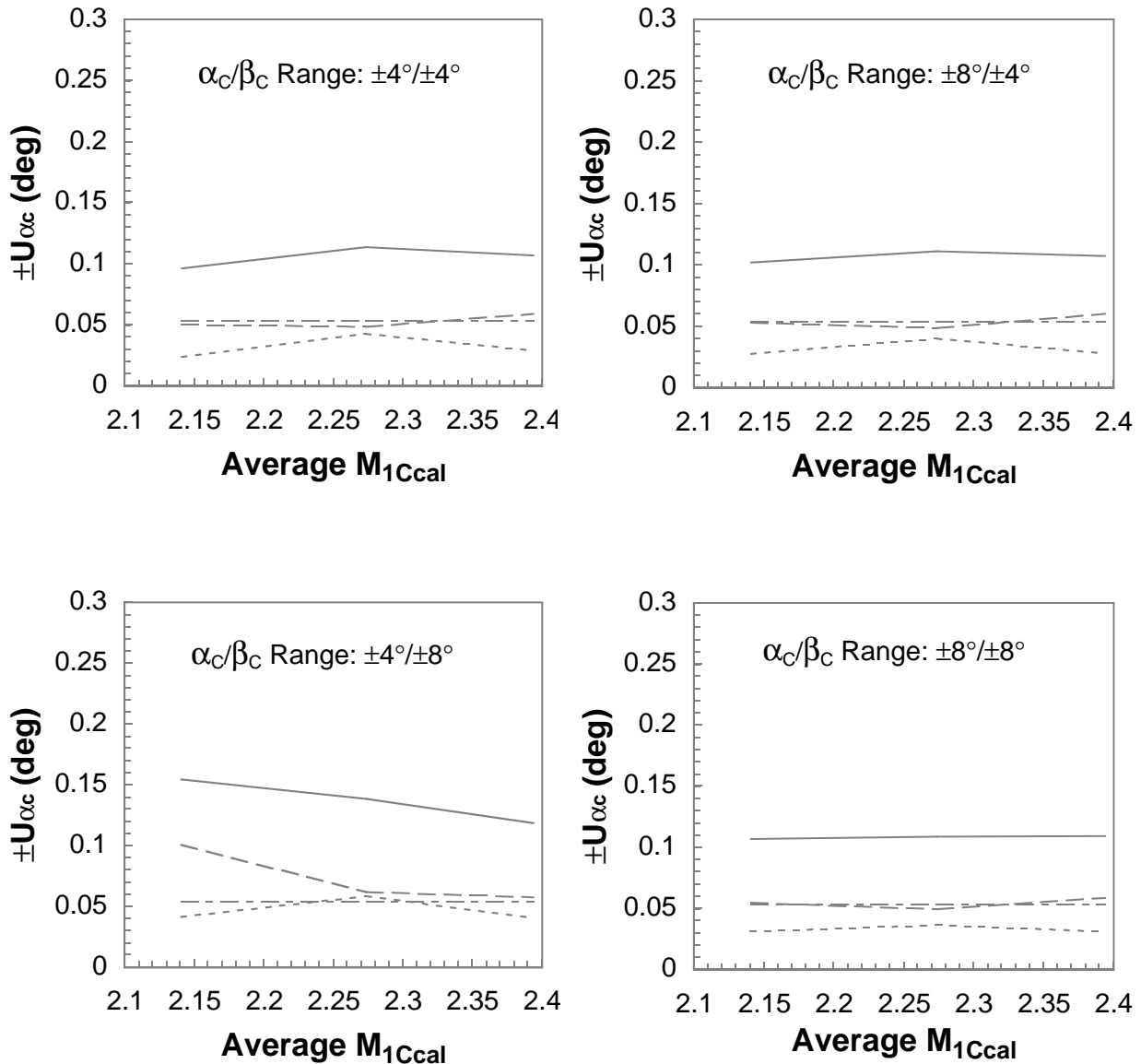
Figure 70. Continued.



Probe 8

- 2σ of correlation residuals
- - - Calculation uncertainty
- · - Reference uncertainty
- Absolute uncertainty

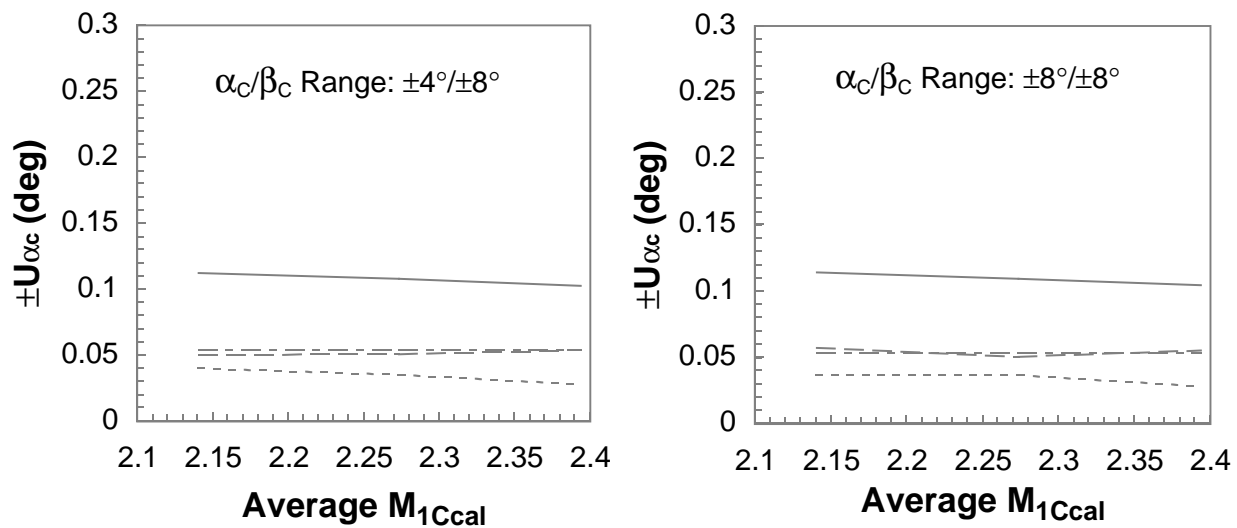
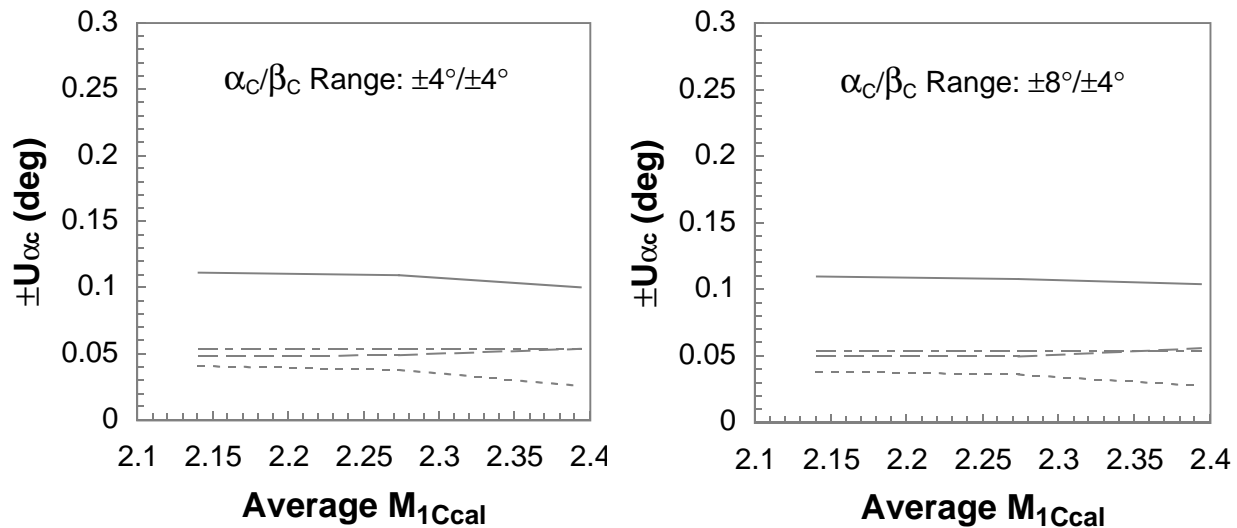
Figure 70. Concluded.



Probe 1

- 2σ of correlation residuals
- - - Calculation uncertainty
- · - Reference uncertainty
- Absolute uncertainty

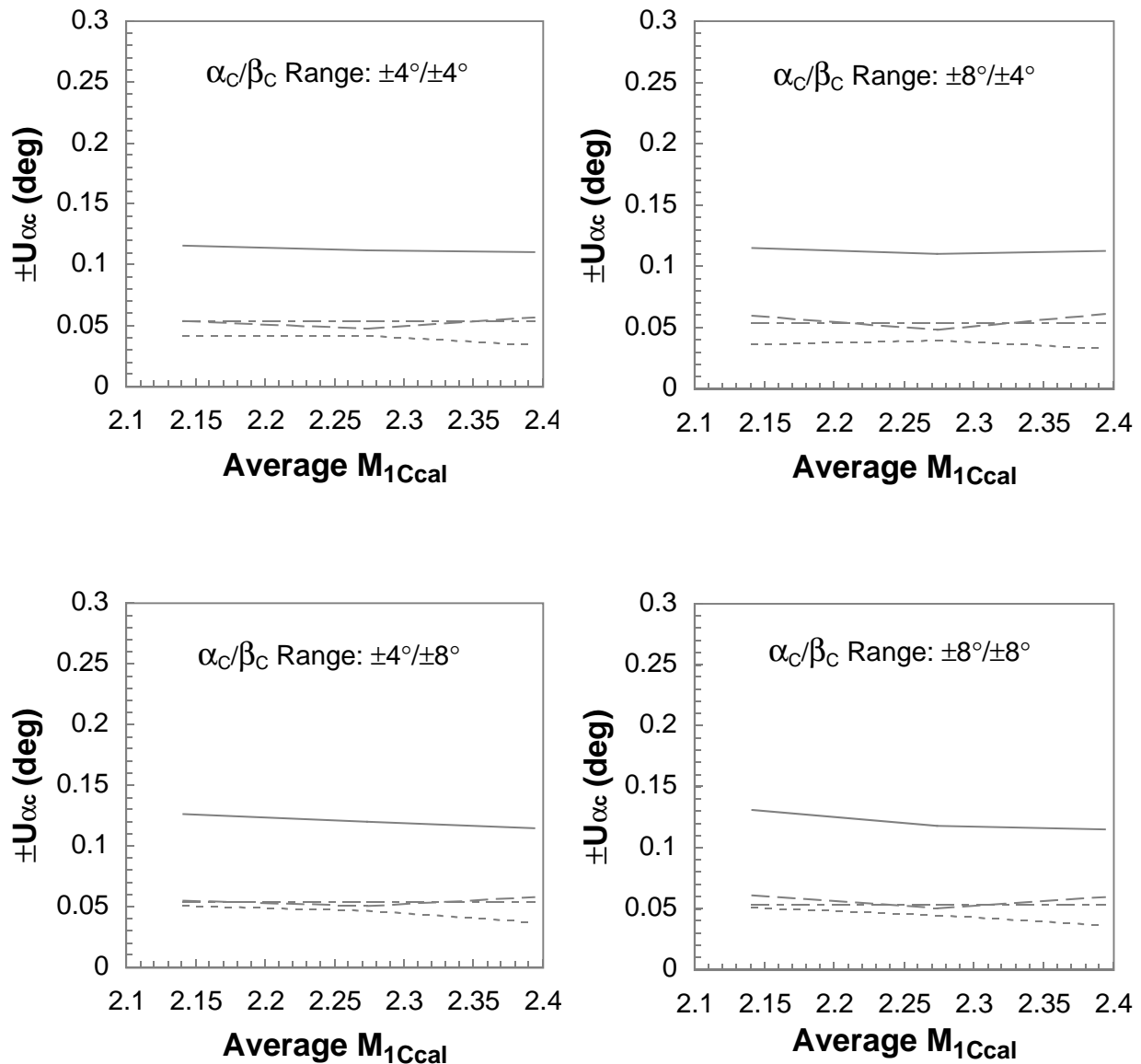
Figure 71. Calibrated angle of attack uncertainty for rake 2.



Probe 2

- 2σ of correlation residuals
- Calculation uncertainty
- Reference uncertainty
- Absolute uncertainty

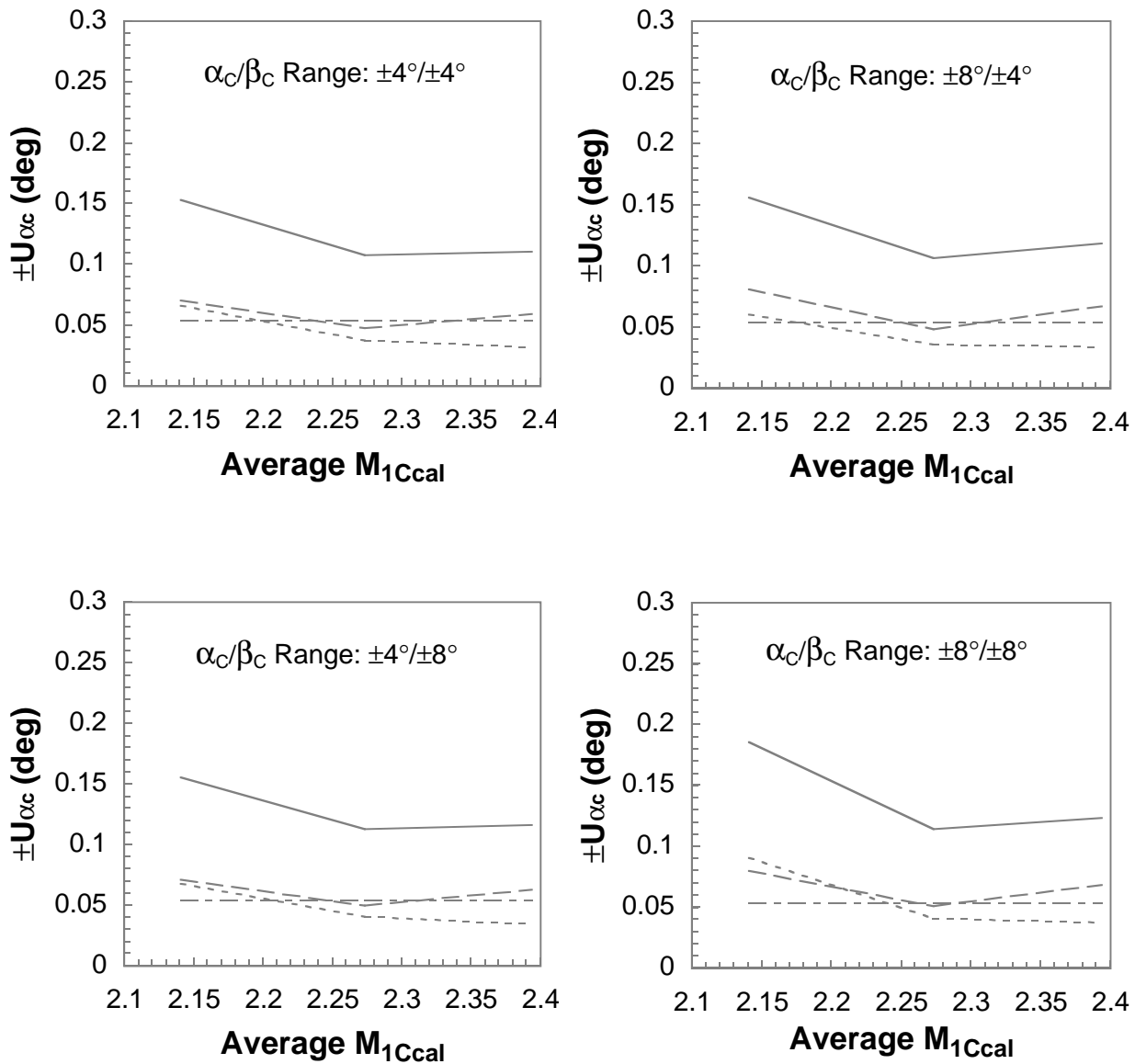
Figure 71. Continued.



Probe 3

- 2σ of correlation residuals
- Calculation uncertainty
- Reference uncertainty
- Absolute uncertainty

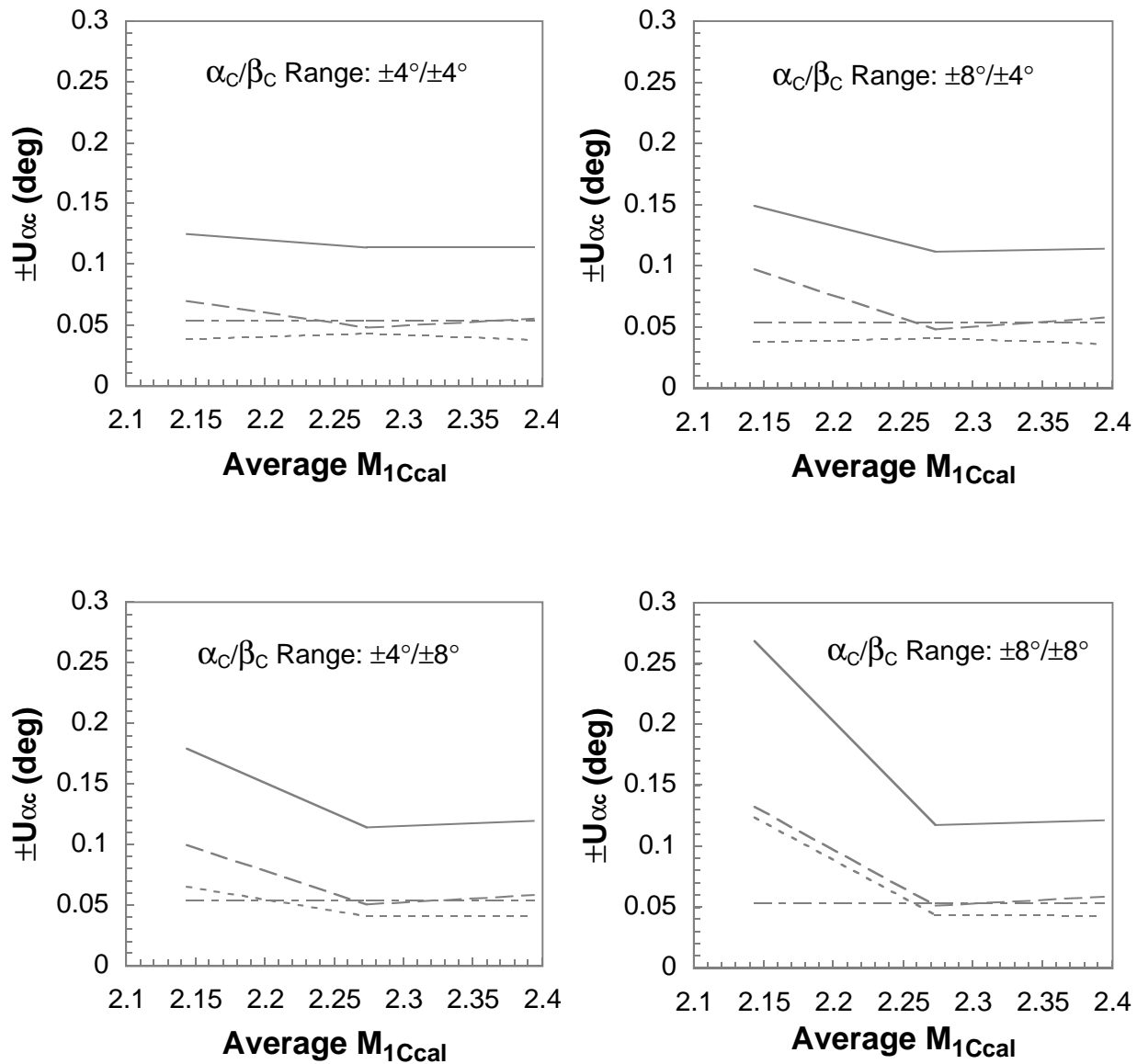
Figure 71. Continued.



Probe 4

- 2σ of correlation residuals
- - - Calculation uncertainty
- · - Reference uncertainty
- Absolute uncertainty

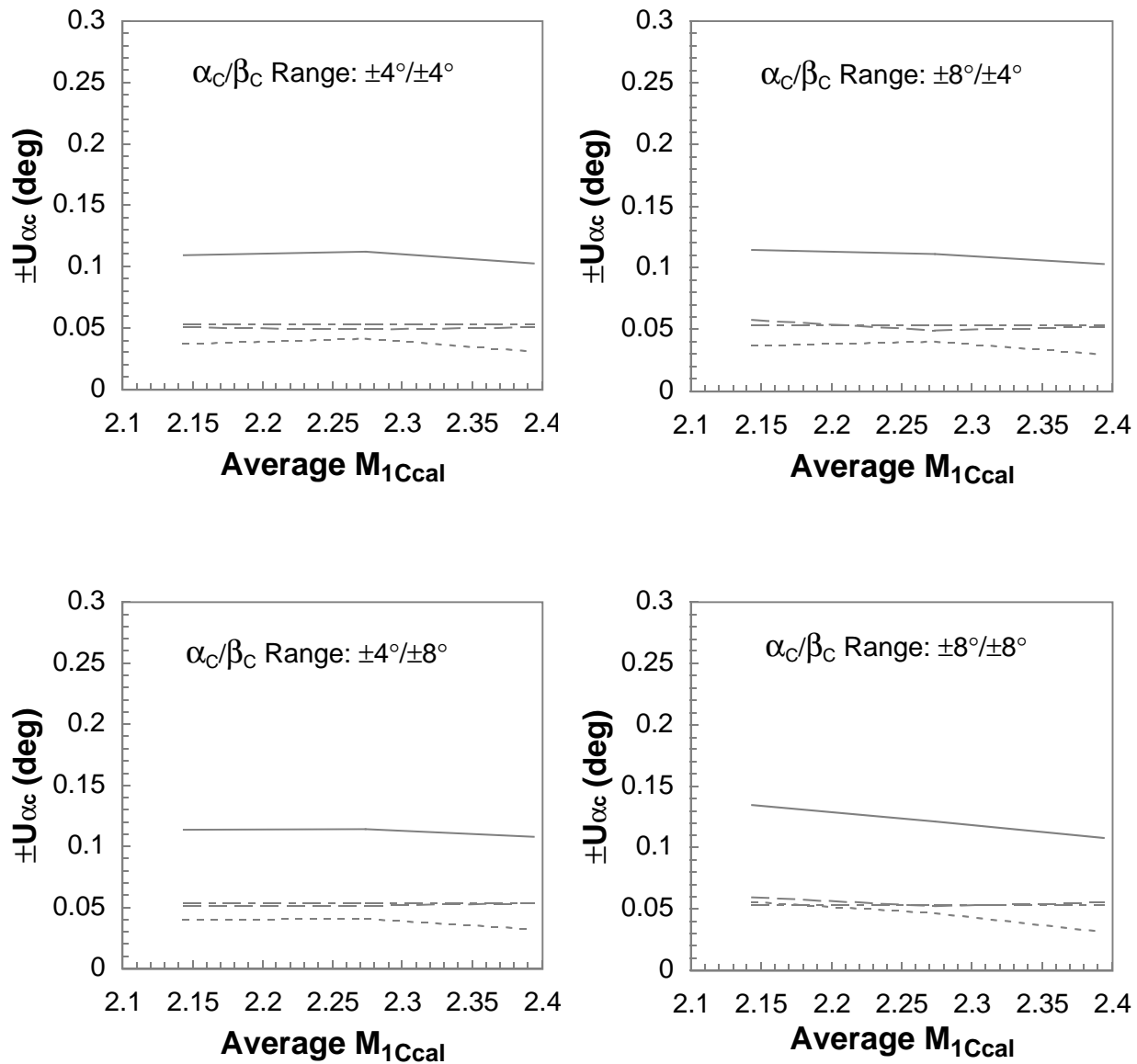
Figure 71. Continued.



Probe 5

- 2σ of correlation residuals
- - - Calculation uncertainty
- · - Reference uncertainty
- Absolute uncertainty

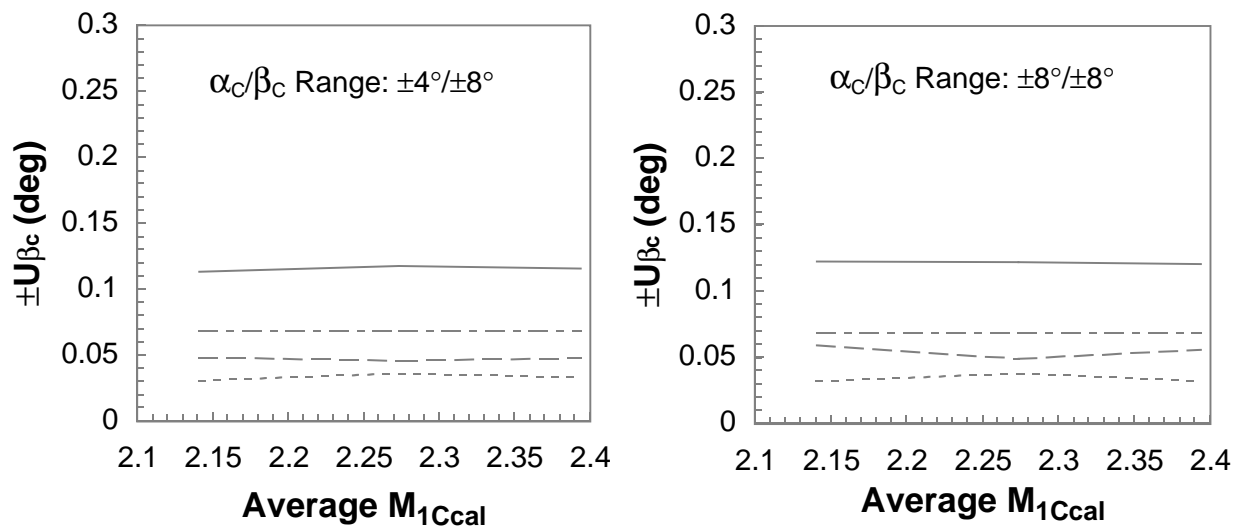
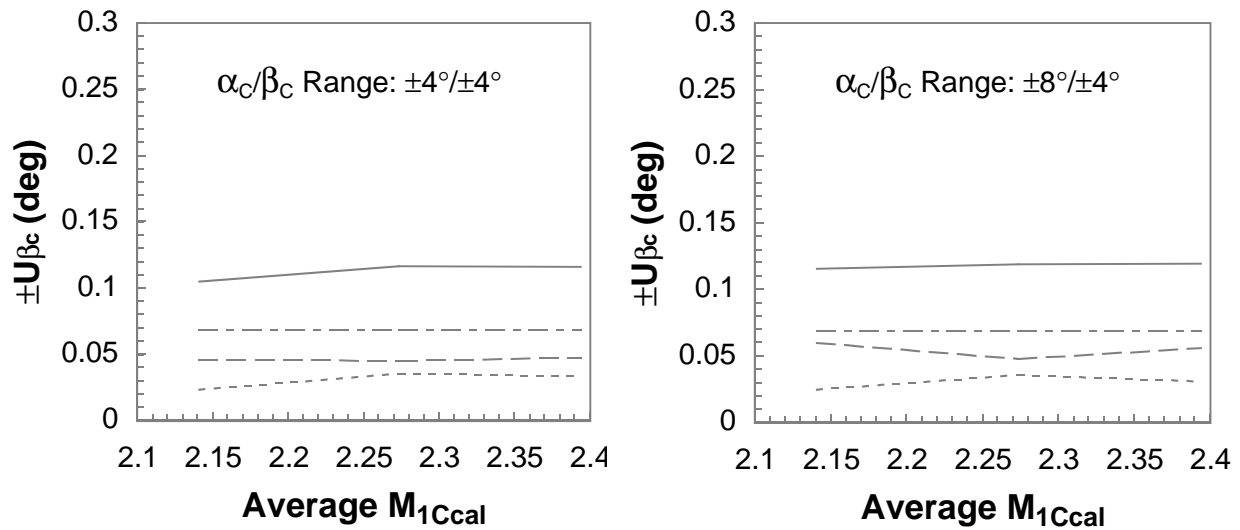
Figure 71. Continued.



Probe 6

- 2σ of correlation residuals
- Calculation uncertainty
- Reference uncertainty
- Absolute uncertainty

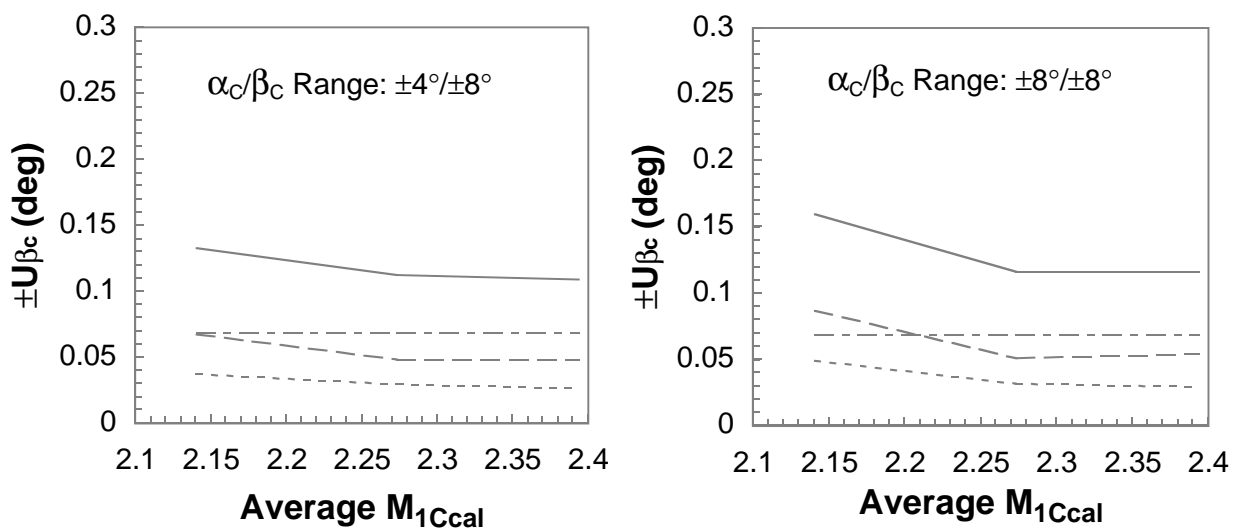
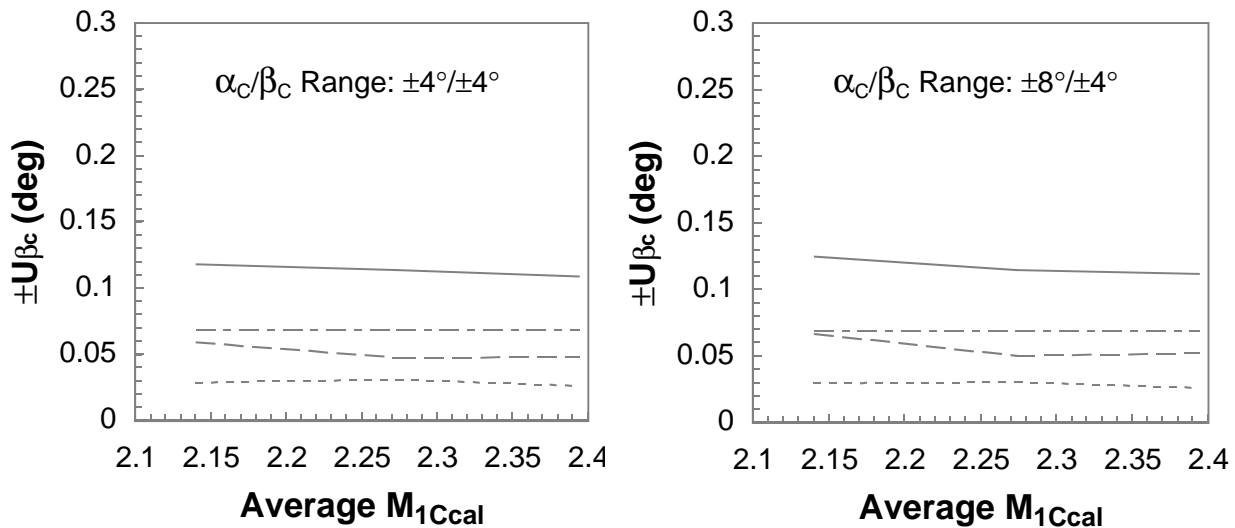
Figure 71. Concluded.



Probe 1

- 2σ of correlation residuals
- - - Calculation uncertainty
- · - Reference uncertainty
- Absolute uncertainty

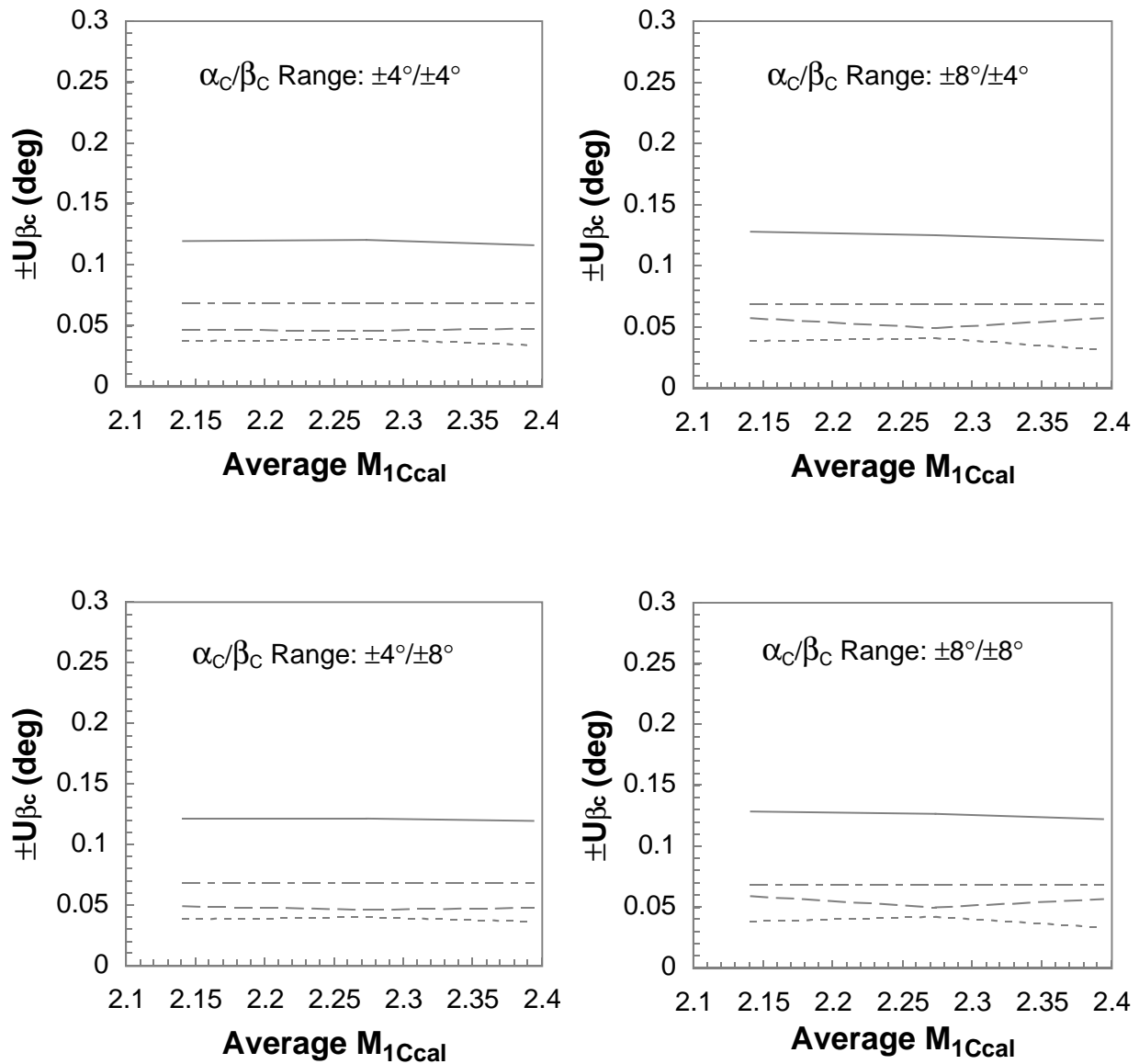
Figure 72. Calibrated angle of sideslip uncertainty for rake 1.



Probe 2

- 2σ of correlation residuals
- - - Calculation uncertainty
- · - Reference uncertainty
- Absolute uncertainty

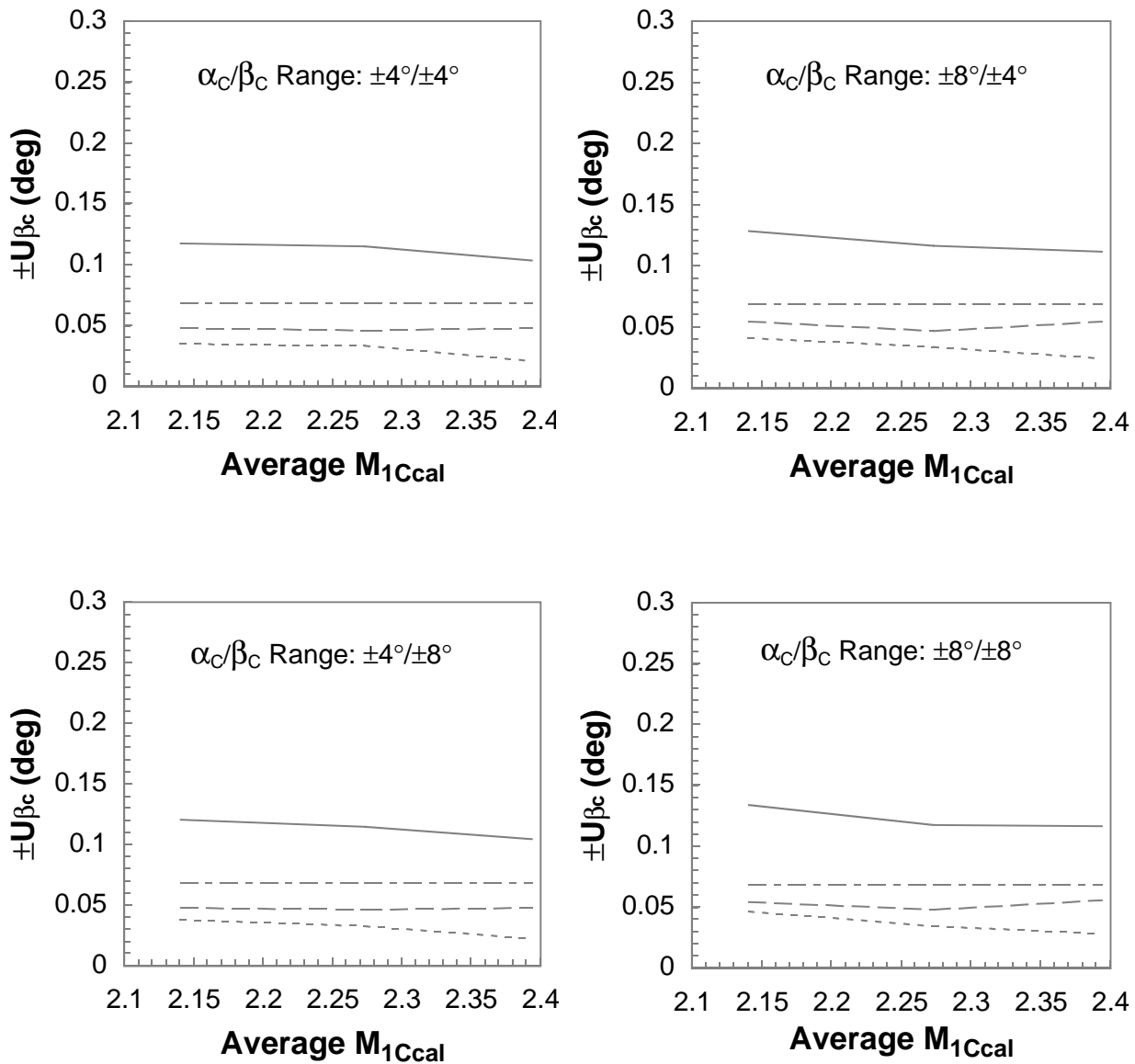
Figure 72. Continued.



Probe 3

- 2σ of correlation residuals
- - - Calculation uncertainty
- · - Reference uncertainty
- Absolute uncertainty

Figure 72. Continued.



Probe 4

- 2σ of correlation residuals
- - - Calculation uncertainty
- · - Reference uncertainty
- Absolute uncertainty

Figure 72. Continued.

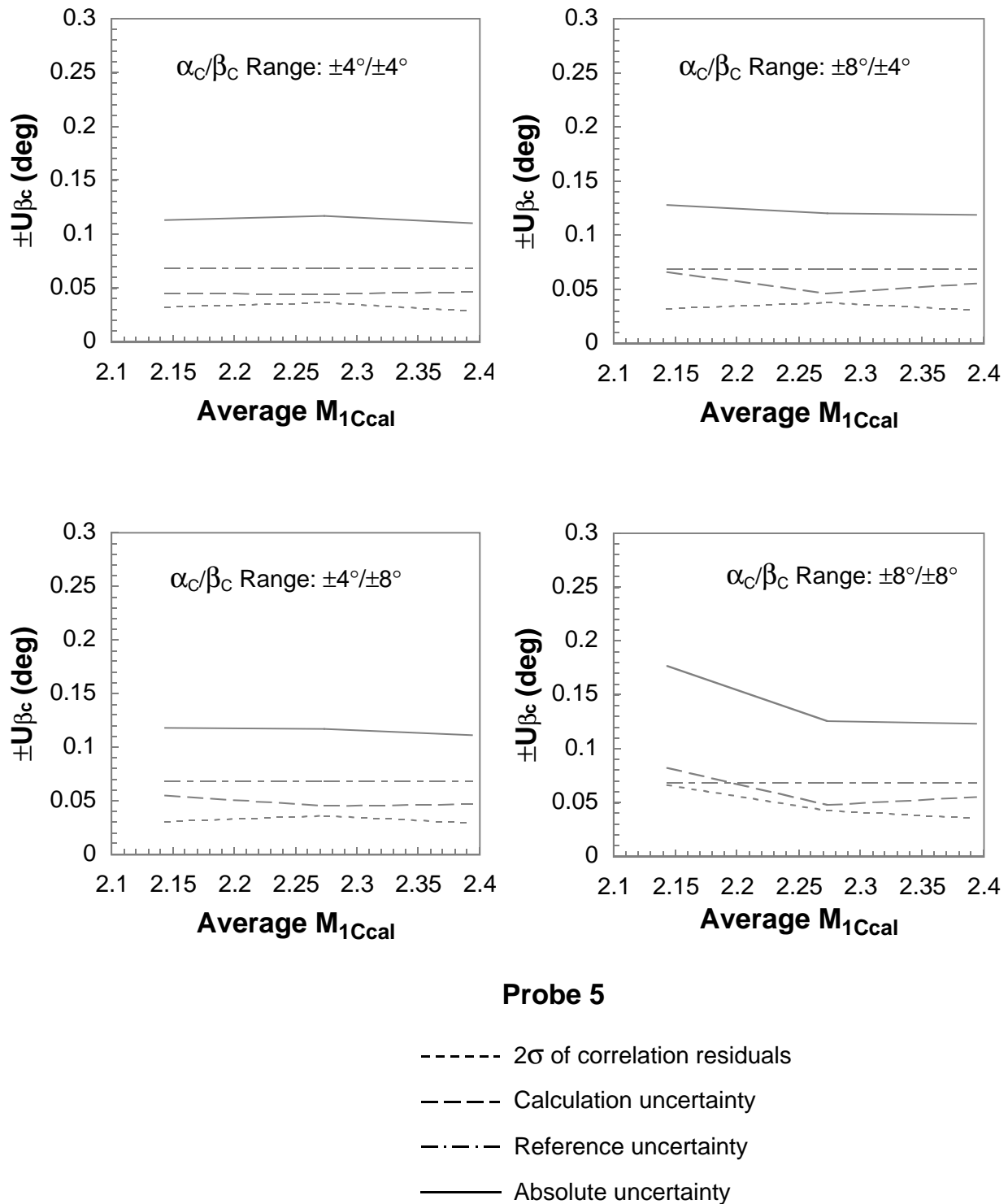
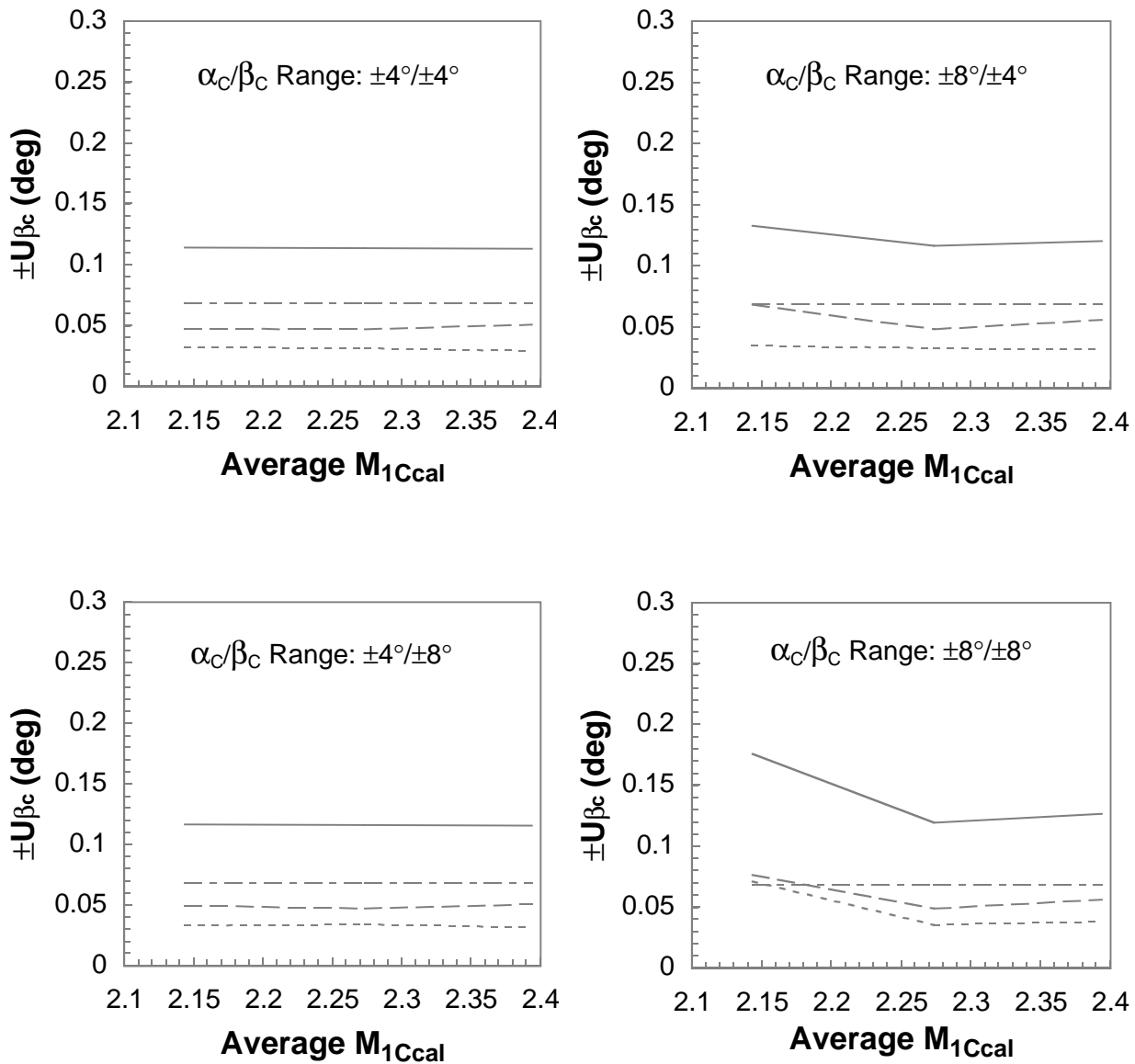


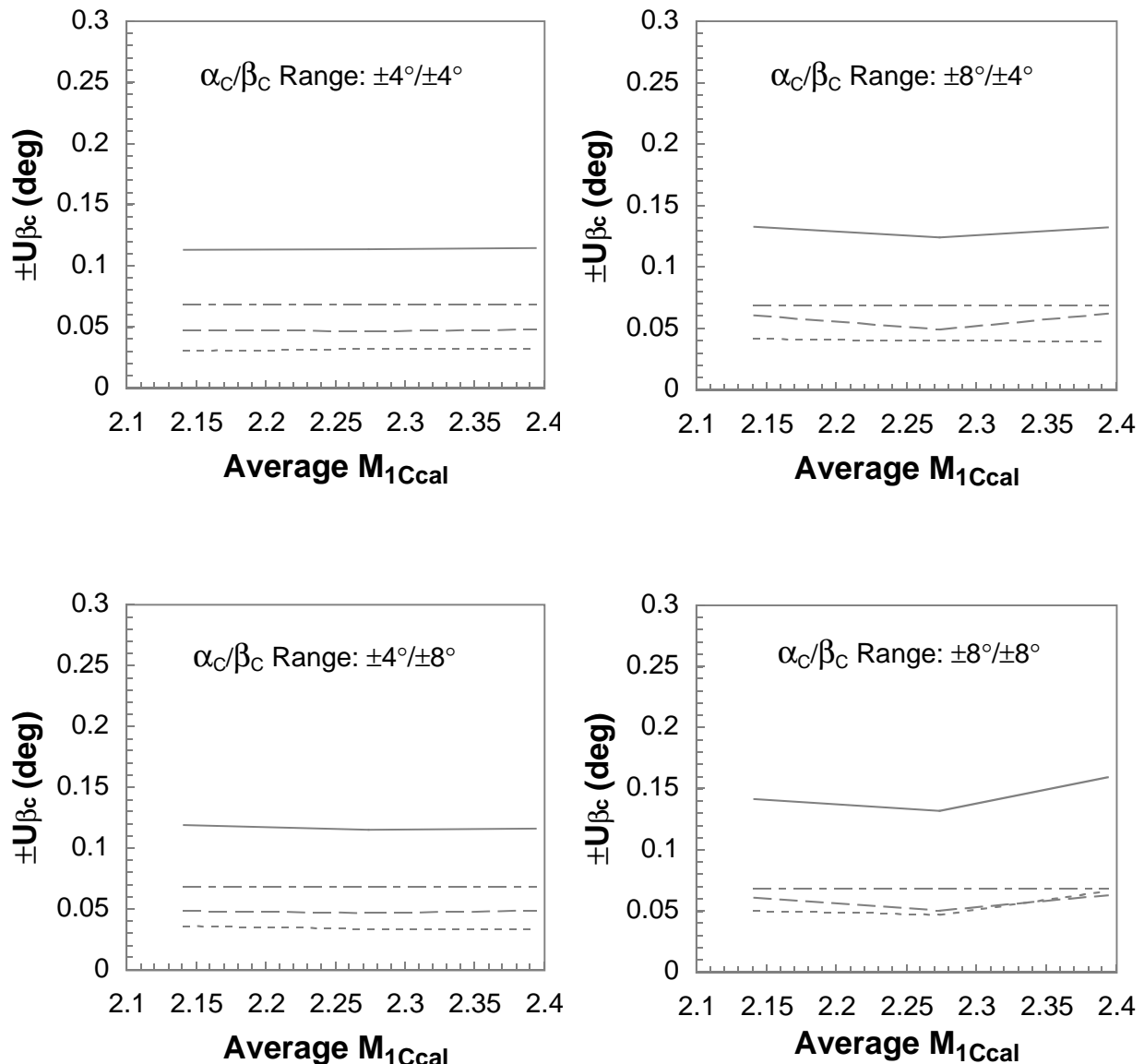
Figure 72. Continued.



Probe 6

- 2σ of correlation residuals
- - - Calculation uncertainty
- · - Reference uncertainty
- Absolute uncertainty

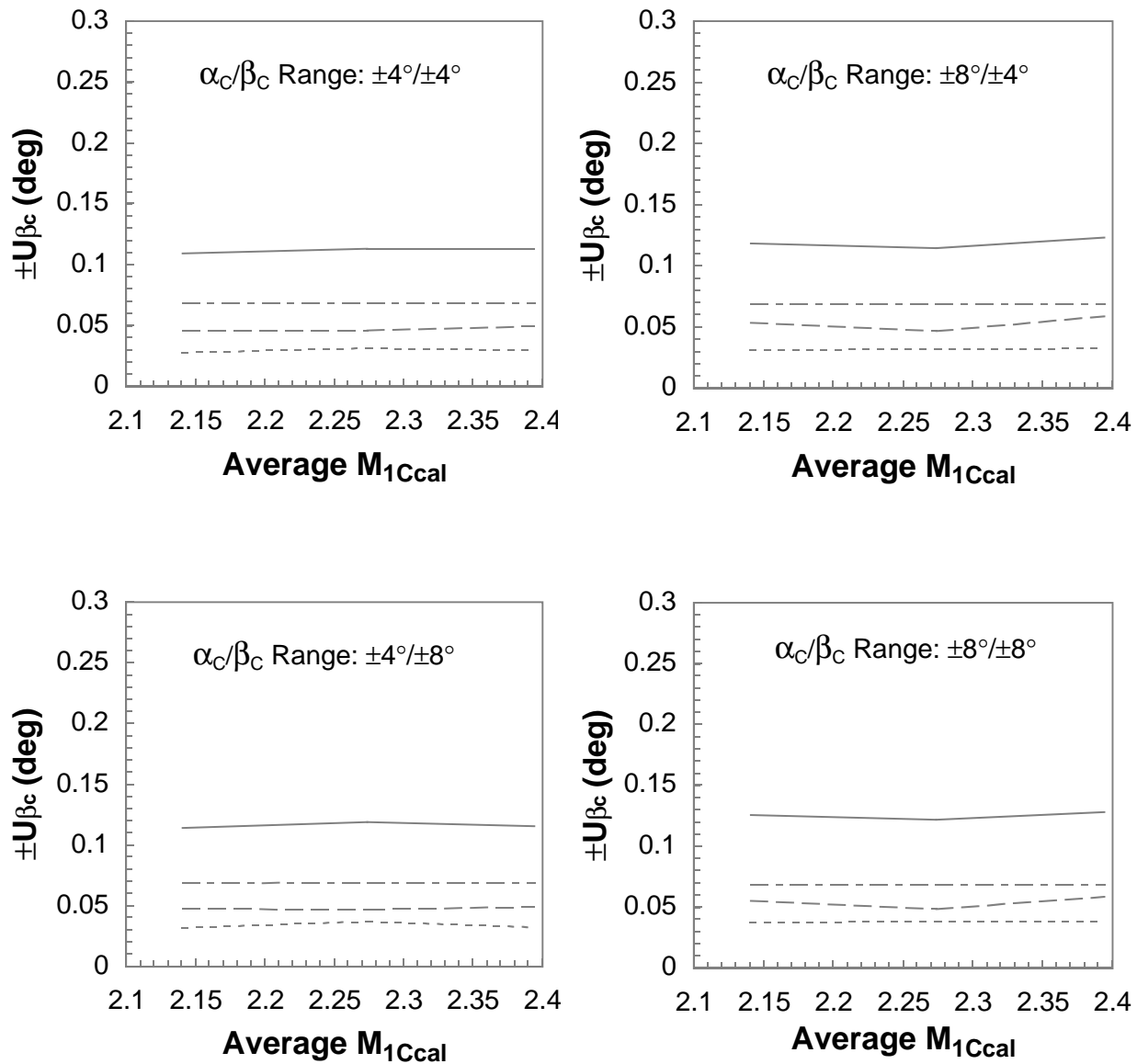
Figure 72. Continued.



Probe 7

- 2σ of correlation residuals
- - - Calculation uncertainty
- · - Reference uncertainty
- Absolute uncertainty

Figure 72. Continued.



Probe 8

- 2σ of correlation residuals
- - - Calculation uncertainty
- · - Reference uncertainty
- Absolute uncertainty

Figure 72. Concluded.

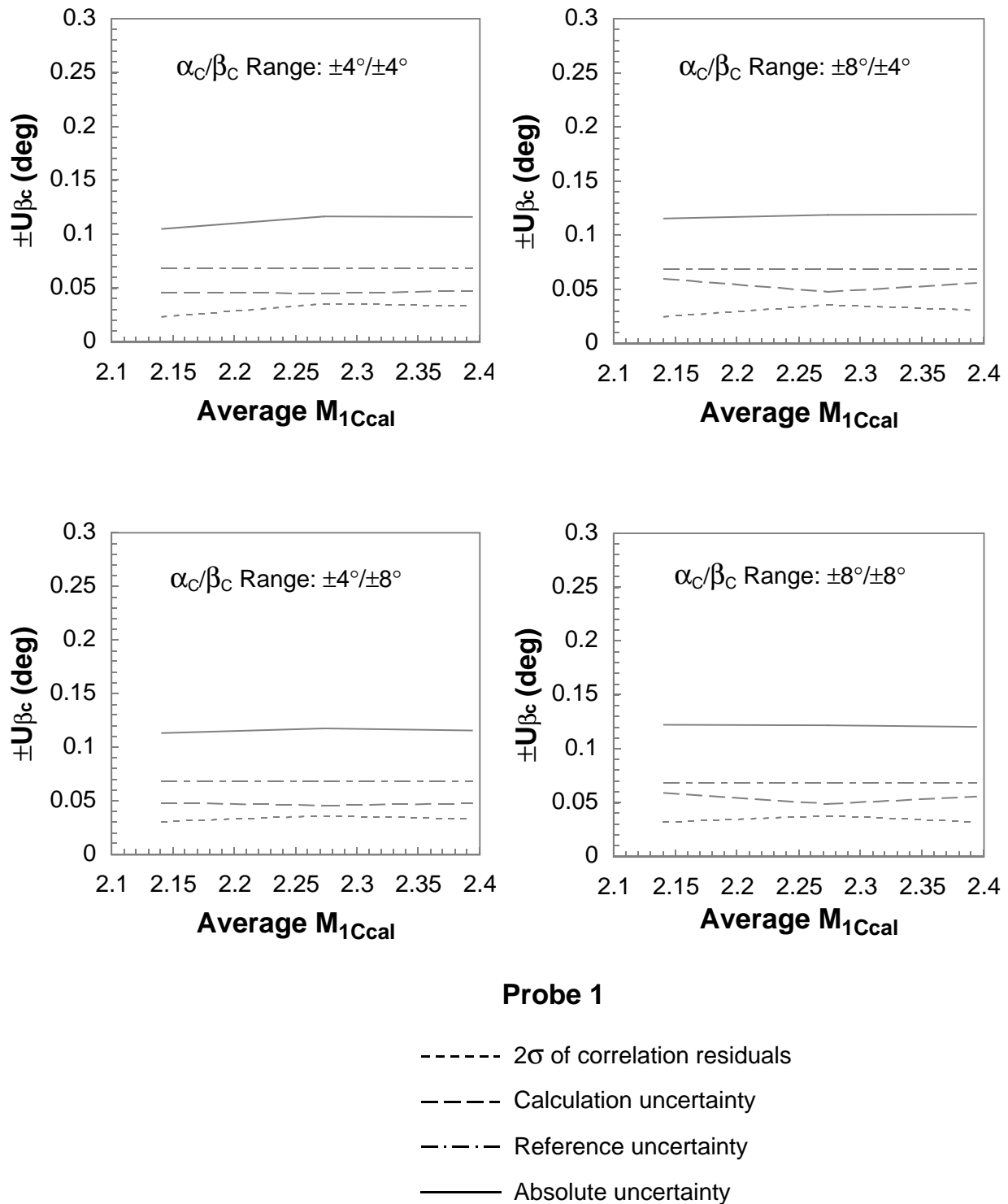
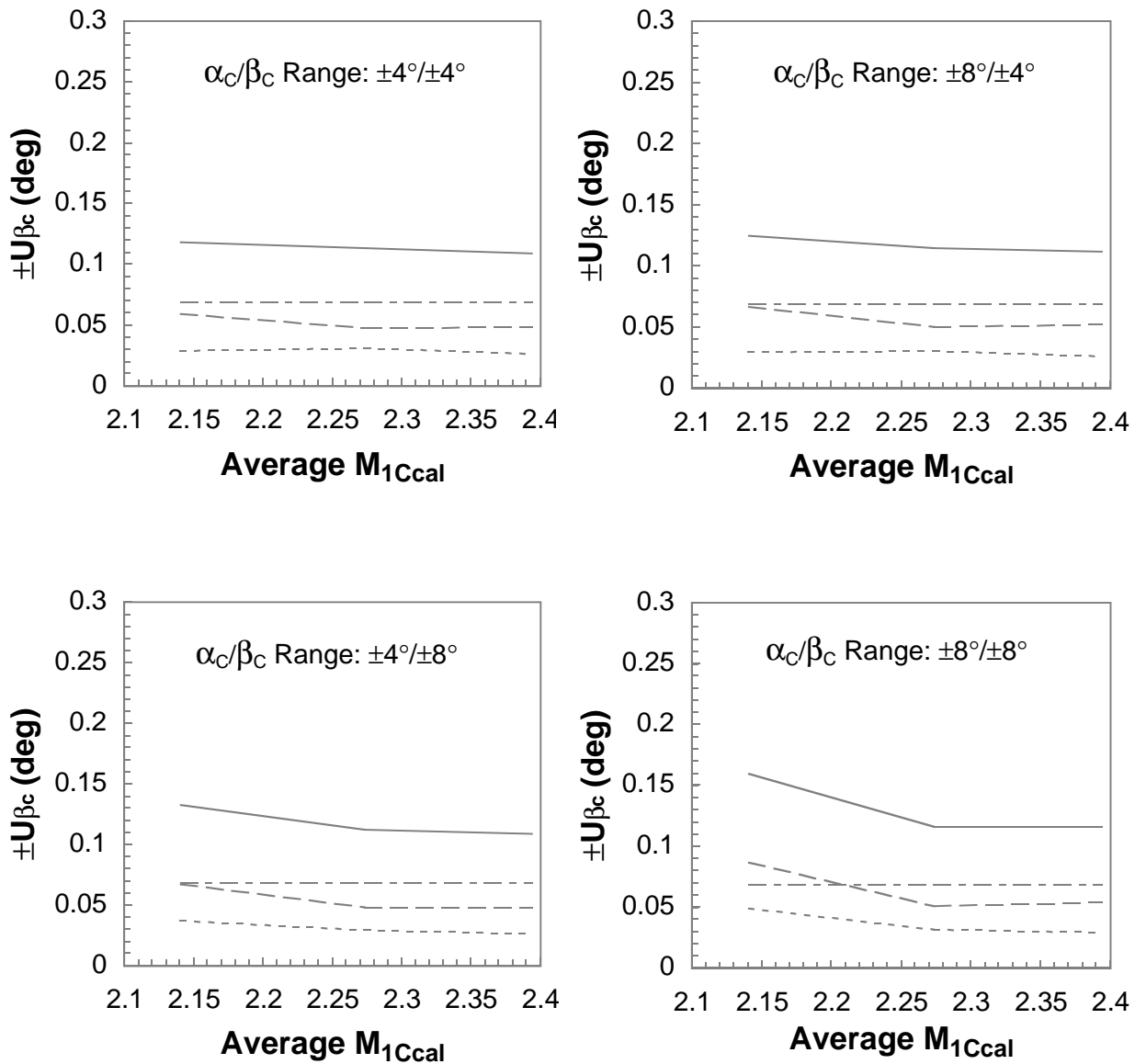


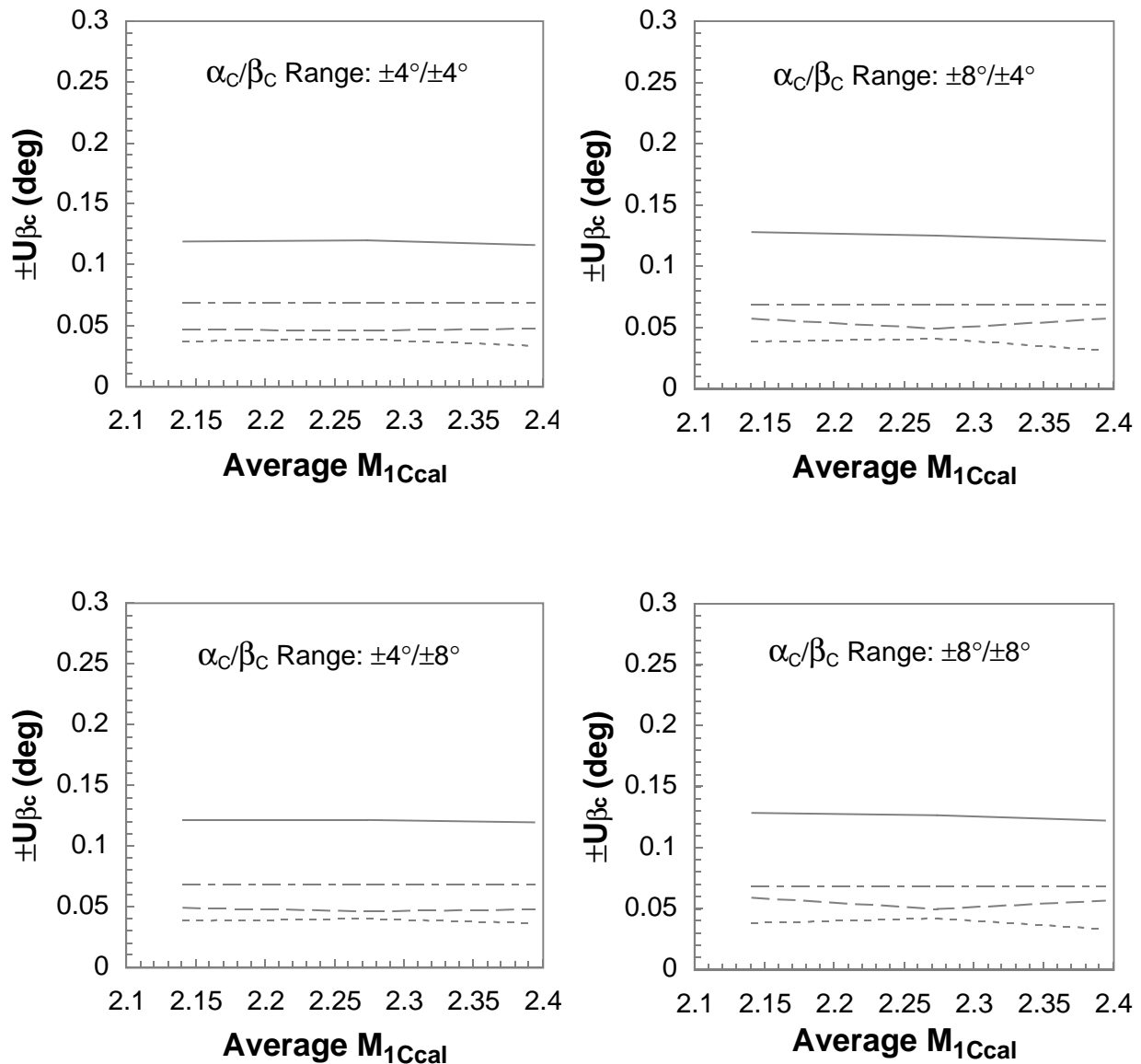
Figure 73. Calibrated angle of sideslip uncertainty for rake 2.



Probe 2

- 2σ of correlation residuals
- - - Calculation uncertainty
- · - Reference uncertainty
- Absolute uncertainty

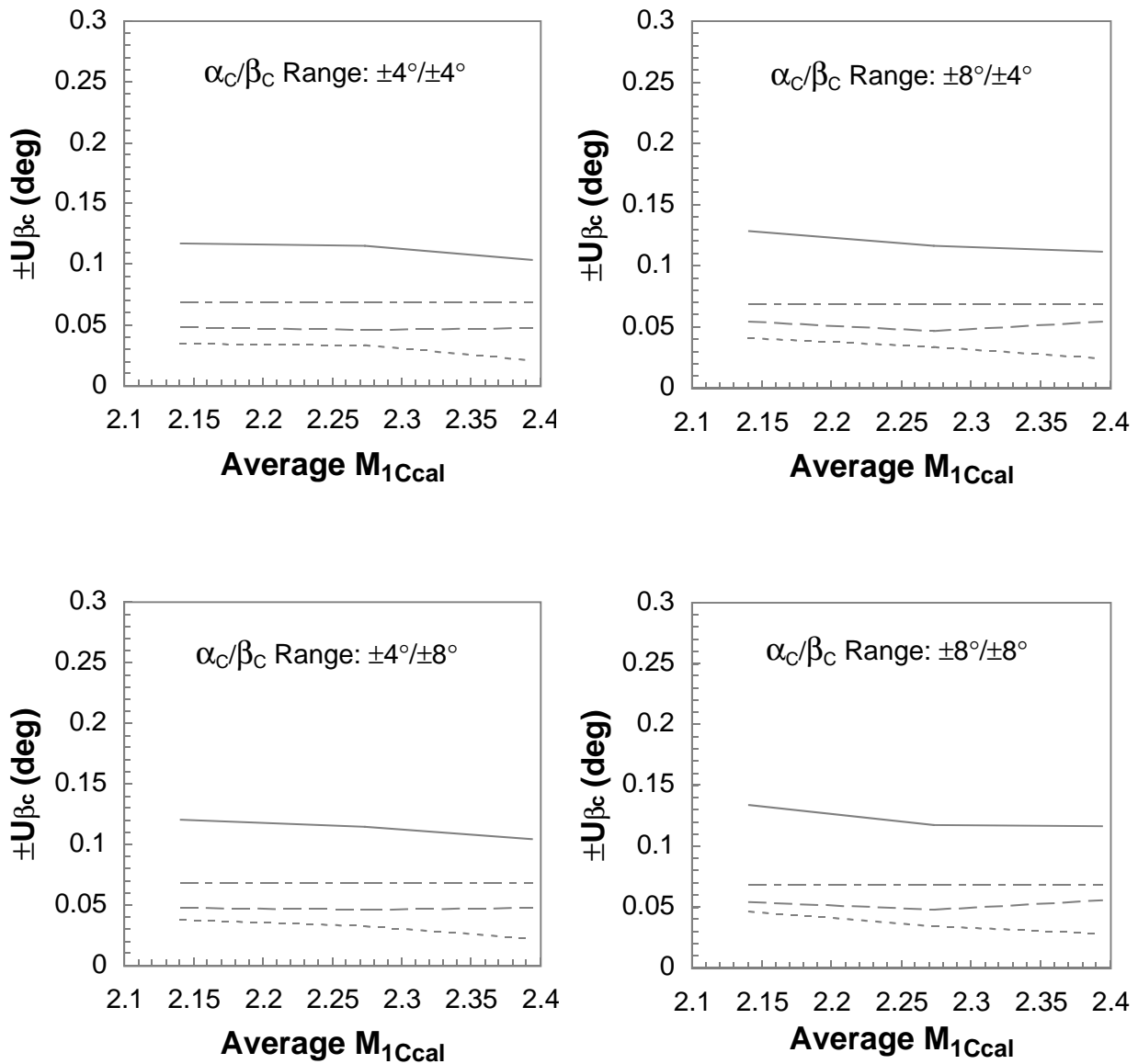
Figure 73. Continued.



Probe 3

- 2σ of correlation residuals
- - - Calculation uncertainty
- · - Reference uncertainty
- Absolute uncertainty

Figure 73. Continued.



Probe 4

- 2σ of correlation residuals
- - - Calculation uncertainty
- · - Reference uncertainty
- Absolute uncertainty

Figure 73. Continued.

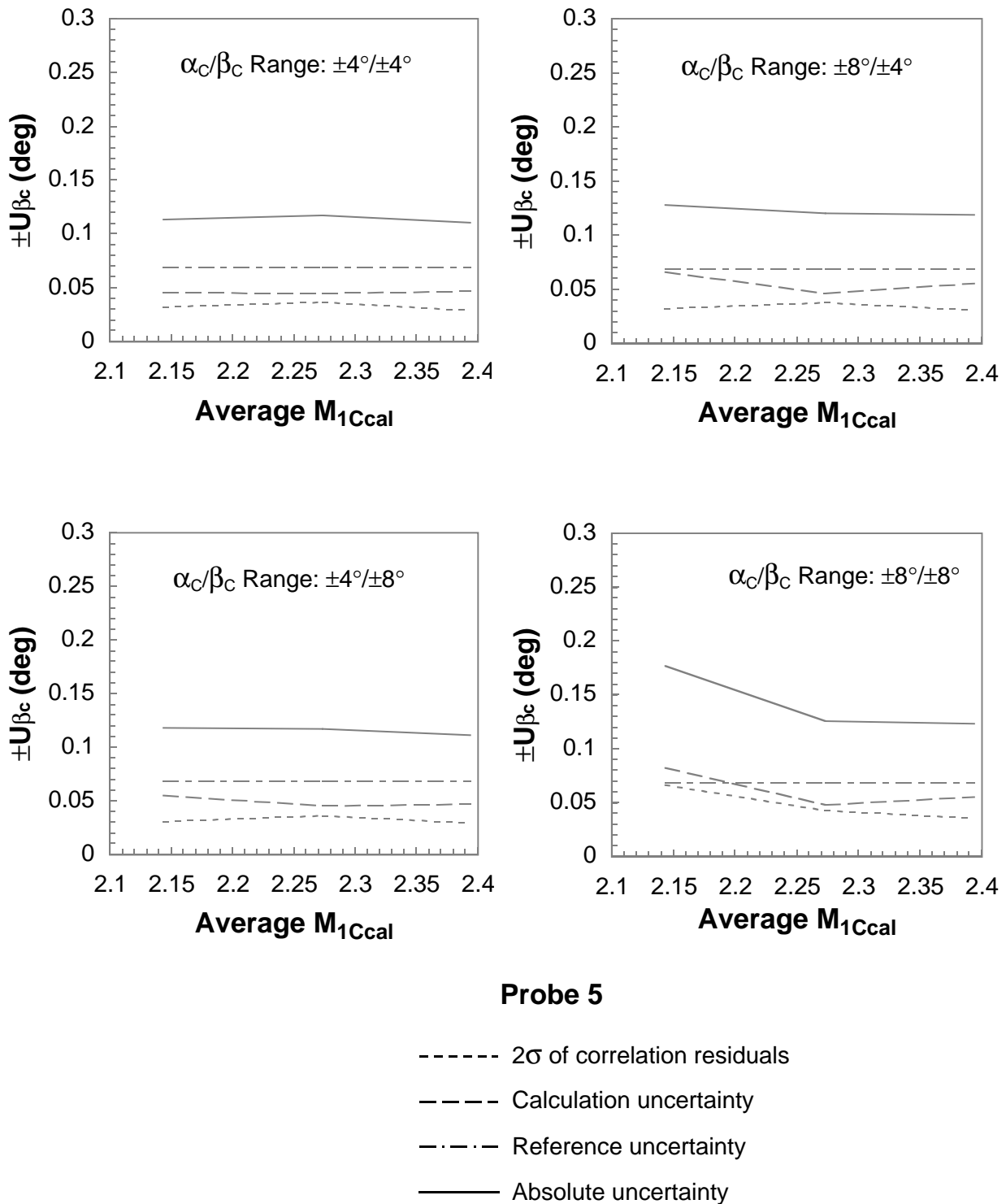
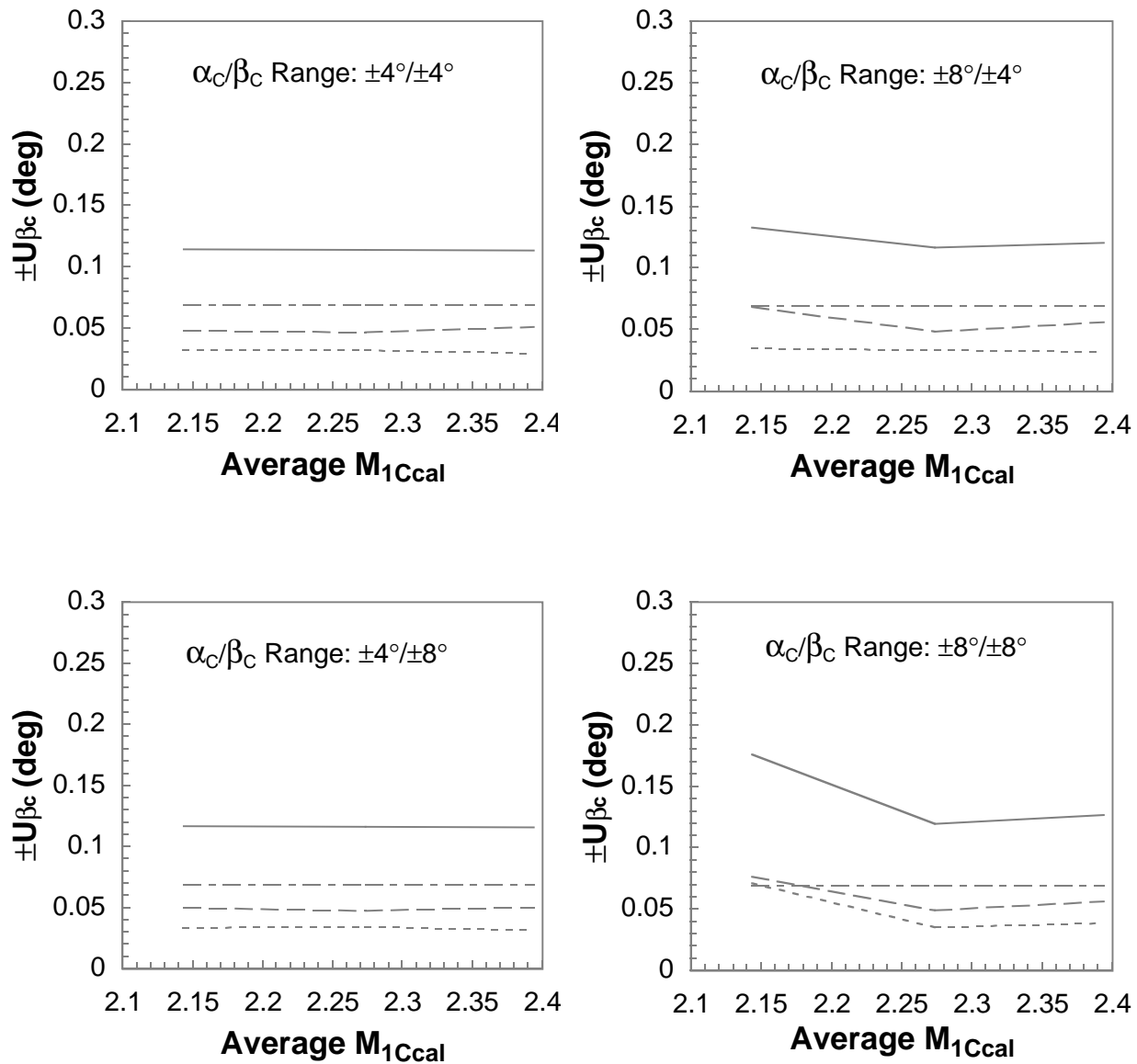


Figure 73. Continued.



Probe 6

- 2σ of correlation residuals
- - - Calculation uncertainty
- · - Reference uncertainty
- Absolute uncertainty

Figure 73. Concluded.

REPORT DOCUMENTATION PAGE

Form Approved
OMB No. 0704-0188

Public reporting burden for this collection of information is estimated to average 1 hour per response, including the time for reviewing instructions, searching existing data sources, gathering and maintaining the data needed, and completing and reviewing the collection of information. Send comments regarding this burden estimate or any other aspect of this collection of information, including suggestions for reducing this burden, to Washington Headquarters Services, Directorate for Information Operations and Reports, 1215 Jefferson Davis Highway, Suite 1204, Arlington, VA 22202-4302, and to the Office of Management and Budget, Paperwork Reduction Project (0704-0188), Washington, DC 20503.

1. AGENCY USE ONLY (Leave blank)			2. REPORT DATE March 1999		3. REPORT TYPE AND DATES COVERED Technical Memorandum		
4. TITLE AND SUBTITLE Cone-Probe Rake Design and Calibration for Supersonic Wind Tunnel Models			5. FUNDING NUMBERS 537-07-20				
6. AUTHOR(S) Mark J. Won							
7. PERFORMING ORGANIZATION NAME(S) AND ADDRESS(ES) Ames Research Center Moffett Field, CA 94035-1000			8. PERFORMING ORGANIZATION REPORT NUMBER A-99V-002				
9. SPONSORING/MONITORING AGENCY NAME(S) AND ADDRESS(ES) National Aeronautics and Space Administration Washington, DC 20546-0001			10. SPONSORING/MONITORING AGENCY REPORT NUMBER NASA/TM-1999-208764				
11. SUPPLEMENTARY NOTES Point of Contact: Mark J. Won, Ames Research Center, MS 227-6, Moffett Field, CA 94035-1000 (650) 604-5865							
12a. DISTRIBUTION/AVAILABILITY STATEMENT Unclassified — Unlimited Subject Category 01 Availability: NASA CASI (301) 621-0390			12b. DISTRIBUTION CODE Distribution: Standard				
13. ABSTRACT (Maximum 200 words) A series of experimental investigations were conducted at the NASA Langley Unitary Plan Wind Tunnel (UPWT) to calibrate cone-probe rakes designed to measure the flow field on 1–2% scale, high-speed wind tunnel models from Mach 2.15 to 2.4. The rakes were developed from a previous design that exhibited unfavorable measurement characteristics caused by a high probe spatial density and flow blockage from the rake body. Calibration parameters included Mach number, total pressure recovery, and flow angularity. Reference conditions were determined from a localized UPWT test section flow survey using a 10° supersonic wedge probe. Test section Mach number and total pressure were determined using a novel iterative technique that accounted for boundary layer effects on the wedge surface. Cone-probe measurements were correlated to the surveyed flow conditions using analytical functions and recursive algorithms that resolved Mach number, pressure recovery, and flow angle to within ±0.01, ±1% and ±0.1°, respectively, for angles of attack and sideslip between ±8°. Uncertainty estimates indicated the overall cone-probe calibration accuracy was strongly influenced by the propagation of measurement error into the calculated results.							
14. SUBJECT TERMS Cone-probe, Wind tunnel instrumentation, Flow quality					15. NUMBER OF PAGES 313		
					16. PRICE CODE A14		
17. SECURITY CLASSIFICATION OF REPORT Unclassified		18. SECURITY CLASSIFICATION OF THIS PAGE Unclassified		19. SECURITY CLASSIFICATION OF ABSTRACT		20. LIMITATION OF ABSTRACT	